Time-Delay Interferometry Simulations for the Laser Interferometer Space Antenna

Referent: Prof. Dr. Karsten Danzmann
Korreferent: Prof. Dr. Klemens Hammerer
Korreferent: Maître de Conférences Dr. Antoine Petiteau
Tag der Promotion: 05.02.2016

Abstract

The planned Laser Interferometer Space Antenna consists of three spacecraft in heliocentric orbits. They form an almost equilateral triangle with million kilometre armlengths. Laser light is exchanged between the spacecraft to detect picometre armlength changes due to gravitational waves interferometrically. The measurements are digitised onboard and telemetered down to Earth. These data include the onboard data streams and sideband measurements. Both comprise gravitational wave signal and noise, mainly laser frequency noise, displacement noise, and clock noise. On Earth, the data is processed with the purpose of noise suppression and data analysis to extract the gravitational waves.

In this thesis, we derive the telemetered data streams that conform to the currently planned split interferometry configuration. They further track the frequency beat-note polarities of the involved lasers. In order to remove the otherwise dominant laser frequency noise from the data, the well-known but revised Time-Delay Interferometry combinations are extended to an algorithm that takes into account the beat-note polarities and uses the ancillary sideband measurements for clock noise correction. Moreover, optical bench displacement noise and back-link fibre noise are suppressed below the common requirements all at once. The developed algorithm is further shown to be unaffected by a recently discussed auxiliary back-link interferometer used for straylight correction from the back-link.

In order to investigate the noise suppression performance, a numerical simulation is developed. It generates measurement phase data onboard the spacecraft which includes a monochromatic gravitational wave signal and noise from lasers, optical bench and test mass displacements as well as from the interferometric readout devices. The data is then processed to remove laser frequency and displacement noise for gravitational wave signal identification. We develop a new technique to compare the data processing outputs to common noise requirements. This scheme regards for the first time the numerically determined overall transfer function between gravitational wave strain and Time-Delay Interferometry output and yields scaling functions with respect to the output of an equal-arm Michelson interferometer, taken as benchmark reference.

We show that the revised Time-Delay Interferometry algorithm suppresses the laser frequency noise and displacement noise of the optical bench below the requirement of $40 \frac{\mathrm{pm}}{\sqrt{\mathrm{Hz}}}$. However, the former secondary readout noise adds up to a level that slightly violates this requirement, which we also establish analytically. Thus, a noise propagation analysis will become necessary as future work, in particular including clock noise.

Keywords: Gravitational waves, Time-Delay Interferometry, LISA simulation

iii

Kurzzusammenfassung

Das geplante Missionskonzept Laser Interferometer Space Antenna besteht aus drei Satelliten, welche sich auf heliozentrischen Orbits bewegen und dabei ein mehrere Millionen Kilometer großes Dreieck aufspannen. Zwischen den Satelliten hin- und hergesendetes Laserlicht detektiert kleinste durch Gravitationswellen verursachte Längenänderungen. Diese haben eine Größenordnung von Pikometern und werden interferometrisch ausgelesen. Die Messsignale und Seitenbandmessungen werden digitalisiert und anschließend zur Erde geschickt. Sie enthalten Gravitationswellensignale, welche vollständig durch Rauschen dominiert werden. Zu den wesentlichen Rauschquellen gehören Laserfrequenzrauschen, Positionsrauschen durch das Wackeln der optischen Bänke und Uhrenrauschen. In der auf der Erde stattfindenden Datenverarbeitung wird mit Hilfe von Algorithmen zunächst das Rauschen unterdrückt und anschließend die Datenanalyse zum Extrahieren der Gravitationswellensignale durchgeführt.

In dieser Dissertation leiten wir zunächst Gleichungen für die zur Erde gesendeten Signale her. Diese werden erstmalig unter Beachtung der aktuell vorgeschlagenen Messkonfiguration, der Split Interferometry Configuration, aufgestellt. Darüber hinaus werden in den aufgestellten Gleichungen die Vorzeichen der Schwebungsfrequenzen der involvierten Laser mitberücksichtigt. Um nun auf der Erde das dominante Laserfrequenzrauschen aus den Daten zu entfernen wird der wohlbekannte, jedoch hier überarbeitete und angepasste Algorithmus der Time-Delay Interferometry benutzt. Die erweiterte Version kompensiert dabei auftretende Vorzeichen in den Schwebungsfrequenzen und benutzt die Seitenbandmessungen zur Uhrenrauschreduktion. Ferner unterdrückt der neue Algorithmus Positionsrauschen (verursacht durch das Wackeln der optischen Bänke) und Rauschen in optischen Fasern. Schließlich zeigen wir, dass sich der Algorithmus auch auf eine Messkonfiguration mit zusätzlichem Interferometer und weiteren Lasern erweitern lässt, mit welcher Streulicht aus den optischen Fasern subtrahiert werden soll.

Weiterhin haben wir eine Simulation entwickelt um die Qualität der Rauschunterdrückung numerisch zu untersuchen. Das Programm generiert im ersten Schritt simulierte Daten der interferometrischen Phasenmessungen auf den Satelliten. Diese Daten enthalten ein monochromatisches Gravitationswellensignal und das Rauschen der Laser, der optischen Bänke und Testmassen sowie Ausleserauschen. In der weiteren Datenverarbeitung werden dann die primären Rauschquellen entfernt und das Gravitationswellensignal extrahiert. Um die Ergebnisse sinnvoll mit gegebenen Rauschanforderungen vergleichen zu können entwickeln wir in dieser Arbeit ein neuartiges Verfahren. Hierdurch kann das Ergebnis der Time-Delay Interferometry mit den Messdaten eines einfachen Michelson-Interferometers mit gleichlangen und senkrechten Armen ins Verhältnis gesetzt und diesbezüglich skaliert werden. Dazu werden Skalierungsfunktionen unter Beachtung der gesamten Transferfunktion zwischen Gravitationswellensignal und dem Ergebnis der Time-Delay Interferometry numerisch berechnet.

Mit Hilfe der Simulation zeigen wir dann, dass der überarbeitete Algorithmus das Laserfrequenz- und Positionsrauschen der optischen Bänke unter die Anforderung von $40 \frac{\text{pm}}{\sqrt{\text{Hz}}}$ reduziert. Allerdings ergibt sich sowohl per Simulation als auch analytisch, dass sich das zuvor sekundäre Ausleserauschen beim Anwenden des Algorithmus aufaddiert und die Rauschanforderung knapp übersteigt. Daher wird zukünftig eine genaue Untersuchung der Rauschfortpflanzung in den Algorithmen nötig sein, vor allem unter Einbeziehen des Uhrenrauschens.

Schlagwörter: Gravitationswellen, Time-Delay Interferometry, LISA-Simulation

Contents

List of Figures and Tables

List of Figures

List of Tables

Index Notation and Einstein Summation Convention

Throughout the thesis, index notation is used. Note, however, that there are two kinds of indices.

The first one denotes components of tensors and is commonly known from the general theory of relativity. We distinguish between Latin indices $i, j, k, \ldots$ counting $1, 2, 3$ and Greek indices $\alpha, \beta, \mu, \nu, \ldots$ counting $0, 1, 2, 3$. These mainly enter in chapter 1. In the case that indices appear twice, subscript and superscript, and nothing different is said, the Einstein summation convention is applied:

$$x^i y_i := \sum_{i=1}^{3} x^i y_i \,, \quad x^\alpha y_\alpha := \sum_{\alpha=0}^{3} x^\alpha y_\alpha \,.$$

The second kind of indices denotes optical benches and laser links in the regarded gravitational wave detector. These indices are introduced in chapter 2 and extensively used in chapters 3 – 6. Latin indices i, j, k run $1, 1', 2, 2', 3, 3'$ accounting for the laser links and directions. It will also be helpful to distinguish primed from unprimed indices. This is written with an underline as $\underline{i} = 1, 2, 3$, and $\underline{i}' = 1', 2', 3'$. For a detailed explanation, we refer to section 2.4.1.

Symbols

Here we list important and frequently used symbols, sorted by the different contexts.

General Relativity

$\mathrm{d}s^2$	line element (4-D) in m^2
$g_{\mu\nu}(x)$	components of the metric tensor $\boldsymbol{g}$, depending on locally defined coordinates $x = (ct, \vec{x})$, dimensionless
$\eta_{\mu\nu}$	components of the Minkowski metric tensor, dimensionless, $(\eta_{\mu\nu}) = \mathrm{diag}(-1, +1, +1, +1)$
$h_{\mu\nu}(x)$	components of the space-time disturbance caused by gravitational waves, depending on x, dimensionless
$h_{+,\times}$	plus-polarised/cross-polarised part of the gravitational wave tensor in TT coordinates, dimensionless
$\boldsymbol{h} = (\bar{h}_{\mu\nu}^{\mathrm{TT}})$	transeverse-traceless (TT) gravitational wave tensor, dimensionless
$\boldsymbol{h}_0$	constant gravitational wave 'amplitude' tensor, dimensionless
$t, t(x)$	time coordinate in s

Gravitational Wave Characteristics

h	gravitational wave strain amplitude, dimensionless
f_{gw}	gravitational wave frequency in Hz
λ_{gw}	wavelength for a gravitational wave in m
ω_{gw}	gravitational wave angular frequency in $\frac{\mathrm{rad}}{\mathrm{s}}$
$\vec{k}_{\mathrm{gw}}$	wave vector denoting propagation direction in $\frac{1}{\mathrm{m}}$

$\hat{k}$	direction vector of wave incidence (normalised), dimensionless
θ, ϕ	spherical angles defining the wave incidence direction in rad
ψ	tilt angle of gravitational wave incidence plane in rad

Armlengths and Light Travel Time

ΔL	change in separation (3-D) in m
L, L_0	absolute (physical) length, often in terms of light travel time, in m
$T(t)$	(overall) light travel time in s
ΔT	light travel time variation due to gravitational waves in s
T_0	light travel time without gravitational wave influence in s
ϵ	perturbation coefficient for light travel time approximation, dimensionless
$T_0^{(0)}, T_0^{(\frac{1}{2})}, T_0^{(1)}$	light travel time contributions for approximations to the order ϵ^0, $\epsilon^{\frac{1}{2}}$ and ϵ^1, respectively, in s
$t_{\text{send}}, t_{\text{recv}}$	time of light emission / reception in s
$\vec{x}_{\text{send}}, \vec{x}_{\text{recv}}$	position vector of sender / receiver in m
$\vec{n}_{\text{send}}, \vec{n}_{\text{recv}}$	unit 3-D directional vector, pointing along the direction of light transmission / reception, dimensionless
v_{rel}	relative velocity between two spacecraft in $\frac{\text{m}}{\text{s}}$

Interferometry

$\Delta\phi$	phase difference between two light fields in rad
ϕ	phase contribution in optical signals in rad
λ	wavelength of light in m
$\vec{E}(\vec{x}, t), \vec{E}_0$	electric field vector / amplitude in $\frac{\text{V}}{\text{m}}$
ρ, τ	reflection / transmission coefficient for electromagnetic waves, dimensionless
ω	angular frequency of light in $\frac{\text{rad}}{s}$
ν	laser frequency in Hz
ω'	Doppler shifted angular frequency of light in $\frac{\text{rad}}{\text{s}}$
P	light power in W
ω_{het}	angular frequency of the heterodyne photodetector signal in $\frac{\text{rad}}{\text{s}}$
f_{ADC}	trigger frequency for the analog-to-digital converter in Hz
f_{samp}	sampling frequency in Hz
f_{PT}	pilot tone frequency in Hz

Transfer Functions, Spectra and Spectral Densities

f	Fourier frequency in Hz
$\mathfrak{T}(f)$	transfer function, various units
$f_{\text{null}}(N)$	frequency of the N-th transfer function zero in Hz
$\widetilde{\text{amp}}(f)$	amplitude or linear spectral density in units of $\frac{[\text{amp}]}{\sqrt{\text{Hz}}}$ dependent on f, for example $\tilde{a}(f)$ denotes the linear spectral density for acceleration noise (in $\frac{\text{m}}{\text{s}^2\sqrt{\text{Hz}}}$)

$\widetilde{\mathrm{amp}}^2(f)$	power spectral density in units of $\frac{[\mathrm{amp}]^2}{\mathrm{Hz}}$
$\widetilde{x}(f)$	linear spectral density of displacement noise in $\frac{\mathrm{m}}{\sqrt{\mathrm{Hz}}}$
$\widetilde{\phi}(f)$	linear spectral density of phase noise in $\frac{\mathrm{rad}}{\sqrt{\mathrm{Hz}}}$
$\widetilde{\nu}(f)$	linear spectral density of frequency noise in $\frac{\mathrm{Hz}}{\sqrt{\mathrm{Hz}}}$
$\widetilde{\phi}_{\mathrm{req}}(f), \widetilde{x}_{\mathrm{req}}(f)$	phase / displacement noise requirement in $\frac{\mathrm{rad}}{\sqrt{\mathrm{Hz}}}$ / $\frac{\mathrm{m}}{\sqrt{\mathrm{Hz}}}$
$\mathrm{C/N_0}$	carrier-to-receiver noise density in Hz
$\mathrm{NSF}(f)$	noise sensitivity function, dimensionless

Onboard Signals

$p(t)$	laser frequency noise in terms of optical phase in rad
$H(t)$	accumulated gravitational wave shift in terms of optical phase in rad
$\vec{\Delta}(t)$	3-D optical bench displacement noise in m
$N^{\mathrm{opt}}(t)$	additional optical path length noise in rad
$N^{\mathrm{S}}(t)$	readout noise and secondary noise in data stream S in rad $\mathrm{S} \in \{s, \varepsilon, \tau, \mathrm{sb}, \rho\}$
$\mu(t)$	back-link fibre noise in terms of phase in rad
$\vec{\delta}(t)$	3-D test mass displacement noise in m

With clocks, but without beat-note polarity:

$q(t)$	clock noise in terms of phase in rad
$\bar{s}(t), \bar{\varepsilon}(t), \bar{\tau}(t)$	science / test mass / reference interferometer signal without clocks in rad
$\bar{s}^q(t), \bar{\varepsilon}^q(t), \bar{\tau}^q(t)$	science / test mass / reference interferometer signal with clocks in rad
$\bar{s}^{\mathrm{sb}}(t)$	sideband interferometer phase signal in rad
$\bar{a}, \bar{b}, \bar{c}$	dimensionless frequency conversion factor from clock to signal for science / test mass and reference / sideband interferometer
m	clock upmultiplication factor for sidebands, dimensionless
$\Delta f_{\bar{\mathrm{S}}}$	beat-note frequency for signal $\bar{\mathrm{S}}$ in Hz with $\bar{\mathrm{S}} \in \{\bar{s}, \bar{\varepsilon}, \bar{\tau}, \mathrm{sb}\}$

With clocks and beat-note polarity:

θ	beat-note polarity factor, dimensionless
$s^{\mathrm{c}}(t), \varepsilon(t), \tau(t)$	science / test mass / reference interferometer carrier signal in rad
$s^{\mathrm{sb}}(t)$	science interferometer sideband signal in rad
$\rho(t)$	auxiliary back-link interferometer signal in rad
a, b, c	dimensionless frequency conversion factor from clock to signal for science / test mass and reference / sideband interferometer
d	dimensionless frequency conversion from clock to signal for $\rho(t)$

Post-Processing Signals

$\widehat{\mathbf{D}}_{i}f(t)$, $f(t)_{;i}$	time-delay operator for constant armlengths L_i applied to a function $f(t)$
$\boldsymbol{\mathcal{D}}_{i}f(t)$, $f(t)_{;i}$	time-dependent time-delay operator with nesting
$f(t)_{,i}$	semi-constant time-delay operator
$\xi(t)$	synthesised optical bench displacement noise free data in rad
$Q(t)$	synthesised data without $\vec{\Delta}(t)$ and with reduced number of free-running laser instances in rad
$Q^{q_1}(t)$	synthesised data referenced to clock 1 without $\vec{\Delta}(t)$ and with reduced number of free-running laser instances in rad
$\bar{\eta}(t)$	synthesised data neglecting clocks and beat-note polarity in rad, used as input for laser frequency noise removal
$\eta(t)$	synthesised data without $\vec{\Delta}(t)$, $q(t)$ and with reduced number of free-running laser instances in rad, used as Time-Delay Interferometry input
X, Y, Z	first generation Michelson Time-Delay Interferometry combinations in rad
X_1, X_2, X_3	second generation Michelson Time-Delay Interferometry combinations in rad
$\alpha, \beta, \gamma, \zeta$	first generation Sagnac Time-Delay Interferometry combinations in rad
$\alpha_1, \alpha_2, \alpha_3,$ $\zeta_1, \zeta_2, \zeta_3$	second generation Sagnac / fully symmetric Sagnac Time-Delay Interferometry combinations in rad

Simulation

f_{cut}	filter cutoff frequency in Hz to prevent high frequency noise in the simulated data
ν_0	central laser frequency in Hz
$s^{\text{sim}}(t), \varepsilon^{\text{sim}}(t)$ $\tau^{\text{sim}}(t)$	simulated interferometric output in terms of phase for science / test mass / reference interferometer in rad
δ, Δ	1-D test mass and optical bench displacement noise, in m
$\boldsymbol{\mathcal{D}}^{\text{sim}}$	numerical time-delay operator
$\xi^{\text{sim}}(t)$	synthesised optical bench displacement noise free data in rad
$\eta^{\text{sim}}(t)$	synthesised data without $\Delta(t)$ and with reduced number of free-running laser instances in rad, used as Time-Delay Interferometry input

Miscellaneous

$\mathcal{O}$	Landau symbol
$\simeq$	approximation, usually in Taylor expansion
$\propto$	proportional, in contrast to $\sim$
$\sim$	neglection of all secondary noise sources
$:$	tensor contraction
$\mathcal{F}$	Fourier transformation
$\mathcal{R}$	regard readout noise terms only

Constants and Units

$\pi = 3.1415926535\ldots$ — pi

$e = 2.718282\ldots$ — Euler's number

i with $i^2 = -1$ — complex number

$c = 299792458\,\frac{\text{m}}{\text{s}}$ — speed of light

$G = 6.67408 \cdot 10^{-11}\,\frac{\text{m}^3}{\text{kg}\,\text{s}^2}$ — Newton's gravitational constant

$h = 6.62607 \cdot 10^{-34}\,\frac{\text{kg}\cdot\text{m}^2}{\text{s}}$ — Planck's constant

$M_\odot \approx 2 \cdot 10^{30}\,\text{kg}$ — solar mass

$1\,\text{pc} = 3.09 \cdot 10^{16}\,\text{m}$ — 1 Parsec

Pictograms

All optical components drawn in the figures were made by the use of the component library.

component **library** version three
by alexander franzen 2k+6

This library was developed in-house by Dr. Alexander Franzen until 2006. It follows a listing of the components frequently used in this thesis.

photodetector

laser

ultra-stable oscillator, clock

mirror

spacecraft telescope

beam splitter

low-pass filter

digital phase readout (phasemeter)

electro-optic modulator

optical fibre with coupler

laser beam

electronic connection

digital connection

Abbreviations

ADC	**a**nalog-to-**d**igital **c**onverter
AEI	**A**lbert **E**instein **I**nstitute
BBO	**B**ig **B**ang **O**bserver
BS	**b**eam **s**plitter
c.c.	**c**omplex **c**onjugated
cf.	see also (Latin: **con**f**er**)
Ch.	**ch**apter
CoM	**c**enter **of** **m**ass
DECIGO	**DECI**hertz **G**ravitational Wave **O**bservatory
DFACS	**d**rag-**f**ree **a**ttitude **c**ontrol **s**ystem
e.g.	for example (Latin: **e**xempli **g**ratia)
eLISA	**e**volved **L**aser **I**nterferometer **S**pace **A**ntenna
EM	**e**lectro**m**agnetic
EOM	**e**lectro-**o**ptic **m**odulator
Eq.	**eq**uation, plural: Eqn.
ESA	**E**uropean **S**pace **A**gency
ESTEC	**E**uropean **S**pace Research and **T**echnology **C**entre
Fig.	**fig**ure
GR	**g**eneral theory of **r**elativity
GW	**g**ravitational **w**aves
i.e.	that is (Latin: **i**d **e**st)
IFO	inter**f**er**o**meter
JPL	**J**et **P**ropulsion **L**aboratory
L3	large ESA satellite mission for **3**rd slot in Cosmic Vision programme
lhs.	left **h**and **s**ide
LIGO	**L**aser **I**nterferometer **G**ravitational Wave **O**bservatory
LISA	**L**aser **I**nterferometer **S**pace **A**ntenna
LO	**l**ocal **o**scillator
LoS	**l**ine **o**f **s**ight
LTPDA	**L**ISA **t**echnology **p**ackage **d**ata **a**nalysis
LSD	**l**inear **s**pectral **d**ensity
NASA	**N**ational **A**eronautics and **S**pace **A**dministration
NGO	**N**ew **G**ravitational wave **O**bservatory
OB	**o**ptical **b**ench
OGO	**O**ctahedral **G**ravitational Wave **O**bservatory
PD	**p**hoto**d**etector
PM	**p**hase**m**eter
PRN	**p**seudo **r**andom **n**oise
PS	**p**ower **s**pectrum
PSD	**p**ower **s**pectral **d**ensity
rhs.	**r**ight **h**and **s**ide
S/C	**s**pace**c**raft
SB	**s**ide**b**and
Sec.	**sec**tion

SNR	**s**ignal-to-**n**oise **r**atio
SR	**s**pecial theory of **r**elativity
SSB	**s**olar **s**ystem **b**arycentric (frame)
Tab.	**tab**le
TDI	**T**ime-**D**elay **I**nterferometry
TDIR	**T**ime-**D**elay **I**nterferometric **r**anging
TDISim	**T**ime-**D**elay **I**nterferometry **Sim**ulation (in developement)
TM	**t**est **m**ass
TT	**t**ransverse-**t**raceless
UFLIS	**U**niversity of **F**lorida **LI**SA **S**imulator
USO	**u**ltra-**s**table **o**scillator

Introduction

The Laser Interferometer Space Antenna (LISA) is a space-based mission concept to detect gravitational waves (GW) [Tea98; ESA11]. These are small variations of space-time that are produced by varying quadrupolar mass moments like, e.g., inspiralling black hole binaries. The mission concept comprises three spacecraft (S/C) in a triangular constellation with million kilometre armlengths that exchange laser light to sense space-time fluctuations caused by gravitational waves. In order to define the measurement path, free-falling test masses (TM) in the spacecraft are used as reference points. Incident gravitational waves will modulate the distance between these reference points and appear as phase modulations of the light which is interferometrically detected onboard.

LISA can in principle be regarded as a Michelson interferometer, but with unequal armlengths due to relative spacecraft motion. By this, laser frequency noise couples into the measurements and makes an immediate gravitational wave detection impossible. Therefore, in post-processing, the onboard measurements are combined to form laser frequency noise free data that is comparable to an equal-armlength Michelson interferometer output signal. This synthesis, called Time-Delay Interferometry (TDI), has been proposed several years ago [TA99], but was based on nowadays outdated optical and metrological setups. Whereas the displacement between two test masses was measured all at once in the former TDI formulation, the current baseline now splits the measurement into three parts [Tho11]. Furthermore, noise from clocks used within the digitisation process of the interferometric data turned out to be significant as well. To remove this clock jitter, auxiliary measurements are performed, the data of which needs to be combined in post-processing properly [HEB+11].

This thesis develops a revised TDI algorithm that resembles the current measurement layout with three measurements per arm. All lasers required for this scheme and their frequency noise are included. Additionally, due to Doppler shifts of the light travelling along the arms and due to applied offset frequency locking schemes [Bar15], the polarity of the measurement beat-note can switch its sign. This beat-note polarity is taken into account by TDI for the first time. The new algorithm further treats clock noise and uses additional sideband measurements to correct for it. Moreover, the new algorithm reduces displacement noise caused by thruster activity and removes the optical path length noise in optical fibres used as intra-spacecraft connections at once. The revised TDI algorithm is finally extended to a recently discussed setup that involves additional interferometers for straylight correction in the fibres, where it was not clear if the laser frequency noise removal is still possible [Ger14].

In order to examine and understand the data processing, in particular TDI, and to verify the revised removal algorithm, a simulation is in developement in the context of this thesis at the Albert Einstein Institute (AEI) in Hannover. It uses orbits that include the Sun, Earth, Moon and Jupiter and then generates phase

measurements of the beat-notes detected in the onboard interferometers. The beat-note phase signals include laser frequency noise, displacement noise, readout noise and sinusoidal gravitational wave signals. The simulated data is then processed by the developed algorithms to first achieve noise suppression, and data combinations are constructed to form the output signal of different interferometric topologies like Michelson and Sagnac.

An open question was how the TDI output can be properly referred to a common noise requirement. We answer this by the inclusion of the overall detector transfer function which is determined numerically within the simulation. It is then put into relation with the gravitational wave response in a reference interferometer, a virtual standard Michelson interferometer with orthogonal arms. With this relation, the TDI output is finally scaled properly and analysed.

This thesis is organised as follows. In Ch. 1, we will explain the fundamentals of gravitational waves and develop the framework for space-based detectors. Ch. 2 introduces the satellite-based mission concept Laser Interferometer Space Antenna and states the common noise requirements. Subsequently, the onboard interferometric signals including gravitational wave signal and various noise contributions are derived. Time-Delay Interferometry is explained in detail in Ch. 3. Besides the final formulation of the telemetered data, the revised TDI algorithm is derived in Ch. 4 and further modified with respect to an alternative optical layout currently under discussion.

The first four chapters can be understood as ingredients to a planned overall simulation of the complete Laser Interferometer Space Antenna. The prototype simulation and its physical models are explained in detail in Ch. 5, followed by the results in Ch. 6. We question the common post-TDI noise level requirement and propose a scheme that establishes an appropriate TDI output scaling. According to this, the rescaled simulation results are investigated for static and flexing S/C constellations and the performance limitations are discussed. The chapter closes with prospects for the future simulation development and is followed by an overall summary and outlook in Ch. 7.

1 Fundamentals of Gravitational Wave Detection

The first chapter discusses the fundamentals of gravitational wave detection with focus on space-based detection. First, we give a short overview on the history of gravitational wave detection research, followed by a section dealing with the theory of gravitational waves. Here, we will introduce the gravitational wave tensor describing the influence on space and time, and which is needed to provide gravitational wave signal data. Next, the main astrophysical sources are introduced and we explain how to detect gravitational waves on Earth and in space in principle. In order to provide the equations for the simulation explained in Ch. 5, we will finally derive the influence of gravitational waves on light that is interchanged between two moving spacecraft in terms of differential light travel time, adding up together with the static gravitational field and orbital effects to the overall light travel time.

1.1 Historical Overview

Since 1687 until the beginning of the 20th century, scientists described gravity by Newton's theory of gravitational forces between two masses [New87]. It worked well in many cases, but failed when considered with respect to the causality principle. In particular, the assumption of instantaneous gravitational attraction regardless of distances let already Newton question his own principle.

This shortcoming in theory was fixed by Einstein in 1916 when he published his famous general theory of relativity (GR) [Ein16]. GR basically includes the gravity into special theory of relativity (SR) and describes it as a geometrical effect in the four dimensional combination of space and time, called space-time. The space-time itself is curved by matter and in turn leads the motion of matter (Fig. 1.1). This picture is the analogon to Newton's theory of gravity, but now without any forces. Instead, mainly geometric aspects enter GR.
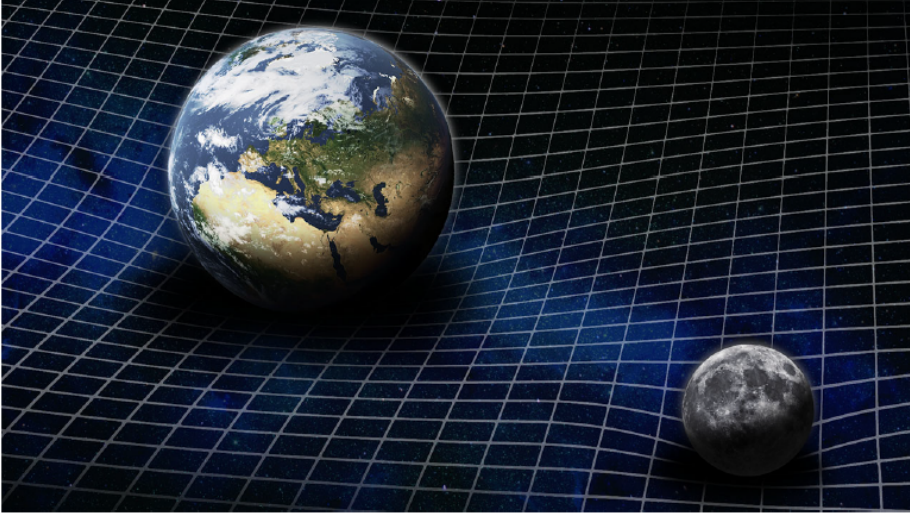
Figure 1.1: Curved space-time in Einstein's picture of gravity. Matter (e.g., the Earth) curves space-time, space-time leads matter (e.g, the Moon surrounding the Earth). This picture of gravity is completely free of forces that act instantaneously [Credits: Simon Barke, AEI Hannover].

An important consequence of GR is the prediction of gravitational waves (GW) [Ein18]. GW are ripples in the four dimensional space-time and travel with the speed of light. They are produced by a mass quadrupole changing with time, for example, by binary stars that circulate around their common center of mass. The waves are stretching the space-time in one direction while shrinking the space-time in the orthogonal direction (Fig. 1.2) with frequencies depending on several parameters of the source like mass ratios, orbital frequencies, etc. Furthermore, GW have in general a very small amplitude and complex polarisation states which makes them extremely hard to measure. Contrariwise, due to their extremely small coupling to mass, the absorption of GW is very small and can negotiate large distances without losses. Hence, GW astronomy can decode undisturbed information in a broad frequency range of nHz – kHz from exotic stellar objects (e.g., black holes), from far away galaxies and perhaps even from the big bang [SS09].

One of the pioneers of gravitational wave detection was Joseph Weber in the early 1960's. He started to build resonant bar detectors, consisting of a roughly 2 m long aluminium bar with resonances in the kHz regime. An incident GW around the bar's resonance frequency would then force oscillations of the bar which can be read out and amplified by transducer systems. In the sixties, Weber claimed the detection of gravitational waves with a bar detector, but it was not possible to verify his results [Web67]. Even today, the *direct* detection of GW is still outstanding.[1]

---

1   Six days after my defense, the direct detection of gravitational waves has been announced on February 11th, 2016 [SCVC16].
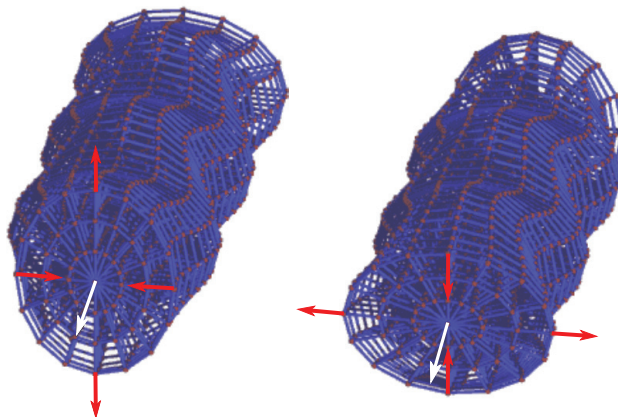
Figure 1.2: Gravitational waves stretching and shrinking space-time. The red dots mark test masses on circular rings. Left: An incident wave (travelling along the direction of the white arrow) would stretch the frontline circle in one direction and simultaneously shrink the circle in a perpendicular direction (red arrows). Right: half a period later, the squeezing and stretching directions on the frontline circle have switched [Ein].

However, in 1993, Robert Hulse and Joseph Taylor were awarded the Nobel prize for an *indirect* detection. They observed for more than 20 years the binary system PSR1913+16 consisting of a radio pulsar, which behaves like a very accurate clock, and an orbiting neutron star. A decrease of the orbital period by few seconds per decade in terms of accumulated phase shifts and hence an increase of the orbiting frequency was observed. This implies a loss of kinetic energy of the system without any outer influence. Hulse and Taylor compared the loss of energy with the theoretical prediction that PSR1913+16 might emit gravitational waves and found an extremely accurate match with the data [TFM79]. This observation counts until today as the first (indirect) detection of GW. In the following years, Hulse and Taylor's observations have been confirmed by the examination of various other binary systems.

Today, technology has advanced to much more sensitive resonant bar detectors consisting of cryogenic cooled bars with temperatures lower than $50\,\mathrm{mK}$, e.g., 'Mario Schenberg' and MiniGrail [AAB$^+$08; ABF$^+$03]. Moreover, since the early 1990's, extreme sensitive laser interferometers came up as an even more promising alternative to the bars. Roughly speaking, in this context an interferometer (IFO) is a device that measures fluctuations of the space-time by sending two laser beams along non-parallel paths (called arms). Due to the interaction with a passing GW, one arm is stretched while the other arm is squeezed and vice versa within a GW period. This fluctuation in space-time is read out by comparing the phases of the output light at a photodetector (PD), a device which converts optical power into electrical current. On Earth, several interferometric gravitational wave detectors are operating: the

(advanced) Laser Interferometer Gravitational Wave Observatory (LIGO/aLIGO), VIRGO and GEO600 [ftLSC10a; AAA$^+$11; ftLSC10b]. They form – together with other detectors – a world-wide network searching for gravitational waves in the GW frequency band from 10 Hz to 10 kHz. Technical developments (e.g., vacuum tubes, signal and power recycling, squeezing) upgrades the detection sensitivity steadily. Currently, third generation detectors (KAGRA/LCGT [Kur10], Einstein Telescope [Tea11a]) located underground are planned or already under construction.

Other promising techniques to detect GW are currently pulsar timing [CBSV$^+$14] and Doppler tracking [Arm06]. The former uses the frequency-stable radio signals of a distant pulsar which travel to Earth and are there compared with a local clock. A long-period change in arrival times might then be an indication for a GW changing the space-time between pulsar and Earth. Doppler tracking is performed by sending radio waves from Earth to spacecraft and back. The Doppler data are compared with a stable frequency reference, e.g., an atomic clock on ground. An incident GW would induce a Doppler frequency shift in the radio signal and could be thus detected.

In 1998, a space-based interferometric gravitational wave detector was proposed: the Laser Interferometer Space Antenna (LISA). LISA consists of three satellites separated by five million kilometre forming a giant triangle. This constellation trails behind the Earth around the Sun. The spacecraft interchange laser light that senses the space-time fluctuations due to gravitational waves. After funding cutoffs in 2011 and a redesign, the evolved Laser Interferometer Space Antenna (eLISA), a LISA version with one million kilometre separation, emerged as a candidate for an European Space Agency (ESA) mission in the early 2030's. It will detect gravitational waves in a frequency regime of $10^{-4} - 10^{-1}$ Hz, which is complementary to that of ground-based detectors and gives insight into interesting stellar objects like black hole binaries and inspiralling neutron stars. Recently, ESA has selected the science theme 'The Gravitational Universe' for the large space mission in the 2030's, the science goals of which would be covered by eLISA [ftec13].

Concluding, there is no direct GW detection yet and it is an extremely challenging enterprise. Nonetheless, scientists are very optimistic to detect GW in the next 10 to 15 years, because the ground-based instruments have reached a sensitity that makes the detection probable. Furthermore, space-based detectors are on the way to launch within the next 10 to 20 years. Both promise exciting discoveries in astrophysics and about our universe soon.

1.2 Gravitational Waves

In this section, we will first sketch how to derive gravitational waves from the Einstein field equations, and then explore the major properties. The goal is here to set the mathematical framework for the description of GW used throughout the thesis and especially in the simulation. Finally, the sources of GW and their detectability are highlighted.

1.2.1 Sketching the Derivation of Gravitational Waves

One of the central statements of GR are the Einstein field equations [Ein16], describing the generation of gravitational fields by matter and energy:

$$G_{\mu\nu} \equiv \mathcal{R}_{\mu\nu} - \frac{1}{2}g_{\mu\nu}\mathcal{R} = \frac{8\pi G}{c^4}T_{\mu\nu} \,. \tag{1.1}$$

On the left hand side (lhs.), $G_{\mu\nu}$ denotes components of the Einstein field tensor, defined as $G_{\mu\nu} \equiv \mathcal{R}_{\mu\nu} - \frac{1}{2}g_{\mu\nu}\mathcal{R}$. Here, $(\mathcal{R}_{\mu\nu})$ is the Ricci tensor and $\mathcal{R}$ the Ricci scalar of the space-time dependent on the metric $\boldsymbol{g} = (g_{\mu\nu})$. The Ricci scalar can be interpreted as the space-time curvature. Both $\mathcal{R}_{\mu\nu}$ and $\mathcal{R}$ are contractions of the Riemann curvature tensor $(\mathcal{R}^{\alpha}_{\beta\mu\nu})$. On the right hand side (rhs.), $T_{\mu\nu}$ describes components of the energy-stress-tensor that comprises the energy density T_{00} and fluxes $T_{0i} = T_{i0}$ as well as pressures and shear stresses $(T_{ij} = T_{ji})$ of the matter which generates a gravitational field.

Putting all together, Eq. (1.1) is the mathematical formulation of the general statement from Einstein's picture of gravity that was presented in Fig. 1.1: matter curves space-time, space-time tells matter how to move. Note eventually that in many astrophysical publications an additional term, containing the cosmological constant, occurs on the lhs. of Eq. (1.1) and thereby includes the possibility for a static universe in the Einstein field equations [Ein17].

Solving the Einstein field equations for the metric components $g_{\mu\nu}$ makes it possible to further compute the motion of bodies within the determined metric. However, a full analytical solution is only possible for approximations and special cases of scenarios. In general, $\mathcal{R}_{\mu\nu}$ and $\mathcal{R}$ both contain various complex combinations of the metric and its derivatives,

$$\mathcal{R}_{\mu\nu} = f(\boldsymbol{g}, \boldsymbol{g}', \boldsymbol{g}'') \,, \quad \mathcal{R} = \mathcal{R}^{\mu}_{\mu} = g^{\mu\alpha}\mathcal{R}_{\alpha\mu} \,,$$

where $'$ denotes the derivative with respect to the space-time coordinates

$$x = (x^{\mu}) = (ct, \vec{x}) \,. \tag{1.2}$$

Hence, solving the coupled second order differential equations (1.1) analytically for $g_{\mu\nu}$ without any approximations turns out to be very complex.

There are several symmetries and identities in the Einstein field equations (concretely, $G_{\mu\nu} = G_{\nu\mu}$ and $g_{\mu\nu} = g_{\nu\mu}$, $T_{\mu\nu} = T_{\nu\mu}$, Bianci identities $\nabla_{\beta}G^{\alpha\beta} = 0$ with ∇_{β} denoting the covariant derivative [MTW73]), which simplify the solution of the Einstein field equations a lot and reduce the sixteen equations for $g_{\mu\nu}$ to six. Nonetheless, currently there are only few analytical solutions known. In the most cases, one has to solve the Einstein field equations numerically.

Weak-Field Approximation

The major approach to derive gravitational waves analytically is the special case of weak gravitational fields. The derivation can be found, e.g., in [Sch09] and [MTW73]. We will provide here only a rough idea of the procedure.

In order to make the problem as easy as possible, we assume that the metric far away from matter (practically in vacuum) is approximately flat, i.e., Minkowskian to first order in locally defined Lorentzian coordinates $x = (ct, \vec{x})$ with local time and space coordinates t and $\vec{x}$:

$$g_{\mu\nu}(x) = \eta_{\mu\nu} + h_{\mu\nu}(x) + \mathcal{O}(\boldsymbol{h}^2) \tag{1.3}$$

with $(\eta_{\mu\nu}) = \mathrm{diag}(-1, 1, 1, 1)$ and $h_{\mu\nu}$ a tiny space-time perturbation, $|h_{\mu\nu}| \ll 1$. Eq. (1.3) is known as the weak-field approximation.

The metric $\boldsymbol{g}$ is related to the space-time interval $\mathrm{d}s^2$ via

$$\mathrm{d}s^2 = g_{\alpha\beta}\,\mathrm{d}x^\alpha\,\mathrm{d}x^\beta\,, \tag{1.4}$$

which can be interpreted as a 4-D distance. Inserting Eq. (1.3) yields

$$\begin{aligned}
\mathrm{d}s^2 &= (\eta_{\alpha\beta} + h_{\alpha\beta}(x))\,\mathrm{d}x^\alpha\,\mathrm{d}x^\beta + \mathcal{O}(\boldsymbol{h}^2) \\
&= \eta_{\alpha\beta}\,\mathrm{d}x^\alpha\,\mathrm{d}x^\beta + h_{\alpha\beta}(x)\,\mathrm{d}x^\alpha\,\mathrm{d}x^\beta + \mathcal{O}(\boldsymbol{h}^2)\,.
\end{aligned} \tag{1.5}$$

The first term denotes the flat space-time without any disturbances while the second term introduces the space-time variation $h_{\alpha\beta}$ due to weak gravitational fields which also change the 4-D distance $\mathrm{d}s^2$.

The weak-field approximation (1.3) can now be inserted into the Einstein field equations (1.1). Therefore, all tensors and derivatives in the Riemann tensor $\mathcal{R}^\alpha_{\beta\mu\nu}$ and its contractions are carried out to first order in $h_{\mu\nu}$. On the way, gauge transformations using gauge freedoms analogously to electrodynamics are performed to simplify the calculation further. For details, we refer to [MTW73] and [Sch09].

It is convenient in the computation of the Einstein tensor $G_{\mu\nu}$ to introduce the trace reverse of the field $\boldsymbol{h}$:

$$\bar{h}^{\alpha\beta} \equiv h^{\alpha\beta} - \frac{1}{2}\eta^{\alpha\beta}h\,, \tag{1.6}$$

with the trace $h := h^\alpha_\alpha$. With the help of this definition, one can compute the Einstein tensor $G_{\mu\nu}$ up to the order $\mathcal{O}(\boldsymbol{h})$.

Weak-Field Einstein Equations

As in electrodynamics, one can make use of a 'clever' gauge choice (Lorenz gauge) to simplify the Einstein field equations enormously:

$$\frac{\partial \bar{h}^{\alpha\beta}}{\partial x^\beta} = 0\,. \tag{1.7}$$

Applying this condition, one finally ends up with the weak-field Einstein equations:

$$\Box \bar{h}^{\mu\nu} = \partial^\alpha \partial_\alpha \bar{h}^{\mu\nu} = -\frac{16\pi G}{c^4} T^{\mu\nu}\,, \tag{1.8}$$

where $\partial_\alpha := \frac{\partial}{\partial x^\alpha}$ denotes the partial derivative with respect to the local space-time coordinates $(x^\alpha) = (ct, \vec{x})$, and $\Box := \partial^\alpha \partial_\alpha$. As known from electrodynamics [Ott11], Eq. (1.8) is a (inhomogeneous) wave equation, even if $h_{\alpha\beta}$ are the components of a tensor and not of a vector field. Hence, we know how the solution of Eq. (1.8) should look like: retarded Greens functions, or – speaking simplified – waves. These are known as gravitational waves. In the next section, we will examine these solutions and discover the properties of GW.

1.2.2 Properties of Gravitational Waves

As sketched before, the Einstein equations reduce in a weak-field approximation to expressions that look like a wave equation. These Eqn. (1.8) account for the time-dependence of gravitational fields $\boldsymbol{h}$, or $\bar{\boldsymbol{h}}$, respectively. In a region far away from any matter, the components of the stress-energy tensor $T^{\mu\nu}$ on the rhs. of Eq. (1.8) completely vanishes:

$$\Box \bar{h}^{\mu\nu} = \partial^\gamma \partial_\gamma \bar{h}^{\mu\nu} = 0\,. \tag{1.9}$$

This again reminds one strongly of electrodynamics and it is not hard to show below that the ansatz of a 'plane' wave solves Eq. (1.9):

$$\bar{h}^{\mu\nu} = A^{\mu\nu} e^{ik_\alpha x^\alpha} \tag{1.10}$$

with complex tensorial 'amplitude' components $A^{\mu\nu}$ and real components k^α with

$$(k^\alpha) = \left(\frac{\omega_{\mathrm{gw}}}{c}, \vec{k}_{\mathrm{gw}}\right)\,, \tag{1.11}$$

both independent of coordinates x^α. Here, $\omega_{\mathrm{gw}} = 2\pi f_{\mathrm{gw}}$ denotes the angular frequency of the gravitational wave with wave vector $\vec{k}_{\mathrm{gw}}$. Note that in the chosen signature,

$$k_\alpha x^\alpha = -\omega_{\mathrm{gw}} t + \vec{k}_{\mathrm{gw}} \cdot \vec{x}\,. \tag{1.12}$$

Speed of Gravitational Waves

The given ansatz (1.10) must satisfy the wave equation. Inserting (1.10) into (1.9) yields the condition

$$\partial^\gamma \partial_\gamma \bar{h}^{\mu\nu} = A^{\mu\nu} \partial^\gamma \partial_\gamma \mathrm{e}^{\mathrm{i}k_\alpha x^\alpha} = A^{\mu\nu} \partial^\gamma \mathrm{i}k_\alpha \delta^\alpha_\gamma \mathrm{e}^{\mathrm{i}k_\beta x^\beta} = A^{\mu\nu} \mathrm{i}k_\alpha \partial^\alpha \mathrm{e}^{\mathrm{i}k_\beta x^\beta}$$

$$= A^{\mu\nu} \mathrm{i}k_\alpha \eta^{\alpha\rho} \partial_\rho \mathrm{e}^{\mathrm{i}k_\beta x^\beta} = A^{\mu\nu} \mathrm{i}k_\alpha \eta^{\alpha\rho} \mathrm{i}k_\rho \mathrm{e}^{\mathrm{i}k_\beta x^\beta}$$

$$= -A^{\mu\nu} k_\alpha k^\alpha \mathrm{e}^{\mathrm{i}k_\beta x^\beta} = 0 \,,$$

where we used the property of locally flatness ($\eta^{\alpha\rho} \partial_\rho = \partial^\alpha$ and $\eta^{\alpha\rho} k_\rho = k^\alpha$ in locally defined coordinates). The wave equations can thus only be satisfied non-trivially (i.e., $A^{\mu\nu} \neq 0$), if

$$k_\alpha k^\alpha = -\frac{\omega^2_{\mathrm{gw}}}{c^2} + \vec{k}^2_{\mathrm{gw}} = 0 \,, \tag{1.13}$$

i. e., k^α are components of a null vector $(k^\alpha) = (\frac{\omega_{\mathrm{gw}}}{c}, \vec{k}_{\mathrm{gw}})$ and subsequently tangent to the world line of a photon. This in turn signifies that the wave is travelling at the speed of light and satisfies the dispersion relation

$$\omega_{\mathrm{gw}}(\vec{k}_{\mathrm{gw}}) = c|\vec{k}_{\mathrm{gw}}| \,. \tag{1.14}$$

Transverse-Traceless Gauge

In the derivation of the weak-field Einstein equations above, we used the Lorenz gauge $\frac{\partial \bar{h}^{\alpha\beta}}{\partial x^\beta} = 0$. Clearly, this condition needs also to be fulfilled by our ansatz (1.10):

$$\frac{\partial \bar{h}^{\alpha\beta}}{\partial x^\beta} = A^{\alpha\beta} \partial_\beta \mathrm{e}^{\mathrm{i}k_\gamma x^\gamma} = A^{\alpha\beta} \mathrm{i}k_\beta \mathrm{e}^{\mathrm{i}k_\gamma x^\gamma} = 0$$

that can be condensed to

$$A^{\alpha\beta} k_\beta = 0 \,. \tag{1.15}$$

We can interpret this statement such that the wave 'amplitude' ($A^{\alpha\beta}$) is orthogonal to the wave vector (k_γ).

A vector field can be added to the coordinates x^α such that the solution of Eq. (1.9) remains unchanged within the weak-field approximation. As can be shown [MTW73], this gauge leads to two further restrictions on $A^{\mu\nu}$:

$$A^\mu_\mu = 0 \,, \quad A_{\mu\nu} U^\nu = 0 \,, \tag{1.16}$$

where U^α denotes the components of a chosen four-velocity vector of the wave. One

can then define $(A_{\mu\nu})$ in the transverse-traceless (TT) gauge as

$$(A_{\mu\nu}^{\mathrm{TT}}) \ :\Longleftrightarrow \ A^{\mu\nu}k_\nu = 0 \ \wedge \ A_{\mu\nu}U^\nu = 0 \wedge \ A_\mu^\mu = 0 \,. \tag{1.17}$$

The lhs. of Eq. (1.17) introduces a new notation. On the rhs., the last condition is the tracelessness of the gravitational 'amplitude' $(A^{\mu\nu})$ and due to (1.10) also of the GW tensor $(\bar{h}^{\mu\nu})$. The first and second condition stand for the transversal behaviour of the wave equation solution. Concluding so far, GW are transversal waves travelling through space-time at the speed of light.

Polarisation

In comparison with electrodynamics and electromagnetic (EM) waves, the most obvious difference is the tensorial property of the gravitational wave. We assume here the polarisation of the GW to be perpendicular to the wave vector $\vec{k}_{\mathrm{gw}}$ (though longitudinal modes in general may exist, as already stated by Einstein [ER37]). One other difference to EM waves is that the linear base polarisations for GW are rotated against each other only by $45°$, while for EM waves, the polarisations are rotated by $90°$.

In the special coordinate system of TT gauge, $(\bar{h}_{\mu\nu}^{\mathrm{TT}})$ is of the form

$$(\bar{h}_{\mu\nu}^{\mathrm{TT}}) = \begin{pmatrix} 0 & 0 & 0 & 0 \\ 0 & \bar{h}_{xx}(t,\vec{x}) & \bar{h}_{xy}(t,\vec{x}) & 0 \\ 0 & \bar{h}_{yx}(t,\vec{x}) & \bar{h}_{yy}(t,\vec{x}) & 0 \\ 0 & 0 & 0 & 0 \end{pmatrix} \,.$$

We can further concretise the elements of $\bar{\boldsymbol{h}}^{\mathrm{TT}}$. We know $g_{\mu\nu} = g_{\nu\mu}$ and due to $\eta_{\mu\nu} = \eta_{\nu\mu}$ and $g_{\mu\nu} = \eta_{\mu\nu} + h_{\mu\nu}$, $\bar{\boldsymbol{h}}^{\mathrm{TT}}$ must also be symmetric. Thus, $\bar{h}_{xy} = \bar{h}_{yx}$. Furthermore, in TT gauge, $\bar{\boldsymbol{h}}^{\mathrm{TT}}$ must be traceless, giving $\bar{h}_{xx} + \bar{h}_{yy} = 0$ or $\bar{h}_{xx} = -\bar{h}_{yy}$. Using a convenient notation,

$$\bar{h}_{xx}(t,\vec{x}) =: h_+(t,\vec{x}) \,, \quad \bar{h}_{xy}(t,\vec{x}) =: h_\times(t,\vec{x}) \,,$$

we end up with

$$(\bar{h}_{\mu\nu}^{\mathrm{TT}}) = \begin{pmatrix} 0 & 0 & 0 & 0 \\ 0 & h_+(t,\vec{x}) & h_\times(t,\vec{x}) & 0 \\ 0 & h_\times(t,\vec{x}) & -h_+(t,\vec{x}) & 0 \\ 0 & 0 & 0 & 0 \end{pmatrix} \,. \tag{1.18}$$

This is the gravitational wave tensor in TT gauge, describing a plane GW that travels along the z-direction.

In TT coordinates, a particle that is initially at rest will remain at rest forever, even if a GW is passing by. The position of the particle will not change. However,

the proper distance given by $\mathrm{d}s^2$ between two particles (we call them test masses in the following) will change. We will come back to that in Sec. 1.3 and 1.4. It will turn out to be a key feature for the GW detection.

The Gravitational Wave Tensor

For the sake of simplicity, from now on we will drop the TT-notation and denote by $\boldsymbol{h}$ the tensor $(\bar{h}_{\mu\nu}^{\mathrm{TT}})$ given in Eq. (1.18). $\boldsymbol{h}$ can be decomposed via

$$\boldsymbol{h} = \begin{pmatrix} 0 & 0 & 0 & 0 \\ 0 & h_+ & h_\times & 0 \\ 0 & h_\times & -h_+ & 0 \\ 0 & 0 & 0 & 0 \end{pmatrix} = h_+ \begin{pmatrix} 0 & 0 & 0 & 0 \\ 0 & 1 & 0 & 0 \\ 0 & 0 & -1 & 0 \\ 0 & 0 & 0 & 0 \end{pmatrix} + h_\times \begin{pmatrix} 0 & 0 & 0 & 0 \\ 0 & 0 & 1 & 0 \\ 0 & 1 & 0 & 0 \\ 0 & 0 & 0 & 0 \end{pmatrix},$$

or for short:

$$\boldsymbol{h} = h_+ \boldsymbol{e}_+ + h_\times \boldsymbol{e}_\times. \tag{1.19}$$

In (1.19), we introduced the polarisation basis tensors of the gravitational wave,

$$\boldsymbol{e}_+ = \begin{pmatrix} 0 & 0 & 0 & 0 \\ 0 & 1 & 0 & 0 \\ 0 & 0 & -1 & 0 \\ 0 & 0 & 0 & 0 \end{pmatrix}, \quad \boldsymbol{e}_\times = \begin{pmatrix} 0 & 0 & 0 & 0 \\ 0 & 0 & 1 & 0 \\ 0 & 1 & 0 & 0 \\ 0 & 0 & 0 & 0 \end{pmatrix}, \tag{1.20}$$

which will be of use later. From the polarisation basis matrices $\boldsymbol{e}_+$ and $\boldsymbol{e}_\times$ we can again see the behavior of stretching space-time in one direction (h_+ component) while squeezing in an orthogonal direction ($-h_+$ component).

The effect of a passing gravitational wave is to cause a tidal variation of a circular TM ring. Note that only in the TT-picture the test masses remain at rest while GW pass by. Essentially, the metric between the test masses changes. Contrary, in an arbitrary coordinate chart, the test masses will follow a tidal variation. This behaviour is displayed in Fig. 1.3 for both plus and cross polarisations. Besides the transversality, one can see clearly the 45° angular tilt between $+$ and $\times$. Both incident waves are linear polarised. When combined, one yields elliptical polarisations.

In the case of arbitrarily chosen coordinates, the polarisation tensors $\boldsymbol{e}_+$ and $\boldsymbol{e}_\times$ of a gravitational wave propagating along the unit vector

$$\hat{k} := \frac{\vec{k}_{\mathrm{gw}}}{|\vec{k}_{\mathrm{gw}}|} \tag{1.21}$$

can be computed via

$$\boldsymbol{e}_+ = \hat{u} \otimes \hat{u} - \hat{v} \otimes \hat{v}, \quad \boldsymbol{e}_\times = \hat{u} \otimes \hat{v} + \hat{v} \otimes \hat{u}, \tag{1.22}$$

where $\hat{u}, \hat{v}$ and $\hat{k}$ span an orthogonal basis travelling along the gravitational wave.
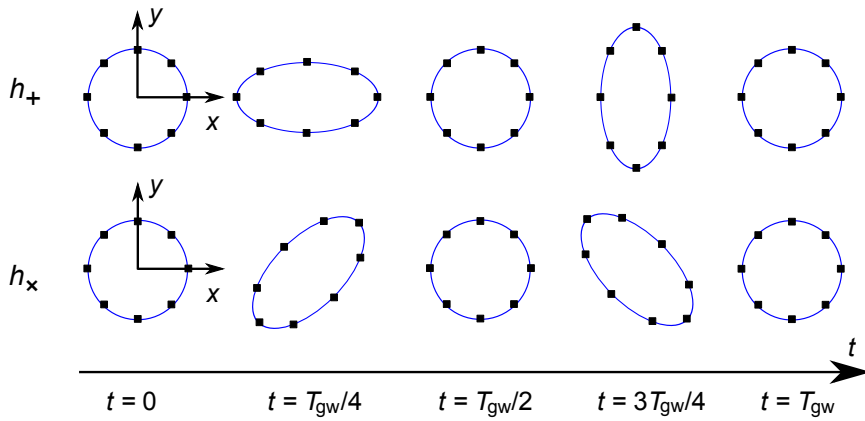
Figure 1.3: Gravitational waves acting on a TM circle for both plus (+) and cross (×) polarisation. The transverse, quadrupolar wave propagates orthogonal to the page. The time-dependent deformation is shown for one whole gravitational wave period T_{gw}.
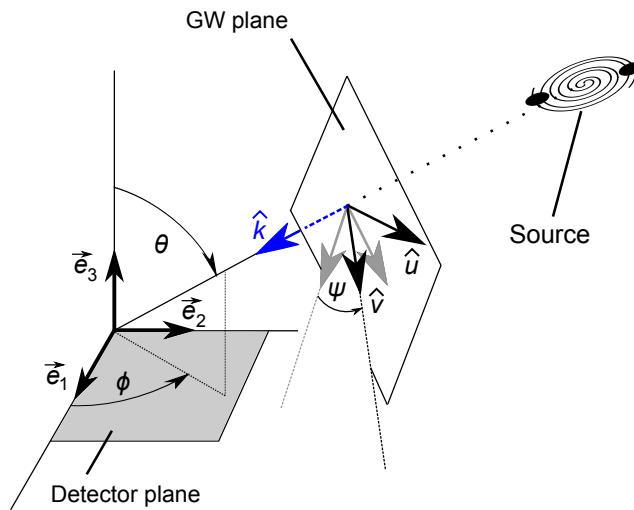
Figure 1.4: Definition of gravitational wave polarisation basis $\hat{k}$, $\hat{u}$ and $\hat{v}$. The three vectors $\hat{u}, \hat{v}$ and $\hat{k}$ form an orthogonal basis. ψ is the tilt angle of the gravitational wave polarisation plane (spanned by $\hat{u}$ and $\hat{v}$) with respect to the projection of the detector plane into the GW polarisation plane (spanned by the grey arrows).

In spherical coordinates (θ, ϕ), they are given by

$$\hat{k} = \begin{pmatrix} -\sin(\theta)\cos(\phi) \\ -\sin(\theta)\sin(\phi) \\ -\cos(\theta) \end{pmatrix}, \quad \hat{u} = \begin{pmatrix} \cos(\theta)\cos(\phi) \\ \cos(\theta)\sin(\phi) \\ -\sin(\theta) \end{pmatrix}, \quad \hat{v} = \begin{pmatrix} \sin(\phi) \\ -\cos(\phi) \\ 0 \end{pmatrix}, \quad (1.23)$$

as shown in Fig. 1.4.

In the case of a GW polarisation tilted by an angle ψ with respect to the detector plane (Fig. 1.4), the wave plane has to be rotated by $-\psi$. Only then, the detector response in terms of relative length variations can be computed. Concluding, the general polarisation tensor is given by

$$\boldsymbol{\epsilon}_+ = \cos(2\psi)\boldsymbol{e}_+ - \sin(2\psi)\boldsymbol{e}_\times, \quad \boldsymbol{\epsilon}_\times = \sin(2\psi)\boldsymbol{e}_+ + \cos(2\psi)\boldsymbol{e}_\times, \quad (1.24)$$

where the factor of two in the trigonometric functions enters by the fact that GW have a 45° angle between its modes. Hence, one should extend Eq. (1.19) to

$$\boldsymbol{h}(t,\vec{x}) = h_+(t,\vec{x})\boldsymbol{\epsilon}_+ + h_\times(t,\vec{x})\boldsymbol{\epsilon}_\times. \quad (1.25)$$

1.2.3 Gravitational Wave Amplitude, Strain and Frequency

We will now introduce the GW characteristics amplitude, strain and frequency [SS09]. They will be used in the simulation (Ch. 5) to generate a gravitational wave signal in the detector.

Amplitude and Strain

The most relevant observable for the detection is the amplitude of the radiated wave. The following formula can be derived in a far field approximation. That is, the GW wavelength λ_{gw} is small compared to the distance R from observer to source, $\lambda_{\mathrm{gw}} \ll R$. Additionally, space-time is flat in first order, such that one finds in a so-called Post-Newtonian expansion in $\frac{v^2}{c^2}$ the quadrupolar formula [MTW73]:

$$h_{ij} = \frac{2}{Rc^2}\ddot{I}_{ij} = \frac{2}{Rc^2}\frac{\partial^2}{\partial t^2}\left[\int \mathrm{d}^3x \, \varrho(\vec{x})(\delta_{ij}\vec{x}^2 - x_i x_j)\right]. \quad (1.26)$$

Here, $I_{ij} \equiv \int \mathrm{d}^3x \, \varrho(\vec{x})(\delta_{ij}\vec{x}^2 - x_i x_j)$ denotes the components of second moment of the radiating mass distribution, which can be interpreted as the moment of inertia, and $\varrho(\vec{x})$ denotes the mass density of the source.

The strength of gravitational waves is given by the strain h, a dimensionless quantity and defined as

$$h \equiv 2\frac{\Delta L}{L}, \quad (1.27)$$

where ΔL is the absolute change in separation between two points in space induced by an incident GW with respect to an overall distance L (e.g., from source to observer). A nice discussion can be found in the appendix of [Wan10]. Moreover, h could be understood roughly as the projection of the gravitational wave tensor $\boldsymbol{h}$ on the observation line of sight. Strains down to the order of magnitude of $h \approx 10^{-22}$ may be detectable with current and future detectors (Fig. 1.5) [RHT08].

Gravitational Wave Frequency

Each cosmic GW source has its own signal frequency that can serve as a fingerprint of the radiating object. In many cases (e.g., inspiralling black hole binaries), the frequency depends on the moment of observation and gives insight into the evolution history of the observed system. Inspiralling objects far away from merger and ringdown have a good frequency stability such that the detected gravitational wave is not changing its behaviour in the detector for an adequate observation duration and can be used to identify the radiating system. However, for systems close to merger, the frequency decoding and determination from a detected signal is a challenging issue, for that the frequency is a complicated function of time.

For a binary star system with orbiting period T_{orb}, one can derive the frequency f_{gw} of the radiated gravitational waves using pure classical mechanics methods [Sch09]:

$$f_{\mathrm{gw}} = 2f_{\mathrm{orb}} \,, \tag{1.28}$$

where $f_{\mathrm{orb}} = \frac{2\pi}{T_{\mathrm{orb}}}$ is the orbital frequency of the binary system.

For the simulation results in Ch. 6, we assume one system orbiting at $2 \cdot 10^{-3}\,\mathrm{Hz}$ giving rise to gravitational waves with frequency $f_{\mathrm{gw}} = 0.004\,\mathrm{Hz}$. The strain is taken to be 10^{-20}, hence a strong signal is assumed. These parameters are characteristic for inspiralling black hole binaries with one million solar masses each, as can be seen in Fig. 1.5.

1.2.4 Sources of Gravitational Waves

It can be shown by using the quadrupolar formula (1.26) that it is not possible to build a device on Earth that produces detectable gravitational waves [Sau94]. However, there exist various sources in the universe producing waves with strain amplitudes of the order $h \approx 10^{-23} - 10^{-20}$ on or near the Earth that could in principle be detected. First, there are binary star systems like pairs of neutron stars or inspiralling black holes which emit strong gravitational waves with $h \approx 10^{-20} - 10^{-21}$. Next, fast rotating pulsars with mm-scale deviations from a perfectly spherical form are interesting sources to study by ground-based detectors as well as bursts from supernovae, both detectable in the audio frequency range of kHz. Other sources might be the stochastic gravitational background [HMOP08; Ott08], perhaps even from the big bang [Col14]. Furthermore, some more speculative sources like cosmic strings are under discussion. A nice overview can be found in [SS09].
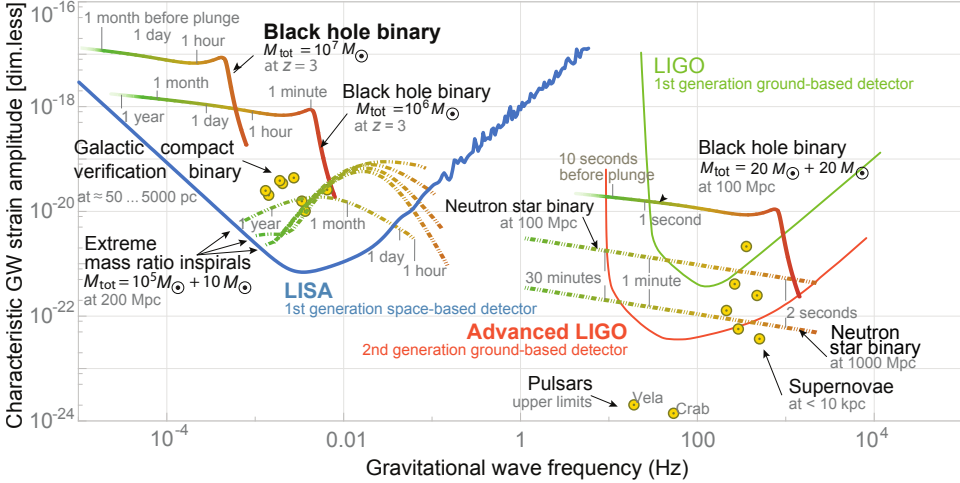
Figure 1.5: Frequency bands of gravitational wave sources and detectors, displayed with the Gravitational Wave Observatory Designer [Bar15]. Shown is the characteristic (strain) amplitude of GWs produced by various astrophysical sources dependent on the signal frequency. The detector sensitivities (blue curve for spaceborne LISA, green and red curve for ground-based LIGO and aLIGO) indicate which sources are detectable. The detectability of some sources (e.g., black hole binaries) is further depending on the inspiral stage and the distance to the observer.

A schematic overview of the GW sources and the detection bands of space- and ground-based detectors is presented in Fig. 1.5 and shows the characteristic strain amplitudes for several GW sources along a logarithmic frequency axis. It compares the detection ability of ground-based detectors (LIGO and advanced LIGO in the audio frequency range) and space-based GW detectors (e.g., LISA, in the sub-Hertz frequency band) in terms of strain, defined in equation (1.27). Sources located above the sensitivity curve are detectable by the respective detector. For more information about sensitivity curves for LISA we refer to [LHH00].

Since this thesis concentrates on the space-based gravitational wave detector LISA, we will now focus on the left hand side of Fig. 1.5. First of all, the best detector strain sensitivity of $\approx 10^{-21}$ is achieved at $f \approx 3\,\mathrm{mHz}$. Astrophysical GW sources with a strain above the blue sensitivity line could be seen by LISA. These are black hole binaries with total masses of $> 10^6\,M_\odot$ at redshift distances $z \lesssim 3$ corresponding to 10^{10} parsecs, where one parsec is $1\,\mathrm{pc} = 3.09 \cdot 10^{16}\,\mathrm{m}$. Moreover, galactic compact binaries at distances between 50 and 5000 parsecs may be observed. Finally, even weak signals from extreme mass ratio inspirals with mass ratios of 10^4 and higher are possible to detect.

At this point, we know what gravitational waves and their properties are, and we have learned about the sources. The next sections in this chapter deal with the principles and mathematical framework of interferometric gravitational wave

detection on ground and in space. Subsequently, the main equations for the numerical simulation of incident gravitational waves will be introduced.

1.3 Interferometric Detection of Gravitational Waves

In Sec. 1.2.4, the sources of gravitational waves and their characteristic strain amplitudes and strains have been presented. The question now arises how one could detect gravitational waves. The principle answer is given in this section and a detection apparatus used for ground-based GW detectors, the Michelson interferometer, is explained in detail.

1.3.1 How to Detect Gravitational Waves

In Sec. 1.2, we derived the matrix equation (1.18) for the gravitational wave tensor $\boldsymbol{h}$ in a special coordinate system (the TT frame). As seen in Sec. 1.2.2, an incident GW would then squeeze space-time in one direction and simultaneously stretch space-time in the orthogonal direction. Thus, if we want to detect gravitational waves, we need a device that can measure these differential space-time variations precisely.

The question now arises how to sense space-time variations, or, speaking differently, distance variations. One convenient way to measure distances, in particular, differential length changes, is to use light. By measuring the light travel time along a certain path, one directly can deduce the distance via distance $= c \times$ light travel time.

Instead of measuring the time for photon travel and its variation due to GW, it is technically much easier to detect differential distance changes $\Delta s = c\Delta T$ by the phase difference

$$\Delta\phi = \frac{2\pi}{\lambda}\Delta s = \frac{2\pi c}{\lambda}\Delta T \qquad (1.29)$$

between two light rays with wavelength λ. Here, ΔT denotes the light travel time variation along the measurement path due to incident gravitational waves.

A device converting relative distance changes to phase shifts is the well known (Michelson) interferometer, depicted in Fig. 1.6. The interferometer basically consists of a coherent (laser) source emitting light which is split at a beam splitter (BS), that sends the light into the two orthogonal arms. Light travelling along the arms gets reflected at the end mirrors and interferes at the BS. A photodetector measures the power fluctuation at the output port. The fluctuations in the photo current can then be converted to phase changes. If the armlengths vary in time, the interference and hence the PD signal also change.

This is exactly what we need to do to detect gravitational waves. A disturbance in space-time, i.e., a gravitational wave, changes the 'length' of the interferometer
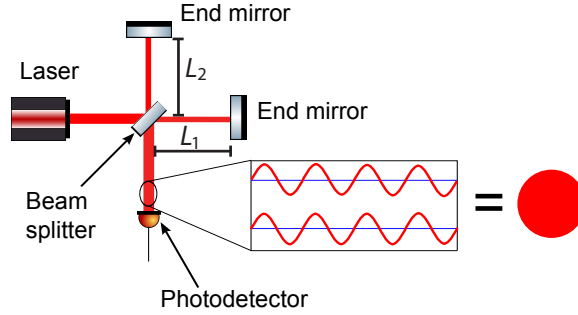
Figure 1.6: Schematic of a Michelson interferometer consisting of a laser source, beam splitter, two arms with physical length L_1 and L_2, respectively, where each arm equipped with an end mirror, and a photodetector readout scheme.

arms. More precisely, the light travel time along the arms is changing according to the TT picture, where positions (e.g., of the mirrors) are fixed and only the distances between (i.e., the metric) varies. This appears as power fluctuations within the optical readout signal. Therefore, we are in principle able to detect gravitational waves with a Michelson interferometer.

However, the strain amplitude of GW, defined as the ratio of length change ΔL in the detector and total armlength L according to Eq. (1.27), is extremely small. In maximum, one could expect $h \approx 10^{-21}$, a signal from a supernova in a neighbour galaxy [SC09]. This number corresponds to a path length variation of $\Delta L = 10^{-18}$ m in a $L = 1$ km long Michelson IFO. That in turn means an exceptional metrological challenge and needs extreme effort to suppress any noise that could be misinterpreted as path length variation due to GW. In the following, we will describe the principles of interferometry more quantitatively.

1.3.2 Phase Detection in Michelson Interferometers

We will now derive an expression for the phase detection in a Michelson interferometer and consider Fig. 1.7. The incoming complex electric field $\vec{E}_L$ from the laser is given in the plane wave approximation for an arbitrary moment t at position $\vec{x}$ by

$$\vec{E}_L(\vec{x},t) = \vec{E}_0 e^{i(\omega t - i\vec{k}\cdot\vec{x})} + \text{c.c.},$$

where $\vec{E}_0 = E_0\vec{\varepsilon}$ combines the electric field amplitude E_0 with the normalised polarisation vector $\vec{\varepsilon}$ of the electromagnetic wave. $\omega = 2\pi\nu$ denotes the angular frequency of the monochromatic laser light, where ν is the frequency in Hz, and the wave vector $\vec{k}$ gives the direction of light travel. Note here that the subsequent calculation is valid only in the case of plane waves. In many cases, the light emitted from the laser has Gaussian beam properties and the computation of the phase signal gets complex, since the wave changes along the light path.
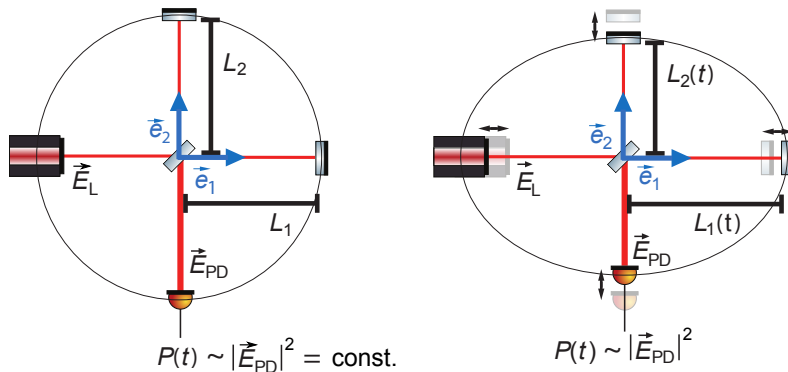
Figure 1.7: IFO setup with armlengths L_1 of arm 1 and L_2 of arm 2 and coordinate basis vectors $\vec{e}_1$ and $\vec{e}_2$. An incident GW (perpendicular to the plane of projection) would then stretch arm 1 while shrinking arm 2. The PD detects relative armlength changes. That is, the affection of the optical path between laser and BS as well as BS to PD does not change the interference signal. However, the relative armlength changes between arm 1 and 2 will enter the PD signal.

For a detailed treatment of Gaussian light, we refer to [Wan10; WHK$^+$12]. However, for the rest of this thesis, we will assume all laser beams to be plane waves which is a good approximation for light that has travelled along the long arms, especially in the space-based detectors.

For the derivation of the phase detection, we will further neglect polarisation issues and omit the explicit c.c. part. Thus, we implicitly use only the real part as a physical quantity but maintain complex notation for convenience in handling quantities with phase. As presented in Fig. 1.7, a coordinate chart with basis vectors $\vec{e}_1$ and $\vec{e}_2$ along the perpendicular interferometer arms with geometric lengths $L_1 = L_1(t)$ and $L_2 = L_2(t)$ is chosen. $\Delta L(t) = L_2(t) - L_1(t)$ comprises the geometric time-dependent differential length change in the two arms which will be computed for the case of incident gravitational waves in Sec. 1.3.3.

The incoming light is split at the semi transmissive (50:50) beam splitter such that one half of the light power travels along $\vec{e}_1$ (arm 1) and the other portion along $\vec{e}_2$ (arm 2). Both light fields are reflected at the end mirrors, travel along $-\vec{e}_1$ and $-\vec{e}_2$, respectively, recombine at the beam splitter and are measured by a photodetector. Quantitatively, we can model the reflections and transmissions at the BS by coefficients ρ and τ. They describe the reflection and transmission coefficient of the electric field. Since absorption is neglected, $\rho^2 + \tau^2 = 1$ is valid, which corresponds to energy conservation.

According to [FS10], for energy conservation, we define that the light collects a phase shift of $\frac{\pi}{2}$ by transmission at the beam splitter, while the reflection at the BS and the end mirrors does not add any phase shift. Hence, we set for the reflected electric field component $\vec{E}_\mathrm{r} = \rho \vec{E}_0$ and for the transmissive part, $\vec{E}_\mathrm{t} = \mathrm{i}\tau \vec{E}_0$. The

values for reflection and transmission coefficients are $\rho_{\mathrm{BS}} = \tau_{\mathrm{BS}} = \frac{1}{\sqrt{2}}$ for the 50:50 BS and $\rho_{\mathrm{M}} = 1, \tau_{\mathrm{M}} = 0$ for the perfect end mirrors. Hence, the two electric fields at the PD read as

$$
\begin{aligned}
\vec{E}_1 &= \mathrm{i}\tau_{\mathrm{BS}}\rho_{\mathrm{M}}\rho_{\mathrm{BS}}\vec{E}_0\mathrm{e}^{\mathrm{i}(\omega t - k_1 \cdot 2L_1)} \\
&= \mathrm{i}\cdot\frac{1}{\sqrt{2}}\cdot 1 \cdot \frac{1}{\sqrt{2}}\cdot\vec{E}_0\mathrm{e}^{\mathrm{i}(\omega t - k_1 \cdot 2L_1)} = \frac{\mathrm{i}}{2}\vec{E}_0\mathrm{e}^{\mathrm{i}(\omega t - k_1 \cdot 2L_1)}\,, \\
\vec{E}_2 &= \rho_{\mathrm{BS}}\rho_{\mathrm{M}}\mathrm{i}\tau_{\mathrm{BS}}\vec{E}_0\mathrm{e}^{\mathrm{i}(\omega t - k_2 \cdot 2L_2)} \\
&= \frac{1}{\sqrt{2}}\cdot 1 \cdot \mathrm{i}\cdot\frac{1}{\sqrt{2}}\cdot\vec{E}_0\mathrm{e}^{\mathrm{i}(\omega t - k_2 \cdot 2L_2)} = \frac{\mathrm{i}}{2}\vec{E}_0\mathrm{e}^{\mathrm{i}(\omega t - k_2 \cdot 2L_2)}\,,
\end{aligned}
$$

and the recombined electric field at the PD is given by the superposition

$$
\vec{E}_{\mathrm{PD}} = \vec{E}_1 + \vec{E}_2 = \frac{\mathrm{i}}{2}\vec{E}_0\mathrm{e}^{\mathrm{i}(\omega t - k_1 \cdot 2L_1)} + \frac{\mathrm{i}}{2}\vec{E}_0\mathrm{e}^{\mathrm{i}(\omega t - k_2 \cdot 2L_2)}.
$$

The intensity at the PD is proportional to the electric field amplitude, $I_{\mathrm{PD}} \propto |\vec{E}_{\mathrm{PD}}|^2$. Hence,

$$
\begin{aligned}
|\vec{E}_{\mathrm{PD}}|^2 &= \left|\frac{\mathrm{i}}{2}\vec{E}_0\mathrm{e}^{\mathrm{i}(\omega t - k_1 \cdot 2L_1)} + \frac{\mathrm{i}}{2}\vec{E}_0\mathrm{e}^{\mathrm{i}(\omega t - k_2 \cdot 2L_2)}\right|^2 \\
&= \frac{|\vec{E}_0|^2}{4}|\mathrm{e}^{\mathrm{i}\omega t}|^2(\mathrm{e}^{-2\mathrm{i}k_1 L_1} + \mathrm{e}^{-2\mathrm{i}k_2 L_2})(\mathrm{e}^{-2\mathrm{i}k_1 L_1} + \mathrm{e}^{-2\mathrm{i}k_2 L_2})^* \\
&= \frac{|\vec{E}_0|^2}{4}(2 + \mathrm{e}^{2\mathrm{i}(k_2 L_2 - k_1 L_1)} + \mathrm{e}^{-2\mathrm{i}(k_2 L_2 - k_1 L_1)}) \\
&= \frac{|\vec{E}_0|^2}{4}(2 + 2\cos(2[k_2 L_2 - k_1 L_1])) \\
&= \frac{|\vec{E}_0|^2}{2}(1 + \cos(2[k_2 L_2 - k_1 L_1]))\,,
\end{aligned}
$$

where we used the trigonometric relation $\cos(u) = \frac{\mathrm{e}^{\mathrm{i}u} + \mathrm{e}^{-\mathrm{i}u}}{2}$.

The detected power is the surface integral of the intensity over the whole PD detection area. For plane waves, the intensity is constant over the complete surface. Subsequently, the integration is trivial and adds only a constant factor accounting for the surface area. The detected power is thus as well proportional to

$$
P(t) \propto \frac{|\vec{E}_0|^2}{2}(1 + \cos(2[k_2 L_2 - k_1 L_1]))\,. \tag{1.30}
$$

Since we neglect Doppler modulation of light in the ground-based IFO, the laser wavelength in the two arms does not change. We can then write $\lambda_1 = \lambda_2 =: \lambda$, and thus, $k_1 = \frac{2\pi}{\lambda_1} = \frac{2\pi}{\lambda_2} = k_2 = \frac{2\pi}{\lambda}$. This yields

$$
P(t) \propto \frac{|\vec{E}_0|^2}{2}(1 + \cos(2[\tfrac{2\pi}{\lambda}L_2 - \tfrac{2\pi}{\lambda}L_1]) = \frac{E_0^2}{2}(1 + \cos(2\tfrac{2\pi}{\lambda}\Delta L))\,,
$$

with $\Delta L(t) = L_2(t) - L_1(t)$. Hence, the power fluctuation due to optical path length change $\Delta s(t) = 2\Delta L(t)$ is finally:

$$P(t) \propto \frac{|\vec{E}_0|^2}{2}(1 + \cos(\Delta\phi(t))), \quad \Delta\phi(t) = \frac{2\pi}{\lambda}\Delta s(t) = 2 \cdot \frac{2\pi}{\lambda}\Delta L(t). \quad (1.31)$$

The power on the PD fluctuates with the relative optical phase change $\Delta\phi(t)$ introduced by the gravitational wave. The question now arises how one can compute $\Delta\phi(t)$ for incident GW. This will be explained subsequently.

1.3.3 Light Travel Time in a Michelson Interferometer

In this section, an expression for the optical phase shift $\Delta\phi$ in the case of a ground-based Michelson interferometer (Fig. 1.7) with different armlengths L_1 and L_2, respectively, is derived. This is useful for space-based GW detectors, since they basically consist of unequal-arm interferometers (Sec. 1.4). The principal assumptions and calculation steps for the Michelson IFO are similar, though simpler.

First, we assume a weak gravitational wave with $|h_{\mu\nu}| \ll 1$ (Sec. 1.2). It propagates along $\hat{k} = \frac{\vec{k}_{\text{gw}}}{|\vec{k}_{\text{gw}}|} = -\vec{e}_3$ towards the IFO, whose arms are again oriented along $\vec{e}_1$ and $\vec{e}_2$ as depicted in Fig. 1.7. The gravitational wave is described by the tensor $\boldsymbol{h}$ (Eq. (1.18)). From GR, we know the space-time interval $\mathrm{d}s^2$ (Eq. (1.5)) representing the four dimensional distance in space-time. An explicit expression for $\mathrm{d}s^2$ can be derived by inserting Eq. (1.18) into (1.5), using $(\eta_{\mu\nu}) = \mathrm{diag}(-1, +1, +1, +1)$:

$$\mathrm{d}s^2 \overset{(1.5)}{=} (\eta_{\alpha\beta} + h_{\alpha\beta})\,\mathrm{d}x^\alpha\,\mathrm{d}x^\beta$$
$$\overset{(1.18)}{=} -c^2\,\mathrm{d}t^2 + (1 + h_+)\,\mathrm{d}x^2 + (1 - h_+)\,\mathrm{d}y^2 + 2h_\times\,\mathrm{d}x\,\mathrm{d}y + \mathrm{d}z^2$$
$$= -c^2\,\mathrm{d}t^2 + \mathrm{d}x^2 + \mathrm{d}y^2 + \mathrm{d}z^2 + (\mathrm{d}x^2 - \mathrm{d}y^2)h_+ + 2h_\times\,\mathrm{d}x\,\mathrm{d}y\,.$$

The difference $\mathrm{d}x^2 - \mathrm{d}y^2$ indicates the differential distance variation due to gravitational waves (stretch in x-direction while simultaneously squeeze in y-direction). For the sake of simplicity, in the further derivation, we will assume a plus-polarised GW only, i.e., $h_\times = 0$.

We will now compute the light travel time for a photon trajectory along arm 1 (Fig. 1.7) as seen from an outside observer at rest and follow closely [Sch09]. A photon travel in the direction of $\vec{e}_1$ yields $\mathrm{d}y = \mathrm{d}z = 0$ and

$$\mathrm{d}s^2 = -c^2\,\mathrm{d}t^2 + (1 + h_+)\,\mathrm{d}x^2\,.$$

For photon paths, $\mathrm{d}s^2 = 0$, and we can thus write:

$$c^2\,\mathrm{d}t^2 = (1 + h_+)\,\mathrm{d}x^2 \quad \Longleftrightarrow \quad \left(\frac{\mathrm{d}t}{\mathrm{d}x}\right)^2 = \frac{1 + h_+}{c^2}\,.$$

Now we can integrate along arm 1, first from BS to end mirror:

$$\int_{t_{\mathrm{BS}}}^{t_{\mathrm{mirror},1}} \mathrm{d}t = \frac{1}{c}\int_0^{L_1} \mathrm{d}x\sqrt{1+h_+} = \frac{1}{c}\int_0^{L_1} \mathrm{d}x\sqrt{1+h_+(t(x))}\,. \tag{1.32}$$

Here, $h_+ = h_+(t)$ is a function of time t, while t itself implicitly depends on x. This can be seen as follows. A photon emitted at t_{BS} from the beam splitter arrives at coordinate x at time $t(x)$ given by

$$t(x) = t_{\mathrm{BS}} + \frac{x}{c}\,.$$

This, of course, is only true in flat space-time. However, the relativistic corrections in $t(x)$ will enter in the integral in terms of order h_+^2, which are negligible due to our assumption $|h_{\mu\nu}| \ll 1$ made above. Inserting $t(x)$, we can Taylor expand the root for small h_+:

$$\int_{t_{\mathrm{BS}}}^{t_{\mathrm{mirror},1}} \mathrm{d}t = \frac{1}{c}\int_0^{L_1} \mathrm{d}x\sqrt{1+h_+(t(x))} = \frac{1}{c}\int_0^{L_1} \mathrm{d}x\sqrt{1+h_+(t_{\mathrm{BS}}+\tfrac{x}{c})}$$

$$\simeq \frac{1}{c}\int_0^{L_1} \mathrm{d}x\left(1+\tfrac{1}{2}h_+(t_{\mathrm{BS}}+\tfrac{x}{c})\right),$$

since $\sqrt{1+h_+} = 1 + \tfrac{1}{2}h_+ + \mathcal{O}(h_+^2)$. Evaluating the integrals on both sides as far as possible gives

$$t_{\mathrm{mirror},1} \simeq t_{\mathrm{BS}} + \frac{L_1}{c} + \frac{1}{2c}\int_0^{L_1} \mathrm{d}x\, h_+(t_{\mathrm{BS}}+\tfrac{x}{c})\,. \tag{1.33}$$

This is the time a photon arrives at the mirror after travelling from the BS of the interferometer along arm 1 to the mirror (Fig. 1.7), having started at time t_{BS}. A similar argument gives the return time at the beam splitter:

$$t_{\mathrm{return},1} \quad\simeq\quad t_{\mathrm{mirror},1} + \frac{1}{c}\int_{L_1}^0 (-\mathrm{d}x)\sqrt{1+h_+(t_{\mathrm{BS}}+\tfrac{L_1}{c}+\tfrac{x}{c})}$$

$$\simeq\quad t_{\mathrm{mirror},1} + \frac{1}{c}\int_0^{L_1} \mathrm{d}x\left(1+\tfrac{1}{2}h_+(t_{\mathrm{BS}}+\tfrac{L_1}{c}+\tfrac{x}{c})\right),$$

or, inserting $t_{\mathrm{mirror},1}$ from Eq. (1.33) and evaluating the first part of the integral,

$$t_{\mathrm{return},1} = t_{\mathrm{BS}} + \frac{2L_1}{c} + \frac{1}{2c} \int_0^{L_1} \mathrm{d}x\, h_+(t_{\mathrm{BS}} + \tfrac{x}{c}) + \frac{1}{2c} \int_0^{L_1} \mathrm{d}x\, h_+(t_{\mathrm{BS}} + \tfrac{L_1}{c} + \tfrac{x}{c})\,. \quad (1.34)$$

An analogous derivation for the other arm starts with

$$\int_{t_{\mathrm{BS}}}^{t_{\mathrm{mirror},2}} \mathrm{d}t = \frac{1}{c}\int_0^{L_2} \mathrm{d}y\, \sqrt{1 - h_+(t_{\mathrm{BS}} + \tfrac{y}{c})} \simeq \frac{1}{c}\int_0^{L_2}\mathrm{d}y\,\left(1 - \tfrac{1}{2}h_+(t_{\mathrm{BS}} + \tfrac{y}{c})\right),$$

and proceeds in a similar manner as shown above for the return path, yielding the photon round-trip time in arm 2 (BS → end mirror → BS). Note that, due to the stretching and shrinking of space-time by the GW expressed by $h_{22} = -h_{11} = -h_+$ (cf. Eq. (1.18)), the second arm is shrunk, and hence a minus sign appears in front of h_+ for arm 2. The differential light travel time Δt is then given by:

$$\begin{aligned}
\Delta t &= t_{\mathrm{return},1} - t_{\mathrm{return},2} \\[2mm]
&= 2\frac{L_1 - L_2}{c} + \frac{1}{2c}\int_0^{L_1}\mathrm{d}x\,\left(h_+(t_{\mathrm{BS}} + \tfrac{x}{c}) + h_+(t_{\mathrm{BS}} + \tfrac{L_1}{c} + \tfrac{x}{c})\right) \\[2mm]
&\quad - \frac{1}{2c}\int_0^{L_2}\mathrm{d}y\,\left(-h_+(t_{\mathrm{BS}} + \tfrac{y}{c}) - h_+(t_{\mathrm{BS}} + \tfrac{L_2}{c} + \tfrac{y}{c})\right). \quad (1.35)
\end{aligned}$$

Finally, the optical phase shift due to GW incidence perpendicular to the detector is measured by the PD of the IFO and can be computed via

$$\Delta\phi(t) = \frac{2\pi}{\lambda}\Delta s(t) = \frac{2\pi}{\lambda}(2\Delta L(t)) = \frac{4\pi c}{\lambda}\Delta t\,. \quad (1.36)$$

Here, Δt is the differential light travel time given by Eq. (1.35) which results in an optical phase shift $\Delta\phi(t)$ that enters the power measurement (1.31). Note again that only the relative phase shift between the *different* light paths is detected at the PD. Common mode changes, e.g., between laser and BS, cannot be detected.

1.3.4 Transfer Function of the Michelson Interferometer

We will now calculate the response of a Michelson interferometer to an incident gravitational wave. This quantity will be frequency-dependent and gives insight how the interferometer reacts to a gravitational wave of a certain frequency. We call the response in the following transfer function, which defines the ratio of the output signal to the input signal of a system.

In order to compute the transfer function, we will use a monochromatic gravitational wave signal with angular frequency ω_{gw} that travels perpendicular to the

detector in $-z$-direction. The interferometer is taken to be oriented as in Sec. 1.3.3, and the strain of the GW can be written as

$$h_+(t) = h_0 \cos(\omega_{\text{gw}} t) \,. \tag{1.37}$$

Furthermore, we assume the nominal armlengths of the Michelson interferometer to be equal, $L_1 = L_2 = L$, which was sketched in the left part of Fig. 1.7.

The differential light travel time shift Δt in the output signal is known from Eq. (1.35). For the monochromatic signal (1.37), this becomes

$$
\begin{aligned}
\Delta t \;=\;& \frac{1}{2c} \int_0^L \mathrm{d}x \, \left[h_0 \cos\left(\omega_{\text{gw}}(t_{\text{BS}} + \tfrac{x}{c})\right) + h_0 \cos\left(\omega_{\text{gw}}(t_{\text{BS}} + \tfrac{L}{c} + \tfrac{x}{c})\right) \right] \\
&+ \frac{1}{2c} \int_0^L \mathrm{d}y \, \left[h_0 \cos\left(\omega_{\text{gw}}(t_{\text{BS}} + \tfrac{y}{c})\right) + h_0 \cos\left(\omega_{\text{gw}}(t_{\text{BS}} + \tfrac{L}{c} + \tfrac{y}{c})\right) \right] \\
=\;& \frac{h_0}{2c} \frac{c}{\omega_{\text{gw}}} \left[\sin\left(\omega_{\text{gw}}(t_{\text{BS}} + \tfrac{x}{c})\right)\big|_0^L + \sin\left(\omega_{\text{gw}}(t_{\text{BS}} + \tfrac{L}{c} + \tfrac{x}{c})\right)\big|_0^L \right. \\
&\left. + \sin\left(\omega_{\text{gw}}(t_{\text{BS}} + \tfrac{y}{c})\right)\big|_0^L + \sin\left(\omega_{\text{gw}}(t_{\text{BS}} + \tfrac{L}{c} + \tfrac{y}{c})\right)\big|_0^L \right] \\
=\;& \frac{h_0}{2\omega_{\text{gw}}} \left[\sin\left(\omega_{\text{gw}}(t_{\text{BS}} + \tfrac{L}{c})\right) - \sin(\omega_{\text{gw}} t_{\text{BS}}) + \sin\left(\omega_{\text{gw}}(t_{\text{BS}} + \tfrac{2L}{c})\right) \right. \\
&- \sin\left(\omega_{\text{gw}}(t_{\text{BS}} + \tfrac{L}{c})\right) + \sin\left(\omega_{\text{gw}}(t_{\text{BS}} + \tfrac{L}{c})\right) - \sin(\omega_{\text{gw}} t_{\text{BS}}) \\
&\left. + \sin\left(\omega_{\text{gw}}(t_{\text{BS}} + \tfrac{2L}{c})\right) - \sin\left(\omega_{\text{gw}}(t_{\text{BS}} + \tfrac{L}{c})\right) \right] \,.
\end{aligned}
$$

The intermediate sinusoidal terms with time stamp $t_{\text{BS}} + \tfrac{L}{c}$ pairwise vanish and we are left with

$$\Delta t = \frac{h_0}{2\omega_{\text{gw}}} \left[2 \sin\left(\omega_{\text{gw}}(t_{\text{BS}} + \tfrac{2L}{c})\right) - 2 \sin\left(\omega_{\text{gw}} t_{\text{BS}}\right) \right] \,.$$

The use of the relation $\sin(u) - \sin(v) = 2 \sin\left(\tfrac{u-v}{2}\right) \cos\left(\tfrac{u+v}{2}\right)$ simplifies Δt to

$$\Delta t = 2 \frac{h_0}{\omega_{\text{gw}}} \sin\left(\frac{\omega_{\text{gw}} L}{c}\right) \cos\left(\omega_{\text{gw}}(t_{\text{BS}} + \tfrac{L}{c})\right) \,.$$

Finally, this translates according to Eq. (1.29) to the optical phase shift $\Delta\phi$ due to gravitational waves sensed by laser light of wavelength λ in an equal-arm interferometer (cf. [Hei95]):

$$\Delta\phi = \frac{2\pi c}{\lambda} \Delta t = \frac{4 h_0 \pi c}{\lambda \omega_{\text{gw}}} \sin\left(\frac{\omega_{\text{gw}} L}{c}\right) \cos\left(\omega_{\text{gw}}(t_{\text{BS}} + \tfrac{L}{c})\right) \,. \tag{1.38}$$

Transfer function for an equal−armlength Michelson interferometer
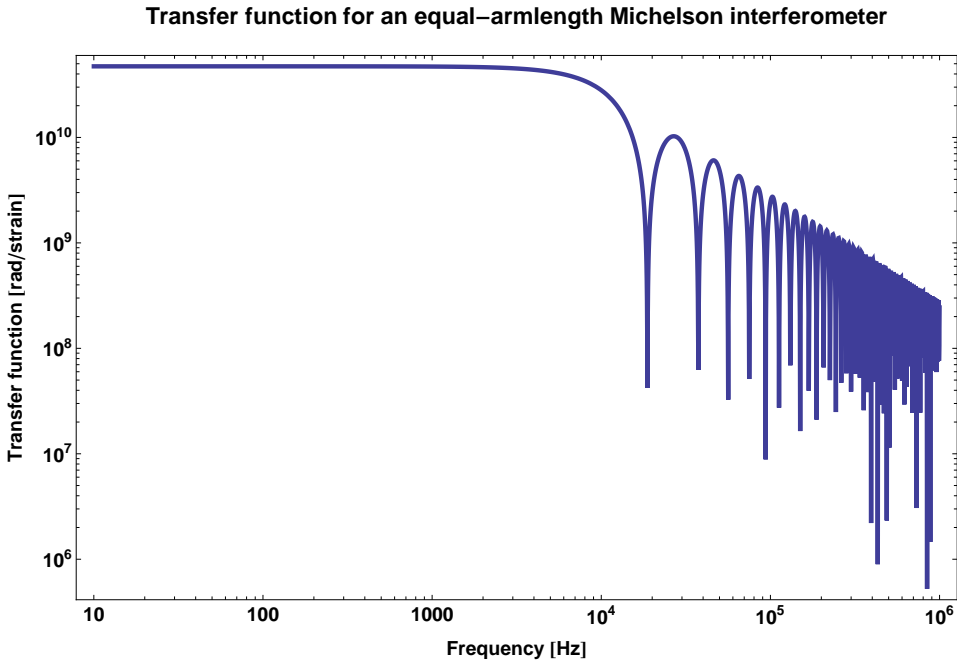
Figure 1.8: Transfer function from strain amplitude to optical phase shift suffered by laser light of $\lambda = 1064\,\mathrm{nm}$ for an equal-armlength Michelson interferometer with $4\,\mathrm{km}$ armlengths. For low frequencies, the detector response is flat with value $4.7 \cdot 10^{10}\,\mathrm{rad}$, while towards high frequencies, it decays with f_{gw}^{-1}. The null pattern appears for frequencies where the GW signal vanishes in the detector (here for multiples of $18750\,\mathrm{Hz}$, explained below).

The transfer function

$$\mathfrak{T}_{h_0 \to \Delta\phi}(f_{\mathrm{gw}}) := \frac{\Delta\phi}{h_0} = \frac{2c}{\lambda f_{\mathrm{gw}}} \sin\left(2\pi f_{\mathrm{gw}}\tfrac{L}{c}\right) \cos\left(2\pi f_{\mathrm{gw}}(t_{\mathrm{BS}} + \tfrac{L}{c})\right) \tag{1.39}$$

is defined here as the ratio of optical phase shift to input strain and varies with the GW frequency $f_{\mathrm{gw}} = \frac{\omega_{\mathrm{gw}}}{2\pi}$. $\mathfrak{T}_{h_0 \to \Delta\phi}(f_{\mathrm{gw}})$ is presented in Fig. 1.8 and further discussed for a choice of $t_{\mathrm{BS}} = 0$, laser wavelength $\lambda = 1064\,\mathrm{nm}$ and nominal interferometer armlength $L = 4000\,\mathrm{m}$ (ground-based detector LIGO).

First of all, the transfer function $\mathfrak{T}_{h_0 \to \Delta\phi}(f_{\mathrm{gw}})$ directly translates the strain amplitude h_0 of a gravitational wave with frequency f_{gw} to the optical phase shift $\Delta\phi$ in the interferometer readout. As an example, the expectable optical phase shift in the interferometer output for an incident gravitational wave with frequency $f_{\mathrm{gw}} = 1000\,\mathrm{Hz}$ and strain $h_0 = 10^{-20}$ can be determined using Fig. 1.8. We read off $\mathfrak{T}_{h_0 \to \Delta\phi}(f_{\mathrm{gw}} = 1000\,\mathrm{Hz}) \approx 4.6 \cdot 10^{10}\,\mathrm{rad} \overset{(1.39)}{=} \frac{\Delta\phi(1000\,\mathrm{Hz})}{h_0}$, and this yields an optical phase shift of $\Delta\phi(1000\,\mathrm{Hz}) = 10^{-20} \cdot 4.6 \cdot 10^{10}\,\mathrm{rad} = 4.6 \cdot 10^{-10}\,\mathrm{rad}$.

Next, the shape of the transfer function is characteristic for Michelson interferometers and interferometer-like systems and will show up several times in this thesis. For low GW frequencies, the transfer function is constant, and towards high frequencies (here $f_{\mathrm{gw}} > 10^4\,\mathrm{Hz}$) it rolls off with f_{gw}^{-1}. That is, waves with higher frequencies show a smaller impact on the optical phase of laser light sensing the space-time than waves with low frequencies, since the stretching effect on the space-time partially cancel for $\lambda_{\mathrm{gw}} < 2L$. The absolute term towards low frequencies emphasise that GWs in this band vary too slowly to have a suppressing impact on the light travel time (for $\lambda_{\mathrm{gw}} \gg 2L$).

In order to proof this mathematically, we need to rewrite the transfer function as follows. For the sake of simplicity, we set $t_{\mathrm{BS}} = 0$ arbitrarily. Then, the fraction in Eq. (1.39) can be expanded by $2\pi L$ and becomes

$$
\begin{aligned}
\mathfrak{T}_{h_0 \to \Delta\phi}(f_{\mathrm{gw}}) &= \frac{2c \cdot 2\pi L}{\lambda f_{\mathrm{gw}} \cdot 2\pi L} \sin\left(2\pi f_{\mathrm{gw}} \tfrac{L}{c}\right) \cos\left(2\pi f_{\mathrm{gw}} \tfrac{L}{c}\right) \\
&= \frac{4\pi L}{\lambda} \frac{\sin\left(2\pi f_{\mathrm{gw}} \tfrac{L}{c}\right)}{2\pi f_{\mathrm{gw}} \tfrac{L}{c}} \cos\left(2\pi f_{\mathrm{gw}} \tfrac{L}{c}\right) \\
&= \frac{4\pi L}{\lambda} \mathrm{sinc}\left(2\pi f_{\mathrm{gw}} \tfrac{L}{c}\right) \cos\left(2\pi f_{\mathrm{gw}} \tfrac{L}{c}\right)
\end{aligned}
$$

with the cardinal sine function $\mathrm{sinc}(x) := \frac{\sin(x)}{x}$. For high frequencies, the f_{gw}^{-1}-behaviour provided by the sinc-function gets dominant, since the sine and the cosine are both bounded to $[-1,1]$. For low frequencies the cosine becomes one, and so does the sinc-function, since $\lim\limits_{x \to 0} \frac{\sin(x)}{x} = 1$. Hence, for low frequencies, the transfer function is constant with the value $\frac{4\pi L}{\lambda}$, which yields for the 4 km interferometer $\frac{4\pi L}{\lambda} = \frac{4\pi \cdot 4000\,\mathrm{m}}{1064 \cdot 10^{-9}\,\mathrm{m}} \approx 4.7 \cdot 10^{10}$ rad (Fig. 1.8).

Finally, deep drops in the roll-off are notable. These nulls appear at frequencies for which the transfer function gives zero. This is the case if the sine or the cosine vanishes in Eq. (1.39). We find

$$
\mathfrak{T}_{h_0 \to \Delta\phi}(f_{\mathrm{gw}}) = 0 \iff 2\pi f_{\mathrm{gw}} \tfrac{L}{c} = N\pi \ \lor \ 2\pi f_{\mathrm{gw}} \tfrac{L}{c} = (2N+1)\tfrac{\pi}{2}\,,
$$

where N is an integer number. The first condition determines for which frequencies the sine vanishes (for arguments $\pi, 2\pi, \ldots, N\pi$, i.e., all even multiples of $\frac{\pi}{2}$), the second condition when the cosine vanishes (for arguments $\frac{\pi}{2}, \frac{3\pi}{2}, \ldots, (2N+1)\frac{\pi}{2}$, i.e. all uneven multiples of $\frac{\pi}{2}$). Altogether, we find

$$
\mathfrak{T}_{h_0 \to \Delta\phi}(f_{\mathrm{null}}^{\mathrm{IFO}}(N)) = 0 \iff \frac{2\pi f_{\mathrm{null}}^{\mathrm{IFO}}(N)L}{c} = N \cdot \frac{\pi}{2} \iff f_{\mathrm{null}}^{\mathrm{IFO}}(N) = N \cdot \frac{c}{4L}\,, \tag{1.40}
$$

with the frequencies at which the N-th zero in the interferometer transfer function appear, $f_{\mathrm{null}}^{\mathrm{IFO}}(N)$. Exemplarily, for the 4 km interferometer discussed above, the first null appears at $f_{\mathrm{null}}^{\mathrm{IFO}}(N = 1) = 1 \cdot \frac{3 \cdot 10^8\,\frac{\mathrm{m}}{\mathrm{s}}}{4 \cdot 4\,\mathrm{km}} = 18750\,\mathrm{Hz}$.

We have studied the Michelson interferometer in sufficient detail for this thesis and can identify it as a possible apparatus to detect gravitational waves with a well-known transfer function. Nonetheless, we will now sketch the limitations.

1.3.5 Limits for Ground-Based Interferometers

The Michelson interferometer seems to be a suitable apparatus to detect gravitational waves. However, every IFO is limited by noise sources. First of all, the most challenging noise in LIGO, GEO600 and VIRGO is nowadays the gravity gradient noise due to local gravitational field variations, e.g., by clouds or moving rocks under the Earth's surface. The gravity gradient noise prevents the ground-based laser interferometers from the detection of gravitational waves below 10 Hz [HT98].

Second, the sensitivity performance is limited at the optimal frequency by shot noise. That is, the light in the interferometer can be described by discrete photons and their emission from the laser obeys a Poisson statistic. Thus, the detector does not measure a constant light power incidence, but is in danger to misinterprete the varying optical power as GW influence according to Eq. (1.31). Turning up the laser power will reduce this noise. However, a fundamental threshold seems to stop the infinite enhancement of laser power. This is the 'standard quantum limit' that describes the interplay between shot noise and radiation pressure noise. The latter originates from the photons hitting the mirror's surface and transferring momentum to them on reflection [Cav97] and counteract the shot noise decrease. However, techniques like squeezing are existing which can bypass the standard quantum limit [GKSftLSC11].

Third, seismic noise shakes the optics which define the optical path in the IFO and degrades the detector performance towards low frequencies. This manifests itself in the steep rise in Fig. 1.5 for LIGO and Advanced LIGO below 10 Hz. In order to prevent displacement noise due to seismic motion, the end mirrors are suspended and decoupled from the Earth's vibration. This in turn gives new noise contributions which we will not describe any further since they are out of scope for this thesis. A detailed noise analysis of ground-based GW laser interferometers can be found in [Mag08; Sau94].

The question now arises how the sensitivity of ground-based GW detectors could be increased besides an increase of laser power. Lowering the laser wavelength raises the detector performance, since smaller armlength changes could be sensed. However, the laser wavelength could be decreased only by a small amount. Below 300 nm, the optics start to absorb the energetic ultra-violet radiation, heat up and could be destroyed in the worst case. Far more promising is the increase of the armlength, since then the measurement track becomes longer and the differential distance change $\Delta L(t)$ from Eq. (1.31) grows. However, the armlengths are limited on Earth by cost, space and the curvature of the Earth's surface.

The limited detection frequency regime from some Hz to kHz were the main reasons to think about alternatives and add-ons for ground-based detectors on Earth.

In order to prevent the gravity gradient noise from spoiling the measurements, one seeks for a place where it vanishes. For gravitation can not be shielded, such a place does not exist. However, in space, the gradient of gravity is much weaker than on Earth and does not limit the performance towards low frequencies. Going to space has even more advantages. Due to the capability of building long arm interferometers (million kilometre), the detection window moves to the frequency regime of $10^{-4} - 1\,\text{Hz}$. Thus, the space-based detectors do not compete against the interferometers on Earth but instead complement their detection frequency range. Moreover, much more GW sources lie in the mHz band than in the higher frequency band of ground-based detectors. The rest of this thesis deals with the challenges and opportunities of gravitational wave detection in space.

1.4 Gravitational Wave Detection in Space

In this section, we will derive the light travel time for a photon interchanged between two S/C and influenced by an incident gravitational wave. The first approach is to calculate the time of flight between two static spacecraft, which is extended to moving S/C in the subsequent step. As a special case, the result for a monochromatic GW signal is formulated as implemented in the simulation (Ch. 5). The derivation is in principle similar to that in Sec. 1.3.3, but now more generalised. Additionally, relativistic effects on the photon path are introduced.

1.4.1 Principles of Space-Based Gravitational Wave Detection

In the last section, we discussed a Michelson interferometer as an appropriate device for gravitational wave detection on Earth. In order to minimise the gravity gradient noise, and to bridge to the low frequency part of the gravitational wave spectrum, it is reasonable to bring the detector to space.

The principle setup of the currently planned space-based gravitational wave detectors such as LISA or the DECI-Hertz Gravitational wave Observatory (DECIGO) [KAN+08] consists of laser light sensing the distance between two spacecraft for incident gravitational wave shifts. Due to the giant distances (several thousands (DECIGO) to millions of kilometre (LISA)) between the spacecraft and the resulting power loss of the exchanged light due to diffraction, the back-reflection of (weak) incoming laser light is not practical. Instead, one-way measurements are performed. The interferometric signals for GW signal decoding are then combined from the one-way measurements in post-processing. Exemplarily, the Michelson interferometer from Sec. 1.3 can be combined by four links. Roughly speaking, these are BS → end mirror in arm 1, end mirror in arm 1 → BS, BS → end mirror in arm 2 and end mirror in arm 2 → BS.

Each S/C is equipped with a local laser and an optical readout system which sends out light to the distant S/C and simultaneously detects the beat-note between incoming weak light and strong local laser light, as shown in Fig. 1.9.
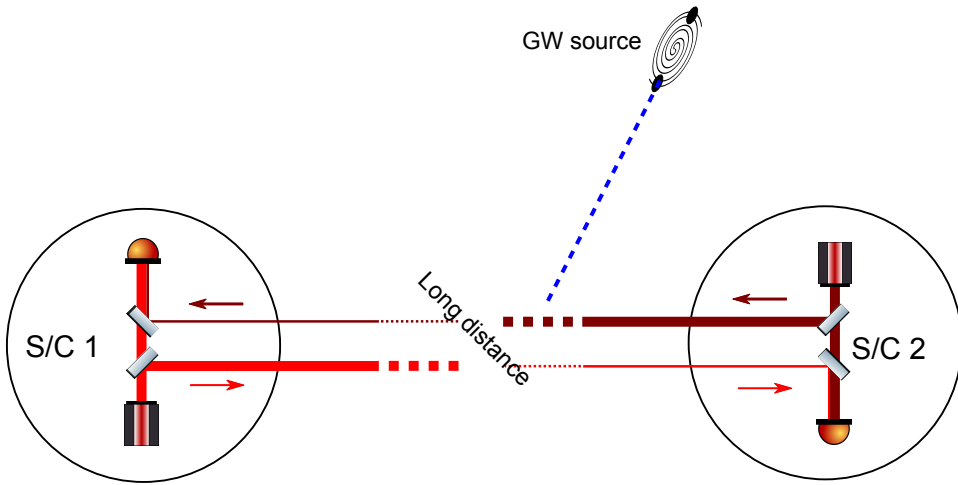
Figure 1.9: The link readout scheme for space-based detectors, shown for one arm consisting of two laser links. Each spacecraft is equipped with a laser transmitting light to the distant spacecraft which probes the space-time for gravitational waves. The received weak light is mixed with the strong onboard laser and gives a beat-note in which the accumulated phase shift due to GW (propagating along the blue line) is decoded.

The light propagating between the S/C accumulates phase shifts due to gravitational waves along the link. The gravitational wave signal itself can be extracted from the combination of multiple one-link measurements in post-processing as described in Ch. 3 and 4. We will now derive the phase shift $\Delta\phi(t)$ due to GW for a single link in space.

1.4.2 Generic Gravitational Wave Signal in a Static One-Way Link

In the following, we will investigate the gravitational wave detection in a *static* one-link measurement in space. Static means in this context that the macroscopic length L_0 of the detection link is not changing with time. In other words, L_0 excludes any variation (e.g., due to displacement noise).

Two S/C are interchanging light as depicted in Fig. 1.10. The first one is sending, indexed in the following as 'send', with constant position $\vec{x}_{\text{send}}$. The second S/C is receiving, indexed in the following as 'recv', with constant position $\vec{x}_{\text{recv}}$. The fixed spacecraft are separated by a nominal distance of L_0 in space with a unit vector $\vec{n}_{\text{send}}$ pointing from sending to receiving spacecraft contrary to the unit vector $\vec{n}_{\text{recv}}$ pointing from the receiving S/C in the direction of light reception. Note that only for a static case, $\vec{n}_{\text{send}} = -\vec{n}_{\text{recv}}$. In general, for moving spacecraft, point-ahead effects occur (Sec. 1.4.3).

In Fig. 1.10 and the subsequent derivation, the S/C are taken to be point masses for the sake of simplicity. A gravitational wave is assumed to travel along an
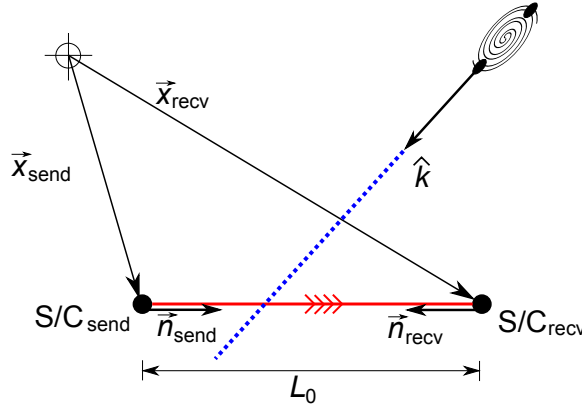
Figure 1.10: A single link with an incident gravitational wave. L_0 is the undisturbed spatial distance between sending and receiving spacecraft with constant position vectors $\vec{x}_{\text{send}}$ and $\vec{x}_{\text{recv}}$, respectively. They interchange laser light (red line) along the S/C-to-S/C link. The GW propagates along $\hat{k}$, marked here by the blue line, and is in general non-perpendicular to the measuring track.

arbitrary direction $\hat{k}$. We now want to compute the armlength variation due to the incident GW and follow [CR03]. Another approach based on Doppler tracking was discussed by [EW75].

Since the disturbance of a GW is weak, we have seen in Sec. 1.2, Eq. (1.3), that the components of the metric tensor can be expanded in a Taylor series:

$$g_{\mu\nu} = \eta_{\mu\nu} + h_{\mu\nu} + \mathcal{O}(h_{\mu\nu}^2) \,,$$

with small perturbation $h_{\mu\nu}$ in a flat Minkowskian space described by the metric $(\eta_{\mu\nu}) = \text{diag}\,(-1,1,1,1)$. In GR, the 4-D geodetic distance $\mathcal{L}$ in space-time between the events 'S/C$_{\text{send}}$ sends light at time t_{send}', denoted $(ct_{\text{send}}, \vec{x}_{\text{send}})$, and 'S/C$_{\text{recv}}$ receives light at time t_{recv}', designated $(ct_{\text{recv}}, \vec{x}_{\text{recv}})$, can in principle be calculated via the path length integral

$$\mathcal{L} = \int\limits_{(ct_{\text{send}}, \vec{x}_{\text{send}})}^{(ct_{\text{recv}}, \vec{x}_{\text{recv}})} \mathrm{d}s = \int\limits_{(ct_{\text{send}}, \vec{x}_{\text{send}})}^{(ct_{\text{recv}}, \vec{x}_{\text{recv}})} \sqrt{g_{\mu\nu}\,\mathrm{d}x^\mu\,\mathrm{d}x^\nu} \,, \tag{1.41}$$

where $\mathrm{d}s^2 = g_{\mu\nu}\,\mathrm{d}x^\mu\,\mathrm{d}x^\nu$ from Eq. (1.4) was used. Since we are investigating the interchange of light (that is, $\mathrm{d}s^2 = 0$), we can write down the line element

$$0 = \mathrm{d}s^2 = g_{\mu\nu}\,\mathrm{d}x^\mu\,\mathrm{d}x^\nu = -c^2\,\mathrm{d}t^2 + \delta_{ij}\,\mathrm{d}x^i\,\mathrm{d}x^j + h_{ij}\,\mathrm{d}x^i\,\mathrm{d}x^j \,,$$

with Latin indices i, j running $1, 2, 3$. t denotes (to first order) the proper time of a photon sent from $\vec{x}_{\text{send}}$ to $\vec{x}_{\text{recv}}$ sensing the geodesic distance $\mathcal{L}$. The timelike

components of $\boldsymbol{h}$, i.e. $h_{\alpha 0}$ and $h_{0\alpha}$, are zero since we found out in Sec. 1.2 that the GW tensor is purely spatial in the TT system (cf. Eq. (1.18)). Rearrangement gives the *spatial* line element $\mathrm{d}r$, and we emphasize the time and space dependence of the gravitational wave tensor:

$$\mathrm{d}r = c\,\mathrm{d}t = \sqrt{\delta_{ij}\,\mathrm{d}x^i\,\mathrm{d}x^j + h_{ij}(t,\vec{x})\,\mathrm{d}x^i\,\mathrm{d}x^j} = \sqrt{\mathrm{d}x^i\,\mathrm{d}x^j\left(\delta_{ij} + h_{ij}(t,\vec{x})\right)}\,.$$

We can write the GW with an arbitrary wave vector $\vec{k}_{\mathrm{gw}}$ and a tensorial 'amplitude' $\boldsymbol{h}_0$ including the polarisation in a plane wave approximation as

$$\boldsymbol{h}(t,\vec{x}) = \boldsymbol{h}_0 \mathrm{e}^{\mathrm{i}(\omega_{\mathrm{gw}}t - \vec{k}_{\mathrm{gw}}\cdot\vec{x})} = \boldsymbol{h}_0 \mathrm{e}^{\mathrm{i}(c|\vec{k}_{\mathrm{gw}}|t - \vec{k}_{\mathrm{gw}}\cdot\vec{x})} = \boldsymbol{h}_0 \mathrm{e}^{\mathrm{i}c|\vec{k}_{\mathrm{gw}}|(t - \frac{\hat{k}\cdot\vec{x}}{c})}$$

where we used Eq. (1.14), $\omega_{\mathrm{gw}} = c|\vec{k}_{\mathrm{gw}}|$, and $\hat{k} = \frac{\vec{k}_{\mathrm{gw}}}{|\vec{k}_{\mathrm{gw}}|}$. Thus, it is reasonable to write in the following

$$h_{ij}(t,\vec{x}) = h_{ij}(t - \tfrac{\hat{k}\cdot\vec{x}}{c})\,. \tag{1.42}$$

Altogether, we have reduced the 4-D integral for the geodetic distance $\mathcal{L}$, Eq. (1.41), to a 3-D integral yielding the spatial distance $\ell(t)$:

$$\ell(t) = \int\limits_{\vec{x}_{\mathrm{send}}}^{\vec{x}_{\mathrm{recv}}} \mathrm{d}r = \int\limits_{\vec{x}_{\mathrm{send}}}^{\vec{x}_{\mathrm{recv}}} \sqrt{\mathrm{d}x^i\,\mathrm{d}x^j\left(\delta_{ij} + h_{ij}(t - \tfrac{\hat{k}\cdot\vec{x}}{c})\right)}\,. \tag{1.43}$$

The integration along the photon path between the S/C with respect to x^i and x^j is here very inconvenient. The first obvious step is to substitute the argument of the integrand by a new function ξ. Though, in order to perform the substitution process within the integral, the derivative of ξ with respect to x^i is needed and we end up with the same inconvenience. The second step is thus to formulate the variables t and $\vec{x}$ dependent of a parameter, w, that describes the photon path and that can then be used as the integration variable:

$$\xi(w) := t(w) - \frac{\hat{k}\cdot\vec{x}(w)}{c}\,. \tag{1.44}$$

We introduced here the functions $t(w)$ and $\vec{x}(w)$ giving space-time coordinates $(ct,\vec{x})$ along the photon path. Since the simulation described in Ch. 5 computes the GW signal with respect to the receiving spacecraft, it is benefical to formulate $t(w)$ and $\vec{x}(w)$ with the use of the receiving time t_{recv} and the unit direction vector $\vec{n}_{\mathrm{recv}} = \frac{\vec{x}_{\mathrm{send}} - \vec{x}_{\mathrm{recv}}}{|\vec{x}_{\mathrm{send}} - \vec{x}_{\mathrm{recv}}|}$ of light reception (Fig. 1.10). That is,

$$t(w) := t_{\mathrm{recv}} - \frac{1}{c}(w_{\mathrm{recv}} - w)\,, \quad \vec{x}(w) := \vec{x}_{\mathrm{recv}} + (w_{\mathrm{recv}} - w)\vec{n}_{\mathrm{recv}}\,, \tag{1.45}$$

introducing w with units of length that parametrises the spatial distance to the sending spacecraft with position $\vec{x}_{\mathrm{send}}$.

$t(w)$ is defined here as follows. For light just sent from the far spacecraft, i.e., $w = 0$, the time coordinate function gives $t(0) = t_{\text{recv}} - \frac{w_{\text{recv}}}{c}$, which equals the sending time t_{send}. Furthermore, if S/C_{recv} receives the light, $w = w_{\text{recv}}$, we find $t(w_{\text{recv}}) = t_{\text{recv}}$. Correspondingly, $\vec{x}(w = 0) = \vec{x}_{\text{recv}} + w_{\text{recv}}\vec{n}_{\text{recv}} = \vec{x}_{\text{send}}$ and $\vec{x}(w_{\text{recv}}) = \vec{x}_{\text{recv}}$. Inserting (1.45) in (1.44) yields

$$\xi(w) = t_{\text{recv}} - \frac{1}{c}(w_{\text{recv}} - w) - \frac{\hat{k} \cdot (\vec{x}_{\text{recv}} + (w_{\text{recv}} - w)\vec{n}_{\text{recv}})}{c} \ . \tag{1.46}$$

The time-dependent spatial distance $\ell(t)$ from Eq. (1.43) becomes by integral substitution

$$\ell(t) = \int_{\vec{x}_{\text{send}}}^{\vec{x}_{\text{recv}}} \mathrm{d}r = \int_{\vec{x}_{\text{send}}}^{\vec{x}_{\text{recv}}} \sqrt{\mathrm{d}x^i \, \mathrm{d}x^j \left[\delta_{ij} + h_{ij}\left(t(w) - \frac{\hat{k}\cdot\vec{x}(w)}{c}\right)\right]}$$

$$= \int_{w_{\text{send}}}^{w_{\text{recv}}} \mathrm{d}w \sqrt{\frac{\mathrm{d}x^i}{\mathrm{d}w}\frac{\mathrm{d}x^j}{\mathrm{d}w} \left[\delta_{ij} + h_{ij}\left(t(w) - \frac{\hat{k}\cdot\vec{x}(w)}{c}\right)\right]}$$

$$= \int_{0}^{w_{\text{recv}}} \mathrm{d}w \sqrt{(-n_{\text{recv}}^i)(-n_{\text{recv}}^j) \left[\delta_{ij} + h_{ij}\left(t(w) - \frac{\hat{k}\cdot\vec{x}(w)}{c}\right)\right]}$$

due to $\frac{\mathrm{d}x^i(w)}{\mathrm{d}w} = \frac{\mathrm{d}}{\mathrm{d}w}[x_{\text{recv}}^i - wn_{\text{recv}}^i] = -n_{\text{recv}}^i$. The expressions n_{recv}^i and n_{recv}^j are the components of the unit vector $\vec{n}_{\text{recv}}$ (i.e., $\vec{n}_{\text{recv}}^2 = 1$), while δ_{ij} denote the components of the identity matrix. Hence, $n_{\text{recv}}^i \delta_{ij} n_{\text{recv}}^j = \vec{n}_{\text{recv}}^2 = 1$ and

$$\ell(t) = \int_{0}^{w_{\text{recv}}} \mathrm{d}w \sqrt{1 + n_{\text{recv}}^i h_{ij}\left(t(w) - \frac{\hat{k}\cdot\vec{x}(w)}{c}\right) n_{\text{recv}}^j} \ .$$

Next, we perform a Taylor expansion with respect to small $|h_{ij}| \ll 1$ as in Sec. 1.3.3:

$$\ell(t) \simeq \int_{0}^{w_{\text{recv}}} \mathrm{d}w \left(1 + \frac{1}{2}n_{\text{recv}}^i h_{ij}\left(t(w) - \frac{\hat{k}\cdot\vec{x}(w)}{c}\right) n_{\text{recv}}^j\right)$$

$$= w_{\text{recv}} + \frac{1}{2}n_{\text{recv}}^i n_{\text{recv}}^j \int_{0}^{w_{\text{recv}}} \mathrm{d}w \, h_{ij}\left(t(w) - \frac{\hat{k}\cdot\vec{x}(w)}{c}\right) \ . \tag{1.47}$$

The parametric value w_{recv} corresponds exactly to the unperturbed distance between the two spacecraft, L_0. However, Eq. (1.47) is still an unpractical formula, because the components of the GW tensor h_{ij} are dependent on the function $\xi(w) = t(w) - \frac{\hat{k}\cdot\vec{x}(w)}{c}$. At this point it is possible to perform the second integral substitution.

It directly follows from (1.46) that

$$\frac{\mathrm{d}\xi(w)}{\mathrm{d}w} = \frac{1}{c} + \frac{\hat{k} \cdot \vec{n}_{\mathrm{recv}}}{c} = \frac{1}{c}(1 + \hat{k} \cdot \vec{n}_{\mathrm{recv}})$$

because t_{recv}, w_{recv} and $\vec{x}_{\mathrm{recv}}$ are constant in w, and therefore the substitution of the integral in (1.47) yields:

$$
\begin{aligned}
\ell(\xi(t)) &= L_0 + \frac{1}{2} n^i_{\mathrm{recv}} n^j_{\mathrm{recv}} \int\limits_{\xi(0)}^{\xi(w_{\mathrm{recv}})} \frac{\mathrm{d}\xi}{\frac{1}{c}(1 + \hat{k} \cdot \vec{n}_{\mathrm{recv}})} \, h_{ij}(\xi) \\
&= L_0 + \frac{c}{2} \cdot \frac{n^i_{\mathrm{recv}} n^j_{\mathrm{recv}}}{1 + \hat{k} \cdot \vec{n}_{\mathrm{recv}}} \int\limits_{\xi(0)}^{\xi(w_{\mathrm{recv}})} \mathrm{d}\xi \, h_{ij}(\xi) \, .
\end{aligned}
\tag{1.48}
$$

From this, we can see the impact of GW on a single link. The nominal separation L_0 of sending and receiving S/C varies by the amount of the second term, depending on the orientation of the detector arm with respect to the wave incidence. Here, the integral bounds are according to Eq. (1.46) given by

$$
\begin{aligned}
\xi(0) &= t_{\mathrm{recv}} - \frac{\hat{k} \cdot \vec{x}_{\mathrm{recv}}}{c} - \frac{L_0}{c}(1 + \hat{k} \cdot \vec{n}_{\mathrm{recv}}) \, , \tag{1.49a} \\
\xi(w_{\mathrm{recv}} = L_0) &= t_{\mathrm{recv}} - \frac{\hat{k} \cdot \vec{x}_{\mathrm{recv}}}{c} \, . \tag{1.49b}
\end{aligned}
$$

Before we proceed, note that if we choose $\vec{n}_{\mathrm{recv}} = \vec{e}_1$, $w_{\mathrm{recv}} = L_1$, make use of Eq. (1.18) and further assume normal incidence (that is here $\hat{k} = \vec{e}_3$ and thus $\hat{k} \cdot \vec{x}_{\mathrm{recv}} = \hat{k} \cdot \vec{n}_{\mathrm{recv}} = 0$) we can derive the result from Sec. 1.3.3 for the Michelson IFO, Eq. (1.33) for $t_{\mathrm{BS}} = t_{\mathrm{recv}} - \frac{L_1}{c}$.

Taking ℓ from (1.48) and divide it by the speed of light c, one gets a formula for the light travel time between the two spacecraft:

$$
\begin{aligned}
T(t_{\mathrm{recv}}) &= \frac{L_0}{c} + \frac{1}{2} \cdot \frac{n^i_{\mathrm{recv}} n^j_{\mathrm{recv}}}{1 + \hat{k} \cdot \vec{n}_{\mathrm{recv}}} \int\limits_{t_{\mathrm{recv}} - \frac{\hat{k} \cdot \vec{x}_{\mathrm{recv}}}{c} - \frac{L_0}{c}(1 + \hat{k} \cdot \vec{n}_{\mathrm{recv}})}^{t_{\mathrm{recv}} - \frac{\hat{k} \cdot \vec{x}_{\mathrm{recv}}}{c}} \mathrm{d}\xi \, h_{ij}(\xi) \\
&=: T_0 + \Delta T(t_{\mathrm{recv}}) \, .
\end{aligned}
\tag{1.50}
$$

$T_0 = \frac{L_0}{c}$ is here the *static* light travel time between sender and receiver. The integral term in $\Delta T(t_{\mathrm{recv}})$, however, describes the accumulated variation of light travel time

along the optical path due to incident gravitational waves:

$$\Delta T(t_{\text{recv}}) = \frac{1}{2} \cdot \frac{n_{\text{recv}}^i n_{\text{recv}}^j}{1 + \hat{k} \cdot \vec{n}_{\text{recv}}} \int\limits_{t_{\text{recv}} - \frac{\hat{k} \cdot \vec{x}_{\text{recv}}}{c} - \frac{L_0}{c}(1 + \hat{k} \cdot \vec{n}_{\text{recv}})}^{t_{\text{recv}} - \frac{\hat{k} \cdot \vec{x}_{\text{recv}}}{c}} \mathrm{d}\xi \, h_{ij}(\xi) \,. \tag{1.51}$$

Finally, the optical phase shift $\Delta\phi$ for light travel between sending and receiving spacecraft is computed at an arbitrary time t via

$$\Delta\phi(t) \overset{(1.29)}{=} \frac{2\pi}{\lambda} \Delta s(t) = \frac{2\pi c}{\lambda} \Delta T(t) \tag{1.52a}$$

$$= \frac{\pi c}{\lambda} \cdot \frac{\vec{n}_{\text{recv}} \otimes \vec{n}_{\text{recv}}}{1 + \hat{k} \cdot \vec{n}_{\text{recv}}} : \int\limits_{t - \frac{\hat{k} \cdot \vec{x}_{\text{recv}}}{c} - \frac{L_0}{c}(1 + \hat{k} \cdot \vec{n}_{\text{recv}})}^{t - \frac{\hat{k} \cdot \vec{x}_{\text{recv}}}{c}} \mathrm{d}\xi \, \boldsymbol{h}(\xi) \,. \tag{1.52b}$$

This is the formula that describes the optical phase shift of laser light with wavelength λ being sent between two static spacecraft while a GW is passing by. In order to formulate the equation index-free, we introduced the tensor product $\vec{a} \otimes \vec{b}$ with $(\vec{a} \otimes \vec{b})^{ij} := a^i b^j$ and make further use of the tensor contraction $\boldsymbol{A}{:}\boldsymbol{B} := A^{ij} B_{ij}$.

As a concluding remark, note that this calculation is not complete, since lensing of the photon path by external gravitational fields is neglected for the sake of simplicity. However, it could be shown recently that even with lensing, fortuitous cancellations in the TT gauge lead to the same result. We refer to [Fin09; Cor09] for further details.

1.4.3 Light Travel Time Between Two Moving Spacecraft

In practice, the spacecraft are of course not fixed and will drift relative to each other with typical velocities of up to a few $10 \, \frac{\text{m}}{\text{s}}$. It is thus important to consider the evolution of the S/C positions and the direction vector of light reception during light propagation. However, the previous calculations need only small modifications.

First, the photon path is parametrised by

$$t(w) = t_{\text{recv}} - \frac{1}{c}(w_{\text{recv}} - w) \,, \tag{1.53a}$$

$$\vec{x}(w) = \vec{x}_{\text{recv}}(t_{\text{recv}}) + (w_{\text{recv}} - w)\vec{n}_{\text{recv}}(t_{\text{recv}}) \,, \tag{1.53b}$$

$$\xi(w) = t_{\text{recv}} - \frac{w_{\text{recv}} - w}{c} - \frac{\hat{k} \cdot (\vec{x}_{\text{recv}}(t_{\text{recv}}) + (w_{\text{recv}} - w)\vec{n}_{\text{recv}}(t_{\text{recv}}))}{c} \tag{1.53c}$$

with the time-dependent unit vector $\vec{n}_{\text{recv}}(t_{\text{recv}})$. Since the constellation is not regarded as static, the position vector of the receiving spacecraft, $\vec{x}_{\text{recv}}(t_{\text{recv}})$, is time-dependent as well.
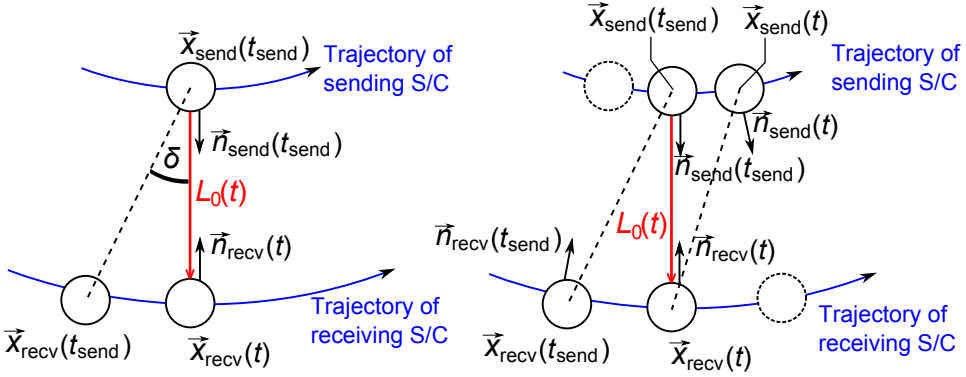
Figure 1.11: Time-dependent unit vector definition and the time argument problem. Since the spacecraft are on different trajectories (blue), the pointing direction between the spacecraft vary in time. Note that with $t_{\text{send}} = t - \frac{L_0(t)}{c}$, we found that $\vec{n}_{\text{send}}(t_{\text{send}}) = -\vec{n}_{\text{recv}}(t)$, but $\vec{n}_{\text{send}}(t_{\text{send}}) \neq -\vec{n}_{\text{recv}}(t_{\text{send}})$ and $\vec{n}_{\text{send}}(t) \neq -\vec{n}_{\text{recv}}(t)$, because all these direction vectors point ahead or backwards to future or recent S/C positions (dashed circles). The dashed line connects the positions of the S/C at the same time stamp. Since the receiving spacecraft is moving within the laser light exchange, the sender has to point ahead by an angle δ. This is the angle between the line of connection of sender and receiver at sending time (dashed) and the line of connection of sender at time emission and receiver at time of reception t. δ is called point-ahead angle.

We define the propagation direction to consider a point-ahead angle due to finite speed of light:

$$\vec{n}_{\text{recv}}(t) := \frac{\vec{x}_{\text{send}}(t - \frac{L_0(t)}{c}) - \vec{x}_{\text{recv}}(t)}{|\vec{x}_{\text{send}}(t - \frac{L_0(t)}{c}) - \vec{x}_{\text{recv}}(t)|} = -\vec{n}_{\text{send}}(t - \tfrac{L_0(t)}{c}). \tag{1.54}$$

This unit vector points at an arbitrary time of photon reception t from the receiving spacecraft to the position of the sending spacecraft at time of emission, $t - \frac{L_0(t)}{c}$, with the absolute spacecraft separation $L_0(t)$ varying in time. One has to be careful not to mix up the time arguments. Fig. 1.11 depicts spacecraft positions and unit direction vectors for different moments in time. The angle δ formed by the line of sight (LoS) between sending and receiving spacecraft both at $t - \frac{L_0(t)}{c}$ and the line of sight between sending spacecraft at time $t - \frac{L_0(t)}{c}$ and receiving S/C at time of reception t is called the point-ahead angle. For LISA, δ is less than mrad [PR10].

Second, the integration in analogy to Sec. 1.4.2 yields the time-dependent light travel time $T(t_{\text{recv}})$ between sending and receiving spacecraft at time of light reception. This includes effects due to gravitational waves as well and is given by

$$T(t_{\text{recv}}) = T_0(t_{\text{recv}}) + \Delta T(t_{\text{recv}}) \tag{1.55}$$

where the time shift due to gravitational waves reads as

$$\Delta T(t_{\text{recv}}) = \frac{1}{2} \cdot \frac{\vec{n}_{\text{recv}}(t_{\text{recv}}) \otimes \vec{n}_{\text{recv}}(t_{\text{recv}})}{1 + \hat{k} \cdot \vec{n}_{\text{recv}}(t_{\text{recv}})} : \int\limits_{\xi(0)}^{\xi(w_{\text{recv}})} \mathrm{d}\xi \, \boldsymbol{h}(\xi) \tag{1.56}$$

with the integral limits

$$\xi(0) = t_{\text{recv}} - \frac{\hat{k} \cdot \vec{x}_{\text{recv}}(t_{\text{recv}})}{c} - \frac{L_0(t_{\text{recv}})}{c}(1 + \hat{k} \cdot \vec{n}_{\text{recv}}(t_{\text{recv}})), \tag{1.57a}$$

$$\xi(w_{\text{recv}}) = t_{\text{recv}} - \frac{\hat{k} \cdot \vec{x}_{\text{recv}}(t_{\text{recv}})}{c}. \tag{1.57b}$$

$T_0(t_{\text{recv}})$ in Eq. (1.55) is again the physical travel time for a photon between receiving and sending S/C. We will specify the relativistic effects on T_0 in Sec. 1.4.4. Contrariwise, $L_0(t_{\text{recv}})$ is the absolute separation of sender and receiver, i.e.,

$$L_0(t_{\text{recv}}) = |\vec{x}_{\text{recv}}(t_{\text{recv}}) - \vec{x}_{\text{send}}(t_{\text{send}})|. \tag{1.58}$$

Note again that the change in light travel time due to incident GW, $\Delta T(t)$, converts to an optical phase shift of the sensing light with wavelength λ via $\Delta\phi(t) = \frac{2\pi c}{\lambda}\Delta T(t)$.

In the special case of a monochromatic gravitational wave $\boldsymbol{h}(\xi) = \boldsymbol{h}_0 e^{\mathrm{i}\omega_{\text{gw}}\xi}$ with angular frequency ω_{gw} and the coordinate ξ given by Eq. (1.53c), the integral in Eq. (1.56) yields for an arbitrary time coordinate t:

$$\Delta T(t) = \frac{L_0(t)}{2c} \cdot (\vec{n}_{\text{recv}}(t) \otimes \vec{n}_{\text{recv}}(t)) \cdot \text{sinc}\left(\frac{\omega_{\text{gw}} L_0(t)}{2c}(1 + \hat{k} \cdot \vec{n}_{\text{recv}}(t))\right) \cdot$$
$$\cdot e^{\mathrm{i}\frac{\omega_{\text{gw}} L_0(t)}{2c}(1 + \hat{k} \cdot \vec{n}_{\text{recv}}(t))} : \boldsymbol{h}_0 e^{\mathrm{i}\omega_{\text{gw}}\xi(0)} \tag{1.59}$$

with the cardinal sine function $\text{sinc}(x) \equiv \frac{\sin(x)}{x}$ and the S/C-to-S/C distance $L_0(t)$. Eq. (1.59) is used in Ch. 5 in a slightly simplified manner for the simulation of the GW phase shift in interferometric single-link measurements. A derivation of (1.59) can be found in appendix B.

The absolute of the (normalised) gravitational wave single-link transfer function

$$\mathfrak{T}_{\text{link}}(f_{\text{gw}}) := \text{sinc}\left(\frac{2\pi f_{\text{gw}} L_0(t)}{2c}(1 + \hat{k} \cdot \vec{n}_{\text{recv}}(t))\right) \cdot e^{\mathrm{i}\frac{2\pi f_{\text{gw}} L_0(t)}{2c}(1 + \hat{k} \cdot \vec{n}_{\text{recv}}(t))}, \tag{1.60}$$

is presented in Fig. 1.12 for $\hat{k} \cdot \vec{n}_{\text{recv}}(t) \equiv 0$ and $L_0(t) \equiv 5 \cdot 10^9 \, \text{m}$ neglecting any time dependence here. It is called normalised here since the absolute term at low frequencies has the value 1.

The frequency-dependent behaviour is remarkably similar to that of the transfer function for the Michelson interferometer discussed in Sec. 1.3.4 except for the different frequency regions of $10^{-5} \dots 1 \, \text{Hz}$ versus $10 \dots 10^6 \, \text{Hz}$, which are basically due to the order of magnitude discrepancies in the armlengths. At low frequencies,

Gravitational wave transfer function for one LISA link
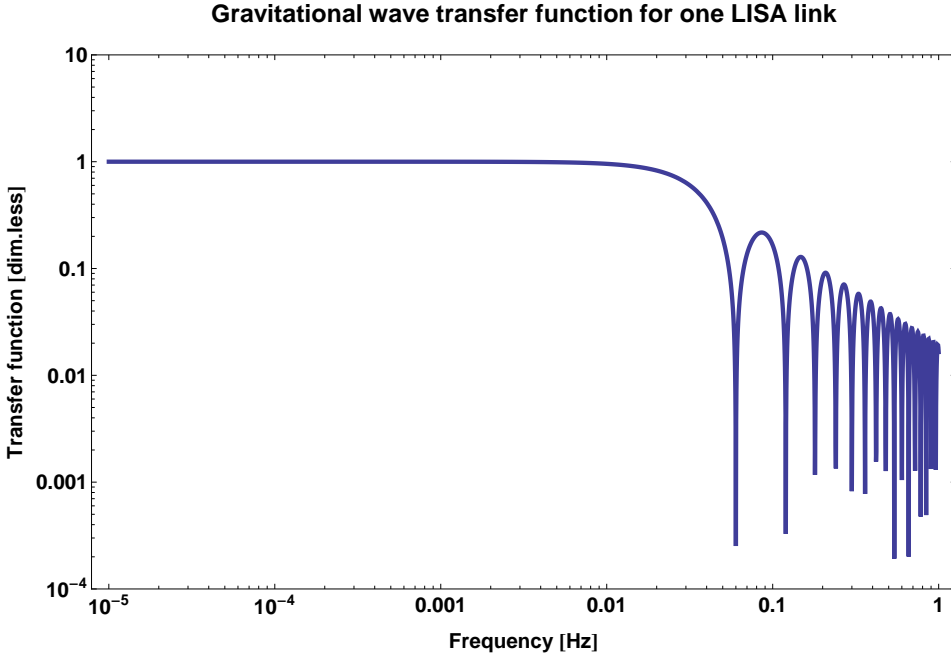
Figure 1.12: Absolute of the (normalised) single link transfer function $\mathfrak{T}_{\text{link}}(f_{\text{gw}})$ for LISA. At low frequencies, the transfer function has the constant value of one (hence it is called normalised), and for frequencies $f_{\text{gw}} > 0.01\,\text{Hz}$ it rolls off with f_{gw}^{-1}. Furthermore, $|\mathfrak{T}_{\text{link}}(f_{\text{gw}})|$ comprises nulls for multiples of $0.06\,\text{mHz}$. That is, the time variation $\varDelta T$ for incident gravitational waves with these frequencies will vanish in the single link signal.

the (normalised) transfer function has a constant value and rolls off with f_{gw}^{-1} towards high frequencies. Furthermore, the high frequency zeros appear as well, with the above choice ($\hat{k} \cdot \vec{n}_{\text{recv}} = 0$ and $L_0 = 5 \cdot 10^9\,\text{m}$) at

$$f_{\text{null}}^{\text{link}}(N) = N \cdot \frac{c}{L_0}\,. \tag{1.61}$$

The first zero can thus be found at $f_{\text{null}}^{\text{link}}(N = 1) = 0.06\,\text{Hz}$.

1.4.4 Relativistic Laser Links

In the previous section, we derived expressions for the overall light travel time, $T(t) = T_0(t) + \varDelta T(t)$, describing light sent between two moving spacecraft in the presence of gravitational waves. In that derivation, no GR effects entered in the expression for $T_0(t)$ that would account for static gravitational fields. We will now resolve this issue. Following [CRVP05], a perturbation coefficient ϵ comparing the relativistic (rest) energy and gravitational potential of a gravitational field source

can be introduced, defined as

$$\epsilon := \frac{GM}{rc^2} \, , \tag{1.62}$$

where $G = 6.67 \cdot 10^{-11} \, \frac{\text{m}^3}{\text{kg}\,\text{s}^2}$ denotes Newton's gravitational constant. In our scenario, $M = M_\odot = 2 \cdot 10^{30}$ kg is the mass of the Sun and r the distance between the receiving spacecraft and the Sun. Note that the spacecraft are assumed to be placed in the solar system on a heliocentric orbit. Hence, $r \approx 150 \cdot 10^6$ km and $\epsilon \approx 10^{-8}$. Using this perturbation parameter, we can approximate the light travel time between two spacecraft without gravitational waves by

$$T_0(t) = \overset{(0)}{T_0}(t) + \overset{(\frac{1}{2})}{T_0}(t) + \overset{(1)}{T_0}(t) + \mathcal{O}(\epsilon^{\frac{3}{2}}) \tag{1.63}$$

with $\overset{(\alpha)}{T_0}$ denoting the time shift of the order ϵ^α. This expansion is known as 'Post Newtonian bookkeeping' [Wil85]. The order $\epsilon^{\frac{3}{2}}$ can be neglected because it corresponds to a time accuracy of 10^{-12} s or mm in length. However, the S/C separation of space-based GW detectors could be determined not better than on a meter level, corresponding to first order in ϵ or, equivalently, to 10^{-8} s light travel time accuracy. Thus, ϵ^1 is sufficient for our purposes.

The following expressions for the different approximation terms $\overset{(0)}{T_0}, \overset{(\frac{1}{2})}{T_0}$ and $\overset{(1)}{T_0}$ can be derived by solving the geodesic equations for the sending and receiving spacecraft. Subsequently, one can compute the photon path by solving the geodesic equation between sender and receiver with the boundaries computed before. The underlying space-time geometry is taken to be the Schwarzschild metric, the spacecraft orbits are Keplerian. For more details, we refer to [Pac14] and [CRVP05].

Zero Order Contribution

In 0-th order one gets

$$\overset{(0)}{T_0}(t) = \frac{1}{c} |\vec{x}_{\text{recv}}(t) - \vec{x}_{\text{send}}(t)| \, , \tag{1.64a}$$

where $\vec{x}_{\text{recv}}(t)$ and $\vec{x}_{\text{send}}(t)$ are dependent on an arbitrary photon reception time t. Hence, $\overset{(0)}{T_0}(t)$ is the light travel time at one moment t in time in a flat space-time for two spacecraft being fixed relative to each other. The direction of the light ray is further given by

$$\overset{(0)}{\vec{n}_{\text{recv}}}(t) = \frac{\vec{x}_{\text{send}}(t) - \vec{x}_{\text{recv}}(t)}{|\vec{x}_{\text{send}}(t) - \vec{x}_{\text{recv}}(t)|} \, . \tag{1.64b}$$

Corrections of Order One-Half

Obviously, zero order corrections are neither realistic nor as exact as needed. In order to increase the accuracy, the motion of the receiving spacecraft during the light travel time and the resulting aberration are included. The corrections of order $\epsilon^{\frac{1}{2}}$ are accordingly given by

$$\overset{(\frac{1}{2})}{T_0}(t) = \frac{\vec{v}_{\text{recv}}(t)}{c^2} \cdot (\vec{x}_{\text{recv}}(t) - \vec{x}_{\text{send}}(t)), \tag{1.65a}$$

$$\overset{(\frac{1}{2})}{\vec{n}}_{\text{recv}} = \frac{\frac{1}{c}[\vec{v}_{\text{recv}}(t) - \overset{(0)}{\vec{n}}_{\text{recv}}(t)(\overset{(0)}{\vec{n}}_{\text{recv}}(t) \cdot \vec{v}_{\text{recv}}(t))]}{|\frac{1}{c}[\vec{v}_{\text{recv}}(t) - \overset{(0)}{\vec{n}}_{\text{recv}}(t)(\overset{(0)}{\vec{n}}_{\text{recv}}(t) \cdot \vec{v}_{\text{recv}}(t))]|}, \tag{1.65b}$$

where $\vec{v}_{\text{recv}}(t) = \dot{\vec{x}}_{\text{recv}}(t)$ is the velocity of the receiving spacecraft with respect to the solar system.

Corrections of Order One

Finally, the inclusion of the Sun's gravitational field in the framework of GR (and therefore an acceleration along the line of sight of the S/C) gives the contribution

$$\overset{(1)}{T_0}(t) = \frac{1}{2}\left(\frac{\vec{v}^2_{\text{recv}}(t)}{c^2} + \left(\frac{\overset{(0)}{\vec{n}}_{\text{recv}}(t) \cdot \vec{v}_{\text{recv}}(t)}{c}\right)^2\right)\overset{(0)}{T_0}(t)$$

$$+ \overset{(0)}{\vec{n}}_{\text{recv}}(t)\left(\frac{2GM_\odot}{c^3}\overset{(0)}{\chi}(\overset{(0)}{T_0}, \overset{(0)}{\vec{n}}_{\text{recv}}) - \frac{GM_\odot\vec{x}_{\text{recv}}(t)}{2|\vec{x}_{\text{recv}}(t)|^3 c}[\overset{(0)}{T_0}(t)]^2\right), \tag{1.66a}$$

and for the normalised reception vector contribution,

$$\overset{(1)}{\vec{n}}_{\text{recv}}(t) = -\frac{1}{2c^2}\overset{(0)}{\vec{n}}_{\text{recv}}(t)[\vec{v}^2_{\text{recv}}(t) - (\overset{(0)}{\vec{n}}_{\text{recv}}(t) \cdot \vec{v}_{\text{recv}}(t))^2]$$

$$- \frac{GM_\odot}{2|\vec{x}_{\text{recv}}(t)|^2 c}[\vec{x}_{\text{recv}}(t) - \overset{(0)}{\vec{n}}_{\text{recv}}(t)(\overset{(0)}{\vec{n}}_{\text{recv}}(t) \cdot \vec{x}_{\text{recv}}(t))]$$

$$+ \frac{2GM_\odot}{c^3\overset{(0)}{T_0}(t)}[\overset{(0)}{\chi}(\overset{(0)}{T_0}, \overset{(0)}{\vec{n}}_{\text{recv}}) - \overset{(0)}{\vec{n}}_{\text{recv}}(t)(\overset{(0)}{\vec{n}}_{\text{recv}}(t) \cdot \overset{(0)}{\chi}(\overset{(0)}{T_0}, \overset{(0)}{\vec{n}}_{\text{recv}}))], \tag{1.66b}$$

where the vector function

$$\overset{(0)}{\chi}(\overset{(0)}{T_0}(t), \overset{(0)}{\vec{n}}_{\text{recv}}(t)) = \frac{\vec{x}_{\text{send}}(t) - \vec{n}_{\text{recv}}(t)(\vec{n}_{\text{recv}}(t) \cdot \vec{x}_{\text{send}}(t))}{r^2_{\text{send}}(t) - (\vec{n}_{\text{recv}}(t) \cdot \vec{x}_{\text{send}}(t))^2} \cdot (\overset{(0)}{r}(t) - r_{\text{send}}(t))$$

$$+ \vec{n}_{\text{recv}}(t)\ln\left(\frac{\overset{(0)}{\vec{n}}_{\text{recv}}(t) \cdot (\vec{x}_{\text{send}}(t) + c\overset{(0)}{T_0}(t)) + \overset{(0)}{r}(t)}{\overset{(0)}{\vec{n}}_{\text{recv}}(t) \cdot \vec{x}_{\text{send}}(t) + r_{\text{send}}(t)}\right) \tag{1.66c}$$

provides the Shapiro time-delay effect [Sha64], i.e. the prolongation of light travel time close to massive objects. r_{send} denotes the instantaneous physical distance to the sending spacecraft from the gravitational field source, i.e., the Sun. Hence, since the Sun is placed in the origin, $r_{\mathrm{send}}(t) = |\vec{x}_{\mathrm{send}}(t)|$. Furthermore, $\overset{(0)}{r}(t)$ is defined by

$$\overset{(0)}{r}(t) := (c\overset{(0)}{T_0}(t) + \overset{(0)}{\vec{n}}_{\mathrm{recv}}(t) \cdot \vec{x}_{\mathrm{send}}(t))^2 + \vec{x}_{\mathrm{send}}^2(t) - (\overset{(0)}{\vec{n}}_{\mathrm{recv}}(t) \cdot \vec{x}_{\mathrm{send}}(t))^2 . \quad (1.66\mathrm{d})$$

A comparison between the different orders is shown in Ch. 6. Eqn. (1.64a), (1.65a) and (1.66a) are used in the simulation to generate the overall light travel time $T(t)$ including gravitational wave shifts ΔT from Eq. (1.59).

Iterative Procedure without Gravitational Effects

An alternative to the one-half order corrections is an iterative procedure to determine the S/C separations. In order to estimate the light travel time between sending and receiving spacecraft, T_0, one can iterate [MG11]

$$T_0[i+1] = \frac{1}{c}|\vec{x}_{\mathrm{send}}(t - T_0[i]) - \vec{x}_{\mathrm{recv}}(t)|, \quad T_0[0] = \frac{L_0}{c} , \quad (1.67)$$

where $i \in \mathbb{N}_0$ counts the number of iterations and L_0 denotes the undisturbed and time-independent spacecraft separation. In this formula, $\vec{x}_{\mathrm{send}}(t - T_0)$ denotes the position of the sending spacecraft at time T_0 before reception on the far spacecraft at position $\vec{x}_{\mathrm{recv}}(t)$, as sketched before in Fig. 1.11. The iteration of (1.67) yields the light travel time between moving spacecraft, but excludes GR effects. However, since we need models accurate to nanoseconds for the light travel time computation, gravitational effects must be included. Thus, the simulational results in Ch. 6 are obtained with the analytic approach to first order in ϵ.

In this chapter, we first introduced the mathematical framework for GW theory, and listed properties and sources. In the last sections, we discussed the detection principle on ground and in space. Subsequently, we derived in detail equations for the observable quantity: the differential light travel time in terms of optical phase shifts due to incident gravitational waves in the detector arms. Furthermore, we introduced equations for the light travel time influenced by static gravitational fields from the Sun. Accurate models for the light travel time are important for implementing noise cancellation schemes discussed in Ch. 3. In the next chapter, we will discuss a proposed GW detector in space, the Laser Interferometer Space Antenna.

2 The Laser Interferometer Space Antenna

In this chapter, we will give an overview of the space-based mission concept Laser Interferometer Space Antenna that aims at gravitational wave detection in the low frequency band. The first section deals with a mission outline including a sketch of its history, followed by a section about the mission details relevant for this thesis. Next, the various noise sources in the LISA data streams and possible suppression strategies are discusssed briefly. In order to find a mathematical formulation for the detector outputs, a consistent index notation used throughout the thesis is introduced and phase readout signals are carefully defined. The chapter's overall goal is finally the formulation of the interferometric phase measurements as recorded onboard the spacecraft, which are extensively used in the subsequent chapters.

2.1 Mission Description

This section deals with the mission concept Laser Interferometer Space Antenna. In Sec. 2.1.1, we will give a short introduction to the historical evolution since the early 90's, followed by an overview about the LISA mission in Sec. 2.1.2.

2.1.1 Concept History

The Laser Interferometer Space Antenna is a deep space satellite mission concept to detect and study gravitational waves in the low frequency band ($10^{-4} - 10^{-1}$ Hz, cf. Fig. 1.5). LISA was first proposed as a cornerstone mission to ESA in 1993 within the Horizon 2000 program. This early proposal consisted of four S/C forming a five million kilometre armlength interferometer in space. However, cost targets could not be met. Instead, in 1997, knowledge and money from ESA and the National Aeronautics and Space Administration (NASA) was bundled to review and advance the design of LISA resulting in the Pre-Phase-A Report in 1998 [Tea98]. The constellation consisted of three identical spacecraft forming an equilateral triangle with five million kilometre lateral length. This constellation should trail the Earth

on an orbit around the Sun with 20° angular shift. Its mission duration was planned to be five years [BDF$^+$11]. An industrial LISA mission formulation study in Europe by the company Astrium started in 2005, and throughout the study, the three S/C constellation with five million kilometre armlength was maintained.

Recently in 2011, NASA cut off financing and LISA needed a reformulation to save costs. A smaller version of it, the evolved Laser Interferometer Space Antenna, also called New Gravitational wave Observatory (eLISA/NGO), was the output of this phase [ESA11]. eLISA mainly differs from LISA in its armlength (one million kilometre instead of five million to save propellent and thus launch mass) and the number of arms (two instead of three). eLISA consists of one mother and two daughter satellites forming a 'V'-shaped constellation. Orbits and the main measurement principle remained the same. The mission duration was shortened to two years.

Currently, the term 'LISA-like mission' summarises all million kilometre armlength laser interferometer concepts in space with the purpose to detect gravitational waves. In 2013, the science theme 'Gravitational Universe' has been selected for the ESA L3 mission in the 2030's [ftec13] which can best be covered by a LISA-like mission.

However, for the rest of the thesis, we will ignore this discussion and regard the original LISA mission with five million kilometre armlength and three arms, as it was formulated in [Tea11b].

2.1.2 LISA – A Mission Overview

The science objectives of the Laser Interferometer Space Antenna include the observation of the formation, growth and merger of massive black holes as well as the survey of stellar populations and dynamics in galactic nuclei. Other important science topics are the investigation of compact stellar-mass binaries, the structure of galaxy and, possibly, the detection of primordial gravitational waves from the early universe. Subsequently, LISA tests the principles of GR as well as cosmology and could discover unforeseen GW sources (Sec. 1.2.4). Its best sensitivity is at 3 mHz and, as often said, it will open a complete new window of astronomy, since it aims at signals complementary to both the whole EM spectrum but also to that of ground-based detectors.

LISA consists of three identical spacecraft following heliocentric orbits around the Sun with a small eccentricity of $< 10^{-2}$. They form a giant triangle shape with five million kilometre armlength. The center of mass (CoM) is trailing the Earth at an angle of 20° as shown in Fig. 2.1. The constellation plane is tilted by 60° to the ecliptic. As a result, the triangle is roughly preserving its form and moreover performs a clockwise cartwheel motion with the orbital frequency of one cycle per year. The orbits are designed such that the constellation remains as 'rigid' as possible and flexing is kept small at an amount of $\approx 1\,\%$ of the detector armlength [NKDV05], i.e., 50000 km in total armlength change over one year.
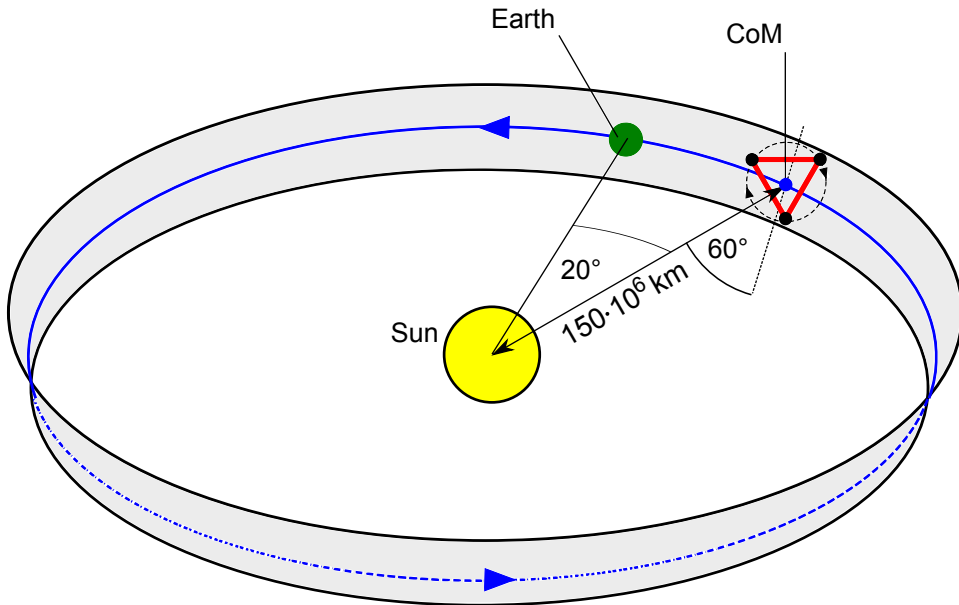
Figure 2.1: The constellation and orbit for LISA. The detector's center of mass (blue dot) trails the Earth (green) on a heliocentric orbit with 150 million kilometre radius. The angle between Earth and the constellation's CoM is 20°. Within a one-year cycle around the Sun, the triangular constellation performs a clockwise cartwheel motion by 360°. In order to sustain the triangular formation as rigid as possible, the constellation plane (grey) is tilted by 60° with respect to the ecliptic.

This will become important when the interferometric measurements performed on each S/C are combined to extract the gravitational wave signal, as we will see in Ch. 3 and 4.

The spacecraft dynamics vary the angles of the triangular constellation by $\pm 1°$ and the orbits shown in Fig. 2.1 provide a constant angle of the constellation with respect to the Sun [ESA11]. The latter ensures a thermally stable environment and, more important, that the solar panels constantly collect sunlight to charge batteries onboard the spacecraft. Not least, the distance to Earth on the heliocentric orbit is roughly constant (≈ 50 million kilometre) and thus the radio communication with the Earth including the data downlink is stable.

Each spacecraft contains two identical optical benches (OB) which are made of Zerodur® to guarantee sufficient path length stability in the presence of temperature variations. A vacuum chamber associated with each OB houses a golden cube test mass designed to follow geodesic motion only. These test masses are marking the endpoints of the detector arms, as sketched in Fig. 2.2. Note here that due to the variation of the angle between two detector arms, it is not possible to rigidly connect the optical benches.
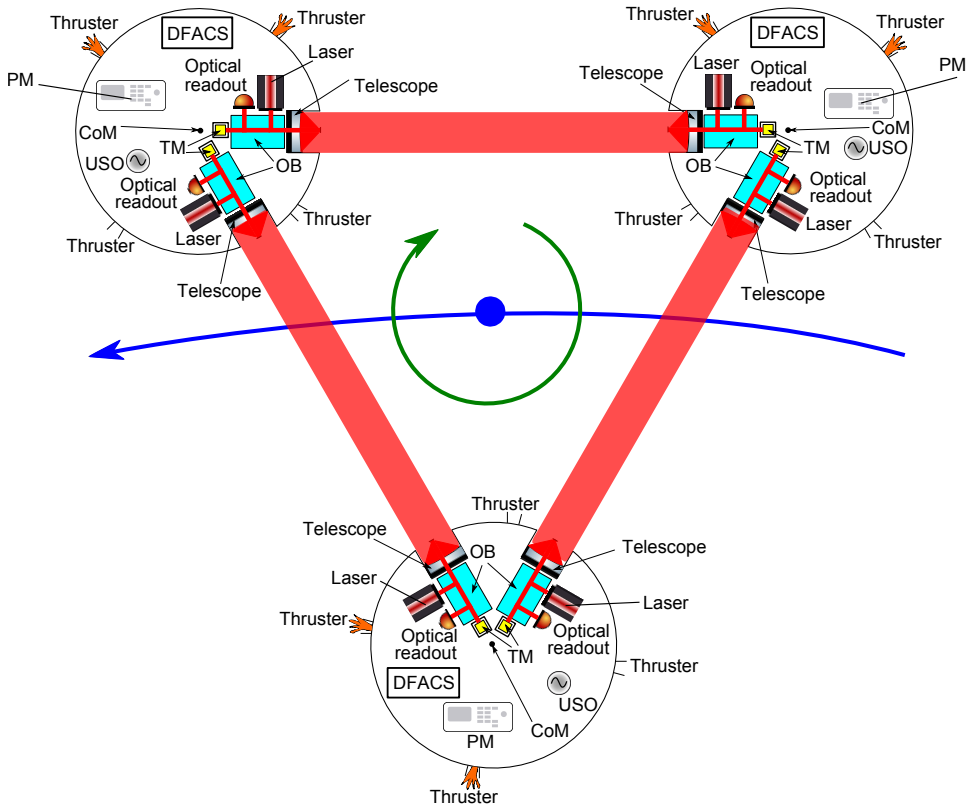
Figure 2.2: Overview of the LISA constellation scheme. Three identical satellites form a triangular detector constellation with its CoM (blue dot) following a heliocentric orbit (blue line) while performing a cartwheel rotation (green arrow). Each S/C is equipped with two optical benches (OB), and each OB is housing a test mass (TM) defining the ends of the detector arms, lasers, telescopes and an optical readout system. The analogue data from the readout scheme is digitised and analysed by an onboard phasemeter (PM), which itself is triggered by an onboard clock signal provided by the ultra-stable oscillator (USO). The test mass position is read out to high precision by sensors, and the drag-free attitude control system (DFACS) controls the thrusters to counteract unwanted acceleration of the test masses.

Each optical bench is further connected to a laser, an optical readout scheme, a telescope to receive light from and send light to the distant spacecraft, and further optics and electronics discussed in detail in Sec. 2.5. In order to analyse the readout signals, the S/C hosts a phasemeter (PM) and an ultra-stable oscillator (USO) as a clock. Furthermore, a drag-free attitude control system (DFACS) reduces unwanted acceleration relative to the test masses, controlling the S/C position with micro-Newton thrusters relative to the undisturbed TM.

Laser light with a wavelength of 1064 nm and power of 1.2 W is sent through the 40 cm telescope to the distant spacecraft where heterodyne interferometry between the incoming and the local laser beam is performed [ESA11]. Heterodyne means the comparison of two laser beams with different frequencies. This measurement yields a beat-note, the phase of which here carries information about the gravitational waves that modulate the space-time, and hence the light travel time between the satellites, as we derived in Ch. 1.

It is not hard to see that LISA-like missions need extraordinary techniques to achieve their goal. To get a feeling for this, we can calculate the absolute armlength shift due to a GW via Eq. (1.27). For a strong GW with a strain amplitude $h = 10^{-21}$ along the LISA arms of nominal armlength $L = 5 \cdot 10^9$ m, we get an armlength variation of $\Delta L = \frac{1}{2}hL = 2.5 \cdot 10^{-12}$ m. Thus, interferometry to picometre precision in space is required to detect GW, which is an extraordinary challenge. Therefore, a technology demonstrator called LISA Pathfinder was launched in December of 2015 and is on its way to the Lagrange point L1 to test the functionality of critical components as, e.g., the test mass position readout and the drag-free control of the satellite to picometre precision [ABB+09; MAA+13].

2.2 Details of the Mission Concept LISA

This section comprises a survey of the technical details for the LISA mission that are relevant for this thesis. At first, we will discuss absolute frequency shifts due to the chosen spacecraft orbits, followed by a deeper elucidation of the LISA measurement principle and an overview of the subsequent data processing steps onboard and on ground.

2.2.1 Doppler Shifts

As explained in Sec. 2.1.2, LISA will move on a heliocentric orbit with a tilted constellation plane such that the constellation rotates by one cycle per year. Furthermore, gravitational effects acting on the S/C from, e.g., the Earth and Jupiter can not be shielded and the constellation will flex. Both effects result in relative velocities between the spacecraft along the arms and hence interchanged light will obtain a Doppler shift. Due to the Sagnac effect introduced by the cartwheel rotation, the Doppler effect is directional dependent. We will now estimate the orbital shift of the laser frequency without Sagnac effect.

The Doppler frequency change for light exchanged between sender (send) with frequency ν_{send} and receiver (recv) with received frequency ν_{recv} for a relative line of sight velocity v_{rel} is given by

$$\nu_{\text{recv}} = \nu_{\text{send}} \sqrt{\frac{1 + \frac{v_{\text{rel}}}{c}}{1 - \frac{v_{\text{rel}}}{c}}} \, .$$

The relative Doppler shift due to orbital motion of the S/C then reads as

$$\frac{\Delta\nu}{\nu_{\text{send}}} = \frac{\nu_{\text{recv}} - \nu_{\text{send}}}{\nu_{\text{send}}} = \sqrt{\frac{1 + \frac{v_{\text{rel}}}{c}}{1 - \frac{v_{\text{rel}}}{c}}} - 1 \,,$$

where $\Delta\nu := \nu_{\text{recv}} - \nu_{\text{send}}$ denotes the absolute frequency shift between sender and receiver frequency. However, the relative motion between the satellites is in maximum $v_{\text{rel}} \approx \pm 15 \, \frac{\text{m}}{\text{s}}$ [ESA11] and very small compared to c, i.e., $\frac{v_{\text{rel}}}{c} \ll 1$. Thus, we can use the approximation $\frac{1}{1-\epsilon} \simeq 1 + \epsilon$ (with $\epsilon \ll 1$) to obtain

$$\frac{\Delta\nu}{\nu_{\text{send}}} \simeq \sqrt{(1 + \tfrac{v_{\text{rel}}}{c})(1 + \tfrac{v_{\text{rel}}}{c})} - 1 = 1 + \tfrac{v_{\text{rel}}}{c} - 1 = \tfrac{v_{\text{rel}}}{c}$$

and finally end up with

$$\Delta\nu \simeq \frac{v_{\text{rel}}}{c} \nu_{\text{send}} \,. \tag{2.1}$$

Eq. (2.1) yields $\Delta\nu \approx \frac{\pm 15 \, \frac{\text{m}}{\text{s}}}{3 \cdot 10^8 \, \frac{\text{m}}{\text{s}}} \cdot 3 \cdot 10^{14} \, \text{Hz} = \pm 15 \, \text{MHz}$ for a relative LoS velocity of $15 \, \frac{\text{m}}{\text{s}}$ and a central laser frequency of $300 \, \text{THz}$. This is the maximal expected Doppler shift for LISA in the detection beat-note due to the arm flexing. As a result, the interferometry between incoming and local lasers onboard each S/C is performed with two laser beams of different frequencies, since the local laser is not shifted in frequency.

2.2.2 Measurement Principle

The science measurement in the LISA mission consists of detecting in-band changes at picometre level in the million kilometre separation between the spacecraft. The reference points are marked by free-falling test masses, housed in the satellites. The spacecraft will follow the geodesics of the test masses, even under presence of disturbances like, e.g., solar wind. In order to establish this so-called drag-free mode, the positions of the TM are read out interferometrically and capacitively. These signals are then used as error signals to control the onboard micro-Newton thrusters in order to actuate and correct for the disturbance displacements of the spacecraft. Hence, the spacecraft is maneuvered to be kept centered around the TM in the sensitive axis without acting on the TM.

The S/C equipment principle is depicted in Fig. 2.3. In order to sense the separation variation, weak laser light ($\approx 300 \, \text{pW}$, narrow wine red line in Fig. 2.3) from the distant S/C is received by the telescope and interferes with light (red line) from the local laser (with a frequency different by several MHz), in the following called local oscillator (LO). A gravitational wave is then recorded as a change in the phase of the beat-note at the photodetector of this so-called science interferometer. The picometre level of precision necessary for GW detection (Sec. 2.1.2) is realised by measuring the phase using a digital phasemeter with microcycle accuracy [EN09]. Note that the overall TM-to-TM separation and its variation due to GW is combined
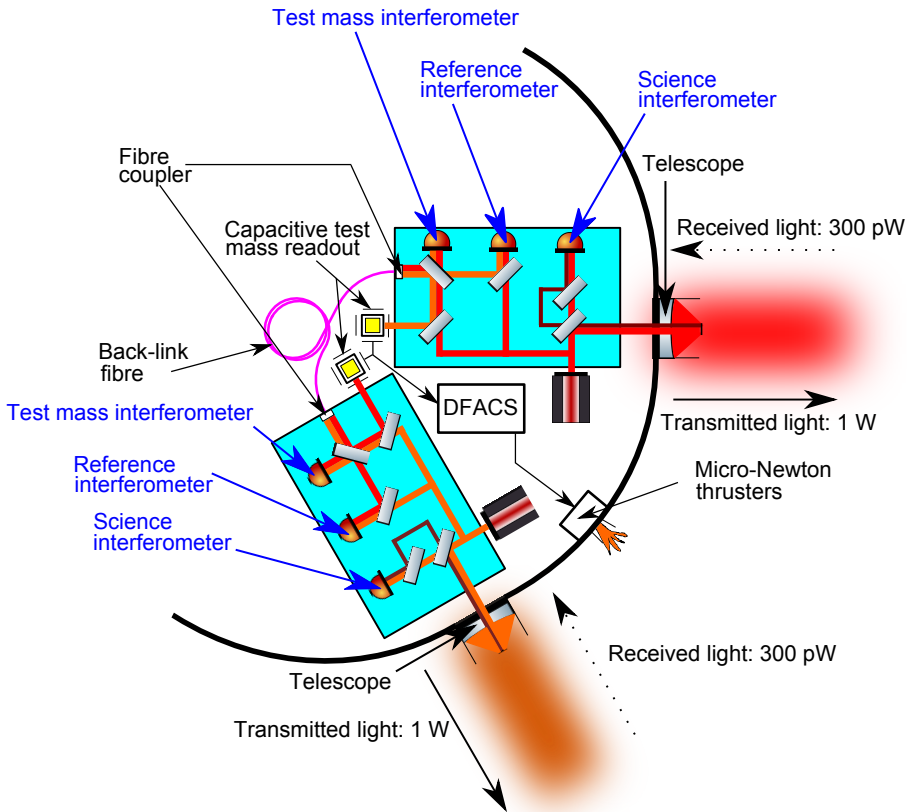
Figure 2.3: Interferometric measurements on one LISA satellite, exemplarily explained for the horizontally drawn OB. Light of a local laser (red) is used for transmission to the distant S/C and to sense the space-time variation between for GW interaction. Simultaneously, the light interferes on the local optical bench with the received weak light (wine red) to form the science interferometer beat-note. The test mass motion is read out in the TM interferometer using light (orange) from the adjacent optical bench transmitted through a back-link fibre. The reference IFO directly compares local laser and adjacent local laser. Moreover, the spacecraft is controlled by DFACS including TM position readout and thruster actuation such that the S/C follows the test masses.

from three interferometric measurements: TM-to-OB on the far spacecraft, OB-to-OB between sending and receiving S/C, and OB-to-TM on the receiving spacecraft. This concept is called 'split interferometry configuration' and we will come back to it in Sec. 2.5.

Laser light (orange) from the adjacent optical bench is used for the interferometric TM readout. Since the benches are not rigidly connected to provide the angular pointing flexibility of $\pm 1°$ (Sec. 2.1.2), the OB-to-OB connection is established by

an extensile optical fibre. Laser light is transmitted through this so-called back-link fibre and senses the motion of the test mass relative to the optical bench. As a reference, the light from the local laser (red) is used to form the beat-note within the test mass interferometer. Additionally, we will see in Ch. 3 that it is crucial for the data processing to compare the two local lasers without any test mass signal. This task is performed with the use of a reference interferometer. Therefore, again the laser light from the adjacent optical bench needs to be transferred through the back-link fibre, and vice versa for the adjacent reference interferometer.

For LISA, the obvious difference to ground-based detection explained in Sec. 1.3.2 is the comparison of lasers with *different* frequencies on each S/C. This has basically two reasons. First, by motion of the S/C constellation, the travelling light suffers an orbital Doppler shift and hence a frequency shift, e.g., for LISA-like missions $\approx \pm 15\,\text{MHz}$ in maximum, as calculated in Sec. 2.2.1. Second, the photodetectors on each S/C have only a limited detection band of $\approx 20\,\text{MHz}$. Therefore, due to orbital Doppler shifts aditionally to the heterodyne frequencies of some MHz, one needs to tune and control the laser frequencies of all lasers such that the detected beat-note signal lies within the detection range of the PDs. This procedure is called frequency lock relying on a so-called frequency plan. We will examine this in more detail in Ch. 4.

2.2.3 Data Processing

In contrast to ground-based gravitational wave detectors, LISA performs one-way measurements for the science signal. This is due to the power loss of about a factor of 10^{10} along the 5 million kilometre track. That is, if the distant spacecraft sends $1\,\text{W}$ of laser power, only a few $100\,\text{pW}$ will be received on the local spacecraft, and passive reflection with the same diffraction loss would result in undetectable low power. The one-way measurements make it impossible to remove laser frequency fluctuations, which is the dominant noise source (Sec. 2.3), by simply differencing incoming and local light at a beam splitter on the receiving optical bench. Moreover, heterodyne interferometry is performed on the S/C such that the simple Michelson scheme discussed in Sec. 1.3 does not apply here. Hence, the interferometric Michelson combination needs to be synthesised in post-processing on ground and, therefore, the data are to be digitally converted and sent to Earth by a radio downlink.

The interferometric beat-notes of the science, reference and TM interferometer are passed through an anti-alias filter and then digitised onboard via an analog-to-digital converter (ADC) [BBB+14]. This ADC is triggered by a reference clock from the USO as schematically drawn in Fig. 2.4. After the digitisation process, a high precision phasemeter determines the phase of each signal with microcycle precision. The phasemeter uses digital phase lock loops integrated in field programmable gate arrays to generate digital tracking copies of the beat-notes. The phasemeter output data is transmitted to Earth via a radio downlink and then prepared within a data pre-processing procedure for the synthesis of virtual interferometer signals. We will explain this more deeply in Sec. 5.1.
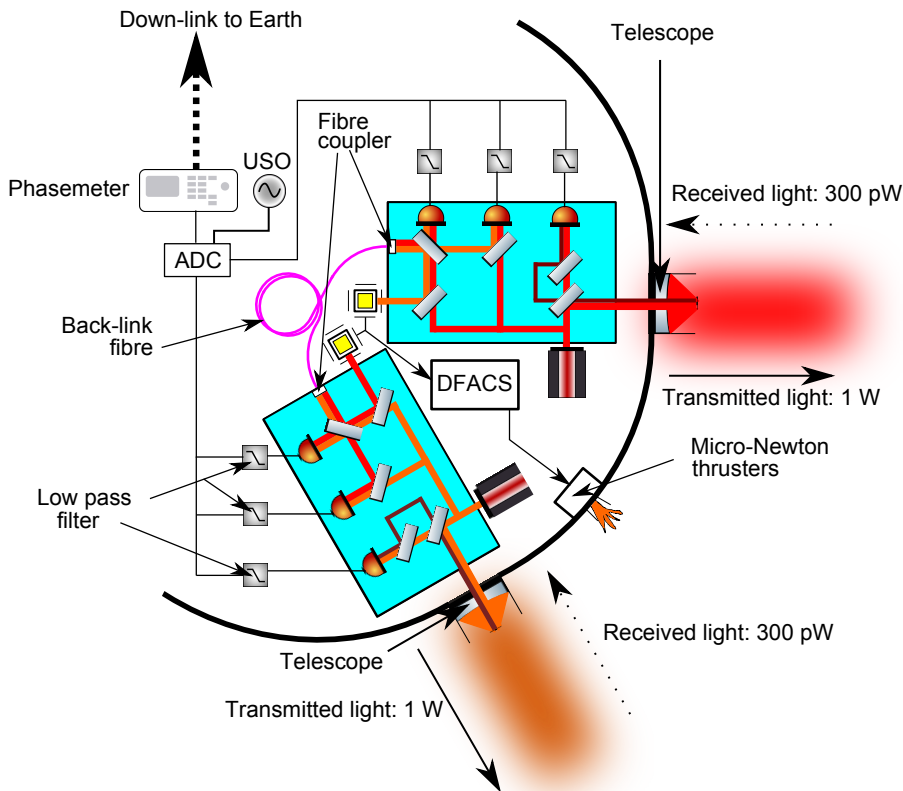
Figure 2.4: Complete LISA onboard measurement principle. Each interferometric output is fed into an anti-alias filter to suppress mirrored noise > 20 MHz and then into an analog-to-digital converter, which is triggered from an ultra-stable oscillator providing a time reference. The phase of the digitised data is determined to microcycle precision in a phasemeter, low-pass filtered and downsampled and then transmitted to Earth for further data processing and analysis.

The USO itself introduces clock jitter in the digitised data streams and, furthermore, in the additional ranging signal, thereby affecting the armlength measurements and limiting the overall performance. Additionally, the ADCs on each S/C contribute inherent jitter. Therefore, the inclusion of a pilot tone, i.e., a stable sinusoidal reference signal derived from the USO, will be used for ADC jitter correction [Bar15]. In order to suppress the differential clock jitter of the three onboard USOs, a clock tone transfer chain was proposed by [BTS+10] using sideband (SB) modulations with amplified clock noise on the outgoing light. After defining one of the clocks as a reference, these SB modulations yield sufficient data to completely remove the clock noise and allow for correction of relative clock drifts in post-processing with respect to one clock chosen as the master clock [WKB+13]. We will discuss this issue in detail in Ch. 4.

Besides clock noise, many other noise sources enter the measured data, as we will see in the subsequent section. The dominant noise source is the laser phase noise, which enters via the orbital armlength difference (up to $1\% \approx 50000\,\text{km}$) and completely swamps the science measurement, even after various laser stabilisation schemes have been applied [TML11]. To remove the laser phase noise, a post-processing method called Time-Delay Interferometry, first proposed by [AET99], has to be applied before one can search the data for gravitational waves.

Time-Delay Interferometry synthesises virtual equal-armlength interferometers by combining the measured data of the three spacecraft after time-shifting by multiples of the light travel times in the arms. Therefore, the absolute armlengths need to be determined by a separate ranging method not shown in Fig. 2.4 [EGMB+09; EGMB+11], and Kalman filters [Wan14] can be applied to achieve approximately meter accuracy between the spacecraft. The ranging scheme basically modulates pseudo random noise (PRN) as weak phase modulation on the outgoing beam sent to the far spacecraft. The receiving spacecraft can then correlate the transmitted code with the same pseudo random noise code locally generated onboard the receiving spacecraft and thus can determine the armlength with meter precision [Est12]. A detailed analysis of the post-processing method Time-Delay Interferometry will follow in Ch. 3 – 6. We will now concentrate on the various noise sources for LISA.

2.3 Noise

This section deals with the main noise sources that enter the LISA data streams, and their suppression strategies. The expressions are formulated in terms of an amplitude spectral density or linear spectral density (LSD) $\widetilde{\text{amp}}_{\text{label}}(f)$, providing information about how much noise is in a certain frequency bandwidth. The notation here is the following: 'amp' is a placeholder for the quantity that is described by the linear spectral density, e.g., ϕ for phase in radian, or ν for frequency in Hz. 'label' emphasises the special application. f is the Fourier frequency. It emphasises that the linear spectral density, defined by the square root of the Fourier transformation of the autocorrelation function of the corresponding noise time series, is in general frequency-dependent (i.e., non-white noise). Its unit is

$$[\widetilde{\text{amp}}_{\text{label}}(f)] = 1\,\frac{[\text{amp}]}{\sqrt{\text{Hz}}}\,. \tag{2.2}$$

For an overview about spectral densities we refer to [HRS02] and appendix A.

2.3.1 Inevitable Noise Sources

For the sake of simplicity, it is assumed for now that technical noise from the lasers, USOs etc. could be suppressed to an arbitrary level. However, there are inevitable noise sources where this is not possible. For LISA, the limiting physical noise contributions are acceleration and readout noise, which we will explain in the following.

Acceleration Noise

The TMs onboard each spacecraft are shielded in vacuum chambers from outer disturbances. However, self-gravity of the S/C, magnetic fields, residual gas pressure, electrostatic disturbances etc. could act on the test masses. An estimate for the TM displacement noise in terms of acceleration is given by the LSD [Tea11b]

$$\widetilde{a}_{\text{TM}} = 3 \cdot 10^{-15} \, \frac{\text{m}}{\text{s}^2 \sqrt{\text{Hz}}} \, , \tag{2.3a}$$

which is a key parameter to be verified by LISA Pathfinder. The acceleration noise converts to optical path length disturbance by $\widetilde{x}_{\text{TM}}(f) = \frac{1}{\omega^2}\widetilde{a}_{\text{TM}}$, where $\omega = 2\pi f$, since acceleration is the second time derivative of the position and thus, in Fourier space, $\mathcal{F}[a(t)] = \mathcal{F}[\ddot{x}(t)] = (\mathrm{i}\omega)^2 \mathcal{F}[x(t)]$. Taking the absolute value gives

$$\widetilde{x}_{\text{TM}}(f) = \frac{1}{\omega^2}\widetilde{a}_{\text{TM}} = 3 \cdot 10^{-15} \, \frac{\text{m}}{\text{s}^2 \sqrt{\text{Hz}}} \frac{1}{(2\pi f)^2} \, , \quad [\widetilde{x}_{\text{TM}}(f)] = 1 \, \frac{\text{m}}{\sqrt{\text{Hz}}} \, . \tag{2.3b}$$

This noise in terms of displacement can be finally translated to phase noise by multiplication with $\frac{2\pi}{\lambda}$ according to Eq. (1.36). Hence, the linear spectral density of displacement noise in terms of optical phase is given by

$$\widetilde{\phi}_{\text{TM}}(f) = \frac{2\pi}{\lambda}\widetilde{x}_{\text{TM}}(f) \approx 4.5 \cdot 10^{-10} \, \frac{\text{rad}}{\sqrt{\text{Hz} \cdot \text{s}^2}} \cdot \frac{1}{f^2} \, , \quad \left[\widetilde{\phi}_{\text{TM}}(f)\right] = 1 \, \frac{\text{rad}}{\sqrt{\text{Hz}}} \, . \tag{2.3c}$$

The wavelength of the laser light is here and elsewhere taken to be $\lambda = 1064 \, \text{nm}$.

Readout Noise

The second inevitable noise source is the readout noise entering via power measurements at the photodetectors. Shot noise, electronic noise from the PD electronics and relative power noise from the laser light add up to readout noise. In the following, a short overview about the three contributions is given.

Measuring optical power can be understood as counting photons per unit time. The photons obey a statistical Poisson distribution due to the quantum mechanical fluctuations in the laser beam, and hence the PD output is affected by fluctuations in power as well. The linear spectral density for shot noise is then [Bar15]

$$\widetilde{\phi}_{\text{shot}} = \sqrt{\frac{2e(P_{\text{sig}} + P_{\text{LO}})}{\eta\gamma P_{\text{sig}} P_{\text{LO}}}} \, . \tag{2.4a}$$

Here, $e = 1.6 \cdot 10^{-19} \, \text{C}$ is the elementary charge and P_{sig} and P_{LO} are the light powers of incoming and local laser. The quantities η and $\gamma = \gamma(\eta) = \eta\frac{e\lambda}{hc}$ with Planck's constant $h = 6.6 \cdot 10^{-34} \, \text{Js}$ and laser wavelength $\lambda = 1064 \, \text{nm}$ describe the quantum efficiency (η, dimensionless) and the resulting photodetector responsivity ($[\gamma] = 1 \, \frac{\text{A}}{\text{W}}$), respectively. A derivation and further extension of Eq. (2.4a) for sideband modulations can be found, e.g., in [Bar15]. Using the numbers from the

web application 'Gravitational Wave Observatory Designer' [BWD$^+$15; spa], we get

$$\widetilde{\phi}_{\text{shot}} = \sqrt{\frac{2 \cdot 1.6 \cdot 10^{-19}\,\text{As} \cdot (259.1 \cdot 10^{-12}\,\text{W} + 2.1 \cdot 10^{-3}\,\text{W})}{0.7 \cdot 0.69\,\frac{\text{A}}{\text{W}} \cdot 259.1 \cdot 10^{-12}\,\text{W} \cdot 2.1 \cdot 10^{-3}\,\text{W}}} = 5 \cdot 10^{-5}\,\frac{\text{rad}}{\sqrt{\text{Hz}}}\,.$$

$$(2.4\text{b})$$

The other contributions, phase noise from the photodetector electronics ($\widetilde{\phi}_{\text{el}}$) and from relative intensity noise ($\widetilde{\phi}_{\text{rin}}$) originating from laser power fluctuations, are given by [TDB$^+$12]:

$$\widetilde{\phi}_{\text{el}} = 2\frac{\widetilde{I}_{\text{el}}}{\gamma\sqrt{\eta P_{\text{sig}} P_{\text{LO}}}}\,, \quad \widetilde{\phi}_{\text{rin}} = \frac{\widetilde{n}_{\text{rin}}(P_{\text{sig}} + P_{\text{LO}})}{\sqrt{2\eta P_{\text{sig}} P_{\text{LO}}}}\,. \tag{2.5a}$$

Here, $\widetilde{I}_{\text{el}}$ and $\widetilde{n}_{\text{rin}}$ specify the electronic noise in units of $\frac{\text{A}}{\sqrt{\text{Hz}}}$ and the relative intensity noise in the laser beams in units of $\frac{1}{\sqrt{\text{Hz}}}$. With $\widetilde{I}_{\text{el}} = 5.1 \cdot 10^{-12}\,\frac{\text{A}}{\sqrt{\text{Hz}}}$ and $\widetilde{n}_{\text{rin}} = 10^{-8}\,\frac{1}{\sqrt{\text{Hz}}}$, this yields

$$\widetilde{\phi}_{\text{el}} = 2.4 \cdot 10^{-5}\,\frac{\text{rad}}{\sqrt{\text{Hz}}}\,, \quad \widetilde{\phi}_{\text{rin}} = 2.4 \cdot 10^{-5}\,\frac{\text{rad}}{\sqrt{\text{Hz}}}\,. \tag{2.5b}$$

Since shot, electronic and relative intensity noise are uncorrelated, they add up quadratically to the total readout noise, $\widetilde{\phi}_{\text{readout}}$:

$$\widetilde{\phi}_{\text{readout}} = \sqrt{(\widetilde{\phi}_{\text{shot}})^2 + (\widetilde{\phi}_{\text{el}})^2 + (\widetilde{\phi}_{\text{rin}})^2}\,. \tag{2.6a}$$

The equality of electronic noise and relative intensity noise in Eq. (2.5b) is no coincidence. The laser power P_{LO} is optimised again by the tool 'Gravitational Wave Observatory Designer' [BWD$^+$15; spa], such that the total readout noise is minimal, which occurs at this equality.

Finally, Eqn. (2.4b) and (2.5b) can be inserted in $\widetilde{\phi}_{\text{readout}}$ and give for LISA a readout noise of

$$\widetilde{\phi}_{\text{readout}} \approx 6.1 \cdot 10^{-5}\,\frac{\text{rad}}{\sqrt{\text{Hz}}}\,. \tag{2.6b}$$

Although several photodetectors are used for the LISA measurements, readout noise is by far not the dominant noise source and is considered as a secondary noise source. However, after removing the timing (laser frequency, clocks) and displacement noise in post-processing (Ch. 4), readout noise dominates the TDI output signals (cf. Ch. 6). Its largest contribution is the fundamental shot noise, which is indeed a normal design goal, i.e., not to tare technical noise sources be dominant.
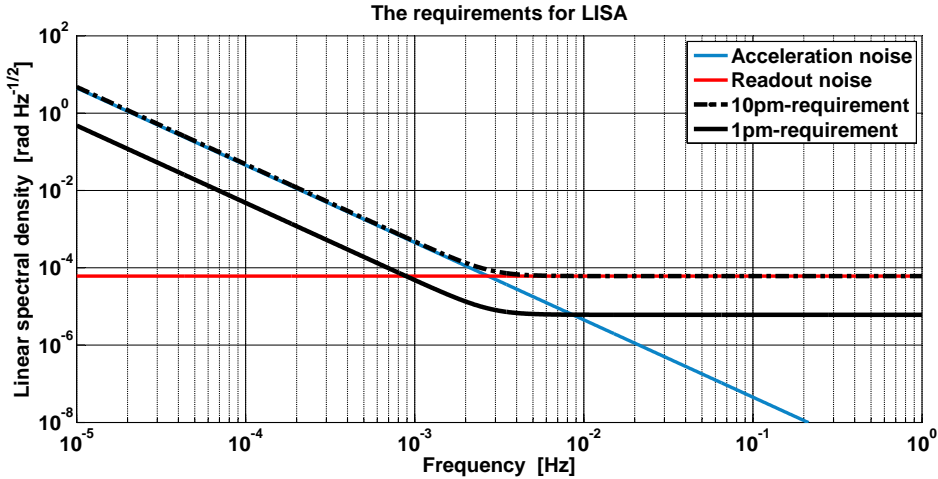
Figure 2.5: 10 pm- and 1 pm-requirement for LISA in terms of optical phase. The 10 pm-requirement (dashed black) described by the NSF is constructed from the constant readout noise limit (red) and the $\frac{1}{f^2}$-behaviour of the acceleration noise limit (blue). The inclusion of a 'safety' factor of $\frac{1}{10}$ gives then the 1 pm-requirement (solid black). Any noise below this line will not spoil the LISA measurements.

Finally, note that the light power strongly differs between the discussed interferometers. As explained in Sec. 2.2.2, we have three interferometers on each OB. For the science IFO, weak laser light from the far spacecraft is interfered with the strong local laser, whereas for the TM readout, the two local lasers are compared, the same holds for the reference interferometer. Hence, the level of readout noise will differ between the different interferometers due to their respective shot noise levels. We will come back to this in Sec. 5.2.4 for the noise simulation.

2.3.2 Noise Shape Function and the LISA Requirements

$\widetilde{\phi}_{\mathrm{TM}}(f)$ and $\widetilde{\phi}_{\mathrm{readout}}$ are the LSDs of the noise sources limiting the performance of LISA. They are plotted in Fig. 2.5. Any technical noise should be suppressed below those two contributions. However, uncorrelated noise adds up quadratically, and hence it could happen that technical noise marginally below displacement and readout noise add up to a technical noise floor larger than the physically limiting noise contributions. Therefore, in order to formulate requirements for the technical noise such as laser frequency noise or USO phase noise, it is common practice to use a conservative 'engineering factor' of $\frac{1}{10}$ for all requirements. Furthermore, a frequency dependence, the noise shape function, was introduced in order to account for the dominance of the $\frac{1}{f^2}$-acceleration noise towards low frequencies and of constant

readout noise towards high frequencies:

$$\mathrm{NSF}(f) = \sqrt{1 + \left(\frac{3\,\mathrm{mHz}}{f}\right)^4}. \tag{2.7}$$

With the noise shape function $\mathrm{NSF}(f)$ at hand, we are able to formulate the overall requirement for LISA: any individual technical noise source should be suppressed below

$$
\begin{aligned}
\widetilde{\phi}_{\mathrm{req}}(f) &= \frac{1}{10} \cdot 6.1 \cdot 10^{-5}\,\frac{\mathrm{rad}}{\sqrt{\mathrm{Hz}}}\sqrt{1 + \left(\frac{3\,\mathrm{mHz}}{f}\right)^4} \\
&= 6.1\,\frac{\mathrm{\mu rad}}{\sqrt{\mathrm{Hz}}}\sqrt{1 + \left(\frac{3\,\mathrm{mHz}}{f}\right)^4},
\end{aligned} \tag{2.8a}
$$

which corresponds to some $\frac{\mathrm{\mu rad}}{\sqrt{\mathrm{Hz}}}$ at the design frequency of $3\,\mathrm{mHz}$. Note that this is only a first guideline and not a final strict requirement. If it turns out that Eq. (2.8a) is impossible or very hard to reach for one particular noise source, reallocation is possible and the engineering factor could change.

A common formulation of Eq. (2.8a) in terms of displacement noise which ex- and includes the 'engineering factor' of $\frac{1}{10}$ is the so-called $10\,\mathrm{pm}$- and $1\,\mathrm{pm}$-requirement, respectively:

$$\widetilde{x}_{\mathrm{req},10\,\mathrm{pm}}(f) = 10 \cdot \frac{\lambda}{2\pi}\widetilde{\phi}_{\mathrm{req}}(f) = 10\,\frac{\mathrm{pm}}{\sqrt{\mathrm{Hz}}}\sqrt{1 + \left(\frac{3\,\mathrm{mHz}}{f}\right)^4}, \tag{2.8b}$$

$$\widetilde{x}_{\mathrm{req},1\,\mathrm{pm}}(f) = \frac{\lambda}{2\pi}\widetilde{\phi}_{\mathrm{req}}(f) = 1\,\frac{\mathrm{pm}}{\sqrt{\mathrm{Hz}}}\sqrt{1 + \left(\frac{3\,\mathrm{mHz}}{f}\right)^4}, \tag{2.8c}$$

both presented in Fig. 2.5 together with acceleration and readout noise in terms of phase. In various documents, this $10\,\mathrm{pm}$-requirement is called single-link requirement and limits the allocation of all technical noise sources in one link which are not suppressed by post-processing algorithms. In other words, it sets the noise budget for the noise level before data processing.

We will now discuss the primary technical noise sources like laser frequency and USO clock noise. Therefore, the assumption of technical noise suppression to an arbitrary level from Sec. 2.3.1 is dropped.

2.3.3 Laser Frequency Noise

Laser frequency noise is by far the dominant noise for LISA. Its origin lies in the frequency instability of the onboard Nd:YAG-lasers. They emit laser light at a wavelength of $1064\,\mathrm{nm}$. However, the THz frequency ν naturally fluctuates by several MHz. This frequency jitter couples into the long arm interferometric

measurements, since the armlengths vary in time and moreover one-way phase measurements are performed. Contrary to the case for ground-based detectors, the frequency fluctuations will not cancel naturally, but instead spoil the data. The linear spectral density of the frequency noise of free-running lasers (i.e, not frequency stabilised) is roughly

$$\widetilde{\nu}_{\text{free}}(f) = \frac{10^4\,\text{Hz}}{f}\,\frac{\text{Hz}}{\sqrt{\text{Hz}}}\,, \tag{2.9}$$

with Fourier frequency f. For LISA, we need $\frac{\mu\text{rad}}{\sqrt{\text{Hz}}}$ accuracy in order to detect the small disturbances in space-time induced by gravitational waves. Hence, it is self-evident to put some effort in laser frequency stabilisation techniques. Today, techniques exist [Tin08a], e.g., the stabilisation on a Fabry Pérot resonator with a precise resonance frequency, called Pound-Drever Hall locking [DHK$^+$83; Bla00].

In particular for LISA, a sophisticated technique called arm locking was proposed [SGMS03; YMM14]. The main idea is to stabilise the lasers on the LISA arms, serving as an extremely stable reference. However, arm locking is at present not part of the mission formulation mainly due to its technical complexity.

The linear spectral density of stabilised lasers is assumed to be

$$\widetilde{\nu}_{\text{stab}} = 280\,\frac{\text{Hz}}{\sqrt{\text{Hz}}} \tag{2.10a}$$

at $3\,\text{mHz}$. This corresponds to a phase noise level of

$$\widetilde{\phi}_{\text{stab}} = \frac{2\pi\Delta L}{c}\cdot\widetilde{\nu}_{\text{stab}} \approx 3\cdot 10^4\,\frac{\text{rad}}{\sqrt{\text{Hz}}} \tag{2.10b}$$

and will be derived in Ch. 3. The level of $\widetilde{\phi}_{\text{stab}}$ is completely out of the plot range of Fig. 2.5 and there is a crucial need for the suppression below at least the $10\,\text{pm}$-requirement. Therefore, Time-Delay Interferometry was developed to suppress the laser frequency noise in post-processing and will be studied in detail in Ch. 3.

2.3.4 Clock Noise

The next largest disturbance in the measurements is the clock noise. Each S/C hosts a free-running USO that triggers the ADCs used for digitisation of the interferometric heterodyne beat-notes. Therefore, a sampling clock with $80\,\text{MHz}$ is generated from the USO. However, this trigger signal does not have an exactly constant frequency and hence the digitised signal is corrupted by clock phase errors. The danger is then to misinterpret this phase shift as a gravitational wave signal. Experiments could show that the linear spectral density of common USOs can be described by [Edl14]

$$\widetilde{\phi}_{\text{USO}}(f) \approx 30\,\frac{\text{rad}}{\sqrt{\text{Hz}}}\cdot\left(\frac{3\,\text{mHz}}{f}\right)^{\frac{9}{5}}. \tag{2.11}$$

Currently, one tries to develop more sophisticated clock noise models verified by lab results [Wan14].

Additionally, as already stated in Sec. 2.2.3, the ADCs itself jitter and inherently distort the sampling process. In order to correct for both clock and ADC noise, a pilot tone is inserted. Since the pilot tone sets a sinusoidal reference signal, it is then possible to determine the noisy sampling times of the ADC digitisation and to correct for them. A schematic is shown in Fig. 2.6 [BBB$^+$14].
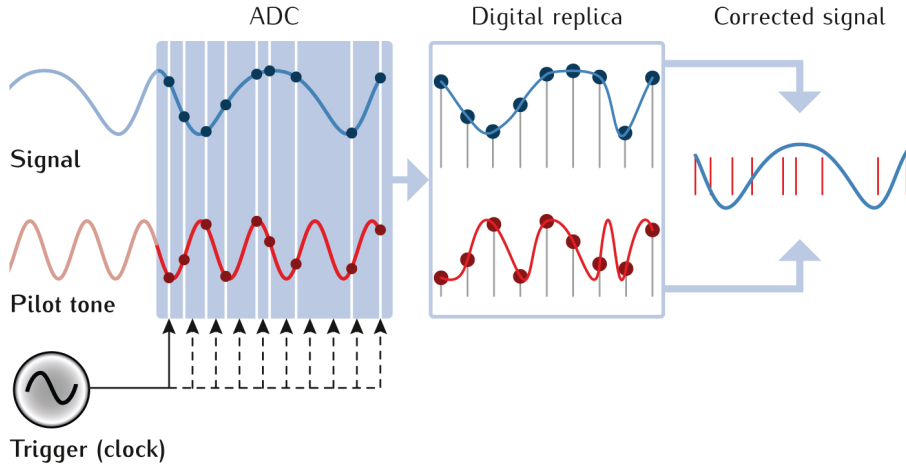
Figure 2.6: A sketch of the pilot tone correction [BBB$^+$14]. The heterodyne signal (blue curve) is digitised with non-equidistant time intervals given by the distorted sampling clock constructed from the USO signal. A stable reference signal, the pilot tone (red) is inserted in the ADC and suffers the same ADC sampling jitter. The digital replica of the heterodyne beat-note signal is then corrected for the ADC and clock jitter identified by the pilot tone. Finally, the input signal is recovered.

A second effect occurs if the USOs on each S/C are running with relative offset frequencies (which yields a frequency drift) and jitter over time. These offsets are also present in the trigger signals and pilot tones on each S/C. The drift can be estimated by Kalman filters and then corrected for [Wan14]. However, differential clock jitter is present in any phasemeter output signal and can not be suppressed technically. Therefore, a scheme was recently developed to transmit the amplified pilot tone between the spacecraft in order to extract the differential clock jitter and then remove it in post-processing from the recorded data. The scheme is called inter spacecraft pilot tone distribution or equivalently clock tone transfer chain and will be discussed extensively in Ch. 4. It could be shown that with the additional data from the clocks it is possible to suppress clock noise to an amount which makes a gravitational wave detection possible.

2.3.5 Optical Bench Displacement Noise

The third largest source is the displacement noise of the optical benches with respect to the test masses. The latter are shielded from other disturbances such that they are force-free down to a level of several femto-Newtons (Eq. (2.3a)). Hence, they should follow their geodesics with utmost precision. Using them as a position reference, the spacecraft are controlled such that they follow the test masses. Therefore, thrusters are used to adjust the satellite position relative to the test masses. However, by thruster firing, the spacecraft suffer shaking and accelerations that change the interferometrically measured relative distances between TMs and OBs. This disturbance is called optical bench displacement noise and has its major origin in the thruster activity. It will be several orders of magnitude above the 1 pm-requirement and hence also a contribution that must be removed in post-processing. Since the displacement noise highly depends on the DFACS controller, the thruster model and the coupling model between TM and S/C, it is not practical to give a formula for the spectral density here. A complex simulation from LISA Pathfinder simulation tools will be used to mimic the optical bench displacement as explained in Ch. 5.

2.3.6 Fibre Noise

In order to deliver the laser light from the adjacent OB for the TM readout and the reference interferometer, an intra-S/C connection between the two local optical benches needs to be established. Currently, two techniques are discussed and investigated. Specifically, these are free beam link and back-link fibre. In the former setup, two turnable mirrors at the exit of each optical bench are controlled such that the link is established. In the latter case (which is the current baseline), the two benches are connected via an optical fibre, through which the laser light is interchanged.

However, an important problem occurs. In case the of a fibre, the light that is sent through the fibre suffers a non-reciprocal phase shift. That is, light travelling from the left hand optical bench to the right hand optical bench (Fig. 2.7) collects a phase shift different from that of light travelling from the right hand to the left hand bench. The requirement is that the variation in the optical path length is below $1\,\frac{\text{pm}}{\sqrt{\text{Hz}}}$, yielding

$$\widetilde{\phi}_{\text{fibre}} < 6\,\frac{\text{μrad}}{\sqrt{\text{Hz}}}\,. \tag{2.12}$$

It could be shown experimentally that this unreciprocity could be removed by additional measurements to a level just sufficient to fulfill the 10 pm-requirement, but not the 1 pm-requirement [Fle12]. However, since the fibre noise does not violate the 10 pm-requirement, we assume for the rest of the thesis that the used fibres are reciprocal and differencing will suppress the phase noise sufficiently.
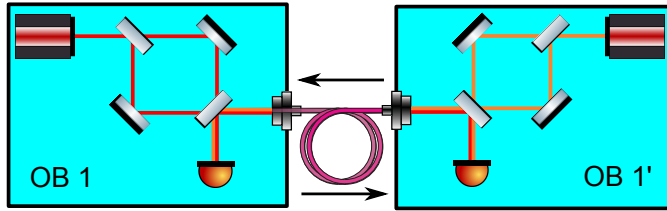
Figure 2.7:   Fibre reciprocity sketch. The two adjacent optical benches onboard the S/C are connected via an optical fibre, shown here schematically for S/C 1. Laser light from OB 1 (red) is sent through the fibre towards OB $1'$ and used there for reference measurements and (not shown) for TM readout, cf. Fig. 2.3. Similarly, light from OB $1'$ (orange) is transmitted to OB 1 through the same fibre. In the worst case, the two lasers do not have the same frequencies such that the collected phase shift in the bent fibre (black arrows) is direction-dependent.

Finally, note that further secondary noise sources occur in the measurement process and the telemetered data which are not regarded explicitly for the rest of this thesis. These are, inter alia, phasemeter noise and displacement noise due to temperature fluctuations. They will be subsumed in optical path length and readout noise terms.

2.4 The One-Link Interferometric Signal

In this section, we will introduce a helpful index notation which is extensively used to enumerate the spacecraft and the optical benches with their lasers, clocks and readout signals. Furthermore, the general phase signal detected onboard is carefully derived in analogy to Sec. 1.3.2.

2.4.1 Notation

We will introduce the following consistent notation according to Fig. 2.8 and refer to it for the rest of this thesis. A translation table between other notations used in the literature can be found in appendix D.

LISA consists of three spacecraft (S/C 1, 2 and 3), counted clockwise. As explained previously, each of the three spacecraft carries two nearly identical optical benches, where one is denoted by unprimed numbers $(1, 2, 3)$ and the other by primed numbers $(1', 2', 3')$, as shown in Fig. 2.8. The armlengths of the triangle in terms of light travel time $T_{0,i}(t)$ with $i = 1, 1', 2, 2', 3, 3'$ are given by

$$L_i(t) = cT_{0,i}(t) . \tag{2.13}$$

Here, $T_{0,i}(t)$ excludes the GW signal and is given in Sec. 1.4.4. t is the so-called constellation time, assuming a perfect clock synchronisation between all S/C. The armlengths are marked as follows: the opposite side of, e.g., S/C 1 is denoted by L_1
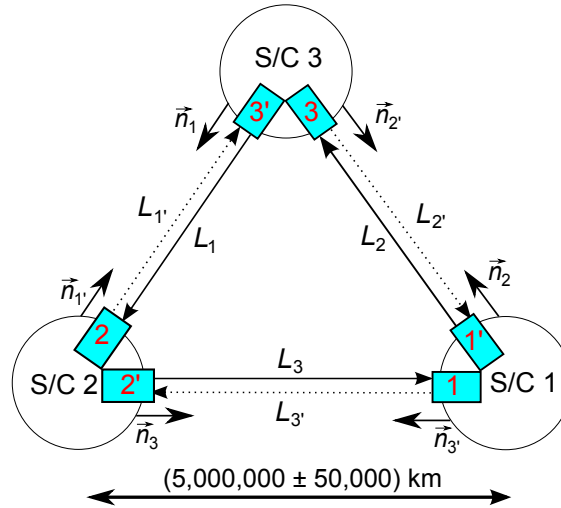
Figure 2.8: Index notation for LISA spacecraft $(1, 2, 3)$, optical benches (red numbers) and links $(L_1, L_{1'}, \text{etc.})$. Note that for the link direction unit vectors $\vec{n}_{1'} \neq -\vec{n}_1$, $\vec{n}_{2'} \neq -\vec{n}_2$ and $\vec{n}_{3'} \neq -\vec{n}_3$ apply in general due to aberration of the constellation (cf. Sec. 1.4).

and $L_{1'}$, respectively, depending on the direction of light travel (counter-clockwise or clockwise). We have to distinguish them because the light travel times differ due to the aberration of the constellation.

It turns out to be convenient to introduce three kinds of indices. Several equations use the full index series $1, 1', 2, 2', 3, 3'$, e.g., for labeling the optical benches or onboard lasers. We mark this with indices i in the following. Indices with an underbar but without a prime, i.e., $\underline{i} = 1, 2, 3$, account for the links pointing in the counter-clockwise direction or for optical benches receiving light along unprimed links, respectively. Complementary, underbarred and primed indices $\underline{i}' = 1', 2', 3'$ account for links pointing in a clockwise manner or for optical benches receiving light along primed links.

Furthermore, we define time-dependent unit direction vectors $\vec{n}_i$ pointing along the LISA arms. $\vec{n}_{\underline{i}}$ aims along arm $\underline{i}$ in the counter-clockwise direction, while $\vec{n}_{\underline{i}'}$ is oriented due to point-ahead effects (Sec. 1.4) approximately, but not exactly, in the opposite direction of $\vec{n}_{\underline{i}}$. That is, $\vec{n}_{\underline{i}} \neq -\vec{n}_{\underline{i}'}$ applies in general. More precisely, the unit direction vectors aim from each OB in the direction of light incidence (as shown in Fig. 2.9) at time of reception and are given for the links 1 and 1' by

$$\vec{n}_1(t_{\mathrm{recv},3}) = \frac{\vec{x}_2(t_{\mathrm{send},2}) - \vec{x}_3(t_{\mathrm{recv},3})}{|\vec{x}_2(t_{\mathrm{send},2}) - \vec{x}_3(t_{\mathrm{recv},3})|}, \quad \vec{n}_{1'}(t_{\mathrm{recv},2}) = \frac{\vec{x}_3(t_{\mathrm{send},3}) - \vec{x}_2(t_{\mathrm{recv},2})}{|\vec{x}_3(t_{\mathrm{send},3}) - \vec{x}_2(t_{\mathrm{recv},2})|}.$$

$$(2.14)$$
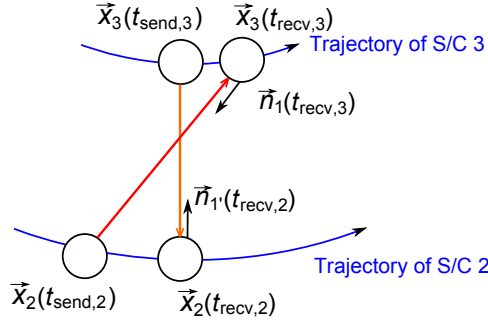
Figure 2.9: Definition of the unit vectors $\vec{n}_i$ for LISA, exemplarily shown for $\vec{n}_1$ and $\vec{n}_{1'}$. Spacecraft 2 and 3 move along their trajectories (blue lines). S/C 2 sends light (red) at time $t_{\mathrm{send},2}$ to the (pre-calculated) position $\vec{x}_3(t_{\mathrm{recv},3})$ where S/C 3 will receive the light at time $t_{\mathrm{recv},3}$. The direction of reception is given by the unit vector $\vec{n}_1(t_{\mathrm{recv},3})$. The construction of $\vec{n}_{1'}(t_{\mathrm{recv},2})$ is similar.

Here, $\vec{x}_{\underline{i}}(t_0)$ denotes the position of the CoM of S/C $\underline{i}$ relative to the solar system barycentric frame (SSB) at an arbitrary time stamp t_0, measured by the onboard clock on S/C $\underline{i}$. $t_{\mathrm{recv},\underline{i}}$ is the time of reception on S/C $\underline{i}$, while $t_{\mathrm{send},\underline{i}}$ is the sending time from S/C $\underline{i}$, always measured with respect to the onboard clock. Note again that two adjacent optical benches use the same clock for the phase measurements.

All other unit vectors $\vec{n}_{\underline{i}}$ can be constructed from Eq. (2.14) by cyclic permutation of the unprimed and primed indices: $1 \rightarrow 2$, $2 \rightarrow 3$ and $3 \rightarrow 1$ as well as $1' \rightarrow 2'$, $2' \rightarrow 3'$ and $3' \rightarrow 1'$. This permutation procedure is a general rule and can be applied here and, if nothing else is said, in the following for the rest of this thesis.

2.4.2 One-Way Phase Measurements

One has to define carefully the phase signals and their signs. Therefore, we will consider one LISA arm as shown in Fig. 2.10 and compute the measured electric field at the photodetector. The following calculation is strongly related to that performed in Sec. 1.3.2 for the Michelson interferometer output.

Neglecting geometric and amplitude factors (cf. Sec. 1.3), the electric field from the local laser detected onboard OB 1 at receiving time $t_{\mathrm{recv},1}$ can be written schematically as

$$
\begin{aligned}
E_1(t_{\mathrm{recv},1}) &= \mathrm{i}\tau_{\mathrm{BS}} \exp(\mathrm{i}[\phi_{\mathrm{Laser},1}(t_{\mathrm{recv},1}) + \phi_{\mathrm{n},1}(t_{\mathrm{recv},1})]) \\
&= \frac{\mathrm{i}}{\sqrt{2}} \exp(\mathrm{i}[\phi_{\mathrm{Laser},1}(t_{\mathrm{recv},1}) + \phi_{\mathrm{n},1}(t_{\mathrm{recv},1})]) ,
\end{aligned}
$$

where $\mathrm{i}\tau_{\mathrm{BS}} = \frac{\mathrm{i}}{\sqrt{2}}$ enter through the transmission at the BS in Fig. 2.10 according to Sec. 1.3.2. $\phi_{\mathrm{n},1}(t_{\mathrm{recv},1})$ contains all optical path length fluctuations on OB 1 at the
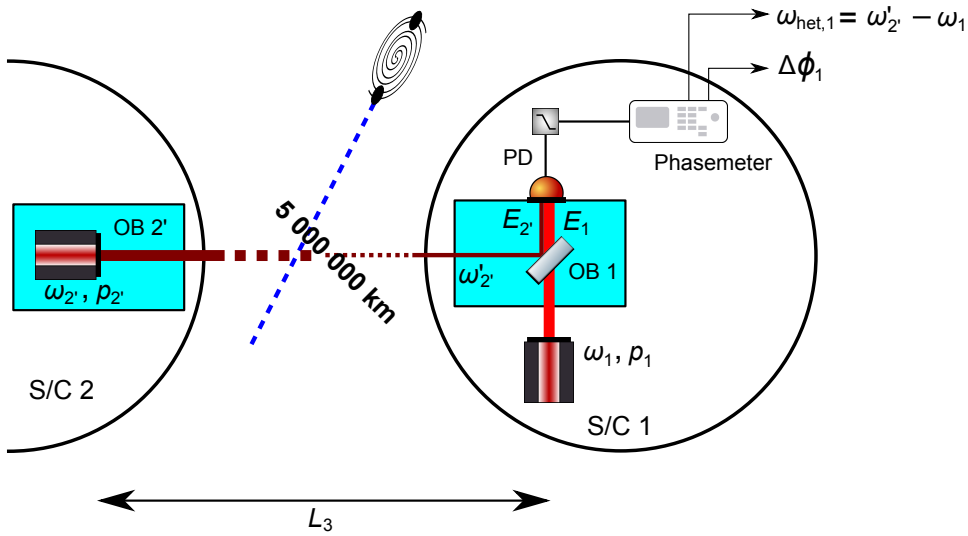
Figure 2.10: One schematic LISA link. $E_{2'}$ is the electric field of the incoming light with phase noise $p_{2'}$ and former angular frequency $\omega_{2'}$. The transmitted light received on OB 1 suffered a Doppler shift and has thus the frequency $\omega_{2'}'$. Furthermore, E_1 denotes the electric field of the local laser with phase noise p_1 and frequency ω_1 on optical bench 1. The photodetector measures the power of the sum of the electric fields (again in plane wave approximation), i.e. $P \propto |E_1 + E_{2'}|^2$, providing a beat-note with frequency $\omega_{\mathrm{het},1}$ and relative phase $\Delta\phi_1$ read out by the onboard phasemeter.

time of detection. The laser phase $\phi_{\mathrm{Laser},i}(t)$ could generally be written as

$$\phi_{\mathrm{Laser},i}(t) = \omega_i t + p_i(t) = 2\pi \int \mathrm{d}t\, \nu_i(t) \tag{2.15}$$

with $\nu_i(t)$ denoting laser frequency noise time series, ω_i the angular frequency of the laser on OB i and $p_i(t)$ its phase noise at an arbitrary time stamp t. Hence, the phase contribution $\phi_{\mathrm{Laser},1}(t_{\mathrm{recv},1})$ of the laser housed on OB 1 is

$$\phi_{\mathrm{Laser},1}(t_{\mathrm{recv},1}) = \omega_1 t_{\mathrm{recv},1} + p_1(t_{\mathrm{recv},1}) \tag{2.16}$$

and the electric field reads as

$$E_1 = \frac{1}{\sqrt{2}} \exp\left(\mathrm{i}\left[\omega_1 t_{\mathrm{recv},1} + p_1(t_{\mathrm{recv},1}) + \phi_{\mathrm{n},1}(t_{\mathrm{recv},1}) + \tfrac{\pi}{2}\right]\right) \,,$$

where we used $\mathrm{e}^{\mathrm{i}\frac{\pi}{2}} = \mathrm{i}$. Note that the travel time from the local laser to the detector is neglected. That is, received light from the distant spacecraft is detected and beaten against light from the local laser at time of reception onboard S/C 1, $t_{\mathrm{recv},1}$.

Similarly, the incoming electric field $E_{2'}$ can be written as

$$
\begin{aligned}
E_{2'} &= \frac{1}{\sqrt{2}} \exp(\mathrm{i}[\omega'_{2'} t_{\mathrm{recv},1} + p_{2'}(t_{\mathrm{send},2}) + \phi_{\mathrm{n},2'}(t_{\mathrm{send},2}) \\
&\quad + \phi_{2'\to 1}(t_{\mathrm{recv},1}) + \phi_{\mathrm{n},1}(t_{\mathrm{recv},1})]) \,,
\end{aligned}
$$

again with the amplitude $\frac{1}{\sqrt{2}}$ due to reflection at the BS.

Let us investigate this expression in detail. First, remark here that the frequency $\omega'_{2'}$ of $E_{2'}$ detected onboard OB 1 is slightly different from the frequency ω_1 of E_1 (by an amount of $\omega'_{2'} - \omega_1$, assumed positive here) and as well different from $\omega_{2'}$ (the frequency of the laser on OB $2'$) due to Doppler shifts. The prime emphasises the frequency Doppler shift that originates from orbital motion of the whole satellite constellation (Sec. 2.2.1) and we should carefully distinguish between $\omega_{2'}$ and $\omega'_{2'}$. Second, the phase shift from the frequency ramp (2.15) of the laser on OB $2'$ is evaluated at the time of reception at OB 1, $t_{\mathrm{recv},1}$, since this is the time at which both beams arrive superimposed at the PD. Third, the laser light from OB $2'$ comprises laser phase noise at time of emission $t_{\mathrm{send},2}$. It is given from the point of view of S/C 1 as

$$
t_{\mathrm{send},2} = t_{\mathrm{recv},1} - \frac{L_3(t_{\mathrm{recv},1})}{c} \,.
$$

This means that the phase noise of the incoming laser beam detected on OB 1 is that generated on OB $2'$, but delayed by the light travel time between the spacecraft.

Between OB $2'$ and 1, the light collects further phase shifts $\phi_{2'\to 1}(t_{\mathrm{recv},1})$ by gravitational wave influence and optical path length noise. Moreover, relative optical bench displacement will have influence on the light track. Finally, noise instances $\phi_{\mathrm{n},1}(t_{\mathrm{recv},1})$ and $\phi_{\mathrm{n},2'}(t_{\mathrm{send},2})$ from the receiving and sending optical benches at time of reception and sending, respectively, enter the phase of the electric field $E_{2'}$ as well.

For the sake of simplicity we will now subsume all phase shifts with the exception of the laser frequency ramp in a phase function $\phi_i(t)$ at an arbitrary time of detection t, called constellation time in the following. That is,

$$
E_1(t) = \frac{1}{\sqrt{2}} \exp(\mathrm{i}[\omega_1 t + \phi_1(t)]) \,, \quad E_{2'}(t) = \frac{1}{\sqrt{2}} \exp(\mathrm{i}[\omega'_{2'} t + \phi_{2'}(t)]) \,.
$$

Again, for plane waves, the photodetector measures the power of the sum of incoming and local laser light fields, i.e. $P \propto |E_{2'} + E_1|^2$:

$$
\begin{aligned}
P(t) &\propto |E_{2'} + E_1|^2 = |E_{2'}|^2 + |E_1|^2 + E_{2'} E_1^* + E_1 E_{2'}^* \\
&= 1 + \tfrac{1}{2} \mathrm{e}^{\mathrm{i}[\omega'_{2'} t + \phi_{2'}(t)]} \mathrm{e}^{-\mathrm{i}[\omega_1 t + \phi_1(t)]} + \tfrac{1}{2} \mathrm{e}^{\mathrm{i}[\omega_1 t + \phi_1(t)]} \mathrm{e}^{-\mathrm{i}[\omega'_{2'} t + \phi_{2'}(t)]} \\
&= 1 + \tfrac{1}{2} \mathrm{e}^{\mathrm{i}[(\omega'_{2'} - \omega_1)t + (\phi_{2'}(t) - \phi_1(t))]} + \tfrac{1}{2} \mathrm{e}^{-\mathrm{i}[(\omega'_{2'} - \omega_1)t + (\phi_{2'}(t) - \phi_1(t))]} \\
&= 1 + \cos[(\omega'_{2'} - \omega_1)t + \phi_{2'}(t) - \phi_1(t)] \,,
\end{aligned}
$$

where we used the trigonometric relation $\cos(u) = \frac{e^{iu}+e^{-iu}}{2}$. Hence, the heterodyne power signal is:

$$P(t) \propto \cos(\omega_{\mathrm{het},1}t + \Delta\phi_1(t)) \tag{2.17}$$

with the heterodyne beat-note frequency detected onboard OB 1 in the science interferometer, $\omega_{\mathrm{het},1} := \omega'_{2'} - \omega_1$ and a phase shift $\Delta\phi_1(t) = \phi_{2'}(t) - \phi_1(t)$ including noise and the gravitational wave signal.

Eq. (2.17) gives the change in phase due to an optical path length change and is commonly referred to as the beat-note. The phase $\Delta\phi_1(t)$ at time of reception $t = t_{\mathrm{recv},1}$ is given on optical bench 1 by

$$
\begin{aligned}
\Delta\phi_1(t_{\mathrm{recv},1}) &= p_{2'}(t_{\mathrm{send},2}) + \phi_{\mathrm{n},2'}(t_{\mathrm{send},2}) + \phi_{2'\to1}(t_{\mathrm{recv},1}) \\
&\quad + \phi_{\mathrm{n},1}(t_{\mathrm{recv},1}) - p_1(t_{\mathrm{recv},1}) - \phi_{\mathrm{n},1}(t_{\mathrm{recv},1}) - \tfrac{\pi}{2} \\
&= p_{2'}(t_{\mathrm{send},2}) - p_1(t_{\mathrm{recv},1}) + \phi_{\mathrm{n},2'}(t_{\mathrm{send},2}) \\
&\quad + \phi_{2'\to1}(t_{\mathrm{recv},1}) - \tfrac{\pi}{2}
\end{aligned}
\tag{2.18}
$$

and will be further specified in Sec. 2.5. Note that the common phase noise for both local and received light onboard OB 1, $\phi_{\mathrm{n},1}(t_{\mathrm{recv},1})$, cancels. $\Delta\phi_1$ reverses its sign for $\omega_{\mathrm{het},1} < 0$ according to the definition (2.17), i.e., if the received light has due to Doppler shifts along L_3 a lower frequency than the light from laser 1. We will discuss this beat-note frequency polarity more deeply in Ch. 4. Constant phases $(-\frac{\pi}{2})$ are neglected in the following, since only the time varying effects are in danger to be misinterpreted as a GW signal.

Similar calculations as above can be performed for all LISA arms and onboard interferometers. In the next section, the different contributions to the phase shifts in Eq. (2.18) are explained for the onboard science, reference and test mass interferometers and we will specify the different terms.

2.5 Onboard Interferometric Signals

We will now explain the current OB design and the onboard data streams in the case of a rotating and flexing LISA constellation [OHD12]. Therefore, we assume here for the sake of simplicity a perfect phasemeter operation without clock offsets and jitter as well as any beat-note frequency polarity of the lasers. Ch. 4 will include these issues and extend the discussion.

2.5.1 Split Interferometry Concept

Some changes in the optical bench design make it necessary to reconsider in detail the LISA-like data streams and TDI-equations [Tho11; HEB+11]. In particular, in contrast to ealier designs, the incoming light from the distant S/C is not reflected off the test mass. The current setup with an auxiliary test mass IFO (Sec. 2.2.2)

benefits from a higher intensity of the laser light hitting the TM and a reduction of the readout noise. It also simplifies alignment, integration and testing.

However, the distance variations between the TMs are not measured directly as in previous designs [ESA00]. Instead, the measurement is divided into three separate measurements: TM to OB (on the far S/C), OB (distant) to OB (local) and OB to TM (on the local S/C). This separation is called 'split interferometry concept' and is depicted schematically in Fig. 2.11.
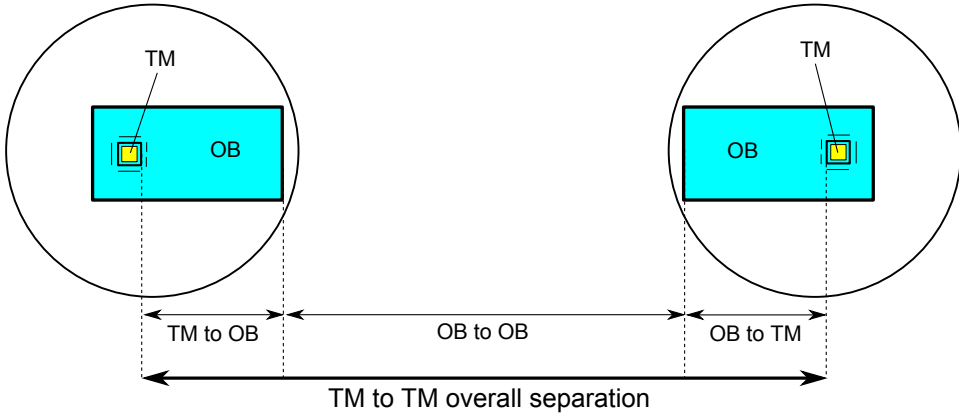
Figure 2.11: Schematic of the split interferometry concept for one LISA arm. The separation measurement between two test masses defining the endpoints of the arm is split in three parts: TM to OB of the distant S/C, OB to OB, and OB to TM on local S/C.

Note here that the separation between the test masses is not measured directly, but instead constructed in post-processing from the phase measurements on the optical benches. The data stream combinations that provide the separation measurements are derived in Ch. 4.

2.5.2 Optical Bench Layout

Fig. 2.12 shows a sketch of one LISA optical bench. The incoming laser beam from the distant S/C (from the left) is interfered with the local laser from the OB. The test mass motion is read out by a separate interferometer using laser light from the adjacent optical bench on the common S/C transmitted through a 'back-link' fibre in addition to the same local oscillator. We will now exemplarily discuss the measurements on OB 1. The setup of the other optical benches is similar.

Three measurements are performed on each OB. First, the incoming laser beam from the distant S/C is interfered with a local oscillator (left PD in Fig. 2.12). Due to the fact that the incoming laser light carries information about a passing gravitational wave, this measurement is referred to as the 'science' interferometer
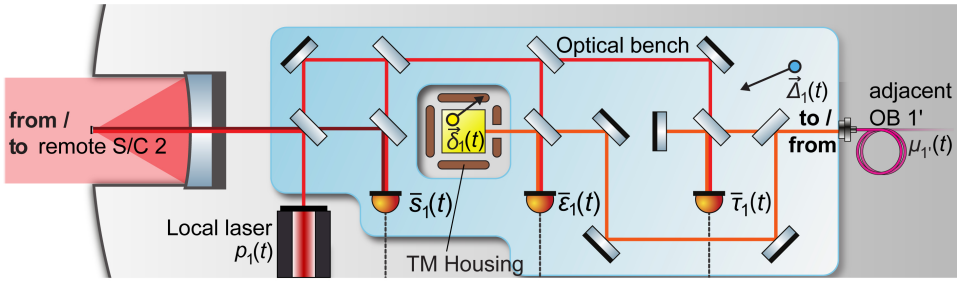
Figure 2.12: Schematic of the LISA OB setup, shown for bench '1' as an example. The science IFO compares the lasers from OB 2′ and 1 and gives $\bar{s}_1(t)$, while test mass and reference IFO use light from OB 1 and adjacent OB 1′, yielding the PD signals $\bar{\varepsilon}_1(t)$ and $\bar{\tau}_1(t)$, respectively. Additionally, optical bench displacement noise, $\vec{\Delta}_1(t)$, test mass displacement noise, $\vec{\delta}_1(t)$, and the fibre noise, $\mu_{1'}(t)$, are sketched. Telescope (left), laser and OB are all fixed with respect to each other. In contrast to the previous TDI literature, here we use the optical bench layout of the year 2010 (baseline since 2006), with the so-called split interferometry configuration. See the text for further explanation.

signal and is denoted for OB 1 by $\bar{s}_1(t)$. This signal was already partially formulated in Sec. 2.4.2. Note that the bar emphasises here (and as well for the test mass and reference interferometer output discussed below) that issues like the digitisation process and the introduction of clock noise are ignored. Thus, $\bar{s}_1(t)$ denotes the phase of the raw optical beat-note signal at the photodetector of the science IFO on OB 1.

Next, the test mass motion is read out interferometrically. For this purpose, the local oscillator of OB 1 is interfered with the local oscillator from the adjacent optical bench 1′, delivered through the 'back-link' fibre and reflected off the test mass. This interferometric readout $\bar{\varepsilon}_1(t)$ is called the test mass interferometer output. In the third, so-called reference interferometer, both lasers of the adjacent OBs 1 and 1′ are interfered (the right PD in Fig. 2.12), and this gives the reference interferometer output $\bar{\tau}_1(t)$.

We will now describe the phase signals of the three onboard interferometric signals neglecting any change in the refractive index (e.g., by windows of the TM chamber). As before, we denote by t the constellation time. That is, the clocks on each S/C are perfectly synchronised without any offsets and drifts, and $t_{\mathrm{recv},\underline{i}}$ is then similar to t. Additionally, for the sake of simplicity, we will here neglect the disturbances from the digitisation process and the phasemeter readout, and denote that by the bar. A comprehensive treatment can be found in Ch. 4.

2.5.3 The Science Interferometer

The science interferometer signal $\bar{s}_1(t)$, expressed as the phase of the beat-note (comparable with $\Delta\phi_1(t)$ of Eq. (2.18)), contains the laser phase noise $p_{2'}$ from the

distant OB, delayed by the light travel time $\frac{L_3(t)}{c}$, compared with p_1 from the local OB. Next, the term $\phi_{2'\to 1}(t)$ in (2.18) includes the cumulated gravitational phase shift collected by the transmitted laser light along $L_3(t)$ and received by OB 1, designated by $H_1(t)$ (capital H reminds one that this is the integrated GW impact and should not be mixed up with the strain h), together with optical phase shifts due to OB motion of the sending ($\phi_{\text{OB},2'}$) and receiving OB ($\phi_{\text{OB},1}$). Note again, as for the laser phase noise from the distant OB, the optical bench displacement noise of the sending S/C is time-shifted by $\frac{L_3(t)}{c}$. Finally, further effects like readout noise at the photodetector on the local optical bench or optical path length noise from OB 2' (former $\phi_{\text{n},2'}$) enter the phase signal, summarised in $\phi_{\text{Noise},1}(t)$. Thus,

$$\bar{s}_1(t) = H_1(t) + p_{2'}\left(t - \frac{L_3(t)}{c}\right) - p_1(t) + \phi_{\text{OB},2'}\left(t - \frac{L_3(t)}{c}\right) + \phi_{\text{OB},1}(t) + \phi_{\text{Noise},1}(t)\,.$$
(2.19)

We will now specify the GW signal and the last three terms.

Gravitational Wave Contribution

The optical phase shift due to gravitational waves incident along $\hat{k}$, which modulate the space-time between the OB 2' and 1, is given, according to Eq. (1.56), by the accumulation

$$H_1(t) := \frac{2\pi c}{\lambda_{2'}}\Delta T_1(t) = \frac{\pi c}{\lambda_{2'}}\frac{\vec{n}_{3'}(t) \otimes \vec{n}_{3'}(t)}{(1 + \hat{k}\cdot\vec{n}_{3'}(t))} \;:\; \int\limits_{\xi(0)}^{\xi(w_{\text{recv}}=L_3(t))} \mathrm{d}\xi\,\boldsymbol{h}(\xi)$$
(2.20a)

with the integration limits

$$\xi(0) \;=\; t - \frac{\hat{k}\cdot\vec{x}_1(t)}{c} - \frac{L_3(t)}{c}(1 + \hat{k}\cdot\vec{n}_{3'}(t))\,,$$
(2.20b)

$$\xi(w_{\text{recv}}) \;=\; t - \frac{\hat{k}\cdot\vec{x}_1(t)}{c}$$
(2.20c)

given in Sec. 1.4.3. Note in Eq. (2.20a) that $\lambda_{2'}$ is the sensing wavelength and $\vec{x}_1(t)$ denotes the center of mass of S/C 1 at an arbitrary receiving time t.

Optical Bench Displacement Noise

The phase due to optical bench displacement noise must be carefully studied. According to Fig. 2.13, we consider the optical phase shift experienced by interchanged light due to optical bench displacement noise $\vec{\Delta}_i$ of OB i relative to an inertial frame defined by the test masses. Again, without loss of generality, a single link is regarded.
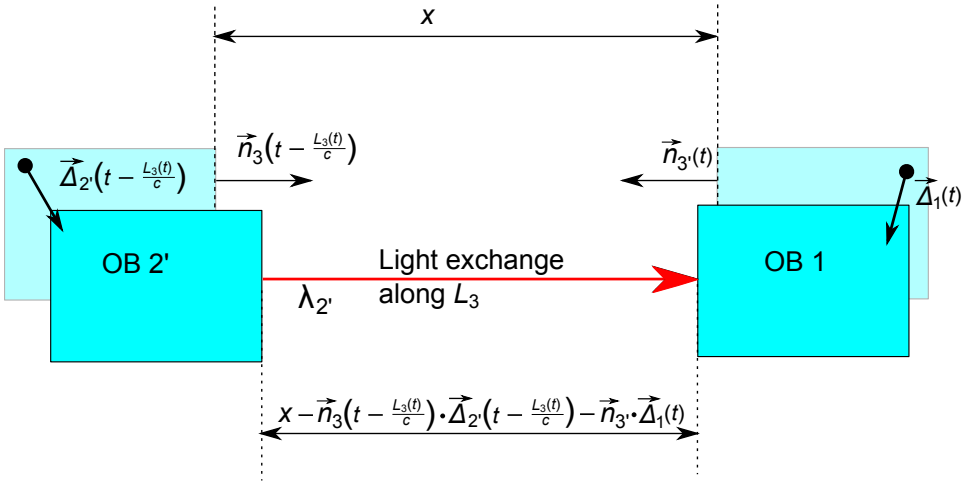
Figure 2.13: Displacement noise for the link L_3. Components of the optical bench displacements $\vec{\Delta}_{2'}$ and $\vec{\Delta}_1$ with respect to $\vec{n}_3$ and $\vec{n}_{3'}$ will change the path length x between the OB $2'$ and 1. Components perpendicular to the unit direction vectors have no influence on x. The situation is from the point of view of OB 1 at time of reception.

The change in separation measured as optical phase shift from OB $2'$ to 1 is then given by

$$\phi_{\mathrm{OB},2'}(t - \tfrac{L_3(t)}{c}) + \phi_{\mathrm{OB},1}(t) = -\frac{2\pi}{\lambda_{2'}}\vec{n}_3(t - \tfrac{L_3(t)}{c}) \cdot \vec{\Delta}_{2'}(t - \tfrac{L_3(t)}{c}) - \frac{2\pi}{\lambda_{2'}}\vec{n}_{3'}(t) \cdot \vec{\Delta}_1(t)\,,$$

$$(2.21)$$

as illustrated in Fig. 2.13. Both displacements are sensed by the laser on OB $2'$ which is sent along L_3 and recorded at OB 1. The direction of light incidence seen from receiving S/C 1 is given by $\vec{n}_{3'}(t)$, the unit direction vector between the CoM of S/C 1 at time of reception and the CoM of S/C 2 at the time of sending (Fig. 2.9). Note again that $\vec{n}_i \neq -\vec{n}_{i'}$ in general due to relative constellation motion (cartwheel rotation and breathing).

If the displacement vector $\vec{\Delta}_{2'}(t - \tfrac{L_3(t)}{c})$ has a positive component with respect to $\vec{n}_3(t - \tfrac{L_3(t)}{c})$, then the distance between the two optical benches shrinks, explaining the first minus sign in Eq. (2.21). The same argument holds for OB 1: If the displacement vector $\vec{\Delta}_1(t)$ has a positive component in the direction of $\vec{n}_{3'}$, the distance between OB $2'$ and OB 1 again shrinks (second minus sign in Eq. (2.21)). Note that the two OBs on one spacecraft are not rigidly connected, that is here, $\vec{\Delta}_{\underline{i}}(t) \neq \vec{\Delta}_{\underline{i}'}(t)$.

However, we make here and in the following a crucial simplification assumption:

$$\vec{n}_i(t - \tfrac{L_i(t)}{c}) \simeq \vec{n}_i(t) \,, \tag{2.22}$$

since in the light travel time of $\approx 17\,$s the S/C move only marginally perpendicular to the line of sight relative to each other. Subsequently, the direction of light reception changes meanwhile by an angle less than mrad [Cer09]. This angle is called point-ahead angle. Using the previous assumption, Eq. (2.21) could be simplified to

$$\phi_{\mathrm{OB},2'}(t - \tfrac{L_3(t)}{c}) + \phi_{\mathrm{OB},1}(t) \simeq -\frac{2\pi}{\lambda_{2'}} \vec{n}_3(t) \cdot \vec{\Delta}_{2'}(t - \tfrac{L_3(t)}{c}) - \frac{2\pi}{\lambda_{2'}} \vec{n}_{3'}(t) \cdot \vec{\Delta}_1(t) \,. \tag{2.23}$$

For the rest of this thesis, we will neglect the small error ($\simeq$) in Eq. (2.23) and subsequent formulas.

Science Interferometer Phase Signal

Finally, $\phi_{\mathrm{Noise},1}(t)$ in Eq. (2.19) comprises additional non-common optical path length noise $N_1^{\mathrm{opt}}(t)$ and readout noise of the PD (shot noise, relative intensity and electronic noise) $N_1^s(t)$. The superscript s labels here the science IFO. This leads to

$$\begin{aligned}
\bar{s}_1(t) \;=\; & H_1(t) + p_{2'}\left(t - \tfrac{L_3(t)}{c}\right) - p_1(t) - \frac{2\pi}{\lambda_{2'}} \vec{n}_3(t) \cdot \vec{\Delta}_{2'}\left(t - \tfrac{L_3(t)}{c}\right) \\
& - \frac{2\pi}{\lambda_{2'}} \vec{n}_{3'}(t) \cdot \vec{\Delta}_1(t) + N_1^{\mathrm{opt}}(t) + N_1^s(t) \,.
\end{aligned} \tag{2.24}$$

Again, the barred notation $\bar{s}_1(t)$ in Eq. (2.24) indicates that the frequency order of the lasers (discussed in Sec. 4.2) as well as the digitising process via analog-to-digital converters triggered by the onboard clocks (Sec. 4.1) is not considered here. The derived signal (2.24) describes the data inserted into the ADCs to form the phasemeter input from the science interferometer. Though, in order to understand the laser noise removal schemes (Ch. 3), the phase signals derived here and in the following are sufficient.

2.5.4 Test Mass and Reference Interferometer

In this section, we will derive the phase signals for the two auxiliary interferometers which read out the test mass motion (test mass IFO) as well as the lasers of the local and the adjacent OB (reference IFO).

Test Mass Interferometer

According to Fig. 2.12, the test mass interferometer signal $\bar{\varepsilon}_1(t)$ contains laser phase noise from the local laser, $p_1(t)$, and from the laser on the adjacent optical bench $1'$, $p_{1'}(t)$, which is delivered through the back-link fibre. Moreover, shot noise, relative intensity and electronic readout noise from the photodetector, subsumed in $N_1^{\bar{\varepsilon}}(t)$,

as well as test mass displacement noise and optical bench displacement noise both relative to the reception direction $\vec{n}_{3'}(t)$, subsumed in $\phi_{\text{TM}-\text{OB},1}(t)$, will enter the phase signals. Furthermore, we have to introduce fibre noise, $\mu_{1'}(t)$, collected by light coming from OB $1'$. Note that the associated time delay by fibre propagation is neglected. Thus, the test mass interferometer output phase signal reads as

$$\bar{\varepsilon}_1(t) = p_{1'}(t) - p_1(t) + \phi_{\text{TM}-\text{OB},1}(t) + \mu_{1'}(t) + N_1^{\varepsilon}(t)\,, \tag{2.25}$$

where we have to specify the relative displacement noise between TM and OB in terms of optical phase shift, $\phi_{\text{TM}-\text{OB},1}(t)$. This will be done with help of Fig. 2.14, since the effect is twofold. That is, the optical bench displacement noise, $\vec{\Delta}_1(t)$, and the test mass displacement noise, $\vec{\delta}_1(t)$, both change the relative distance between TM and OB.
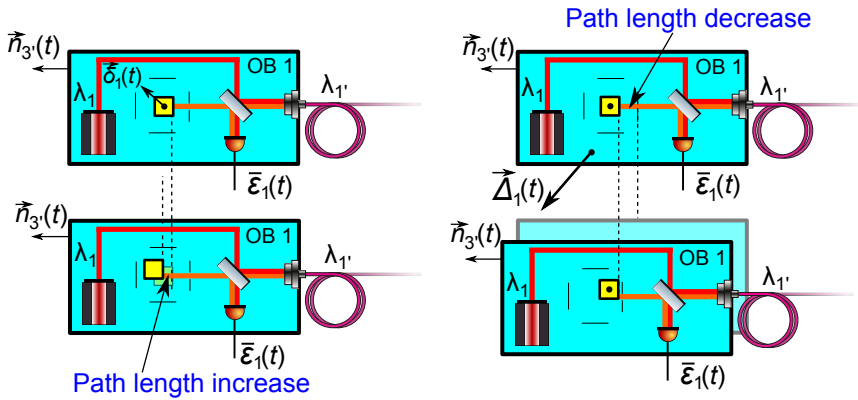
Figure 2.14: Sketch of the test mass interferometer. Light from the adjacent OB $1'$ with wavelength $\lambda_{1'}$, transmitted through a fibre, is used for sensing the TM position. Left: The TM has residual displacement $\vec{\delta}_1(t)$ with components parallel to $\vec{n}_{3'}(t)$; the OB-TM-measurement gains an additional positive phase shift. Right: The OB displacement vector $\vec{\Delta}_1(t)$ has components parallel to $\vec{n}_{3'}(t)$; the OB-TM-measurement gains an additional negative phase shift, since the TM remains at its initial position.

First, if the test mass moves due to the displacement noise $\vec{\delta}_1(t)$ in the direction of $\vec{n}_{3'}(t)$ while the optical bench is at rest, the optical path length for the sensing light from the adjacent optical bench with wavelength $\lambda_{1'}$ grows by $+2(\vec{n}_{3'}(t) \cdot \vec{\delta}_1(t))$. The factor of 2 comes from the light travelling back and forth to the test mass and thus experiencing the shift twice. Second, and vice versa, if the TM is at rest and the optical bench moves in the direction of $\vec{n}_{3'}$, the optical path length shrinks by $-2(\vec{n}_{3'}(t) \cdot \vec{\Delta}_1(t))$. The addition of both effects gives rise to a relative optical phase shift of

$$\phi_{\text{TM}-\text{OB},1}(t) = 2\left(\frac{2\pi}{\lambda_{1'}}\vec{n}_{3'}(t)\cdot\vec{\delta}_1(t) - \frac{2\pi}{\lambda_{1'}}\vec{n}_{3'}(t)\cdot\vec{\Delta}_1(t)\right),$$

finally resulting in the test mass interferometer phase signal:

$$\bar{\varepsilon}_1(t) = p_{1'}(t) - p_1(t) + 2\left(\frac{2\pi}{\lambda_{1'}}\vec{n}_{3'}(t) \cdot \vec{\delta}_1(t) - \frac{2\pi}{\lambda_{1'}}\vec{n}_{3'}(t) \cdot \vec{\Delta}_1(t)\right) + \mu_{1'}(t) + N_1^\varepsilon(t).$$

$$(2.26)$$

The Reference Interferometer

The reference IFO output, $\bar{\tau}_1(t)$, contains the beat-note of the lasers of OB 1 and $1'$, readout noise, $N_1^\tau(t)$, and fibre noise, $\mu_{1'}(t)$, collected by the laser light coming from OB $1'$, and is hence given by

$$\bar{\tau}_1(t) = p_{1'}(t) - p_1(t) + \mu_{1'}(t) + N_1^\tau(t).$$

$$(2.27)$$

Finally, we end up with three interferometric phase signals on optical bench 1:

$$\bar{s}_1(t) = H_1(t) + p_{2'}(t - \tfrac{L_3(t)}{c}) - p_1(t) - \frac{2\pi}{\lambda_{2'}}\vec{n}_3(t) \cdot \vec{\Delta}_{2'}(t - \tfrac{L_3(t)}{c})$$

$$- \frac{2\pi}{\lambda_{2'}}\vec{n}_{3'}(t) \cdot \vec{\Delta}_1(t) + N_1^{\mathrm{opt}}(t) + N_1^s(t),$$

$$(2.28a)$$

$$\bar{\varepsilon}_1(t) = p_{1'}(t) - p_1(t) + 2\left(\frac{2\pi}{\lambda_{1'}}\vec{n}_{3'}(t) \cdot \vec{\delta}_1(t) - \frac{2\pi}{\lambda_{1'}}\vec{n}_{3'}(t) \cdot \vec{\Delta}_1(t)\right)$$

$$+ \mu_{1'}(t) + N_1^\varepsilon(t),$$

$$(2.28b)$$

$$\bar{\tau}_1(t) = p_{1'}(t) - p_1(t) + \mu_{1'}(t) + N_1^\tau(t).$$

$$(2.28c)$$

Similar arguments yield the interferometric signals of the adjacent OB $1'$:

$$\bar{s}_{1'}(t) = H_{1'}(t) + p_3(t - \tfrac{L_{2'}(t)}{c}) - p_{1'}(t) - \frac{2\pi}{\lambda_3}\vec{n}_{2'}(t) \cdot \vec{\Delta}_3(t - \tfrac{L_{2'}(t)}{c})$$

$$- \frac{2\pi}{\lambda_3}\vec{n}_2(t) \cdot \vec{\Delta}_{1'}(t) + N_{1'}^{\mathrm{opt}}(t) + N_{1'}^s(t),$$

$$(2.28d)$$

$$\bar{\varepsilon}_{1'}(t) = p_1(t) - p_{1'}(t) + 2\left(\frac{2\pi}{\lambda_1}\vec{n}_2(t) \cdot \vec{\delta}_{1'}(t) - \frac{2\pi}{\lambda_1}\vec{n}_2(t) \cdot \vec{\Delta}_{1'}(t)\right)$$

$$+ \mu_1(t) + N_{1'}^\varepsilon(t),$$

$$(2.28e)$$

$$\bar{\tau}_{1'}(t) = p_1(t) - p_{1'}(t) + \mu_1(t) + N_{1'}^\tau(t).$$

$$(2.28f)$$

All other interferometric signals from S/C 2 and 3 can be constructed by cyclic permutation of the indices, as explained in Sec. 2.4.1.

In this chapter, after having treated gravitational waves and their detection in principle, we focussed on the space-based detector Laser Interferometer Space Antenna. In the first section, a short overview of the mission history was given, followed by details about the measurement principles and noise sources. After having defined a consistent notation for labelling optical benches, spacecraft, links etc., we proceeded to the formulation of the pure interferometric signals onboard, i.e.,

the science, test mass and reference IFO outputs. They are given by Eqn. (2.28a) – (2.28f) with cyclic permutations for the other spacecraft.

The accumulated phase shifts $H_i(t)$ due to gravitational waves are to be extracted from the six science signals $\bar{s}_i(t)$ in order to determine the input strain signal. However, many noise sources, first and foremost laser phase noise, p_i, swamp the data by orders of magnitude and make it impossible to extract the GW signal directly. Therefore, an algorithm to cancel the primary noise sources is needed. The input to this algorithm can only consist of the available onboard phase measurements, i.e., the 18 data streams derived in this chapter and auxiliary data streams which will be discussed in Ch. 4. The algorithm itself that removes laser phase noise is called Time-Delay Interferometry and is discussed extensively in the following chapters.

Chapter 2

3 Time-Delay Interferometry

This chapter will explain in detail an algorithm to remove the laser frequency noise from the onboard data streams discussed in Sec. 2.5. The algorithm, called Time-Delay Interferometry (TDI), was first proposed by [AET99] for a simplified model of the LISA onboard measurements and is based on previous work [GHTF96]. TDI is performed on ground in post-processing. Its functionality is crucial for LISA-like missions, because otherwise laser frequency noise will swamp completely the data and make it impossible to extract the gravitational wave signal. We will first give an overview about the basic procedure and notation, followed by the treatment of a non-flexing and a flexing LISA constellation. The last two sections discuss experimental verification test beds on ground and in space, and possible prospects for Time-Delay Interferometry in other space-based GW detectors than LISA.

3.1 Fundamentals of Time-Delay Interferometry

In this section, we will state the problem Time-Delay Interferometry deals with and discuss the algorithm in an extremely simplified LISA case. Furthermore, a standardisation of TDI is given and a powerful time-delay operator notation introduced, which we will use extensively for the rest of the thesis.

3.1.1 Problem Statement

The interferometric detection of GWs requires phase measurements with μrad precision. However, due to armlength mismatches in ground- and space-based interferometers, the laser phase noise does not completely cancel at the recombining beam splitter, and the residual phase noise will be orders of magnitude above the μrad requirement. We will now estimate the remaining noise and start with an idealised Michelson interferometer, extend the discussion to an unequal-arm interferometer and will finally estimate the remaining laser phase noise in the science interferometer for LISA.
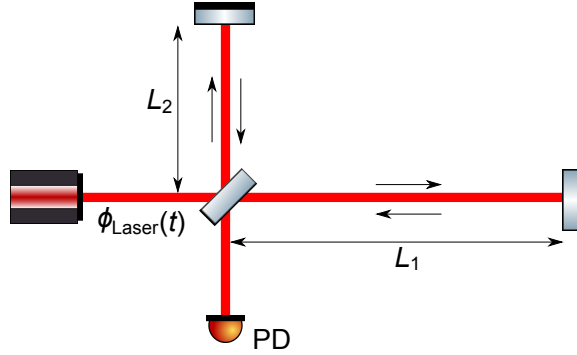
Figure 3.1: An unequal-arm Michelson interferometer with armlengths L_1 and L_2 and physical round-trip times $\frac{2L_1}{c}$ and $\frac{2L_2}{c}$. The laser comprises light with phase $\phi_{\text{Laser}}(t) = \omega t + p(t)$ propagated through the unequal arms. The PD at the output port detects the differential phase of the two light rays.

Idealised Michelson Interferometer

The interferometer arms in an idealised Michelson interferometer would be matched such that they have both the same length (Fig. 1.6, with $L_1 = L_2$ assumed). In that case, it is not hard to see that the phase noise from the (common) laser source cancels exactly at the PD, as we will show subsequently. Therefore, consider the two accumulated optical phases $y_1(t)$ and $y_2(t)$ of light that arrives at the PD of an unequal-arm Michelson IFO as depicted in Fig. 3.1:

$$
\begin{aligned}
y_1(t) &= H_1(t) + \phi_{\text{Laser}}(t - \tfrac{2L_1}{c}) + \phi_{\text{n},1}(t) \\
&= H_1(t) + \omega(t - \tfrac{2L_1}{c}) + p(t - \tfrac{2L_1}{c}) + \phi_{\text{n},1}(t)\,, \\
y_2(t) &= H_2(t) + \phi_{\text{Laser}}(t - \tfrac{2L_2}{c}) + \phi_{\text{n},2}(t) \\
&= H_2(t) + \omega(t - \tfrac{2L_2}{c}) + p(t - \tfrac{2L_2}{c}) + \phi_{\text{n},2}(t)\,.
\end{aligned}
$$

Here, H_1 and H_2 are the accumulated phase shifts collected in the perpendicular arms 1 and 2 due to gravitational waves, p is the laser phase noise, in each case delayed by the corresponding round-trip time in the interferometer arms, and $\phi_{\text{n},1}(t)$, $\phi_{\text{n},2}(t)$ denote all appearing secondary noise sources in the IFO arms which are not further specified here. Moreover, since $\phi_{\text{Laser}}(t)$ includes the frequency ramp ωt according to Eq. (2.15), it appears time-delayed by the corresponding round-trip time $\frac{2L_1}{c}$ and $\frac{2L_2}{c}$, too. Note here that the common optical path from the laser to the BS and from the BS to the PD does not add any relative phase shift and is thus neglected.

The subtraction of the two data streams, i.e., $y_{\text{PD}}(t) = y_1(t) - y_2(t)$, corresponds here physically to the interference of the two laser beams at the beam splitter (Sec. 2.4.2). The differential phase is then given by

$$y_{\text{PD}}(t) = H_1(t) - H_2(t) + \omega(\tfrac{2L_2}{c} - \tfrac{2L_1}{c}) + p(t - \tfrac{2L_1}{c}) - p(t - \tfrac{2L_2}{c}) + \phi_{\text{n},1}(t) - \phi_{\text{n},2}(t) \quad (3.1)$$

and cancels the frequency ramp ωt. In the case of equal arms and thus equal round-trips, $\frac{2L_1}{c} = \frac{2L_2}{c}$, the laser phase noise completely cancels. Hence, in the photodetector, laser frequency noise does not appear and it is in principle possible to extract the GW signal.

Unequal-Arm Michelson Interferometer

However, if imperfections and noise affect the armlengths of the idealised Michelson interferometer and make them unequal, laser phase noise will not completely cancel in (3.1). If we assume a small constant difference $\Delta L = L_2 - L_1$ between the arms, then the PD phase output including readout noise (subsumed together with $\phi_{n,1}(t)$ and $\phi_{n,2}(t)$ in $N(t)$), but excluding the constant term $\frac{\omega \Delta L}{c}$ according to the phase definition (2.17), could be described by

$$y_{\mathrm{PD}}(t) \approx H_1(t) - H_2(t) + p(t - \tfrac{2L_1}{c}) - p\left(t - \tfrac{2(L_1 + \Delta L)}{c}\right) + N(t)\,.$$

In order to estimate the effect of the residual laser phase noise on the interferometer sensitivity, we can use the formula [BMR$^+$79]

$$\frac{\widetilde{x}(f)}{\Delta L} = \frac{\widetilde{\nu}(f)}{\nu} \quad \Longleftrightarrow \quad \widetilde{x}(f) = \Delta L \cdot \frac{\widetilde{\nu}(f)}{\nu}\,. \tag{3.2}$$

This equation translates an inequality of the interferometer armlengths, $\Delta L \neq 0$, to relative frequency fluctuations $\frac{\widetilde{\nu}(f)}{\nu}$ with laser frequency ν. The quantities $\widetilde{x}(f)$ and $\widetilde{\nu}(f)$ denote the linear spectral density for displacement and frequency noise, respectively.

In Sec. 2.3, the frequency noise of a pre-stabilised, space-qualified laser was assumed to be around $280\,\frac{\mathrm{Hz}}{\sqrt{\mathrm{Hz}}}$. For ground-based lasers, a stabilisation to a level of $1\,\frac{\mathrm{Hz}}{\sqrt{\mathrm{Hz}}}$ is possible in the frequency range of $10\,\mathrm{Hz} - 10^4\,\mathrm{Hz}$ [KJLS09]. An armlength mismatch of $1\,\mathrm{mm}$ translates then to

$$\widetilde{x}_{\mathrm{ground}}(f) = \Delta L \cdot \frac{\widetilde{\nu}_{\mathrm{ground}}(f)}{\nu} = 1\,\mathrm{mm} \cdot \frac{1\,\frac{\mathrm{Hz}}{\sqrt{\mathrm{Hz}}}}{3 \cdot 10^{14}\,\mathrm{Hz}} \approx 3.3 \cdot 10^{-18}\,\frac{\mathrm{m}}{\sqrt{\mathrm{Hz}}}\,.$$

Compared to a typical total armlength of the order $L = 1\,\mathrm{km}$, $\widetilde{x}_{\mathrm{ground}}(f)$ translates to an equivalent strain linear spectral density according to Eq. (1.27) of

$$\widetilde{h} = 2 \cdot \frac{\widetilde{x}_{\mathrm{ground}}(f)}{L} \approx 6.6 \cdot 10^{-21}\,\frac{1}{\sqrt{\mathrm{Hz}}}\,. \tag{3.3}$$

In order to transform this to strain, we can compute the averaged (root mean square) value h_{rms} in a certain frequency band $\Delta \nu = \nu_2 - \nu_1$, where the linear spectral

density $\widetilde{h}(f)$ is known:

$$h_{\mathrm{rms}} = \sqrt{\int\limits_{\nu_1}^{\nu_2} \mathrm{d}f\, (\widetilde{h}(f))^2}\,. \tag{3.4a}$$

In the case of constant spectral densities, this reduces to

$$h_{\mathrm{rms}} = \widetilde{h}(f)\sqrt{\Delta\nu}\,. \tag{3.4b}$$

Hence, for $\Delta\nu = 10^4\,\mathrm{Hz} - 10\,\mathrm{Hz} = 9990\,\mathrm{Hz}$, this yields here

$$h_{\mathrm{rms}} = \widetilde{h} \cdot \sqrt{\Delta\nu} \approx 6.7 \cdot 10^{-19}\,, \tag{3.5}$$

which corresponds to a strain due to laser frequency noise in the ground-based detectors. Since the strain of a strong signal is around $h \approx 10^{-21}$ and thus below h_{rms}, it is necessary (and possible) with further techniques to suppress laser frequency noise such that it does not limit the detection of GW on Earth (e.g., by using the average length of both arms as reference in power recycling [GTV$^+$13]).

LISA Case

For space-based gravitational wave detectors, the armlength mismatch within the science interferometer will not lie in the range of mm or cm as in ground-based detectors. Rather, it lies in the range of million kilometre, since one interferometer arm is between the S/C, and the other onboard only. Making use of Eq. (3.2), we get

$$\widetilde{x}_{\mathrm{stab}} = \Delta L \cdot \frac{\widetilde{\nu}_{\mathrm{stab}}}{\nu} = 5 \cdot 10^9\,\mathrm{m} \cdot \frac{280\,\frac{\mathrm{Hz}}{\sqrt{\mathrm{Hz}}}}{3 \cdot 10^{14}\,\mathrm{Hz}} \approx 4.7 \cdot 10^{-3}\,\frac{\mathrm{m}}{\sqrt{\mathrm{Hz}}} \tag{3.6a}$$

corresponding to phase noise $\widetilde{\phi}_{\mathrm{stab}}$ (cf. Eq. (2.10b)) of

$$\widetilde{\phi}_{\mathrm{stab}} = \frac{2\pi}{\lambda}\widetilde{x}_{\mathrm{stab}} = \frac{2\pi}{\lambda} \cdot \Delta L \cdot \frac{\widetilde{\nu}_{\mathrm{stab}}}{\nu} = \frac{2\pi\Delta L}{c}\widetilde{\nu}_{\mathrm{stab}} \approx 3 \cdot 10^4\,\frac{\mathrm{rad}}{\sqrt{\mathrm{Hz}}} \tag{3.6b}$$

which is fifteen orders of magnitude above the value for ground-based detectors. Hence, by the direct recombination of two light beams at a BS, the laser frequency noise will not cancel naturally as it was the case for ground-based interferometers [Tin08b].

Hence, one needs a post-processing algorithm that synthesises the output of an equal-armlength interferometer from one-way link measurements in order to cancel the laser frequency noise as shown above for the ground-based Michelson interferometer case. The required scheme should of course preserve the gravitational wave signal. An algorithm for LISA-like missions fulfilling this is Time-Delay Interferometry.
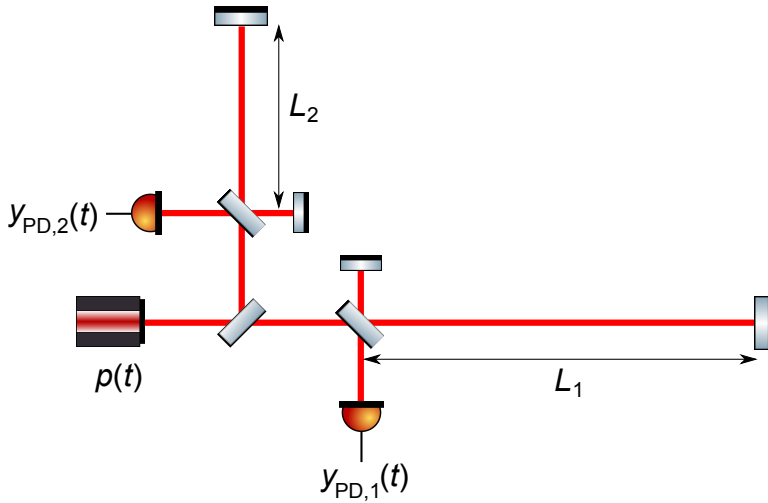
Figure 3.2: An unequal-arm interferometric setup with two separate arm readout PDs. The separations of the recombination beam splitters are negligible compared with the armlengths L_1 and L_2.

3.1.2 Basic Idea of Time-Delay Interferometry

In the following, we will discuss the TDI functionality in a very simplified example. In order to get a rough idea of the algorithm, we consider the interferometric setup at rest shown in Fig. 3.2.

The light sent from the laser is split into two beams entering the arms, called 1 and 2. In each arm, a 50:50 beam splitter routes half of the light power to a PD. The other half of the light travels along the arm with length L_1 or L_2, is then reflected off an end mirror and sent back to the PD. There, the interferometric readout is performed giving phase signals $y_{\mathrm{PD},1}(t)$ and $y_{\mathrm{PD},2}(t)$ according to the phase definition (2.17). Neglecting any frequency ramp ω_{het} (from Doppler shifts in the arms) and common mode optical paths (from laser to BS, and BS to PD), we find

$$
\begin{aligned}
y_{\mathrm{PD},1}(t) &= H_1(t) + p(t - \mathcal{T}_1) - p(t) + N_1(t)\,, & \text{(3.7a)} \\
y_{\mathrm{PD},2}(t) &= H_2(t) + p(t - \mathcal{T}_2) - p(t) + N_2(t)\,. & \text{(3.7b)}
\end{aligned}
$$

Here, $\mathcal{T}_1 = \frac{2L_1}{c}$ and $\mathcal{T}_2 = \frac{2L_2}{c}$ are the photon round-trip times of arm 1 and 2 (in contrast to $T_{0,i}$ for one-link light travel times for LISA), and $H_1(t)$ and $H_2(t)$ denote the gravitational wave phase shift in each arm. $N_1(t)$ and $N_2(t)$ include all kinds of noise contributions within the PD readout signal. Note here that, in contrast to the simple Michelson interferometer from Sec. 3.1.1, the instantaneous laser phase noise $p(t)$ enters the measurement and is compared with light that was sent from the laser a certain time $\mathcal{T}_1$ or $\mathcal{T}_2$ earlier and that gives rise to phase noise $p(t - \mathcal{T}_1)$ and $p(t - \mathcal{T}_2)$, respectively.

We can easily see that pure subtraction of the data streams will not remove the laser phase noise p as it was the case for the Michelson IFO in the last section:

$$y_{\text{PD},1}(t) - y_{\text{PD},2}(t) = H_1(t) - H_2(t) + p(t - \mathcal{T}_1) - p(t - \mathcal{T}_2) + N_1(t) - N_2(t). \quad (*)$$

The crucial trick is now to delay the photodetector signals by the round-trip time of the *other* arm, i.e., $y_{\text{PD},1}(t)$ by $\mathcal{T}_2$ and $y_{\text{PD},2}(t)$ by $\mathcal{T}_1$:

$$y_{\text{PD},1}(t - \mathcal{T}_2) \overset{(3.7a)}{=} H_1(t - \mathcal{T}_2) + p(t - \mathcal{T}_1 - \mathcal{T}_2) - p(t - \mathcal{T}_2) + N_1(t - \mathcal{T}_2),$$

$$y_{\text{PD},2}(t - \mathcal{T}_1) \overset{(3.7b)}{=} H_2(t - \mathcal{T}_1) + p(t - \mathcal{T}_2 - \mathcal{T}_1) - p(t - \mathcal{T}_1) + N_2(t - \mathcal{T}_1).$$

As we can clearly see, the term $p(t - \mathcal{T}_1 - \mathcal{T}_2)$ appears in both equations and thus can be subtracted:

$$y_{\text{PD},1}(t - \mathcal{T}_2) - y_{\text{PD},2}(t - \mathcal{T}_1) = \begin{aligned}& H_1(t - \mathcal{T}_2) - H_2(t - \mathcal{T}_1) + p(t - \mathcal{T}_1) \\ & -p(t - \mathcal{T}_2) + N_1(t - \mathcal{T}_2) - N_2(t - \mathcal{T}_1). \quad (**)\end{aligned}$$

In this combination, the laser phase noise enters exactly with the same time stamps as in $(*)$. Thus, if we subtract $(*)$ from $(**)$ and call this combination $x(t)$, we finally get

$$\begin{aligned} x(t) \; &:= \; \big(y_{\text{PD},1}(t - \mathcal{T}_2) - y_{\text{PD},2}(t - \mathcal{T}_1) \big) - \big(y_{\text{PD},1}(t) - y_{\text{PD},2}(t) \big) & (3.8a) \\ &= \; H_1(t - \mathcal{T}_2) - H_2(t - \mathcal{T}_1) + H_2(t) - H_1(t) + N_1(t - \mathcal{T}_2) - N_2(t - \mathcal{T}_1) \\ & \quad + N_2(t) - N_1(t) & (3.8b) \\ &\sim \; H_1(t - \mathcal{T}_2) - H_2(t - \mathcal{T}_1) + H_2(t) - H_1(t). & (3.8c) \end{aligned}$$

Here, we introduced a new notation. The $\sim$ denotes the neglection of all secondary noise sources (here, N_1 and N_2 at arbitrary time stamps) and simultaneously the consideration of the target contribution (here, the GW). This means, e.g., for the photodetector outputs of Fig. 3.2:

$$y_{\text{PD},1}(t) \overset{(3.7a)}{\sim} H_1(t) + p(t - \mathcal{T}_1) - p(t), \quad y_{\text{PD},2}(t) \overset{(3.7b)}{\sim} H_2(t) + p(t - \mathcal{T}_2) - p(t).$$

In Eq. (3.8c), a laser phase noise free data stream is constructed with gravitational wave signals H_1 and H_2 that enter at three time stamps t, $t - \mathcal{T}_1 = t - \frac{2L_1}{c}$ and $t - \mathcal{T}_2 = t - \frac{2L_2}{c}$. Eq. (3.8a) finally emphasises the basic idea of TDI: the construction of laser phase noise free data streams by properly adding and time-shifting the interferometric PD measurements. This data combination should then of course preserve the GW signal.

Gravitational Wave Signal Preservation and the Transfer Function

The mere existence of a term or a combination with H_i in the output data does not guarantee GW signal preservation. Instead, we have to regard the response to gravitational waves in the Fourier domain. We will demonstrate the procedure here

for the simple case of the interferometric setup presented in Fig. 3.2. For the sake of simplicity, the round-trip light travel times in both arms are assumed to be equal, $\mathcal{T}_1 = \mathcal{T}_2 =: \mathcal{T}$.

Converting Eq. (3.8c) to Fourier space using the definition and transformation rule [Ott11]

$$
\mathcal{F}[u(t)] := \int\limits_{-\infty}^{\infty} \mathrm{d}t\, u(t)\mathrm{e}^{-\mathrm{i}\cdot 2\pi f t} \,, \quad \mathcal{F}[u(t - t_0)] = \mathcal{F}[u(t)] \cdot \mathrm{e}^{-\mathrm{i}\cdot 2\pi f t_0} \,, \tag{3.9}
$$

we get

$$
\begin{aligned}
\mathcal{F}[x(t)] \quad &\sim \quad \mathcal{F}[H_1(t - \mathcal{T})] - \mathcal{F}[H_2(t - \mathcal{T})] + \mathcal{F}[H_2(t)] - \mathcal{F}[H_1(t)] \\
&= \quad \mathcal{F}[H_1]\mathrm{e}^{-\mathrm{i}\cdot 2\pi f \mathcal{T}} - \mathcal{F}[H_2]\mathrm{e}^{-\mathrm{i}\cdot 2\pi f \mathcal{T}} + \mathcal{F}[H_2] - \mathcal{F}[H_1] \\
&= \quad (\mathcal{F}[H_1] - \mathcal{F}[H_2])(\mathrm{e}^{-\mathrm{i}\cdot 2\pi f \mathcal{T}} - 1) \,.
\end{aligned}
$$

The frequency-dependent function in the second bracket translates in Fourier space an input differential strain $\mathcal{F}[\Delta H] = \mathcal{F}[H_1] - \mathcal{F}[H_2]$ to the unequal-arm interferometric output $\mathcal{F}[x]$, and this is per definition the transfer function. For the sake of legibility, we will denote the transfer function without the Fourier $\mathcal{F}$ as $\mathfrak{T}_{\Delta H \to x}(f)$ (instead of $\mathfrak{T}_{\mathcal{F}[\Delta H] \to \mathcal{F}[x]}(f)$). Thus,

$$
\mathfrak{T}_{\Delta H \to x}(f) = \mathrm{e}^{-\mathrm{i}\cdot 2\pi f \mathcal{T}} - 1 = \left(\mathrm{e}^{-\mathrm{i}\cdot \pi f \mathcal{T}} - \mathrm{e}^{\mathrm{i}\cdot \pi f \mathcal{T}}\right) \mathrm{e}^{-\mathrm{i}\cdot \pi f \mathcal{T}} = -2\mathrm{i}\sin(\pi f \mathcal{T})\mathrm{e}^{-\mathrm{i}\cdot \pi f \mathcal{T}}
$$

with the absolute value

$$
|\mathfrak{T}_{\Delta H \to x}(f)| = 2\sin(\pi f \mathcal{T}) \,, \tag{3.10}
$$

which is plotted in Fig. 3.3 with the choice of the photon round-trip time $\mathcal{T} = 33.4\,\mathrm{s}$.

The above calculation can be performed analogously for the noise contributions in Eq. (3.8b) which yields the identical transfer function for the noise. That is, both the noise and the gravitational wave signal show the same modulation. This in turn means that the signal-to-noise ratio (SNR) in the presented LISA-like interferometric setup (Fig. 3.2) is for approximately equal armlengths similar to the signal-to-noise ratio achievable with an equal-arm detector, where the gravitational wave reconstruction is possible [TA99].

In the following, 'preservation of gravitational waves' connotes the statement that a data combination maximises the SNR. Hence, for a data combination that preserves the GW signal it can then be shown in a similar manner as here that the transfer function is comparable to that of an equal-arm interferometer.

Transfer function for the simplified TDI scheme
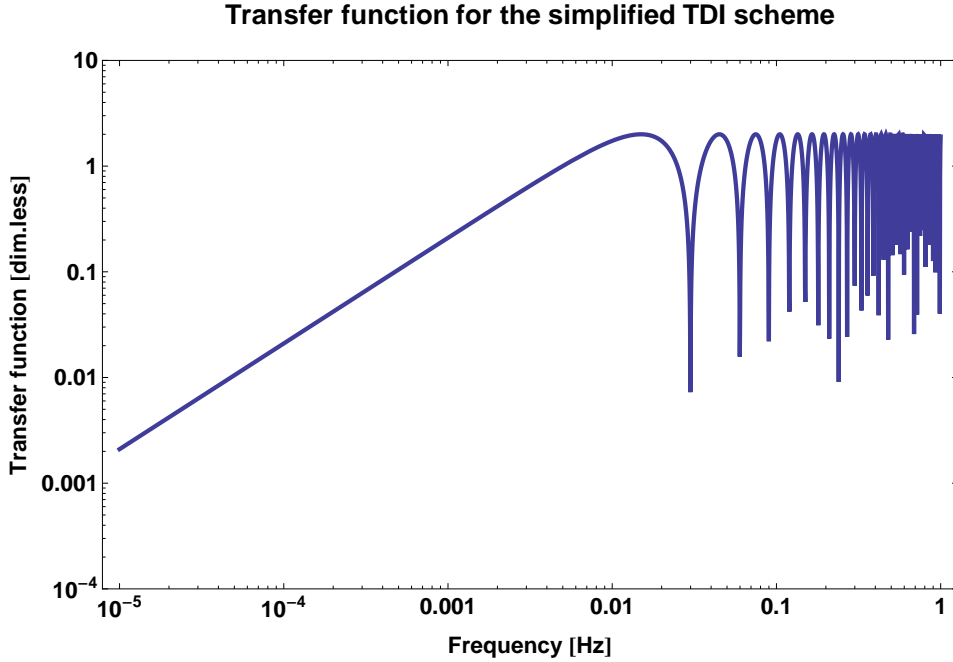
Figure 3.3: Absolute of the transfer function $\mathfrak{T}_{\Delta H \to x}$ of the simplified TDI scheme for a setup with 10 million kilometre round-trip armlength, neglecting any optical losses. For frequencies $f < 10\,\mathrm{mHz}$, the transfer function rolls off with f^{-1} towards low frequencies, while for $f > 10\,\mathrm{mHz}$ the transfer function shows an absolute term, and nulls of the round-trips enter the transfer function. At multiples of frequencies equal to the inverse of twice the armlength, i.e., $f_{\mathrm{null}}^{\mathrm{unequal}}(N) = N \cdot \frac{3 \cdot 10^8\,\frac{\mathrm{m}}{\mathrm{s}}}{2 \cdot 5 \cdot 10^9\,\mathrm{m}} = 0.03 \cdot N\,\mathrm{Hz}$, the gravitational wave effect cancels naturally, as can be seen from the sine function in $\mathfrak{T}_{\Delta H \to x}$.

The Synthesised Photon Path

The combination $x(t)$ synthesises the interferometric signal of two photon beams shown in Fig. 3.4 (black and blue).

In order to understand the photon path, we rewrite Eq. (3.8a) in the form

$$x(t) = (\, y_{\mathrm{PD},2}(t) + y_{\mathrm{PD},1}(t - \mathcal{T}_2)\,) - (\, y_{\mathrm{PD},1}(t) + y_{\mathrm{PD},2}(t - \mathcal{T}_1)\,) \tag{3.11}$$

and then go backwards in time along the track presented in Fig. 3.4.

As explained previously, the laser beam is split in two parts and arrives at the BS of the long arm interferometers. For the blue path, the Eastern BS is the starting point (marked by the arrow tail), while for the black line it is the end point (marked by the final dot). Vice versa, the photon path in black starts at the Northern BS, and the blue line has its destination there.
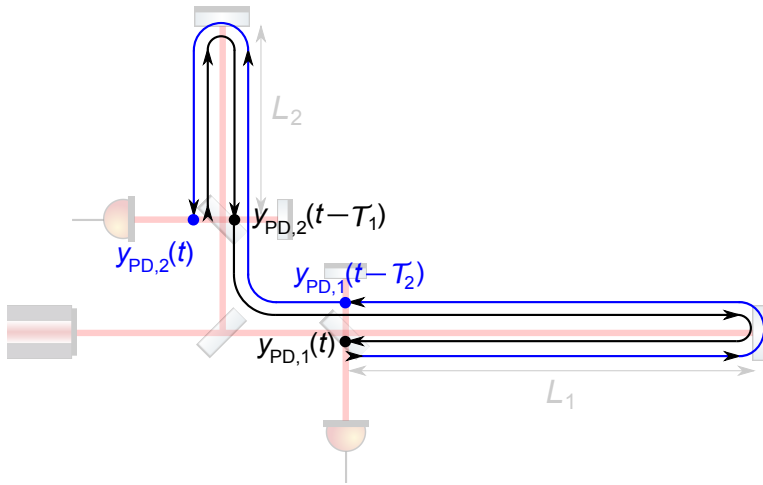
Figure 3.4: Synthesised photon path of the combination $x(t)$ with its phase contributions (marked by the dots). The photon beam from the laser is split at the PD into two beams (black and blue). One portion (blue) is virtually travelling down arm 1 forth and back and then entering arm 2 again travelling forth and back. Simultaneously, the other part of the split light (black line) propagates virtually first through arm 2 and then through arm 1. Both light rays are reaching the 'sender' (i.e., the BS) at the same receiving time t in the case that the IFO is at rest. Hence, both light rays have travelled the same optical path and, as in the Michelson IFO, the laser frequency noise cancels naturally.

The first contribution of $x(t)$ in Eq. (3.11) is the instantaneous measurement $y_{\mathrm{PD},2}(t)$ at PD 2 and is marked by a dot. This corresponds to the destination of the blue line. The second term in $x(t)$ is, however, no direct measurement, but instead interpolated using the proper time shifts. That is, light starting from the Eastern BS has performed one round-trip along L_1 and is read out interferometrically by PD 1 (marked again by a blue dot). In order to add this measurement properly to $y_{\mathrm{PD},2}(t)$, it needs to be shifted by $\mathcal{T}_2 = \frac{2L_2}{c}$, which corresponds to a physical round-trip in the Northern interferometer arm. The sum of the instantaneous measurement $y_{\mathrm{PD},2}(t)$ and the delayed contribution $y_{\mathrm{PD},1}(t - \mathcal{T}_2)$ in Eq. (3.11) forms the first bracket in $x(t)$. Graphically, this addition is illustrated by the end-to-end blue line in Fig. 3.4.

The same description holds for the black colored photon path, where only the chronological order of the arm round-trips is switched. In the case of a fixed optical setup, both photon paths will have covered exactly the same distance at its destinations. Therefore, if differenced as in $x(t)$, laser frequency noise cancels naturally as it was the case for the Michelson interferometer. Note, however, that the shown light path is a virtual path synthesisation in post-processing, but no 'real' path, since light from arm 1 will not enter arm 2 and vice versa.

TDI in the LISA Case

It should be emphasised that we assumed L_1, L_2 to be constant in time and known to an extremely high accuracy in the previous scenario. However, the LISA arms are of course not exactly equal and vary in time due to the complex spacecraft orbits. Hence, it is not as easy as claimed above to eliminate laser phase noise p from the photodetector signals. Furthermore, in contrast to the Michelson interferometer, LISA relies on a laser receiver transponder scheme with up to six different lasers. The laser frequency noise cancellation scheme, TDI for LISA, will be much more complex than the demonstration of the basic principle here. The details will be discussed in Sec. 3.2 and 3.3.

3.1.3 Time-Delay Interferometry Generations

The TDI theory can in principle be divided into four classes, called TDI generations. They are displayed schematically in Fig. 3.5 and are discriminated as follows.

- **TDI 1.0 or TDI 1st generation** is valid for a static LISA constellation and does not account for rotation and flexing:

$$L_i(t) = L_i = \text{const.} , \quad L_{\underline{i}} = L_{i'} . \tag{3.12a}$$

  The laser phase noise cancellation is (in principle) exact. Note that the first condition emphasises that all armlengths $(i = 1, 1', 2, 2', 3, 3')$ are constant in time, while the second condition implies that the light travel time in one arm is independent of the light propagation direction.

- **TDI 1.5 or modified TDI generation** is valid for a rigid but rotating spacecraft constellation:

$$L_i(t) = L_i = \text{const.} , \quad L_{\underline{i}} \neq L_{i'} . \tag{3.12b}$$

  The laser phase noise cancellation is still (in principle) exact. Here, the armlengths are assumed to be fixed, but one distinguishes the propagation direction in the arms.

- **TDI 2.0 or TDI 2nd generation** combinations account for a rotating and flexing LISA constellation with nominal armlengths L_i^0 and relative LoS velocities $v_{\text{rel},i}$:

$$L_i(t) = L_i^0 + v_{\text{rel},i} \cdot t , \quad L_{\underline{i}} \neq L_{i'} . \tag{3.12c}$$

  That is, the armlengths vary linearly in time on a well-defined time scale, and due to the rotation, the propagation direction in the arms needs to be distinguished carefully. As a consequence, the laser phase noise cancellation is here not exact anymore, but at least within an approximation to a linear flexing of the arms.
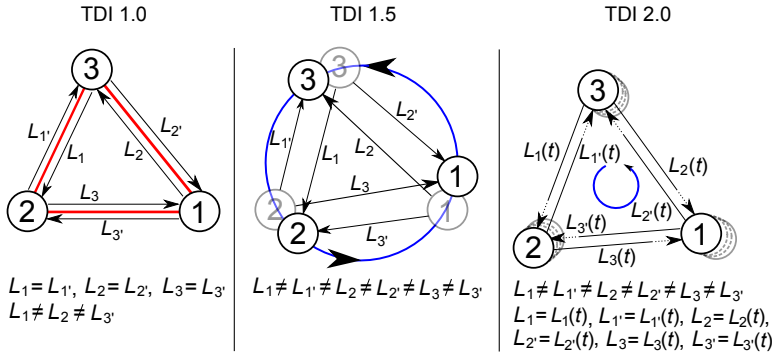
Figure 3.5: Schematic discrimination between TDI generations. Left: The algorithm for TDI 1.0 takes LISA with fixed S/C without any relative motion; the armlengths in terms of light travel time are then constant. Center: TDI 1.5 accounts for the rotation of a rigid constellation; the armlengths depend on the direction of laser propagation, i.e., $L_{\underline{i}} \neq L_{\underline{i}'}$ in general. Right: Higher TDI generations (as, e.g., TDI 2.0) account for the rotation (blue arrow) and flexing of the constellation; the armlengths become additionally time-dependent; for TDI 2.0, a linear LoS velocity is regarded, while for TDI 3.0 relative acceleration terms enter the algorithm.

- **TDI 3.0 or TDI 3rd generation** is in analogy to TDI 2.0, but within an approximation for S/C that have a constant acceleration $a_{\mathrm{rel},i}$ relative to each other along the line of sight:

$$L_i(t) = L_i^0 + v_{\mathrm{rel},i} \cdot t + \frac{1}{2} a_{\mathrm{rel},i} \cdot t^2, \quad L_{\underline{i}} \neq L_{\underline{i}'}, \tag{3.12d}$$

and so on for higher orders. For our purpose, TDI 2.0 is enough to fulfill the requirements for laser frequency noise cancellation given in Sec. 2.3. Therefore, this thesis will only deal with TDI generations up to 2.0.

3.1.4 Time-Delay Shorthand Notation

Instead of using the timestamp notation for time delays (e.g., $p(t - \frac{L_3(t)}{c})$), we will introduce shorthand notations and extensively make use of it. Note that in the common TDI papers [AET99; TEA04; SWSV04; DNV02] various conflicting notations coexist (see appendix D). We will define two kinds of notations.

Time-Delay Operator

It is convenient to introduce time-delay operators $\widehat{\mathbf{D}}$ which act on continuous functions $f(t)$ as [TD14]

$$\widehat{\mathbf{D}}_{\boldsymbol{j}} f(t) = f\left(t - \frac{L_j}{c}\right), \quad \widehat{\mathbf{D}}_{\boldsymbol{k}} \widehat{\mathbf{D}}_{\boldsymbol{j}} f(t) = f\left(t - \frac{L_k}{c} - \frac{L_j}{c}\right). \tag{3.13}$$

Here, j, k can take the values of $1, 1', 2, 2', 3, 3'$ according to Fig. 2.8. These time-delay operator definitions are sufficient in the case of a non-flexing, rotating LISA constellation, denoted by the hat, since all armlengths are constant in time.

Powers of time-delay operators mean multiple applications of $\widehat{\mathbf{D}}$, e.g.,

$$\widehat{\mathbf{D}}_{\boldsymbol{j}}^2 f(t) = \widehat{\mathbf{D}}_{\boldsymbol{j}} \widehat{\mathbf{D}}_{\boldsymbol{j}} f(t) = \widehat{\mathbf{D}}_{\boldsymbol{j}} f(t - \tfrac{L_j}{c}) = f((t - \tfrac{L_j}{c}) - \tfrac{L_j}{c}) = f(t - \tfrac{2L_j}{c}) \,.$$

Hence, as an example, the unequal-arm Michelson output variable $x(t)$ from Eq. (3.8a) can be written as

$$
\begin{aligned}
x(t) &= (\, y_{\mathrm{PD},1}(t - \mathcal{T}_2) - y_{\mathrm{PD},2}(t - \mathcal{T}_1)\,) - (\, y_{\mathrm{PD},1}(t) - y_{\mathrm{PD},2}(t)\,) \\
&= y_{\mathrm{PD},1}(t - \tfrac{2L_2}{c}) - y_{\mathrm{PD},2}(t - \tfrac{2L_1}{c}) - y_{\mathrm{PD},1}(t) + y_{\mathrm{PD},2}(t) \\
&= \widehat{\mathbf{D}}_{\boldsymbol{2}}^2 y_{\mathrm{PD},1}(t) - \widehat{\mathbf{D}}_{\boldsymbol{1}}^2 y_{\mathrm{PD},2}(t) - y_{\mathrm{PD},1}(t) + y_{\mathrm{PD},2}(t) \\
&= (\widehat{\mathbf{D}}_{\boldsymbol{2}}^2 - \mathbb{1}) y_{\mathrm{PD},1}(t) - (\widehat{\mathbf{D}}_{\boldsymbol{1}}^2 - \mathbb{1}) y_{\mathrm{PD},2}(t) \,,
\end{aligned}
\tag{3.14}
$$

where we introduced the identity operator

$$\mathbb{1} f(t) = f(t - 0) = f(t) = \widehat{\mathbf{D}}_{\boldsymbol{j}}^0 f(t) \,. \tag{3.15}$$

However, in the case of arm flexing, the armlengths L_k are time-dependent and the time-delay operators need to be defined in a more complex way as follows. In order to emphasise the time-dependent character of the time-delay operators, we drop the hat notation:

$$\boldsymbol{\mathcal{D}_j} f(t) = f\left(t - \frac{L_j(t)}{c}\right), \tag{3.16a}$$

$$\boldsymbol{\mathcal{D}_k} \boldsymbol{\mathcal{D}_j} f(t) = \boldsymbol{\mathcal{D}_k} f\left(t - \frac{L_j(t)}{c}\right) = f\left(t - \frac{L_k(t)}{c} - \frac{L_j\left(t - \frac{L_k(t)}{c}\right)}{c}\right), \tag{3.16b}$$

and so on for multiple time delays. Note that the delay operator $\boldsymbol{\mathcal{D}_i}$ shifts *all* time-dependent functions (also as arguments) by the corresponding light travel time $\frac{L_i(t)}{c}$. That is, the time t is substituted *everywhere* by $t - \frac{L_i(t)}{c}$. Therefore, if applied twice, the time t as well as the argument in the function $L_j(t)$ is time-shifted itself (Eq. (3.16b)).

In order to handle calculations for TDI 2.0 with the nested delay operator $\boldsymbol{\mathcal{D}_i}$, an approximation is derived in Sec. 3.3.1 that uses semi-constant time delays. That is, applying it once, it just gives the expressions of Eq. (3.16a). However, multiple application of the semi-constant time delays give a non-nested, but time-dependent time shift of the series. Exemplarily, for $f(t)$, this gives $f(t - \frac{L_j(t)}{c} - \frac{L_k(t)}{c})$ if delayed by the light travel time of link j and k. In some sense, the semi-constant time shift is a time-dependent version of $\widehat{\mathbf{D}}_{\boldsymbol{i}}$. As a remark, note that, in order to

emphasise the application of semi-constant time delays, we will use a shorthand notation introduced subsequently.

Colon, Comma and Semicolon Notation

In various papers dealing with TDI, the comma and semicolon notation is used to denote time-independent and time-dependent time delays. However, we previously mentioned a third kind of delay, that deals with (in some sense constant) time delays of time-dependent armlengths and need therefore a further distinction.

Instead of a comma, we will denote the time-independent time shifts by a colon:

$$f(t)_{:j} := \widehat{\mathbf{D}}_{\boldsymbol{j}} f(t) = f\left(t - \frac{L_j}{c}\right), \quad f(t)_{:jk} = \widehat{\mathbf{D}}_{\boldsymbol{k}} \widehat{\mathbf{D}}_{\boldsymbol{j}} f(t) = f\left(t - \frac{L_k}{c} - \frac{L_j}{c}\right). \tag{3.17}$$

Both equations only hold for armlengths that do not depend on time.

Next, a semicolon denotes time delays with time-dependent armlengths:

$$f(t)_{;j} \quad := \quad \boldsymbol{\mathcal{D}}_{\boldsymbol{j}} f(t) = f\left(t - \frac{L_j(t)}{c}\right), \tag{3.18a}$$

$$f(t)_{;jk} \quad = \quad \boldsymbol{\mathcal{D}}_{\boldsymbol{k}} \boldsymbol{\mathcal{D}}_{\boldsymbol{j}} f(t) = f\left(t - \frac{L_j(t)}{c}\right)_{;k} \tag{3.18b}$$

$$= \quad f\left(t - \frac{L_k(t)}{c} - \frac{L_j(t - \frac{L_k(t)}{c})}{c}\right). \tag{3.18c}$$

The semi-constant time shift is connotated by a comma in the following to emphasise the time-dependence of the delay time, but the neglection of nesting. Exemplarily,

$$f(t)_{,jk} = f\left(t - \frac{L_k(t)}{c} - \frac{L_j(t)}{c}\right).$$

In summary, a colon marks a delay by constant armlengths, and a comma denotes the application of the delay operator based on armlengths taken to be constant at a certain time stamp t for the time period of light travel. Contrary, the semicolon denotes the application of the time-delay operator based on varying armlengths.

Properties of Operators

One has to deal carefully with the order of operators in the flexing case as can be seen easily. It is

$$f(t)_{;jk} = f\left(t - \frac{L_k(t)}{c} - \frac{L_j(t - \frac{L_k(t)}{c})}{c}\right),$$

but vice versa we have

$$f(t)_{;kj} = f\left(t - \frac{L_j(t)}{c} - \frac{L_k(t - \frac{L_j(t)}{c})}{c}\right),$$

which is in general not equal, since $L_k(t) \neq L_k(t - \frac{L_j(t)}{c})$ and $L_j(t) \neq L_j(t - \frac{L_k(t)}{c})$ due to breathing and aberration. In other words, the time-delay operators $\boldsymbol{\mathcal{D}_j}$ and $\boldsymbol{\mathcal{D}_k}$ do not commute for $j \neq k$:

$$[\boldsymbol{\mathcal{D}_j}, \boldsymbol{\mathcal{D}_k}]f(t) = (\boldsymbol{\mathcal{D}_j}\boldsymbol{\mathcal{D}_k} - \boldsymbol{\mathcal{D}_k}\boldsymbol{\mathcal{D}_j})f(t) = f(t)_{;kj} - f(t)_{;jk} \neq 0\,. \tag{3.19a}$$

Here, we used the quantum mechanical notation for commutators, $[A,B] := AB - BA$. In contrast, the delay operators $\widehat{\mathbf{D}}_j$ and $\widehat{\mathbf{D}}_k$ commute. That is,

$$[\widehat{\mathbf{D}}_j, \widehat{\mathbf{D}}_k]f(t) = (\widehat{\mathbf{D}}_j\widehat{\mathbf{D}}_k - \widehat{\mathbf{D}}_k\widehat{\mathbf{D}}_j)f(t) = f(t)_{:kj} - f(t)_{:jk} = 0\,, \tag{3.19b}$$

and for the semi-constant delay, we find

$$f(t)_{,kj} - f(t)_{,jk} = 0\,. \tag{3.19c}$$

This again shows that one has to distinguish carefully between colon, comma and semicolon as well as the ordering of the indices in the case of time-dependent time delays. In particular, the notation requires

$$(f(t)_{;j})_{;k} = \boldsymbol{\mathcal{D}_k}(\boldsymbol{\mathcal{D}_j}f(t)) = f(t)_{;jk}\,. \tag{3.20}$$

As a final remark, it is straighforward to show that the delay operators apply 'linearly' to sums/differences of time-dependent functions, i.e., for two functions $f(t)$ and $g(t)$ and factors A and B constant in time. We have

$$\boldsymbol{\mathcal{D}_j}(A \cdot f(t) \pm B \cdot g(t)) = A \cdot \boldsymbol{\mathcal{D}_j}f(t) \pm B \cdot \boldsymbol{\mathcal{D}_j}g(t)\,, \tag{3.21}$$

which is also valid for $\widehat{\mathbf{D}}$ and the semi-constant delay. For the rest of this thesis, we will use the introduced notation and switch between operator and index notation.

3.2 TDI Combinations for Non-Flexing Arms

In this section, we will learn about the first generation TDI combinations and their functionality. Therefore, we will give an idea how to 'derive' the combinations algebraically, followed by a list of the common TDI combinations and their graphical representations.

3.2.1 Derivation Sketch of TDI Combinations

We start with a brief derivation sketch of the laser frequency noise cancelling TDI equations assuming LISA to be static. Note, in particular, that in a static case,

$L_{\underline{i}} = L_{\underline{i}'}$, and thus $\widehat{\mathbf{D}}_{\underline{i}} = \widehat{\mathbf{D}}_{\underline{i}'}$. A more detailed algebraic treatment for a rotating and flexing case can be found in [DNV02; NV04; NV05].

Starting Point

The starting point for the derivation are Eqn. (2.28a) – (2.28f), the set of phase measurements onboard the spacecraft. They are combined to extract the encoded gravitational wave signal such that the primary noise contributions are removed, first and foremost the laser phase noise. Therefore, combinations of the onboard interferometric measurements free of laser phase noise are needed. In order to understand the procedure, we will now make two steps back and only consider the gravitational wave signal together with laser frequency noise in terms of phase in the *static* LISA case (thus, no primed time delays). Any other noise source is neglected for now (denoted here by "→"). Exemplarily, this gives for OB 1:

$$
\begin{aligned}
\bar{s}_1(t) &= H_1 + p_{2':\mathbf{3}} - p_1 - \frac{2\pi}{\lambda_{2'}}\vec{n}_3 \cdot \vec{\Delta}_{2':\mathbf{3}} - \frac{2\pi}{\lambda_{2'}}\vec{n}_{3'} \cdot \vec{\Delta}_1 + N_1^{\mathrm{opt}} + N_1^s \\
&\rightarrow H_1 + p_{2':\mathbf{3}} - p_1 =: \sigma_1(t)\,, \\
\bar{\tau}_1(t) &= p_{1'} - p_1 + \mu_{1'} + N_1^\tau \rightarrow p_{1'} - p_1 =: \varsigma_1(t)\,.
\end{aligned}
$$

Note that due to the non-flexing LISA constellation, the time-delay operator is denoted as a colon. Furthermore, the TM interferometer outputs $\bar{\varepsilon}_i(t)$ are not necessary here. They are needed to remove the displacement noise (Ch. 4). When neglecting the optical bench and TM displacement noise, the outputs $\bar{\varepsilon}_i(t)$ give only information redundant with that of $\bar{\tau}_i(t)$, i.e., $\bar{\varepsilon}_1(t) \rightarrow p_{1'} - p_1 = \varsigma_1(t)$. Altogether we have

$$
\begin{aligned}
\bar{s}_1(t) &\rightarrow \sigma_1(t) := H_1 + p_{2':\mathbf{3}} - p_1\,, & \bar{\tau}_1(t) &\rightarrow \varsigma_1(t) := p_{1'} - p_1\,, \\
\bar{s}_{1'}(t) &\rightarrow \sigma_{1'}(t) := H_{1'} + p_{3:\mathbf{2}} - p_{1'}\,, & \bar{\tau}_{1'}(t) &\rightarrow \varsigma_{1'}(t) := p_1 - p_{1'}\,, \\
\bar{s}_2(t) &\rightarrow \sigma_2(t) := H_2 + p_{3':\mathbf{1}} - p_2\,, & \bar{\tau}_2(t) &\rightarrow \varsigma_2(t) := p_{2'} - p_2\,, \\
\bar{s}_{2'}(t) &\rightarrow \sigma_{2'}(t) := H_{2'} + p_{1:\mathbf{3}} - p_{2'}\,, & \bar{\tau}_{2'}(t) &\rightarrow \varsigma_{2'}(t) := p_2 - p_{2'}\,, \\
\bar{s}_3(t) &\rightarrow \sigma_3(t) := H_3 + p_{1':\mathbf{2}} - p_3\,, & \bar{\tau}_3(t) &\rightarrow \varsigma_3(t) := p_{3'} - p_3\,, \\
\bar{s}_{3'}(t) &\rightarrow \sigma_{3'}(t) := H_{3'} + p_{2:\mathbf{1}} - p_{3'}\,, & \bar{\tau}_{3'}(t) &\rightarrow \varsigma_{3'}(t) := p_3 - p_{3'}\,.
\end{aligned}
$$

The goal is now to combine the $\sigma_i(t)$ and $\varsigma_i(t)$ such that all laser phase noise terms (p_i, delayed and instantaneous) will completely vanish.

Elimination with Local Measurements

We use the simplified reference interferometer signals $\varsigma_i(t)$ to eliminate the laser noise from primed optical benches, i.e., $p_{1'}, p_{2'}$ and $p_{3'}$ and its delayed parts. Therefore, we can construct

$$
\varsigma_1(t) - \varsigma_{1'}(t) = 2p_{1'} - 2p_1 \iff \frac{\varsigma_1(t) - \varsigma_{1'}(t)}{2} = p_{1'} - p_1\,,
$$

and cyclic. One could now think that this is the same as $\varsigma_1(t)$ and thus there is no advantage to combine $\varsigma_1(t)$ and $\varsigma_{1'}(t)$. However, in the above equations we have neglected the fibre noise that directly enters $\tau_i(t)$. As stated in Sec. 2.3, the fibre is assumed to be reciprocal, i.e., $\mu_{\underline{i}}(t) - \mu_{\underline{i}'}(t) \simeq 0$. This of course does not mean that single fibre noise terms $\mu_i(t)$ are negligible. Therefore, we always need to ensure that the fibre noise enters each data stream combination in a difference with its counterpart. If we include the fibres, we can see the advantage:

$$\frac{\varsigma_1(t) - \varsigma_{1'}(t)}{2} = p_{1'} - p_1 + \mu_{1'} - \mu_1 \simeq p_{1'} - p_1 + 0 \,,$$

but

$$\varsigma_1(t) = p_{1'} - p_1 + \mu_{1'} \not\simeq p_{1'} - p_1 + 0 \,.$$

In the latter case, the fibre noise enters without its counterpart $\mu_{1'}$ and we can not make use of the reciprocity. We will come back to this later.

Properly adding or subtracting and time-shifting the above combinations gives

$$\begin{aligned}
\sigma_1(t) - \widehat{\mathbf{D}}_3 \left(\frac{\varsigma_2(t) - \varsigma_{2'}(t)}{2} \right) &= H_1 + p_{2':\mathbf{3}} - p_1 - (p_{2'} - p_2)_{:\mathbf{3}} \\
&= H_1 + p_{2':\mathbf{3}} - p_1 - (p_{2':\mathbf{3}} - p_{2:\mathbf{3}}) \\
&= H_1 + p_{2:\mathbf{3}} - p_1 \,,
\end{aligned}$$

and cyclic, which removes the laser phase noise originating from primed optical benches. We therefore define data streams with three lasers only:

$$\bar{\eta}_1(t) \quad \equiv \quad \sigma_1(t) - \widehat{\mathbf{D}}_3 \left(\frac{\varsigma_2(t) - \varsigma_{2'}(t)}{2} \right) = H_1 + p_{2:\mathbf{3}} - p_1 \,, \qquad (3.22a)$$

$$\bar{\eta}_{1'}(t) \quad \equiv \quad \sigma_{1'}(t) + \frac{\varsigma_1(t) - \varsigma_{1'}(t)}{2} = H_{1'} + p_{3:\mathbf{2}} - p_1 \,, \qquad (3.22b)$$

and cyclic. These six synthesised data streams are the input to the TDI algorithm. The bar again emphasises the neglection of clocks and the beat-note polarity, as before for the onboard interferometric measurements. Additionally, fibre noise is not comprised by $\bar{\eta}_i(t)$, since $\sigma_i(t)$ and $\varsigma_i(t)$ exclude it.

The Central Condition

The TDI algorithm should take the data streams with a reduced number of different lasers, (3.22a), (3.22b) and cyclic, to form laser phase noise free data combinations. The central condition to find these is

$$\sum_{j \in \{1, 1', 2, 2', 3, 3'\}} \mathfrak{F}_j(\widehat{\mathbf{D}}_1, \widehat{\mathbf{D}}_2, \widehat{\mathbf{D}}_3) \bar{\eta}_j(t) = f(H_1, \ldots, H_{3'}) + 0 \,. \qquad (3.23)$$

That is, we need to combine all input data $\bar{\eta}_1(t), \ldots, \bar{\eta}_{3'}(t)$ to construct data streams without laser frequency noise (emphasized by the zero) but with a non-zero combination of gravitational wave signals, $f(H_1, \ldots, H_{3'})$. This is exactly the core idea of Time-Delay Interferometry. Note that the coefficients $\mathfrak{F}_j(\widehat{\mathbf{D}}_{\mathbf{1}}, \widehat{\mathbf{D}}_{\mathbf{2}}, \widehat{\mathbf{D}}_{\mathbf{3}})$ are polynomial functions of the delay operators $\widehat{\mathbf{D}}_{\underline{i}}$. These polynomials $\mathfrak{F}_j$ are to be determined algebraically.

Exemplarily, Eq. (3.23) reads for the laser phase noise free data combination $x(t)$ for the unequal-arm Michelson interferometric setup discussed in Sec. 3.1.2 as

$$
\begin{aligned}
x(t) &\stackrel{(3.8a)}{=} \left(y_{\text{PD},1}(t - \mathcal{T}_2) - y_{\text{PD},2}(t - \mathcal{T}_1) \right) - \left(y_{\text{PD},1}(t) - y_{\text{PD},2}(t) \right) \\
&= y_{\text{PD},1}(t - \tfrac{2L_2}{c}) - y_{\text{PD},1}(t) - y_{\text{PD},2}(t - \tfrac{2L_1}{c}) + y_{\text{PD},2}(t) \\
&\stackrel{(3.14)}{=} (\widehat{\mathbf{D}}_{\mathbf{2}}^2 - \mathbb{1}) y_{\text{PD},1}(t) + (\mathbb{1} - \widehat{\mathbf{D}}_{\mathbf{1}}^2) y_{\text{PD},2}(t) \stackrel{(3.8c)}{=} H_{1:\mathbf{22}} - H_{2:\mathbf{11}} + H_2 - H_1 \, .
\end{aligned}
$$

We now compare the last line with the central condition, i.e.,

$$
\stackrel{!}{\Longleftrightarrow} \sum_{j \in \{1,2\}} \mathfrak{F}_j(\widehat{\mathbf{D}}_{\mathbf{1}}, \widehat{\mathbf{D}}_{\mathbf{2}}) y_{\text{PD},j}(t) \stackrel{(3.23)}{=} f(H_1, H_2) + 0
$$

and find the combination of GW signal contributions on the rhs.:

$$
f(H_1, H_2) = H_{1:\mathbf{22}} - H_{2:\mathbf{11}} + H_2 - H_1 \, .
$$

Furthermore, the polynomial functions can be directly identified as

$$
\{\mathfrak{F}_1, \mathfrak{F}_2\} = \{\widehat{\mathbf{D}}_{\mathbf{2}}^2 - \mathbb{1}, \mathbb{1} - \widehat{\mathbf{D}}_{\mathbf{1}}^2\} \, ,
$$

where the brackets denote the set of polynomial prefactors in the lexicographical order {Prefactor of $y_{\text{PD},1}$, Prefactor of $y_{\text{PD}2}$}.

In the case of an unequal-arm Michelson interferometer with one laser and one interferometric measurement per arm, it was not hard to find the polynomial combination that removes laser frequency noise and simultaneously preserves the GW signal (Sec. 3.1.2). However, even for the simplified LISA case considered here with six data streams $\bar{\eta}_i(t)$ reduced to three different lasers, it is a complex challenge to find the polynomials $\mathfrak{F}_j(\widehat{\mathbf{D}}_{\mathbf{1}}, \widehat{\mathbf{D}}_{\mathbf{2}}, \widehat{\mathbf{D}}_{\mathbf{3}})$, as we will sketch now.

First, we insert Eqn. (3.22a) and (3.22b) in the central condition (3.23),

$$
\begin{aligned}
&\mathfrak{F}_1(H_1 + p_{2:\mathbf{3}} - p_1) + \mathfrak{F}_{1'}(H_{1'} + p_{3:\mathbf{2}} - p_1) + \mathfrak{F}_2(H_2 + p_{3:\mathbf{1}} - p_2) \\
&+ \mathfrak{F}_{2'}(H_{2'} + p_{1:\mathbf{3}} - p_2) + \mathfrak{F}_3(H_3 + p_{1:\mathbf{2}} - p_3) + \mathfrak{F}_{3'}(H_{3'} + p_{2:\mathbf{1}} - p_3) \\
&= f(H_1, \ldots, H_{3'}) + 0 \, ,
\end{aligned}
$$

and then sort the terms:

$$\iff \quad \mathfrak{F}_1(p_{2:\mathbf{3}} - p_1) + \mathfrak{F}_{1'}(p_{3:\mathbf{2}} - p_1) + \mathfrak{F}_2(p_{3:\mathbf{1}} - p_2) + \mathfrak{F}_{2'}(p_{1:\mathbf{3}} - p_2)$$
$$+\mathfrak{F}_3(p_{1:\mathbf{2}} - p_3) + \mathfrak{F}_{3'}(p_{2:\mathbf{1}} - p_3) + \mathfrak{F}_1 H_1 + \mathfrak{F}_{1'}H_{1'} + \mathfrak{F}_2 H_2 + \mathfrak{F}_{2'}H_{2'}$$
$$+\mathfrak{F}_3 H_3 + \mathfrak{F}_{3'}H_{3'} = f(H_1, \ldots, H_{3'})$$
$$\iff \quad (-\mathfrak{F}_1 - \mathfrak{F}_{1'} + \mathfrak{F}_{2'}\widehat{\mathbf{D}}_{\mathbf{3}} + \mathfrak{F}_3\widehat{\mathbf{D}}_{\mathbf{2}})p_1 + (\mathfrak{F}_1\widehat{\mathbf{D}}_{\mathbf{3}} - \mathfrak{F}_2 - \mathfrak{F}_{2'} + \mathfrak{F}_{3'}\widehat{\mathbf{D}}_{\mathbf{1}})p_2$$
$$+(\mathfrak{F}_{1'}\widehat{\mathbf{D}}_{\mathbf{2}} + \mathfrak{F}_2\widehat{\mathbf{D}}_{\mathbf{1}} - \mathfrak{F}_3 - \mathfrak{F}_{3'})p_3 = 0\,,$$

where we identified $f(H_1, \ldots, H_{3'}) = \sum_j \mathfrak{F}_j H_j$. The equation including $p_{\underline{i}}$ can only be fulfilled non-trivially if all brackets vanish, i.e.,

$$-\mathfrak{F}_1 - \mathfrak{F}_{1'} + \mathfrak{F}_{2'}\widehat{\mathbf{D}}_{\mathbf{3}} + \mathfrak{F}_3\widehat{\mathbf{D}}_{\mathbf{2}} = 0\,, \qquad \text{(I)}$$
$$\mathfrak{F}_1\widehat{\mathbf{D}}_{\mathbf{3}} - \mathfrak{F}_2 - \mathfrak{F}_{2'} + \mathfrak{F}_{3'}\widehat{\mathbf{D}}_{\mathbf{1}} = 0\,, \qquad \text{(II)}$$
$$\mathfrak{F}_{1'}\widehat{\mathbf{D}}_{\mathbf{2}} + \mathfrak{F}_2\widehat{\mathbf{D}}_{\mathbf{1}} - \mathfrak{F}_3 - \mathfrak{F}_{3'} = 0\,. \qquad \text{(III)}$$

We can now eliminate $\mathfrak{F}_{1'}$ and $\mathfrak{F}_{2'}$ using the first two equations (I) and (II):

$$\mathfrak{F}_{1'} = -\mathfrak{F}_1 + \mathfrak{F}_{2'}\widehat{\mathbf{D}}_{\mathbf{3}} + \mathfrak{F}_3\widehat{\mathbf{D}}_{\mathbf{2}}\,, \quad \mathfrak{F}_{2'} = \mathfrak{F}_1\widehat{\mathbf{D}}_{\mathbf{3}} - \mathfrak{F}_2 + \mathfrak{F}_{3'}\widehat{\mathbf{D}}_{\mathbf{1}}\,.$$

Inserting this in the third equation (III) yields

$$(-\mathfrak{F}_1 + \mathfrak{F}_{2'}\widehat{\mathbf{D}}_{\mathbf{3}} + \mathfrak{F}_3\widehat{\mathbf{D}}_{\mathbf{2}})\widehat{\mathbf{D}}_{\mathbf{2}} + \mathfrak{F}_2\widehat{\mathbf{D}}_{\mathbf{1}} - \mathfrak{F}_3 - \mathfrak{F}_{3'} = 0$$
$$\iff \quad (-\mathfrak{F}_1 + [\mathfrak{F}_1\widehat{\mathbf{D}}_{\mathbf{3}} - \mathfrak{F}_2 + \mathfrak{F}_{3'}\widehat{\mathbf{D}}_{\mathbf{1}}]\widehat{\mathbf{D}}_{\mathbf{3}} + \mathfrak{F}_3\widehat{\mathbf{D}}_{\mathbf{2}})\widehat{\mathbf{D}}_{\mathbf{2}} + \mathfrak{F}_2\widehat{\mathbf{D}}_{\mathbf{1}} - \mathfrak{F}_3 - \mathfrak{F}_{3'} = 0$$
$$\iff \quad -\mathfrak{F}_1\widehat{\mathbf{D}}_{\mathbf{2}} + \mathfrak{F}_1\widehat{\mathbf{D}}_{\mathbf{3}}\widehat{\mathbf{D}}_{\mathbf{3}}\widehat{\mathbf{D}}_{\mathbf{2}} - \mathfrak{F}_2\widehat{\mathbf{D}}_{\mathbf{3}}\widehat{\mathbf{D}}_{\mathbf{2}} + \mathfrak{F}_{3'}\widehat{\mathbf{D}}_{\mathbf{1}}\widehat{\mathbf{D}}_{\mathbf{3}}\widehat{\mathbf{D}}_{\mathbf{2}} + \mathfrak{F}_3\widehat{\mathbf{D}}_{\mathbf{2}}\widehat{\mathbf{D}}_{\mathbf{2}}$$
$$+\mathfrak{F}_2\widehat{\mathbf{D}}_{\mathbf{1}} - \mathfrak{F}_3 - \mathfrak{F}_{3'} = 0$$

and finally end up with

$$\widehat{\mathbf{D}}_{\mathbf{2}}(\widehat{\mathbf{D}}_{\mathbf{3}}^2 - \mathbb{1})\mathfrak{F}_1 + (\widehat{\mathbf{D}}_{\mathbf{1}} - \widehat{\mathbf{D}}_{\mathbf{3}}\widehat{\mathbf{D}}_{\mathbf{2}})\mathfrak{F}_2 + (\widehat{\mathbf{D}}_{\mathbf{2}}^2 - \mathbb{1})\mathfrak{F}_3 + (\widehat{\mathbf{D}}_{\mathbf{1}}\widehat{\mathbf{D}}_{\mathbf{3}}\widehat{\mathbf{D}}_{\mathbf{2}} - \mathbb{1})\mathfrak{F}_{3'} = 0\,. \quad (3.24)$$

This equation can be solved for $\mathfrak{F}_1, \mathfrak{F}_2, \mathfrak{F}_3$ and $\mathfrak{F}_{3'}$. From the result, it is possible to deduce several laser phase noise free data combinations, partially presented in the subsequent section. However, for the solution of (3.24), familiar tools from linear algebra do not apply here, since the combinations of time-delay operators, i.e., the prefactors, could not be inverted. Hence, algebraic tools like Buchberger algorithm and Gröbner bases as well as structures like the second module of Syzygies need to be used. For details we refer to [Buc70; DNV02], since a full treatment is beyond the scope for this thesis. An even more complex algebraic treatment for a rotating LISA constellation, i.e., for $L_{\underline{i}} \neq L_{\underline{i}'}$, is given in [NV04]. Remarkably, for time-dependent time-delay operators (second generation TDI variables), no closed algebraic treatment could be performed until today [TD14].

3.2.2 Overview of the First Generation TDI Combinations

We will now list several TDI combinations that are not only used for laser frequency noise suppression (Michelson combinations), but also for redundancy of data in order to estimate, e.g., GW polarisation and other properties as well as the instrumental noise of the space-based detectors. Furthermore, the access to several combinations enables a proper treatment of link failure scenarios. That is, laser links between the S/C break down and it is not anymore possible to access the corresponding science interferometer output data. A link failure analysis can be found in [VCT08]. All combinations presented here are comprised in the algebraic module of Syzygy and fulfill the central condition (3.23) as will be exemplarily shown.

Previously, Eqn. (3.22a) and (3.22b) were announced to be adequate inputs for TDI in a static LISA case, i.e., for 1st generation TDI. For LISA in an orbiting, but non-flexing constellation, it is possible to construct data streams of the form

$$\eta_1(t) \quad \sim \quad H_1 + p_{2:\mathbf{3}} - p_1 + \frac{\mu_{2:\mathbf{3}} - \mu_{2':\mathbf{3}}}{2} \,, \tag{3.25a}$$

$$\eta_{1'}(t) \quad \sim \quad H_{1'} + p_{3:\mathbf{2'}} - p_1 - \frac{\mu_1 - \mu_{1'}}{2} \,, \tag{3.25b}$$

and use those as appropriate TDI 1.5 input. This is even possible with clocks included (cf. Ch. 4), and that is why we have now dropped the bar notation. Note that the laser phase noise from the primed optical benches have been already removed by combining the reference interferometer outputs as in Sec. 3.2.1.

It is crucial for the TDI functionality that the input has the form (3.25a) and (3.25b) plus secondary noise contributions that are neglected here for the sake of simplicity (such as readout and optical path length noise), again emphasised by '$\sim$'. In contrast to Sec. 3.2.1, time delays by primed links enter the synthesised data combinations as well. For the rest of this chapter, we will assume the fibres to be perfectly reciprocal, i.e., $\mu_{\underline{i}} = \mu_{\underline{i}'}$ for the sake of brevity, and also since we concentrate here on the laser phase noise suppression. The full treatment is dealt with in Ch. 4.

Michelson Combinations

The Michelson combinations are laser phase noise free data streams given by [AET99]:

$$X(t) \;=\; (\eta_{2':\mathbf{322'}} + \eta_{1:\mathbf{22'}} + \eta_{3:\mathbf{2'}} + \eta_{1'}) - (\eta_{3:\mathbf{2'3'3}} + \eta_{1':\mathbf{3'3}} + \eta_{2':\mathbf{3}} + \eta_1), \tag{3.26a}$$

$$Y(t) \;=\; (\eta_{3':\mathbf{133'}} + \eta_{2:\mathbf{33'}} + \eta_{1:\mathbf{3'}} + \eta_{2'}) - (\eta_{1:\mathbf{3'1'1}} + \eta_{2':\mathbf{1'1}} + \eta_{3':\mathbf{1}} + \eta_2), \tag{3.26b}$$

$$Z(t) \;=\; (\eta_{1':\mathbf{211'}} + \eta_{3:\mathbf{11'}} + \eta_{2:\mathbf{1'}} + \eta_{3'}) - (\eta_{2:\mathbf{1'2'2}} + \eta_{3':\mathbf{2'2}} + \eta_{1':\mathbf{2}} + \eta_3). \tag{3.26c}$$

Note here the cyclic permutation of the indices and thus the formation symmetry. Fig. 3.6 displays the synthesised photon paths of the three combinations.

We will examine the data combination $X(t)$ (often also called TDI-X) closer now and assume that S/C 2 and 3 are replaced by perfect mirrors. Hence, the phase
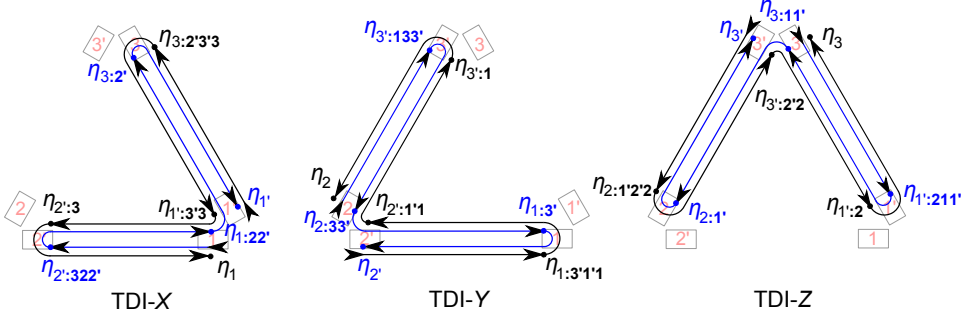
Figure 3.6: Synthesised photon paths of the Michelson combinations. Shown are the paths for X, Y and Z and its synthesised contributions $\eta_i(t)$ in analogy to Fig. 3.4. Note the cyclic permutation of links for Y and Z. The blue path corresponds to the first bracket in Eqn. (3.26a) – (3.26c), the black path to the second bracket.

measurements $\bar{s}_{2'}(t)$ and $\bar{s}_3(t)$ do not exist. Since $\eta_i(t)$ is constructed from the corresponding $\bar{s}_i(t)$ comparable to Eq. (3.22a) and (3.22b), $\eta_{2'}(t)$ and $\eta_3(t)$ are not accessible in turn and X reduces to

$$X(t) \rightarrow \eta_{1:\mathbf{22'}} + \eta_{1'} - \eta_{1':\mathbf{3'3}} - \eta_1 = (\widehat{\mathbf{D}}_{\mathbf{2'}}\widehat{\mathbf{D}}_{\mathbf{2}} - \mathbb{1})\eta_1 - (\widehat{\mathbf{D}}_{\mathbf{3}}\widehat{\mathbf{D}}_{\mathbf{3'}} - \mathbb{1})\eta_{1'}\,.$$

For a static case, $\widehat{\mathbf{D}}_{\underline{i}} = \widehat{\mathbf{D}}_{\underline{i}'}$ and hence

$$X(t) \rightarrow (\widehat{\mathbf{D}}_{\mathbf{2}}^2 - \mathbb{1})\eta_1 - (\widehat{\mathbf{D}}_{\mathbf{3}}^2 - \mathbb{1})\eta_{1'}\,,$$

which corresponds to Eq. (3.14), the laser phase noise free combination for the unequal-arm Michelson interferometric setup discussed in Sec. 3.1.2. This is why the X-combination is commonly called TDI Michelson variable.

It can be shown explicitly for TDI-X that it is laser phase noise free, even in the case that we have to distinguish between $\widehat{\mathbf{D}}_{\underline{k}}$ and $\widehat{\mathbf{D}}_{\underline{k}'}$ (TDI 1.5). Therefore, we insert the signals $\eta_i(t)$ given by Eqn. (3.25a) and (3.25b) into X, use the fibre reciprocity and further neglect any secondary noise ('$\sim$'):

$$\begin{aligned}
X(\eta_1,\ldots,\eta_{3'}) \sim\ & [(H_{2'} + p_{1:\mathbf{3'}} - p_2)_{:\mathbf{322'}} + (H_1 + p_{2:\mathbf{3}} - p_1)_{:\mathbf{22'}} + (H_3 + p_{1:\mathbf{2}} - p_3)_{:\mathbf{2'}} \\
& + H_{1'} + p_{3:\mathbf{2'}} - p_1] - [(H_3 + p_{1:\mathbf{2}} - p_3)_{:\mathbf{2'3'3}} + (H_{1'} + p_{3:\mathbf{2'}} - p_1)_{:\mathbf{3'3}} \\
& + (H_{2'} + p_{1:\mathbf{3'}} - p_2)_{:\mathbf{3}} + H_1 + p_{2:\mathbf{3}} - p_1]\,.
\end{aligned}$$

Using the rules for the delay operators, Eqn. (3.20) and (3.21), and sorting the

terms gives

$$
\begin{aligned}
X \sim\ & H_{2':\mathbf{322'}} + p_{1:\mathbf{3'322'}} - p_{2:\mathbf{322'}} + H_{1:\mathbf{22'}} + p_{2:\mathbf{322'}} - p_{1:\mathbf{22'}} + H_{3:\mathbf{2'}} + p_{1:\mathbf{22'}} \\
& - p_{3:\mathbf{2'}} + H_{1'} + p_{3:\mathbf{2'}} - p_1 - H_{3:\mathbf{2'3'3}} - p_{1:\mathbf{22'3'3}} + p_{3:\mathbf{2'3'3}} - H_{1':\mathbf{3'3}} - p_{3:\mathbf{2'3'3}} \\
& + p_{1:\mathbf{3'3}} - H_{2':\mathbf{3}} - p_{1:\mathbf{3'3}} + p_{2:\mathbf{3}} - H_1 - p_{2:\mathbf{3}} + p_1 \\
=\ & H_{2':\mathbf{322'}} + H_{1:\mathbf{22'}} + H_{3:\mathbf{2'}} + H_{1'} - H_{3:\mathbf{2'3'3}} - H_{1':\mathbf{3'3}} - H_{2':\mathbf{3}} - H_1 \\
& + (p_{1:\mathbf{3'322'}} - p_{1:\mathbf{22'3'3}}) + (-p_{2:\mathbf{322'}} + p_{2:\mathbf{322'}}) + (-p_{1:\mathbf{22'}} + p_{1:\mathbf{22'}}) \\
& + (-p_{3:\mathbf{2'}} + p_{3:\mathbf{2'}}) + (-p_1 + p_1) + (p_{3:\mathbf{2'3'3}} - p_{3:\mathbf{2'3'3}}) + (p_{1:\mathbf{3'3}} - p_{1:\mathbf{3'3}}) \\
& + (p_{2:\mathbf{3}} - p_{2:\mathbf{3}}).
\end{aligned}
$$

Except for the first bracket, all laser phase noise contributions cancel pairwise. Finally, we make use of the fact that the time-delay operators commute as was stated in Eq. (3.19b) and hence the index ordering in the first bracket is without importance. That is, all brackets vanish and we get

$$
X \sim H_{2':\mathbf{22'}} + H_{1:\mathbf{22'}} + H_{3:\mathbf{2'}} + H_{1'} - H_{3:\mathbf{2'3'3}} - H_{1':\mathbf{3'3}} - H_{2':\mathbf{3}} - H_1.
$$

Thus, X (and in analogy Y and Z) is laser phase noise free, since it fulfills the central condition Eq. (3.23). Furthermore, as shown above, the Michelson combination can be reduced to a Michelson interferometer combination and thus preserves the gravitational wave signal.

The transfer function between the accumulated phase shift $H_i(t)$ and the $X(t)$-output can be computed by a similar procedure to that in Sec. 3.1.2. For this, the light travel times are assumed to be equal, $T_i = T_0$, and furthermore, $H_{1'} = H_3 =: H_A$ and $H_1 = H_{2'} =: H_B$ is assumed (long wavelength limit, GW effect is reciprocal per arm). Subsequently, with $\Delta H := H_A - H_B$, the transfer function reads as

$$
\mathfrak{T}_{\Delta H \to X}(f) = 1 + e^{-i \cdot 2\pi f T_0} - e^{-i \cdot 2\pi f \cdot 2T_0} - e^{-i \cdot 2\pi f \cdot 3T_0}. \tag{3.27}
$$

The absolute of the transfer function is presented in Fig. 3.7. Its shape is remarkably similar to the transfer function of the simplified TDI scheme discussed in Sec. 3.1.2.

Fully Symmetric Sagnac Combination

One combination that senses the constellation rotation is the fully symmetric Sagnac variable [AET99]:

$$
\begin{aligned}
\zeta(t) & \equiv \eta_{2':\mathbf{2'}} - \eta_{3:\mathbf{3}} + \eta_{3':\mathbf{3'}} - \eta_{1:\mathbf{1}} + \eta_{1':\mathbf{1'}} - \eta_{2:\mathbf{2}} \\
& = (\eta_{1':\mathbf{1'}} + \eta_{2':\mathbf{2'}} + \eta_{3':\mathbf{3'}}) - (\eta_{1:\mathbf{1}} + \eta_{2:\mathbf{2}} + \eta_{3:\mathbf{3}}). \tag{3.28}
\end{aligned}
$$

The symmetric Sagnac combination has the property that each of the $\eta_i(t)$ enters exactly once and is lagged by exactly one of the one-way light travel times. $\zeta(t)$ synthesises a photon path shown in Fig. 3.8 and is sensitive to constellation rotation. Thus, the laser frequency noise is not cancelled exactly, only for static LISA case.

Chapter 3

Transfer function for TDI–X
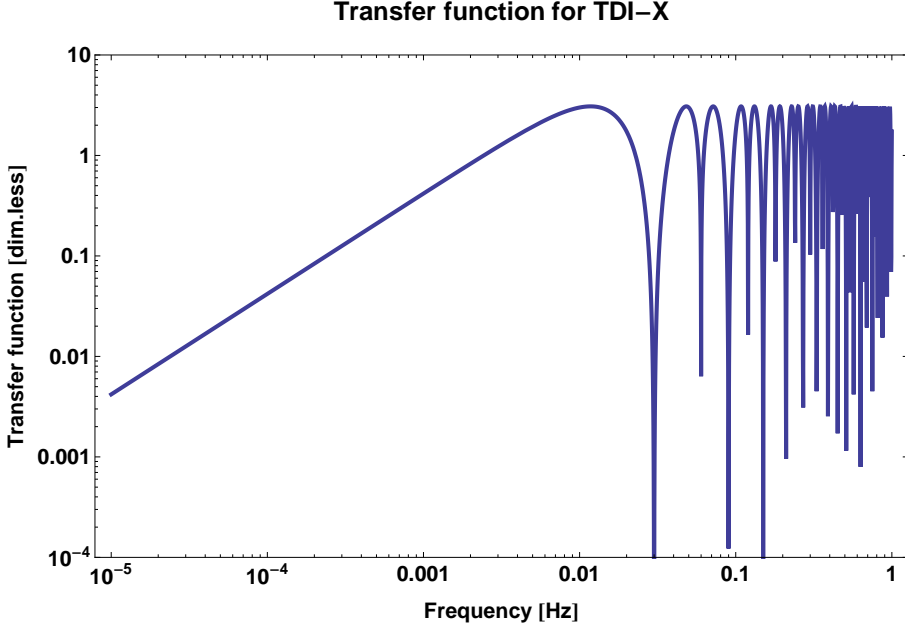
Figure 3.7:   Transfer function for the gravitational wave response in the X-combination. Towards low frequencies, the same f^{-1}-behaviour as in Fig. 3.3 can be determined, and the high frequency part is comparable. As in the simplified TDI scheme, the first transfer function null appears here at $f_{\mathrm{null}}^{X}(N=1) = 0.03\,\mathrm{Hz} = \frac{c}{2L_0}$. This is (due to one synthesised round-trip per arm) half of the frequency of the single link GW transfer function zero in Fig. 1.12.

However, $\zeta(t)$ has good coupling to GWs at frequencies comparable to or larger than the reciprocal of the LISA light travel time, but poor coupling at lower frequencies, as can be seen from the transfer function computed, e.g., in [AET99]. This characteristic can be used to distinguish between GW background and instrumental noise [AET03].

Even without explicitly inserting the data streams, it is rapidly shown that ζ fulfills the central condition for static LISA. We can make use of Eq. (3.24), which was derived from Eq. (3.23), and insert the $\mathfrak{F}_j$'s given by ζ. For static LISA, $\widehat{\mathbf{D}}_{\underline{i}} = \widehat{\mathbf{D}}_{\underline{i}'}$ and hence $\zeta = (\widehat{\mathbf{D}}_{\mathbf{1}}\eta_{1'} + \widehat{\mathbf{D}}_{\mathbf{2}}\eta_{2'} + \widehat{\mathbf{D}}_{\mathbf{3}}\eta_{3'}) - (\widehat{\mathbf{D}}_{\mathbf{1}}\eta_1 + \widehat{\mathbf{D}}_{\mathbf{2}}\eta_2 + \widehat{\mathbf{D}}_{\mathbf{3}}\eta_3)$ with the set of polynomial factors $\{\mathfrak{F}_1, \mathfrak{F}_{1'}, \mathfrak{F}_2, \mathfrak{F}_{2'}, \mathfrak{F}_3, \mathfrak{F}_{3'}\} = \{-\widehat{\mathbf{D}}_{\mathbf{1}}, \widehat{\mathbf{D}}_{\mathbf{1}}, -\widehat{\mathbf{D}}_{\mathbf{2}}, \widehat{\mathbf{D}}_{\mathbf{2}}, -\widehat{\mathbf{D}}_{\mathbf{3}}, \widehat{\mathbf{D}}_{\mathbf{3}}\}$. This yields in Eq. (3.24):

$$-\widehat{\mathbf{D}}_{\mathbf{2}}(\widehat{\mathbf{D}}_{\mathbf{3}}^2 - \mathbb{1})\widehat{\mathbf{D}}_{\mathbf{1}} - (\widehat{\mathbf{D}}_{\mathbf{1}} - \widehat{\mathbf{D}}_{\mathbf{3}}\widehat{\mathbf{D}}_{\mathbf{2}})\widehat{\mathbf{D}}_{\mathbf{2}} - (\widehat{\mathbf{D}}_{\mathbf{2}}^2 - \mathbb{1})\widehat{\mathbf{D}}_{\mathbf{3}} + (\widehat{\mathbf{D}}_{\mathbf{1}}\widehat{\mathbf{D}}_{\mathbf{3}}\widehat{\mathbf{D}}_{\mathbf{2}} - \mathbb{1})\widehat{\mathbf{D}}_{\mathbf{3}}$$
$$= -\widehat{\mathbf{D}}_{\mathbf{2}}\widehat{\mathbf{D}}_{\mathbf{3}}^2\widehat{\mathbf{D}}_{\mathbf{1}} + \widehat{\mathbf{D}}_{\mathbf{2}}\widehat{\mathbf{D}}_{\mathbf{1}} - \widehat{\mathbf{D}}_{\mathbf{1}}\widehat{\mathbf{D}}_{\mathbf{2}} + \widehat{\mathbf{D}}_{\mathbf{3}}\widehat{\mathbf{D}}_{\mathbf{2}}^2 - \widehat{\mathbf{D}}_{\mathbf{2}}^2\widehat{\mathbf{D}}_{\mathbf{3}} + \widehat{\mathbf{D}}_{\mathbf{3}} + \widehat{\mathbf{D}}_{\mathbf{1}}\widehat{\mathbf{D}}_{\mathbf{3}}^2\widehat{\mathbf{D}}_{\mathbf{2}} - \widehat{\mathbf{D}}_{\mathbf{3}} = 0\,,$$

due to the commuting time delays. Hence, at least for static LISA, the laser phase noise removal by TDI-ζ is expected to be exact.

clockwise paths   counter-clockwise paths

TDI-ζ
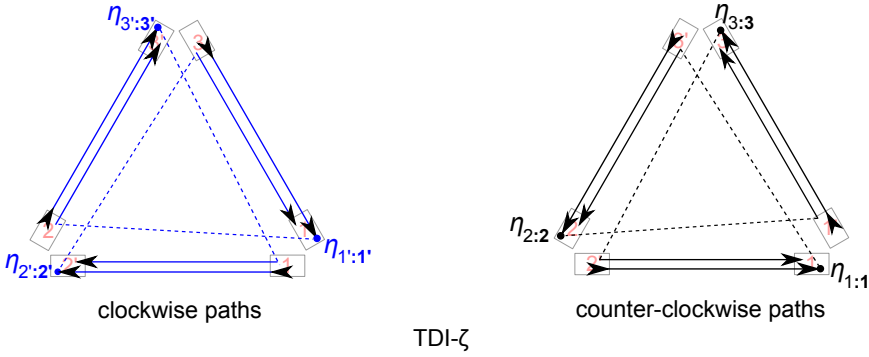
Figure 3.8: Synthesised photon path of the Sagnac combination ζ, where the blue paths are described by the first bracket in Eq. (3.28) and the black paths represent the second bracket. The contributions $\eta_1, \ldots, \eta_{3'}$ are here delayed by the light travel time of the adjacent link. Therefore, the dashed lines display the virtual transfer of the respective data streams $\eta_i(t)$. Note that at the receiving OB (at the arrows) no measurement is performed in contrast to the Michelson combination.

Sagnac Combinations

Further rotational sensitive data streams are the Sagnac combinations [AET99]:

$$\alpha(t) \;=\; (\eta_{2':\mathbf{1'2'}} + \eta_{3':\mathbf{2'}} + \eta_{1'}) - (\eta_{3:\mathbf{13}} + \eta_{2:\mathbf{3}} + \eta_1), \tag{3.29a}$$

$$\beta(t) \;=\; (\eta_{3':\mathbf{2'3'}} + \eta_{1':\mathbf{3'}} + \eta_{2'}) - (\eta_{1:\mathbf{21}} + \eta_{3:\mathbf{1}} + \eta_2), \tag{3.29b}$$

$$\gamma(t) \;=\; (\eta_{1':\mathbf{3'1'}} + \eta_{2':\mathbf{1'}} + \eta_{3'}) - (\eta_{2:\mathbf{32}} + \eta_{1:\mathbf{2}} + \eta_3). \tag{3.29c}$$

Though often claimed to cancel laser phase noise completely, it can be shown by inserting the input $\eta_i(t)$ from Eqn. (3.25a) and (3.25b) that this is only the case for TDI 1.0:

$$
\begin{aligned}
\alpha(\eta_1, \ldots, \eta_{3'}) \sim\; & (H_{2'} + p_{1:\mathbf{3'}} - p_2)_{:\mathbf{1'2'}} + (H_{3'} + p_{2:\mathbf{1'}} - p_3)_{:\mathbf{2'}} + (H_{1'} + p_{3:\mathbf{2'}} - p_1) \\
& - (H_3 + p_{1:\mathbf{2}} - p_3)_{:\mathbf{13}} - (H_2 + p_{3:\mathbf{1}} - p_2)_{:\mathbf{3}} - (H_1 + p_{2:\mathbf{3}} - p_1) \\
=\; & H_{2':\mathbf{1'2'}} + p_{1:\mathbf{3'1'2'}} - p_{2:\mathbf{1'2'}} + H_{3':\mathbf{2'}} + p_{2:\mathbf{1'2'}} - p_{3:\mathbf{2'}} + H_{1'} + p_{3:\mathbf{2'}} \\
& - p_1 - H_{3:\mathbf{13}} - p_{1:\mathbf{213}} + p_{3:\mathbf{13}} - H_{2:\mathbf{3}} - p_{3:\mathbf{13}} + p_{2:\mathbf{3}} - H_1 - p_{2:\mathbf{3}} + p_1 \\
=\; & H_{1'} + H_{3':\mathbf{2'}} + H_{2':\mathbf{1'2'}} - H_1 - H_{2:\mathbf{3}} - H_{3:\mathbf{13}} + (p_{1:\mathbf{3'1'2'}} - p_{1:\mathbf{213}}).
\end{aligned}
$$

For a static LISA configuration, $L_{\underline{i}} = L_{\underline{i'}}$, and thus the difference in the bracket would vanish. For a rotating constellation, this is not anymore the case and the Sagnac combinations do not cancel laser frequency noise exactly. An estimate for the residual laser noise in the case of a flexing LISA constellation is presented in Sec. 3.3. Fig. 3.9 shows the synthesised photon path.
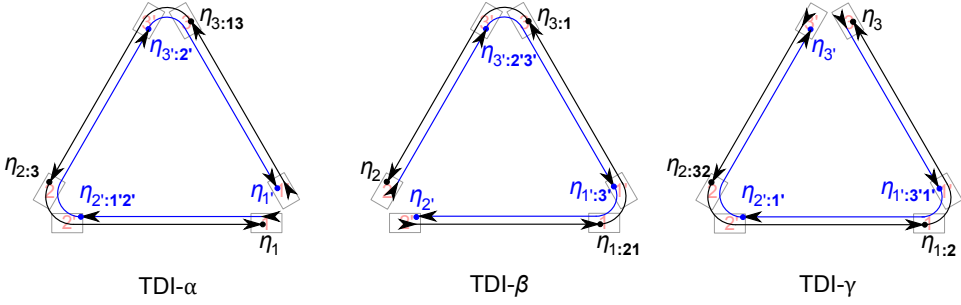
Figure 3.9: Photon paths of the synthesised Sagnac combinations α, β and γ. They form — as the symmetric Sagnac variable — a closed area and are thus sensitive to constellation rotations.

Link Failure Surviving Combinations

An important issue for LISA-like missions is the breakdown of one laser link (e.g., due to laser source breakdown). In that case, one can use several TDI combinations relying on one-link measurements to reconstruct the GW signal. These are called Beacon, Monitor and Relay. The Relay combinations are given according to the photon paths shown in Fig. 3.10 by

$$U(t) = (\eta_{1':\mathbf{3'1'1}} + \eta_{2':\mathbf{1'1}} + \eta_{3':\mathbf{1}} + \eta_2) - (\eta_{2:\mathbf{1'2'3'}} + \eta_{3':\mathbf{2'3'}} + \eta_{1':\mathbf{3'}} + \eta_{2'}), \quad (3.30\text{a})$$

$$V(t) = (\eta_{2':\mathbf{1'2'2}} + \eta_{3':\mathbf{2'2}} + \eta_{1':\mathbf{2}} + \eta_3) - (\eta_{3:\mathbf{2'3'1'}} + \eta_{1':\mathbf{3'1'}} + \eta_{2':\mathbf{1'}} + \eta_{3'}), \quad (3.30\text{b})$$

$$W(t) = (\eta_{3':\mathbf{2'3'3}} + \eta_{1':\mathbf{3'3}} + \eta_{2':\mathbf{3}} + \eta_1) - (\eta_{1:\mathbf{3'1'2'}} + \eta_{2':\mathbf{1'2'}} + \eta_{3':\mathbf{2'}} + \eta_{1'}). \quad (3.30\text{c})$$

However, Monitor (E, F, G) and Beacon (P, Q, R) do not form a reasonable photon path to display (except for a simplified picture given in [Val05]), therefore we list only the equations and refer to [TEA04]. Monitor is given by

$$E(t) = \eta_{2:\mathbf{12}} + \eta_{3':\mathbf{2}} - \eta_{3':\mathbf{1'3'}} - \eta_{2:\mathbf{3'}} - \eta_{1':\mathbf{11'}} + \eta_{1:\mathbf{1'1}} + \eta_{1'} - \eta_1, \quad (3.31\text{a})$$

$$F(t) = \eta_{3:\mathbf{23}} + \eta_{1':\mathbf{3}} - \eta_{1':\mathbf{2'1'}} - \eta_{3:\mathbf{1'}} - \eta_{2':\mathbf{22'}} + \eta_{2:\mathbf{2'2}} + \eta_{2'} - \eta_2, \quad (3.31\text{b})$$

$$G(t) = \eta_{1:\mathbf{31}} + \eta_{2':\mathbf{1}} - \eta_{2':\mathbf{3'2'}} - \eta_{1:\mathbf{2'}} - \eta_{3':\mathbf{33'}} + \eta_{3:\mathbf{3'3}} + \eta_{3'} - \eta_3. \quad (3.31\text{c})$$

The Monitor variables include one S/C as listen-only. That is, one spacecraft only contributes to the TDI combinations by 'monitoring' receiving signals, while its signals being sent are not taken into account [ETA00]. For $E(t)$, this is the case for S/C 1, since measurements on OB $2'$ and 3 do not appear in the combinations.

The variables P, Q and R could be useful in case of link failure modes and are called Beacon, because each data stream involves data received at only two of the S/C, while the third spacecraft is only transmitting and provides an independent
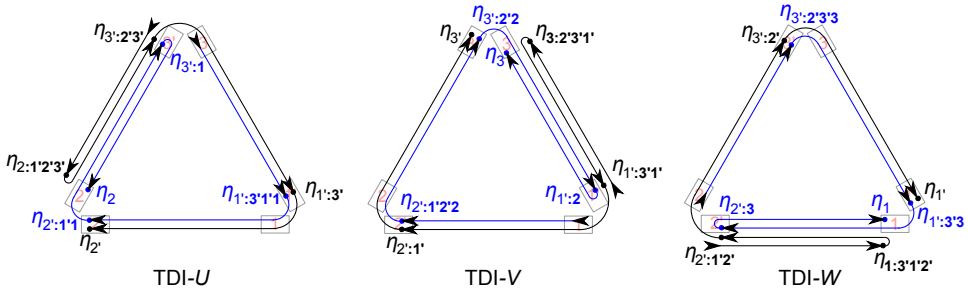
Figure 3.10: Photon paths of the link failure Relay combinations.

frequency 'beacon' [ETA00]:

$$P(t) = \eta_{2:\mathbf{13}} + \eta_{3':\mathbf{3}} - \eta_{3':\mathbf{1'2'}} - \eta_{2:\mathbf{2'}} - \eta_{2':\mathbf{2'11'}} + \eta_{3:\mathbf{311'}} + \eta_{2':\mathbf{2'}} - \eta_{3:\mathbf{3}}\,, \quad (3.32\text{a})$$

$$Q(t) = \eta_{3:\mathbf{21}} + \eta_{1':\mathbf{1}} - \eta_{1':\mathbf{2'3'}} - \eta_{3:\mathbf{3'}} - \eta_{3':\mathbf{3'22'}} + \eta_{1:\mathbf{122'}} + \eta_{3':\mathbf{3'}} - \eta_{1:\mathbf{1}}\,, \quad (3.32\text{b})$$

$$R(t) = \eta_{1:\mathbf{32}} + \eta_{2':\mathbf{2}} - \eta_{2':\mathbf{3'1'}} - \eta_{1:\mathbf{1'}} - \eta_{1':\mathbf{1'33'}} + \eta_{2:\mathbf{233'}} + \eta_{1':\mathbf{1'}} - \eta_{2:\mathbf{2}}\,. \quad (3.32\text{c})$$

Optimal Combinations

In gravitational wave data analysis, optimal combinations are used for the estimation of unknown source parameters (e.g., wave frequency, polarisation, source location). Therefore, one can additionally define the optimal TDI variables using the Michelson combinations [PTLA02]:

$$A(t) = \frac{1}{\sqrt{2}}(Z - X)\,, \quad E(t) = \frac{1}{\sqrt{6}}(X - 2Y + Z)\,, \quad T(t) = \frac{1}{\sqrt{3}}(X + Y + Z)\,, \quad (3.33)$$

named after the inventors of TDI, Armstrong (A), Estabrook (E) and Tinto (T). The instrumental noise that enter the Michelson TDI variables X, Y and Z are correlated by construction. However, for GW data analysis, it is more convenient to have data streams with uncorrelated noise. The combinations A, E and T are optimal in the sense that they are constructed orthogonal such that the correlations between them are minimised. Note, however, that in the current simulation (Ch. 5) only one GW source is implemented and there is (yet) no need to build the A,E,T-combinations.

In this section, the main first generation TDI combinations were introduced and a rough algebraic derivation sketch was presented. All equations are valid for a rotating, but rigid LISA constellation. In reality, the S/C are of course not fixed with respect to each other and relative motions will occur. Hence, we need to extend the existing equations to the case of a flexing LISA constellation.

Chapter 3

3.3 Time-Delay Interferometry for Flexing LISA

We will now explore the more complex TDI 2.0 combinations [STEA03; DVN08; TD14]. The main difference to TDI 1.0 and 1.5 is that the armlengths are no longer considered to be time-independent. Hence, the time-delay operators are defined in a more complex way (Eq. (3.18a)) than before, and this in turn results for multiple delays in complicated nested functions that can hardly be handled analytically without approximations. Therefore, we need to expand the armlengths $L_i(t)$ up to terms of $\frac{\dot{L}_i(t)}{c} \approx 10^{-8}$. Here, $\dot{L}_i(t)$, which is often called Doppler rate, is the relative velocity along the line of sight between two S/C and was stated in Ch. 2 to be $\approx 15 \frac{\text{m}}{\text{s}}$. Note again that an algebraic derivation of the 2nd generation combinations as in Sec. 3.2.1 was not found yet [TD14].

3.3.1 Multiple Time-Delay Operator Application

As explained before in Sec. 3.1.4, the multiple application of time delays results in nested delays, since the armlengths are now time-dependent as well and need to be shifted, too. In order to get an analytical handling for this case, an approximation of multiple time-delay operations is required. For a twofold time delay, it was defined in Eq. (3.16b) that

$$
f(t)_{;jk} = f\left(t - \frac{L_j(t)}{c}\right)_{;k} = f\left(t - \frac{L_k(t)}{c} - \frac{L_j\left(t - \frac{L_k(t)}{c}\right)}{c}\right).
$$

Obviously, these nested implicit functions are hard to handle analytically. Hence, we expand the complete argument by a Taylor expansion up to order $\frac{\dot{L}}{c} \approx 10^{-8}$ and start with

$$
\begin{aligned}
L_j\left(t - \frac{L_k(t)}{c}\right) &= L_j(t) + \dot{L}_j(t)\left(-\frac{L_k(t)}{c}\right) + \mathcal{O}(\tfrac{\ddot{L}(t)}{c^2}) \\
&\simeq L_j(t) - \frac{1}{c}\dot{L}_j(t)L_k(t),
\end{aligned}
$$

where $\simeq$ denotes the approximation. Note that terms of $\frac{\ddot{L}(t)}{c}$ are neglected, since relative LoS accelerations are negligible for LISA due to the smooth spacecraft orbits. This is justified subsequently.

As an order of magnitude estimate, we can approximate the relative LoS acceleration for two spacecraft that drift away with maximal speed of $15 \frac{\text{m}}{\text{s}}$, decelerate, and then reduce their separation with the same speed, by

$$
\ddot{L} \simeq \frac{\Delta v_{\text{rel}}}{\Delta t} \approx \frac{(15 - (-15)) \frac{\text{m}}{s}}{0.5\,\text{yr}} \approx 2 \cdot 10^{-6}\,\frac{\text{m}}{\text{s}^2}\,.
$$

The whole procedure is assumed to take half a year, since the LISA triangle performs one complete breathing period within one year. The second order term in the above

Taylor expansion of $L_j\left(t - \frac{L_k(t)}{c}\right)$ is then

$$\frac{1}{2}\ddot{L}_j(t)(-\tfrac{L_k}{c})^2 \approx \frac{1}{2} \cdot 2 \cdot 10^{-6}\,\frac{\mathrm{m}}{\mathrm{s}^2} \cdot 289\,\mathrm{s}^2 \approx 3 \cdot 10^{-4}\,\mathrm{m}\,.$$

In terms of light travel time, we thus find approximately

$$\frac{L_k(t)}{c} \approx 17\,\mathrm{s}\,, \qquad \frac{\frac{1}{c}\dot{L}_j(t)L_k(t)}{c} \approx 9 \cdot 10^{-7}\,\mathrm{s}\,, \qquad \frac{\frac{1}{2}\ddot{L}_j(t)(-\tfrac{L_k}{c})^2}{c} \approx 10^{-12}\,\mathrm{s}\,. \quad (3.34)$$

For TDI functionality, the light travel times must be known to nanosecond precision [EGMB$^+$11], and it gets obvious that the acceleration term is neglible. Therefore, we do not need to consider relative accelerations between the spacecraft (what TDI 3.0 or higher accounts for) for the rest of this thesis and can use

$$L_j\left(t - \frac{L_k(t)}{c}\right) \simeq L_j(t) - \frac{1}{c}\dot{L}_j(t)L_k(t)\,, \qquad (3.35)$$

since $\frac{1}{c}\dot{L}_j(t)L_k(t) \approx 270\,\mathrm{m}$ is non-negligible for meter accuracy and needs to be taken into account.

After more analogously performed expansions (appendix C.1) we end up with the following expression:

$$
\begin{aligned}
f(t)_{;\boldsymbol{jk}} &\simeq f(t)_{,\boldsymbol{jk}} + \frac{1}{c^2}\dot{f}(t)_{,\boldsymbol{jk}}\dot{L}_j(t)L_k(t) \qquad\qquad (3.36)\\
&= f\left(t - \frac{L_k(t)}{c} - \frac{L_j(t)}{c}\right) + \frac{1}{c^2}\dot{f}\left(t - \frac{L_k(t)}{c} - \frac{L_j(t)}{c}\right)\dot{L}_j(t)L_k(t)\,.
\end{aligned}
$$

Note here that the nested delays $f(t)_{;\boldsymbol{jk}}$ (marked by the semicolon) are replaced by expressions with unnested delays (marked by comma). $\dot{f}(t)_{,\boldsymbol{jk}}$ denotes the time derivative of the function $f(t)$, evaluated at the time $t - \frac{L_k(t)}{c} - \frac{L_j(t)}{c}$. For the sake of legibility, we will drop the t-dependence for $L, \dot{L}$ and $\ddot{L}$ in the following.

From (3.36) it can be deduced that even in the approximated case the delays do not commute, i.e., $f(t)_{;\boldsymbol{jk}} \neq f(t)_{;\boldsymbol{kj}}$ for $j \neq k$:

$$
\begin{aligned}
f(t)_{;\boldsymbol{jk}} - f(t)_{;\boldsymbol{kj}} &\simeq \left(f(t)_{,\boldsymbol{jk}} + \frac{1}{c^2}\dot{f}(t)_{,\boldsymbol{jk}}\dot{L}_j L_k\right) - \left(f(t)_{,\boldsymbol{kj}} + \frac{1}{c^2}\dot{f}(t)_{,\boldsymbol{kj}}\dot{L}_k L_j\right)\\
&= \frac{1}{c^2}\dot{f}(t)_{,\boldsymbol{jk}}(\dot{L}_j L_k - L_j \dot{L}_k) \neq 0\,,
\end{aligned}
$$

where we used $f(t)_{,\boldsymbol{jk}} = f(t)_{,\boldsymbol{kj}}$ and $\dot{f}(t)_{,\boldsymbol{jk}} = \dot{f}(t)_{,\boldsymbol{kj}}$ from Eq. (3.19c). For the case of time-independent armlengths, the relative LoS velocities $\dot{L}_j$ and $\dot{L}_k$ would vanish and the delay operators commute (cf. TDI 1.5).

In general, for an arbitrary number of time delays, the rule

$$f(t)_{;j_1...j_n} \simeq f(t)_{,j_1...j_n} + \frac{1}{c^2} \dot{f}(t)_{,j_1...j_n} \cdot \sum_{k=1}^{n-1} \left(\dot{L}_{j_k} \sum_{\ell=k+1}^{n} L_{j_\ell} \right) \tag{3.37}$$

applies to first order in $\frac{\dot{L}}{c}$. A derivation sketch can be found in appendix C.

3.3.2 Overview of the Second Generation TDI Combinations

The flexing arms make it necessary to sense the armlength change of the spacecraft constellation by more than single photon round-trips as it was the case for 1st generation. TDI 2.0 combinations thus extend the 1st generation variables by synthesising photon paths where each arm is sensed twice, as illustrated in Fig. 3.11 for the TDI-X enhancement, labelled by X_1.
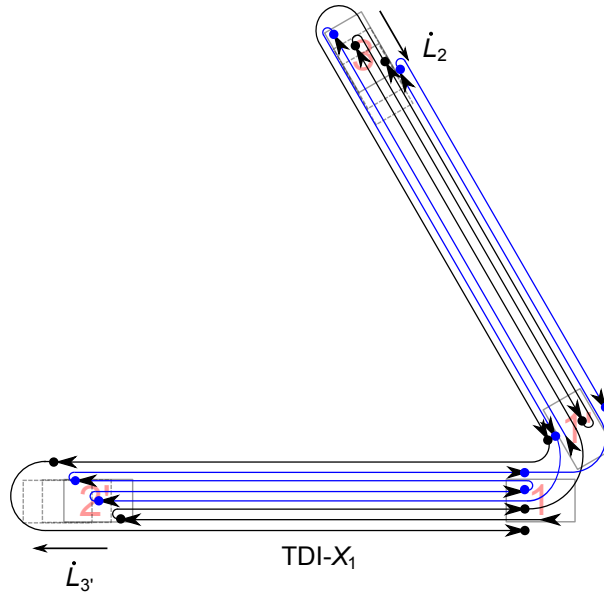
Figure 3.11: Photon path for the TDI 2.0 Michelson X_1 combination. In order to account for the breathing, each arm is sensed twice. The points mark again the virtual 'measurements' performed on each optical bench. Exemplarily, the relative LoS velocity of S/C 2 and 3 are chosen such that the armlengths L_2 and $L_{2'}$ shrink with time and meanwhile L_3 and $L_{3'}$ grow with time in this representation.

This in turn makes the equations messy. For the sake of readability, we will therefore only present one combination per variable class (e.g., X_1 for Michelson). The other variables of that class (e.g., X_2 and X_3) can be found by cyclic permutation of the indices (Sec. 2.4.1). Many combinations do not cancel anymore the laser frequency noise, even to first order in $\frac{\dot{L}}{c}$.

The form of the required input data streams $\eta_i(t)$ for TDI 2.0 is similar to that of the non-flexing constellation, Eqn. (3.25a) and (3.25b). The only difference is here that the time shifts are time-dependent. That is, we replace the colons in Eqn. (3.25a) and (3.25b) by semicolons:

$$\eta_1(t) \sim H_1 + p_{2;\mathbf{3}} - p_1 + \frac{\mu_{2;\mathbf{3}} - \mu_{2';\mathbf{3}}}{2} \,, \quad \eta_{1'}(t) \sim H_{1'} + p_{3;\mathbf{2'}} - p_1 - \frac{\mu_1 - \mu_{1'}}{2} \,, \quad (3.38)$$

others cyclic. Note again that the lasers from the primed optical benches have already been removed with help of the reference IFO output in a previous step, as described in Sec. 3.2.1, and the perfect reciprocity of fibre noise is assumed in the following

Michelson Combinations

The scientifically most important 2nd generation combinations are the Michelson combinations

$$
\begin{aligned}
X_1(t) \;=\; & \eta_{1'} + \eta_{3;\mathbf{2'}} + \eta_{1;\mathbf{22'}} + \eta_{2';\mathbf{322'}} + \eta_{1;\mathbf{3'322'}} + \eta_{2';\mathbf{33'322'}} \\
& + \eta_{1';\mathbf{3'33'322'}} + \eta_{3;\mathbf{2'3'33'322'}} - \eta_1 - \eta_{2';\mathbf{3}} - \eta_{1';\mathbf{3'3}} - \eta_{3;\mathbf{2'3'3}} \\
& - \eta_{1';\mathbf{22'3'3}} - \eta_{3;\mathbf{2'22'3'3}} - \eta_{1;\mathbf{22'22'3'3}} - \eta_{2';\mathbf{322'22'3'3}}
\end{aligned}
\quad (3.39)
$$

and $X_2(t)$, $X_3(t)$ similarly by cyclic permutation of the indices. After a tedious computation (appendix E.1) neglecting secondary noise sources and using the approximations to first order in $\frac{\dot{L}}{c}$ from Sec. 3.3.1, $X_1(t)$ turns out to be laser phase noise free and preserves the gravitational wave signal:

$$
\begin{aligned}
X_1 \;\simeq\; & H_{1'} + H_{3;\mathbf{2'}} + H_{1;\mathbf{22'}} + H_{2';\mathbf{322'}} + H_{1;\mathbf{3'322'}} + H_{2';\mathbf{33'322'}} \\
& + H_{1';\mathbf{3'33'322'}} + H_{3;\mathbf{2'3'33'322'}} - H_1 - H_{2';\mathbf{3}} - H_{1';\mathbf{3'3}} - H_{3;\mathbf{2'3'3}} \\
& - H_{1';\mathbf{22'3'3}} - H_{3;\mathbf{2'22'3'3}} - H_{1;\mathbf{22'22'3'3}} - H_{2';\mathbf{322'22'3'3}} \,.
\end{aligned}
\quad (3.40)
$$

The synthesised photon path of X_1 is shown in Fig. 3.11. The armlength variations were chosen there such that $L_{3'}$ grows and L_2 shrinks with time. The double round-trips of each arm sense the relative LoS motion.

The absolute of the transfer function for X_1 in a simplified equal-arm and time-independent case with the conventions and assumptions from Sec. 3.2.2 is shown in Fig. 3.12, and compared with the first generation X-combination. It is given by

$$
\begin{aligned}
\mathfrak{T}_{\Delta H \to X_1}(f) \;=\; & 1 + \mathrm{e}^{-\mathrm{i}\cdot 2\pi f T_0} - \mathrm{e}^{-\mathrm{i}\cdot 2\pi f \cdot 2T_0} - \mathrm{e}^{-\mathrm{i}\cdot 2\pi f \cdot 3T_0} - \mathrm{e}^{-\mathrm{i}\cdot 2\pi f \cdot 4T_0} \\
& - \mathrm{e}^{-\mathrm{i}\cdot 2\pi f \cdot 5T_0} + \mathrm{e}^{-\mathrm{i}\cdot 2\pi f \cdot 6T_0} + \mathrm{e}^{-\mathrm{i}\cdot 2\pi f \cdot 7T_0} \,.
\end{aligned}
\quad (3.41)
$$

The main difference to the first generation combination $X(t)$ lies in the low frequency behaviour, where in X_1 the transfer function rolls off with $\propto f^{-2}$ towards low frequencies, while for X this is according to $\propto f^{-1}$.

Chapter 3

Transfer function for TDI−X_1 and TDI−X
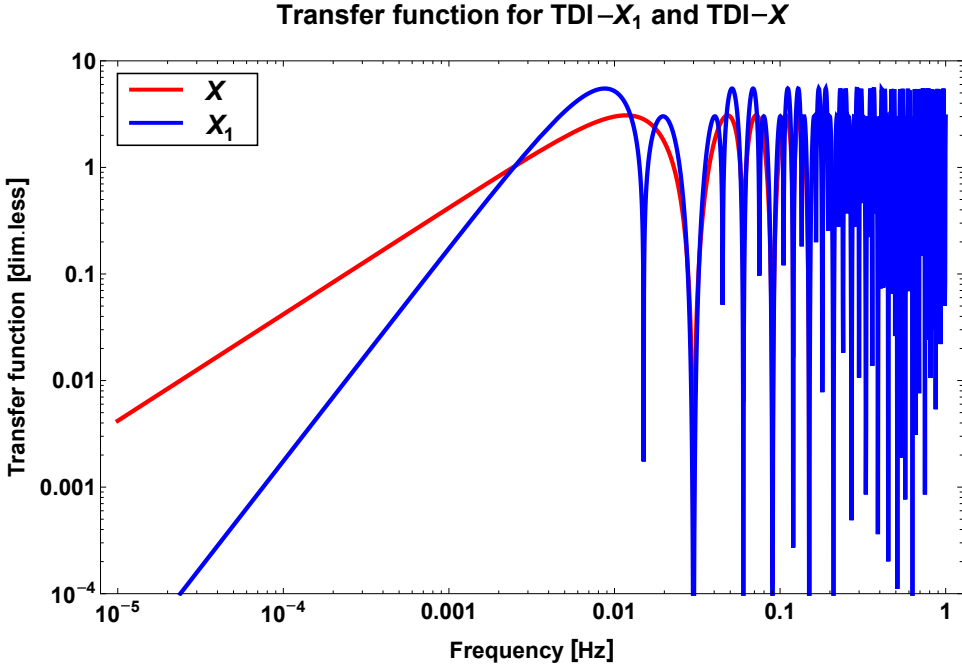
Figure 3.12: Transfer function for gravitational waves in the X_1-combination (blue), compared with TDI-X (red). The most obvious difference lies in the low frequency behaviour. While for TDI-X, the transfer function rolls off with f^{-1} towards low frequencies, the transfer function of the second generation combination X_1 follows a f^{-2} law. This stronger roll-off results from the inclusion of not only the armlengths L_i, but also the rate of change $\dot{L}_i$ in the synthesisation process of an equal-armlength interferometer. Further distinctions are in the level of the transfer function (twice as large for high frequencies as for X) and the appearance of the first null at $0.015\,\text{Hz}$. This is half the frequency as for X and results from the double sensing of one arm, where gravitational waves can partially cancel.

Fully Symmetric Sagnac Combination

The next class of TDI variables is the fully symmetric Sagnac. Due to the flexing of the constellation, we have now three symmetric Sagnac combinations ζ_1, ζ_2 and ζ_3 instead of one, ζ, for the static case. They are given by

$$
\begin{aligned}
\zeta_1(t) = \; & \eta_{1';\mathbf{1'2'3'}} - \eta_{2;\mathbf{22'3'}} + \eta_{2';\mathbf{22'3'}} - \eta_{1';\mathbf{1'1}} + \eta_{2;\mathbf{21}} - \eta_{2';\mathbf{21}} \\
& - \eta_{3;\mathbf{3'23}} + \eta_{3';\mathbf{3'23}} - \eta_{1;\mathbf{123}} + \eta_{3;\mathbf{3'1'}} - \eta_{3';\mathbf{3'1'}} + \eta_{1;\mathbf{11'}}, \quad (3.42)
\end{aligned}
$$

and ζ_2, ζ_3 by cyclic permutation. The fully symmetric Sagnac combinations $\zeta_{\underline{i}}(t)$ minimise the GW signal and therefore make it possible to perform a noise analysis of the detector network [TEA04].

Sagnac Combinations

The Sagnac variables do not cancel laser frequency noise to first order in $\frac{\dot{L}}{c}$ anymore. They sense the rotation of the satellite constellation and are given by

$$
\begin{aligned}
\alpha_1(t) \quad = \quad & \eta_{1'} + \eta_{3';\mathbf{2'}} + \eta_{2';\mathbf{1'2'}} + \eta_{1;\mathbf{3'1'2'}} + \eta_{2;\mathbf{33'1'2'}} + \eta_{3;\mathbf{133'1'2'}} \\
& -\eta_1 - \eta_{2;\mathbf{3}} - \eta_{3;\mathbf{13}} - \eta_{1';\mathbf{213}} - \eta_{3';\mathbf{2'213}} - \eta_{2';\mathbf{1'2'213}}
\end{aligned}
\tag{3.43}
$$

and others cyclic. The photon path for $\alpha_1(t)$ is presented in Fig. 3.13.

TDI-α_1
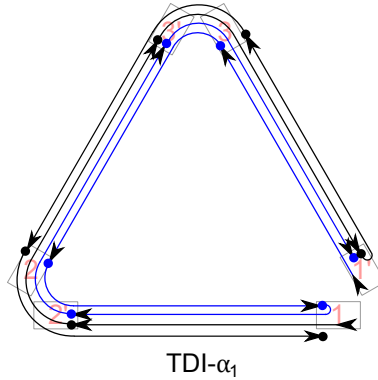
Figure 3.13: Photon path of the TDI 2.0 Sagnac combination α_1. In contrast to TDI 1st generation, the armlengths are sensed twice.

If we now make use of Eq. (3.37) and the η_i-definitions from Eq. (3.38), we can deduce after a tedious computation (appendix E.3) that parts of the laser phase noise will survive within the $\alpha_1(t)$-combination:

$$
\begin{aligned}
p_{1;\mathbf{2133'1'2'}} - p_{1;\mathbf{3'1'2'213}} \quad \simeq \quad & \frac{1}{c^2} \dot{p}_1(t)_{,\mathbf{1231'2'3'}} \left((\dot{L}_{1'} + \dot{L}_{2'} + \dot{L}_{3'})(L_1 + L_2 + L_3) \right. \\
& \left. - (\dot{L}_1 + \dot{L}_2 + \dot{L}_3)(L_{1'} + L_{2'} + L_{3'}) \right) \neq 0 \, .
\end{aligned}
\tag{3.44}
$$

Note again that in the case of non-flexing constellation the Doppler rates are zero and hence $\alpha_1(t)$ is free of laser noise $p_i(t)$. However, in the case of flexing arms, $\dot{L}_{\underline{i}} \neq \dot{L}_{\underline{i}'}$, and $p_{1;\mathbf{2133'1'2'}} - p_{1;\mathbf{3'1'2'213}}$ comprises non-vanishing laser noise.

We will now estimate the residual laser frequency noise according to Eq. (3.44). Therefore, the Doppler rates are assumed to be in sum $\dot{L}_1 + \dot{L}_2 + \dot{L}_3 = 50 \, \frac{m}{s}$, which is the worst case. Since it is expected that the relative velocities change slowly (with $\ddot{L} \approx 2 \cdot 10^{-6} \, \frac{m}{s^2}$ in maximum, Sec. 3.3.1), we can assume $\dot{L}_i$ to be equal over a short time period: $\dot{L}_{1'} + \dot{L}_{2'} + \dot{L}_{3'} \approx \dot{L}_1 + \dot{L}_2 + \dot{L}_3$, which was also stated in [Sha04]. We can then roughly estimate the round-trip armlength difference

$\Delta L = (L_1 + L_2 + L_3) - (L_{1'} + L_{2'} + L_{3'})$ due to the Sagnac effect via

$$\Delta L = \frac{4\vec{\Omega} \cdot \vec{A}}{c}, \tag{3.45}$$

where $\vec{\Omega}$ denotes the angular velocity of the constellation cartwheel motion and the area vector $\vec{A}$ points perpendicular on the constellation plane and its length corresponds to the area. Since constellation plane and ecliptic are tilted by 60° with respect to each other (Fig. 2.1), this yields

$$\Delta L = \frac{4|\vec{\Omega}||\vec{A}| \cos(\sphericalangle(\vec{\Omega},\vec{A}))}{c} = \frac{4\frac{2\pi}{T_{\mathrm{orb}}} \frac{1}{2} L_0 \frac{\sqrt{3}L_0}{2} \cos(60°)}{c} \approx 14.4 \, \mathrm{km} \tag{3.46}$$

with nominal armlength $L_0 = 5 \cdot 10^9 \, \mathrm{m}$. Hence, we can write

$$L_{1'} + L_{2'} + L_{3'} = L_1 + L_2 + L_3 + \Delta L$$

and furthermore

$$
\begin{aligned}
& \left((\dot{L}_{1'} + \dot{L}_{2'} + \dot{L}_{3'})(L_1 + L_2 + L_3) - (\dot{L}_1 + \dot{L}_2 + \dot{L}_3)(L_{1'} + L_{2'} + L_{3'}) \right) \\
\simeq\ & (\dot{L}_1 + \dot{L}_2 + \dot{L}_3)((L_1 + L_2 + L_3) - (L_{1'} + L_{2'} + L_{3'})) \\
=\ & (\dot{L}_1 + \dot{L}_2 + \dot{L}_3)((L_1 + L_2 + L_3) - (L_1 + L_2 + L_3 + \Delta L)) \\
=\ & -(\dot{L}_1 + \dot{L}_2 + \dot{L}_3)\Delta L.
\end{aligned}
$$

Eq. (3.44) then reduces to

$$p_{1;\mathbf{2133'1'2'}} - p_{1;\mathbf{3'1'2'213}} \simeq -\frac{1}{c^2} \dot{p}_1(t),_{\mathbf{1231'2'3'}}(\dot{L}_1 + \dot{L}_2 + \dot{L}_3)\Delta L.$$

However, $\dot{p}_1(t),_{\mathbf{1231'2'3'}}$ is still unknown and needs to be determined in the following.

Since frequency and phase are related via differentiation or integration, respectively, $\dot{p}$ is nothing different than the phase variation of the laser per time, also known as (absolute) frequency variation $\Delta\nu(t)$. With the knowledge of Sec. 3.1, we can compute the frequency variation from a given spectral density for the LISA measurement band:

$$
\begin{aligned}
\Delta\nu_{\mathrm{rms}} &= \sqrt{\int_{10^{-4}\,\mathrm{Hz}}^{10^{-1}\,\mathrm{Hz}} \mathrm{d}f \left(\frac{10^4\,\mathrm{Hz}}{f} \frac{\mathrm{Hz}}{\sqrt{\mathrm{Hz}}} \right)^2} = 10^4\,\mathrm{Hz} \frac{\mathrm{Hz}}{\sqrt{\mathrm{Hz}}} \sqrt{\int_{10^{-4}\,\mathrm{Hz}}^{10^{-1}\,\mathrm{Hz}} \mathrm{d}f \frac{1}{f^2}} \\
&= 10^4 \frac{\mathrm{Hz}^2}{\sqrt{\mathrm{Hz}}} \sqrt{-\frac{1}{f}\Big|_{10^{-4}\,\mathrm{Hz}}^{10^{-1}\,\mathrm{Hz}}} = 10^4 \frac{\mathrm{Hz}^2}{\sqrt{\mathrm{Hz}}} \sqrt{-10 + 10^4} \frac{1}{\sqrt{\mathrm{Hz}}} \\
&\approx 1\,\mathrm{MHz}. \tag{3.47}
\end{aligned}
$$

Finally we make use of the fact that the root mean square value is an averaged

value, and hence $\dot{p}_1(t)_{,\mathbf{1231'2'3'}} \simeq \dot{p}_1(t) \simeq \Delta\nu_{\mathrm{rms}}$. This results in

$$
\begin{aligned}
p_{1;\mathbf{2133'1'2'}} - p_{1;\mathbf{3'1'2'213}} &\simeq -\frac{1}{c^2}\dot{p}_1(t)_{,\mathbf{1231'2'3'}}(\dot{L}_1 + \dot{L}_2 + \dot{L}_3)\Delta L \\
&= \frac{1}{9\cdot10^{16}\,\frac{\mathrm{m^2}}{\mathrm{s^2}}}\cdot 10^6\,\mathrm{Hz}\cdot(50\,\frac{\mathrm{m}}{\mathrm{s}}\cdot 14400\mathrm{m}) \\
&\approx\quad 8\cdot10^{-6}\,\mathrm{rad}\,,
\end{aligned}
\tag{3.48}
$$

and this is below the expected GW phase signal of some 10^{-5} rad. Hence, for 2nd generation Sagnac combinations, we should be able to extract the GW as is also confirmed by the simulation results presented in Ch. 6 even for free-running lasers.

Link Failure Surviving Combinations

Of course, the link failure surviving combinations Beacon, Monitor and Relay also become more complex as for the first generation [TEA04]. Relay extends to

$$
\begin{aligned}
U_1(t) =\ & \eta_{2';\mathbf{2311'}} + \eta_{1';\mathbf{32311'}} + \eta_{3';\mathbf{232311'}} + \eta_{2;\mathbf{1232311'}} - \eta_{2;\mathbf{2311'}} - \eta_{2';\mathbf{1'}} \\
& -\eta_{1';\mathbf{31'}} - \eta_{3';\mathbf{231'}} - \eta_{2;\mathbf{1231'}} + \eta_{2;\mathbf{1'}} + \eta_{2';\mathbf{11'1'}} + \eta_{3';\mathbf{1'1'}} \\
& +\eta_{1';\mathbf{311'1'}} - \eta_{2';\mathbf{11'1'123}} - \eta_{3';\mathbf{1'1'123}} - \eta_{1';\mathbf{311'1'123}}
\end{aligned}
\tag{3.49}
$$

and others cyclic. Next, Beacon changes to

$$
\begin{aligned}
P_1(t) =\ & \eta_{3';\mathbf{3311'2'}} + \eta_{2;\mathbf{13311'2'}} + \eta_{3;\mathbf{1'13311'2'}} - \eta_{3;\mathbf{3311'2'}} - \eta_{3';\mathbf{332'}} - \eta_{2;\mathbf{1332'}} \\
& -\eta_{3;\mathbf{1'1332'}} + \eta_{3;\mathbf{332'}} + \eta_{2;\mathbf{2'2'3}} + \eta_{3';\mathbf{1'2'2'3}} + \eta_{2';\mathbf{11'2'2'3}} - \eta_{2';\mathbf{2'2'3}} \\
& -\eta_{2;\mathbf{2'2'1'13}} - \eta_{3';\mathbf{1'2'2'1'13}} - \eta_{2';\mathbf{11'2'2'1'13}} + \eta_{2';\mathbf{2'2'1'13}}\,,
\end{aligned}
\tag{3.50}
$$

and the Monitor combination enhances to

$$
\begin{aligned}
E_1(t) =\ & \eta_{1'} - \eta_{1';\mathbf{11'}} - \eta_{1';\mathbf{1'1}} + \eta_{1';\mathbf{11'1'1}} - \eta_1 + \eta_{1;\mathbf{11'}} + \eta_{1;\mathbf{1'1}} - \eta_{1;\mathbf{1'111'}} \\
& +\eta_{3';\mathbf{2}} + \eta_{2;\mathbf{12}} - \eta_{2;\mathbf{3'}} - \eta_{3';\mathbf{1'3'}} - \eta_{3';\mathbf{2211'\bar{2}}} - \eta_{2;\mathbf{12211'\bar{2}}} \\
& +\eta_{2;\mathbf{3'3'1'1\bar{3}'}} + \eta_{3';\mathbf{1'3'3'1'1\bar{3}'}}\,.
\end{aligned}
\tag{3.51}
$$

The bar notation of some indices in Eq. (3.51) emphasises here that the inverse time-delay operator $\boldsymbol{\mathcal{D}}^{-1}$ has to be applied. It is defined as $\boldsymbol{\mathcal{D}}\boldsymbol{\mathcal{D}}^{-1} = \mathbb{1}$ to first order in $\frac{\dot{L}}{c}$ and

$$
\boldsymbol{\mathcal{D}_i}^{-1}f(t) = f(t)_{;\bar{i}} = f\left(t + \frac{L_i\left(t + \frac{L_i(t)}{c}\right)}{c}\right).
\tag{3.52}
$$

Note that this operator does not simply advance, since it shifts not by $+\frac{L_i(t)}{c}$, but rather by $+\frac{1}{c}L_i(t + \frac{L_i(t)}{c})$. A proof of the inversion property, i.e., $\boldsymbol{\mathcal{D}}\boldsymbol{\mathcal{D}}^{-1} = \mathbb{1}$, can be found in appendix C.4.

Currently, our simulation explained in Ch. 5 uses TDI-$X_{\underline{i}}$, TDI-$\alpha_{\underline{i}}$ and TDI-$\zeta_{\underline{i}}$ as TDI 2.0 output data streams. These are sufficient to show that laser phase noise can in principle be suppressed below the 10 pm-requirement, even in case of a flexing LISA.

3.4 Experimental TDI Tests

Up to this point, Time-Delay Interferometry comes as a theoretical algorithm for artificial synthesisation of interferometric outputs using digitised one-link measurements. It is therefore reliable to simulate and test it on a software basis. In Ch. 5 and 6 of this thesis, a simulation and its results are explained in detail. However, laser frequency noise and clock noise were rated by NASA's 2004 LISA Technology Development Plan as a primary interferometry technology risk [NAS04]. It is therefore crucial to demonstrate experimentally the critical LISA technologies and data processing techniques like TDI in advance. In this section, we will at first introduce a separate ranging technique relying on the TDI functionality and then proceed to a short overview about ground-based and space-based testbeds for TDI testing.

3.4.1 Time-Delay Interferometric Ranging

Recently, a new tool based on Time-Delay Interferometry came up in order to perform accurate ranging without sophisticated ranging systems onboard which are technically complex. This method is called Time-Delay Interferometric Ranging (TDIR) [TVA05; Tin08b; MMS12].

TDIR uses the TDI output formation, e.g. of $X_1(t)$, and optimises it such that the residual laser phase noise power becomes minimal while the gravitational wave signal power is maximised. This is the case if the artificial delays used in the post-processing to form the TDI combinations coincide with the physical light travel times. Hence, the optimisation, e.g., by least-square methods, is performed with respect to the synthesised armlengths $L_i(t)$ used for the delay operators.

In other words, the goal of the TDIR procedure is to find the minimum of the functional

$$\mathcal{I}^{(p)}(\hat{L}_k) = \frac{1}{T} \int\limits_0^T \mathrm{d}t \, (X_1^{(p)}(\hat{L}_k(t),t))^2 \,.$$

T denotes the overall length of the time series $X_1^{(p)}(\hat{L}_k(t),t)$, while $\hat{L}_k$ is an estimated armlength. $X_1^{(p)}(\hat{L}_k(t),t)$ itself is the TDI 2.0 Michelson combination X_1 with laser phase noise only (denoted by $^{(p)}$). It highly depends on the armlengths $\hat{L}_k(t)$ which are used for the time-delay operators, as can be seen from Eq. (3.39). If the extremum of $\mathcal{I}^{(p)}$ is reached at $\hat{L}_k \simeq L_k$ (where L_k is the real physical armlength and $\hat{L}_k$ the estimated armlength of link k), one can read off the armlengths $\hat{L}_k$ and

gets an extremely good estimate for the 'real' armlength value L_k. Moreover, TDIR could allow the synthesis of TDI combinations even in the case of ranging dropout or glitches in the data.

The baseline in the present prototypes is that ranging via pseudo random noise phase modulation will be performed continuously (Ch. 2). This has been successfully implemented in the ESA-funded Danish/German collaboration phasemeter prototype [Est12; BBB+14]. TDI ranging will be used complementary to calibrate constant biases (offsets due to light travel time delays) in the PRN ranging results. However, the TDIR algorithm is beyond the scope of this thesis.

3.4.2 Ground-Based Testbeds for TDI

Time-Delay Interferometry is a crucial technique for LISA. Unfortunately, an experimental simulator with million kilometre armlength is obviously impossible to build on Earth. Even with the use of optical delay lines one could by far not reach the 17 s light travel times along the LISA inter-spacecraft links. However, various aspects for TDI functionality can be tested on ground, and, with a digital storage trick, even long delays can be mimicked. We will now list the recent and current experimental testbeds.

Experimental TDI Demonstration at the Jet Propulsion Laboratory

In 2003, first plannings to demonstrate the TDI procedure in laboratory started at the Jet Propulsion Laboratory (JPL) [TSSA03] and a first functionality proof followed in 2010 [dVWM+10]. It was for the first time possible to show experimentally that laser frequency noise and clock noise could be suppressed in post-processing by TDI. Therefore, a setup was chosen that could be used to construct the virtual photon path of the Sagnac combination. TDI-α was proven to be only limited by the intrinsic noise floor of the laboratory testbed.

The JPL simulator setup comprises two optical benches, separated by one meter, and simulates two simplified LISA spacecraft. The whole setup is operated in vacuum to minimise external couplings. Each optical bench is equipped with two lasers and one phasemeter triggered by an independent clock. The four lasers are locked to each other with frequency offsets accounting for (static) Doppler shifts. Furthermore, white frequency noise is added to mimic pre-stabilised laser frequency noise (Sec. 2.3.3). The lasers are then interfered and form three beat-notes per optical bench. Two of which correspond to the science signals and the third measurement provides the reference measurement for onboard laser comparison.

Additionally, the clock signal of each OB is sideband-modulated on the outgoing laser beam and transmitted to the other optical bench, where a sideband beat-note is formed to extract the clock signal, as explained in Sec. 2.2.3. Using this transfer chain, the measurements can be corrected for the clock noise. For this, a post-processing reduction algorithm (as explained in Ch. 4 for the complex full LISA
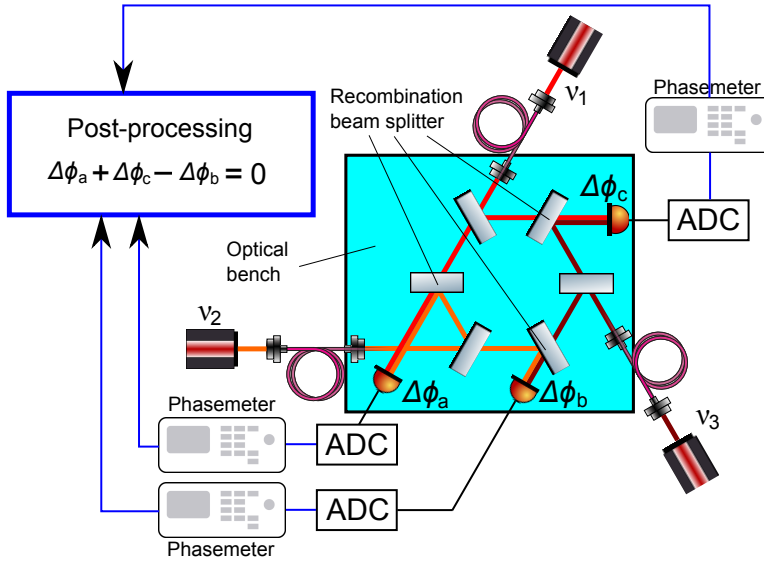
Figure 3.14: Setup of the hexagon interferometer. Three lasers are locked to each other (locking scheme not shown here for simplicity) with slightly different frequencies ν_1, ν_2 and ν_3. Their light is sent via optical fibres to the optical bench, combined to form MHz beat-notes and read out by PDs. The phases of the beat-note signals, $\Delta\phi_a$, $\Delta\phi_b$ and $\Delta\phi_c$, are tracked with phasemeters and finally combined in post-processing to synthesise a virtual zero and thus to perform a phasemeter linearity test.

case) is used to remove the clock noise, and this procedure relies on high accuracy interpolations. The result of this data processing step is then the input for TDI. The JPL simulation provides the validation of the LISA phasemeter and the evidence that the overall TDI performance is not limited by technical phase noise from lasers and clocks. For more details we refer to [TSSA03].

Hexagon Interferometer

Recently, an interferometric metrology testbed was developed in-house at the Albert Einstein Institute Hannover, the so-called hexagon interferometer. Its purpose is to test key technologies for TDI such as ADC jitter correction via pilot tone injection (Sec. 4.1), the performance of the raw ranging and clock measurements, the PM readout and combination of the phase signals to correct for clock noise [Deh12]. Initially, the goal was to perform an ultimate linearity test of the phasemeter. That is, the phase measurement system combines three phase difference outputs in such a way that the sum is virtually zero. In the case of non-linearity of the PM, this is not possible, since unwanted noise couples into the phasemeter channels.

The hexagon interferometric setup is sketched in Fig. 3.14. The optical setup is optimised with respect to several parameters, e.g., straylight disturbances and thermal expansion of the optical bench. It consists of three lasers with small MHz

frequency offsets, locked to each other. The laser light is transmitted through optical fibres to the optical bench. Here, the lasers are interfered at three recombination beam splitters and give rise to PD measurements with phases $\Delta\phi_a$, $\Delta\phi_b$ and $\Delta\phi_c$. These are read out by separate phasemeters and then combined in post-processing to virtually construct a zero. A first test of the measurement concept was performed recently. It showed the successful suppression of the offset frequencies and proved the pilot tone correction for ADC jitter [Ger14].

University of Florida LISA Simulator

The University of Florida LISA Simulator (UFLIS) follows a more LISA-like approach for the experimental demonstration of TDI [MWM10]. Generally, an eLISA-like setup with four 'links' in a 'V'-shaped constellation was chosen. UFLIS uses three lasers plus one reference laser providing the clock, each of these forming beat-notes comparable to the science and reference interferometers in LISA. The delays along the links are mimicked by so-called electronic phase delay units. That is, the beat-note phase of the transmitting laser and the reference laser is tracked by a phasemeter and then interpolated to time-lead or time-lag the phase information. Digitally generated linear variations in this delay according to a constellation with flexing armlengths, Doppler frequency shifts and a GW signal are added and mixed. This mimics the science measurement on the distant spacecraft and is similar for the other links. The digital data streams that correspond to the PM outputs of science and reference interferometers are then combined in post-processing on a computer to form the combination $X(t)$ and $X_1(t)$.

Furthermore, an important aspect for UFLIS is the implementation of a ranging procedure. It consists of the TDIR method (Sec. 3.4.1) using a pilot tone modulated on the lasers. TDIR is then used to constrain the one-way delay times between the spacecraft by the minimisation of the residual phase power in the TDI X_1 combination [MMS12].

Several measurement were recently performed. First of all, the TDI 1.0 performance was successfully tested, while for TDI 2.0, the simulation violated the 10 pm-requirement by a factor of 4, resulting from non-linear electronic phase delay effects due to clock noise. Moreover, one-way ranging via pilot tone and TDIR was simulated, finally including a low frequency background confusion noise which did not spoil the output data significantly. For more details we refer to [MMS12].

For the ground-based experiments discussed above, the armlengths are all limited to some meters in maximum. A reliable approach for the experimental verification of TDI for long arm interferometry without digital storage (as in the UFLIS) is to use appropriate satellite missions as testbeds, as we will sketch now for one future mission.

3.4.3 A Satellite-Based Testbed for TDI

The Gravity Recovery and Climate Experiment (GRACE) is a satellite-based mission to map the Earth's gravitational field [TBWR04; WBC+14]. It consists of two spacecraft that orbit the Earth at an altitude of 450 km. They are separated by 220 km and the distance is tracked by microwaves to micrometer precision. A change in separation can be identified with a variation of the local gravitational field. Since the two GRACE satellites fly in a low-Earth polar orbit with a period of approximately 90 minutes, a monthly update of the gravity field with a spatial resolution of some hundreds of kilometre can be obtained. With this precision it was for example possible to identify the raise of Greenland due to ice loss [VSvdB14] or the water drought in the California Central Valley [SLL12].

In order to measure the Earth's gravity field more precisely, an advanced mission is on track to be launched in 2017. The GRACE Follow-On mission consists basically of the same setup and payload as GRACE. Additionally, the microwave link is supplemented by laser links and heterodyne interferometry is performed on both spacecraft in order to sense the distance to sub-micrometer precision [SSM+12]. This laser ranging instrument relies on LISA techniques and is therefore planned to be used for TDI and TDIR technology testing, as proposed by [Sut14].

3.5 Applications for Time-Delay Interferometry

This section deals with possible prospects for Time-Delay Interferometry. The application of TDI in two other space-based missions with long arm interferometry, the Big Bang Observer and the Octahedron Gravitational Wave Observatory, is briefly presented.

3.5.1 TDI for the Big Bang Observer

The Big Bang Observer (BBO) is a future space-based gravitational wave detector formed by four detectors following the Earth and shifted each by 120° with respect to the Sun, and tilted by 60° with respect to the ecliptic [ea04]. Each detector consists of a LISA-like triangle with armlengths of several 10000 kilometre. Two of these 'small LISAs' are forming a star of David as depicted in Fig. 3.15. This constellation is necessary for the cross-correlation of the science signals in order to extract cosmic gravitational wave background signals [CC05; CH06].

BBO is aiming at the detection of primordial gravitational waves produced at the time of inflation, the phase less than 10^{-30} s after the big bang where the universe expanded rapidly [Gut81; Lin82]. Therefore, it operates in the mid frequency band between 0.1 Hz and 3 Hz and could close the gap between space-based and ground-based detectors (Fig. 1.5).

The detection principle of BBO is comparable to that of LISA. Many problems for LISA, as beam divergence and low power interferometry, are simplified by the
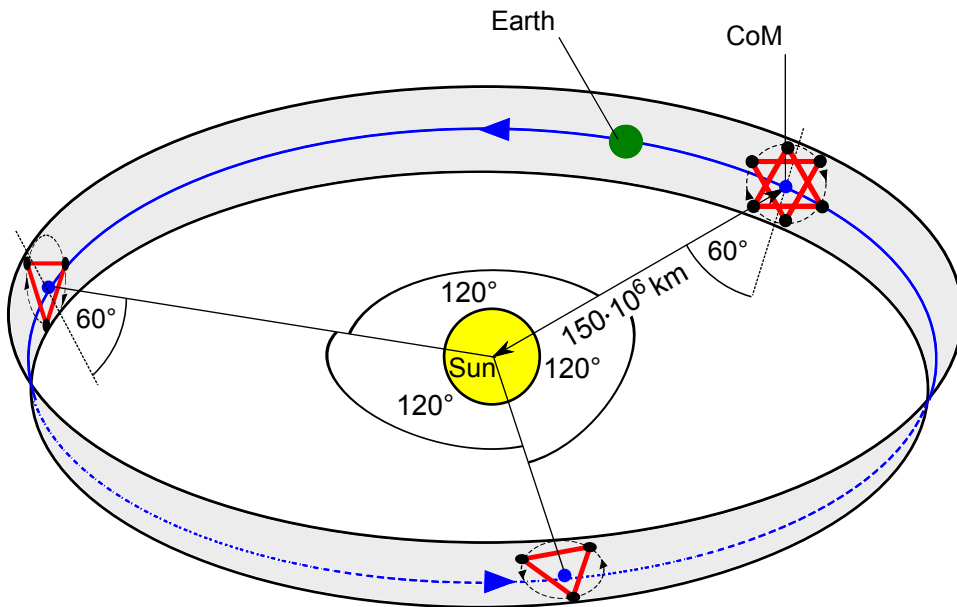
Figure 3.15: Constellation of the Big Bang Observer. The four LISA-like constellations follow a heliocentric orbit and are separated by 120°. Two of the small LISAs form a star of David and are used for cross-correlation of the science signals.

short armlengths of roughly 1% of LISA. However, still laser frequency noise is an issue for BBO, too, due to flexing and cartwheel motion. Hence, TDI is required to remove laser frequency noise. Due to the LISA-like triangular constellations, the TDI combinations in each triangle are similar to those of LISA, and simulations have shown the functionality of TDI for BBO. [HMOP08]

3.5.2 TDI for the Octahedron Gravitational Wave Observatory

The octahedron gravitational wave observatory (OGO) is a space-based mission concept inspired by a 3-dimensional interferometer configuration on ground first examined by [CPS06]. Its key feature is the displacement-noise free interferometry [KC04; CPS06; CK06] and is an improved algorithm upon TDI, since it cancels laser frequency noise and displacement noise simultaneously. The OGO constellation is shown in Fig. 3.16. It consists of six spacecraft separated by one million kilometre, forming an octahedron shape. Each S/C is equipped with lasers, clocks and optical readout systems to perform one-way optical phase measurements similar to the LISA measurement principle. The octahedron configuration gives 24 laser links, each corresponding to a science measurement channel of the distance (photon flight-time) variation between the test masses on adjacent spacecraft. OGO is placed around the Lagrangian point L1 in the Sun-Earth system.
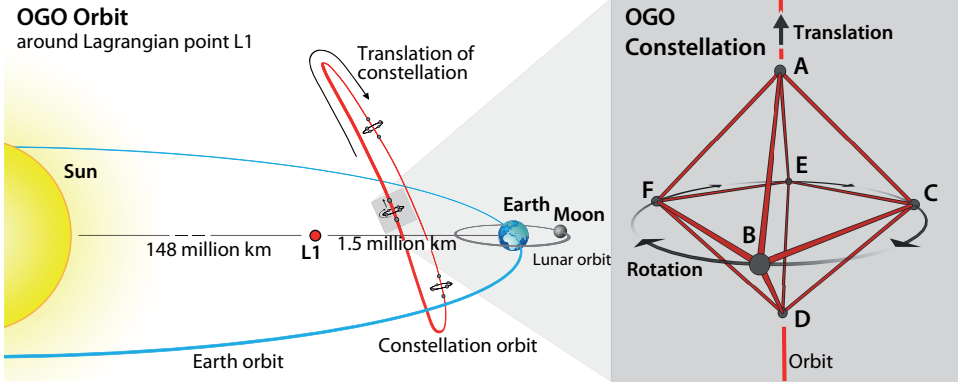
Figure 3.16: The OGO constellation (not to scale). Six S/C labelled A, B, C, D, E and F form the octahedron shape and interchange light probing the space-time for GW. The constellation is placed on a quasi-halo orbit around Lagrangian point L1. [WKB+13]

Onboard Data Streams

Each spacecraft of OGO is located in a corner of the octahedron and exchanges laser light with four adjacent spacecraft. Interference is performed between the laser light emitted from spacecraft I and received by spacecraft J, and light of the local laser beam onboard S/C J. Here, $I, J = \{A, B, C, D, E, F\}$ refer to the labels in Fig. 3.16. We follow [WKB+13] and assume a rigid and non-rotating constellation with all armlengths $L_0 = $ const. Furthermore, any deviations from the equal-arm configuration are taken to be small and can be absorbed into the low frequency part of the acceleration noise. The measurement of the phase change for each link is then given by a similar expression to Eq. (2.24):

$$s_{IJ}(t) = H_{IJ} + \widehat{\mathbf{D}} p_I - p_J + \widehat{\mathbf{D}}\left(\vec{a}_I \cdot \vec{n}_{IJ}\right) - \left(\vec{a}_J \cdot \vec{n}_{IJ}\right) + N_{IJ}\,, \tag{3.53}$$

where we have neglected constant factors to convert acceleration noise to optical phase shifts. Here, H_{IJ} denotes the influence of gravitational waves on the link $I \to J$ (comparable with Eq. (2.20a)), N_{IJ} labels the shot noise and other noise sources at the photodetector and phasemeter of spacecraft J, p_I denotes the local laser phase noise of spacecraft I. The vector $\vec{a}_I$ marks the acceleration noise of spacecraft I and is comparable with the displacement noise $\vec{\Delta}$ from the LISA setup. Furthermore, $\vec{n}_{IJ} = \frac{\vec{x}_J - \vec{x}_I}{L}$ is the unit vector along the arm $I \to J$ (with nominal armlength L_0), where $\vec{x}_I$ and $\vec{x}_J$ mark the positions of the pointwise spacecraft I and J, respectively. Since the constellation is taken to be rigid and non-rotating, the S/C positions are time-independent and the delay operator $\widehat{\mathbf{D}}$ has no arm index: $\widehat{\mathbf{D}} f(t) = f(t - \frac{L_0}{c})$.

Displacement Noise Free Interferometry Combinations

The science data H_{IJ} is again buried in laser frequency and acceleration noise which must be suppressed in post-processing. On each S/C, four measurement data streams are accessible. It could be argued that 24 data streams are enough to remove displacement and laser noise in post-processing, since six lasers plus $6 \times 3 = 18$ components of acceleration noise are involved. Hence, no intra-S/C measurements like the reference or test mass IFO for LISA are needed for OGO.

As for LISA, the challenge is to combine and time-shift the individual one-link measurements from Eq. (3.53) in order to remove acceleration noise $\vec{a}_I$ and laser noise p_I in post-processing. Therefore, we can perform a similar algebra as sketched in Sec. 3.2.1. However, for OGO, we have to deal with 24 science signals (in contrast to 6 for LISA) and the noise-free data combinations become much more complex. Moreover, we need to find combinations that at the same time suppress also the acceleration noise of each spacecraft, since no test mass interferometer measurements are provided.

By using the algebraic tools of [TD14], it was possible to deduce combinations for laser phase and acceleration noise removal for OGO that also preserve the GW signal. A detailed derivation of the displacement and laser phase noise free combinations as well as an analysis of the OGO detector with respect to shot noise limiting properties and astrophysical prospects can be found in [WKB⁺13; Wan14]. However, we will concentrate in the following again on the Laser Interferometer Space Antenna.

Chapter 3

4 Time-Delay Interferometry for a Full LISA Model

In the last chapter, we discussed the laser frequency noise cancellation procedure called Time-Delay Interferometry. As a starting point, we used the onboard interferometric LISA data streams, Eqn. (2.28a) – (2.28f) from Ch. 2, in a very simplified form with laser phase noise and gravitational wave signal only. However, as discussed in Sec. 2.3, the critical primary noise sources that swamp the onboard interferometric data are not only laser frequency noise (which can be removed by TDI), but additionally OB displacement noise (e.g., due to thruster firing). Furthermore, the light transmitted between the optical benches through back-link fibres collects phase noise as well which thus distorts the test mass and reference IFO measurements.

The synthesis of the TDI combinations is performed on ground in post-processing. Therefore, the onboard inferometric readout data need to be digitised by analog-to-digital converters in order to determine the beat-note frequency and relative phase shifts by the phasemeter. A stable clock onboard each spacecraft triggers the digitisation process of the ADCs. However, even the best-stabilised clock underlies fluctuations, the clock noise, which distort the sampling process and needs to be suppressed. The clock noise removal process relies on an auxiliary interferometric sideband measurement discussed below and is as well crucial for the TDI functionality.

The goal of this chapter is to derive a post-processing algorithm to remove all discussed critical primary noise sources: laser frequency noise, OB displacement, fibre phase noise and clock noise. A further issue, the beat-note frequency polarity, is taken into account. The chapter closes with an extended removal scheme for an alternative optical bench setup that uses two lasers for fibre noise cancellation and is under current discussion.

4.1 Inclusion of Clock Noise

This section deals with the impact of differential clock noise. That is, even with pilot tone correction (Sec. 2.3.4), the clock signals on each S/C have relative phase noise that swamp the measurement data. As explained in Sec. 2.3.4, one distinguishes between low frequency noise (called drift) and high frequency components of clock noise (called jitter). For the sake of brevity, we will subsume both the low and high frequency components as clock noise and discuss in the following the impact on the onboard interferometric measurements from Ch. 2. Since there is insufficient data to remove the differential clock noise in post-processing from the digitised data, an inter spacecraft clock tone transfer chain can be used for correcting each clock and is elucidated at last.

4.1.1 USO Signal Distribution

Each spacecraft hosts a stable oscillator as a master clock. In the phase measurement scheme given in [BBB$^+$14] and presented in Fig. 4.1, the USO ticks with a frequency of 2.4 GHz and its signal is used mainly for three purposes. First, it triggers the ADCs and the phasemeter. Therefore, the USO signal is divided down to 80 MHz, which provides the internal clock for both ADC and phasemeter operation. Beside USO phase fluctuations given by Eq. (2.11), the ADCs themself introduce phase noise as was sketched in Fig. 2.6. This noise can be determined with help of an accurately known signal, the pilot tone. The second purpose of the USO is thus the pilot tone generation. We refer to [Bar15] for further details.

The accurate sinusoidal pilot tone at 75 MHz is constructed from the USO signal again by division and fed to the ADC as an input signal. Since the trigger signal is at 80 MHz, the Nyquist-Shannon theorem is violated [Sha49]. That is, any sampling process must be performed with a frequency f_{samp} higher than twice the signal frequency for preventing alias effects in the digitised data. If violated, the signal frequency is aliased to a different value. However, this effect is wanted here, since the 75 MHz are then reflected at $\frac{f_{\mathrm{samp}}}{2} = 40$ MHz and produces a signal at 5 MHz. Since the pilot tone is known accurately, the noisy transfer function of the ADC and the sampling clock can be determined and corrected for in the digitised data from the interferometers. Note that the exact frequency values for the USO, clock and aliased signal are current baseline and may change.

One could now argue that taking a 5 MHz signal is more efficient than the artificial production of a 5 MHz aliased signal. However, the timing jitter in a 5 MHz signal has a small phase impact compared to the 75 MHz signal (the slope of the digitised waveform is 15 times higher). Since the ADC jitter needs to be determined by the pilot tone injection, it is therefore beneficial to insert a high frequency signal where the impact on the phase is large.

Each phasemeter analyses the input data referred to its own time stamps provided by the local USO. However, the USOs on each spacecraft drift and jitter relative to
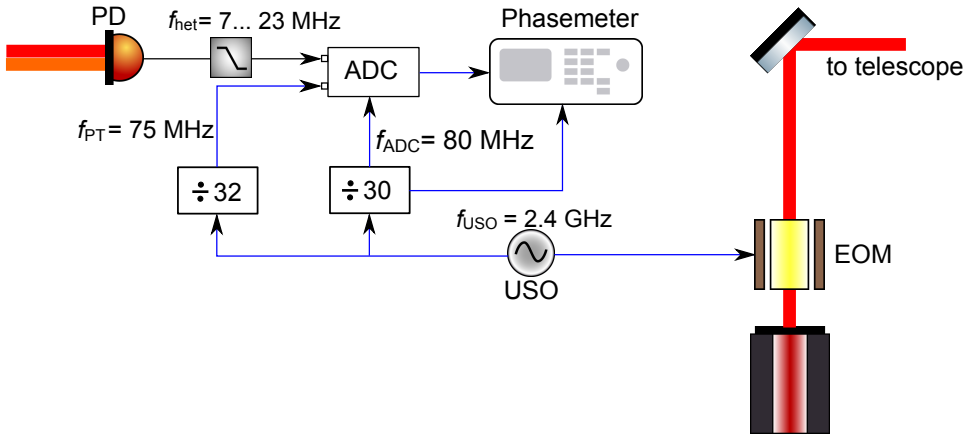
Figure 4.1: USO signal distribution scheme. The photodetector signal at a hete-rodyne frequency of $7\,\text{MHz} < f_{\text{het}} < 23\,\text{MHz}$ is digitised by an ADC, and this ADC is triggered by a clock at $f_{\text{ADC}} = 80\,\text{MHz}$ derived by division from the USO signal with $f_{\text{USO}} = 2.4\,\text{GHz}$. The same 80 MHz clock signal provides the internal clock for phasemeter operation. With the purpose of ADC jitter correction, the USO is further used for the pilot tone construction. Through division by 32, a stable pilot tone at $f_{\text{PT}} = 75\,\text{MHz}$ is derived. Finally, in order to transfer clock data, the USO signal is modulated on the outgoing laser beam by electro-optic modulators and sent to the distant spacecraft.

each other, and the recorded data has thus different time stamps with differential clock noise. In order to correct for this differential phase noise, a companion between the S/C clocks is needed. This requires a transfer of the clock noise information along the arms, called clock tone transfer chain. For this third purpose, the USO signal is modulated via an electro-optic modulator (EOM) on the outgoing beam. A schematic of the three USO signal utilisations is drawn in Fig. 4.1.

Since the pilot tone is an accurate sinusoidal signal, it can be regarded as a stable time reference. Its phase jitter is, compared to the USO signal, smaller. Hence, we will use the pilot tone as the clock reference and formulate clock phase errors with respect to it. The pilot tone phase jitter is denoted by $q(t)$ and we will call it clock noise in the following.

4.1.2 Impact on the Interferometric Signals

The first analysis of the clock noise impact on LISA-like measurement signals and its technical suppression was performed in [HGGT$^+$96]. In Ch. 2, we derived the onboard signals for the science interferometer accounting for the current baseline which resulted in

$$\bar{s}_1(t) = H_1 + p_{2';\mathbf{3}} - p_1 - \frac{2\pi}{\lambda_{2'}}\vec{n}_3 \cdot \vec{\Delta}_{2';\mathbf{3}} - \frac{2\pi}{\lambda_{2'}}\vec{n}_{3'} \cdot \vec{\Delta}_1 + N_1^{\text{opt}} + N_1^s \,.$$

Chapter 4
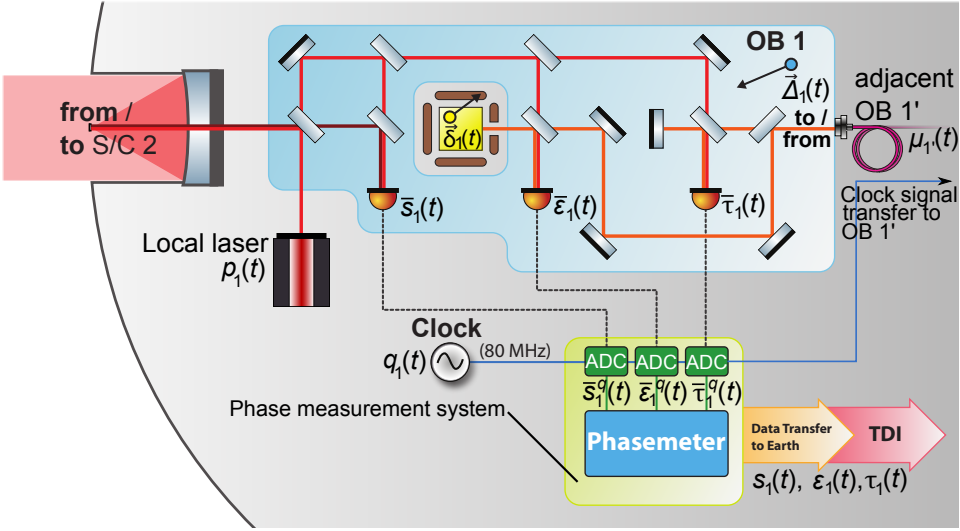
Figure 4.2: Digitisation process on the LISA OB 1. The onboard interferometric measurements for the science IFO ($\bar{s}_1(t)$), the TM IFO ($\bar{\varepsilon}_1(t)$) and reference IFO ($\bar{\tau}_1(t)$) are sampled by analog-to-digital converters giving phasemeter input data $\bar{s}_1^q(t)$, $\bar{\varepsilon}_1^q(t)$ and $\bar{\tau}_1^q(t)$. This sampling process introduces differential phase noise $q_1(t)$ from the internal clock signal at 80 MHz with respect to the pilot tone. The same signal is used for digitisation on the adjacent OB $1'$. After phasemeter operation, the outputs $s_1(t)$, $\varepsilon_1(t)$ and $\tau_1(t)$ are telemetered to Earth for the post-processing.

This equation holds for an idealised perfect measurement at the photodetector. After digitisation, the interferometric data is proceeded to the phase measurement system, the heart of which consists of a phasemeter in order to determine the detected phase changes. The recorded data is then transmitted to Earth via radio link sent to the Deep Space Network (an Earth-based antenna network), resampled on ground, pre-processed and used for TDI input, finally followed by data analysis. This is shown in Fig. 4.2.

The onboard sampling process introduces phase noise $q(t)$ that originates from the pilot tone jitter, and we get an additional term in the science IFO phase signal:

$$\bar{s}_1^q(t) = H_1 + p_{2';\mathbf{3}} - p_1 + \bar{a}_1 q_1 - \frac{2\pi}{\lambda_{2'}} \vec{n}_3 \cdot \vec{\Delta}_{2';\mathbf{3}} - \frac{2\pi}{\lambda_{2'}} \vec{n}_{3'} \cdot \vec{\Delta}_1 + N_1^{\mathrm{opt}} + N_1^s . \quad (4.1a)$$

Here, $\bar{a}_1 := \frac{f_{\mathrm{ADC},1}}{f_{\mathrm{PT},1}} \frac{|\Delta f_{\bar{s}_1}|}{f_{\mathrm{ADC},1}} = \frac{|\Delta f_{\bar{s}_1}|}{f_{\mathrm{PT},1}}$ is the conversion factor from phase noise $q_1(t)$ of the pilot tone, which is introduced via the digitisation process triggered by the ADC signal with frequency $f_{\mathrm{ADC},1}$, to phase noise at the signal frequency $|\Delta f_{\bar{s}_1}| = \frac{|\omega_{2'}' - \omega_1|}{2\pi}$. The absolute values are taken since the phasemeter interprets all beat-note frequencies as positive.

Again, as in Sec. 2.4.2, $\omega'_{2'}$ denotes the frequency of light transmitted from optical bench $2'$ and detected onboard S/C 1 including the Doppler shift due to constellation motion along the LoS of link 3. The superscript q in $\bar{s}^q_1(t)$ stands for the inclusion of the clock noise by the digitisation process, the bar reminds one that the frequency order determined by the phasemeter is still disregarded. Note that $\bar{s}_1(t)$ is the interferometric signal phase detected by the PD while $\bar{s}^q_1(t)$ denotes the phase of the digitised signal after the ADC, i.e., the phasemeter input (Fig. 4.2). The phasemeter outputs will be finally denoted without any 'q' and bar. They are transmitted via the Deep Space Network to Earth and are used there for pre-processing, post-processing and data analysis.

Analogously, we obtain for the phasemeter input of the test mass and reference interferometer readout

$$\bar{\varepsilon}^q_1(t) = p_{1'} - p_1 + \bar{b}_1 q_1 + 2 \left(\frac{2\pi}{\lambda_{1'}} \vec{n}_{3'} \cdot \vec{\delta}_1 - \frac{2\pi}{\lambda_{1'}} \vec{n}_{3'} \cdot \vec{\Delta}_1 \right) + \mu_{1'} + N^\varepsilon_1, \quad (4.1b)$$

$$\bar{\tau}^q_1(t) = p_{1'} - p_1 + \bar{b}_1 q_1 + \mu_{1'} + N^\tau_1, \quad (4.1c)$$

where $\bar{b}_1 = \frac{|\Delta f_{\bar{\varepsilon}_1}|}{f_{\text{PT},1}}$ with $|\Delta f_{\bar{\varepsilon}_1}| = \frac{|\omega_{1'} - \omega_1|}{2\pi} = |\Delta f_{\bar{\tau}_1}|$ is the conversion factor with respect to the beat-note frequency of the two local oscillators. Note that in $|\Delta f_{\bar{\varepsilon}_1}|$ no Doppler shift appears due to the local comparison of light on the same spacecraft. Furthermore, the equality $\Delta f_{\bar{\varepsilon}_1} = \Delta f_{\bar{\tau}_1}$ comes from the fact that in both reference and TM interferometer the same two lasers with the equal sign enter. Finally, Fig. 4.2 illustrates that the corresponding ADCs are triggered by the same clock signal (as for the science interferometer, too), hence the same clock noise q_1 is introduced in $\bar{\varepsilon}^q_1(t)$ and $\bar{\tau}^q_1(t)$.

Adjacent Optical Bench

As stated before, each spacecraft houses a single USO that produces a pilot tone used as a clock reference in all phase measurements onboard this S/C. Hence, the same clock signal also triggers the ADCs on the adjacent optical bench. This leads to the digitised phase signals

$$\bar{s}^q_{1'}(t) = H_{1'} + p_{3;\mathbf{2'}} - p_{1'} + \bar{a}_{1'} q_1 - \frac{2\pi}{\lambda_3} \vec{n}_{2'} \cdot \vec{\Delta}_{3;\mathbf{2'}} - \frac{2\pi}{\lambda_3} \vec{n}_2 \cdot \vec{\Delta}_{1'}$$
$$+ N^{\text{opt}}_{1'} + N^s_{1'}, \quad (4.1d)$$

$$\bar{\varepsilon}^q_{1'}(t) = p_1 - p_{1'} + \bar{b}_{1'} q_1 + 2 \left(\frac{2\pi}{\lambda_1} \vec{n}_2 \cdot \vec{\delta}_{1'} - \frac{2\pi}{\lambda_1} \vec{n}_2 \cdot \vec{\Delta}_{1'} \right) + \mu_1 + N^\varepsilon_{1'}, \quad (4.1e)$$

$$\bar{\tau}^q_{1'}(t) = p_1 - p_{1'} + \bar{b}_{1'} q_1 + \mu_1 + N^\tau_{1'}, \quad (4.1f)$$

where, in the same manner as above, $\bar{a}_{1'} = \frac{|\Delta f_{\bar{s}_{1'}}|}{f_{\text{PT},1}}$ with $|\Delta f_{\bar{s}_{1'}}| = \frac{|\omega'_3 - \omega_{1'}|}{2\pi}$ and $\bar{b}_{1'} = \frac{|\Delta f_{\bar{\varepsilon}_{1'}}|}{f_{\text{PT},1}}$ with $|\Delta f_{\bar{\varepsilon}_{1'}}| = \frac{|\omega_1 - \omega_{1'}|}{2\pi}$.

Eqn. (4.1a) – (4.1f) provide the digitised data streams used as phasemeter inputs per spacecraft. Hence, we have 18 data streams $(\bar{s}_i^q, \bar{\varepsilon}_i^q, \bar{\tau}_i^q)$. However, it is not possible to remove the clock noise from this data alone. This is due to the inappropriate time signature that all clocks enter non-delayed and not in a difference as for the laser frequency noise. As seen from Ch. 3, one distant and one local part of the noise is needed to construct noise-free data streams (cf. Eqn. (3.25a), (3.25b) and (3.38)). As for the laser frequency noise, this holds also true for clock noise. Concluding, we need additional (time-delayed) data from the distant S/C to successfully cancel clock noise.

4.1.3 Sideband Signals and Clock Tone Transfer Chain

As previously stated, there is insufficient data to remove the clock noise, q_i, from the phasemeter inputs $\bar{s}_i^q(t), \bar{\varepsilon}_i^q(t)$ and $\bar{\tau}_i^q(t)$. A clock tone transfer chain using SB modulations, as first proposed in detail in [FST$^+$04] and demonstrated later [BTS$^+$10], provides additional information to cancel clock noise. A sketch of the transfer chain for the link from OB 2′ to 1 is presented in Fig. 4.3.
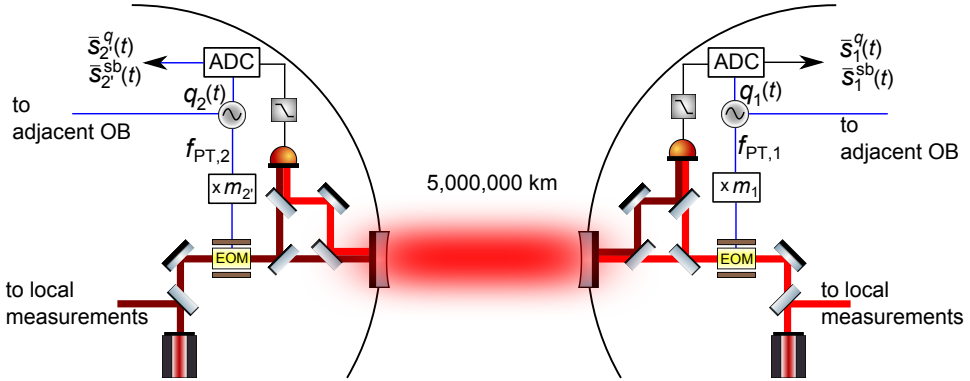
Figure 4.3: A sketch of the clock tone transfer chain. The outgoing laser light on OB 2′ (wine red) passes an electro-optic modulator, which imprints sidebands at a frequency of $f_{\mathrm{PT},2} \cdot m_{2'} = 2.4\,\mathrm{GHz}$ comprising local clock information. This signal is then transmitted over five million kilometre to the receiving S/C. Here, the beat-note with the local laser from OB 1 (red) is formed, which is again sideband-modulated with the local onboard clock ticking at $f_{\mathrm{PT},1}$, upmultiplied to $f_{\mathrm{PT},1} \cdot m_1$ and containing the pilot tone clock noise $q_1(t)$. The beat-note is detected by a photodetector, then low-passed and digitised with the same local clock signal. The phasemeter input is subsequently twofold: the carrier-to-carrier measurement $\bar{s}_1^q(t)$ and the SB measurement $\bar{s}_1^{\mathrm{sb}}(t)$.

The pilot tone phase noise of the distant OB 2′, q_2, is amplified by a large integer ($m_{2'} \approx 32$) and imprinted on the outgoing beam as phase modulation sidebands via an electro-optic-modulator. This is then transmitted to the receiving OB 1. There, the incoming light is interfered with the local laser light that itself is sideband-modulated (with the modulation index m_1) at a slightly different frequency and

therefore includes clock noise from S/C 1, q_1. The resulting sideband-sideband measurements $\bar{s}_1^{\text{sb}}(t)$ (and $\bar{s}_{1'}^{\text{sb}}(t)$ from the adjacent optical bench) are then given in terms of phase by

$$
\begin{aligned}
\bar{s}_1^{\text{sb}}(t) &= H_1 + p_{2';\mathbf{3}} - p_1 + m_{2'}q_{2;\mathbf{3}} - m_1 q_1 + \bar{c}_1 q_1 - \frac{2\pi}{\lambda_{2'}}\vec{n}_3 \cdot \vec{\Delta}_{2';\mathbf{3}} \\
&\quad - \frac{2\pi}{\lambda_{2'}}\vec{n}_{3'} \cdot \vec{\Delta}_1 + N_1^{\text{opt,sb}} + N_1^{\text{sb}},
\end{aligned} \tag{4.2a}
$$

$$
\begin{aligned}
\bar{s}_{1'}^{\text{sb}}(t) &= H_{1'} + p_{3;\mathbf{2'}} - p_{1'} + m_3 q_{3;\mathbf{2'}} - m_{1'}q_1 + \bar{c}_{1'}q_1 - \frac{2\pi}{\lambda_3}\vec{n}_{2'} \cdot \vec{\Delta}_{3;\mathbf{2'}} \\
&\quad - \frac{2\pi}{\lambda_3}\vec{n}_2 \cdot \vec{\Delta}_{1'} + N_{1'}^{\text{opt,sb}} + N_{1'}^{\text{sb}},
\end{aligned} \tag{4.2b}
$$

and cyclic.

In the above expressions, $\bar{c}_1 = \frac{|\Delta f_{\bar{s}_1}^{\text{sb}}|}{f_{\text{PT},1}} = \frac{|\omega_{2'}^{\text{sb}} - \omega_1^{\text{sb}}|}{2\pi f_{\text{PT},1}}$ and $\bar{c}_{1'} = \frac{|\Delta f_{\bar{s}_{1'}}^{\text{sb}}|}{f_{\text{PT},1}} = \frac{|\omega_3'^{\text{sb}} - \omega_{1'}^{\text{sb}}|}{2\pi f_{\text{PT},1}}$ are the conversion factors from the sampling process of the sideband beat-note. Note that $\bar{c}_i$ slightly differs from $\bar{a}_i$ due to the different absolute frequencies of the beat-notes. That is, in general according to Fig. 4.4, $|\Delta f_{\bar{s}_i}^{\text{sb}}| \neq |\Delta f_{\bar{s}_i}|$. Furthermore, since the sidebands have a frequency offset of 2.4 GHz and lower power compared to the carrier, they give rise to different optical path length noise and readout noise, subsumed in $N_1^{\text{opt,sb}}$ and N_1^{sb}, respectively.
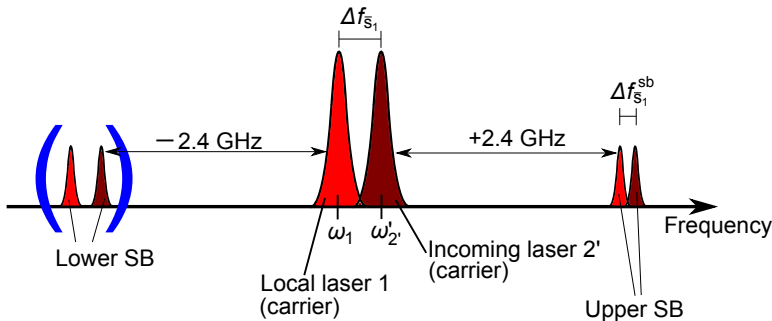
Figure 4.4: The frequency spectrum of the clock tone transfer chain for OB 1. Incoming (wine red) and local laser (red) are frequency-shifted relative to each other due to Doppler shifts (and offset frequency locking, Sec. 4.2). Two beat-notes are detected by the PD: carrier-to-carrier, $\Delta f_{\bar{s}_1}$, and sideband-to-sideband, $\Delta f_{\bar{s}_1}^{\text{sb}}$. Both beat-notes lie in the range of $7 \ldots 23$ MHz. Since lower and upper sideband, separated by ± 2.4 GHz from the carrier, basically contain the same information (i.e., the clock signal), we can disregard the lower SB (emphasised by blue brackets).

The SB signals given in Eqn. (4.2a) and (4.2b) basically contain the same information as $\bar{s}_1^q(t)$ and $\bar{s}_{1'}^q(t)$, but with the pilot tone clock noise amplified by the integer factors m_i. In practice, two SB-SB-measurements are performed (upper and lower sideband, Fig. 4.4) to increase the signal-to-noise ratio. However, both

contain redundant information. For the rest of this thesis, we will only consider one SB-SB-measurement.

4.2 Beat-Note Frequency Polarity and Frequency Plan

This section discusses further impacts on the phase signals given in Sec. 4.1. They result from technical issues and have been neglected previously. In particular, these are the beat-note detection problem and the frequency polarity. The goal of this section is the reformulation of the telemetered phasemeter data including these effects.

4.2.1 Frequency Plan

Up to now, we have disregarded an important practical issue. The technically detectable beat-notes lie in the range of $7 \ldots 23 \, \mathrm{MHz}$. The lower bound comes from the relative intensity noise dominating the readout process below $5 \, \mathrm{MHz}$, and above the upper bound, technical noise from the digitisation process becomes dominant. Optical beat-notes of lasers with constant and slighty different frequencies (e.g., from adjacent optical benches) will not be a problem to detect [Bar15]. However, the satellite constellation is flexing and this in turn introduces relative Doppler shifts of $\pm 15 \, \mathrm{MHz}$ (Sec. 2.2.1) along the LoS in each link between sending and receiving spacecraft. This effect can shift the signal frequency of the science interferometer out of the detection band in which case signal loss will occur.

In order to prevent such signal loss, a laser locking scheme is needed to arrange the frequencies of each laser independently such that each single interferometric measurement in science/sideband, reference and test mass interferometer is in-band. Note that this condition must be true for *all* IFO and sideband beat-notes. Hence, we have to deal with a complex optimisation problem where the orbit information gives the relative Doppler shift within the arms.

The solution for this issue is called frequency plan and basically comprises a list containing offset frequencies for all lasers. Depending on the shrinking or growing of the constellation, the introduced Doppler shift could be positive or negative. Hence, the offset frequencies could be as well positive or negative. Exemplarily, beat-notes of the six science and three TM/reference interferometers are shown for a duration of three years in Fig. 4.5. We have dropped the bar notation for the signal beat-notes, since Doppler effects and offset frequencies are now included.

The frequencies are optimised with respect to the duration of each chunk (in minimum one week) using a genetic algorithm [Bar15]. The tolerable frequency band is chosen here from $7 \, \mathrm{MHz}$ to $23 \, \mathrm{MHz}$. Since beat-note frequencies are indistinguishable and equally detectable in the photodetector and phasemeter, the band from $-23 \, \mathrm{MHz}$ to $-7 \, \mathrm{MHz}$ is included. If a beat-note is in danger to run out of the detection band, the laser frequencies are reprogrammed, which is indicated by the vertical black lines.
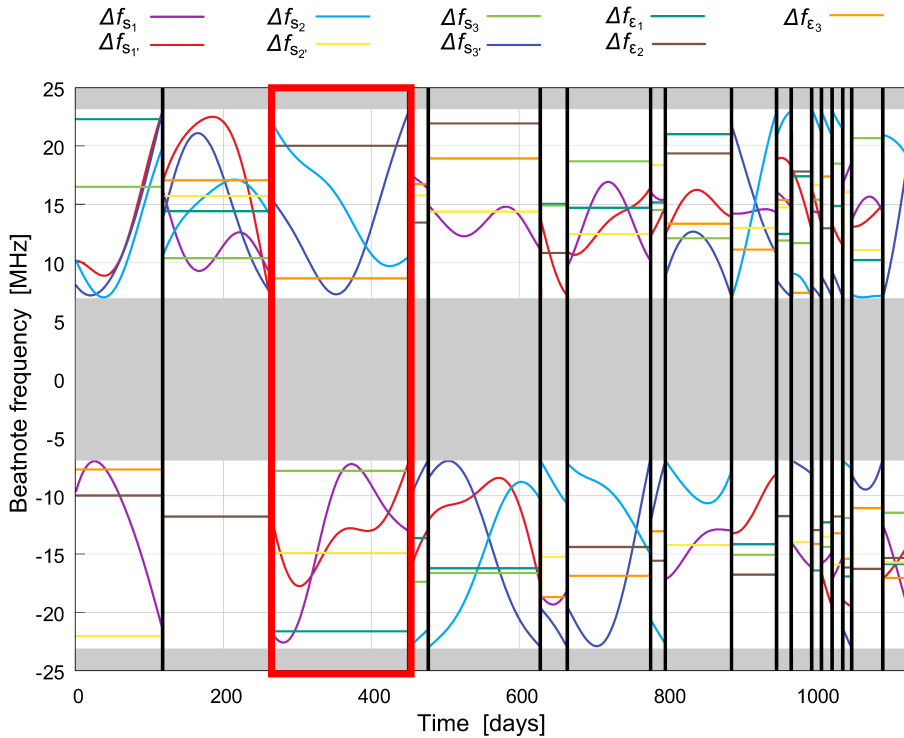
Figure 4.5: Beat-note frequencies Δf_{s_i} (science IFO) and Δf_{ε_i} (TM/reference IFO) for the LISA constellation for three years. The offset frequencies of the lasers are chosen such that the period without frequency tuning (the latter is indicated by the black vertical lines) is as long as possible. Grey areas indicate forbidden beat-note frequencies. Here, the laser on OB $1'$ is chosen to be the master laser, and it was used locking scheme A from [Bar15]. The polarity of the beat-note frequencies within the red box is exemplarily discussed in Sec. 4.2.2.

Concluding, we have to regard the frequency of each beat-note carefully since they vary over time, and we need to define a correct way of comparing the phases within the phasemeter. This will be discussed in the following. More details on the locking schemes and the frequency plan can be found in [Bar15].

4.2.2 Beat-Note Frequency Polarity

As we have seen in the previous section, the lasers are not running at the same central frequency but have different relative offsets which are also introduced in the onboard heterodyne beat-notes $\Delta f_{s_i}, \Delta f_{s_i}^{\mathrm{sb}}, \Delta f_{\varepsilon_i}$ and Δf_{τ_i}. However, the phasemeter, while reading out the phases of each input signal $\bar{s}_i^q(t)$, interprets all beat-note frequencies as positive, even though they might originate from a negative frequency difference implying the opposite sign of length-related phase shifts (Sec. 2.4.2 and Fig. 4.5). Hence, in each data stream it has to be checked if the heterodyne frequency

determined by the phasemeter is positive or negative. In the negative case, the input has to be inverted, and this effect needs to be included in the data streams.

We therefore introduce the total frequencies, $\omega_{j \to i}^{\text{tot}}$, for laser light sent from OB j and detected onboard the receiving optical bench i, where it is interfered with light of the local laser. The frequency of the local laser is denoted by ω_i^{tot}. $\omega_{j \to i}^{\text{tot}}$ includes offset frequencies and Doppler shifts, while the light from the local laser with frequency ω_i^{tot} does not suffer any Doppler shift, since it is not transferred along the link, and only accounts for the offset frequency lock. In this notation, we find

$$\Delta f_{s_1} = \frac{\omega_{2' \to 1}^{\text{tot}} - \omega_1^{\text{tot}}}{2\pi} , \qquad \Delta f_{s_{1'}} = \frac{\omega_{3 \to 1'}^{\text{tot}} - \omega_{1'}^{\text{tot}}}{2\pi} , \qquad (4.3a)$$

$$\Delta f_{\varepsilon_1} = \frac{\omega_{1'}^{\text{tot}} - \omega_1^{\text{tot}}}{2\pi} , \qquad \Delta f_{\varepsilon_{1'}} = \frac{\omega_1^{\text{tot}} - \omega_{1'}^{\text{tot}}}{2\pi} = -\Delta f_{\varepsilon_1} , \qquad (4.3b)$$

where $\Delta f_{\varepsilon_i} = \Delta f_{\tau_i}$ and $\Delta f_{\varepsilon_{\underline{i}}} = -\Delta f_{\varepsilon_{\underline{i}'}}$.

In order to account for the frequency polarity in the following, the factor

$$\theta_i^j = \begin{cases} +1 & \text{if } \omega_{j \to i}^{\text{tot}} - \omega_i^{\text{tot}} > 0 \\ -1 & \text{if } \omega_{j \to i}^{\text{tot}} - \omega_i^{\text{tot}} < 0 \end{cases} , \quad (\theta_i^j)^2 = 1 , \quad \theta_{\underline{i}}^{i'} = -\theta_{\underline{i}'}^i \qquad (4.4)$$

is introduced to keep track of the polarity of the PM input, valid for one segment of the frequency plan, which typically lasts several days to weeks. The upper case index of θ marks the incoming laser, while the lower case index labels the local laser. If, for example, $\Delta f_{s_1} = \omega_{2' \to 1}^{\text{tot}} - \omega_1^{\text{tot}} < 0$, then the beat-note of $\bar{s}_1^q(t)$, defined by Eq. (2.17), is inverted by the PM. This in turn has to be compensated by inverting the phase vice versa by the prefactor $\theta_1^{2'} = -1$. Noise that contributes like readout noise or ADC sampling jitter after the optical beat-note detection needs not to be inverted by the factor θ_i^j. Tab. 4.1 displays the values of θ_i^j for the beat-note frequencies given in Fig. 4.5 using the section between days 260 and 440, marked by the red box.

	$i = 1$	$i = 1'$	$i = 2$	$i = 2'$	$i = 3$	$i = 3'$
$j = 1$	–	+1	–	−1	–	–
$j = 1'$	−1	–	–	–	−1	–
$j = 2$	–	–	–	−1	–	−1
$j = 2'$	−1	–	+1	–	–	–
$j = 3$	–	−1	–	–	–	−1
$j = 3'$	–	–	+1	–	+1	–

Table 4.1: Values of the beat-note frequency polarity factor θ_i^j, exemplarily shown for the chunk from day 260 to 440 of Fig. 4.5. As an example, the factor for the science interferometer beat-note on OB 2 gives $\theta_{i=2}^{j=3'} = +1$, since the beat-note of Δf_{s_2} is positive in that chunk.

4.2.3 The Telemetered Phasemeter Output Signals

The previously discussed beat-note polarities of course have an impact on the onboard data streams. We take it into account by the factor θ_i^j from Eq. (4.4) and get the following system of equations:

$$s_1^{\mathrm{c}}(t) = \theta_1^{2'}\left[H_1 + p_{2';\mathbf{3}} - p_1 - \frac{2\pi}{\lambda_{2'}}\vec{n}_3 \cdot \vec{\Delta}_{2';\mathbf{3}} - \frac{2\pi}{\lambda_{2'}}\vec{n}_{3'} \cdot \vec{\Delta}_1 + N_1^{\mathrm{opt}} \right]$$
$$+ a_1 q_1 + N_1^s \,, \tag{4.5a}$$

$$s_1^{\mathrm{sb}}(t) = \theta_1^{2'}\left[H_1 + p_{2';\mathbf{3}} - p_1 + m_{2'} q_{2;\mathbf{3}} - m_1 q_1 - \frac{2\pi}{\lambda_{2'}}\vec{n}_3 \cdot \vec{\Delta}_{2';\mathbf{3}} \right.$$
$$\left. - \frac{2\pi}{\lambda_{2'}}\vec{n}_{3'} \cdot \vec{\Delta}_1 + N_1^{\mathrm{opt,sb}} \right] + c_1 q_1 + N_1^{\mathrm{sb}} \,, \tag{4.5b}$$

$$\varepsilon_1(t) = \theta_1^{1'}\left[p_{1'} - p_1 + 2\left(\frac{2\pi}{\lambda_{1'}}\vec{n}_{3'} \cdot \vec{\delta}_1 - \frac{2\pi}{\lambda_{1'}}\vec{n}_{3'} \cdot \vec{\Delta}_1 \right) + \mu_{1'} \right]$$
$$+ b_1 q_1 + N_1^\varepsilon \,, \tag{4.5c}$$

$$\tau_1(t) = \theta_1^{1'}[p_{1'} - p_1 + \mu_{1'}] + b_1 q_1 + N_1^\tau \,, \tag{4.5d}$$

and others cyclic. Now the bar notation as well as the superscript q-notation is dropped, since all relevant issues for the phasemeter outputs are included. In particular, we add the superscript 'c' in order to emphasise the carrier-carrier science measurement. Note that the polarity factor θ_i^j only influences all optical noise contributions, but not shot noise and digitisation clock noise.

Similar equations can be found for the adjacent optical bench:

$$s_{1'}^{\mathrm{c}}(t) = \theta_{1'}^{3}\left[H_{1'} + p_{3;\mathbf{2'}} - p_{1'} - \frac{2\pi}{\lambda_3}\vec{n}_{2'} \cdot \vec{\Delta}_{3;\mathbf{2'}} - \frac{2\pi}{\lambda_3}\vec{n}_2 \cdot \vec{\Delta}_{1'} + N_{1'}^{\mathrm{opt}} \right]$$
$$+ a_{1'} q_1 + N_{1'}^s \,, \tag{4.5e}$$

$$s_{1'}^{\mathrm{sb}}(t) = \theta_{1'}^{3}\left[H_{1'} + p_{3;\mathbf{2'}} - p_{1'} + m_3 q_{3;\mathbf{2'}} - m_{1'} q_1 - \frac{2\pi}{\lambda_3}\vec{n}_{2'} \cdot \vec{\Delta}_{3;\mathbf{2'}} \right.$$
$$\left. - \frac{2\pi}{\lambda_3}\vec{n}_2 \cdot \vec{\Delta}_{1'} + N_{1'}^{\mathrm{opt,sb}} \right] + c_{1'} q_1 + N_{1'}^{\mathrm{sb}} \,. \tag{4.5f}$$

$$\varepsilon_{1'}(t) = \theta_{1'}^{1}\left[p_1 - p_{1'} + 2\left(\frac{2\pi}{\lambda_1}\vec{n}_2 \cdot \vec{\delta}_{1'} - \frac{2\pi}{\lambda_1}\vec{n}_2 \cdot \vec{\Delta}_{1'} \right) + \mu_1 \right]$$
$$+ b_{1'} q_1 + N_{1'}^\varepsilon \,, \tag{4.5g}$$

$$\tau_{1'}(t) = \theta_{1'}^{1}[p_1 - p_{1'} + \mu_1] + b_{1'} q_1 + N_{1'}^\tau \,, \tag{4.5h}$$

The corresponding translation factors are finally

$$a_1 = \frac{|\Delta f_{s_1}|}{f_{\mathrm{PT},1}} = \frac{|\omega_{2'\to 1}^{\mathrm{tot}} - \omega_1^{\mathrm{tot}}|}{2\pi f_{\mathrm{PT},1}}, \qquad a_{1'} = \frac{|\Delta f_{s_{1'}}|}{f_{\mathrm{PT},1}} = \frac{|\omega_{3\to 1'}^{\mathrm{tot}} - \omega_{1'}^{\mathrm{tot}}|}{2\pi f_{\mathrm{PT},1}}, \qquad (4.6a)$$

$$b_1 = \frac{|\Delta f_{\varepsilon_1}|}{f_{\mathrm{PT},1}} = \frac{|\omega_{1'}^{\mathrm{tot}} - \omega_1^{\mathrm{tot}}|}{2\pi f_{\mathrm{PT},1}}, \qquad b_{1'} = \frac{|\Delta f_{\varepsilon_{1'}}|}{f_{\mathrm{PT},1}} = \frac{|\omega_1^{\mathrm{tot}} - \omega_{1'}^{\mathrm{tot}}|}{2\pi f_{\mathrm{PT},1}}, \qquad (4.6b)$$

$$c_1 = \frac{|\Delta f_{s_1}^{\mathrm{sb}}|}{f_{\mathrm{PT},1}} = \frac{|\omega_{2'\to 1}^{\mathrm{sb,tot}} - \omega_1^{\mathrm{sb,tot}}|}{2\pi f_{\mathrm{PT},1}}, \qquad c_{1'} = \frac{|\Delta f_{s_{1'}}^{\mathrm{sb}}|}{f_{\mathrm{PT},1}} = \frac{|\omega_{3\to 1'}^{\mathrm{sb,tot}} - \omega_{1'}^{\mathrm{sb,tot}}|}{2\pi f_{\mathrm{PT},1}}, \qquad (4.6c)$$

and all others cyclic.

One could regard the above signal equations (4.5a) – (4.5h) together with (4.6a) – (4.6c) as the 'real' phasemeter outputs telemetered to Earth according to Fig. 4.2. The main goal is now to use these data streams and combine and time-shift them properly in order to suppress the critical primary noise sources provided by the given system of equations. These are laser phase noise, p_i, clock noise, $q_{\underline{i}}$, optical bench displacement noise, $\vec{\Delta}_i$, and fibre noise, μ_i.

4.3 Full Removal Algorithm

An algorithm combining laser phase noise and USO noise cancellation was first proposed by [Hel01], further modified and extended to optical bench displacement jitter removal by [TEA02]. However, the papers were based on an old OB layout where the incoming light bounces first off the TM and is then beaten against the local laser. Moreover, issues like the phasemeter beat-note polarity or the ADC digitisation noise were neglected. Thus, it is necessary to review the developed algorithms. We will now derive the full removal algorithm for the state-of-the-art OB layout of LISA, using the split interferometry configuration, as it was introduced in Ch. 2. Furthermore, we will regard a worst-case scenario of six free-running lasers (in contrast to the relaxed case of locked lasers, Sec. 4.2), which are also used in the simulation explained in Ch. 5.

4.3.1 Overview

Eqn. (4.5a) – (4.5h) describe the phasemeter outputs from S/C 1 sent to Earth. They are assumed to be perfectly synchronised with respect to a constellation time, denoted by t, which can be assured by the use of Kalman filters in a pre-processing step (Ch. 5). Thus, we are left with $3 \times 8 = 24$ data streams each containing phase shifts due to gravitational waves, laser phase noise, optical bench displacement noise, clock noise, fibre noise and secondary noise (mainly readout noise).

The goal is now to remove all primary noise sources in post-processing. An intermediate goal is to construct a data combination in the form of Eqn. (3.38), i.e.,

$$\eta_1(t) \sim H_1 + p_{2;\mathbf{3}} - p_1 + \frac{\mu_{2;\mathbf{3}} - \mu_{2';\mathbf{3}}}{2}, \quad \eta_{1'}(t) \sim H_{1'} + p_{3;\mathbf{2}'} - p_1 - \frac{\mu_1 - \mu_{1'}}{2}, \quad (4.7)$$

others cyclic. It was shown in Ch. 3 that this is an appropriate TDI input for successful laser phase noise removal and simultaneous GW perservation. Additionally, we have to take care that the noise $\mu_{\underline{i}}$ introduced by the 'back-link' fibre phase delay only appears as a difference to its counterpart, $\mu_{\underline{i}'}$. In the case that the fibre can be assumed to be reciprocal, these terms will cancel [FST$^+$09]. The intermediate data combinations (4.7) can finally be used as input forming the TDI combinations. It is therefore obviously necessary to remove optical bench displacement noise $\vec{\Delta}_i$ and clock noise $q_{\underline{i}}$ in a previous step.

The procedure is as follows. First, we will combine the test mass IFO data streams together with the corresponding reference IFO output to remove the optical bench displacement from the science signal. The optical bench displacement noise free combinations will be denoted by $\xi_i(t)$. Second, we will reduce the contributing laser phase noise instances to three (from the unprimed optical benches), as in Sec. 3.2.1. Therefore, we use the reference IFO outputs and define data streams $Q_i(t)$ with three (unprimed) lasers only, including laser, clock and fibre noise. Third, we define one USO as master clock and use the sideband signals for the removal of clock noise relative to the master clock. These clock noise free data combinations $\eta_i(t)$ are exactly of the form (4.7) and finally taken as input for TDI which suppresses the laser phase noise for GW extraction.

4.3.2 Optical Bench Displacement Noise Suppression

First, the OB motion is removed from the carrier science signal $s_i^c(t)$. The presented algorithm is different to the literature in that it does not assume perfectly locked lasers with the same wavelength. In that idealised case, one could build an intermediate combination $\sim \mathcal{D}p - p + \mathcal{D}\Delta - \Delta + H$ with projections Δ of the vectorial optical bench displacement $\vec{\Delta}$ onto the detector arm unit vector $\vec{n}$. For the sake of simplicity, we have omitted here the indices and prefactors. Due to the signature $\mathcal{D}\Delta - \Delta$ (same as for the lasers), forming the TDI equations with this intermediate combination would remove the optical bench displacements naturally. However, we will here remove the displacement noise $\vec{\Delta}$ for the general and more realistic case of six lasers with different frequencies and wavelengths including the beat-note frequency polarity issue.

The combination of reference and TM interferometer data on the same optical bench gives, e.g., for OB 1 with help of Eqn. (4.5c) and (4.5d):

$$
\begin{aligned}
\varepsilon_1(t) - \tau_1(t) &= \theta_1^{1'}\left[p_{1'} - p_1 + 2\left(\frac{2\pi}{\lambda_{1'}}\vec{n}_{3'} \cdot \vec{\delta}_1 - \frac{2\pi}{\lambda_{1'}}\vec{n}_{3'} \cdot \vec{\Delta}_1 \right) + \mu_{1'} \right] \\
&\quad + b_1 q_1 + N_1^\varepsilon - \theta_1^{1'}[p_{1'} - p_1 + \mu_{1'}] - b_1 q_1 - N_1^\tau \\
&= 2\theta_1^{1'}\left(\frac{2\pi}{\lambda_{1'}}\vec{n}_{3'} \cdot \vec{\delta}_1 - \frac{2\pi}{\lambda_{1'}}\vec{n}_{3'} \cdot \vec{\Delta}_1 \right) + N_1^\varepsilon - N_1^\tau .
\end{aligned}
$$

That is, the optical bench displacement can be extracted and removed by comparing the test mass IFO output with the reference IFO:

$$\varepsilon_1(t) - \tau_1(t) \sim -2\theta_1^{1'} \frac{2\pi}{\lambda_{1'}} \vec{n}_{3'} \cdot \vec{\Delta}_1 \,, \tag{4.8}$$

neglecting all secondary noise sources, emphasised by $\sim$. One can see that, due to redundant information in TM and reference IFO, the combination $\varepsilon_1(t) - \tau_1(t)$ is free of clock and laser phase noise, as well as fibre noise. The only primary noise left in $\varepsilon_1(t) - \tau_1(t)$ is the optical bench displacement of OB 1.

However, we could not simply take (4.8) and subtract it from $s_1^{\mathrm{c}}(t)$ given by Eq. (4.5a) to cancel the instantaneous displacement term $-\theta_1^{2'} \frac{2\pi}{\lambda_{2'}} \vec{n}_{3'} \cdot \vec{\Delta}_1$. Before, we need to adjust the prefactor properly. First, the factor of two in (4.8) can be removed by division by two, i.e., by forming $\frac{\varepsilon_1(t) - \tau_1(t)}{2}$. Second, we can use $(\theta_i^j)^2 = 1$ from Eq. (4.4) to eliminate the polarity factor $\theta_1^{1'}$ in (4.8) by forming $\theta_1^{1'} \frac{\varepsilon_1(t) - \tau_1(t)}{2}$. Third, the sensing wavelength needs to be transformed by multiplication with $\frac{\lambda_{1'}}{\lambda_{2'}}$. Forth and finally, we multiply the result with the frequency plan factor $\theta_1^{2'}$ and end up with

$$
\theta_1^{2'} \theta_1^{1'} \frac{\lambda_{1'}}{\lambda_{2'}} \frac{\varepsilon_1(t) - \tau_1(t)}{2} \stackrel{(4.8)}{\sim} \theta_1^{2'} \theta_1^{1'} \frac{\lambda_{1'}}{\lambda_{2'}} \left(\frac{-2\theta_1^{1'} \frac{2\pi}{\lambda_{1'}} \vec{n}_{3'} \cdot \vec{\Delta}_1}{2} \right)
$$
$$
= -\theta_1^{2'} (\theta_1^{1'})^2 \frac{\lambda_{1'}}{\lambda_{2'}} \frac{2\pi}{\lambda_{1'}} \vec{n}_{3'} \cdot \vec{\Delta}_1 \stackrel{(4.4)}{=} -\theta_1^{2'} \frac{2\pi}{\lambda_{2'}} \vec{n}_{3'} \cdot \vec{\Delta}_1 \,.
$$

This can then be used to remove the instantaneous displacement noise on the local OB from $s_1^{\mathrm{c}}(t)$ as follows:

$$
s_1^{\mathrm{c}}(t) - \theta_1^{2'} \theta_1^{1'} \frac{\lambda_{1'}}{\lambda_{2'}} \frac{\varepsilon_1(t) - \tau_1(t)}{2}
$$
$$
\stackrel{(4.5a)}{\sim} \theta_1^{2'} \left[H_1 + p_{2';\mathbf{3}} - p_1 - \frac{2\pi}{\lambda_{2'}} \vec{n}_3 \cdot \vec{\Delta}_{2';\mathbf{3}} - \frac{2\pi}{\lambda_{2'}} \vec{n}_{3'} \cdot \vec{\Delta}_1 \right] + a_1 q_1
$$
$$
- \left(-\theta_1^{2'} \frac{2\pi}{\lambda_{2'}} \vec{n}_{3'} \cdot \vec{\Delta}_1 \right)
$$
$$
= \theta_1^{2'} \left[H_1 + p_{2';\mathbf{3}} - p_1 - \frac{2\pi}{\lambda_{2'}} \vec{n}_3 \cdot \vec{\Delta}_{2';\mathbf{3}} \right] + a_1 q_1 \,.
$$

Note that in the procedure discussed previously and in the following, the wavelengths λ_i and the beat-note polarity factors θ_i^j are known from commissioning. Hence, we insert no 'extra' information and the data combinations rely on accessible data only.

In a similar manner, it is possible to remove the delayed optical bench displacement term from the sending spacecraft in $s_1^{\mathrm{c}}(t)$, $-\theta_1^{2'} \frac{2\pi}{\lambda_{2'}} \vec{n}_3 \cdot \vec{\Delta}_{2';\mathbf{3}}$. Consider therefore the

combination

$$
\begin{aligned}
\varepsilon_{2'}(t) - \tau_{2'}(t) &= 2\theta_{2'}^2 \left(\frac{2\pi}{\lambda_2} \vec{n}_3 \cdot \vec{\delta}_{2'} - \frac{2\pi}{\lambda_2} \vec{n}_3 \cdot \vec{\Delta}_{2'} \right) + N_{2'}^\varepsilon - N_{2'}^\tau \\
&\sim -2\theta_{2'}^2 \frac{2\pi}{\lambda_2} \vec{n}_3 \cdot \vec{\Delta}_{2'} \, .
\end{aligned}
\tag{4.9}
$$

The only principle difference to the derivation above is that one has to delay the difference $\varepsilon_{2'}(t) - \tau_{2'}(t)$ properly by $L_3(t)$, since $\vec{n}_3$ can taken as constant in time, as stated in Eq. (2.22). The rest is similar: Divide by 2, multiply with $\theta_{2'}^2$, $\frac{\lambda_2}{\lambda_{2'}}$ and $\theta_1^{2'}$. Hence,

$$
\begin{aligned}
s_1^{\text{c}}(t) &- \theta_1^{2'} \theta_{2'}^2 \frac{\lambda_2}{\lambda_{2'}} \frac{\varepsilon_{2';\mathbf{3}}(t) - \tau_{2';\mathbf{3}}(t)}{2} \\
&\sim \theta_1^{2'} \left[H_1 + p_{2';\mathbf{3}} - p_1 - \frac{2\pi}{\lambda_{2'}} \vec{n}_{3'} \cdot \vec{\Delta}_1 \right] + a_1 q_1
\end{aligned}
$$

is free of delayed displacement noise from the distant spacecraft. Putting all together,

$$
\begin{aligned}
\xi_1(t) &\equiv s_1^{\text{c}}(t) - \theta_1^{2'} \theta_1^{1'} \frac{\lambda_{1'}}{\lambda_{2'}} \frac{\varepsilon_1(t) - \tau_1(t)}{2} - \theta_1^{2'} \theta_{2'}^2 \frac{\lambda_2}{\lambda_{2'}} \frac{\varepsilon_{2';\mathbf{3}}(t) - \tau_{2';\mathbf{3}}(t)}{2} \\
&\sim \theta_1^{2'} (H_1 + p_{2';\mathbf{3}} - p_1) + a_1 q_1 \, , \tag{4.10a} \\
\xi_{1'}(t) &\equiv s_{1'}^{\text{c}}(t) - \theta_{1'}^3 \theta_{1'}^1 \frac{\lambda_1}{\lambda_3} \frac{\varepsilon_1(t) - \tau_{1'}(t)}{2} - \theta_{1'}^3 \theta_3^{3'} \frac{\lambda_{3'}}{\lambda_3} \frac{\varepsilon_{3;\mathbf{2'}}(t) - \tau_{3;\mathbf{2'}}(t)}{2} \\
&\sim \theta_{1'}^3 (H_{1'} + p_{3;\mathbf{2'}} - p_{1'}) + a_{1'} q_1 \tag{4.10b}
\end{aligned}
$$

synthesise displacement noise free data streams. Note that these combinations in some sense form the TM-to-TM measurements, as discussed for the split interferometry configuration in Ch. 2 and depicted in Fig. 2.11. $\xi_1(t)$ virtually constructs the TM-to-TM measurement between S/C 2 and S/C 1. It is combined from the distant TM-to-OB measurement (synthesised here by $-\theta_1^{2'} \theta_{2'}^2 \frac{\lambda_2}{\lambda_{2'}} \frac{\varepsilon_{2';\mathbf{3}}(t) - \tau_{2';\mathbf{3}}(t)}{2}$) plus the OB-to-OB measurement (which corresponds to $s_1^{\text{c}}(t)$) plus the local OB-to-TM measurement (constructed via $-\theta_1^{2'} \theta_1^{1'} \frac{\lambda_{1'}}{\lambda_{2'}} \frac{\varepsilon_1(t) - \tau_1(t)}{2}$).

4.3.3 Reduction to Three Free-Running Laser Instances

The next step on the way to an intermediate data stream as targeted in Eq. (4.7) is to remove contributions of lasers housed on primed OBs from (4.10a) and (4.10b). This can be achieved with help of the reference interferometer outputs of two adjacent optical benches, $\tau_{\underline{i}}(t)$ and $\tau_{\underline{i}'}(t)$, where the two local lasers are compared. This is basically in analogy to Sec. 3.2.1 for the TDI combinations derivation sketch (compare with the elimination with local measurements). However, the payoff is now that we have to deal with another primary noise source: phase noise due to the 'back-link' fibre.

In order to remove the primed laser phase noise term exemplarily in $\xi_{1'}(t)$, i.e., $-\theta_{1'}^3 p_{1'}$, one obvious ansatz might be

$$
\begin{aligned}
\tau_{1'}(t) - \tau_1(t) \quad &\sim \quad (\theta_{1'}^1 [p_1 - p_{1'} + \mu_1] + b_{1'} q_1) - (\theta_1^{1'} [p_{1'} - p_1 + \mu_{1'}] + b_1 q_1) \\
&\overset{(4.4)}{=} \quad \theta_{1'}^1 (p_1 - p_{1'} + p_{1'} - p_1) + (b_{1'} - b_1) q_1 + \theta_{1'}^1 (\mu_1 + \mu_{1'}) \\
&= \quad (b_{1'} - b_1) q_1 + \theta_{1'}^1 (\mu_1 + \mu_{1'}) \, ,
\end{aligned}
$$

where we used the antisymmetry $\theta_i^{i'} = -\theta_{i'}^i$. However, the laser phase noise totally cancels here and thus $\tau_{1'}(t) - \tau_1(t)$ can not be used to eliminate laser phase noise contributions with primed indices from (4.10b). Moreover, the fibre noise does not appear as a difference with its counterpart as required for the TDI input (4.7). In order to fix the naive ansatz, we adjust the prefactors properly:

$$
\begin{aligned}
\theta_{1'}^1 \tau_{1'}(t) - \theta_1^{1'} \tau_1(t) \quad &\sim \quad (\theta_{1'}^1)^2 [p_1 - p_{1'} + \mu_1] + \theta_{1'}^1 b_{1'} q_1 - (\theta_1^{1'})^2 [p_{1'} - p_1 + \mu_{1'}] \\
&\qquad - \theta_1^{1'} b_1 q_1 \\
&\overset{(4.4)}{=} \quad p_1 - p_{1'} + \mu_1 + \theta_{1'}^1 b_{1'} q_1 - p_{1'} + p_1 - \mu_{1'} - \theta_1^{1'} b_1 q_1 \\
&\overset{(4.4)}{=} \quad 2 p_1 - 2 p_{1'} + \theta_{1'}^1 (b_{1'} + b_1) q_1 + \mu_1 - \mu_{1'} \, ,
\end{aligned}
$$

where again $(\theta_i^j)^2 = 1$ and $\theta_1^{1'} = -\theta_{1'}^1$ applied. As a useful intermediate step, we define

$$
\kappa_1(t) \equiv \frac{\theta_{1'}^1 \tau_{1'}(t) - \theta_1^{1'} \tau_1(t)}{2} \sim p_1 - p_{1'} + \frac{\theta_{1'}^1 (b_{1'} + b_1)}{2} q_1 + \frac{\mu_1 - \mu_{1'}}{2} \, , \quad (4.11)
$$

others cyclic, which will now be of use for the reduction to three free-running lasers. That is, we form $\theta_{1'}^3 \xi_{1'}(t)$ with a proper prefactor $\theta_{1'}^3$, in order to free the laser terms in Eq. (4.10b) from the phasemeter polarity factor and then subtract $\kappa_1(t)$ from it. This construction will remove $p_{1'}$:

$$
\begin{aligned}
\theta_{1'}^3 \xi_{1'}(t) - \kappa_1(t) \quad &\overset{(4.11)}{\sim} \quad (\theta_{1'}^3)^2 (H_{1'} + p_{3;2'} - p_{1'}) + \theta_{1'}^3 a_{1'} q_1 - p_1 + p_{1'} \\
&\qquad - \frac{\theta_{1'}^1 (b_{1'} + b_1)}{2} q_1 - \frac{\mu_1 - \mu_{1'}}{2} \\
&= \quad H_{1'} + p_{3;2'} - p_1 + \theta_{1'}^3 a_{1'} q_1 - \frac{\theta_{1'}^1 (b_{1'} + b_1)}{2} q_1 - \frac{\mu_1 - \mu_{1'}}{2} \, .
\end{aligned}
$$

In a similar manner, the delayed primed laser from Eq. (4.10a), $\theta_1^{2'} p_{2';\mathbf{3}}$, could be removed. Therefore, we take a properly delayed version of $\kappa_2(t)$, i.e.,

$$
\begin{aligned}
\kappa_{2;\mathbf{3}}(t) \quad &\overset{(4.11)}{\sim} \quad \left(p_2 - p_{2'} + \frac{\theta_{2'}^2 (b_{2'} + b_2)}{2} q_2 + \frac{\mu_2 - \mu_{2'}}{2} \right)_{;\mathbf{3}} \\
&= \quad p_{2;\mathbf{3}} - p_{2';\mathbf{3}} + \frac{\theta_{2'}^2 (b_{2'} + b_2)}{2} q_{2;\mathbf{3}} + \frac{\mu_{2;\mathbf{3}} - \mu_{2';\mathbf{3}}}{2} \, .
\end{aligned}
$$

Adding this to $\theta_1^{2'}\xi_1(t)$ will substitute $p_{2';\mathbf{3}}$ by $p_{2;\mathbf{3}}$:

$$\theta_1^{2'}\xi_1(t) + \kappa_{2;\mathbf{3}}(t) \overset{(4.10a)}{\sim} (\theta_1^{2'})^2(H_1 + p_{2';\mathbf{3}} - p_1) + \theta_1^{2'}a_1q_1 + p_{2;\mathbf{3}} - p_{2';\mathbf{3}}$$
$$+ \frac{\theta_{2'}^2(b_{2'} + b_2)}{2}q_{2;\mathbf{3}} + \frac{\mu_{2;\mathbf{3}} - \mu_{2';\mathbf{3}}}{2}$$
$$= H_1 + p_{2;\mathbf{3}} - p_1 + \theta_1^{2'}a_1q_1 + \frac{\theta_{2'}^2(b_{2'} + b_2)}{2}q_{2;\mathbf{3}} + \frac{\mu_{2;\mathbf{3}} - \mu_{2';\mathbf{3}}}{2},$$

and similar for $\xi_2(t)$ and $\xi_3(t)$. Summing up, the data combinations

$$Q_1(t) \equiv \theta_1^{2'}\xi_1(t) + \kappa_{2;\mathbf{3}}(t) = \theta_1^{2'}\xi_1(t) + \frac{\theta_{2'}^2\tau_{2';\mathbf{3}}(t) - \theta_2^{2'}\tau_{2;\mathbf{3}}(t)}{2}$$
$$\sim H_1 + p_{2;\mathbf{3}} - p_1 + \theta_1^{2'}a_1q_1 + \frac{\theta_{2'}^2(b_{2'} + b_2)}{2}q_{2;\mathbf{3}} + \frac{\mu_{2;\mathbf{3}} - \mu_{2';\mathbf{3}}}{2}, \quad (4.12a)$$

$$Q_{1'}(t) \equiv \theta_{1'}^3\xi_{1'}(t) - \kappa_1(t) = \theta_{1'}^3\xi_{1'}(t) - \frac{\theta_{1'}^1\tau_{1'}(t) - \theta_1^{1'}\tau_1(t)}{2}$$
$$\sim H_{1'} + p_{3;\mathbf{2'}} - p_1 + \theta_{1'}^3a_{1'}q_1 - \frac{\theta_{1'}^1(b_{1'} + b_1)}{2}q_1 - \frac{\mu_1 - \mu_{1'}}{2} \quad (4.12b)$$

are free of optical bench displacement noise and deal with three lasers only (the unprimed). Note that the $Q_i(t)$ have, except for the clock noise, already the form of the TDI inputs $\eta_i(t)$ from Eq. (4.7) and were shown in Ch. 3 to cancel laser phase noise and fibre noise (in the case of reciprocity). However, the differential clock noise contributions will not vanish automatically. We need to remove them in a further algorithm step.

4.3.4 Clock Noise Removal

By using only the synthesised data streams $Q_i(t)$ from (4.12a) and (4.12b), it is not possible to remove all clock errors $q_{\underline{i}}$. This is due to the fact that the data combinations are insensitive to a common-mode error in all clocks. We therefore need to set a reference. In the following, we choose

$$q_1(t) = 0. \quad (4.13)$$

Thus, all terms with q_2 and q_3 can be considered as relative clock drifts to the reference master clock signal onboard S/C 1. In that case, the $Q_i(t)$-data streams from (4.12a) and (4.12b) take the form

$$Q_1^{q_1}(t) \sim H_1 + p_{2;\mathbf{3}} - p_1 + 0 + \frac{\theta_{2'}^2(b_{2'} + b_2)}{2}q_{2;\mathbf{3}} + \frac{\mu_{2;\mathbf{3}} - \mu_{2';\mathbf{3}}}{2}, \quad (4.14a)$$

$$Q_{1'}^{q_1}(t) \sim H_{1'} + p_{3;\mathbf{2'}} - p_1 + 0 - 0 - \frac{\mu_1 - \mu_{1'}}{2}, \quad (4.14b)$$

$$Q_2^{q_1}(t) \sim H_2 + p_{3;\mathbf{1}} - p_2 + \theta_2^{3'}a_2q_2 + \frac{\theta_{3'}^3(b_{3'} + b_3)}{2}q_{3;\mathbf{1}} + \frac{\mu_{3;\mathbf{1}} - \mu_{3';\mathbf{1}}}{2}, \quad (4.14c)$$

$$Q_{2'}^{q_1}(t) \sim H_{2'} + p_{1;\mathbf{3'}} - p_2 + \theta_{2'}^1 a_{2'} q_2 - \frac{\theta_{2'}^2 (b_{2'} + b_2)}{2} q_2 - \frac{\mu_2 - \mu_{2'}}{2} \,, \quad (4.14d)$$

$$Q_3^{q_1}(t) \sim H_3 + p_{1;\mathbf{2}} - p_3 + \theta_3^{1'} a_3 q_3 + 0 + \frac{\mu_{1;\mathbf{2}} - \mu_{1';\mathbf{2}}}{2} \,, \quad (4.14e)$$

$$Q_{3'}^{q_1}(t) \sim H_{3'} + p_{2;\mathbf{1'}} - p_3 + \theta_{3'}^3 a_{3'} q_3 - \frac{\theta_{3'}^3 (b_{3'} + b_3)}{2} q_3 - \frac{\mu_3 - \mu_{3'}}{2} \,. \quad (4.14f)$$

We emphasise here by the superscript 'q_1' that the data combinations $Q_i(t)$ comprise clock noise with respect to the master clock of S/C 1. The zeros appear for terms making use of $q_1(t) = 0$ or $q_{1;i} = 0$. One can clearly see that the cyclical symmetry is then broken due to the choice of a master clock.

In the following, we will remove the clock noise q_2 and q_3 from $Q_1^{q_1}(t), \ldots, Q_{3'}^{q_1}(t)$. Therefore, we can make use of the sideband information $s_i^{\mathrm{sb}}(t)$ introduced in Sec. 4.1.3. We will demonstrate the procedure for $Q_{2'}^{q_1}(t)$, because in this data stream both instantaneous clocks as well as delayed clocks enter. Furthermore, the procedure will show how to extract $q_2(t)$ and $q_3(t)$ (remember: $q_1(t) = 0$).

First, we will extract q_2 and q_3 from the given system of PM outputs. Consider the combination

$$
\begin{aligned}
s_{2'}^{\mathrm{c}}(t) - s_{2'}^{\mathrm{sb}}(t) \quad \sim \quad & \left(\theta_{2'}^1 \left[H_{2'} + p_{1;\mathbf{3'}} - p_{2'} - \frac{2\pi}{\lambda_1} \vec{n}_{3'} \cdot \vec{\Delta}_{1;\mathbf{3'}} - \frac{2\pi}{\lambda_1} \vec{n}_3 \cdot \vec{\Delta}_{2'} \right] + a_{2'} q_2 \right) \\
& - \left(\theta_{2'}^1 \left[H_{2'} + p_{1;\mathbf{3'}} - p_{2'} + m_1 q_{1;\mathbf{3'}} - m_{2'} q_2 - \frac{2\pi}{\lambda_1} \vec{n}_{3'} \cdot \vec{\Delta}_{1;\mathbf{3'}} \right. \right. \\
& \left. \left. - \frac{2\pi}{\lambda_1} \vec{n}_3 \cdot \vec{\Delta}_{2'} \right] + c_{2'} q_2 \right) \\
= \quad & a_{2'} q_2 - \theta_{2'}^1 m_1 \underbrace{q_{1;\mathbf{3'}}}_{=0} + \theta_{2'}^1 m_{2'} q_2 - c_{2'} q_2 = (a_{2'} + \theta_{2'}^1 m_{2'} - c_{2'}) q_2 \,.
\end{aligned}
$$

Since the carrier and sideband data streams of the same optical bench comprise the same information except for the clock tone transfer, laser phase noise and optical bench displacement noise cancel fortunately in the difference, as well as the GW signal. The leftover primary noise is clock noise only. The important implication is now that we can extract the clock noise from carrier and sideband data via

$$\frac{s_{2'}^{\mathrm{c}}(t) - s_{2'}^{\mathrm{sb}}(t)}{a_{2'} + \theta_{2'}^1 m_{2'} - c_{2'}} \sim q_2 \,. \quad (4.15a)$$

The denominator is not zero due to the large modulation factor $m_{2'} \gg a_{2'}, c_{2'}$ (Sec. 4.1.3). Note here again that all constants are known from operation.

A similar data combination makes it possible to extract q_3:

$$s_3^{\mathrm{c}}(t) - s_3^{\mathrm{sb}}(t) \sim a_3 q_3 - \theta_3^{1'} m_{1'} \underbrace{q_{1;\mathbf{2}}}_{=0} + \theta_3^{1'} m_3 q_3 - c_3 q_3 = (a_3 + \theta_3^{1'} m_3 - c_3) q_3 \,.$$

This yields

$$\frac{s_3^{\mathrm{c}}(t) - s_3^{\mathrm{sb}}(t)}{a_3 + \theta_3^{1'} m_3 - c_3} \sim q_3 \, . \tag{4.15b}$$

Second, with the appropriate prefactors, q_2 and q_3 can be removed from (4.14a) – (4.14f). That is, e.g., for $Q_2^{q_1}(t)$:

$$Q_2^{q_1}(t) - \theta_2^{3'} a_2 \frac{s_{2'}^{\mathrm{c}}(t) - s_{2'}^{\mathrm{sb}}(t)}{a_{2'} + \theta_{2'}^1 m_{2'} - c_{2'}} \sim H_2 + p_{3;\mathbf{1}} - p_2 + \frac{\theta_{3'}^3 (b_{3'} + b_3)}{2} q_{3;\mathbf{1}} + \frac{\mu_{3;\mathbf{1}} - \mu_{3';\mathbf{1}}}{2}$$

yields data free of instantaneous clock noise from S/C 2, and similarly

$$Q_2^{q_1}(t) - \frac{\theta_{3'}^3 (b_{3'} + b_3)}{2} \frac{s_{3;\mathbf{1}}^{\mathrm{c}}(t) - s_{3;\mathbf{1}}^{\mathrm{sb}}(t)}{a_3 + \theta_3^{1'} m_3 - c_3} \sim H_2 + p_{3;\mathbf{1}} - p_2 + \theta_2^{3'} a_2 q_2 + \frac{\mu_{3;\mathbf{1}} - \mu_{3';\mathbf{1}}}{2}$$

subtracts the time-delayed clock noise from S/C 3. The combination of both will form clock noise free data. Finally,

$$\begin{aligned}
\eta_1(t) &\equiv Q_1^{q_1}(t) - \frac{\theta_{2'}^2 (b_{2'} + b_2)}{2} \frac{s_{2';\mathbf{3}}^{\mathrm{c}}(t) - s_{2';\mathbf{3}}^{\mathrm{sb}}(t)}{a_{2'} + \theta_{2'}^1 m_{2'} - c_{2'}} \\
&\sim H_1 + p_{2;\mathbf{3}} - p_1 + \frac{\mu_{2;\mathbf{3}} - \mu_{2';\mathbf{3}}}{2} \, , \tag{4.16a}
\end{aligned}$$

$$\begin{aligned}
\eta_2(t) &\equiv Q_2^{q_1}(t) - \theta_2^{3'} a_2 \frac{s_{2'}^{\mathrm{c}}(t) - s_{2'}^{\mathrm{sb}}(t)}{a_{2'} + \theta_{2'}^1 m_{2'} - c_{2'}} - \frac{\theta_{3'}^3 (b_{3'} + b_3)}{2} \frac{s_{3;\mathbf{1}}^{\mathrm{c}}(t) - s_{3;\mathbf{1}}^{\mathrm{sb}}(t)}{a_3 + \theta_3^{1'} m_3 - c_3} \\
&\sim H_2 + p_{3;\mathbf{1}} - p_2 + \frac{\mu_{3;\mathbf{1}} - \mu_{3';\mathbf{1}}}{2} \, , \tag{4.16b}
\end{aligned}$$

$$\begin{aligned}
\eta_3(t) &\equiv Q_3^{q_1}(t) - \theta_3^{1'} a_3 \frac{s_3^{\mathrm{c}}(t) - s_3^{\mathrm{sb}}(t)}{a_3 + \theta_3^{1'} m_3 - c_3} \\
&\sim H_3 + p_{1;\mathbf{2}} - p_3 + \frac{\mu_{1;\mathbf{2}} - \mu_{1';\mathbf{2}}}{2} \, , \tag{4.16c}
\end{aligned}$$

$$\begin{aligned}
\eta_{1'}(t) &\equiv Q_{1'}^{q_1}(t) \\
&\sim H_{1'} + p_{3;\mathbf{2'}} - p_1 - \frac{\mu_1 - \mu_{1'}}{2} \, , \tag{4.16d}
\end{aligned}$$

$$\begin{aligned}
\eta_{2'}(t) &\equiv Q_{2'}^{q_1}(t) - \theta_{2'}^1 a_{2'} \frac{s_{2'}^{\mathrm{c}}(t) - s_{2'}^{\mathrm{sb}}(t)}{a_{2'} + \theta_{2'}^1 m_{2'} - c_{2'}} + \frac{\theta_{2'}^2 (b_{2'} + b_2)}{2} \frac{s_{2'}^{\mathrm{c}}(t) - s_{2'}^{\mathrm{sb}}(t)}{a_{2'} + \theta_{2'}^1 m_{2'} - c_{2'}} \\
&\sim H_{2'} + p_{1;\mathbf{3'}} - p_2 - \frac{\mu_2 - \mu_{2'}}{2} \, , \tag{4.16e}
\end{aligned}$$

$$\begin{aligned}
\eta_{3'}(t) &\equiv Q_{3'}^{q_1}(t) - \theta_{3'}^2 a_{3'} \frac{s_3^{\mathrm{c}}(t) - s_3^{\mathrm{sb}}(t)}{a_3 + \theta_3^{1'} m_3 - c_3} + \frac{\theta_{3'}^3 (b_{3'} + b_3)}{2} \frac{s_3^{\mathrm{c}}(t) - s_3^{\mathrm{sb}}(t)}{a_3 + \theta_3^{1'} m_3 - c_3} \\
&\sim H_{3'} + p_{2;\mathbf{1'}} - p_3 - \frac{\mu_3 - \mu_{3'}}{2} \tag{4.16f}
\end{aligned}$$

yield the analytical form of Eq. (4.7), as demanded for TDI input. The phase noise $\mu_{\underline{i}}$ and its counterpart $\mu_{\underline{i}'}$ enter as a difference, and if the fibre is taken to be

reciprocal, the difference (even if time-delayed by the same light travel time) will vanish. Thus, the shown algorithm yields clock noise free, and optical bench motion free data combinations and, furthermore, keeps track of the beat-note polarity for each PM input. TDI is the final step of the full removal algorithm and uses the combinations $\eta_i(t)$ as input data.

4.3.5 Laser Phase Noise Cancellation

Application of TDI will suppress the laser phase noise by orders of magnitude to a level below the gravitational wave signal. Exemplarily, X_1 applies as before:

$$
\begin{aligned}
X_1 \;=\; & \eta_{1'} + \eta_{3;\mathbf{2'}} + \eta_{1;\mathbf{22'}} + \eta_{2';\mathbf{322'}} + \eta_{1;\mathbf{3'322'}} + \eta_{2';\mathbf{33'322'}} \\
& + \eta_{1';\mathbf{3'33'322'}} + \eta_{3;\mathbf{2'3'33'322'}} - \eta_1 - \eta_{2';\mathbf{3}} - \eta_{1';\mathbf{3'3}} - \eta_{3;\mathbf{2'3'3}} \\
& - \eta_{1';\mathbf{22'3'3}} - \eta_{3;\mathbf{2'22'3'3}} - \eta_{1;\mathbf{22'22'3'3}} - \eta_{2';\mathbf{322'22'3'3}}.
\end{aligned}
$$

It is remarkable that no phasemeter polarity factors θ_j^i enter anymore, and this is the same for all TDI combinations discussed in Ch. 3. Hence, the algorithm presented in Sec. 4.3.2 – 4.3.4 accounts completely for the phasemeter beat-note frequency polarity. Inserting (4.16a) – (4.16f) in X_1 yields finally the explicit output

$$
\begin{aligned}
X_1 \;\sim\; & H_{1'} + H_{3;\mathbf{2'}} + H_{1;\mathbf{22'}} + H_{2';\mathbf{322'}} + H_{1;\mathbf{3'322'}} + H_{2';\mathbf{33'322'}} \\
& + H_{1';\mathbf{3'33'322'}} + H_{3;\mathbf{2'3'33'322'}} - H_1 - H_{2';\mathbf{3}} - H_{1';\mathbf{3'3}} - H_{3;\mathbf{2'3'3}} \\
& - H_{1';\mathbf{22'3'3}} - H_{3;\mathbf{2'22'3'3}} - H_{1;\mathbf{22'22'3'3}} - H_{2';\mathbf{322'22'3'3}} \\
& + \frac{\mu_{1'} - \mu_1}{2} + \frac{\mu_{1;\mathbf{3'3}} - \mu_{1';\mathbf{3'3}}}{2} + \frac{\mu_{1;\mathbf{22'}} - \mu_{1';\mathbf{22'}}}{2} \\
& + \frac{\mu_{1';\mathbf{22'22'3'3}} - \mu_{1;\mathbf{22'22'3'3}}}{2} + \frac{\mu_{1';\mathbf{3'33'322'}} - \mu_{1;\mathbf{3'33'322'}}}{2} \\
& + \frac{\mu_{1;\mathbf{22'3'33'322'}} - \mu_{1';\mathbf{22'3'33'322'}}}{2} + \mathcal{O}(\tfrac{\dot{L}^2}{c^2}),
\end{aligned}
\tag{4.17}
$$

and other combinations similarly. In the derivation that can be found in appendix E.1, we used the approximation (3.37) to first order in $\frac{\dot{L}}{c}$ and neglected higher terms of $\mathcal{O}(\frac{\dot{L}^2}{c^2})$. In that approximation, laser frequency noise is removed while the gravitational wave signal H is preserved. Furthermore, the phase noise $\mu_{\underline{i}}$ in the fibres appears in each term of (4.17) as a difference with its counterpart $\mu_{\underline{i}'}$, as required above.

Concluding, we have found a sophisticated and suitable algorithm to remove all critical primary noise sources of lasers, clocks, optical fibres and optical bench displacement by combining and properly time-shifting the phasemeter outputs. At the same time, the algorithm accounts for the beat-note frequency polarity at the phasemeter input and treats the beat-note polarities correctly, such that the TDI equations for laser phase noise removal presented in Ch. 3 remain invariant.

4.4 Removal Algorithms for an Alternative Back-Link Interferometer

Currently, a discussion on the back-link between the two adjacent optical benches has been arisen. The main idea is to remove back-scattered straylight in the reference and test mass interferometer output originating from the fibre transmission. Therefore, an additional laser with a slightly different frequency than the local laser is transmitted through the fibre to get measurements at shifted frequencies with reduced susceptibility to back-scatter [Hen13]. The optical setup is shown in Fig. 4.6.

Since TM and reference IFO data were used in Sec. 4.3 for the reduction to three lasers and for optical bench displacement noise suppression, and since the additional laser appears in both IFOs, it is clear that the full removal algorithm from the previous section is affected. The aim of this section is hence the reformulation of the full removal algorithm in the case of alternative back-link interferometers with one additional laser per optical bench.

Onboard Data Streams

In the new setup, each optical bench hosts two independent lasers, the transmitting (TX) laser and the local oscillator (LO), which can be a low-power laser with few mW. An additional reference measurement on each OB between TX-laser and LO, $\rho_i(t)$, is needed to remove all laser frequency noise instances.

According to Fig. 4.6, the phasemeter output is given by

$$
\begin{aligned}
s_1^{\mathrm{c}}(t) & = \theta_{\mathrm{TX},1}^{\mathrm{TX},2'} \left[H_1 + p_{\mathrm{TX},2';\mathbf{3}} - p_{\mathrm{TX},1} - \frac{2\pi}{\lambda_{\mathrm{TX},2'}} \vec{n}_3 \cdot \vec{\Delta}_{2';\mathbf{3}} \right. \\
& \qquad \left. - \frac{2\pi}{\lambda_{\mathrm{TX},2'}} \vec{n}_{3'} \cdot \vec{\Delta}_1 + N_1^{\mathrm{opt}} \right] + a_1 q_1 + N_1^s \,, \tag{4.18a}
\end{aligned}
$$

$$
\begin{aligned}
s_1^{\mathrm{sb}}(t) & = \theta_{\mathrm{TX},1}^{\mathrm{TX},2'} \left[H_1 + p_{\mathrm{TX},2';\mathbf{3}} - p_{\mathrm{TX},1} + m_{2'} q_{2;\mathbf{3}} - m_1 q_1 - \frac{2\pi}{\lambda_{\mathrm{TX},2'}} \vec{n}_3 \cdot \vec{\Delta}_{2';\mathbf{3}} \right. \\
& \qquad \left. - \frac{2\pi}{\lambda_{\mathrm{TX},2'}} \vec{n}_{3'} \cdot \vec{\Delta}_1 + N_1^{\mathrm{opt,sb}} \right] + c_1 q_1 + N_1^{s,\mathrm{sb}} \,, \tag{4.18b}
\end{aligned}
$$

$$
\begin{aligned}
\varepsilon_1(t) & = \theta_{\mathrm{TX},1}^{\mathrm{LO},1'} \left[p_{\mathrm{LO},1'} - p_{\mathrm{TX},1} + 2 \left(\frac{2\pi}{\lambda_{\mathrm{LO},1'}} \vec{n}_{3'} \cdot \vec{\delta}_1 - \frac{2\pi}{\lambda_{\mathrm{LO},1'}} \vec{n}_{3'} \cdot \vec{\Delta}_1 \right) + \mu_{1'} \right] \\
& \qquad + b_1 q_1 + N_1^{\varepsilon} \,, \tag{4.18c}
\end{aligned}
$$

$$
\rho_1(t) = \theta_{\mathrm{LO},1}^{\mathrm{TX},1}[p_{\mathrm{TX},1} - p_{\mathrm{LO},1}] + d_1 q_1 + N_1^{\rho} \,, \tag{4.18d}
$$

$$
\tau_1(t) = \theta_{\mathrm{TX},1}^{\mathrm{LO},1'}[p_{\mathrm{LO},1'} - p_{\mathrm{TX},1} + \mu_{1'}] + b_1 q_1 + N_1^{\tau} \,, \tag{4.18e}
$$

with the clock noise translation factor $d_1 = \frac{|\Delta f_{\rho_1}|}{f_{\mathrm{PT},1}} = \frac{|\omega_{\mathrm{TX},1}^{\mathrm{tot}} - \omega_{\mathrm{LO},1}^{\mathrm{tot}}|}{2\pi f_{\mathrm{PT},1}}$ for the additional interferometer. Similar phasemeter data can be formulated for the adjacent optical
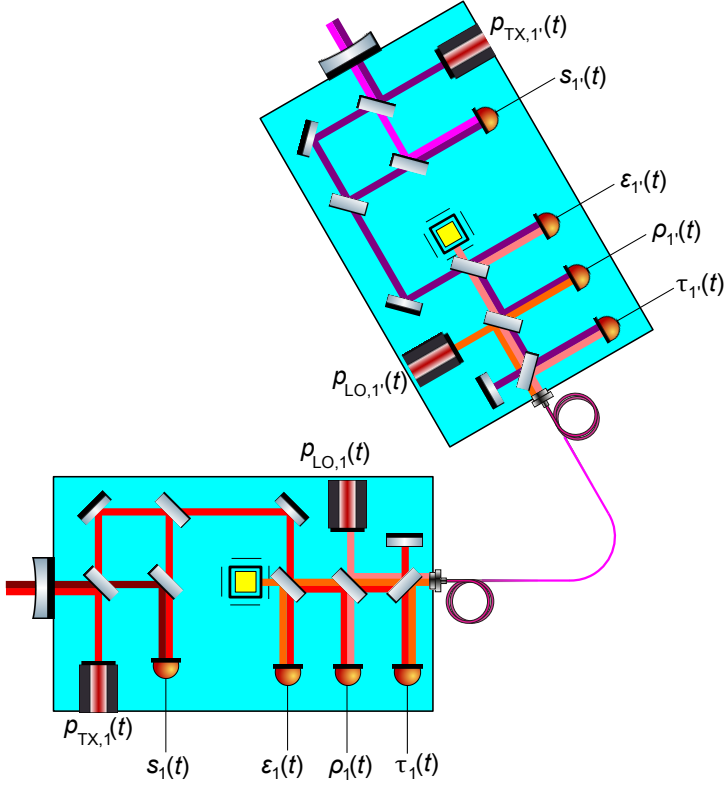
Figure 4.6: Optical setup for the alternative back-link interferometer. The additional local oscillator (LO1 and LO1′, respectively) contributes to the TM and reference IFO of each optical bench, but not to the science/sideband IFO. The local laser light is therefore not transmitted to the distant S/C. An auxiliary beat-note phase signal between transmission laser (TX1 and TX1′) and local oscillator, denoted by $\rho_1(t)$ and $\rho_{1'}(t)$, is formed for laser frequency noise removal.

bench:

$$
\begin{aligned}
s_{1'}^{c}(t) &= \theta_{\mathrm{TX},1'}^{\mathrm{TX},3} \left[H_{1'} + p_{\mathrm{TX},3;\mathbf{2'}} - p_{\mathrm{TX},1'} - \frac{2\pi}{\lambda_{\mathrm{TX},3}} \vec{n}_{2'} \cdot \vec{\Delta}_{3;\mathbf{2'}} \right. \\
&\quad \left. - \frac{2\pi}{\lambda_{\mathrm{TX},3}} \vec{n}_2 \cdot \vec{\Delta}_{1'} + N_{1'}^{\mathrm{opt}} \right] + a_{1'} q_1 + N_{1'}^{s} \,, \tag{4.18f}
\end{aligned}
$$

$$
\begin{aligned}
s_{1'}^{\mathrm{sb}}(t) &= \theta_{\mathrm{TX},1'}^{\mathrm{TX},3} \left[H_{1'} + p_{\mathrm{TX},3;\mathbf{2'}} - p_{\mathrm{TX},1'} + m_3 q_{3;\mathbf{2'}} - m_{1'} q_1 - \frac{2\pi}{\lambda_{\mathrm{TX},3}} \vec{n}_{2'} \cdot \vec{\Delta}_{3;\mathbf{2'}} \right. \\
&\quad \left. - \frac{2\pi}{\lambda_{\mathrm{TX},3}} \vec{n}_2 \cdot \vec{\Delta}_{1'} + N_{1'}^{\mathrm{opt,sb}} \right] + c_{1'} q_1 + N_{1'}^{\mathrm{sb}} \,, \tag{4.18g}
\end{aligned}
$$

$$
\begin{aligned}
\varepsilon_{1'}(t) &= \theta_{\mathrm{TX},1'}^{\mathrm{LO},1} \left[p_{\mathrm{LO},1} - p_{\mathrm{TX},1'} + 2 \left(\frac{2\pi}{\lambda_{\mathrm{LO},1}} \vec{n}_2 \cdot \vec{\delta}_{1'} - \frac{2\pi}{\lambda_{\mathrm{LO},1}} \vec{n}_2 \cdot \vec{\Delta}_{1'} \right) + \mu_1 \right] \\
&\quad + b_{1'} q_1 + N_{1'}^{\varepsilon} \,, \tag{4.18h}
\end{aligned}
$$

$$
\rho_{1'}(t) = \theta_{\mathrm{LO},1'}^{\mathrm{TX},1'} (p_{\mathrm{TX},1'} - p_{\mathrm{LO},1'}) + d_{1'} q_1 + N_{1'}^{\rho} \,, \tag{4.18i}
$$

$$
\tau_{1'}(t) = \theta_{\mathrm{TX},1'}^{\mathrm{LO},1} [p_{\mathrm{LO},1} - p_{\mathrm{TX},1'} + \mu_1] + b_{1'} q_1 + N_{1'}^{\tau} \,. \tag{4.18j}
$$

All other data streams follow per cyclic permutation of the indices.

The well-known task is again to remove all primary noise sources. Before we proceed, some remarks are essential. First, one has to deal carefully with the correct laser wavelengths in the data streams. In the science IFO of the alternative optical setup shown in Fig. 4.6, the TX laser from the distant optical bench with wavelength $\lambda_{\text{TX},2'}$ is sensing the optical bench displacement noise $\vec{\Delta}_{2'}$ and $\vec{\Delta}_1$. In contrast to the 'original' layout, the TM motion is not read out by the transmission laser of the adjacent optical bench (the TX laser), but instead by the local oscillator of the adjacent bench. Second, note that no measurement between the two local oscillators is performed since it is not necessary for laser phase noise removal.

Third, the frequency conversion factors need a revision. With the additional laser, they read as

$$a_1 = \frac{|\Delta f_{s_1}|}{f_{\text{PT},1}} = \frac{|\omega^{\text{tot}}_{\text{TX},2'\to 1} - \omega^{\text{tot}}_{\text{TX},1}|}{2\pi f_{\text{PT},1}}, \qquad a_{1'} = \frac{|\Delta f_{s_{1'}}|}{f_{\text{PT},1}} = \frac{|\omega^{\text{tot}}_{\text{TX},3\to 1'} - \omega^{\text{tot}}_{\text{TX},1'}|}{2\pi f_{\text{PT},1}},$$
$$\text{(4.19a)}$$

$$b_1 = \frac{|\Delta f_{\varepsilon_1}|}{f_{\text{PT},1}} = \frac{|\omega^{\text{tot}}_{\text{TX},1'} - \omega^{\text{tot}}_{\text{LO},1}|}{2\pi f_{\text{PT},1}}, \qquad b_{1'} = \frac{|\Delta f_{\varepsilon_{1'}}|}{f_{\text{PT},1}} = \frac{|\omega^{\text{tot}}_{\text{TX},1} - \omega^{\text{tot}}_{\text{LO},1'}|}{2\pi f_{\text{PT},1}},$$
$$\text{(4.19b)}$$

$$c_1 = \frac{|\Delta f^{\text{sb}}_{s_1}|}{f_{\text{PT},1}} = \frac{|\omega^{\text{sb,tot}}_{\text{TX},2'\to 1} - \omega^{\text{sb,tot}}_{\text{LO},1}|}{2\pi f_{\text{PT},1}}, \qquad c_{1'} = \frac{|\Delta f^{\text{sb}}_{s_{1'}}|}{f_{\text{PT},1}} = \frac{|\omega^{\text{sb,tot}}_{\text{TX},3\to 1'} - \omega^{\text{sb,tot}}_{\text{TX},1'}|}{2\pi f_{\text{PT},1}},$$
$$\text{(4.19c)}$$

$$d_1 = \frac{|\Delta f_{\rho_1}|}{f_{\text{PT},1}} = \frac{|\omega^{\text{tot}}_{\text{TX},1} - \omega^{\text{tot}}_{\text{LO},1}|}{2\pi f_{\text{PT},1}}, \qquad d_{1'} = \frac{|\Delta f_{\rho_{1'}}|}{f_{\text{PT},1}} = \frac{|\omega^{\text{tot}}_{\text{TX},1'} - \omega^{\text{tot}}_{\text{LO},1'}|}{2\pi f_{\text{PT},1}},$$
$$\text{(4.19d)}$$

and all others cyclic. Here, $\omega^{\text{tot}}_{\text{TX},j\to i}$ denotes again the overall frequency of transmitting laser from OB j received on OB i and which includes Doppler shift and frequency offsets. $\omega^{\text{tot}}_{\text{TX},i}$ and $\omega^{\text{tot}}_{\text{LO},i}$ mark the total frequencies of transmissive and local laser onboard OB i, respectively, both accounting for the frequency offset only. As a consequence of the auxiliary laser instance, note that $\Delta f_{\varepsilon_i} \neq \Delta f_{\varepsilon_{i'}}$ and $\Delta f_{\varepsilon_i} \neq \Delta f_{\tau_i}$ in contrast to the baseline LISA layout.

Spacecraft Jitter Elimination

First, the elimination of displacement jitter is necessary for gravitational wave extraction. In order to remove the term $-\theta^{\text{TX},2'}_{\text{TX},1} \frac{2\pi}{\lambda_{\text{TX},2'}} \vec{n}_{3'} \cdot \vec{\Delta}_1$ from $s^{\text{c}}_1(t)$, we use $\tau_1(t)$ and $\varepsilon_1(t)$ as before:

$$\varepsilon_1(t) - \tau_1(t) \sim -2\theta^{\text{LO},1'}_{\text{TX},1} \frac{2\pi}{\lambda_{\text{LO},1'}} \vec{n}_{3'} \cdot \vec{\Delta}_1(t).$$

Hence, we have to adjust the prefactors properly and find that

$$
s_1^{\mathrm{c}}(t) - \theta_{\mathrm{TX},1}^{\mathrm{TX},2'} \theta_{\mathrm{TX},1}^{\mathrm{LO},1'} \frac{\lambda_{\mathrm{LO},1'}}{\lambda_{\mathrm{TX},2'}} \frac{\varepsilon_1(t) - \tau_1(t)}{2}
$$

removes $-\theta_{\mathrm{TX},1}^{\mathrm{TX},2'} \frac{2\pi}{\lambda_{\mathrm{TX},2'}} \vec{n}_{3'} \cdot \vec{\Delta}_1$ in Eq. (4.18a). A similar calculation to that of Sec. 4.3.2 shows that

$$
s_1^{\mathrm{c}}(t) - \theta_{\mathrm{TX},1}^{\mathrm{TX},2'} \theta_{\mathrm{TX},2'}^{\mathrm{LO},2} \frac{\lambda_{\mathrm{LO},2}}{\lambda_{\mathrm{TX},2'}} \frac{\varepsilon_{2';\mathbf{3}}(t) - \tau_{2';\mathbf{3}}(t)}{2}
$$

cancels $-\theta_{\mathrm{TX},1}^{\mathrm{TX},2'} \frac{2\pi}{\lambda_{\mathrm{TX},2'}} \vec{n}_3 \cdot \vec{\Delta}_{2';\mathbf{3}}(t)$. Hence, the spacecraft jitter free combinations are given by

$$
\begin{aligned}
\xi_1(t) &= s_1^{\mathrm{c}}(t) - \theta_{\mathrm{TX},1}^{\mathrm{TX},2'} \theta_{\mathrm{TX},1}^{\mathrm{LO},1'} \frac{\lambda_{\mathrm{LO},1'}}{\lambda_{\mathrm{TX},2'}} \frac{\varepsilon_1(t) - \tau_1(t)}{2} \\
&\quad - \theta_{\mathrm{TX},1}^{\mathrm{TX},2'} \theta_{\mathrm{TX},2'}^{\mathrm{LO},2} \frac{\lambda_{\mathrm{LO},2}}{\lambda_{\mathrm{TX},2'}} \frac{\varepsilon_{2';\mathbf{3}}(t) - \tau_{2';\mathbf{3}}(t)}{2} \\
&\sim \theta_{\mathrm{TX},1}^{\mathrm{TX},2'} \left[H_1 + p_{\mathrm{TX},2';\mathbf{3}} - p_{\mathrm{TX},1} \right] + a_1 q_1 , \qquad (4.20a) \\
\xi_{1'}(t) &= s_{1'}^{\mathrm{c}}(t) - \theta_{\mathrm{TX},1'}^{\mathrm{TX},3} \theta_{\mathrm{TX},1'}^{\mathrm{LO},1} \frac{\lambda_{\mathrm{LO},1}}{\lambda_{\mathrm{TX},3}} \frac{\varepsilon_{1'}(t) - \tau_{1'}(t)}{2} \\
&\quad - \theta_{\mathrm{TX},1'}^{\mathrm{TX},3} \theta_{\mathrm{TX},3}^{\mathrm{LO},3'} \frac{\lambda_{\mathrm{LO},3'}}{\lambda_{\mathrm{TX},3}} \frac{\varepsilon_{3;\mathbf{2'}}(t) - \tau_{3;\mathbf{2'}}(t)}{2} \\
&\sim \theta_{\mathrm{TX},1'}^{\mathrm{TX},3} \left[H_{1'} + p_{\mathrm{TX},3;\mathbf{2'}} - p_{\mathrm{TX},1'} \right] + a_{1'} q_1 , \qquad (4.20b)
\end{aligned}
$$

which exactly compares to the optical bench noise free data in the case of one laser per OB, Eqn. (4.10a) and (4.10b).

Reduction of Free-Running Laser Instances

Again, we need to reduce $\xi_i(t)$ to only three different laser entities. However, simply subtracting the reference interferometer outputs of the adjacent optical benches $(\tau_{\underline{i}}(t) - \tau_{i'}(t))$ in order to remove contributions of TX lasers on primed OBs from the science signals will not work here either, even with the adequate phasemeter polarity factors θ_i^j. This is due to the different laser contributions in the reference interferometer, where we compare the *transmitting* laser of the first OB with the *local* oscillator of the adjacent OB, both assumed to run independently.

Instead, we have to make use of the additional comparison between the onboard

lasers, $\rho_i(t)$, where the transmitted and local laser is interfered. By forming

$$\theta_{\mathrm{LO},1}^{\mathrm{TX},1'}\rho_{1'}(t) + \theta_{\mathrm{TX},1}^{\mathrm{LO},1'}\tau_1(t)$$
$$\sim \quad (p_{\mathrm{TX},1'} - p_{\mathrm{LO},1'}) + \theta_{\mathrm{LO},1}^{\mathrm{TX},1'}d_{1'}q_1 + [p_{\mathrm{LO},1'} - p_{\mathrm{TX},1} + \mu_{1'}] + \theta_{\mathrm{TX},1}^{\mathrm{LO},1'}b_1 q_1$$
$$= \quad p_{\mathrm{TX},1'} - p_{\mathrm{TX},1} + \theta_{\mathrm{LO},1}^{\mathrm{TX},1'}d_{1'}q_1 + \theta_{\mathrm{TX},1}^{\mathrm{LO},1'}b_1 q_1 + \mu_{1'}\,,$$

we could in principle eliminate the primed TX lasers as in Sec. 4.3.3. However, $\mu_{1'}$ would then enter without its counterpart μ_1 in difference, as required for TDI input (Eq. (4.7)). The solution is here to form additionally

$$\theta_{\mathrm{LO},1}^{\mathrm{TX},1}\rho_1(t) + \theta_{\mathrm{TX},1'}^{\mathrm{LO},1}\tau_{1'}(t) \sim p_{\mathrm{TX},1} - p_{\mathrm{TX},1'} + \theta_{\mathrm{LO},1}^{\mathrm{TX},1}d_1 q_1 + \theta_{\mathrm{TX},1'}^{\mathrm{LO},1}b_{1'}q_1 + \mu_1\,,$$

which comprises the same laser phase noise entities as the formation above, and further provides the required counterpart of the fibre noise, μ_1. We can now subtract the two constructs and get

$$(\theta_{\mathrm{LO},1}^{\mathrm{TX},1}\rho_1(t) + \theta_{\mathrm{TX},1'}^{\mathrm{LO},1}\tau_{1'}(t)) - (\theta_{\mathrm{LO},1}^{\mathrm{TX},1'}\rho_{1'}(t) + \theta_{\mathrm{TX},1}^{\mathrm{LO},1'}\tau_1(t))$$
$$\sim \quad 2p_{\mathrm{TX},1} - 2p_{\mathrm{TX},1'} - \theta_{\mathrm{LO},1}^{\mathrm{TX},1'}d_{1'}q_1 - \theta_{\mathrm{TX},1}^{\mathrm{LO},1'}b_1 q_1 + \theta_{\mathrm{LO},1}^{\mathrm{TX},1}d_1 q_1 + \theta_{\mathrm{TX},1'}^{\mathrm{LO},1}b_{1'}q_1$$
$$+ \mu_1 - \mu_{1'}\,.$$

We thus define data streams $\kappa_i(t)$, containing TX lasers only, in analogy to Eq. (4.11), via:

$$\kappa_1(t) \quad \equiv \quad \frac{(\theta_{\mathrm{LO},1}^{\mathrm{TX},1}\rho_1(t) + \theta_{\mathrm{TX},1'}^{\mathrm{LO},1}\tau_{1'}(t)) - (\theta_{\mathrm{LO},1}^{\mathrm{TX},1'}\rho_{1'}(t) + \theta_{\mathrm{TX},1}^{\mathrm{LO},1'}\tau_1(t))}{2}$$
$$\sim \quad p_{\mathrm{TX},1} - p_{\mathrm{TX},1'} - \frac{1}{2}\left(\theta_{\mathrm{LO},1}^{\mathrm{TX},1'}d_{1'} + \theta_{\mathrm{TX},1}^{\mathrm{LO},1'}b_1 - \theta_{\mathrm{LO},1}^{\mathrm{TX},1}d_1 - \theta_{\mathrm{TX},1'}^{\mathrm{LO},1}b_{1'}\right)q_1$$
$$+ \frac{1}{2}(\mu_1 - \mu_{1'})\,, \tag{4.21}$$

and cyclic. They can now be used to remove the primed TX lasers from $\xi_i(t)$. In analogy to Sec. 4.3.3, one can find data combinations where only three TX lasers, $p_{\mathrm{TX},1}, p_{\mathrm{TX},2}$ and $p_{\mathrm{TX},3}$, appear:

$$Q_1(t) \quad = \quad \theta_{\mathrm{TX},1}^{\mathrm{TX},2'}\xi_1(t) + \kappa_{2;\mathbf{3}}(t)$$

$$\sim \quad H_1 + p_{\mathrm{TX},2;\mathbf{3}} - p_{\mathrm{TX},1} + \theta_{\mathrm{TX},1}^{\mathrm{TX},2'}a_1 q_1 - \frac{\theta_{\mathrm{LO},2'}^{\mathrm{TX},2'}d_{2'}q_{2;\mathbf{3}}}{2}$$

$$- \frac{\theta_{\mathrm{TX},2}^{\mathrm{LO},2'}b_2 q_{2;\mathbf{3}}}{2} + \frac{\theta_{\mathrm{LO},2}^{\mathrm{TX},2}d_2 q_{2;\mathbf{3}}}{2} + \frac{\theta_{\mathrm{TX},2'}^{\mathrm{LO},2}b_{2'}q_{2;\mathbf{3}}}{2} + \frac{\mu_{2;\mathbf{3}} - \mu_{2';\mathbf{3}}}{2}$$

$$= \quad H_1 + p_{\mathrm{TX},2;\mathbf{3}} - p_{\mathrm{TX},1} + \theta_{\mathrm{TX},1}^{\mathrm{TX},2'}a_1 q_1 + \left(-\frac{\theta_{\mathrm{LO},2'}^{\mathrm{TX},2'}d_{2'}}{2} - \frac{\theta_{\mathrm{TX},2}^{\mathrm{LO},2'}b_2}{2}\right.$$

$$\left. + \frac{\theta_{\mathrm{LO},2}^{\mathrm{TX},2}d_2}{2} + \frac{\theta_{\mathrm{TX},2'}^{\mathrm{LO},2}b_{2'}}{2}\right)q_{2;\mathbf{3}} + \frac{\mu_{2;\mathbf{3}} - \mu_{2';\mathbf{3}}}{2}\,, \tag{4.22a}$$

$$
\begin{aligned}
Q_{1'}(t) \;=\;& \theta^{\mathrm{TX},3}_{\mathrm{TX},1'}\xi_{1'}(t) - \kappa_1(t) \\[6pt]
\sim\;& H_{1'} + p_{\mathrm{TX},3;\mathbf{2'}} - p_{\mathrm{TX},1} + \theta^{\mathrm{TX},3}_{\mathrm{TX},1'}a_{1'}q_1 + \frac{\theta^{\mathrm{TX},1'}_{\mathrm{LO},1'}d_{1'}q_1}{2} \\[6pt]
&+ \frac{\theta^{\mathrm{LO},1'}_{\mathrm{TX},1}b_1 q_1}{2} - \frac{\theta^{\mathrm{TX},1}_{\mathrm{LO},1}d_1 q_1}{2} - \frac{\theta^{\mathrm{LO},1}_{\mathrm{TX},1'}b_{1'}q_1}{2} + \frac{\mu_{1'}-\mu_1}{2} \\[6pt]
\;=\;& H_{1'} + p_{\mathrm{TX},3;\mathbf{2'}} - p_{\mathrm{TX},1} + \left(\theta^{\mathrm{TX},3}_{\mathrm{TX},1'}a_{1'} + \frac{\theta^{\mathrm{TX},1'}_{\mathrm{LO},1'}d_{1'}}{2} \right. \\[6pt]
&\left. + \frac{\theta^{\mathrm{LO},1'}_{\mathrm{TX},1}b_1}{2} - \frac{\theta^{\mathrm{TX},1}_{\mathrm{LO},1}d_1}{2} - \frac{\theta^{\mathrm{LO},1}_{\mathrm{TX},1'}b_{1'}}{2} \right) q_1 + \frac{\mu_{1'}-\mu_1}{2} . \quad (4.22\mathrm{b})
\end{aligned}
$$

We have reduced the primed laser entities and remain with that of the transmitting lasers, $p_{\mathrm{TX},1}$, $p_{\mathrm{TX},2}$ and $p_{\mathrm{TX},3}$. Neglecting clock noise, $\eta_i(t)$ has the required signature (4.7) and all laser phase noise instances can be removed by TDI.

Clock Noise Removal

Finally, we have to address the issue of clock noise removal. The basic principle is exactly the same as in Sec. 4.3.4: choose one clock as master (as before, $q_1(t) := 0$), extract the clock signals with respect to the master from the sidebands and subtract it from $\eta_i(t)$.

As before, we can use $s^{\mathrm{c}}_{2'}(t) - s^{\mathrm{sb}}_{2'}(t)$ and $s^{\mathrm{c}}_3(t) - s^{\mathrm{sb}}_3(t)$ in order to remove q_2 and q_3, respectively:

$$
\frac{s^{\mathrm{c}}_{2'}(t) - s^{\mathrm{sb}}_{2'}(t)}{a_{2'} + \theta^{\mathrm{TX},1}_{\mathrm{TX},2'}m_{2'} - c_{2'}} \sim q_2 , \qquad \frac{s^{\mathrm{c}}_3(t) - s^{\mathrm{sb}}_3(t)}{a_3 + \theta^{\mathrm{TX},1'}_{\mathrm{TX},3}m_3 - c_3} \sim q_3 . \tag{4.23}
$$

With this and appropriate prefactors we end up with the following clock noise free data combinations:

$$
\begin{aligned}
\eta_1(t) \;=\;& Q^{q_1}_1(t) - \left(-\frac{\theta^{\mathrm{TX},2'}_{\mathrm{LO},2'}d_{2'}}{2} - \frac{\theta^{\mathrm{LO},2'}_{\mathrm{TX},2}b_2}{2} + \frac{\theta^{\mathrm{TX},2}_{\mathrm{LO},2}d_2}{2} \right. \\[6pt]
&\left. + \frac{\theta^{\mathrm{LO},2}_{\mathrm{TX},2'}b_{2'}}{2} \right) \frac{s^{\mathrm{c}}_{2';\mathbf{3}}(t) - s^{\mathrm{sb}}_{2';\mathbf{3}}(t)}{a_{2'} + \theta^{\mathrm{TX},1}_{\mathrm{TX},2'}m_{2'} - c_{2'}} , \tag{4.24a} \\[10pt]
\eta_2(t) \;=\;& Q^{q_1}_2(t) - a_2\theta^{\mathrm{TX},3}_{\mathrm{TX},2}\frac{s^{\mathrm{c}}_{2'}(t) - s^{\mathrm{sb}}_{2'}(t)}{a_{2'} + \theta^{\mathrm{TX},1}_{\mathrm{TX},2'}m_{2'} - c_{2'}} - \left(-\frac{\theta^{\mathrm{TX},3'}_{\mathrm{LO},3'}d_{3'}}{2} \right. \\[6pt]
&\left. - \frac{\theta^{\mathrm{LO},3'}_{\mathrm{TX},3}b_3}{2} + \frac{\theta^{\mathrm{TX},3}_{\mathrm{LO},3}d_3}{2} + \frac{\theta^{\mathrm{LO},3}_{\mathrm{TX},3'}b_{3'}}{2} \right) \frac{s^{\mathrm{c}}_{3;\mathbf{1}}(t) - s^{\mathrm{sb}}_{3;\mathbf{1}}(t)}{a_3 + \theta^{\mathrm{TX},1'}_{\mathrm{TX},3}m_3 - c_3} , \tag{4.24b} \\[10pt]
\eta_3(t) \;=\;& Q^{q_1}_3(t) - a_3\theta^{\mathrm{TX},1'}_{\mathrm{TX},3}\frac{s^{\mathrm{c}}_3(t) - s^{\mathrm{sb}}_3(t)}{a_3 + \theta^{\mathrm{TX},1'}_{\mathrm{TX},3}m_3 - c_3} , \tag{4.24c}
\end{aligned}
$$

and furthermore

$$\eta_{1'}(t) = Q_{1'}^{q_1}(t), \tag{4.24d}$$

$$\eta_{2'}(t) = Q_{2'}^{q_1}(t) - \left(\theta_{\mathrm{TX},2'}^{\mathrm{TX},1} a_{2'} + \frac{\theta_{\mathrm{LO},2'}^{\mathrm{TX},2'} d_{2'}}{2} + \frac{\theta_{\mathrm{TX},2}^{\mathrm{LO},2'} b_2}{2} \right.$$
$$\left. - \frac{\theta_{\mathrm{LO},2}^{\mathrm{TX},2} d_2}{2} - \frac{\theta_{\mathrm{TX},2'}^{\mathrm{LO},2} b_{2'}}{2} \right) \frac{s_{2'}^{\mathrm{c}}(t) - s_{2'}^{\mathrm{sb}}(t)}{a_{2'} + \theta_{\mathrm{TX},2'}^{\mathrm{TX},1} m_{2'} - c_{2'}}, \tag{4.24e}$$

$$\eta_{3'}(t) = Q_{3'}^{q_1}(t) - \left(\theta_{\mathrm{TX},3'}^{\mathrm{TX},2} a_{3'} + \frac{\theta_{\mathrm{LO},3'}^{\mathrm{TX},3'} d_{3'}}{2} + \frac{\theta_{\mathrm{TX},3}^{\mathrm{LO},3'} b_3}{2} \right.$$
$$\left. - \frac{\theta_{\mathrm{LO},3}^{\mathrm{TX},3} d_3}{2} - \frac{\theta_{\mathrm{TX},3'}^{\mathrm{LO},3} b_{3'}}{2} \right) \frac{s_{3}^{\mathrm{c}}(t) - s_{3}^{\mathrm{sb}}(t)}{a_3 + \theta_{\mathrm{TX},3}^{\mathrm{TX},1'} m_3 - c_3}. \tag{4.24f}$$

Formation of these data streams will give exactly the same result (except of secondary noise and the superscript 'TX') as in Eqn. (4.16a) – (4.16f). We know that the TDI Michelson combinations (Ch. 3) are then laser noise free to first order in $\frac{\dot{L}}{c}$.

In summary, by taking a new intra spacecraft measurement between the local oscillator and transmitting laser into account, it is again possible to remove all primary noise sources in post-processing, even in the worst case scenario of free-running lasers. Hence, from the TDI point of view, nothing argues against the presented alternative back-link configuration, because the post-processing will still be accurate. However, for the rest of the thesis, we will come back to the LISA model baseline with only one laser per optical bench.

Chapter 4

5 Time-Delay Interferometry Simulations

In the last decade, several computer-based TDI simulations, e.g., LISA Simulator [CR03; CH03], Synthetic LISA [Val05] and LISACode [PAH+08], were developed. Their goal is to have a simulation at hand that mimics as closely as possible the 'real' LISA detector, and, as a side aspect, to test and examine Time-Delay Interferometry. This includes data generation, processing and analysis. In particular, the simulations were used extensively for the Mock LISA data challenge [BBB+10]. However, the LISA mission has evolved (Ch. 2 and 4) and new technologies and subsystems have entered the LISA design. Therefore, a new comprehensive simulation combined with several existing data processing and analysis tools is needed, which is called LISA data processing chain.

In this chapter, we will give an overview about the LISA data processing chain that (as an overall goal) needs to be fully simulated in the future. Furthermore, we will explain in detail the parts implemented in the TDI Simulator (TDISim) at the AEI Hannover, followed by a code overview.

5.1 The LISA Data Processing Chain

The LISA data processing chain is depicted in Fig. 5.1 and consists in principle of eight steps that can be divided in two parts: (a) the generation of simulated phasemeter output data streams, and (b) (after virtual telemetry to Earth) the data processing and analysis part taking place on ground. It should be emphasised that (a) and (b) have a fundamental difference. In (a) we have complete information available including the GW tensor $\boldsymbol{h}(t)$, precise orbits and numerical values for all noise sources. However, in (b) we only have the simulated telemetry data at hand and aim at the reconstruction of $\boldsymbol{h}(t)$ and numerous auxiliary intermediate variables without the knowledge used in (a).
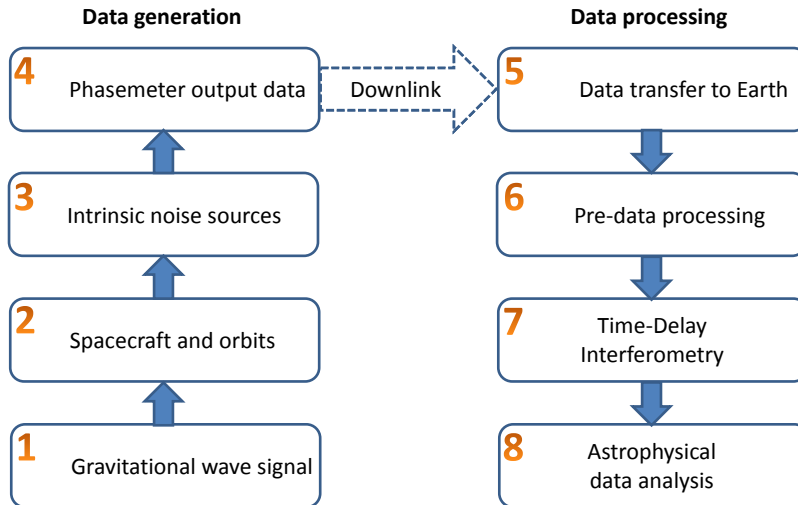
Data generation

Figure 5.1: Overview about the LISA data processing chain. It basically consists of eight steps. On the lhs., the data generation part takes place, while, after transmission to Earth via downlink, the data is processed and analysed (rhs.).

We will now sketch the single steps presented in Fig. 5.1. In step 1, the gravitational wave signal is generated. Therefore, the observable sources within the LISA detection band need to be simulated. In order to account for the constellation's motion, the satellite orbits are then calculated in step 2 using ephemeris data including several celestial bodies and interpolation routines.

The third step provides the generation of laser, clock, optical bench, test mass and fibre noise as well as secondary noise. This is followed in step 4 by the OB measurement scheme and synthesisation of raw phasemeter outputs. They include the science and sideband signal, reference and test mass interferometer. Moreover, auxiliary measurement data as from the ranging procedure between the satellites and differential wavefront sensing should be implemented [HEB$^+$11; Jen09].

While the optical signals are sampled onboard at 80 MHz, the relevant phase information is downsampled to 3 Hz in order to prevent data overflow. The compressed data is then telemetered down to Earth (left to right column in Fig. 5.1 and step 5). On ground, in step 6, the raw data is used to estimate orbit parameters (armlengths, relative velocities) and clock noise by the use of Kalman filters. Furthermore, the data is synchronised on a common time stamp, the constellation time. Besides, data is smoothed out and further prepared for the full removal TDI algorithm input in step seven which suppresses all primary noise sources as discussed in Ch. 4 of this thesis. The TDI output is finally processed to the data analysis and GW signal extraction (step 8).

We will now focus on some aspects of the LISA data processing chain which have been included in TDISim. For more information about the single processing steps of the chain shown in Fig. 5.1, we refer to [Wan14].

5.2 The Prototype Simulation TDISim

In this section, we will explain in detail the prototype simulator TDISim, developed at the AEI Hannover by the author together with Andreas Schreiber and Sarah Paczkowski [Sch13; Pac14].

5.2.1 Overview

TDISim is a prototype Time-Delay Interferometry simulation tool programmed in MATLAB. It uses extensively the tools of the LISA technology package data analysis (LTPDA) toolbox developed for LISA Pathfinder data analysis. The simulation fully operates in the time domain and provides in a simplified manner steps $1 - 4$ and 7 of the LISA data processing chain shown in Fig. 5.1.

Currently (December 15, 2015), TDISim produces a monochromatic GW signal in the LISA laser links. The impact on the links is given in terms of optical phase shifts by Eq. (2.20a). In order to compute the light travel times, TDISim uses the expressions from Sec. 1.4. The required orbit data for the spacecraft positions is taken from a separate program run in a previous generation step performed by Oliver Jennrich from the European Space Research and Technology Centre (ESTEC), and is then interpolated. In our model, the spacecraft are taken as point masses and we therefore neglect any rotational effects of the satellites itself. As a further simplification, the laser light travel times used for data generation and data processing, in particular for TDI, are equal and exactly known in both the steps 4 and 7.

The simulation then generates the photodetector signals from science measurements (carrier only), test mass and reference IFOs in terms of optical phase as derived in Ch. 2. Therefore, as a worst case scenario, free-running laser phase noise, characterised by a pole-zero transfer function given in Sec. 5.2.4, is produced. Furthermore, readout noise is generated according to a white noise spectral density with different magnitudes according to the power levels in the three interferometers (Sec. 5.2.4). An external 1-D test mass simulation block based on state space modelling and LISA Pathfinder data analysis methods provides residual test mass and optical bench displacement noise. The combination of the time series of gravitational wave signal, laser noise, test mass, optical bench and readout noise yields the PD signals. Note that clock noise is completely neglected in the simulation and all data is assumed to be perfectly synchronised. This is an important issue to be fixed within the future. Due to this simplification, and since the beat-note polarity was neglected as well for the sake of simplicity, the phasemeter output data in the current version of TDISim is identical to the PD output signals.

The downlink to the Earth and in particular the data synchronisation and estimation by Kalman filter are not included in this prototype, since all data are known from generation. Instead, the TDI input data streams are constructed immediately from the photodetector signals. Finally, the TDI 1.0 and 2.0 output variables (Michelson, Sagnac and fully symmetric Sagnac) from Sec. 3.2 and 3.3 are synthesised.

Currently, the time domain TDI output signals are analysed directly. Matched filtering is not needed here, because the induced gravitational wave signal is monochromatic and assumed to be known exactly. However, it is planned to use parts of the LISACode from Antoine Petiteau [PAH+08] for the gravitational wave data analysis in TDISim in the future.

Synthetic vs. Mother Nature Quantities

The overall goal is a comprehensive simulation of LISA-like missions including data generation, processing and analysis. As discussed before, several simplifications were made in our simulator TDISim. Besides those, the most crucial simplification is the absolute knowledge about the mother nature quantities. These are quantities generally not known to the required precision, as armlengths or relative LoS velocities. In order to verify the functionality and performance of the steps $5-8$ in a realistic scenario, these steps should not know the input mother nature quantities used for data generation. However, in the current version of TDISim, we make no difference between synthetic and mother nature quantities and assume all of them to be perfectly known. In particular, the TDI algorithm takes the armlengths from the data generation part to compute the time delays. In other words, the ranging inaccuracies that would be experienced in reality are not taken into account here.

The next subsections deal with details about the numerical implementation of the simulation blocks discussed previously, i.e., steps $1-4$ and 7 in Fig. 5.1.

5.2.2 Spacecraft and Orbit Simulation

Within TDISim, three orbit cases for LISA are implemented. The user can choose between LISA on algebraic Keplerian orbits and LISA in a realistic flexing mode. Furthermore, for testing, we implemented a static LISA configuration. Each scenario takes the spacecraft as point masses.

Keplerian Orbit Simulation

For the Keplerian orbits, TDISim makes use of a straightforward analytical approximation of the LISA orbits with respect to the small orbit eccentricity e, according to [RCP04]. The coordinates of the spacecraft positions, $\vec{x}_{\underline{i}}(t) = (x_{\underline{i}}(t), y_{\underline{i}}(t), z_{\underline{i}}(t))$, are then given in the solar system barycentric (SSB) frame [MG11] as
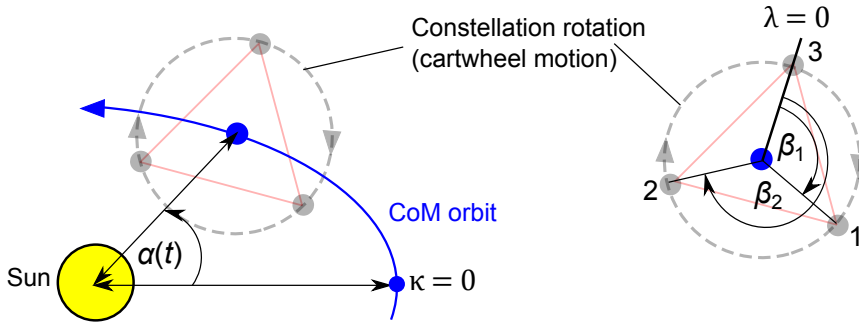
Figure 5.2: Orbit parameters for the Keplerian orbits. Left: $\alpha(t)$ describes the orbital constellation's CoM motion with initial offset κ. Right: $\beta_{\underline{i}}$ gives the shift of S/C $\underline{i}$ within the constellation with respect to an initial value λ.

$$
\begin{aligned}
x_{\underline{i}}(t) &= R\cos(\alpha(t)) + \frac{1}{2}eR[\cos(2\alpha(t) - \beta_{\underline{i}}) - 3\cos(\beta_{\underline{i}})] \\
&\quad + \frac{1}{8}e^2R[3\cos(3\alpha(t) - 2\beta_{\underline{i}}) - 10\cos(\alpha(t)) - 5\cos(\alpha(t) - 2\beta_{\underline{i}})], \quad (5.1a) \\
y_{\underline{i}}(t) &= R\sin(\alpha(t)) + \frac{1}{2}eR[\sin(2\alpha(t) - \beta_{\underline{i}}) - 3\sin(\beta_{\underline{i}})] \\
&\quad + \frac{1}{8}e^2R[3\sin(3\alpha(t) - 2\beta_{\underline{i}}) - 10\sin(\alpha(t)) + 5\cos(\alpha(t) - 2\beta_{\underline{i}})], \quad (5.1b) \\
z_{\underline{i}}(t) &= -\sqrt{3}eR\cos(\alpha(t) - \beta_{\underline{i}}) \\
&\quad + \sqrt{3}e^2R[\cos^2(\alpha(t) - \beta_{\underline{i}}) + 2\sin^2(\alpha(t) - \beta_{\underline{i}})], \quad (5.1c)
\end{aligned}
$$

since the S/C are again taken to be point masses and are negligible compared to the mass of the Sun. Subsequently, the CoM of detector and Sun, and hence the origin of the SSB frame, is placed in the Sun with sufficient accuracy. R defines the nominal distance between the CoM of the constellation and the Sun, while e denotes the orbit eccentricity.

Moreover, the angle $\alpha(t)$ describes the orbital CoM evolution of the constellation, while $\beta_{\underline{i}}$ defines the angular shift of S/C $\underline{i}$ within the constellation as shown in Fig. 5.2:

$$
\alpha(t) = 2\pi f_{\mathrm{orb}}t + \kappa, \quad \beta_{\underline{i}} = \frac{2\pi}{3}\underline{i} + \lambda. \tag{5.1d}
$$

Here, f_{orb} gives the orbital frequency for the closed Keplerian orbit and κ and λ denote the initial angular values. By the choice of κ and λ, the orbit is uniquely defined. Note that the orbits are closed, i.e., after one roundtrip of the CoM, the S/C will pass exactly the same coordinates as before.

TDISim uses the parametric values for the Keplerian orbit computation as follows. Since the CoM of LISA trails the Earth on a heliocentric orbit, the orbital frequency

is $f_{\rm orb} = 1\,\frac{\rm cycle}{\rm yr}$ and $R = 149\,597\,870\,700\,{\rm m}$ is the nominal distance of the Keplerian orbit. The eccentricity is slightly different from the Earth orbit: $e = 0.00965$ [RCP04], which is due to the angular tilt of the orbit with respect to the ecliptic. Finally, the initial values are set to $\kappa = \lambda = 0$.

Static LISA

In order to construct test cases (e.g., for TDI 1.0) we implemented a static LISA configuration. The spacecraft 'orbits' are constructed by using the positions on the Keplerian orbits at a fixed time of $t = 50\,\text{days}$. These are then, according to Eqn. (5.1a) – (5.1d):

$$
\begin{aligned}
\vec{x}_1 &\equiv \vec{x}_1(t=50\,{\rm d}) = (99274616.474, 111285788.222, -781427.816)\,{\rm km}\,, \\
\vec{x}_2 &\equiv \vec{x}_2(t=50\,{\rm d}) = (98031927.256, 114846658.468, 2482027.437)\,{\rm km}\,, \\
\vec{x}_3 &\equiv \vec{x}_3(t=50\,{\rm d}) = (95227505.512, 114150741.534, -1592018.785)\,{\rm km}\,.
\end{aligned}
$$

With these positions, we build the models of the spacecraft in the static case.

LISA Orbits from ESA

The orbit data for the flexing constellation is provided by Oliver Jennrich from ESTEC. His sophisticated simulator includes the Sun, the Earth as well as the planets of the solar system and further details relying on astrometric ephemeris data [NAS]. The simulation gives positions, Doppler velocities, angles, etc., of the LISA constellation as the excerpt shows in Fig. 5.3. The data is given with respect to the SSB frame. Since no launch date for LISA is fixed currently, preliminary test data is provided by the simulator.

Figure 5.3: Excerpt of the orbit data provided by Oliver Jennrich from ESTEC. $\vec{x}_{\underline{i}}(t) = (x_{\underline{i}}(t), y_{\underline{i}}(t), z_{\underline{i}}(t))$ are the CoM coordinates of S/C $\underline{i}$ with respect to SSB coordinates with the Sun as the origin, given in km. Furthermore, the S/C velocities $\vec{v}_{\underline{i}}(t) = (v_{x,\underline{i}}(t), v_{y,\underline{i}}(t), v_{z,\underline{i}}(t))$ in km/s are provided, as well with respect to the SSB frame. Note that there is only one data point per day.

The simulator produces one data point per day. Hence, in order to form the delay shifts ($\approx 17\,\text{s}$ for a single link) of the onboard measurements for data generation and TDI processing, high accuracy (Lagrangian) interpolation of the orbit data is

necessary. This is fortunately possible due to the smooth LISA orbits. We implemented the Lagrange interpolation routine in the form of the recursive Neville and Aitken algorithm [Ait32], by default of the order 18. This fast algorithm computes directly an interpolated value of the polynomial at a certain time stamp without first calculating the Lagrange polynomials itself and hence saves computational costs [Sch13].

5.2.3 Gravitational Wave Signal

The gravitational wave signal is generated in principle in two sections. The first section consists of the gravitational wave tensor computation (according to step 1 in Fig. 5.1) for a single, monochromatic GW source. Within the second section, the projections on the detector arms and thus the spacecraft separation variations are calculated and converted to optical phase shifts.

Section 1 starts with defining the direction to a GW source in spherical coordinates (θ,ϕ). By default, this is $\theta = -\frac{\pi}{6}$ and $\phi = \frac{\pi}{4}$. From this information, the direction vector of GW incidence $\hat{k}$ as well as the dreibein companion vectors $\hat{u}$ and $\hat{v}$ can be directly constructed following Eq. (1.23). Next, the generalised polarisation tensors $\boldsymbol{\epsilon}_{+,\times}$ are built as given by (1.24) with default $\psi = 0$. Finally, in section 1, TDISim generates the complete gravitational wave tensor, where we implemented an oscillation function for $h_+(t)$ and $h_\times(t)$ such that (1.25) reads as

$$\boldsymbol{h}(t,\vec{x}) = (h_+\boldsymbol{\epsilon}_+ + h_\times\boldsymbol{\epsilon}_\times)\cos(2\pi f_{\mathrm{gw}}(t - \tfrac{\hat{k}\cdot\vec{x}}{c})). \tag{5.2}$$

Here, f_{gw} denotes the gravitational wave frequency, t the simulation time and $\vec{x}$ an arbitrary position input vector. Note that h_+ and $h_\times$ are constants with default values $h_+ = 10^{-20}$ and $h_\times = 0$, and the gravitational wave frequency is taken to be $f_{\mathrm{gw}} = 4\,\mathrm{mHz}$. The used model is adequate for GW radiation from an inspiralling binary or a ringing black hole [SS09].

Section 2 computes the optical phase shifts $H_i(t)$ detected onboard. $H_i(t)$ is the phase shift that photons will suffer from the light travel time variation between the spacecraft due to GW, i.e.,

$$H_i(t) = 2\pi\nu_0\Delta T_i(t), \tag{5.3}$$

where the central laser frequency $\nu_0 = 3\cdot 10^{14}\,\mathrm{Hz}$ is the same for all onboard lasers within the current version of TDISim. The light travel time variation due to gravitational waves, $\Delta T_i(t)$, is implemented according to Eq. (1.59). However, the simulation makes use of a real value version and neglect the (approximately constant) phase term $\mathrm{e}^{\mathrm{i}\frac{\omega_{\mathrm{gw}}L_0(t)}{2c}(1+\hat{k}\cdot\vec{n}_{\mathrm{recv}}(t))}$. For the detection in the science IFO of,

e.g., OB 1 this results in:

$$\Delta T_1(t) \quad = \quad \frac{|\vec{x}_1(t) - \vec{x}_2(t - T_{0,3}(t))|}{2c} \left(\vec{n}_{3'}(t) \otimes \vec{n}_{3'}(t)\right) : \boldsymbol{h}(t, \vec{x}_1(t))$$
$$\cdot \operatorname{sinc}\left(2\pi f_{\text{gw}} \frac{|\vec{x}_1(t) - \vec{x}_2(t - T_{0,3}(t))|}{2c}(1 + \hat{k} \cdot \vec{n}_{3'}(t))\right), \quad (5.4)$$

where the time of flight $T_{0,3}(t)$ without GW influence along link 3 is computed by the formulas explained in Sec. 1.4.4. Similar (cyclic) expressions hold true for the light travel time variations in the other links. Note that the factor $\mathrm{e}^{\mathrm{i}\omega\xi(0)}$ from Eq. (1.59) is implicitly included in the GW model (5.2).

5.2.4 Noise Generation

In this section, we will give details about how the noise sources of the gravitational wave detector model are generated in TDISim and how they affect the simulated data.

Laser noise generation

The free-running laser frequency noise contributes to the PD signal of each interferometer as given by Eqn. (4.5a) – (4.5h) and is by far the dominant noise source. We generate it according to its filter transfer function given by the following pole-zero model [Hei08]:

$$H(s) = G\frac{(s - z_1)(s - z_2)}{(s - p_1)(s - p_2)(s - p_3)} \tag{5.5}$$

with gain $G = 228.2 \cdot 10^6$, zeros $z_1 = 36.019 \cdot 10^{-3}$, $z_2 = 310.55 \cdot 10^{-3}$, and poles $p_1 = 59.054 \cdot 10^{-6}$, $p_2 = 118.62 \cdot 10^{-3}$, $p_3 = 983.77 \cdot 10^{-3}$. s denotes here the Laplace variable, $s = \mathrm{i}\omega$. Note that the six (free-running) laser output signals are generated independently with help of a random number generator, the seed of which is reset for each run. The linear spectral density of the laser frequency noise is shown in Fig. 5.4.

For the simulation, it is numerically cost expensive to generate and process MHz signals. Therefore, the generated noise is at first band-limited to $f_{\text{cut}} = 1\,\text{Hz}$ by a low-pass filter of order 8, then converted to phase by simple numerical integration (trapezoidal rule) and finally processed through the laser links in order to contribute to the interferometer outputs. Moreover, by low-pass filtering, the alias effects on the high frequency components are suppressed. The linear spectral density of the filtered laser frequency noise is presented in Fig. 5.5.
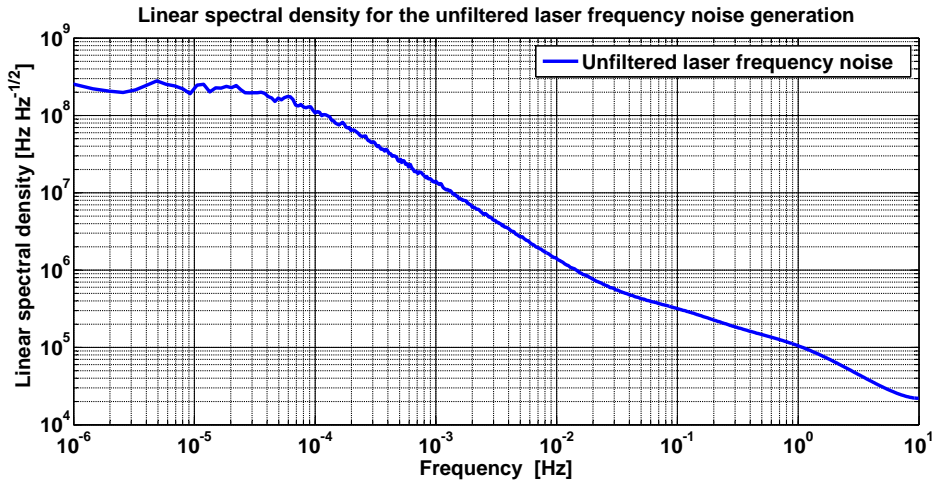
Linear spectral density for the unfiltered laser frequency noise generation

Figure 5.4: Linear spectral density $\tilde{\nu}_{\mathrm{unfilt}}$ of the unfiltered laser frequency noise. The noise for frequencies below 10^{-5} Hz has a level of $2 \cdot 10^8 \frac{\mathrm{Hz}}{\sqrt{\mathrm{Hz}}}$ and rolls off down to $10^5 \frac{\mathrm{Hz}}{\sqrt{\mathrm{Hz}}}$ at 1 Hz.

Linear spectral density comparison between filtered and unfiltered laser frequency noise generation
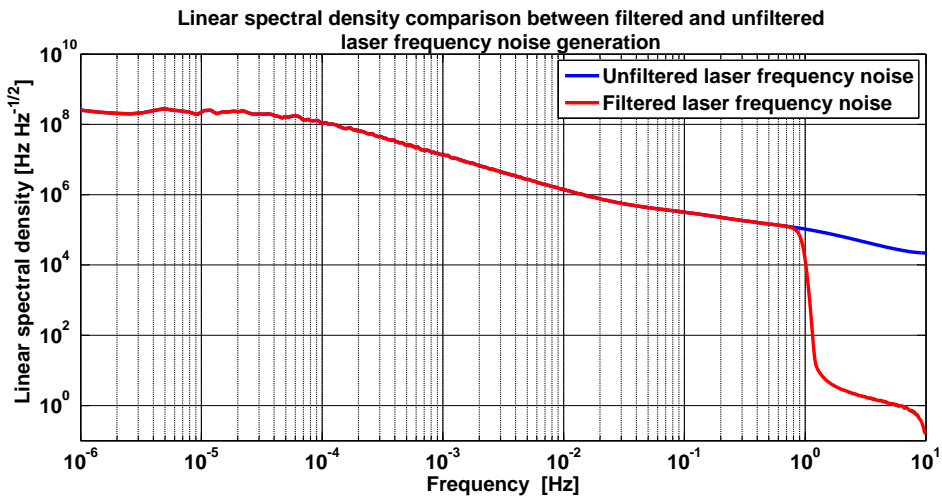

Figure 5.5: Linear spectral density $\widetilde{\nu}$ of the filtered laser frequency noise. The cutoff frequency lies at $f_{\mathrm{cut}} = 1$ Hz and noise from alias effects is hence suppressed. The choice of f_{cut} is suitable since LISA targets GW signals at frequencies between $0.1 - 100\,\mathrm{mHz} < f_{\mathrm{cut}}$.

Chapter 5

Note finally that first test results of the ranging accuracy are presented in Ch. 6. For this, *stabilised* lasers (with a flat noise spectrum in the frequency band of 5 mHz to 1 Hz) are used. They are generated according to the requirement Eq. (2.10a), i.e., having a noise level of $280 \frac{\text{Hz}}{\sqrt{\text{Hz}}}$ at 3 mHz and further relaxing towards low frequencies in accordance with the noise sensitivity function given in Eq. (2.7).

Test Mass and Optical Bench Displacement Noise

Besides laser frequency noise, TDISim includes additional phase noise from residual test mass and optical bench displacement. However, a 3-D simulation of that is extremely challenging and not the scope of this thesis (for this, we refer to [Inc15]). Instead, a simplified model was developed externally using LTPDA tools, and TDISim employs the output time series as input [Pac14]. Fig. 5.6 shows a sketch of the test mass model.
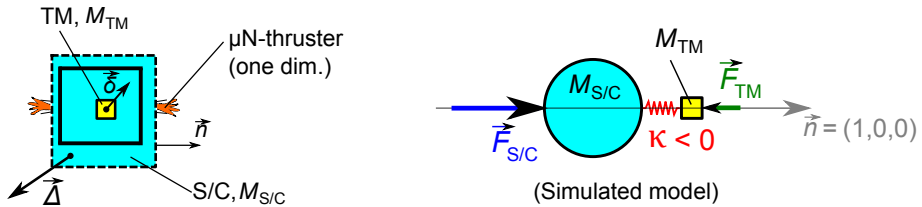

Figure 5.6: Left: Sketch of the TM housing. The test mass underlies relative displacements $\vec{\delta}$ (projected onto $\vec{n}$) due to gravity gradient and residual electro- and magnetostatic forces. Since the OBs are taken to be rigidly mounted on the S/C, the thruster firing will shake the OB and introduce further noise $\vec{\Delta}$, again projected on $\vec{n}$ to give displacement. Right: The simplified test mass model without housing consists of two point masses $M_{\text{S/C}}$ and M_{TM} (again $M_{\text{S/C}} \gg M_{\text{TM}}$) for the S/C and test mass. Both masses are modelled as connected by a spring (red) with negative spring constant, i.e., $\kappa < 0$, to mimic the gravitational attraction that can not be balanced out by the spacecraft payload. Residual TM forces F_{TM} act on M_{TM}, while the S/C position jitters by acceleration forces $F_{\text{S/C}}$ due to thruster firing. The sensitive axis is directed along $\vec{n} = (1,0,0)$.

The simplifications made are explained in the following. First, the TMs and spacecraft are taken as point masses with one degree of freedom only, and rotational effects of the TM with respect to the OB are disregarded. The masses are chosen to be $M_{\text{TM}} = 2 \, \text{kg}$ and $M_{\text{S/C}} = 800 \, \text{kg}$. Second, the gravitational coupling (e.g., the gravity gradient) between TM and S/C is modelled as a spring with negative spring constant $\kappa = -1 \cdot 10^{-7} \frac{\text{kg}}{\text{s}^2}$. That is, the further away the TM is from the CoM of the S/C, the weaker is the self gravity. All other influences on the relative TM position, e.g., of electro- and magnetostatic nature, are subsumed in residual forces F_{TM} directly acting on the test mass. The linear spectral density of the residual forces applied to the TM is presented in Fig. 5.7.
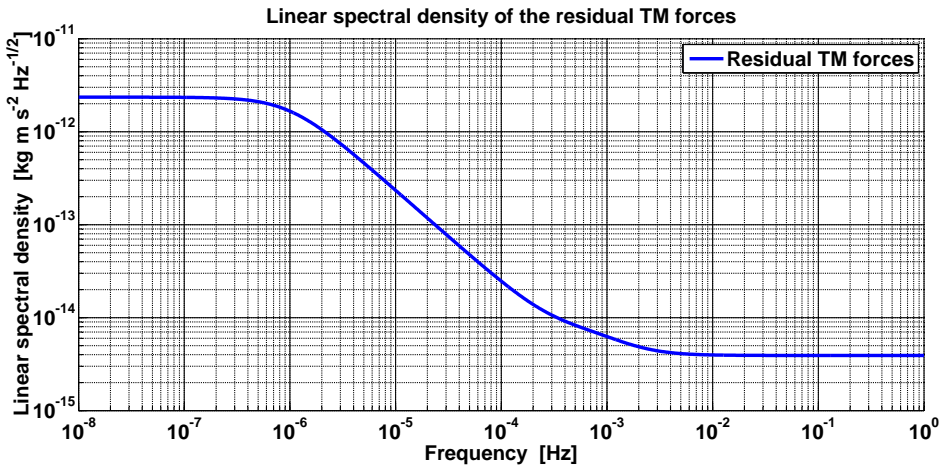
Figure 5.7: Linear spectral density $\widetilde{F}_{\text{TM}}$ of the residual forces acting on the TM in the simulation. For $M_{\text{TM}} = 2\,\text{kg}$, $\widetilde{a} = \frac{\widetilde{F}}{M_{\text{TM}}}$ fulfills the acceleration noise requirements from Ch. 2.
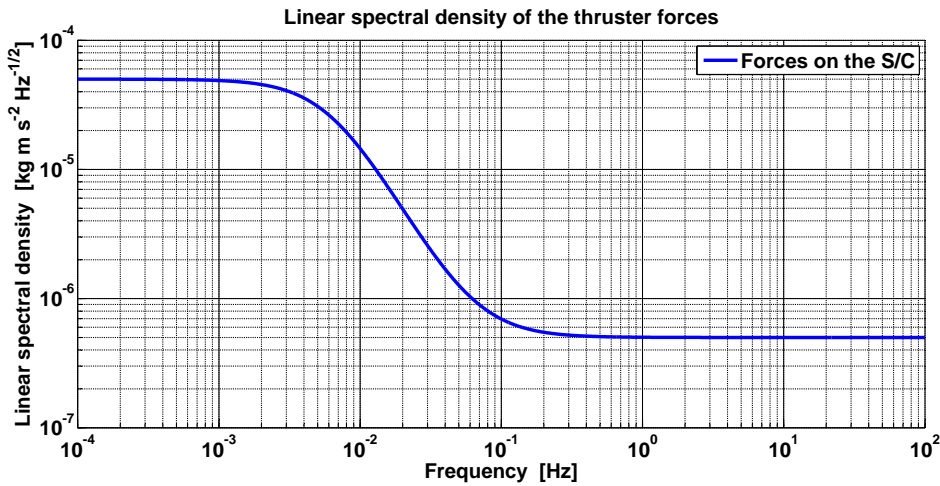
Figure 5.8: Linear spectral density $\widetilde{F}_{\text{S/C}}$ of the thruster forces acting directly on the S/C in the simulation. The forces are highly frequency-dependent in the target frequency band of $10^{-4}\,\text{Hz}$ to $10^{-1}\,\text{Hz}$ and vary between $5 \cdot 10^{-5}\,\frac{\text{N}}{\sqrt{\text{Hz}}}$ for low frequencies and $5 \cdot 10^{-7}\,\frac{\text{N}}{\sqrt{\text{Hz}}}$ towards higher frequencies.

Chapter 5

Forces acting on the spacecraft (e.g., by thruster firing), and, due to an assumed rigid connection, as well acting on the optical benches, are modelled by the linear spectral density presented in Fig. 5.8. By the weak spring connection, the forces also drive the test mass to a small amount. Note that any spatial limitations due to the test mass chamber walls are neglected, as is the case for drag-free control systems, too.

Third, the displacement is not projected onto the unit vectors $\vec{n}_i$ of light reception for each optical bench, but taken already as an 1-D displacement noise along the sensitive axis. Fourth, the displacements are not connected with the spacecraft setup in the simulation and hence not properly correlated. Instead, they are generated independently. This means that the two OBs on each S/C can move uncorrelated in the model which is not true in reality. Nonetheless, we use this simplified model in order to test the optical bench displacement noise suppression in the manner of the full removal algorithm from Ch. 4.

The outputs of the external TM simulation are six plus six noisy data streams for the optical bench displacement due to thruster activity, $\Delta_i(t) := \vec{n} \cdot \vec{\Delta}_i$, and for the relative OB-TM displacement, $\delta_i(t) - \Delta_i(t) = \vec{n} \cdot (\vec{\delta}_i - \vec{\Delta}_i)$, with $\delta_i(t) := \vec{n} \cdot \vec{\delta}_i$ and unit vector $\vec{n} = \vec{e}_1$. All outputs are generated with help of a so-called state space model. This model applies for linear and time-invariant systems [ZD76] and is described by two main equations:

$$\dot{\vec{X}}(t) = \boldsymbol{A} \cdot \vec{X}(t) + \boldsymbol{B} \cdot \vec{U}(t), \quad \vec{Y}(t) = \boldsymbol{C} \cdot \vec{X}(t) + \boldsymbol{D} \cdot \vec{U}(t). \tag{5.6}$$

The first vectorial equation describes the evolution of the state vector $\vec{X}(t)$ that contains here positions and velocities. $\boldsymbol{A}$ is called the system matrix that characterises the spring system shown in Fig. 5.6 and contains the corresponding first order ordinary differential equation coefficients. An external force on the system, e.g., the electro- and magnetostatic residual forces on the TMs, can be included by the input vector $\vec{U}(t)$. Thus, $\boldsymbol{B}$ is called input matrix. By solving the coupled differential equation for $\vec{X}(t)$, the evolution of the system can be determined. The second vectorial equation connects the system output vector $\vec{Y}(t)$ (e.g., the optical phase for the interferometric test mass readout) to the state vector by the output matrix $\boldsymbol{C}$. Here, readout noise contributions are taken into account by the feedthrough matrix $\boldsymbol{D}$. The detailed matrices $\boldsymbol{A}, \boldsymbol{B}, \boldsymbol{C}$ and $\boldsymbol{D}$ for the explained model are presented in [Pac14].

The simulation showed that in absence of a feedback control of the optical bench, the TM position relative to the OB will diverge. In other words, the TM will collide after few minutes of simulation time with the housing, which of course is unwanted. Therefore, a feedback control loop simulating the counteracting thruster firing was designed and implemented. It could be shown that even in the presence of OB noise and residual forces that directly act on the TM (fulfilling $\tilde{a} < 3 \cdot 10^{-15} \frac{\frac{\text{m}}{\text{s}^2}}{\sqrt{\text{Hz}}}$ (Sec. 2.3.2)), it is possible to hold the relative position of OB and TM constant to a

level of $\approx 10^{-8} \frac{\text{m}}{\sqrt{\text{Hz}}}$ within the frequency band of $10^{-4} - 10^{-1}$ Hz [Pac14]. It further emerged that the displacement noise of the optical bench is the limiting factor. The results of the TM and OB modelling in TDISim are presented in Ch. 6.

Readout Noise

A reasonable model for readout noise is white noise according to Sec. 2.3.1, and can thus be described by a noise spectral density independent of the frequency. In TDISim, different noise magnitudes are implemented for the science, reference and test mass interferometers accounting for the power loss through inter-spacecraft exchange and fibre transmission. The magnitudes for reference and test mass interferometer are determined by ground-based experimental simulations of the LISA optical bench. TDISim uses the experimentally verified numbers given in [TDB$^+$12] which correspond to the real values onboard. For the reference interferometer, it was found $P_{\text{LO}} = 1.33\,\text{mW}$ and $P_{\text{sig}} = 0.88\,\text{mW}$. The values for the test mass IFO are $P_{\text{LO}} = 0.73\,\text{mW}$ and $P_{\text{sig}} = 20.6\,\mu\text{W}$. Inserting these in Eqn. (2.4a), (2.5a) and (2.6a) yields the readout noise levels in terms of phase noise for each interferometer separately:

$$\widetilde{\phi}^s_{\text{readout}} \quad = \quad 6.1 \cdot 10^{-5} \frac{\text{rad}}{\sqrt{\text{Hz}}}\,, \tag{5.7a}$$

$$\widetilde{\phi}^\varepsilon_{\text{readout}} \quad = \quad 2.4 \cdot 10^{-7} \frac{\text{rad}}{\sqrt{\text{Hz}}}\,, \tag{5.7b}$$

$$\widetilde{\phi}^\tau_{\text{readout}} \quad = \quad 4.4 \cdot 10^{-8} \frac{\text{rad}}{\sqrt{\text{Hz}}}\,. \tag{5.7c}$$

Remarkably, the readout noise levels of the reference and test mass interferometer are by two orders of magnitude or more lower than the readout noise level of the science interferometer. This is due to the low light power received from the distant spacecraft ($\approx 10^2\,\text{pW}$), while in both reference and TM interferometer the local lasers are interfered. There, the optical power is by four to six orders of magnitude higher and thus the shot noise as the main readout noise contribution lower (and so is the overall readout noise).

Based on the frequency-independent linear spectral densities (5.7a) – (5.7c), TDISim generates time series for the readout noise in terms of phase, i.e., N_i^s, N_i^τ and N_i^ε. Note finally that the readout noise level in the science interferometers is comparable to the single-link 10 pm-requirement (Sec. 2.3.2).

5.2.5 Onboard Data Streams

We have now all ingredients (GW, noise) together to proceed to the last step in data generation: the formation of the phasemeter output data streams. As stated in Sec. 5.2.1, the PM output is assumed to be equal to the anti-alias filtered PD output, since clock noise and any beat-note frequency polarity is completely neglected in TDISim.

Chapter 5

Thus, the telemetered data from the PM consists of GW signal, laser frequency noise, optical bench displacement noise, relative displacement noise between OB and TM, and readout noise. It is given according to Eqn. (4.5a) – (4.5h) by

$$
\begin{array}{rcll}
s_1^{\text{sim}}(t) & = & H_1 + \boldsymbol{\mathcal{D}_3^{\text{sim}}} p_{2'} - p_1 + \frac{2\pi\nu_0}{c}\left(\boldsymbol{\mathcal{D}_3^{\text{sim}}}\Delta_{2'} - \Delta_1\right) + N_1^s \,, & (5.8a) \\[4pt]
s_{1'}^{\text{sim}}(t) & = & H_{1'} + \boldsymbol{\mathcal{D}_{2'}^{\text{sim}}} p_3 - p_{1'} - \frac{2\pi\nu_0}{c}\left(\boldsymbol{\mathcal{D}_{2'}^{\text{sim}}}\Delta_3 - \Delta_{1'}\right) + N_{1'}^s \,, & (5.8b) \\[4pt]
\varepsilon_1^{\text{sim}}(t) & = & p_{1'} - p_1 + 2\cdot\frac{2\pi\nu_0}{c}\left(\delta_1 - \Delta_1\right) + N_1^\varepsilon \,, & (5.8c) \\[4pt]
\varepsilon_{1'}^{\text{sim}}(t) & = & p_1 - p_{1'} - 2\cdot\frac{2\pi\nu_0}{c}\left(\delta_{1'} - \Delta_{1'}\right) + N_{1'}^\varepsilon \,, & (5.8d) \\[4pt]
\tau_1^{\text{sim}}(t) & = & p_{1'} - p_1 + N_1^\tau \,, & (5.8e) \\[4pt]
\tau_{1'}^{\text{sim}}(t) & = & p_1 - p_{1'} + N_{1'}^\tau \,, & (5.8f)
\end{array}
$$

and others cyclic. $\boldsymbol{\mathcal{D}_i^{\text{sim}}}$ emphasises the numerical nature of the delay operator that makes it possible for the user to switch between $\widehat{\mathbf{D}}$ and $\boldsymbol{\mathcal{D}}$. The optical bench displacement as well as the test mass noise (in terms of optical phase) is uncorrelated and sensed by lasers with a central frequency of ν_0. Furthermore, since the displacements are simulated in a 1-D model, we need to account for the missing scalar products of $\vec{\delta}_i$ and $\vec{\Delta}_i$ with the unit vectors $\vec{n}_j$ pointing along the arms, as given in Eqn. (4.5a) – (4.5h). Therefore, minus signs are added for the displacement noise contributions in the signals on primed optical benches.

Note again that we do not simulate the sideband measurements, since no clock tone transfer chain is implemented. Moreover, beat-note polarities resulting from the frequency plan (Ch. 4) are completely neglected in TDISim. Finally, the phase signals (5.8a) – (5.8f) are then fed to the post-processing algorithm.

5.2.6 Full Removal Algorithm and Time-Delay Interferometry

In this section, we will explain the central part of the simulation: implementation of the full removal algorithm and TDI. First, we will have a closer look at the time-delay operators and then proceed to the full removal algorithm.

The Time-Delay Operators

A key algorithm for the TDI simulation is the time delay of data series. Therefore, it is essential to have light travel times with maximum accuracy. In our simulation, two independent methods are implemented that determine the light travel time and are explained in Sec. 1.4.4. That is, an iterative solution according to [MG11] and a calculation based on the results of [CRVP05] can be used individually. Note that in reality, the light travel time will be estimated from the PRN ranging signal.

The iterative algorithm converges after maximal seven runs such that the necessary precision of the order $3\,\text{m} \approx 10^{-8}\,\text{s}$ is reached for TDI functionality [MMS12]. In the more sophisticated analytical approach, which is used to obtain the results of Ch. 6, the expansion can be executed up to order one in $\epsilon = \frac{GM_\odot}{rc^2}$ and gives corrections of

10^{-8} s. The expansion term of order $\epsilon^{\frac{3}{2}}$ (also neglected in Sec. 1.4.4) is $\approx 10^{-12}$ s, and this exceeds the necessary exactness and is thus neglected. For our purpose, the directional vectors of light incidence, $\vec{n}_i$, can be considered as unaffected by the higher orders of the expansion, because stretching even in the order of $\epsilon^{\frac{1}{2}}$ is way beyond the required accuracy, as discussed in Sec. 2.5.3.

The operators $\widehat{\mathbf{D}}$ and $\boldsymbol{\mathcal{D}}$ do not *backtrack* a measured signal rather than *shift* a time series by a chosen delay time determined by the light travel times $T_{0,i}(t)$. Since these are in general not multiples of $\frac{1}{f_{\text{samp}}}$ (i.e., the temporal distance between two samples), the data must be interpolated between samples by high order Lagrangian interpolation [SWSV04] (commonly called fractional delay filtering). This is schematically shown in Fig. 5.9.
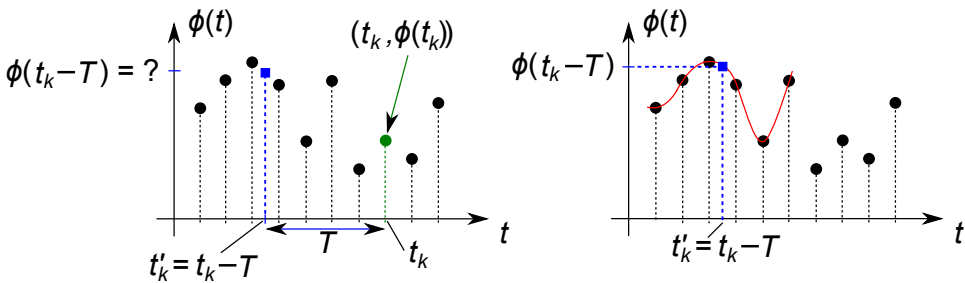

Figure 5.9: Interpolation scheme for the delay of the time series. Data at time t_k (green) needs to be delayed by an arbitrary time T. Since at $t'_k = t_k - T$ no data point is existing, interpolation of the time series at time t'_k is needed (marked by the blue box). Therefore, a polynomial (red) is constructed, e.g., by Lagrangian interpolation, and then evaluated at time t'_k to give the interpolated value $\phi(t'_k)$.

For the LISA case, the delay time is given by the light travel time per link. Each data point $(t_k, \phi(t_k))$ (with $k = 1, \ldots, N$) of the time series $\phi(t)$ to be delayed is thus interpolated at a time $t'_k = t_k - T_{0,i}(t_k)$, where N denotes the overall number of samples within the time series. In this notation, t'_k marks the temporary interpolation time stamp of the k-th data point, while t_k is the time stamp of the k-th data point, and $T_{0,i}(t_k)$ denotes the light travel time of the corresponding arm i without GW at time t_k. We will now explain the implementation of the delay operators.

For the different TDI generations, we should distinguish between the time-delay operators $\widehat{\mathbf{D}}$ and $\boldsymbol{\mathcal{D}}$ (Sec. 3.1.4). Note that in the current version of TDISim, no analytical approximation using the semi-constant time delay is implemented. The first kind of operator, $\widehat{\mathbf{D}}$, accounts for constant armlengths in a static LISA constellation. The corresponding delay algorithm takes each data point from a time series and shift it by the same amount of (pre-calculated light travel) time, even in the case of multiple application. For example, data need to be shifted by the arms 1 and 2 with light travel time $T_{0,1} = 16.6605$ s and $T_{0,2} = 16.7594$ s. Thus, the

algorithm shifts each data point (no matter at which time stamp) by the constant amount of $T = T_{0,1} + T_{0,2} = 33.4199\,\text{s}$ and has thus to interpolate the data series at $t'_k = t_k - 33.4199\,\text{s}$ for all k. Fig. 5.10 illustrates the procedure.
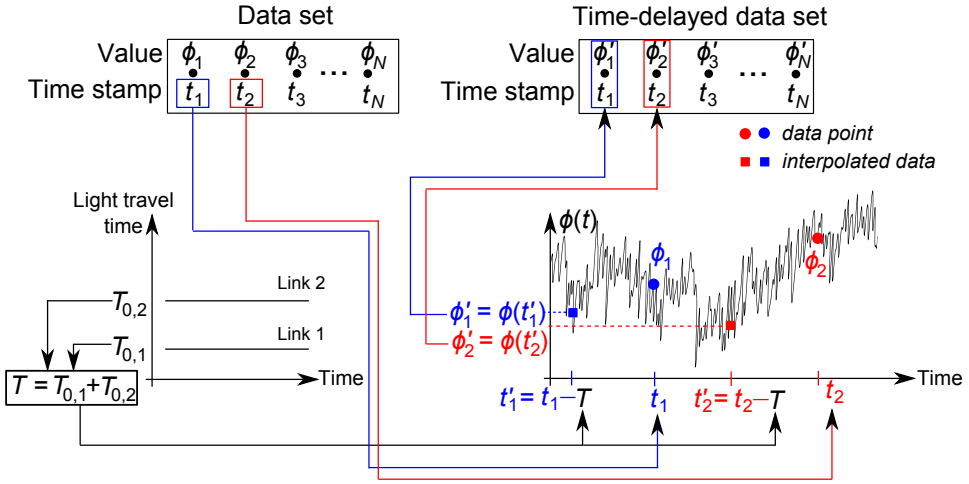

Figure 5.10: Graphical illustration of the time-*in*dependent time-delay operator for the data shift by constant links 1 and 2. The time series $\phi(t)$ to be time-delayed is given by the data set $(t_k, \phi_k) = (t_k, \phi(t_k))$ with $k = 1, \ldots, N$ and the number of data points N. The time-independent time-delay algorithm takes the pre-calculated light travel times per link, $T_{0,1}$ and $T_{0,2}$, directly without interpolation and computes the sum $T = T_{0,1} + T_{0,2}$. For each new temporary time stamp $t'_k = t_k - T$, the signal $\phi(t)$ is interpolated (marked by boxes). That is, e.g., for t_1 (blue arrows), the data series $\phi(t)$ has to be interpolated at time $t'_1 = t_1 - T$ and gives the data point $(t_1, \phi'_1) = (t_1, \phi(t_1 - T))$ of the delayed series $\phi(t - T)$. The same procedure is performed with all other data points yielding a time-shifted copy $\phi(t - T)$ of the input series. Note that the original time signature $t_1, \ldots, t_N$ is preserved.

The implementation of the time-dependent time-delay operator, $\mathcal{D}$, is in general different. For single application, it uses a scheme as follows. We need to compute the corresponding light travel time for *each* data point separately due to the time-dependence of the LISA armlengths and hence the time dependence of the shifting time. That is, e.g., the data point at time $100\,\text{s}$ needs to be shifted in the previously explained interpolation manner by the light travel time $T_{0,2}(100\,\text{s}) = 16.6372694\,\text{s}$, but data at $200\,\text{s}$ must be shifted by $T_{0,2}(200\,\text{s}) = 16.6372698\,\text{s}$. Since we account for ns accuracy for TDI functionality, this change in light travel time can not be neglected. A schematic of the time-dependent time-delay operator is shown in Fig. 5.11.
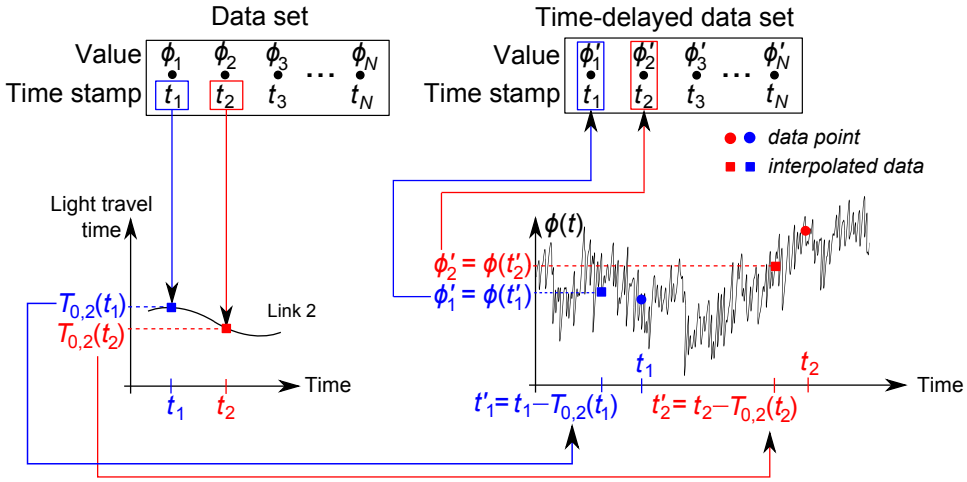
Figure 5.11: Schematic for a single time-dependent time delay operation step. The procedure is shown for data samples with the time stamps t_1 and t_2, but is performed in a similar manner for all other data points. The algorithm takes t_1 and interpolates the light travel time $T_{0,2}(t)$ at time t_1, yielding $T_{0,2}(t_1)$. This value is processed to the time-shifting operation, where the phase signal function $\phi(t)$ is interpolated at time stamp $t_1' = t_1 - T_{0,2}(t_1)$. The value $\phi_1' = \phi(t_1')$ is finally returned and forms together with the origin time stamp t_1 the first data point (t_1, ϕ_1') of the delayed data series. The same procedure is performed with all other data points.

Multiple Time-Dependent Time-Shifts

In the case of multiple delays, the algorithm for time-dependent time delays gets much more complex since the nested delay operation defined in Eq. (3.16b) has to be used and the time delay needs to be computed recursively. This in turn means more interpolations. In order to form, e.g., $\boldsymbol{\mathcal{D}_2}\boldsymbol{\mathcal{D}_1}\phi(t) = \phi_{;\mathbf{12}} = \phi\left(t - \frac{L_2(t)}{c} - \frac{L_1\left(t - \frac{L_2(t)}{c}\right)}{c}\right)$, the algorithm has to interpolate $L_2(t)$ at time t, furthermore $L_1(t)$ at time $t - \frac{L_2(t)}{c}$ and finally ϕ at time $t' = t - \frac{L_2(t)}{c} - \frac{L_1\left(t - \frac{L_2(t)}{c}\right)}{c}$. Note that this becomes numerically expensive since this scheme has to be applied for any data point separately. It gets even more complex for threefold delays, fourfold delays etc. Furthermore, it is remarkable that the algorithm first interpolates L_2 at time t and then L_1 at the delayed time $t - \frac{L_2(t)}{c}$, though one would expect it on the first sight vice versa, since in $\phi_{;\mathbf{12}}$ the second index is the time-shift temporally farther away in the past. The nested algorithm with respect to two links is illustrated in Fig. 5.12.
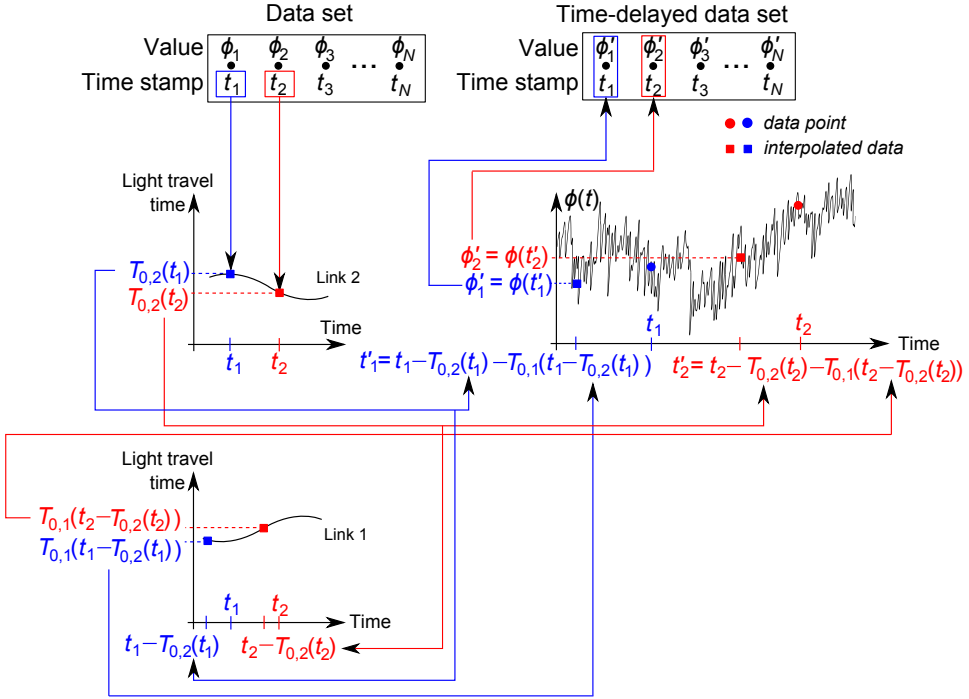
Chapter 5

Figure 5.12: Scheme for multiple time-dependent time delays. The procedure is again shown for the data points with time stamps t_1 and t_2, but is performed in a similar manner for all other data points. The algorithm takes t_1 and computes by interpolation routines the light travel time for link 2 at time t_1, that is $T_{0,2}(t_1)$. This value is needed for the interpolation of the light travel time for link 1 at time $t_1 - T_{0,2}(t_1)$ and gives $T_{0,1}(t_1 - T_{0,2}(t_1))$. This is then processed to the time-shifting operation, where the phase signal function $\phi(t)$ is interpolated at time stamp $t_1' = t_1 - T_{0,2}(t_1) - T_{0,1}(t_1 - T_{0,2}(t_1))$. Note that $T_{0,2}(t_1)$ is here again needed and taken from the first light travel time interpolation step. The value $\phi_1' = \phi(t_1')$ is finally returned and forms together with the origin time stamp t_1 the first data point (t_1, ϕ_1') of the delayed data series replica $\phi_{;12}$. The same procedure is performed with all other data points. Analogously, the procedure works for threefold, fourfold, etc. delays.

Full Removal Algorithm

After generation of the onboard data $s_i^{\mathrm{sim}}(t), \tau_i^{\mathrm{sim}}(t)$ and $\varepsilon_i^{\mathrm{sim}}(t)$ (Sec. 5.2.5) by properly time-shifting and combining the noise contributions and the gravitational wave phase signal, TDISim combines these signals to form at first the optical bench noise free combinations

$$\xi_1^{\mathrm{sim}}(t) \;=\; s_1^{\mathrm{sim}}(t) - \frac{\varepsilon_1^{\mathrm{sim}}(t) - \tau_1^{\mathrm{sim}}(t)}{2} - \frac{\boldsymbol{\mathcal{D}_3^{\mathrm{sim}}} \left[\varepsilon_{2'}^{\mathrm{sim}}(t) - \tau_{2'}^{\mathrm{sim}}(t) \right]}{2}, \quad (5.9\mathrm{a})$$

$$\xi_{1'}^{\mathrm{sim}}(t) \;=\; s_{1'}^{\mathrm{sim}}(t) - \frac{\varepsilon_{1'}^{\mathrm{sim}}(t) - \tau_{1'}^{\mathrm{sim}}(t)}{2} - \frac{\boldsymbol{\mathcal{D}_{2'}^{\mathrm{sim}}} \left[\varepsilon_3^{\mathrm{sim}}(t) - \tau_3^{\mathrm{sim}}(t) \right]}{2}, \quad (5.9\mathrm{b})$$

and cyclic, according to Eqn. (4.10a) and (4.10b) with the constant wavelengths $\lambda_1 = \lambda_{1'} = \ldots = \lambda_{3'} = 1064\,\text{nm}$ and neglected beat-note polarity factors, i.e., $\theta_i^j = +1$ for all i and j.

The algorithm proceeds with the formation of TDI input data. Due to the complete neglection of clock jitter in the current simulation, the combinations $Q_i(t)$ given by Eqn. (4.12a) and (4.12b) can already be used as TDI input,

$$\eta_1^{\text{sim}}(t) \quad = \quad \xi_1^{\text{sim}}(t) + \frac{\boldsymbol{\mathcal{D}_3^{\text{sim}}}\left[\tau_{2'}^{\text{sim}}(t) - \tau_2^{\text{sim}}(t)\right]}{2}\,, \tag{5.10a}$$

$$\eta_{1'}^{\text{sim}}(t) \quad = \quad \xi_{1'}^{\text{sim}}(t) - \frac{\tau_{1'}^{\text{sim}}(t) - \tau_1^{\text{sim}}(t)}{2}\,, \tag{5.10b}$$

and cyclic. $\eta_i^{\text{sim}}(t)$ contains now the GW signal and laser frequency noise of the three lasers on OB 1, 2 and 3. It was shown in Ch. 3 that these can be successfully removed by the Time-Delay Interferometry combinations given in Sec. 3.3. Currently implemented for TDI 2.0 are the Michelson variables $X_{\underline{i}}$, Sagnac variables $\alpha_{\underline{i}}$ and fully symmetric Sagnac combinations $\zeta_{\underline{i}}$, all making use of multiple time delays as seen in Sec. 3.3. For TDI 1.0, all combinations from Sec. 3.2 can be computed. Before we present the results of the simulations in Ch. 6, we will give a brief overview about the code structure of TDISim in the next section.

5.3 Code Overview

The prototype simulator TDISim consists of two main scripts which are called `SCRIPT_TDI_10_w_TM.m` and `SCRIPT_TDI_20_w_TM.m` and that compute TDI outputs in the previously described manner. The first script calculates the output in the case of TDI 1.0 with optional contribution of the externally generated test mass signal, the second does the same in the case of 2nd generation TDI. Besides, several scripts for analysis and aside-simulations can be used which will not be regarded here. Each script executes global functions and methods provided by the three classes `gw.m`, `sc.m` and `link.m`. TDISim is written such that it can use several routines and functions provided by the LTPDA toolbox. This implies the usage of analysis objects in the code, wherever possible.

In the following, we will illustrate the functional structure of the scripts and explain the three classes. Furthermore, the parameter setting file `FLAG.m` is elucidated in detail in order to introduce the reader to the features provided by the simulation prototype TDISim. The section closes with a flow diagram of the overall simulation structure. For a more detailed explanation of the implemented methods and functions, we refer to [Sch13].

5.3.1 The Executing Scripts

Both scripts `SCRIPT_TDI_10_w_TM.m` and `SCRIPT_TDI_20_w_TM.m` consist mainly of five blocks. The first one sets the simulation parameters as shown in listing 5.1.

Chapter 5

```
1   y = 0; m = 0; w = 0; d = 0; h = 0; min = 0; sec = 10000;
2   T_sim = y*31536000 + m*2419200 + w*604800 + d*86400 + h*3600 + min*60 +sec;
3
4   L0 = FLAG('STANDARD_LISA_ARMLENGTH');
5
6   % default sampling rates
7   f_sampl = 3;
8   f_sampl_pos = 1;
9   f_sampl_noise = 20;
10  f_sampl_pd = 3;
```

Listing 5.1: Simulation parameter settings in TDISim. Line 1 and 2 determine the simulation time, line 4 (if needed for a static LISA constellation) the nominal armlength for S/C construction. This is followed by the default sampling rate settings in line 7 – 10, where we distinguish between the normative sample rate `f_sampl`, the orbit sample rate `f_sampl_pos`, the noise and GW generation sample rate `f_sampl_noise` and the detection sample rate at the photodetector, `f_sampl_pd`. All frequencies are given in units of Hz.

```
1   monochrGW = gw(1e-20,0,-pi/6,pi/4,0,4e-3);
2
3   p_sc1 = plist(...
4       'constellation','series',...
5       'sc_num',1, ...
6       'T_start', 0, ...
7       'T_end', T_sim, ...
8       'f_sampl_pos', f_sampl_pos, ...
9       'f_sampl_noise', f_sampl_noise, ...
10      'f_sampl_pd', f_sampl_pd, ...
11      'OB_noise', true, ...
12      'TM_noise', true, ...
13      'laser_lock', FLAG('LASER_LOCK'));
14
15  sc1 = sc(p_sc1);
```

Listing 5.2: Spacecraft object construction in TDISim. Line 1 creates the GW as an object of the class `gw.m`. This object comprises the gravitational wave tensor with strain amplitudes $h_+ = 10^{-20}$, $h_\times = 0$, and incident angles $\theta = -\frac{\pi}{6}$, $\phi = \frac{\pi}{4}$ according to Fig. 1.4. Furthermore, the tilt angle between the detector plane and GW plane, ψ, is set to zero, and the GW frequency is defined as $f_{\mathrm{gw}} = 4\,\mathrm{mHz}$. In lines 3 – 13, the constructor parameter list `p_sc1` for S/C 1 (assigned by `'sc_num'`) is defined. The constellation parameter in line 4 is set to `'series'`, which implies the orbit construction relying on the ESA orbits. Lines 6 – 10 use the previously chosen simulation parameters (cf. listing 5.1). In line 11 and 12, the user can explicitly 'turn off' the OB and TM displacement noise. Next, in line 13, the lasers on adjacent optical benches can be locked to reduce the complete detector system to a three free-running laser system. Finally, in line 15, the spacecraft object is built in the class `sc.m` (Sec. 5.3.2) with the settings of the parameter list `p_sc1`.

Either the parameters are imported from `FLAG.m`, the content of which is explained in detail in Sec. 5.3.3, or the flag parameters are overwritten by manual settings within the scripts.

The second block of the simulation script builds objects of the spacecraft class `sc.m`. This includes orbit computations (Sec. 5.2.2) and intrinsic noise generation according to the models of Sec. 5.2.4. Furthermore, the GW tensor is built. The MATLAB commands are exemplarily shown for S/C 1 in listing 5.2.

In the third branch, the six laser link objects are constructed with help of the class `link.m`. It provides the phasemeter signals of each OB placed at the end of the relative link as presented in listing 5.3. The PM output consists of a gravitational wave signal, laser frequency noise as well as readout noise, optical bench and test mass displacement noise (if called in the S/C constructor, listing 5.2).

The fourth block shown in listing 5.4 provides the TDI input data formed by the photodetector signals according to Sec. 5.2.6. Furthermore, the various TDI combinations are formed. Finally, in the fifth branch, the TDI output data is monitored and stored. In order to compute the power spectral densities, at the beginning of the data series (the so-called initialisation phase) a splitting is indispensable, as we will see in Ch. 6. The split procedure is exemplarily shown for X_1 in listing 5.5. In the next section, the three classes are explained.

5.3.2 The TDISim Classes

The executing scripts `SCRIPT_TDI_10_w_TM.m` and `SCRIPT_TDI_20_w_TM.m` make use of several methods and functions (e.g., for interpolation, light travel time computation, time delay). These methods are called rarely from the simulation script, but instead from the classes used to form the desired spacecraft, gravitational wave and link objects (Sec. 5.3.1). We will now give a brief introduction to the classes `sc.m`, `gw.m` and `link.m`. The properties of each are illustrated in Fig. 5.13.

The class `gw.m`

`gw.m` provides the GW tensor $\boldsymbol{h}(t,\vec{x})$ which is used in a later step for the projection onto the laser links yielding the light travel time variation $\Delta T_i(t)$ due to gravitational waves. For the computation of $\boldsymbol{h}(t,\vec{x})$, the class constructor calculates at first the polarisation basis vectors $\hat{u}$, $\hat{v}$ and $\hat{k}$ given in Eq. (1.23) and then the GW polarisation tensors $\boldsymbol{\epsilon}_+$ and $\boldsymbol{\epsilon}_\times$ according to Eqn. (1.22) and (1.24).

The gravitational wave tensor is computed with help of `h(obj,pos,time)`. The first argument of this method has to be a GW object, followed by a position of the spacecraft marking the point of GW signal detection, and a time coordinate. The output of `h` is then the time-dependent tensor from Eq. (5.2).

Chapter 5

```
1  L_3 = link(sc2,sc1,'ccw',monochrGW);
2  s1 = L_3.s;
3  tau1 = L_3.tau;
4  e1 = L_3.e;
```

Listing 5.3: Link object construction in TDISim, exemplarily for link L_3. Line 1 defines L_3 as the link between S/C 2 and 1 in a counter-clockwise manner ('ccw'), influenced by the incident GW described by the object `monochrGW`. The phasemeter outputs $s_1^{\text{sim}}(t)$, $\tau_1^{\text{sim}}(t)$ and $\varepsilon_1^{\text{sim}}(t)$ are generated in lines 2 – 4 according to Sec. 5.2.5.

```
1  xi1 = s1 - (e1 - tau1)/2 - delayCombination_ao(e2prime - tau2prime,L_3)/2;
2  xi1prime = s1prime - (e1prime - tau1prime)/2 - delayCombination_ao(e3 -
       tau3, L_2p)/2;
3  %[...] xi2,..., xi3prime cyclic
4  eta1_ao = xi1 + 0.5*delayCombination_ao(tau2prime-tau2,L_3);
5  eta1prime_ao = xi1prime - 0.5*(tau1prime - tau1);
6  %[...] eta2_ao,..., eta3prime_ao cyclic
7  X1_ao = ( eta1prime_ao - eta1_ao ) ...
8      + ( delayCombination_ao(eta3_ao,L_2p) - delayCombination_ao(
           eta2prime_ao,L_3) ) ...
9      + ( delayCombination_ao(eta1_ao,[L_2p L_2]) - delayCombination_ao(
           eta1prime_ao,[L_3 L_3p]) ) ...
10     + ( delayCombination_ao(eta2prime_ao,[L_2p L_2 L_3]) -
           delayCombination_ao(eta3_ao,[L_3 L_3p L_2p]) ) ...
11     + ( delayCombination_ao(eta1_ao,[L_2p L_2 L_3 L_3p]) -
           delayCombination_ao(eta1prime_ao,[L_3 L_3p L_2p L_2]) ) ...
12     + ( delayCombination_ao(eta2prime_ao,[L_2p L_2 L_3 L_3p L_3]) -
           delayCombination_ao(eta3_ao,[L_3 L_3p L_2p L_2 L_2p]) ) ...
13     + ( delayCombination_ao(eta1prime_ao,[L_2p L_2 L_3 L_3p L_3 L_3p]) -
           delayCombination_ao(eta1_ao,[L_3 L_3p L_2p L_2 L_2p L_2]) ) ...
14     +( delayCombination_ao(eta3_ao,[L_2p L_2 L_3 L_3p L_3 L_3p L_2p]) -
           delayCombination_ao(eta2prime_ao,[L_3 L_3p L_2p L_2 L_2p L_2 L_3]))
           ;
```

Listing 5.4: TDI combinations formation shown here in parts (missing parts abbreviated by the comment `%[...]`), since the synthetic data streams are cyclic in the indices. The core delay operator used for the construction of $\xi_i(t)$ (line 1 and 2, according to Eq. (5.9a) and (5.9b)), $\eta_i(t)$ (line 4 and 5, according to Eq. (5.10a) and (5.10b)) and $X_1(t)$ (lines 7 – 14) is implemented in a global function `delayCombination_ao.m` that takes any time series analysis object as the first input slot, followed by a vector of link objects defining the time delays. Note here that the ordering of the delays is reverse to that of Eq. (3.39). This is due to the recursive computation of the delays and works as presented previously in the float diagram in Fig. 5.12.

```
1  t0 = input('start time: ');
2  t1 = input('end time: ');
3  split_pl = plist('times', [t0 t1]);
4  X1_ao_s = X1_ao.split(split_pl);
```

Listing 5.5: Time series splitting in order to remove the initialisation phase ($\approx 140\,\text{s}$). The procedure is exemplarily shown for X_1. Line 1 and 2 wait for keyboard input (time in seconds), which are used for the splitting parameter list `split_pl` in line 3. The cut is exhibited in line 4 and returns a splitted time series `X1_ao_s`, excluding data points within the time interval from `t0` to `t1`.

The class `sc.m`

The constructor of `sc.m` produces all relevant S/C data for TDISim. First of all, the orbits are computed according to Sec. 5.2.2. This depends on the S/C constellation which is defined by the parameter `'constellation'` (choices are `'static'`, `'algebraic_LISA'`, and `'series'`) in the executing scripts (Sec. 5.3.1). Each spacecraft object gets the computed position time series $\vec{x}_i(t)$ assigned. Furthermore, for the ESA orbits (`'series'`), the velocities of each S/C are provided and assigned to the spacecraft object, too. They are needed for the computation of the analytically approximated light travel times of order $\epsilon^{\frac{1}{2}}$ and ϵ^1 in the `link.m` class, as explained below.

The next step in the S/C class constructor comprises the intrinsic noise source generation for each OB, i.e., laser frequency noise, readout noise, TM and OB displacement noise. Laser frequency noise is generated as explained in Sec. 5.2.4 by a predefined pole-zero model (Eq. (5.5)), is then anti-alias filtered and converted to phase by integration. Furthermore, readout noise contributions are introduced and as well filtered to prevent alias effects. The optional TM and OB displacement noise are read in from the externally generated phase time series `phase_pos_SC_1_cw.mat` and `phase_pos_TM_1_cw.mat` (similar for the counter-clockwise pointing optical benches denoted previously with a prime). It is generally possible to save and reload any noise series. Note that they are assigned separately to the spacecraft object as time series.

The class `link.m`

The class `link.m` provides upmost the phasemeter outputs $s_i^{\text{sim}}(t)$, $\tau_i^{\text{sim}}(t)$ and $\varepsilon_i^{\text{sim}}(t)$ (Eqn. (5.8a) – (5.8f)). In the first step of the constructor, the GW optical phase shift along the respective link is computed. Therefore, the transmitted GW object provides the gravitational wave tensor for the computation of $\Delta T_i(t)$ according to Eq. (5.4) by the link class method `strainOfSpace`, which is then translated to phase $H_i(t)$. For $\Delta T_i(t)$, the S/C positions $\vec{x}_i(t)$ are taken from the previously executed spacecraft initialisation in `sc.m`.
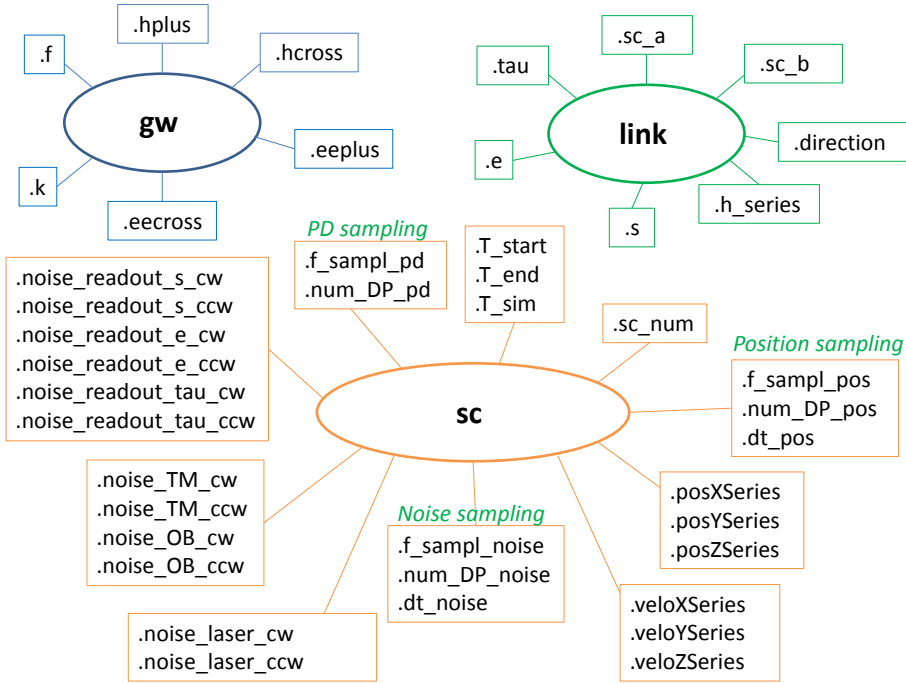
Chapter 5

Figure 5.13: Object properties of `gw.m`, `link.m` and `sc.m`. The GW object is described by the strain amplitudes h_+ and $h_\times$, the polarisation tensors ϵ_+ and $\epsilon_\times$ (`gw.eepluss` and `gw.eecross`), the wave direction vector $\hat{k}$ and the gravitational wave frequency, f_{gw}. Next, the link class object is characterised by information about sending and receiving spacecraft (`link.sc_a` and `link.sc_b`, respectively), the link direction, i.e., clockwise ('cw') or counterclockwise ('ccw'), and the specific GW signal as a time series (`link.h_series`). Furthermore, the OB interferometric measurements $s_i^{\text{sim}}(t)$, $\varepsilon_i^{\text{sim}}(t)$ and $\tau_i^{\text{sim}}(t)$ are assigned. Objects of the class `sc.m` have various properties. At first, the regarded S/C is numbered by `sc.sc_num` and the simulation time with start and end time is assigned. The next properties are information about the S/C position sampling, noise sampling and PD sampling in terms of sampling frequencies, number of datapoints and stepwidths. The time series `sc.posXSeries` and `sc.veloXSeries` provide the first component of the S/C position and velocity (similarly for the other components). Finally, time series for the laser frequency noise, TM/OB displacement noise and readout noise for clockwise and counter-clockwise pointing OBs are assigned to the spacecraft objects.

The second step comprises all phasemeter outputs, the noise contributions which are defined within `FLAG.m`. For the science IFO PM output, a time-delayed replica of the laser frequency noise as well as for the OB displacement noise (both from the distant spacecraft) is built with help of the global function `delayCombination_ao.m`. Note here that this is the same function as used for the TDI combination formation. As explained in Sec. 5.2.1, the program is cheating here, since in reality, the

synthesised time delays within TDI and the physical time delays in the measurements are not the same. For the sake of simplicity, however, TDISim takes them to be exactly known.

In the third and final step of the constructor, the single phase contributions of the GW signal, time-delayed and instantaneous laser noise, readout noise, TM and OB noise are combined to form the phasemeter outputs, for each spacecraft on the clockwise and counter-clockwise pointing optical bench.

Besides the described functionality, `link.m` provides the useful method to determine the light travel time along each link, which is crucial for the global delay function. TDISim computes $T_{0,i}(t)$ either iteratively or in the analytical approximation, both explained in Sec. 1.4.4. The depth of approximation is set externally in `FLAG.m`. For the order $\epsilon^{\frac{1}{2}}$ and ϵ^1, the spacecraft velocities are needed. They are provided either directly by the ESA orbits (again by interpolation), or computed from the spacecraft positions by the numerical derivative $f'(x) \approx \frac{f(x+h)-f(x-h)}{2h}$ with (small) derivative stepwidth h (set by the flag file), which is sufficient for the smooth LISA orbits.

5.3.3 Flags and Parameters

The external file `FLAG.m` provides the simulation parameters shown in Tab. 5.1, which will be explained in the following.

Timing Parameters

The first block of Tab. 5.1 consists of flags for the timing parameters, which basically determine the code runtime. The simulation duration `SIMUL_DURATION` is set by default to $T_{\mathrm{sim}} = 1000\,\mathrm{s}$. The choice has several practical reasons. First, multiple interpolations (each sample for each time-delay operator application, Fig. 5.12) are computationally extremely expensive. However, at least $8 \cdot 17\,\mathrm{s} = 136\,\mathrm{s}$ of simulation time is needed for acquisition (the initialisation phase). That is, the laser signal has to virtually travel back and forth several times along the arms to form the first TDI output sample (Ch. 3). Thus, a choice of $T_{\mathrm{sim}} > 140\,\mathrm{s}$ is reasonable. Second, the GW signal frequency `STANDARD_GW_FREQ` is set by default to $f_{\mathrm{gw}} = 4\,\mathrm{mHz}$, i.e., after acquisition time we need at least $250\,\mathrm{s}$ of time series data to observe one period of GW signal. However, the longer the duration, the better the resolution of the gravitational wave signal in the LSD plot. We decided on $T_{\mathrm{sim}} = 1000\,\mathrm{s}$ as a payoff for fast test runs.

Note that a time offset is needed for TDI in the case of orbit data taken from Oliver Jennrichs simulation (Sec. 5.2.2). Orbit data is generated only once per day, but interpolation of the data down to milliseconds is required. Hence, the choice of `TDI_TIMEOFFSET` (in days) to a sufficient high number prevents interpolation errors due to missing data points in the beginning of the orbit data series.

Parameter	Default	Unit	Description
SIMUL_DURATION	1000	s	overall simulation time
TDI_TIMEOFFSET	50	days	offset preventing interpol. problems
SAMPL_FREQ	2	Hz	simulation sample frequency
LASER_NOISE_SAMPL_FREQ	8	Hz	laser noise sampling frequency
SAMPL_FREQ_PHOTODIODES	3	Hz	PD sampling frequency
STANDARD_GW_FREQ	4e-3	Hz	GW frequency
NEW_ORBITS	f		(re)calculation of orbits
LIGHT_RUNTIME_METHOD	algebraic_10		computation method of
			light travel time
			`iterative_geometric`, `algebraic_0`
			`algebraic_0.5`, `algebraic_1.0`
SATELLITE_RANGING_DEPTH	7		iteration steps for S/C
			distance determination
SATELLITE_RANGING_NOMINAL	16.7	s	initial range between S/C
STANDARD_LASER_FREQ	3e14	Hz	central laser frequency (1064 nm)
PZM_LASER_NOISE	(∗)		laser noise pole-zero model
MODEL_READOUT_NOISE_S	6.1e-5	$\frac{\text{rad}}{\sqrt{\text{Hz}}}$	science IFO readout noise
MODEL_READOUT_NOISE_TAU	4.4e-8	$\frac{\text{rad}}{\sqrt{\text{Hz}}}$	reference IFO readout noise
MODEL_READOUT_NOISE_E	2.4e-7	$\frac{\text{rad}}{\sqrt{\text{Hz}}}$	test mass IFO readout noise
LASER_LOCK	f		intra S/C laser lock
NOISES	[t t f f]		laser, readout, OB, TM noise
NEW_NOISE	[t t]		recomputes laser/readout noise
LOWPASS_ORDER_NOISEGEN	8		order of noise low-pass filter
LOWPASS_CUTOFF_FREQ	1	Hz	noise filter cutoff frequency
DERIVATIVE_NUM_STEPWIDTH	0.001		numerical derivative stepwidth
DELAY_INTERPOL_ALGORITHM	AITKEN		interpolation algorithm for delay
NOISE_INTERPOLATION_ALGORITHM	LSF		noise interpolation algorithm
For all interpolations chose			`'DIRTY'`,`'AITKEN'`,`'LAGRANGE'`
			or `'LEAST_SQUARE_FIT'`
INTERPOLATION_NUM_SAMPLINGPOINTS	32		sets number of interpolation nodes
ORBIT_INTERPOLATION_NUM_	18		sets number of nodes
SAMPLINGPOINTS			for orbit interpolation

Table 5.1: The important fixed parameters and standard values for TDISim provided by `FLAG.m`. `t` and `f` are shortcuts for true and false. LSF is an abbreviation for `'LEAST_SQUARE_FIT'`, and (∗) encrypts the command `pzmodel(228.2e6,{59.054e-6 118.62e-3 983.77e-3},{36.019e-3 310.55e-3})` which implements the laser frequency noise pole zero model introduced in Sec. 5.2.4. All of these parameters are called from the classes and functions.

The second important parameter in terms of computational power is the sample frequency `SAMPL_FREQ`. It is set to $f_{\text{samp}} = 2\,\text{Hz}$. In order to simulate the combination of data with different sampling rates, the laser and photodetector sampling frequency, `LASER_NOISE_SAMPL_FREQ` and `SAMPL_FREQ_PHOTODIODES` are unequal to the simulation frequency, and the noise sampling frequency needs to be 8 or more to establish accurate noise interpolation. The gravitational wave frequency f_{gw} is defined by `STANDARD_GW_FREQ`. It lies at least two orders of magnitude below the overall sampling frequency in order to suppress the aliasing within the detection signal (default: $4\,\text{mHz}$).

Spacecraft Model and Orbits

The next block in `FLAG.m` provides parameters about the orbits used for the S/C construction in `sc.m`. In order to save computation time, the orbits could be computed once and then stored, independent of the constellation that is under consideration. If the parameter `NEW_ORBITS` is `true`, they are computed new.

Furthermore, parameters for the light travel time computation in `link.m` are defined in the second block of Tab. 5.1. The light travel time computation methods described in Sec. 1.4.4 could be selected by `LIGHT_RUNTIME_METHOD`, where the algebraic calculation including effects from static gravitational fields is default. If `iterative_geometric` is chosen, the iteration depth `SATELLITE_RANGING_DEPTH` and the initial value for the light travel time $T_0[0]$ (Eq. (1.67)), defined here by `SATELLITE_RANGING_NOMINAL` with $16.7\,\mathrm{s}$ by default, can be set.

Noise

The third block in Tab. 5.1 predefines the noise parameters such as the central laser frequencies for lasers with $1064\,\mathrm{nm}$ wavelength, the pole-zero-model of (free-running) laser frequency noise (Eq. (5.5)), and readout noise levels in terms of white noise levels according to Eqn. (5.7a) – (5.7c). Besides, a simplification of the locking scheme for the onboard laser to a master laser is available. While setting `LASER_LOCK` true, adjacent lasers on one spacecraft are locked to each other and the overall system reduces from six to three free-running lasers. That is, the frequency noise in terms of phase follow the master laser on each spacecraft: $p_1 = p_{1'}$, $p_2 = p_{2'}$, $p_3 = p_{3'}$. However, note here that the locking is greatly simplified and TDISim does not yet deal with beat-notes that include Doppler shifts and frequency offsets as was discussed in Ch. 4.

In the current code version, four noise sources are implemented. That is, the laser frequency noise and readout noise as well as optical bench displacement and test mass noise. Each of them can be turned on and off by setting `true` and `false`, respectively, in the parameter vector `NOISES`. Note, however, that test mass and OB displacement noise is intrinsically connected in the external generator and could not be switched on and off separately. If components of the parameter vector `NEW_NOISE` are set to `true`, the corresponding readout and/or laser noise are generated new, else taken from savings.

In order to generate laser noise that is suppressed by TDI, a strong low-pass filter of order `LOWPASS_ORDER_NOISEGEN` with cutoff frequency `LOWPASS_CUTOFF_FREQ` is applied to the noise time series (Sec. 5.2.4). Subsequently, the high frequency parts of noise which are in danger to make TDI unfunctional due to aliasing effects are suppressed by several orders of magnitude. The order is set to 8 by default and the cutoff frequency f_{cut} to $1\,\mathrm{Hz}$.

Derivatives and Interpolation

The fourth tabular block lists the flags for frequently used mathematical tools: computing derivatives and the interpolation of data series. `DERIVATIVE_NUM_STEPWIDTH` defines the stepwidth for numerical derivatives used for the light travel time computation according to Eq. (1.65a) and (1.66a), where the relative line of sight velocity between the spacecraft needs to be computed, if not provided directly.

Furthermore, we implemented several interpolation routines to compare runtime and precision. These are: two point interpolation (`DIRTY`), interpolation via Neville-Aitken algorithm (`AITKEN`), complete Lagrange interpolation (`LAGRANGE`) and a least-square-fit (`LEAST_SQUARE_FIT`). Therefore, information on the number of sampling points, both for orbit interpolation (with default 18) and noise interpolation (with default 32) is provided within `FLAG.m`.

Besides, `FLAG.m` consists of an additional block with graphical output parameters that are not listed in Tab. 5.1. The user can switch on and off the plotting of the following power spectral densities: noise (depending on the flag `NOISES`), interferometer outputs, TDI outputs, laser noise transfer functions and readout noise only in the interferometers. This makes it easier to compare the different noise sources and contributions.

5.3.4 Simulation Float Diagram

Before we proceed with the results of the simulator, this chapter closes with a float diagram of the simulation TDISim presented in Fig. 5.14. The interplay between the script `SCRIPT_TDI_20_w_TM.m`, the classes `gw.m`, `sc.m` and `link.m` as well as the global fuction `delayCombination_ao.m`, the filter and interpolation routines is shown. We refer to the caption for further explanation.
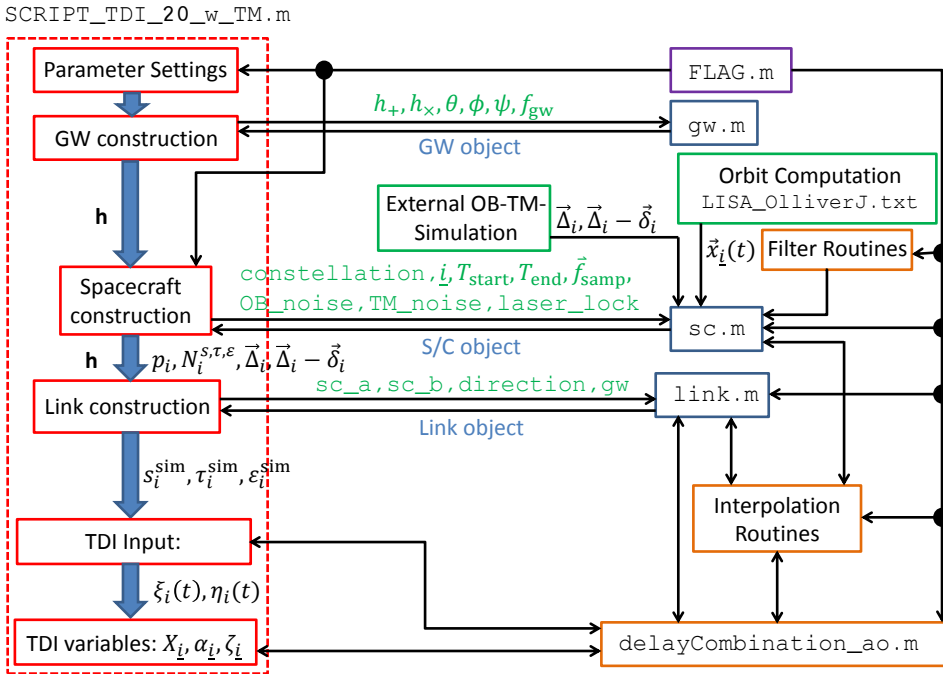
SCRIPT_TDI_20_w_TM.m

Figure 5.14: Simulation float diagram for TDISim. On the left, the dashed red box shows the content of the script SCRIPT_TDI_20_w_TM.m. It consists of the parts explained in Sec. 5.3.1. The file FLAG.m (purple box) provides settings used in all functions (orange), classes (blue) and even within the main script. The green boxes display data generated externally, and the arrows show the connections between the main script, classes, methods and external data. Calling the constructor of each class with necessary input data (green font) as explained in the previous listings gives back the objects of the respective class (blue font) with all properties given in Fig. 5.13. $\vec{f}_{\mathrm{samp}}$ abbreviates the different sampling frequencies for PD, noise and position, i.e., f_sampl_pd, f_sampl_noise and f_sampl_pos. $\underline{i}$ denotes the spacecraft number sc_num and OB_noise as well as TM_noise are Boolean variables that in- or exclude the optical bench and test mass displacement noise from the external generator. Finally, the Boolean laser_lock decides if the lasers are locked or not within the building of the spacecraft object.

Chapter 5

6 Simulation Results

The final chapter of this thesis presents and discusses the simulation results produced by TDISim. We follow the ordering of Sec. 5.2 and start with the orbits, in particular the armlength and light travel time simulation in the case of static LISA, Keplerian orbits and orbits provided by Oliver Jennrich from ESTEC, the latter of which are referenced in the following as ESA orbits for brevity. Next, results for the GW signal in the LISA links are presented for the three orbit cases, followed by the noise contributions to the phasemeter outputs that are completely dominated by laser frequency noise. We will then analyse the TDI outputs for the three constellations and discuss the noise removal performance with respect to the requirements from Sec. 2.3.2. Therefore, a signal calibration scheme is introduced and discussed, since the requirements are formulated for only first generation TDI combinations and additionally in terms of equivalent displacement noise of an equal-armlength Michelson interferometer. Eventually, the limitations of TDI accuracy and the effect of inaccurate armlength knowledge are discussed. The chapter closes with a list of possible next steps to enhance the simulator.

6.1 Orbit Simulation

First of all, the orbit constellations provided by TDISim are elucidated. We distinguish between static LISA, LISA with (analytical) Keplerian orbits, and LISA with ESA orbits, as explained in Sec. 5.2.2. The orbit computation is performed for two years corresponding to $\approx 6.3 \cdot 10^7$ s. In the following, the armlengths and light travel times are shown for the three orbit cases, and we will compare the light travel time contributions introduced in Sec. 1.4.4.

6.1.1 Armlengths

The static LISA constellation consists of three satellites placed at positions predicted by the Keplerian orbit after 50 days. The initial time offset of 50 days is arbitrarily chosen to ensure different L_1, L_2 and L_3 in our model, whereas for an initial time of zero, $L_1 = L_3$. The armlengths for the static LISA test case are shown in Fig. 6.1.
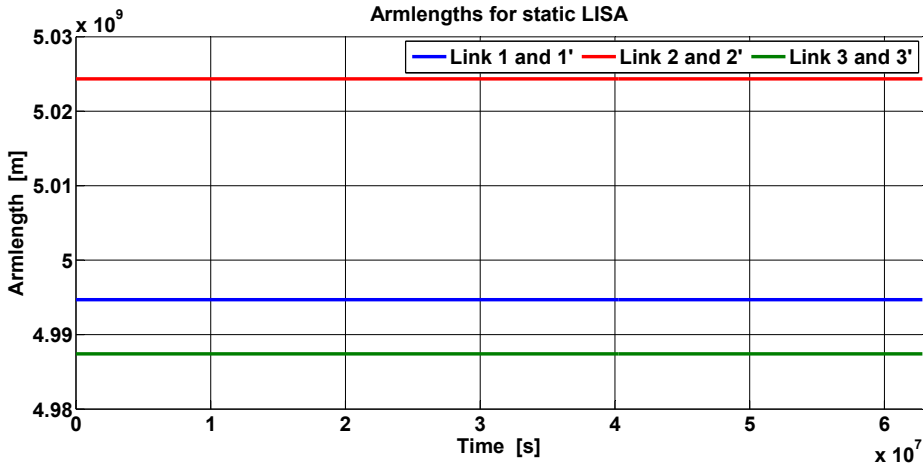
Figure 6.1: Static LISA constellation with fixed armlengths. Note that only three curves are plotted, since the instantaneous armlengths L_1, L_2 and L_3 do not differ in arm direction, i.e., $L_{\underline{i}} = L_{\underline{i}'}$.

Since the spacecraft do not move with respect to each other, the armlengths are fixed over the whole simulation time to $L_1 = L_{1'} \approx 4.995 \cdot 10^9$ m, $L_2 = L_{2'} \approx 5.024 \cdot 10^9$ m and $L_3 = L_{3'} \approx 4.987 \cdot 10^9$ m, whereas relative LoS velocities vanish. The use of such a static constellation is mainly for debugging and testing the simulational results.

The second constellation synthesised by TDISim is based on algebraic Keplerian orbits according to Sec. 5.2.2. The orbits in terms of instantaneous armlengths are presented in Fig. 6.2. Note again that only three curves are plotted, since the instantaneous armlengths do not differ in arm direction. They vary here periodically by an amount of ± 25000 km (roughly 0.5%) around $5 \cdot 10^9$ m within one year, i.e., between $4.977 \cdot 10^9$ m and $5.025 \cdot 10^9$ m. Hence, the Keplerian orbits already imply a flexing of the LISA constellation.

The third orbit is provided by the external simulator from Oliver Jennrich. The instantaneous armlengths have now a complex signature as can be seen from Fig. 6.3. Obviously, the ESA orbits are non-periodic. This is, e.g., due to external gravitational forces not included in the Keplerian orbit computation. The flexing of the constellation is here larger than in the Keplerian orbit case and the armlengths vary by an amount of roughly ± 40000 km within one year. Furthermore, the variation depends on the link that is considered. The maximal flexing is expected for link 1 and 1' between $4.947 \cdot 10^9$ m and $5.035 \cdot 10^9$ m in the first year of simulation time. As before, only three curves are plotted, since the instantaneous armlengths are the same for both directions of each arm.
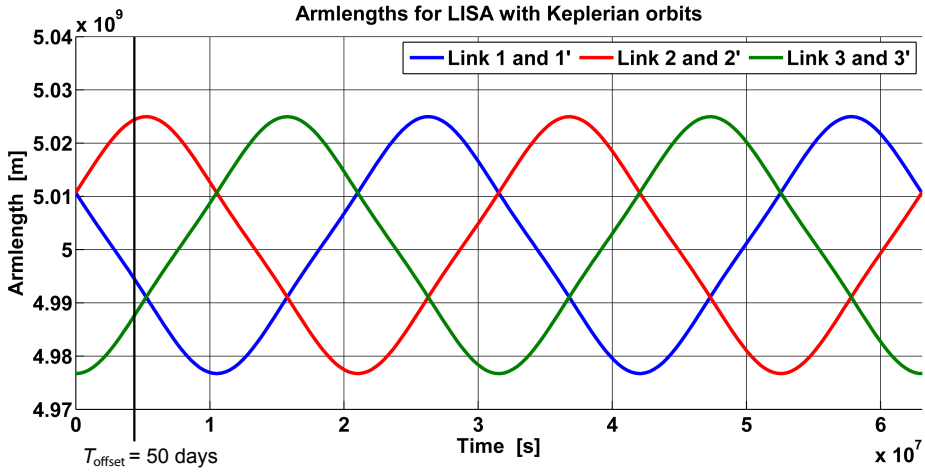
Figure 6.2: Armlengths for a Keplerian LISA constellation. They vary by $\pm 25000\,\mathrm{km}$ around the nominal LISA armlength of five million kilometre within one year. The solid black line marks the time offset $T_{\mathrm{offset}} = 50$ days chosen for the static LISA armlength constellation.
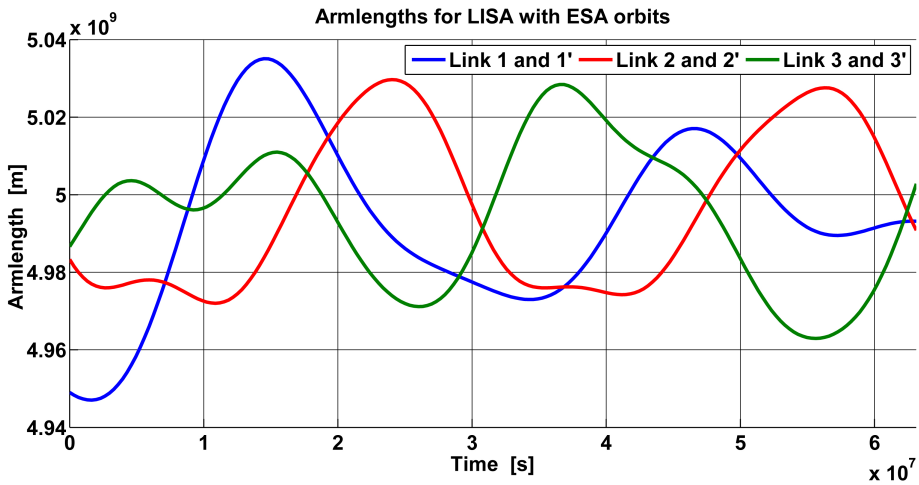

Figure 6.3: Armlengths for LISA with ESA orbits. L_1 varies non-periodically by $\pm 40000\,\mathrm{km}$, L_2 by $\pm 30000\,\mathrm{km}$ and L_3 by $\pm 35000\,\mathrm{km}$ within one year.

Chapter 6

6.1.2 Light Travel Time

For TDI synthesis, the light travel times along the links are needed. In this section they will be presented for all three satellite constellations, and we will also distinguish the different contributions as explained in Ch. 1. The sum of all contributions up to first order in ϵ, denoted by $T_{0,i}(t)$, consists of $\overset{(0)}{T}_{0,i}(t)$ (light travel time between the S/C for a moment at rest), $\overset{(\frac{1}{2})}{T}_{0,i}(t)$ (light travel time correction for moving S/C), and $\overset{(1)}{T}_{0,i}(t)$ (correction including shifts by the gravitational field of the Sun).

In contrast to the armlengths, the light travel times differ with respect to the link direction if the constellation moves or if gravitational effects are included. This is due to non-symmetric time-dependent motions of the spacecraft, the constellation rotation (Sagnac effect, Sec. 3.3.2) and flexing as well as due to the Shapiro delay introduced in Sec. 1.4.4. Additionally, we consider point-ahead effects from now on. That is, while light is travelling from sending to receiving spacecraft, the positions have changed on the orbit and this affects the pointing and light travel time as well (Fig. 1.11). This effect was neglected for the armlengths, since it is of the order of some 100 km and thus not visible in the previous plots. However, in order to compute the light travel time to ns accuracy, we now need to take point-ahead effects into account.

The structure of this section is as follows. First, the overall (static) light travel times per link i without GW influence,

$$T_{0,i}(t) = \overset{(0)}{T}_{0,i}(t) + \overset{(\frac{1}{2})}{T}_{0,i}(t) + \overset{(1)}{T}_{0,i}(t) \,,$$

is shown, and then the different contributions are compared. This is each done for the static LISA case, Keplerian orbits and ESA orbits.

Light Travel Time for Static LISA

The overall light travel time in link i for a static LISA constellation, $T_{0,i}$, is depicted in Fig. 6.4. Since the spacecraft do not move in this constellation, the light travel times will not vary visibly (the same as for the armlengths) and are expected to be constant. That is, the $\epsilon^{\frac{1}{2}}$-contributions vanish, i.e., $\overset{(\frac{1}{2})}{T}_{0,i} = 0$, and moreover $\overset{(0)}{T}_{0,i}$ is constant in a static LISA constellation for all links over the complete simulation time of two years. Its magnitudes are $\overset{(0)}{T}_{0,1} = \overset{(0)}{T}_{0,1'} \approx 16.6605\,\mathrm{s}$, $\overset{(0)}{T}_{0,2} = \overset{(0)}{T}_{0,2'} \approx 16.7594\,\mathrm{s}$ and $\overset{(0)}{T}_{0,3} = \overset{(0)}{T}_{0,3'} \approx 16.6362\,\mathrm{s}$. This constancy is of course not the case for Keplerian and realistic ESA orbits as we will see below.
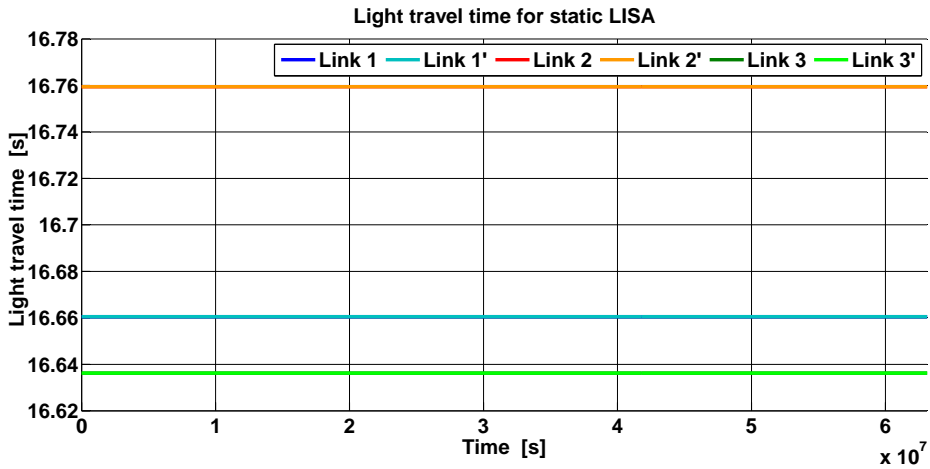
Figure 6.4: Light travel times for static LISA links. Due to the fixed constellation, $T_{0,i}^{(\frac{1}{2})} = 0$, and thus the up- and down-travel times in one link do not differ visibly. Furthermore, as can be seen from Fig. 6.5, the gravitational contribution in each link, $T_{0,i}^{(1)}$, is of the order 10^{-7} s and as well not visible here. The overall light travel times are then $T_{0,1} \simeq T_{0,1'} \approx 16.6605$ s, $T_{0,2} \simeq T_{0,2'} \approx 16.7594$ s and $T_{0,3} \simeq T_{0,3'} \approx 16.6362$ s.
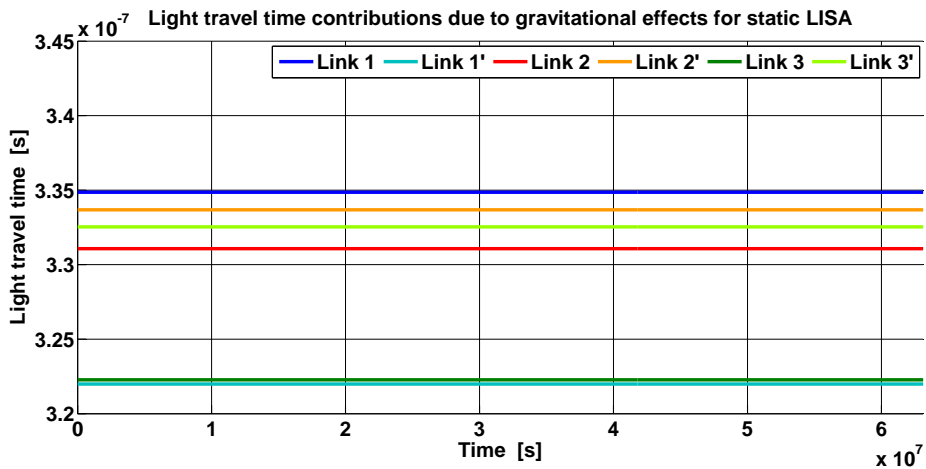

Figure 6.5: Light travel time contributions of order ϵ^1 with gravitational effects for static LISA, $T_{0,i}^{(1)}$. They lie in the order $\approx 3 \cdot 10^{-7}$ s, corresponding to a ranging difference of the order 10^2 m. The shift is different by each link and ranges from 322 ns for link $1'$ to 335 ns for link 1.

However, if we construct the difference between the light travel times up to order ϵ^0 (or here equivalently $\epsilon^{\frac{1}{2}}$) and ϵ^1 for static LISA, we can see a difference of $\approx 320\ldots 340\,$ns caused by static gravitational field effects originating from the Sun that are included in the computation. Those values correspond to armlength differences of $100\,$m and depend on the considered link. Furthermore, the influence turns out to be directional dependent, since clockwise and counter-clockwise light travel does not exactly collect the same shift. This can be seen from Eq. (1.66a) which defines the contribution $\overset{(1)}{T}_{0,i}$. For a fixed S/C constellation, any receiver velocity is $\vec{v}_{\mathrm{recv}} = \vec{0}$, and hence the first term in (1.66a) vanishes. The second term, however, depends in a complex manner on both the receiver and sender position. In particular, the term is non-zero for $\vec{v}_{\mathrm{recv}} = \vec{0}$ and as well not cyclic in the interchange of sender and receiver. This results in the directional dependence of the gravitational induced time shift within one arm. The effect is visible in Fig. 6.5, presenting $\overset{(1)}{T}_{0,i}$.

Light Travel Time for LISA with Keplerian Orbits

The light travel time for a LISA constellation with Keplerian orbits generated according to Eqn. (5.1a) – (5.1d) is presented in Fig. 6.6. As for the armlengths, we again see the annual variation showing up in the light travel time variation between $16.6\,$s and $16.76\,$s. Note that here the link direction matters, since $T_{0,\underline{i}}(t) \neq T_{0,\underline{i}'}(t)$ due to flexing and constellation motion. The difference $T_{0,\underline{i}'}(t) - T_{0,\underline{i}}(t)$ between up- and down-travelling laser light varies annually and can be read off Fig. 6.7 to be $\pm 3.3 \cdot 10^{-3}\,$s in maximum at the turning points of the constellation breathing. The mismatch corresponds then to $1000\,$km and emphasises the necessity of synthesising equal-arm interferometric measurements in post-processing by TDI accounting for a flexing LISA constellation.

Subsequently, the half order contributions $\overset{(\frac{1}{2})}{T}_{0,i}(t)$ are in the Keplerian case not anymore zero, but vary in time. This can be read off Fig. 6.8. The magnitude is $\pm 1.65\,$ms, corresponding to an armlength difference of $500\,$km, which is in perfect agreement with [CRVP05].

The light travel time contribution of the order ϵ^1 is presented in Fig. 6.9. One can identify a shift varying between $410\,$ns and $500\,$ns, again due to the gravitational field of the Sun included in the approximation. Note here that the magnitude is larger than for static LISA, which can be explained as previously with Eq. (1.66a). In the Keplerian case, the velocities of the receiving spacecraft are not zero, hence the first term of Eq. (1.66a) does not vanish anymore and contributes now to $\overset{(1)}{T}_{0,i}(t)$.
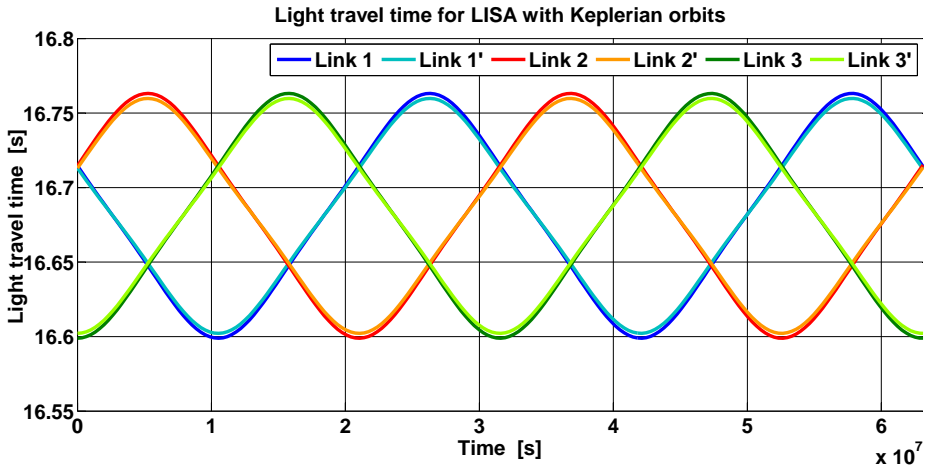
Figure 6.6: Overall light travel time for LISA with Keplerian orbits. $T_{0,i}(t)$ varies between $16.6\,\text{s}$ and $16.76\,\text{s}$ with a period of $f_{\text{orb}} = 1\,\frac{\text{cycle}}{\text{yr}}$ and differs in up- and down-travel per link by an amount presented in Fig. 6.7.
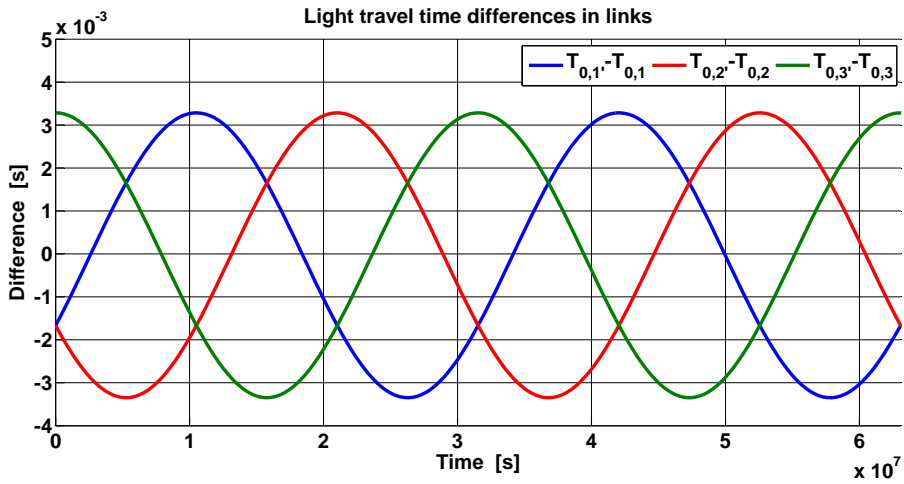

Figure 6.7: Light travel time difference in the links for LISA with Keplerian orbits. The difference between clockwise and counter-clockwise light travel time per link varies between $-3.3\,\text{ms}$ and $+3.3\,\text{ms}$ within one year. The effect is also visible in Fig. 6.6.
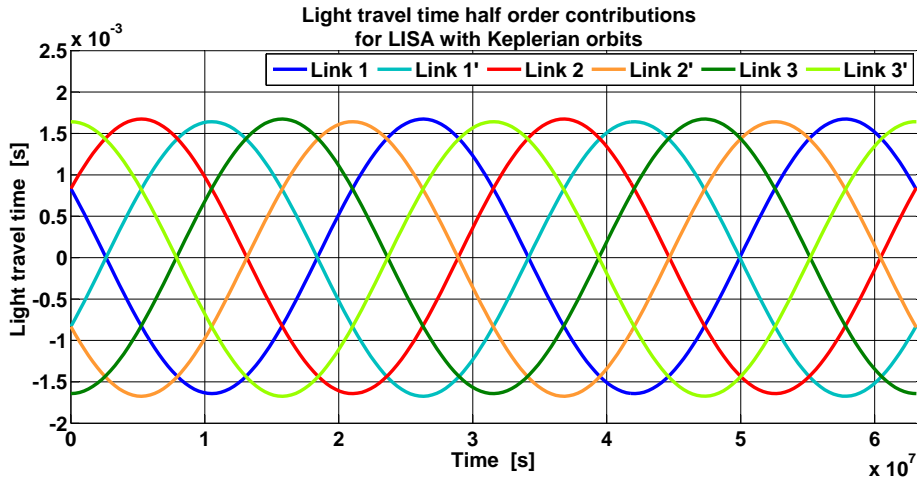
Chapter 6

Figure 6.8: Half order contributions $\overset{(\frac{1}{2})}{T}_{0,i}(t)$ of the light travel time for Keplerian orbits. Their magnitudes are $\pm 1.65\,\text{ms}$ for all links. The contributions change periodically within one year.
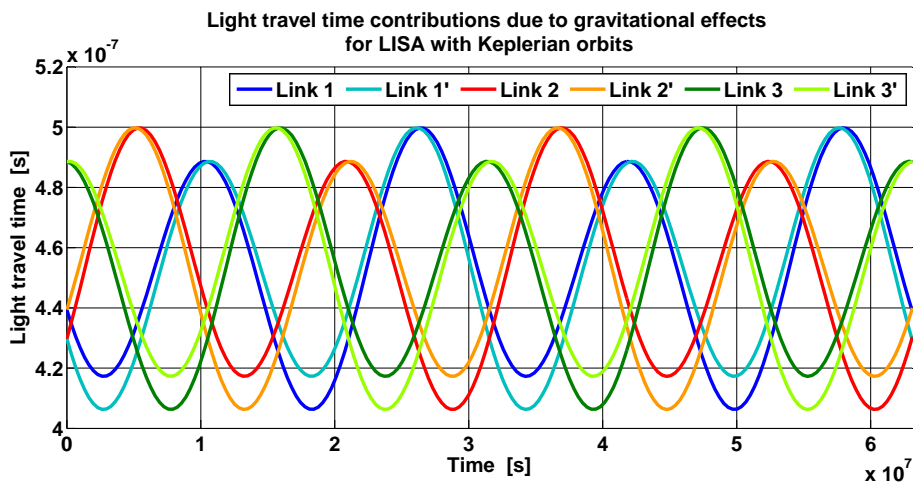

Figure 6.9: Gravitational effects on the light travel time for Keplerian orbits, $\overset{(1)}{T}_{0,i}(t)$. They lie in the range between $410\,\text{ns}$ and $500\,\text{ns}$, varying by maximally $10\,\text{ns}$ between up- and down-link travel.
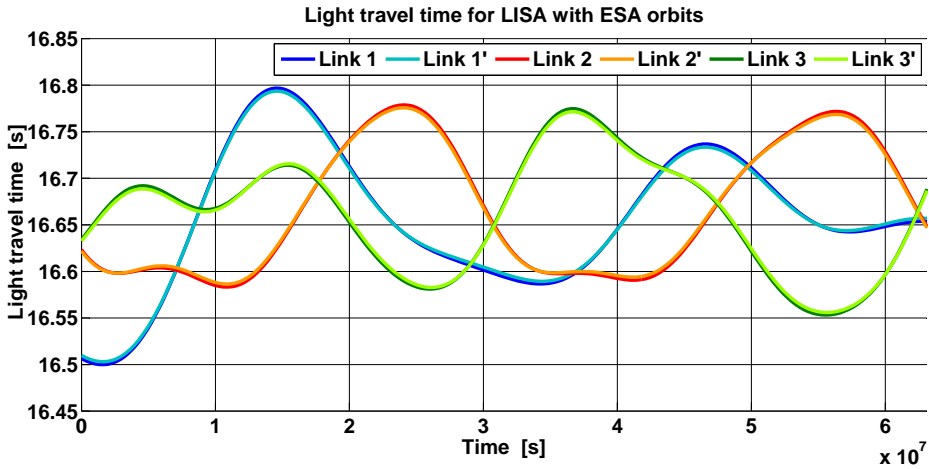
Figure 6.10: Overall light travel time $T_{0,i}(t)$ for LISA with ESA orbits. The pattern is comparable to that of the armlengths from Fig. 6.3. The maximal variation between 16.5 s and 16.8 s is exhibited by link 1 and 1'.

Light Travel Time for LISA with ESA Orbits

Finally, we present the overall light travel times for LISA on realistic orbits provided by ESA. They are depicted in Fig. 6.10. The pattern is of course similar to that of the armlengths from Fig. 6.3. One can see here as well the differences in the direction of light travel between two spacecraft, which result from $\epsilon^{\frac{1}{2}}$ contributions given in Fig. 6.11. However, if we finally include the gravitation of the Sun placed at the origin of the SSB frame by the expansion to ϵ^1, an additional contribution ranging from 405 ns to 500 ns can be found. This contribution is given in Fig. 6.12.

One can see a modulation of gravitational influence on the light travel time of twice the orbital frequency within the variation (as in Fig. 6.9). This originates mainly from the annual constellation rotation that changes the relative S/C acceleration by the Sun's gravitational field. Second, the constellation distance to the Sun varies as well within one year (so does the gravitational shift). This ellipticity of the CoM orbit leads to the different peak heights changing every half a year.

Summing up, the significant difference between Keplerian and ESA orbits is provided in the zero order contributions $\overset{(0)}{T}_{0,i}(t)$, while the half and first order contributions only slightly differ. In the following, we will always use the light travel time up to first order in ϵ, i.e., $T_{0,i}(t)$.
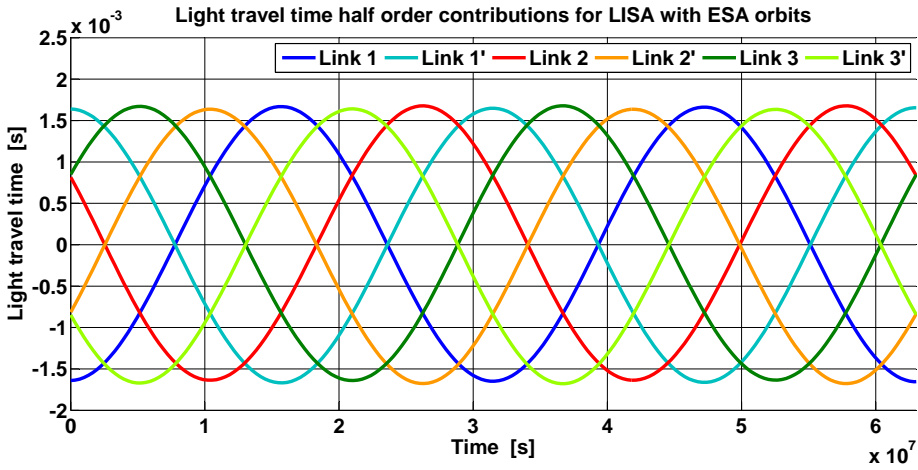
Chapter 6

Figure 6.11: Half order light travel time contributions for LISA with ESA orbits. $T_{0,i}^{(\frac{1}{2})}(t)$ again varies by ± 1.65 ms for all links, as was the case for the Keplerian orbits.
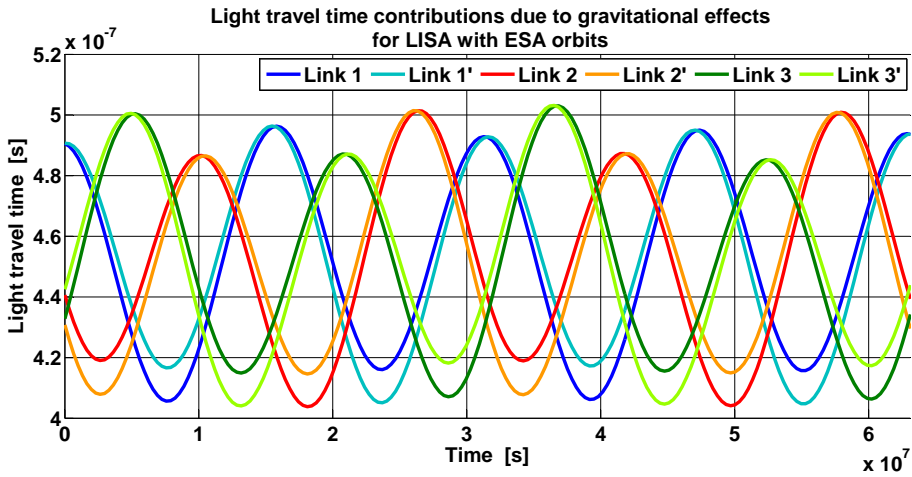

Figure 6.12: Gravitational light travel time shifts for LISA with ESA orbits. They range from 405 ns to 500 ns and are comparable with the values of the Keplerian orbits.
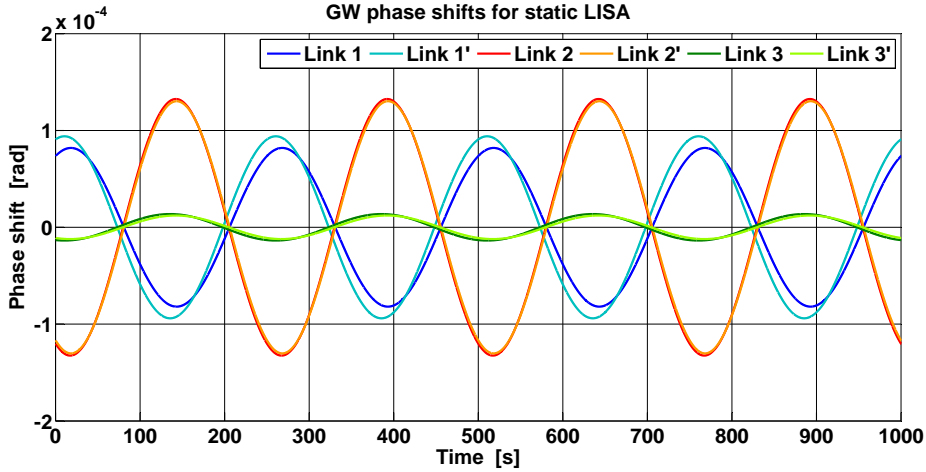
Figure 6.13: Gravitational wave signal in the links of a static LISA constellation, shown for 1000 s. The optical phase shift oscillates by $\pm 1.3 \cdot 10^{-4}$ rad in maximum with GW frequency $f_{\mathrm{gw}} = 0.004$ Hz.

6.2 Gravitational Wave Signal

We will now focus on the results for the GW signal detected onboard the spacecraft for each orbit case. It is generated according to Sec. 5.2.3 in terms of optical phase shifts $H_i(t) = 2\pi\nu_0\Delta T_i(t)$ experienced by laser light (with central frequency ν_0) interchanged between the spacecraft. For all three spacecraft constellations, a GW incidence along $\theta = -\frac{\pi}{6}$ and $\phi = \frac{\pi}{4}$ is assumed with strains $h_+ = 10^{-20}$ and $h_\times = 0$. The GW phase signal plots are drawn for 1000 s. Note that the pattern will significantly change over a year according to the time-dependent detector orientation with respect to the incident gravitational wave.

We will start with the GW signal detected by the static LISA constellation. The corresponding phase shift time series along the links $1, \ldots, 3'$ are depicted for a duration of 1000 s in Fig. 6.13. First of all, a sinusoidal signature of the phase signal with $f_{\mathrm{gw}} = 4$ mHz is obvious. This is also what we expect from Eqn. (5.2) and (5.4), since the GW tensor has a time-depending cosine term including f_{gw}, and we set the GW frequency to be 4 mHz. The amplitudes differ from link to link between $1.4 \cdot 10^{-5}$ rad and $1.3 \cdot 10^{-4}$ rad and the maxima per link are shifted slightly with respect to each other, where the effect on link 1 and 1' is the largest. This is both due to the different orientations of the links relative to the incoming gravitational wave and its polarisation, and moreover due to the complex GW transfer function.
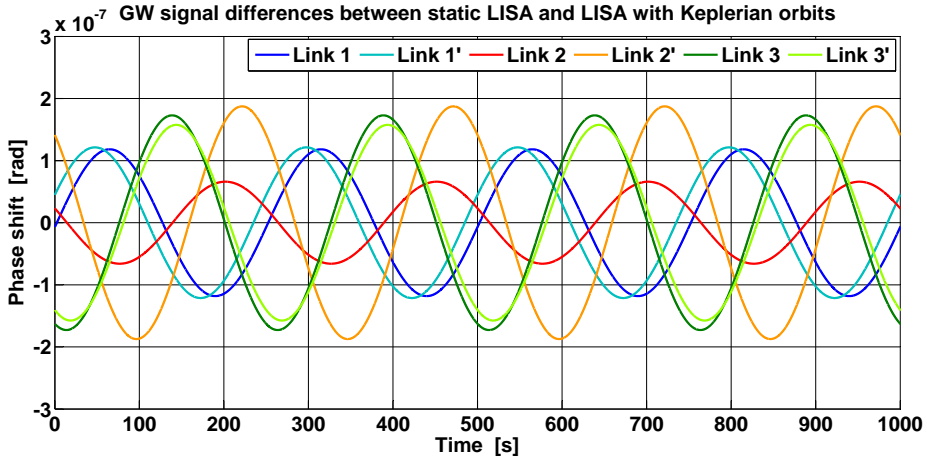
Figure 6.14: Gravitational wave signal differences between static and Keplerian orbits. They vary by less than $\pm 0.2\,\mu\mathrm{rad}$ with the GW signal frequency. Clearly, the differences depend on the links and their directions.
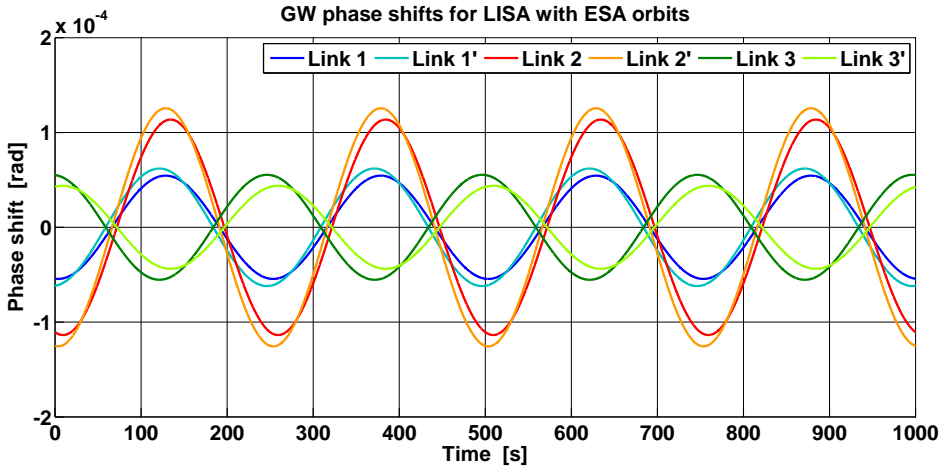
Figure 6.15: Gravitational wave signals for a flexing LISA constellation with ESA orbits. The signal is comparable to the Keplerian case and reaches in maximum $\approx 1.2 \cdot 10^{-4}$ rad of corresponding optical phase shift for link $2'$.

Furthermore, one can see a small discrepancy of 10^{-6} rad in the links 2, 2′, 3 and 3′ in up- and downlink, and $1.2 \cdot 10^{-5}$ rad in link 1 and 1′. Intuitively, one would not expect this in a static LISA constellation. However, the phase shifts $H_i(t)$ are computed with help of $\Delta T_i(t)$ given by Eq. (5.4). There, the scalar product $\hat{k} \cdot \vec{n}_i$ in the sinc-function ranges from -1 to 1 and introduces the difference between optical phase shifts due to GW collected by light travelling up and down the arms, since $\vec{n}_{\underline{i}} \neq \vec{n}_{\underline{i}'}$.

The figures that display the GW phase signal for LISA with algebraic Keplerian orbits look on the first view exactly the same, since the relative LoS velocities are small ($\approx 10\,\frac{\text{m}}{\text{s}}$) and hence one would not expect a large change of gravitational signal pattern within $1000\,\text{s}$, even with point-ahead effects. The difference between the GW signal for static LISA and LISA with Keplerian orbits is shown in Fig. 6.14. It lies within a range of the order 10^{-7} rad and is three orders of magnitude smaller than the gravitational wave phase signal itself. Orbital motion of the detector on a small time scale is thus negligible for the GW signal.

The signals for LISA with ESA orbits are presented in Fig. 6.15. The constellation is here such that the strongest signal is recognized by link 2′ and has its maximum at $1.2 \cdot 10^{-4}$ rad while that of link 3′ is more than two times weaker. The signals clearly differ from the signal pattern of the Keplerian orbits, since the relative positions of the spacecraft and hence the detector orientation with respect to the GW incidence is different.

In summary, the GW phase signals in the detector have an order of magnitude of 10^{-4} rad independent of the chosen spacecraft constellation. However, the signals are buried in noise that is several orders of magnitude higher as we will discuss now.

6.3 Noise Contributions to the Phasemeter Signals

In this section, we will discuss the noise contributions for the generation of the phasemeter signals $s_i^{\text{sim}}(t)$, $\varepsilon_i^{\text{sim}}(t)$ and $\tau_i^{\text{sim}}(t)$ according to Eqn. (5.8a) – (5.8f). This includes the simulation of the involved noise sources, i.e., laser frequency noise, test mass and optical bench displacement noise as well as readout noise. Any input noise above the $10\,\text{pm}$-requirement,

$$\widetilde{x}_{\text{req,input}}(f) = 10\,\frac{\text{pm}}{\sqrt{\text{Hz}}}\sqrt{1 + \left(\frac{3\,\text{mHz}}{f}\right)^4}, \tag{6.1}$$

needs to be suppressed by post-processing and TDI. Therefore, each noise contribution is compared with Eq. (6.1). The $1\,\text{pm}$-requirement is too stringent, and already the input readout noise in the science measurements is violating it by one order of magnitude in TDISim (cf. Eq. (5.7a)).

Chapter 6
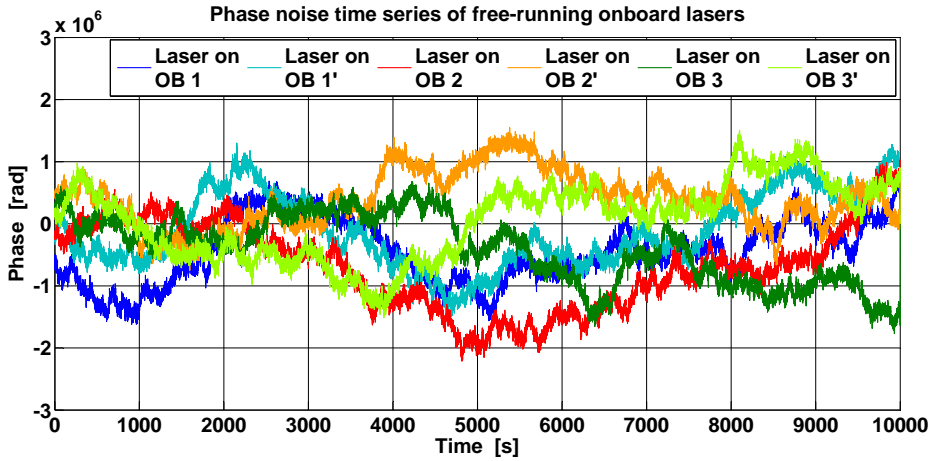
Figure 6.16: Time series of free-running and unlocked laser phase noise, shown for $10000\,\mathrm{s}$. The phase varies by more than $\pm 10^6\,\mathrm{rad}$ for each laser instance.
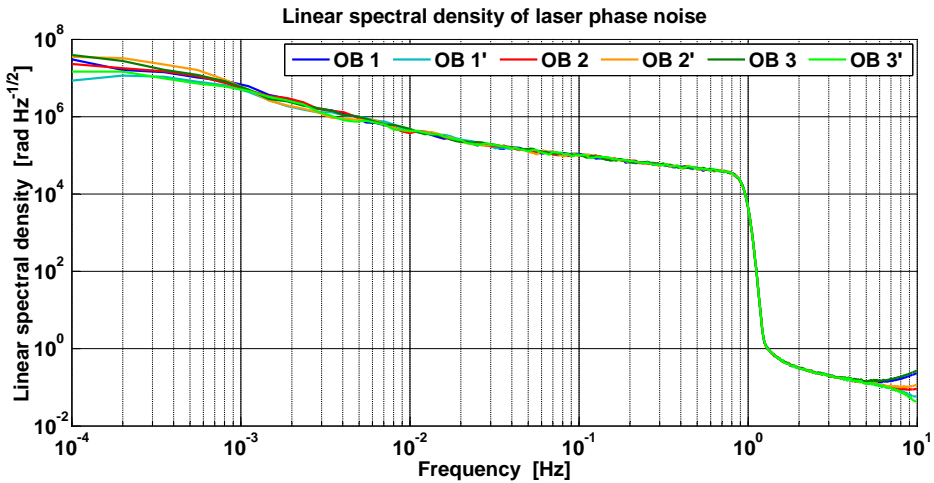
Figure 6.17: Linear spectral density of laser phase noise from each OB. A strong 8th-order band pass filter with cutoff frequency $f_{\mathrm{cut}} = 1\,\mathrm{Hz}$ has been applied. Converted to displacement noise in a single link interferometric measurement, the coupled noise for each instance is 11 orders of magnitude in amplitude or more above the $10\,\mathrm{pm}$-requirement for $f < 0.1\,\mathrm{Hz}$.

6.3.1 Laser Phase Noise

For laser phase noise generation, the filter explained in Sec. 5.2.4 is used to generate independent time domain series of frequency noise for all six lasers. This is then converted to phase via integration over time according to Eq. (2.15). The resulting time series for 10000 s are presented in Fig. 6.16. The lasers are free-running and not locked. They contribute huge optical phase errors of some 10^6 rad to the measurements in each interferometer. Compared with the Figs. 6.13 and 6.15, one can see that the gravitational wave signal in terms of optical phase is more than 9 orders of magnitude smaller than the laser phase noise. Hence, the GW signal is completely buried in laser frequency noise, and it is crucial to suppress the latter one sufficiently by TDI.

Note here that our simulation is conservative in the sense that we assume free-running lasers in contrast to the calculation in Sec. 3.1.1, where a phase jitter of some 10^4 rad was calculated. However, for free-running lasers, TDISim yields a level of 10^6 rad. A spectral point of view on the laser phase noise series is provided by the linear spectral density in terms of phase noise in Fig. 6.17. This phase noise enters the phasemeter directly but should not be mixed up with the phase noise due to laser frequency noise coupling into the interferometric output (cf. Eq. (3.6b)).

The linear spectral densities in Fig. 6.17 have values of $8 \cdot 10^6 \frac{\text{rad}}{\sqrt{\text{Hz}}}$ at 1 mHz, decreasing with $\propto f^{-2}$ to 10 mHz, and from there they roll off with $\propto f^{-1}$ to $5 \cdot 10^4 \frac{\text{rad}}{\sqrt{\text{Hz}}}$ at 0.8 Hz. This is also in accordance with the pole-zero model plotted as a linear spectral density in Fig. 5.5. At $f_{\text{cut}} = 1$ Hz, the LSDs roll off extremely rapid. This is due to the applied 8th-order filter explained in Sec. 5.2.4 which suppresses aliasing noise. Converted to interferometric single-link displacement noise by Eq. (3.6b), we find out that the coupled noise is more than 11 orders of magnitude above the 10 pm-requirement for $f < 0.1$ Hz. Hence, it is crucial to suppress laser frequency noise in post-processing.

As a sidemark, note here and in the following that if the plotted quantity is generalised as, e.g., 'laser noise' without any indices, it implies that only small variations exist between the statistics of the individual laser noise instances. Thus, it would be adequate to plot exemplarily only one curve of Fig. 6.17, since the behaviour is the same for all instances in the frequency band of interest between $10^{-4} \ldots 1$ Hz. The realisations of each noise source in the time domain are of course different.

6.3.2 Displacement Noise

Another primary noise source within the LISA data streams is the displacement noise due to relative OB and TM motion. Fig. 6.18 shows the time series of that displacement noise in the science and test mass interferometer. Note that no displacements enter the reference interferometer output according to Eq. (5.8a) – (5.8f).

Chapter 6
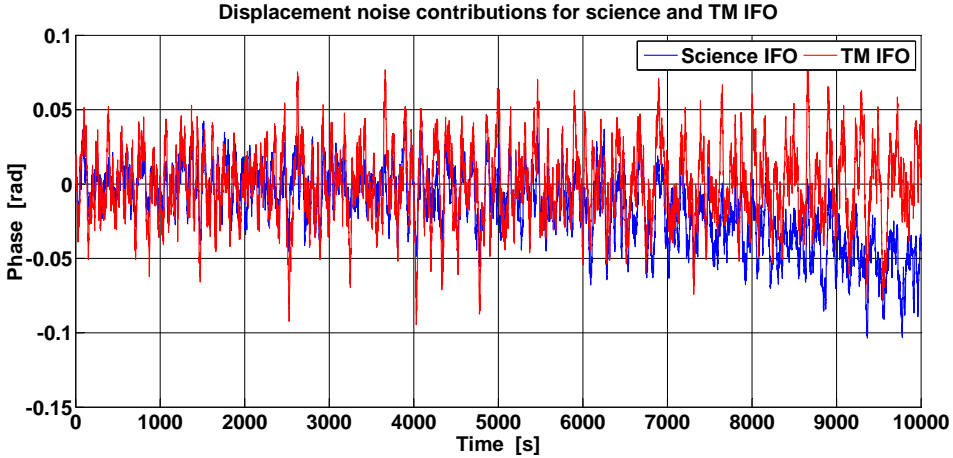
Figure 6.18: Time series of displacement noise in science and TM IFO. The drift originates from the low frequency component of thruster noise acting on the optical benches. The TM is following the OB by the spring coupling, and therefore no relative drift between OB and TM is obvious in the TM interferometer.

Figure 6.19: Time series of displacement noise in all science IFOs. A phase drift explained previously is visible in all interferometers. Since the same displacement noise instances, though time-delayed, enter in the science IFOs, the signals of OB 1 and 2′, 1′ and 3, and 2 and 3′, respectively, appear to follow each other.
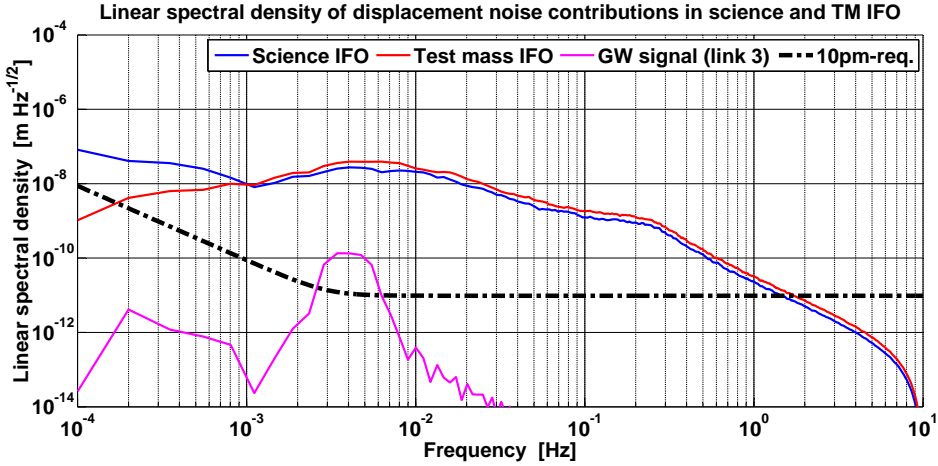
Figure 6.20: Linear spectral density of displacement noise in science and TM interferometers in terms of displacement. It lies several orders of magnitude above the 10 pm-requirement. The GW signal power from LISA with ESA orbits is shown for comparison. It is clear that there is crucial need for a displacement noise suppression scheme.

The first thing to remark is that the noise level lies within the range of ± 0.1 rad and has hence a much smaller contribution than the laser frequency noise. However, it is three orders of magnitude above the gravitational wave phase signal and can be regarded as a primary noise source. Second, a relative phase 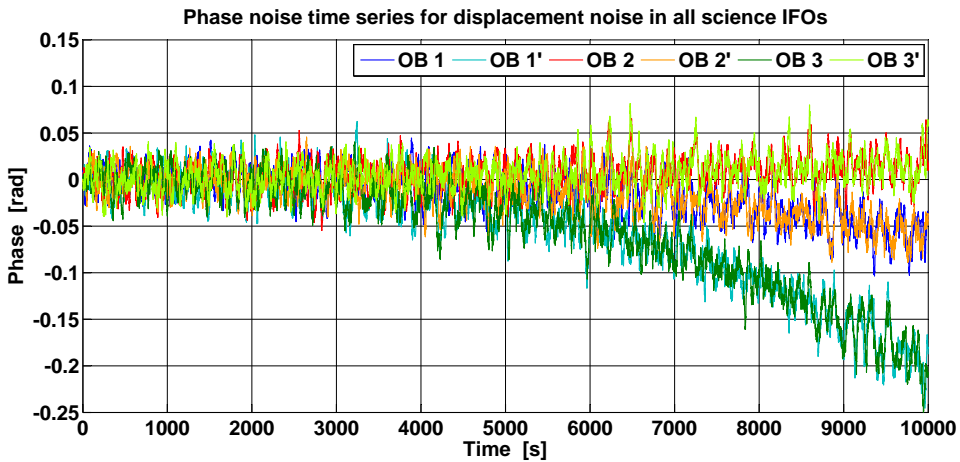drift due to displacement noise in the science IFO is distinct in Fig. 6.18, while the same tendency is absent in the TM interferometer output. This comes from the low frequency part of the displacement noise of both sending and receiving optical benches. As explained in Sec. 5.2.4, a thruster force with strong low frequency components is applied on each optical bench and results in the drift (cf. Fig. 5.8). This effect is obvious in each science interferometer signal, as displayed in Fig. 6.19. Since the TM is coupled by the spring to the respective OB, it will follow the thruster activity. Thus, in the TM interferometer signal, no relative position drift is visible. Remind again that spatial limitations by the chamber walls are neglected in the test mass simulation, as well as drag-free control systems or suspensions.

The displacement noise appear linkwise to follow each other in Fig. 6.19. This is due to the signature of the respective displacement contributions, e.g., for OB 1, $s_1^{\text{sim}}(t) = \ldots + \frac{2\pi\nu_0}{c}(\boldsymbol{\mathcal{D}_3^{\text{sim}}}\Delta_{2'} - \Delta_1) + \ldots$ and $s_{2'}^{\text{sim}}(t) = \ldots - \frac{2\pi\nu_0}{c}(\boldsymbol{\mathcal{D}_{3'}^{\text{sim}}}\Delta_1 - \Delta_{2'}) + \ldots$ according to Eqn. (5.8a) – (5.8f). Here, $-\Delta_1$ and its delayed relative $-\boldsymbol{\mathcal{D}_{3'}^{\text{sim}}}\Delta_1$ as well as $+\Delta_{2'}$ and $+\boldsymbol{\mathcal{D}_3^{\text{sim}}}\Delta_{2'}$ occur. The displacement noise varies by only ± 10 mrad within the light travel time for one link, and so do the delayed and non-delayed instances differ. Since the resolution is very small, the curves then seem to follow each other.

Chapter 6

The linear spectral density of the displacement noise that contributes to science and TM interferometer is presented in Fig. 6.20. In the relevant frequency band it lies two or more orders of magnitude in amplitude above the 10 pm-requirement and therefore needs to be suppressed in post-processing, as is also indicated by the comparison with the gravitational wave signal. For low frequencies, the displacement noise in the science interferometer grows again which occurs as the slow drift behaviour in Fig. 6.19 in the time domain and originates from the thruster activity, as explained previously.

Finally, note that the noise levels slightly differ between TM and science interferometer which is due to the different displacement contributions. That is, e.g., for optical bench 1, the contributions in our model are $\boldsymbol{\mathcal{D}_3^{\mathbf{sim}}} \Delta_{2'} - \Delta_1$ for the science and $\Delta_1 - \delta_1$ for the TM interferometer. δ_1 is several orders of magnitude smaller than Δ_1 (the same for $\widetilde{\delta}_1(f)$) and has a negligible impact on the difference $\Delta_1 - \delta_1$. However, in the science interferometer, the noise levels are comparable and the difference $\boldsymbol{\mathcal{D}_3^{\mathbf{sim}}} \Delta_{2'} - \Delta_1$ of the OB noise contributions is smaller than for the TM interferometer.

6.3.3 Readout Noise

According to Eqn. (5.8a) – (5.8f), readout noise $N_i^{s,\tau,\varepsilon}$ enter in all three interferometers with different noise magnitudes, as discussed in Sec. 5.2.4. The readout noise is maximal in the science IFO. Since the noise levels of reference and test mass interferometer are two to three orders of magnitude in terms of optical phase smaller, only the time series N_1^s is plotted in Fig. 6.21. As can be seen, even the biggest readout noise magnitude of some 10^{-4} rad (for the science IFO) is already comparable in magnitude to the gravitational wave signal.

The same statement can be found in the linear spectral density plot presented in Fig. 6.22. The readout noise level in terms of displacement for science, test mass and reference interferometer is of the order $10^{-11} \frac{\mathrm{m}}{\sqrt{\mathrm{Hz}}}$, $10^{-13} \frac{\mathrm{m}}{\sqrt{\mathrm{Hz}}}$ and $10^{-14} \frac{\mathrm{m}}{\sqrt{\mathrm{Hz}}}$, respectively. For each interferometer output, the readout noise is fulfilling the 10 pm-requirement, and we do not need to remove it in post-processing (this is not possible anyway). Thus, readout noise can be regarded as a secondary noise source in the following.

6.4 Onboard Interferometric Outputs

We will now analyse the synthesised outputs of the onboard interferometers, i.e., from the science IFOs $s_i^{\mathrm{sim}}(t)$, the test mass IFOs $\varepsilon_i^{\mathrm{sim}}(t)$ and the reference interferometers $\tau_i^{\mathrm{sim}}(t)$ according to Eqn. (5.8a) – (5.8f). That is, all noise contributions and the GW phase signal discussed previously are properly combined to form the onboard interferometric phase signals for each OB.
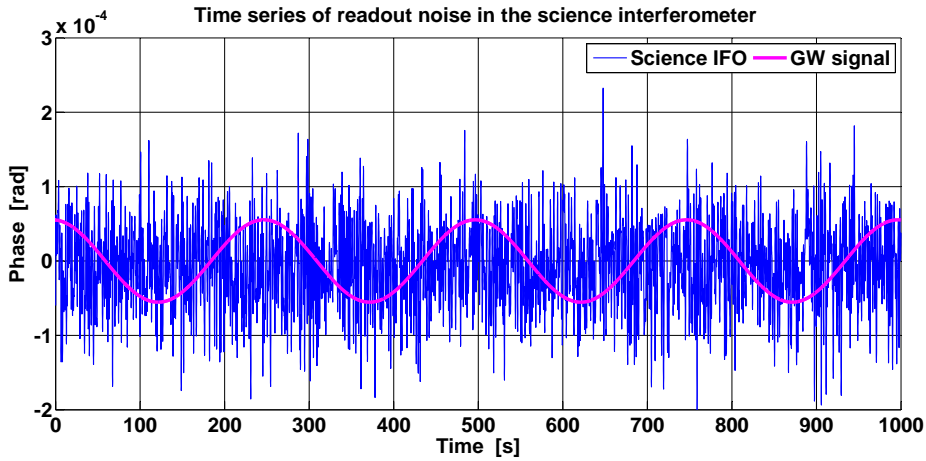
Figure 6.21: Phase noise time series of readout noise for the science interferometer, shown for 1000 s. It has a magnitude of 10^{-4} rad in optical phase, which is in the same order of magnitude as the GW signal amplitude. The readout noise for TM and reference interferometer has an even smaller magnitude according to Eqn. (5.7a) – (5.7c) and is not plotted here.
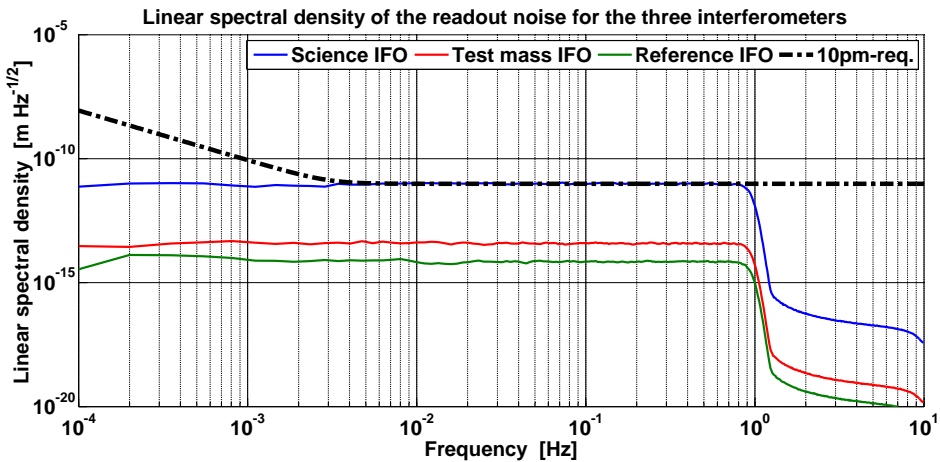
Figure 6.22: Linear spectral density of readout noise for the three IFOs. Since the readout noise in the science interferometer is on the same level as the 10 pm-requirement for $f > 3\,\mathrm{mHz}$, and in the TM and reference interferometer by 2 and 3 orders of magnitude below, we can regard readout noise as a secondary noise.

Chapter 6
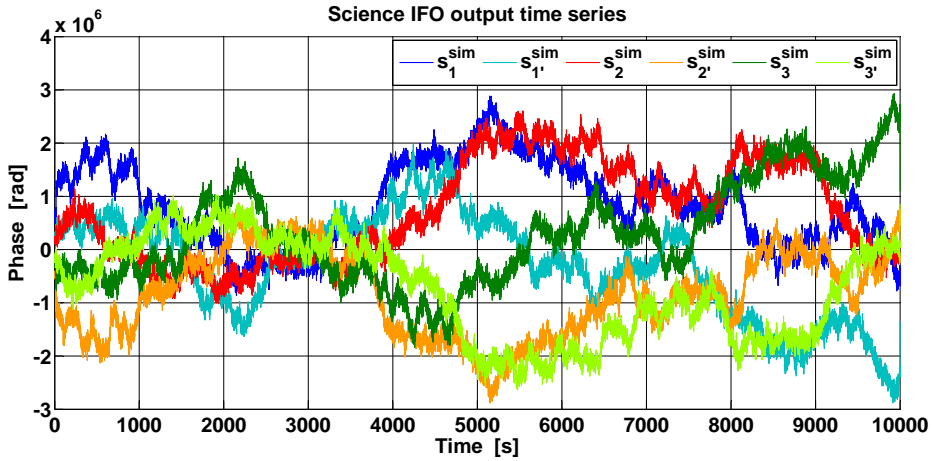
Figure 6.23: Science interferometer signals with six free-running lasers and the buried GW. On the first view, the signals appear pairwise mirrored, but this virtual effect is only due to the small resolution of the time axis. By zooming in, one discover that the curves are time-shifted with respect to each other, as can be read off Fig. 6.24.
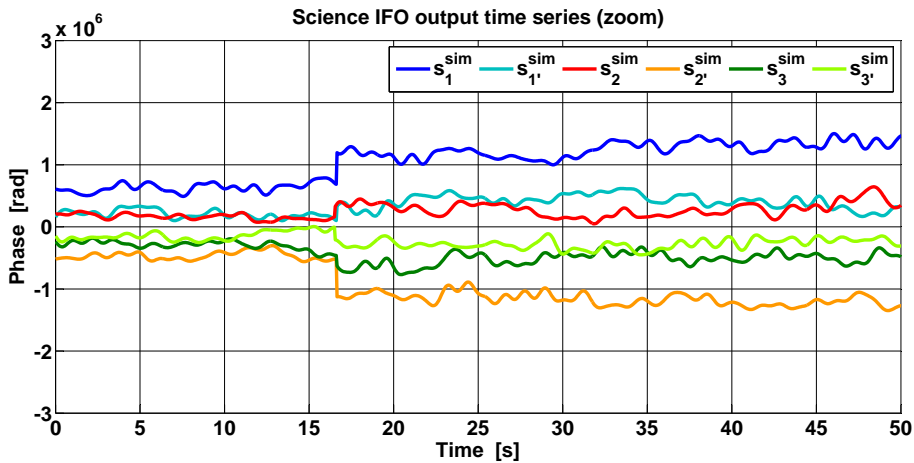
Figure 6.24: Zoom of the science IFO outputs, shown for the first 50 seconds. The onset of the laser phase noise from the distant S/C is distinct by the bump between 16.5 to 17 s. The pretended symmetry from Fig. 6.23 is also not visible here anymore.

6.4.1 Science Interferometer

The generated time series for the six science interferometers are shown in Fig. 6.23. It is obvious that laser frequency noise completely dominates the science IFO outputs such that the gravitational wave is buried, since the phase noise exceeds several 10^6 rad, compared with 10^{-4} rad phase shift by the GW (Fig. 6.13 and 6.15).

On a first view, the phase noise of $s_1^{\text{sim}}(t)$ and $s_{2'}^{\text{sim}}(t)$, $s_{1'}^{\text{sim}}(t)$ and $s_3^{\text{sim}}(t)$, $s_2^{\text{sim}}(t)$ and $s_{3'}^{\text{sim}}(t)$ look mirrored such that the pairwise addition would give zero. However, this impression is only due to the small resolution of the time axis. In fact, the described pairs are all shifted with respect to each other by roughly 17 s, since each science IFO output comprises one time delay. Consider, e.g., the simulated signals $s_1^{\text{sim}}(t) = \ldots + \boldsymbol{\mathcal{D}_3^{\text{sim}}} p_{2'} - p_1 + \ldots$ and $s_{2'}^{\text{sim}}(t) = \ldots + \boldsymbol{\mathcal{D}_{3'}^{\text{sim}}} p_1 - p_{2'} + \ldots$. Since p_1 and $p_{2'}$ (and their delayed replica) are several orders of magnitude larger than all other noise sources plus GW signal in $s_1^{\text{sim}}(t)$ and $s_{2'}^{\text{sim}}(t)$, only the phase noise differences are visible in Fig. 6.23. Moreover, only the two lasers p_1 and $p_{2'}$ enter in the two signals, but crosswise time-delayed and with opposite signs, here for example $-p_1$ in $s_1^{\text{sim}}(t)$ and $\boldsymbol{\mathcal{D}_{3'}^{\text{sim}}} p_1$ in $s_{2'}^{\text{sim}}(t)$. This is the origin of the mirror impression.

If we zoom into the beginning of the time series of Fig. 6.23, a jump at approximately 17 seconds occurs in the science signals (Fig. 6.24). This originates from the time-delayed laser noise instance within the received laser light, which needs these 17 seconds to travel down the link from sending to receiving spacecraft. Then, it is added interferometrically to the local laser and contributes to the overall time series of the science IFO output. Before reception, zeros are added to the local phase signal, and $s_i^{\text{sim}}(t)$ is dominated by phase noise of the local laser, $p_i(t)$, within the first ≈ 17 s.

6.4.2 Test Mass and Reference Interferometer

For the test mass and reference interferometer, no delayed data from a distant spacecraft is involved. The associated time series are plotted in Fig. 6.25. As we have seen, OB and TM displacement as well as readout noise are by far weaker than the laser phase noise. Thus, the signals of TM and reference IFO look pairwise identical on a large scale since they both include the same lasers with the identical signature. Therefore, we only plot the test mass output in Fig. 6.25. The data does not jump at ≈ 17 s since no delayed signal enters the measurement, and the overall phase varies by some 10^6 rad in maximum.

In order to compare the output of the test mass and reference IFOs, the subtraction $\varepsilon_i^{\text{sim}}(t) - \tau_i^{\text{sim}}(t)$ is constructed and shown in Fig. 6.26. It comprises noise of the maximal order ± 0.1 rad, which corresponds to the level of displacement noise (Sec. 6.3.2). The linear spectral density of the difference in Fig. 6.27 has as well a shape similar to the inserted displacement noise (Fig. 6.20). Hence, one can deduce that the primary noise contribution in the difference is the displacement noise, as expected (cf. Sec. 4.3.2), since laser frequency noise does cancel naturally. The readout noise with $10 \frac{\text{pm}}{\sqrt{\text{Hz}}}$ is again only secondarily.
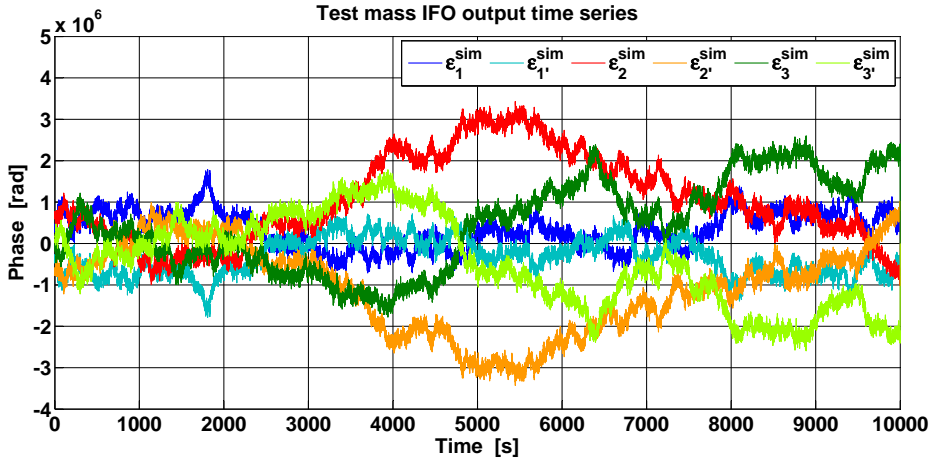
Figure 6.25: Test mass interferometer signals. Since the lasers are dominant and occur with the signature 'adjacent minus local', the TM IFO signals of the adjacent optical benches are approximately the same except for the sign.
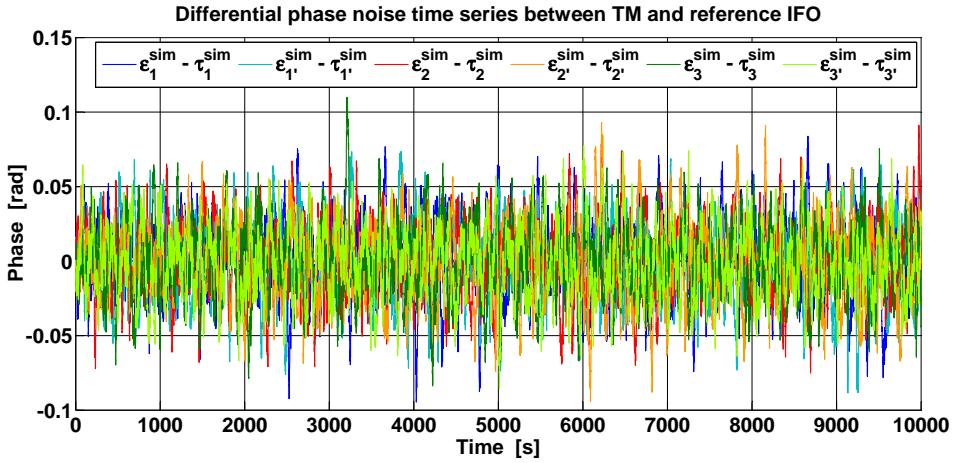
Figure 6.26: Differential phase noise between TM and reference interferometer. The differences $\varepsilon_{\underline{i}}^{\mathrm{sim}}(t) - \tau_{\underline{i}}^{\mathrm{sim}}(t) \sim \frac{4\pi\nu_0}{c}(\Delta_{\underline{i}} - \delta_{\underline{i}})$ and $\varepsilon_{\underline{i'}}^{\mathrm{sim}}(t) - \tau_{\underline{i'}}^{\mathrm{sim}}(t) \sim -\frac{4\pi\nu_0}{c}(\Delta_{\underline{i'}} - \delta_{\underline{i'}})$ give a phase noise time series dominated by the relative displacement noise due to OB and TM motion, since the difference is free of laser frequency noise.
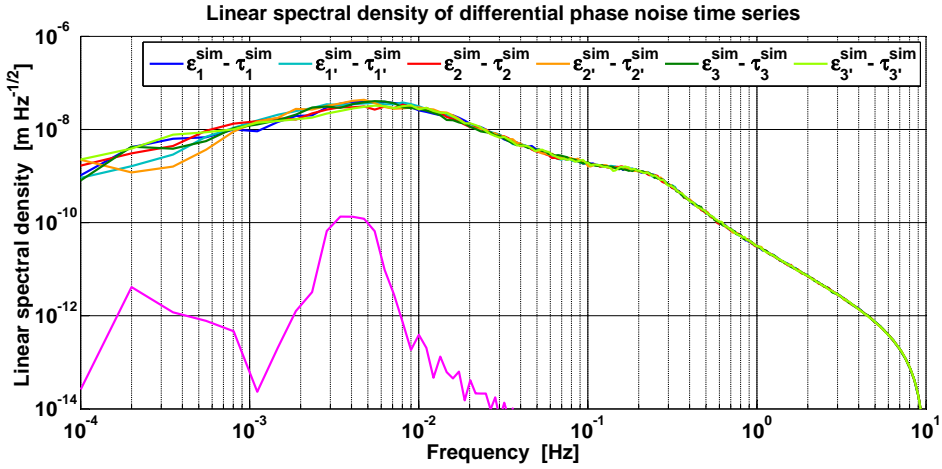
Figure 6.27: Linear spectral density of differential phase noise between TM and reference IFO. Though the displacement noise is 5 or more orders of magnitude in displacement weaker than the laser frequency noise (Fig. 6.17 converted to displacement), it still lies two to three orders of magnitude above the gravitational wave signal (purple) and completely covers it.
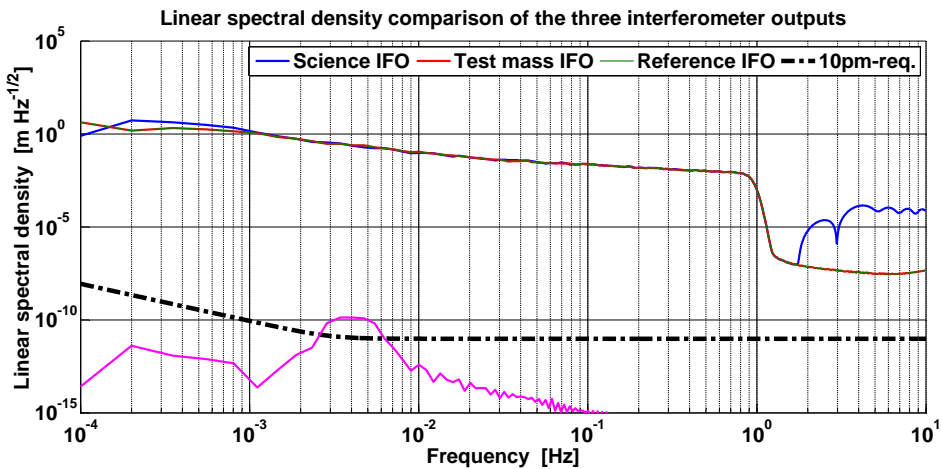
Figure 6.28: Linear spectral density of science, test mass and reference interferometer, compared with the GW signal and the 10 pm-requirement. Obviously, the sum of all input noise contributions in $s_1^{\mathrm{sim}}(t)$, $\varepsilon_1^{\mathrm{sim}}(t)$ and $\tau_1^{\mathrm{sim}}(t)$ is far above the requirement. The same holds true for all other onboard interferometer outputs which are not shown here explicitly, since they have the same shape. Note further that $\widetilde{\varepsilon}_i^{\mathrm{sim}}(t) \simeq \widetilde{\tau}_i^{\mathrm{sim}}(t)$, each dominated by the same laser frequency noise instance. The bumps of $s_i^{\mathrm{sim}}(t)$ at high frequencies come from the time-shifting jumps within the data (Fig. 6.24). The TDI performance must establish a noise suppression of more than 9 orders of magnitude in amplitude to get below the 10 pm-requirement.

Chapter 6

Fig. 6.28 compares the linear spectral densities of the onboard interferometer outputs, exemplarily for $s_1^{\mathrm{sim}}(t)$, $\varepsilon_1^{\mathrm{sim}}(t)$ and $\tau_1^{\mathrm{sim}}(t)$. Furthermore, the LSD of the gravitational wave signal in link 3 as well as the 10 pm-requirement are included for comparison. Since the reference IFO is dominated by the same laser frequency noise instances as the TM IFO, the LSDs look the same on a big scale. In Fig. 6.28 we can notice again the band-limited laser noise filter with cutoff frequency $f_{\mathrm{cut}} = 1\,\mathrm{Hz}$.

The goal is to suppress the noise of $\frac{\mathrm{cm}}{\sqrt{\mathrm{Hz}}}$ to $\frac{\mathrm{m}}{\sqrt{\mathrm{Hz}}}$ in the frequency range $10^{-4} \dots 1\,\mathrm{Hz}$ down to $\frac{\mathrm{pm}}{\sqrt{\mathrm{Hz}}}$-level where the GW signal can be extracted. The 1 pm-requirement can not be reached, because already the readout noise in Fig. 6.22 in the science interferometers is touching the 10 pm-requirement and limits the performance as we will also exhibit soon. In the following, the TDI performance is discussed.

6.5 Time-Delay Interferometry

The generated onboard signals in TDISim are eventually fed to the post-processing and various data combinations are formed to remove optical bench displacement and laser frequency noise. Doing so, the formerly secondary readout noise adds up to a level above the 10 pm-requirement. This effect is taken into account by a relaxed post-TDI requirement defined in [Tea98] and applied in [ESA11]. The total tolerable optical path length noise in the LISA measurements and post-processing due to residual laser frequency noise, shot noise, clock noise, interpolation inaccuracy etc., in the following called post-TDI 40 pm-requirement, is set to

$$\widetilde{x}_{\mathrm{req,output}}(f) = 4 \cdot \widetilde{x}_{\mathrm{req,input}}(f) = 40 \cdot 10^{-12}\,\frac{\mathrm{m}}{\sqrt{\mathrm{Hz}}}\sqrt{1 + \left(\frac{3\,\mathrm{mHz}}{f}\right)^4}. \qquad (6.2)$$

Here, $\widetilde{x}_{\mathrm{req,input}}(f)$ is given by Eq. (6.1).

In this section, we will at first elucidate the 40 pm-requirement in more detail. In order to apply it properly, a reference 90°-Michelson interferometer is constructed to which the TDI outputs are compared. This issue of signal calibration is adressed in Sec. 6.5.1. Next, the optical bench displacement noise suppression is analysed, followed by the main discussion of the TDI output data for different orbit cases in Sec. 6.5.4 and 6.5.5. The TDI 2.0 performance is tested again for pre-stabilised lasers with a lower frequency noise level of $280\,\frac{\mathrm{Hz}}{\sqrt{\mathrm{Hz}}} \cdot \mathrm{NSF}(f)$, and we will find out that in fact the readout noise is the limiting noise contribution after TDI application.

6.5.1 TDI Output Signal Calibration

In the following, the issue of signal amplitude calibration is adressed. Since in the TDI synthesis process various data streams are added together, the output signal amplitude (inlcuding noise and GW signal) is amplified compared to the input. Hence, only a signal-to-noise ratio discussion is useful, and residual noise

requirements are not practical in their original form. Subsequently, a possible adjustment is presented.

To start with, a more detailed look on the 40 pm-requirement is helpful, provided by Tab. 6.1 from [Tea98].

Noise	Contribution	Instances
Detector shot noise	$11 \frac{\text{pm}}{\sqrt{\text{Hz}}}$	4
Master clock noise	$10 \frac{\text{pm}}{\sqrt{\text{Hz}}}$	1
Residual laser phase noise after correction	$10 \frac{\text{pm}}{\sqrt{\text{Hz}}}$	1
Laser beam-pointing instability	$10 \frac{\text{pm}}{\sqrt{\text{Hz}}}$	4
Laser phase measurement and offset lock	$5 \frac{\text{pm}}{\sqrt{\text{Hz}}}$	4
Scattered-light effects	$5 \frac{\text{pm}}{\sqrt{\text{Hz}}}$	4
Other substantial effects	$3 \frac{\text{pm}}{\sqrt{\text{Hz}}}$	32
Total (quadratically) allocation	$40 \frac{\text{pm}}{\sqrt{\text{Hz}}}$	

Table 6.1: Noise allocation for the 40 pm-requirement, formulated in the yellow book [Tea98] in 1998. At that time, TDI was rarely investigated and formulated only for first generation combinations. The first column lists all primary noise sources, and the second column shows the contributions to the overall noise budget, i.e., after data processing, in terms of displacement noise. The third column gives the number of instances of the respective noise source in the synthesised (outdated) TDI combinations. At large, for TDI 1.0, the acceptable noise level is $40 \frac{\text{pm}}{\sqrt{\text{Hz}}}$, again relaxed towards low frequencies by the noise sensitivity function $\text{NSF}(f)$ from Eq. (2.7).

The table shows the primary noise contributions formulated in terms of displacement noise that are expected to allocate to $40 \frac{\text{pm}}{\sqrt{\text{Hz}}}$. This level is then comparable to the total optical path length error in a reference Michelson interferometer with perpendicular arms. Note, however, that this requirement was once formulated for first generation TDI combinations, and the simulation will show that the residual noise level is in a realistic setup with TDI 2.0 variables not reachable.

Additionally, in TDISim, laser beam-pointing instability and light scatter effects are not taken into account at all, and the detector shot noise is below the contribution of Tab. 6.1, since the complete readout noise is comparable to the 10 pm-requirement. That is, we use for TDISim noise inputs even below the noise levels allocated to the 40 pm-requirement and would therefore expect it to fulfill $\widetilde{x}_{\text{req,output}}(f)$. However, we will find out that the requirement is violated in a realistic flexing LISA case (Sec. 6.5.5), and especially in the static case. Hence, a reformulation of the 40 pm-requirement is crucial for the future but is beyond the scope of this thesis.

Chapter 6

Difficulties of Requirement Application

In order to apply the requirement, one has to compare the generated data properly, and we have to pay attention to two issues. First, as said before, the 40 pm-requirement is formulated for an equivalent rectangular interferometer. We therefore need to simulate a calibration 90° Michelson interferometer output and then compare all TDI results with that output. The interferometer should be placed with its beam splitter at the respective center spacecraft of the regarded TDI combination. For example, X_1 synthesises an interferometer with the BS at S/C 1 with both arms sensed twice (Fig. 3.11). Thus, the reference Michelson interferometer should be placed with its BS as well at S/C 1. We will carry out the comparison with the Michelson interferometer below in more detail. The second issue, the inclusion of the total transfer function from strain amplitude to the TDI output (e.g., $X_1(t)$), is complex and needs a detailed elucidation as follows.

One of the main LISA tasks is to determine the input strain for an incident gravitational wave (in our case, $h = 10^{-20}$) from the TDI outputs. This is a non-trivial enterprise as can be seen from Fig. 6.29, which demonstrates the whole chain implemented in TDISim.

An input strain h_+ is used to construct the gravitational wave tensor $\boldsymbol{h}$ (in the parentheses, the corresponding equation numbers are listed), and from this the light travel time variations $\Delta T_i(t)$ and optical phase shifts $H_i(t)$ are computed. The latter are then added with noise to form the phasemeter outputs $s_i^{\mathrm{sim}}(t)$. This first simulation part (blue boxed) is determined by nature, and the transfer function from Fig. 1.12 is shown below. In the second simulation part (green box), the data combinations $\eta_i^{\mathrm{sim}}(t)$ are constructed and the laser frequency noise free combination, here $X_1(t)$, is synthesised. These combinations do not rely on nature, but are instead completely artificial. The generic transfer function for X_1 can be found below the green box (cf. Sec. 3.3).

The synthesis of the TDI variables is in principle arbitrary. For example, a multiplication of the complete TDI-X_1 variable with any non-zero factor will not change the laser frequency noise suppression ability, but will scale the level of residual noise and the GW signal amplitude relative to any requirement. To remove this arbitrariness, we need to define a procedure to determine the gain factors with respect to a reference signal to be determined.

We chose the output of a conventional Michelson interferometer with perpendicular arms as a calibration reference, since the scientifically most important TDI-$X_{\underline{i}}$ combinations synthesise equal-arm Michelson interferometer outputs. Furthermore, it is known to have the best GW response, and we can then define a signal gain with respect to the interferometric output. If the gain is unequal to 1, the LSD outputs need a re-scaling if compared to any requirement. Finally, as explained previously, the 40 pm-requirement is formulated in terms of equivalent displacement noise in a 90°-Michelson interferometer and we need to compare with this anyway.
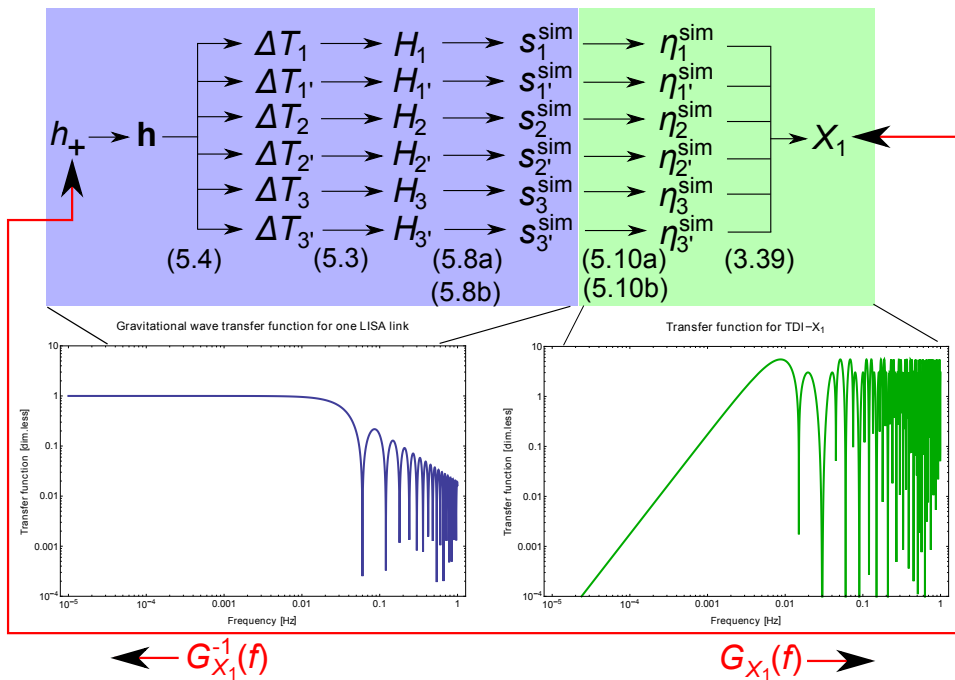
Figure 6.29: Schematic of the simulation chain in TDISim, presented here for X_1-synthesisation. In the blue box, all transitions are given by physical laws. The green box marks transitions by synthesised combinations that are not described by physical laws. Below are sketched the transfer functions of the two parts. The determination of the input strain (here: h_+) from the TDI output (here: X_1) is the crucial missing point in the simulation chain. A determination procedure of the gain function for each TDI combination, exemplarily here $G_{X_1}(f)$, is needed.

Determination Procedure of the Input Strain

For the determination of the gain factors (and subsequently the input strain) we first generate a GW frequency comb signal with amplitudes $h_1 = h_2 = \ldots = h_{81} = 10^{-20}$ distributed over 81 logarithmic equidistant frequencies f_n, $n = 1, \ldots, 81$ between $10^{-4}\,\mathrm{Hz}$ and $1\,\mathrm{Hz}$. The comb is given by

$$h_{\mathrm{comb}}^{\mathrm{tot}}(t) = h_+ \sum_{n=1}^{81} \cos(2\pi f_n t)\,, \tag{6.3}$$

where the polarisation tensors are neglected here for the sake of brevity. This is in accordance with Eq. (5.2), since $h_\times = 0$. Note that peaks at frequencies different by less than $1\,\mathrm{mHz}$ from the nulls of the transfer function (i.e., multiples of $15\,\mathrm{mHz}$ for X_1, Fig. 3.12) are removed from the comb, reducing to 72 peaks. The amplitude spectrum plot of the reduced comb $h_{\mathrm{comb}}(t)$, computed (as all spectra) with the flat-top window SFT3f from the LTPDA-Toolbox, is presented in Fig. 6.30.

Chapter 6
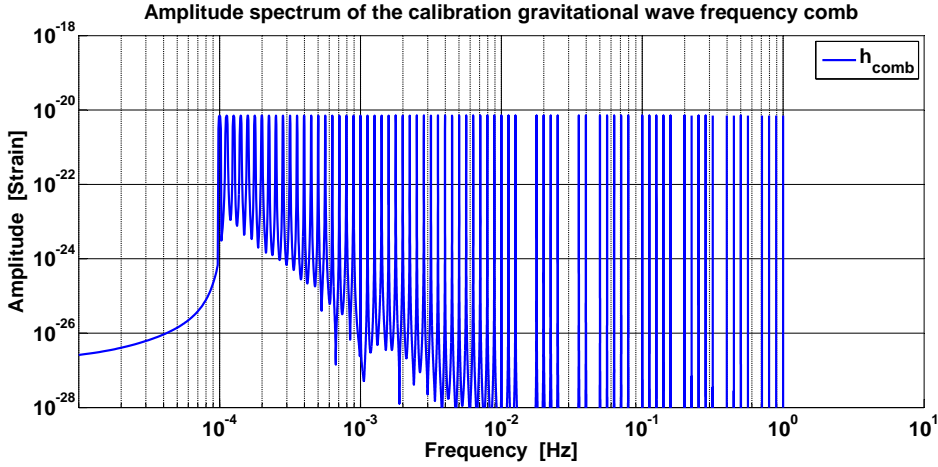
Figure 6.30: Amplitude spectrum of the calibration GW frequency comb. The peak heights are equal over the frequency band of 10^{-4} Hz to 1 Hz, corresponding to the root-mean square value of $h_{\mathrm{comb}}(t)$, i.e. $h_{\mathrm{comb}}^{\mathrm{rms}} = \frac{h_+}{\sqrt{2}} \approx 7 \cdot 10^{-21}$ in strain (Eq. (3.4a)). The reduction by 9 peaks is visible around 15 mHz (two peaks), 30 mHz (two peaks), 45 mHz, 90 mHz, 180 mHz, 360 mHz and 630 mHz.

This comb is processed without any additional noise through the complete TDI algorithm provided by TDISim. The simulation gives the time series $X_{\underline{i}}^H(t)$, $\alpha_{\underline{i}}^H(t)$ and $\zeta_{\underline{i}}^H(t)$, where the uppercase index H indicates that the combinations do not comprise any noise source. The exemplary conversion of the time series $X_1^H(t)$ to an amplitude spectrum is presented in Fig. 6.31.

In the next step, these signals are Fourier transformed to give the amplitude spectral densities $\widetilde{X}_{\underline{i}}^H(f)$, $\widetilde{\alpha}_{\underline{i}}^H(f)$ and $\widetilde{\zeta}_{\underline{i}}^H(f)$. The ratios

$$G_{X_{\underline{i}}}(f) = \frac{\widetilde{X}_{\underline{i}}^H(f)}{\widetilde{h}_{\mathrm{comb}}(f)}, \quad G_{\alpha_{\underline{i}}}(f) = \frac{\widetilde{\alpha}_{\underline{i}}^H(f)}{\widetilde{h}_{\mathrm{comb}}(f)}, \quad G_{\zeta_{\underline{i}}}(f) = \frac{\widetilde{\zeta}_{\underline{i}}^H(f)}{\widetilde{h}_{\mathrm{comb}}(f)} \tag{6.4}$$

yield then the frequency-dependent gain of the complete signal in the respective combinations. That is, for instance, $G_{X_1}(f)$ describes the transition from input strain signal to TDI-X_1 output in terms of optical phase, as depicted in Fig. 6.29, and has units of $[G_{X_1}] = 1 \, \frac{\mathrm{rad\,Hz}^{-\frac{1}{2}}}{\mathrm{strain\,Hz}^{-\frac{1}{2}}} = 1 \, \frac{\mathrm{rad}}{\mathrm{strain}}$. The gain function for X_1 is presented in Fig. 6.32.

From $G_{X1}(f)$, one can directly identify the GW phase modulation amplitude at any Fourier frequency. Exemplarily, for $f = 4$ mHz, one can find a gain factor of $3.85 \cdot 10^{16} \, \frac{\mathrm{rad}}{\mathrm{strain}}$. That is, for an input strain amplitude of $h = 10^{-20}$, a phase amplitude of $10^{-20} \cdot G_{X_1}(4\,\mathrm{mHz}) = 3.85 \cdot 10^{-4}$ rad in X_1 is expected.
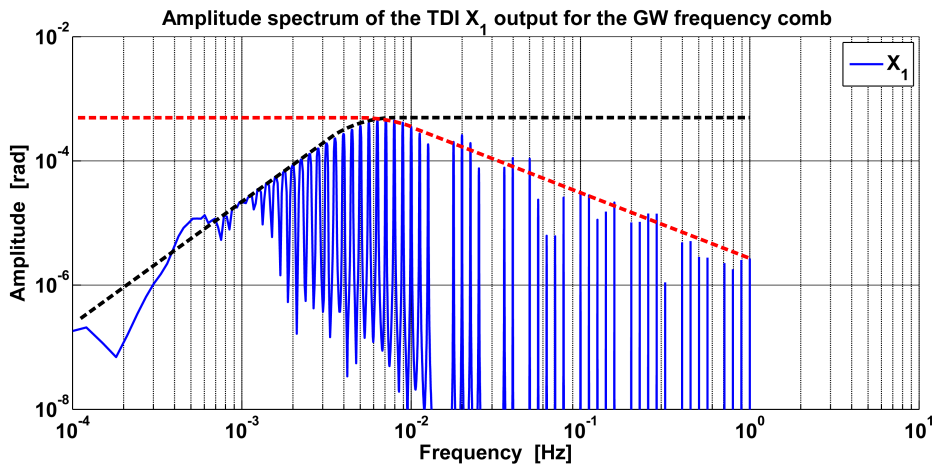
Figure 6.31: Amplitude spectrum of the X_1 output for the GW comb. It is a combination of the arm transfer function (red dashed) from Fig. 1.12 with the f^{-1}-decay for high frequencies and the TDI transfer function (black dashed) shown in Fig. 3.12 with the f^2-slope at low frequencies.
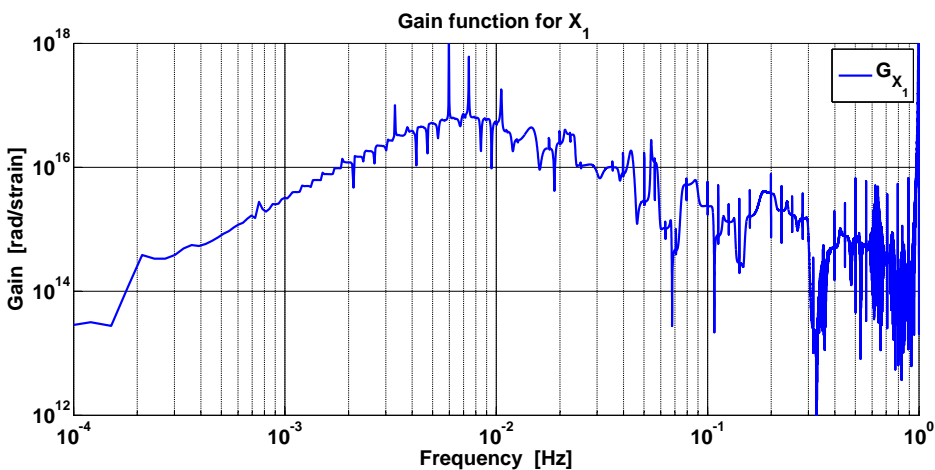
Figure 6.32: Gain function for the X_1 combination. It shows the same frequency behaviour as the amplitude spectrum in Fig. 6.31, since the (constant) amplitude spectrum of the frequency comb only normalises the output amplitude spectrum.

Chapter 6

However, within the real mission, one could not determine the gain factors, because the strain amplitude(s) of the GW(s) are unknown. Contrarily, the strain of the GW is one of the target parameters for the data analysts. It is therefore crucial to simulate GW signals with various locations and incident directions as well as with different strains and frequencies previously before the launch of LISA. These pre-determined gain functions can then vice versa be used to determine the strain. Furthermore, the transfer functions should be determined analytically in future work to cross-check the numerical implementations performed with the comb model.

The Michelson Interferometer Signal

By $G(f)$, we can not yet make any statement about amplifying or attenuating the GW signal in the combinations. In order to compare with a reference signal in TDISim, a conventional Michelson interferometer with equal armlengths as discussed in Sec. 1.3 and 3.1.1 is used for calibration. From this apparatus, it is known that it has the best GW response under normal GW incidence. The Michelson interferometer setup is virtually placed with its beam splitter at S/C 1 for comparison with X_1, α_1 and ζ_1 as shown in Fig. 6.33, and similar for S/C 2 and 3.
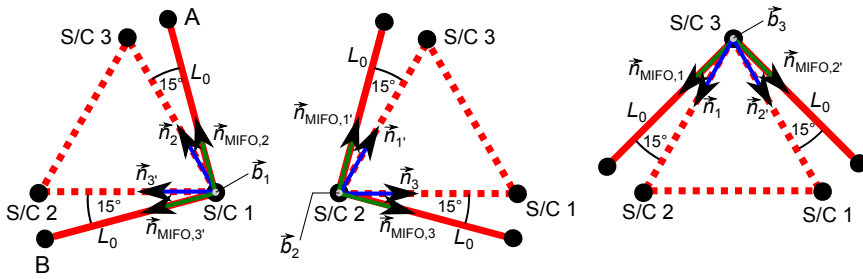
Figure 6.33: Synthesised Michelson interferometer setup relative to the spacecraft. The armlengths of the Michelson interferometer are exactly $L_0 = 5 \cdot 10^9$ km. This value differs by less than 1% from the 'real' armlengths. Furthermore, each arm direction vector in the $60°$ constellation (blue arrows, $\vec{n}_i$) is rotated by $\pm 15°$ with respect to the rotation axis (grey circle within the S/C, $\vec{b}_{\underline{i}}$, pointing perpendicular out of the plane of projection) to define the arm directions of the (almost) orthogonal interferometer arms (green arrows, $\vec{n}_{\mathrm{MIFO},i}$). The angle between the green arrows differs by only $\pm 1°$ from $90°$ in the simulation for each Michelson interferometer.

The arm directions for the perpendicular interferometers, $\vec{n}_{\mathrm{MIFO},i}$, are constructed from the known direction vectors $\vec{n}_i$ of the $60°$-constellation. Exemplarily, for the Michelson interferometer seated with its beam splitter at S/C 1, the receiving vectors $\vec{n}_{3'}$ and $\vec{n}_2$ are used to form a rotation axis by $\vec{b}_1 = \vec{n}_2 \times \vec{n}_{3'}$ (similar for $\vec{b}_2$ and $\vec{b}_3$) which stands perpendicular on the spanned plane (Fig. 6.33). With this, a rotation matrix is constructed via [Ott11]

$$D(\vec{b}_{\underline{i}}, \varphi) = \cos(\varphi) \cdot \mathbb{1} + (1 - \cos(\varphi)) \cdot (\vec{b}_{\underline{i}} \circ \vec{b}_{\underline{i}}) - \sin(\varphi)(\vec{b}_{\underline{i}} \times) \tag{6.5}$$

using the dyadic product $(\vec{b}_{\underline{i}} \circ \vec{b}_{\underline{i}})$ and the operator $(\vec{b}_{\underline{i}} \times)$ waiting for a vector to map (similar for the other spacecraft). $D(\vec{b}_{\underline{i}}, \varphi)$ describes the rotation around $\vec{b}_{\underline{i}}$ by the angle φ according to the right screw rule. One can then determine

$$\vec{n}_{\text{MIFO},3'} = D(\vec{b}_1, \varphi = +15°) \cdot \vec{n}_{3'} \quad \text{and} \vec{n}_{\text{MIFO},2} = D(\vec{b}_1, \varphi = -15°) \cdot \vec{n}_2 . \quad (6.6)$$

This finally gives the positions of the virtual end mirrors A and B (Fig. 6.33, left picture) in the Michelson interferometer centered at S/C 1 by

$$\vec{x}_{\text{A},1} = \vec{x}_1 + L_0 \cdot \vec{n}_{\text{MIFO},2} \quad \text{and} \quad \vec{x}_{\text{B},1} = \vec{x}_1 + L_0 \cdot \vec{n}_{\text{MIFO},3'} . \quad (6.7)$$

Here, $\vec{x}_1$ is the CoM position of S/C 1 (Sec. 5.2.2) and $L_0 = 5 \cdot 10^9$ m denotes the constant armlengths. The construction for the other calibration interferometers is similar.

Relying on the new positions given by Eq. (6.7), TDISim eventually simulates the 90° Michelson interferometer outputs at each spacecraft for the GW frequency comb input signal $h_{\text{comb}}(t)$. The corresponding response amplitude spectrum for the Michelson interferometer placed at the position of S/C 1 is presented in Fig. 6.34. It is flat for low frequencies and decays for frequencies greater than some mHz with $\propto f^{-1}$ which is (except for the frequency region) the same behaviour as in 1.3.4.

Comparable to the described procedure to determine the input strain, the gain function of the Michelson interferometer with respect to S/C $\underline{i}$ can be defined as

$$G_{\text{MIFO},\underline{i}}(f) = \frac{\widetilde{y}^H_{\text{PD},\underline{i}}(f)}{\widetilde{h}_{\text{comb}}(f)} . \quad (6.8)$$

Here, $\widetilde{y}^H_{\text{PD},\underline{i}}(f)$ is the linear spectral density of the conventional Michelson interferometer output from Eq. (3.1) placed with its BS at S/C $\underline{i}$, excluding any noise, and $\widetilde{h}_{\text{comb}}(f)$ marks again the linear spectral density of the calibration comb. Exemplarily, $G_{\text{MIFO},1}(f)$ is plotted in Fig. 6.35.

The TDI Output Scaling Function

Combining the two gains $G_{X_1}(f)$ and $G_{\text{MIFO},1}(f)$, it is finally possible to scale the TDI-X_1 output with respect to a common requirement to be set (other TDI variables similar). This is as well necessary for the first generation TDI, since the 40 pm-requirement refers to a conventional Michelson interferometer. The dimensionless scaling function is defined by

$$k_{X_1}(f) = \frac{G_{X_1}(f)}{G_{\text{MIFO},1}(f)} = \frac{\widetilde{X}^H_1(f)}{\widetilde{y}^H_{\text{PD}}(f)} , \quad (6.9)$$

and analogously for the other combinations.
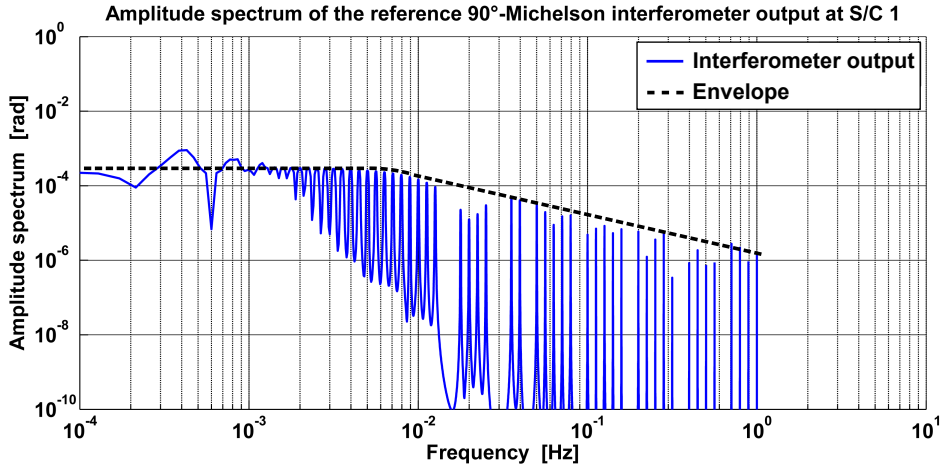
Figure 6.34: Michelson interferometer response to the calibration frequency comb of a $90°$-Michelson interferometer placed at S/C 1. Also shown in dashed-black is the frequency dependence of the response function (without the zero pattern).
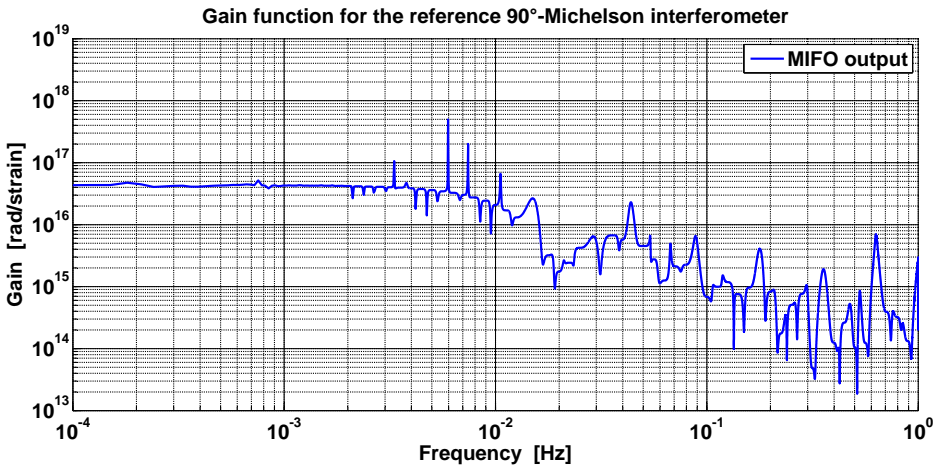
Figure 6.35: Gain function $G_{\mathrm{MIFO},1}(f)$ of the Michelson interferometer placed virtually with its beam splitter at S/C 1. For low frequencies, it has the constant value of $\approx 4 \cdot 10^{16} \, \frac{\mathrm{rad}}{\mathrm{strain}}$ and rolls of with $\propto f^{-1}$ for high frequencies.
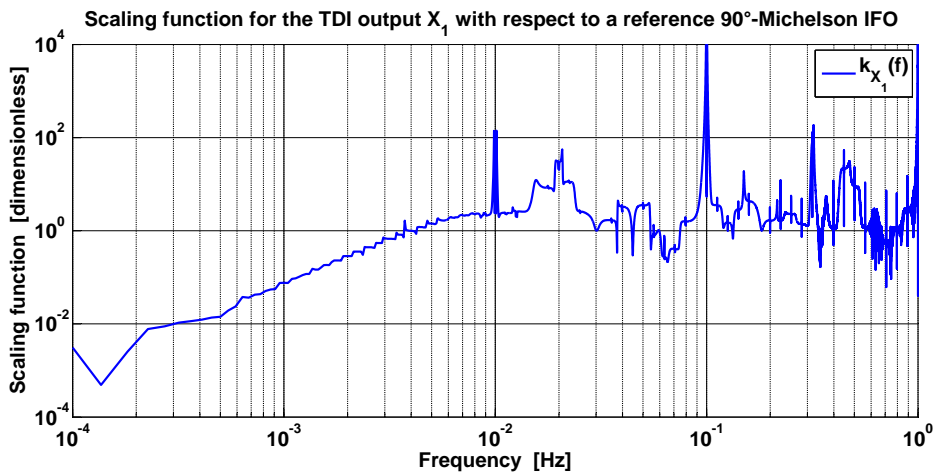
Figure 6.36: Scaling function for the TDI-X_1 output. For low frequencies, it rolls off with $\propto f^{-2}$, and for high frequencies, $k_{X_1}(f)$ yields a factor of 2. For the $4\,\text{mHz}$ GW signal, the scale function yields a factor of $k_{X_1}(4\,\text{mHz}) = 0.997$.
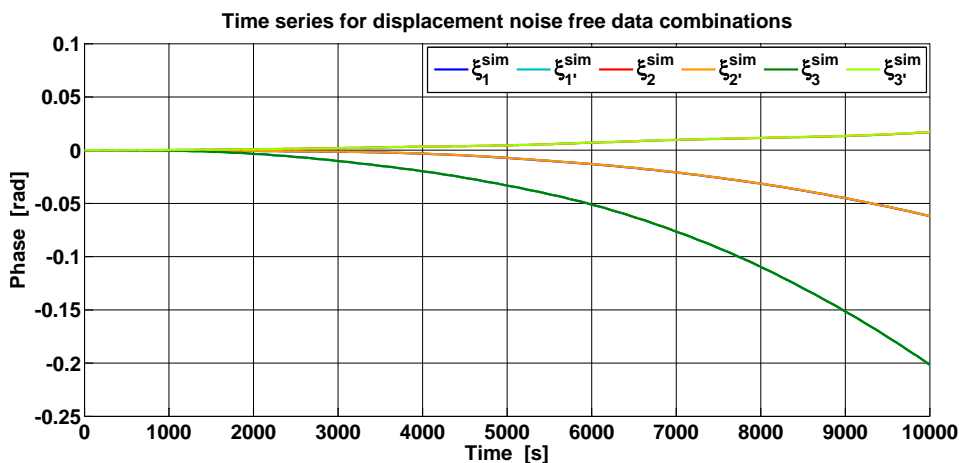
Figure 6.37: Time series $\xi_i^{\text{sim}}(t)$ of simulated phasemeter data with TM and OB noise only. It is corrected for optical bench displacement noise. Laser frequency noise is ignored here since it would otherwise completely swamp the data and make the displacement noise removal invisible. $\xi_i^{\text{sim}}(t)$ is shown here for $10000\,\text{s}$. The relative displacement drifts get distinct and diverge in the worst to $-0.2\,\text{rad}$ for $\xi_{1'}^{\text{sim}}(t)$ and $\xi_3^{\text{sim}}(t)$ within the simulation time. As argued in Sec. 6.3.2, the curves seem to follow each other in pairs $\xi_1^{\text{sim}}(t)$ and $\xi_{2'}^{\text{sim}}(t)$, $\xi_{1'}^{\text{sim}}(t)$ and $\xi_3^{\text{sim}}(t)$, $\xi_2^{\text{sim}}(t)$ and $\xi_{3'}^{\text{sim}}(t)$. This impression is again due to the small resolution.

Chapter 6

The bigger the value of the function $k(f)$, the larger is the amplification of the regarded combination output to a GW signal compared with the response of a 90° Michelson interferometer placed at the corresponding spacecraft. For scaling, the data must therefore be *divided* by $k(f)$. Exemplarily, $k_{X_1}(f)$ is presented in Fig. 6.36. Finally, it should be noted that the spectral density plots in Sec. 6.5.4 – 6.5.6 all include the scaling with respect to a reference Michelson interferometer and are thus comparable to a common requirement, mostly the 40 pm-requirement.

6.5.2 Optical Bench Displacement Noise Suppression

After the discussion about the signal calibration, we will now concentrate on the TDI output signals. As described in Sec. 5.2.6, TDISim constructs in a first processing step data combinations $\xi_i^{\mathrm{sim}}(t)$ free of optical bench displacement noise according to Eqn. (5.9a) and (5.9b). However, since laser frequency noise is by orders of magnitude in amplitude larger than the displacement noise, we could not directly observe the suppression by the formation of $\xi_i^{\mathrm{sim}}(t)$ in the presence of laser noise. Instead, in order to test the performance of the displacement noise suppression scheme, we simulated phasemeter data with displacement noise and GW only for LISA with ESA orbits.

It is expected that the synthesised data $\xi_i^{\mathrm{sim}}(t)$, which combines these 'idealistic' phasemeter outputs, is free of optical bench displacement noise and, due to the absence of laser and readout noise, we can directly observe the TM drift together with the GW signal modulation of some tenth of mrad. Figs. 6.37 and 6.38 confirm this.

As expected, the displacement noise is suppressed by more than two orders of magnitude in amplitude such that the GW signal gets already visible in the data $\xi_i^{\mathrm{sim}}(t)$. This performance is shown in the zoomed Fig. 6.38 and confirmed by the corresponding LSDs in Fig. 6.39. Here, only the low-frequency part of the noise for $f < 0.5\,\mathrm{mHz}$ can not be removed from the input signal $s_1^{\mathrm{sim}}(t)$, showing up as the long-term drift in Fig. 6.37. The LSD of $\xi_i(t)$ rolls off with $\propto f^{-2}$ in amplitude, according to the acceleration noise spectral density from Eq. (2.3c).

Here and in the following, the LSDs of the synthesised data streams are presented for the frequency range $10^{-4}\,\mathrm{Hz}$ up to $2\,\mathrm{Hz}$. The lower bound is due to the practical limitation of our simulated time series of $10000\,\mathrm{s}$. The upper limit of $2\,\mathrm{Hz}$ is set such that the (irrelevant) high frequency behaviour beyond the anti-alias filter cutoff frequency of $f_{\mathrm{cut}} = 1\,\mathrm{Hz}$ is not displayed since the scientific interesting frequency band is from $10^{-4} \ldots 1\,\mathrm{Hz}$.
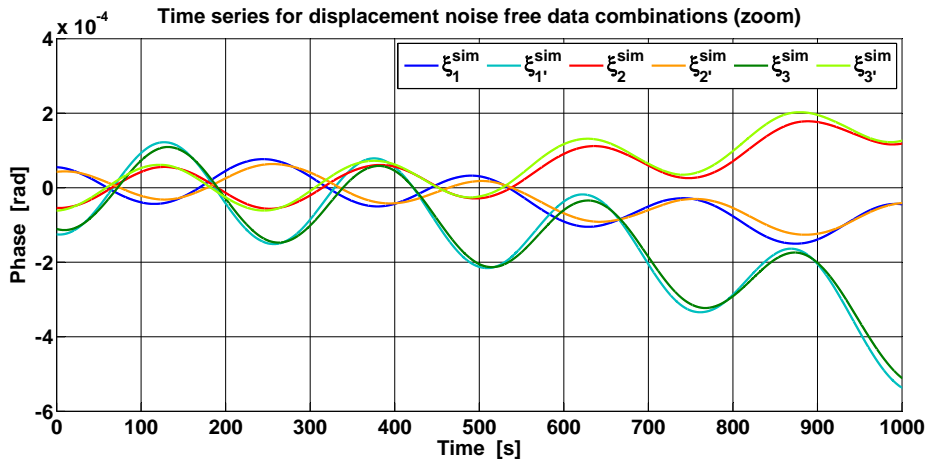
Figure 6.38: Time series of $\xi_i^{\mathrm{sim}}(t)$ (zoom), presented for the first $1000\,\mathrm{s}$. Besides the relative OB-TM-drift, the modulation due to gravitational waves with a maximal amplitude of $10^{-4}\,\mathrm{rad}$ for $\xi_{1'}^{\mathrm{sim}}(t)$ is visible here.
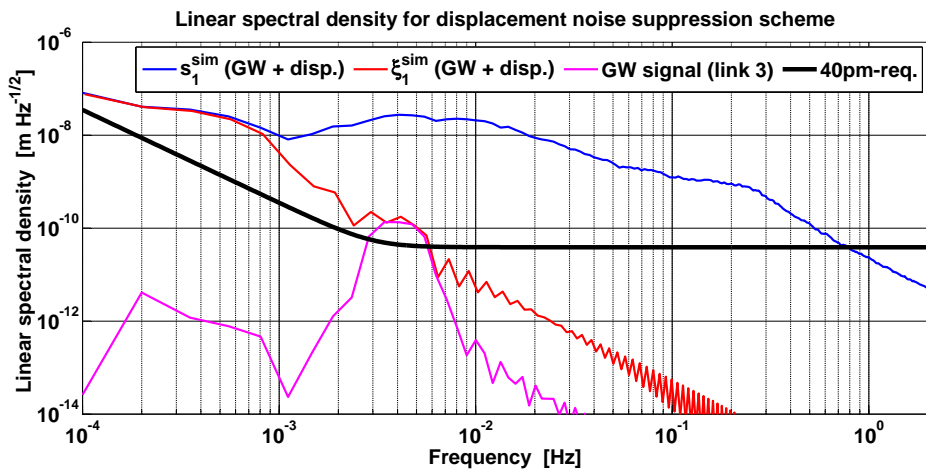
Figure 6.39: Linear spectral density of $\xi_1^{\mathrm{sim}}(t)$ for displacement noise only. Shown are the LSDs $\widetilde{s}_1^{\mathrm{sim}}$ (blue), $\widetilde{\xi}_1^{\mathrm{sim}}$ (red) and the equivalent corresponding GW signal amplitude for comparison (pink). The rise of $\widetilde{\xi}_1^{\mathrm{sim}}$ towards low frequencies shows up as the drift in time domain. The spikes in the GW signal (which are further propagated to ξ_i^{sim} by construction) originate from the single link GW transfer function Eq. (1.60). Similar curves can be found for the other $\xi_i^{\mathrm{sim}}(t)$-combinations.

Chapter 6

Noise contributions to the TDI input data
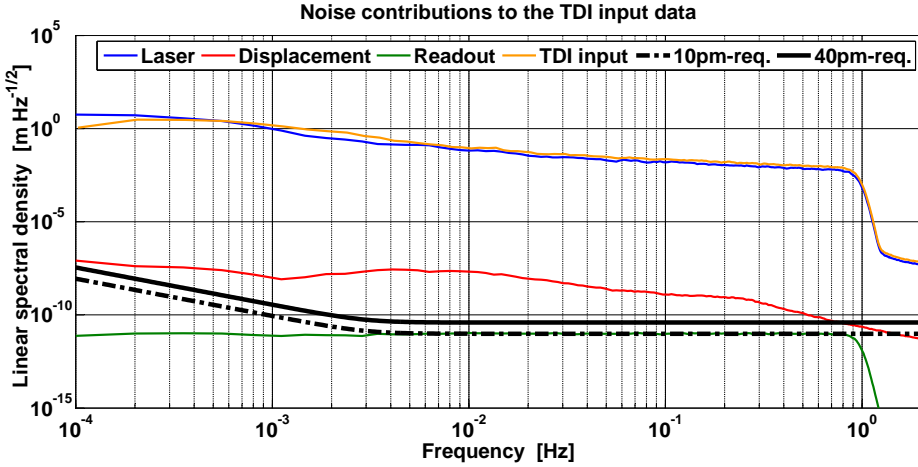
Figure 6.40: Linear spectral density of TDI input data $\eta_i^{\mathrm{sim}}(t)$, exemplarily shown for $\eta_1^{\mathrm{sim}}(t)$. Laser frequency noise is the dominating noise source and covers the GW by several orders of magnitude at the signal frequency of $f_{\mathrm{gw}} = 0.004\,\mathrm{Hz}$. Readout noise will limit the TDI performance but could be regarded as secondary noise, because it is fulfilling the 10 pm-requirement. For comparison, the OB displacement noise (including the TM motion) and the post-TDI 40 pm-requirement is displayed as well.

6.5.3 TDI Input Data

In the following, we move from the simplified scenario of displacement and GW signal only, applied in Sec. 6.5.2, back to our more realistic noise scenario including all noise sources examined in Sec. 6.3. After the discussed OB displacement noise suppression, the last step before forming the Michelson and Sagnac combinations is to reduce the data to three independent laser noise instances by the use of Eqn. (5.10a) and (5.10b).

The linear spectral density plot of these synthesised combinations $\eta_i^{\mathrm{sim}}(t)$ with all their noise ingredients is presented in Fig. 6.40, here for $\eta_1^{\mathrm{sim}}(t)$. The other data streams are similar. As can be seen, the TDI input and 40 pm-requirement are separated by approximately 8 orders of magnitude or more, and laser frequency noise is dominant. It needs to be reduced in post-processing below the 40 pm-requirement to establish TDI functionality. The optical bench displacement (including the TM) is shown here for comparison, but was already removed previously by the formation of $\xi_i^{\mathrm{sim}}(t)$. Note that the (secondary) readout noise at $10\,\frac{\mathrm{pm}}{\sqrt{\mathrm{Hz}}}$ in the relevant frequency band will limit the TDI performance, as will be shown later.

Finally, the $\eta_i^{\mathrm{sim}}(t)$-combinations are fed to the laser frequency noise removal scheme to form the Michelson and Sagnac combinations.

6.5.4 First Generation TDI

Using the discussed input data $\eta_i^{\mathrm{sim}}(t)$, we will at first test the functionality of TDI for the static LISA case. Since no relative orbital drifts are present within that detector model, the algorithms do not need to account for time-dependent detector armlengths. First generation laser phase noise free data combinations (Michelson X, Y, Z and Sagnac $\alpha, \beta, \gamma, \zeta$, cf. Sec. 3.2) are then constructed and we expect them to suppress the laser noise sufficiently.

Scaling Functions

First of all, according to the procedure explained in Sec. 6.5.1, we computed the scaling functions for the first generation TDI combinations. They are plotted in Fig. 6.41 for the Michelson variables X, Y, Z and in Fig. 6.42 for Sagnac types ζ and α, β, γ. A scaling function value smaller 1 implies an attenuation of the signal with respect to a Michelson interferometer reference signal. Exemplarily, for X, this is the case for any signal below $8\,\mathrm{mHz}$. The simulated $4\,\mathrm{mHz}$ signal is hence attenuated by the factor $k_X(f = 4\,\mathrm{mHz}) \approx 0.5$ in the X-combination.

All scaling functions show again the f^1-slope at low frequencies and a vanishing slope at higher frequencies. The appearance of the dips in the high frequency regime can be explained by the nulls of the transfer functions and the spikes of the (numerically determined) gain functions. It is further notable that the scaling differs between X, Y and Z (and the same for the Sagnac variables), which is due to the advantageous and disadvantageous orientation of the (virtual) interferometers with respect to the GW source location and polarisation. Concluding from Figs. 6.41 and 6.42, we will expect the strongest GW signal reconstruction in the combinations Z and γ. For ζ, the GW response is the poorest, as predicted in Sec. 3.2.2, since the combination itself is designed such that it suppresses any GW signal at lower frequencies. However, small fractions of the GW signal should be visible in ζ as well.

The Carrier-to-Receiver Noise Density

We will now analyse the TDI outputs directly. Since the $40\,\mathrm{pm}$-requirement is only partially significant as discussed in Sec. 6.5.1, the second figure of merit for the rest of this chapter is the carrier-to-receiver noise density $\mathrm{C/N_0}$, defined as

$$\mathrm{C/N_0} = \frac{\text{signal power}}{\text{narrow-band noise level}}\,, \quad [\mathrm{C/N_0}] = 1\,\frac{\mathrm{rad}^2}{\frac{\mathrm{rad}^2}{\mathrm{Hz}}} = 1\,\mathrm{Hz}\,. \tag{6.10}$$

Contrary to the common use in communication electronics, the carrier in $\mathrm{C/N_0}$ here refers to the injected gravitational wave of constant small amplitude.

Chapter 6

Scaling functions for the first generation Michelson variables for static LISA
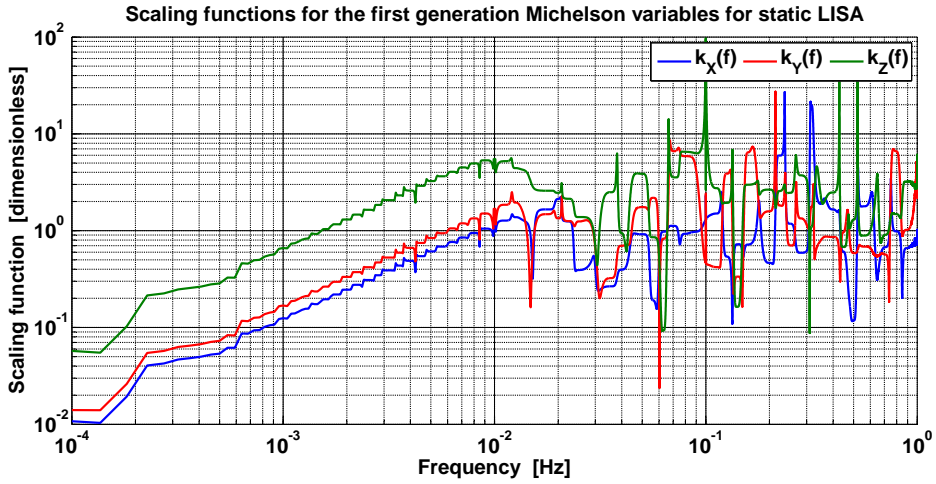
Figure 6.41: Scaling functions for the TDI 1.0 Michelson combinations X, Y and Z. Towards low frequencies, any signal is weakened $\propto f^{-1}$ with respect to the reference Michelson interferometer at the corresponding S/C. Attenuation is the case if $k(f) < 1$, which is here for $f < 8\,\mathrm{mHz}$ in X, $f < 6\,\mathrm{mHz}$ in Y and $f < 1.5\,\mathrm{mHz}$ in Z. Towards high frequencies, the scaling has no slope. The signal in Z is amplified the most within the regarded data series.

Scaling functions for the first generation Sagnac variables for static LISA
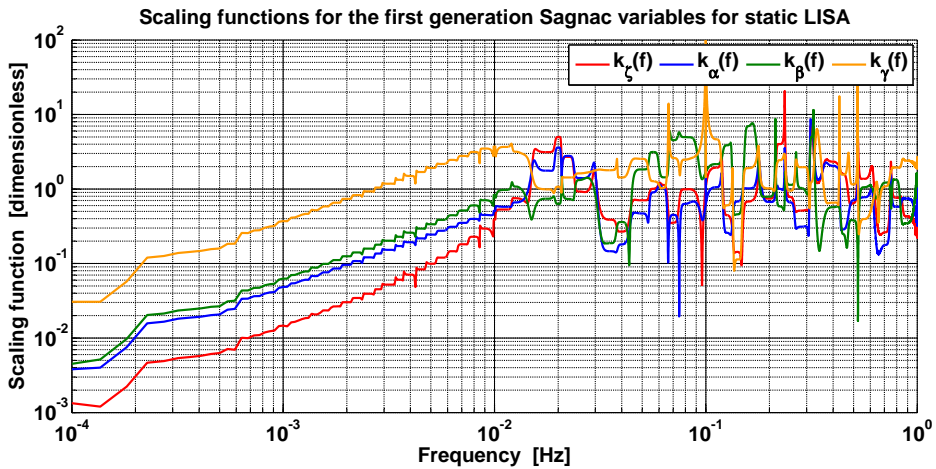
Figure 6.42: Scaling functions for the TDI 1.0 Sagnac combinations ζ and α, β, γ. Again, at low frequencies, the scaling functions rise linearly in f leading to a zero slope for higher frequencies. $k_\zeta(f)$ shows the strongest suppression for $f < 10\,\mathrm{mHz}$.
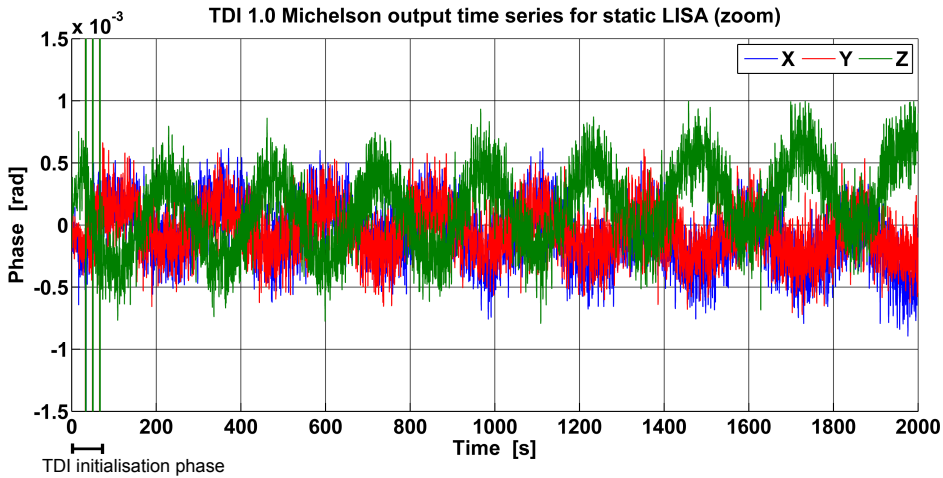
Figure 6.43: TDI Michelson output time series for static LISA (zoom). Shown are the combinations X, Y and Z for the first 2000 s with all noise sources included. Note the TDI initialisation phase from 0 to ≈ 70 s where the laser frequency noise does not cancel properly for short time periods. The TDI outputs oscillate between maximally $-4 \ldots 4 \cdot 10^{-4}$ rad with imprinted residual noise of $\pm 1 \cdot 10^{-4}$ rad.
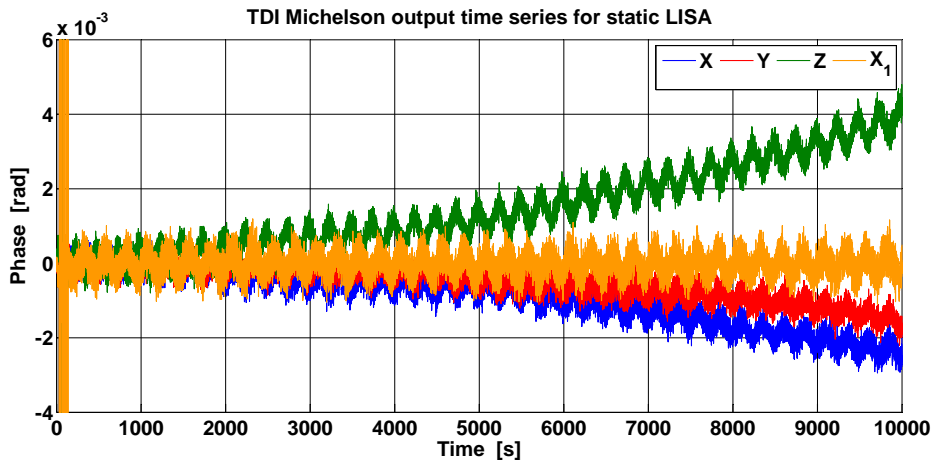
Figure 6.44: TDI Michelson output time series for static LISA. Note the phase drift of the three TDI 1.0 combinations due to the relative OB-TM displacement. It is suppressed within the TDI 2.0 variable X_1, formed in the case of a static LISA constellation.

Chapter 6

The signal power is determined from the power spectrum (PS, in rad^2) of the regarded TDI output by the use of a flat-top window (appendix A), and the noise level can be read off the power spectral density (PSD, in units of $\frac{\text{rad}^2}{\text{Hz}}$) in a narrow frequency band around the signal peak. Eventually, the two quantities are divided by each other and give the value for C/N_0. This quantity is connected to the signal-to-noise ratio by integration over time and by the square root. For example, a C/N_0 of $1\,\text{Hz}$ gives a signal to noise ratio after $T = 10000\,\text{s}$ observation time of $\text{SNR} = \sqrt{C/N_0 \cdot T} = 100$. The determination procedure of C/N_0 is exemplarily shown for the TDI 1.0 Michelson X combination below, and is computed for the other combinations in a similar way.

Michelson Combinations

The Michelson combination output time series $X(t)$, $Y(t)$ and $Z(t)$ are presented in Fig. 6.43 for the time interval 0 to 2000 s. Within the first approximately 70 s, the TDI initialisation phase takes place and the time delays are applied step by step to form the Michelson combinations. Within that procedure, it happens that the laser frequency noise does not cancel properly for short time intervals, indicated by the vertical lines. This is due to the fragmentary formation of all necessary time delays. For the first generation Michelson combinations, this is four times the case, since fourfold time delays are involved in maximum (1 in $\eta_i(t)$, 3 in $X(t)$).

However, after the initialisation (which is omitted in the analysis), a GW signal occurs in each Michelson combination, noise residuals (mainly readout noise) imprinted on each. The combinations show a modulation of $\approx 3 \ldots 4 \cdot 10^{-4}\,\text{rad}$. Additionally, the TDI Michelson outputs are phase-shifted with respect to each other. The deviations in both amplitude and relative phase is due to the different orientations of the detector arms with respect to the incident gravitational wave (Eq. (5.4)) and subsequently due to the slightly different transfer functions.

By a closer look on Fig. 6.43, the curves seem to drift away for emerging time. The whole 10000 s time series in Fig. 6.44 confirms this observation. The drift originates again from the OB-TM displacement. However, this behaviour does not appear anymore if TDI 2.0 combinations (e.g., X_1) are constructed, as will be also the case in a flexing LISA constellation (Sec. 6.5.5). This is due to the difference in the transfer functions at low frequencies presented in Fig. 3.12. X_1 suppresses in a stronger way with $\propto f^2$ the low frequency noise (i.e., displacement noise) and GW signal than X with only $\propto f^1$.

In order to compute any significant linear spectral density, here and in the following the LSD of the TDI output is converted to displacement via $\widetilde{x} = \frac{c}{2\pi\nu_0}\widetilde{\phi}$ and has thus units of $\frac{\text{m}}{\sqrt{\text{Hz}}}$. Moreover, the initialisation phase is not taken into account, since it introduces a large noise amount for frequencies above 1 Hz. This is exemplarily shown for TDI-X in Fig. 6.45. At $f \approx 0.2\,\text{Hz}$, the LSD of the complete TDI output series (including the initialisation phase) jumps by several orders of magnitude on a noise level of the order $10^{-5}\,\frac{\text{m}}{\sqrt{\text{Hz}}}$ and higher for $f > 0.5\,\text{Hz}$.
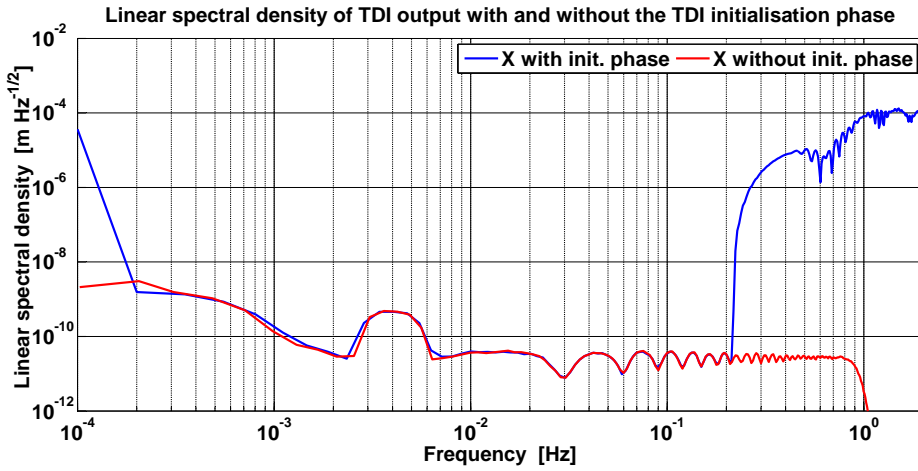
Figure 6.45: Linear spectral density with and without the TDI initialisation phase. The high frequency behaviour differs completely, since the intialisation phase introduces a large amount of noise of more than $10^{-5} \frac{\mathrm{m}}{\sqrt{\mathrm{Hz}}}$ for $f > 0.5 \, \mathrm{Hz}$.
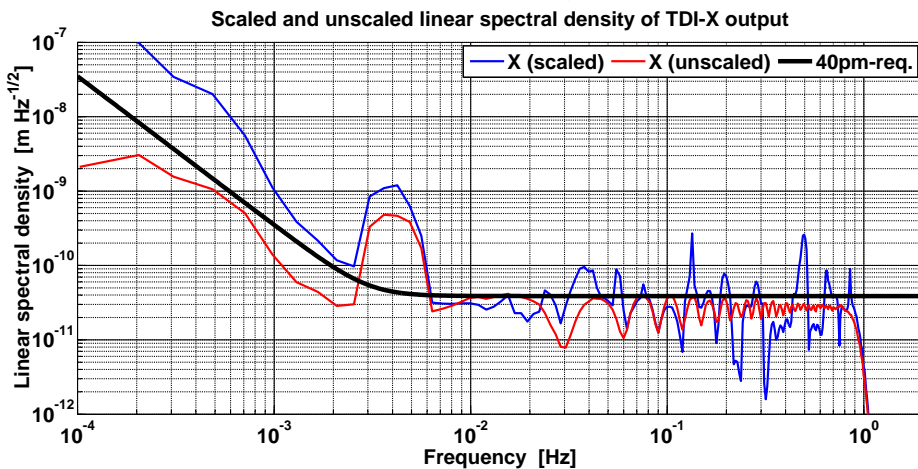
Figure 6.46: Linear spectral density with and without scaling. The red curve displays the linear spectral density of the (sliced) TDI-X output. The nulls of the transfer function are clearly visible at multiples of $3 \, \mathrm{mHz}$, as in Fig. 3.7. The division of the LSD by $k_X(f)$ yields the blue and more spiky curve. For low frequencies, the LSD gets amplified (division by a number < 1), and for high frequencies, the nulls are slightly diluted.

Chapter 6

However, since we are not interested in the TDI initialisation phase but instead in the properly formed TDI combinations, the linear spectral densities are computed from sliced time series beginning at 150 s and ending at 9900 s simulation time (to avoid interpolation errors at the end of the data series as well) for the rest of this thesis.

In a further step, the computed linear spectral densities are scaled with help of the frequency-dependent functions $k(f)$ discussed above. The division changes the low frequency behaviour and lowers the high frequency noise level except for the spikes in the scaling functions, which also appear in the scaled LSD. For X, this is exemplarily presented in Fig. 6.46. On the one hand, the unprocessed TDI output shows an f^2-growth towards low frequencies, while the scaled version has an f^3-slope, and the high frequency part gets spiky. On the other hand, the GW signal is amplified by a factor of two according to the scaling function $k_X(f)$, which has the value 0.5 at $f = 4\,\mathrm{mHz}$ (Fig. 6.41).

Finally, in order to determine the carrier-to-receiver noise density $\mathrm{C/N_0}$, the ratio of the power spectrum at $f = f_\mathrm{gw} = 4\,\mathrm{mHz}$ and the power spectral density in a narrow band around f_gw is computed. For X, the power spectrum is presented in Fig. 6.47 and yields a value of $9 \cdot 10^{-22}\,\mathrm{m^2}$ at $4\,\mathrm{mHz}$, while the power spectral density in Fig. 6.48 has a noise value of $\approx 4 \ldots 6 \cdot 10^{-22}\,\frac{\mathrm{m^2}}{\mathrm{Hz}}$ at signal frequency. Hence, this yields a carrier-to-receiver noise density of $\mathrm{C/N_0} \approx 1.5 \ldots 2.25\,\mathrm{Hz}$ for X.

Note that in the following, the scaling functions are directly included in the linear spectral densities, and the carrier-to-receiver noise density is given without explicitly showing the power spectrum and power spectral density.

The linear spectral densities of the Michelson combinations X, Y and Z, compared with the post-TDI requirement from Eq. (6.2), are presented in Fig. 6.49. The 40 pm-requirement with the noise sensitivity function of $\mathrm{NSF}(f) = \sqrt{1 + \left(\frac{3\,\mathrm{mHz}}{f}\right)^4}$ seems even more outdated here, since the low frequency behaviour is not $\propto f^{-2}$ (what would be expected by $\mathrm{NSF}(f)$), but f^{-3} due to the additional f^1 for low frequencies in the scaling functions depicted in Fig. 6.41. Furthermore, the flat noise level of $40 \cdot 10^{-12}\,\frac{\mathrm{m}}{\sqrt{\mathrm{Hz}}}$ is also exceeded at several frequencies and by all combinations. We will come back to this discussion in Sec. 6.6.

However, the laser frequency noise cancellation works well and suppresses an input noise of several $\frac{\mathrm{Mrad}}{\sqrt{\mathrm{Hz}}}$ by 10 orders of magnitude in amplitude. The residual noise level is mainly due to readout noise, as will be further examined in Sec. 6.5.6. Note finally that the peaks will flatten down by the use of an analytical scaling function instead of a numerically determined one.
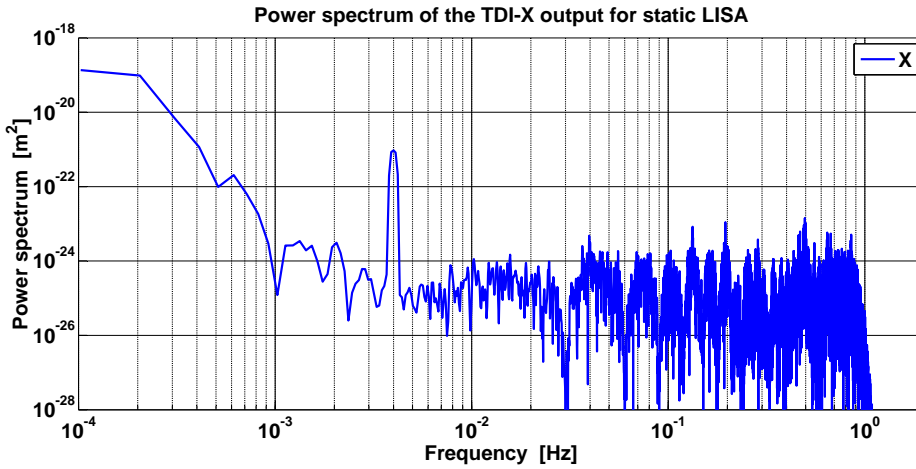
Figure 6.47: Power spectum of X for C/N$_0$-determination. It shows a roll off with $\propto f^{-6} = (f^{-3})^2$ at low frequencies and the characteristic nulls of the detector transfer functions at multiples of $0.03\,$Hz. The significant value at the signal frequency $f_{\text{gw}} = 4\,\text{mHz}$ is $9 \cdot 10^{-22}\,\text{m}^2$.
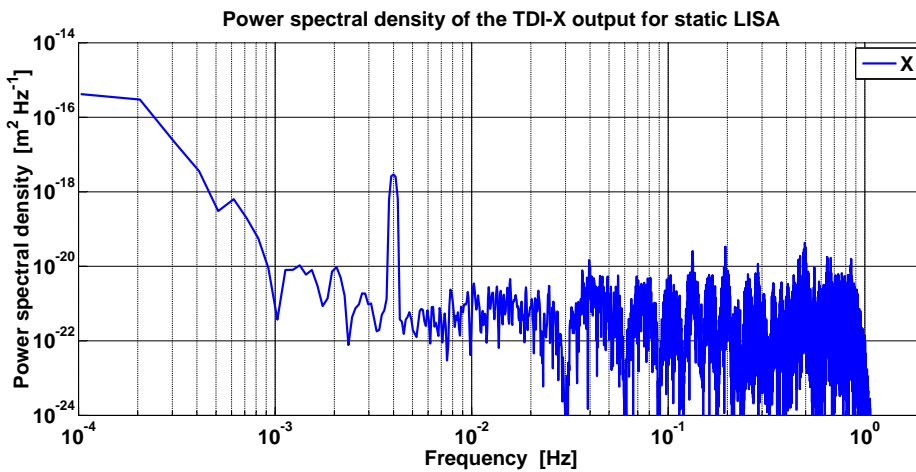
Figure 6.48: Power spectral density of X for C/N$_0$-determination. It shows basically the same characteristics as the power spectrum (Fig. 6.47), and is only scaled differently. The narrow band noise level around $4\,$mHz is at $4 \ldots 6 \cdot 10^{-22}\,\frac{\text{m}^2}{\text{Hz}}$.

Chapter 6
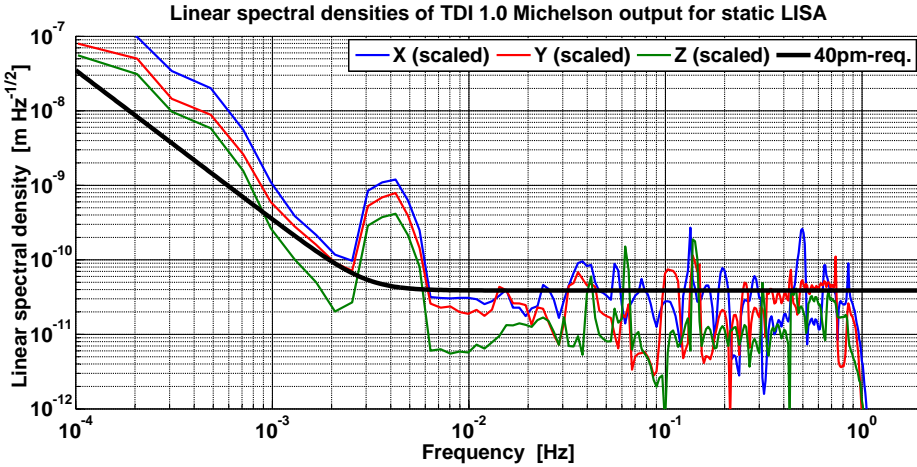
Figure 6.49: Linear spectral densities of TDI Michelson output for static LISA. The relative drift of the OB/TM can be identified in the noise power level rise $\propto f^{-3}$ below 3 mHz. The GW peak at 4 mHz is visible in all combinations. Note that the 40 pm-requirement is violated in both low and high frequency band.

Sagnac Combinations

Besides the Michelson combinations, the formation of Sagnac variables is implemented in TDISim as well. For static LISA, the simulation yields the time series shown in Fig. 6.50. Here, the GW is directly visible in γ with an amplitude of some 10^{-4} rad. The drift in phase due to the growing displacement is obvious in all data combinations, as was the case for the Michelson first generation variables. All Sagnac combinations remove the laser frequency noise sufficiently to a level of 10^{-4} rad. ζ shows the smallest response to gravitational waves, as expected.

The corresponding scaled linear spectral densities for the Sagnac combinations are depicted in Fig. 6.51. On the one hand, in terms of noise suppression, the Sagnac variables α, β and γ remove sufficiently the laser frequency noise to a level where the GW signal can be extracted. On the other hand, again the 40 pm-requirement is violated at several frequencies, and the LSD show an f^{-3}-behaviour at low frequencies. Furthermore, it is remarkable here that the GW signal amplitude in terms of LSD is the same as for the corresponding Michelson variables ($\approx 10^{-9} \frac{m}{\sqrt{Hz}}$ at 4 mHz). The main obvious difference between the LSDs of Sagnac and Michelson is the weaker shaping of the response nulls for frequencies greater than 30 mHz for Sagnac.

For the fully symmetric Sagnac variable ζ, the situation is different. The residual noise level is above that of α, β and γ for $f < 10$ mHz, and for $f > 10$ mHz the level is comparable to the other combinations.
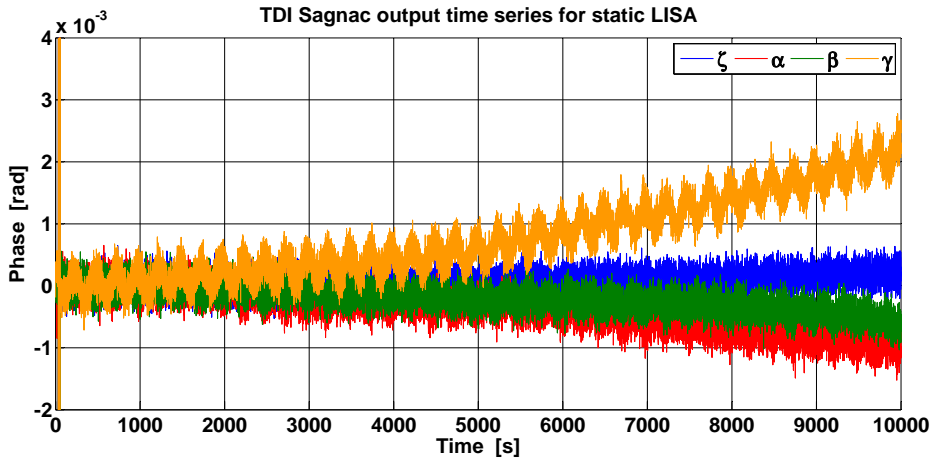
Figure 6.50: Time series for the TDI Sagnac output. α, β and γ provide the GW modulation with a level of ± 0.4 mrad. As for the Michelson combinations, the relative OB-TM drift is visible in all combinations. ζ shows the poorest gravitational wave response.
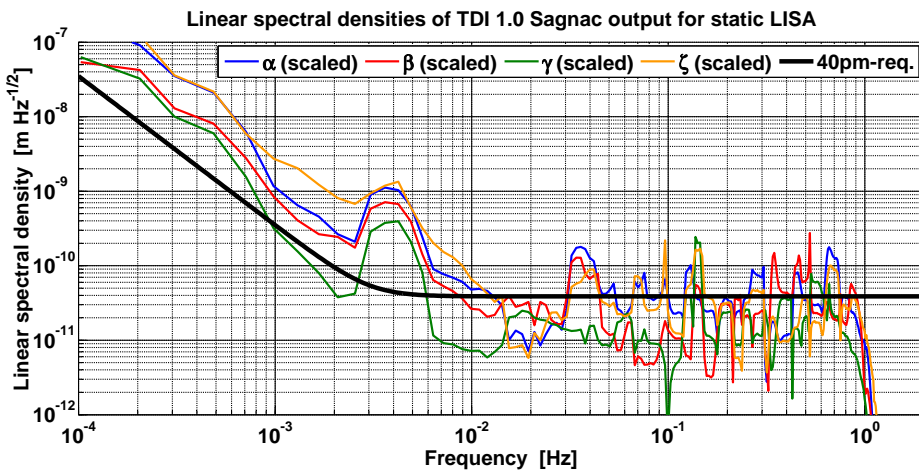
Figure 6.51: Linear spectral densities for TDI 1.0 Sagnac output in a static LISA constellation. All combinations remove laser frequency noise sufficiently, but also violate the 40 pm-requirement. ζ comprises the highest noise level over the low frequency band.

Chapter 6
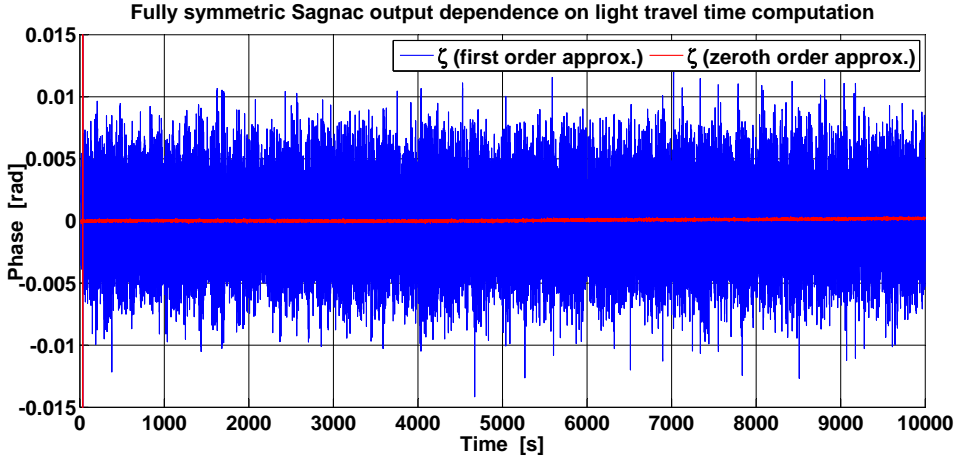
Figure 6.52: Light travel time dependence on ζ for static LISA. By taking into account the gravitational influence on the light travel time (first order approximation in ϵ) the residual noise floor is more than one order of magnitude in phase larger than for time delays computed for a zero order light travel time approximation. Note that the initialisation phase is here only $17\,\mathrm{s}$ long (1 spike), since only single time-delay operators are involved in ζ (Eq. 3.28).

The low frequency behaviour in Fig. 6.51 establishes the statement from Ch. 3 that ζ shows poor coupling for GW signals below frequencies equal to the reciprocal of the light travel time, while the high frequency part confirms the proper laser frequency noise removal by ζ. The latter effect was proven analytically in Sec. 3.2.2. Subsequently, the gravitational wave is not preserved for ζ since it has an inappropriate transfer function. This will also become manifest in the C/N_0 value below.

The algebraic treatment of Ch. 3 showed that $\zeta(t)$ removes exactly the laser frequency noise (in a static LISA case). However, this is only true if the light travel direction in the arms do not matter for the time delays, i.e, only for $\mathcal{D}_{\underline{i}}^{\mathbf{sim}} = \mathcal{D}_{\underline{i'}}^{\mathbf{sim}}$. In a static LISA case, this is valid for light travel times that exclude the direction-dependent gravitational shift taken into account by $\overset{(1)}{T}_{0,i}$. Note that the previously presented outputs for ζ have been computed using time delays which rely on the analytical approach to order ϵ^0. The inclusion of the first order, and therefore the directional dependent gravitational shift, has a significant impact on ζ as can be seen from the time series presented in Fig. 6.52. The residual noise in phase is more than one order of magnitude larger than under exclusion of static gravitational effects.
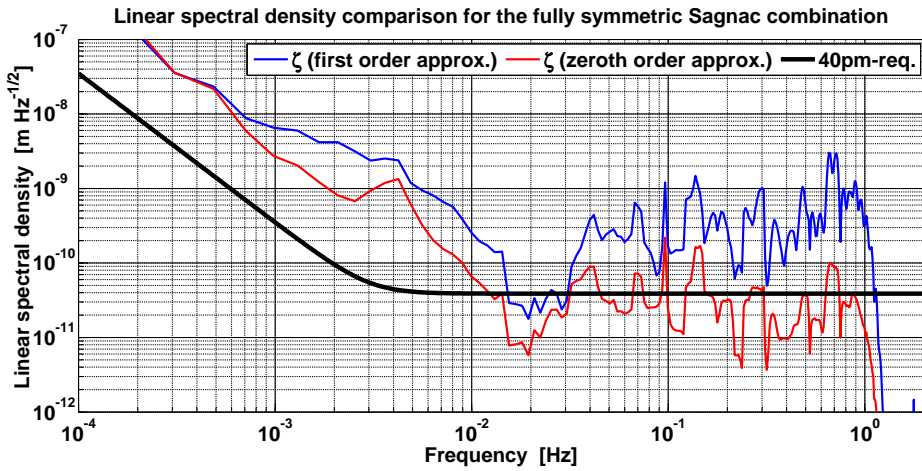
Figure 6.53: Linear spectral density for the light travel time dependence on ζ for static LISA. The formation with time delays that compute light travel times to first order in ϵ result in a significantly higher noise level for $f > 1\,\text{mHz}$. Furthermore, in the high frequency band, an f^1-growth can be observed towards the cutoff frequency. This growth is absent in the zeroth order output.
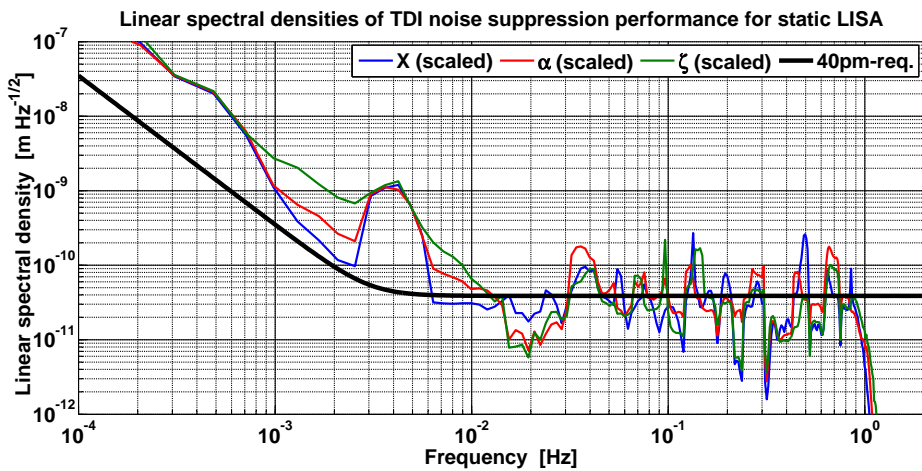
Figure 6.54: Linear spectral densities of the TDI 1.0 noise suppression performance. For both low and high frequencies, the 40 pm-requirement is violated. Furthermore, towards low frequencies, the linear spectral densities for Michelson and Sagnac rise with f^3 and not f^2, as pretended by the requirement. X shows the best signal-to-noise ratio, while ζ shows the poorest response for GW.

The situation in the frequency domain is visualised in Fig. 6.53. For the zeroth order, the residual noise provides a level comparable to the 40 pm-requirement. The residual noise in ζ with time delays relying on the first order approximation (blue) is significantly above the residuals for zeroth order light travel times (red) in the relevant frequency band. Subsequently, in the first order case, the ζ output does by far not fulfill the 40 pm-requirement, and laser frequency noise becomes dominant in the output. Hence, successful laser frequency noise suppression by the fully symmetric Sagnac combination $\zeta(t)$ is only possible for $\boldsymbol{\mathcal{D}}_{\underline{i}}^{\mathbf{sim}} = \boldsymbol{\mathcal{D}}_{\underline{i'}}^{\mathbf{sim}}$. However, the GW signal is suppressed in both zeroth and first order approximation cases, as expected.

Overall First Generation TDI Performance

The overall TDI 1.0 performance in comparison for static LISA can be found in Fig. 6.54. One of the main simulation results is that for static LISA the Time-Delay Interferometry combinations for first generation sufficiently remove the laser frequency noise down to a level where gravitational wave extraction is possible. In particular, for ζ, this is only true for direction-independent time delays that exclude the static gravitional field of the Sun. However, each scaled TDI output violates the 40 pm-requirement and it is further in question if the frequency dependence of the requirement is realistic, since the simulations show an f^3-rise towards low frequencies for the Michelson combinations, which comes from the scaling function for the combinations, in contrast to the predicted f^2-trend.

In terms of carrier-to-receiver noise density, we found that the Michelson combinations provide a one order of magnitude better C/N_0-value than the corresponding Sagnac variables, as can be concluded from Tab. 6.2.

TDI variable	PS($f = 4\,\mathrm{mHz}$)	PSD($f \approx 4\,\mathrm{mHz}$)	C/N_0
X	$9 \cdot 10^{-22}\,\mathrm{m}^2$	$4 \ldots 6 \cdot 10^{-22}\,\frac{\mathrm{m}^2}{\mathrm{Hz}}$	$1.5 \ldots 2.25\,\mathrm{Hz}$
Y	$5 \cdot 10^{-22}\,\mathrm{m}^2$	$3 \ldots 7 \cdot 10^{-22}\,\frac{\mathrm{m}^2}{\mathrm{Hz}}$	$0.7 \ldots 1.7\,\mathrm{Hz}$
Z	$6 \cdot 10^{-22}\,\mathrm{m}^2$	$0.5 \ldots 1 \cdot 10^{-22}\,\frac{\mathrm{m}^2}{\mathrm{Hz}}$	$6 \ldots 12\,\mathrm{Hz}$
α	$4 \cdot 10^{-22}\,\mathrm{m}^2$	$8 \ldots 20 \cdot 10^{-22}\,\frac{\mathrm{m}^2}{\mathrm{Hz}}$	$0.2 \ldots 0.5\,\mathrm{Hz}$
β	$2 \cdot 10^{-22}\,\mathrm{m}^2$	$10 \ldots 30 \cdot 10^{-22}\,\frac{\mathrm{m}^2}{\mathrm{Hz}}$	$0.07 \ldots 0.2\,\mathrm{Hz}$
γ	$3 \cdot 10^{-22}\,\mathrm{m}^2$	$1 \ldots 3 \cdot 10^{-22}\,\frac{\mathrm{m}^2}{\mathrm{Hz}}$	$1 \ldots 3\,\mathrm{Hz}$
ζ	$1 \cdot 10^{-22}\,\mathrm{m}^2$	$20 \ldots 50 \cdot 10^{-22}\,\frac{\mathrm{m}^2}{\mathrm{Hz}}$	$0.02 \ldots 0.05\,\mathrm{Hz}$

Table 6.2: C/N_0-values for first generation TDI. The first column gives the TDI-combination, the second lists the values of the corresponding power spectrum (PS), and the third presents the approximated power spectral density (PSD) value in a frequency band around f_{gw}. The ratio of PS and PSD gives finally the last column, the carrier-to-receiver noise density C/N_0.

The highest signal-to-noise ratio shows the combination with respect to S/C 3, i.e., Z and γ. For Z, an observation with 10 second duration yields a signal-to-noise ratio of ≈ 10. Concluding, as expected, the Michelson variables provide the best possibility to detect and extract the gravitational wave(s).

6.5.5 Second Generation TDI

A static satellite constellation as discussed previously is of course unrealistic for LISA, since the whole constellation will flex. Therefore, the simulation of the noise suppression by TDI for a flexing LISA is crucial and was performed with TDISim for both LISA with Keplerian orbits and ESA orbits. We will now present the results for the ESA orbits and then compare this with the Keplerian orbits.

TDI 2.0 for LISA with ESA Orbits

As for TDI 1.0, the outputs of the data processing need to be re-scaled, since the transfer function amplifies/attenuates each frequency component differently. The scaling functions for the second generation Michelson combinations X_1, X_2, X_3 and Sagnac combinations $\zeta_1, \alpha_1, \alpha_2, \alpha_3$ for ESA orbits are presented in Figs. 6.55 and 6.56. They all role off with f^{-2} towards low frequencies and are again on different levels, as for TDI 1.0 (Figs. 6.41 and 6.42). As expected, ζ_1 has the poorest gain for $f < 0.01\,\mathrm{Hz}$. The scaling functions for ζ_2 and ζ_3 are not displayed here, since it will soon become clear that the fully symmetric Sagnac variables are by far dominated by residual laser frequency noise orders of magnitude above the 40 pm-requirement.

The second generation Michelson variables X_1, X_2 and X_3 show an almost equal scaling behaviour, in particular for low frequencies, as can be seen from Fig. 6.55. They differ for $f > 10\,\mathrm{mHz}$ which is due to the normalisation by the input strain and the (slightly different) contributions from the transfer function nulls. For Sagnac, the low frequency level of $k_{\alpha_1}(f), k_{\alpha_2}(f)$ and $k_{\alpha_3}(f)$ is different, and furthermore $k_{\alpha_3}(f)$ rolls off slightly faster than the others, even than $k_{\zeta_1}(f)$. Further investigation is needed here in future work.

The time series for one Michelson and Sagnac combination (i.e., X_1 and α_1, others similar) are shown in Fig. 6.57. Plotted are the first 2000 s of data. The sinusoidal modulation by the gravitational wave is visible in both combinations and yields amplitudes of 0.4 mrad for X_1 and 0.2 mrad for α_1. However, the residual noise is larger than for the static case, since for TDI 2.0, 16 phasemeter outputs are combined instead of 8, and thus interpolation inaccuracies and noise add up to a higher level (cf. Figs. 6.44 and 6.50). This produces here a phase error of ± 0.3 mrad for Sagnac and ± 0.5 mrad for Michelson, or even more. Note again the TDI initialisation phase in the beginning of the time series, now enduring until approximately $8 \times 17\,\mathrm{s} = 136\,\mathrm{s}$. In analogy to TDI 1.0, several time intervals are visible within that phase where the laser frequency noise does not cancel properly (vertical lines). 1 enters naturally by the link construction, and 7 further for X_1 (blue) and 5 for α_1 (green).

Chapter 6
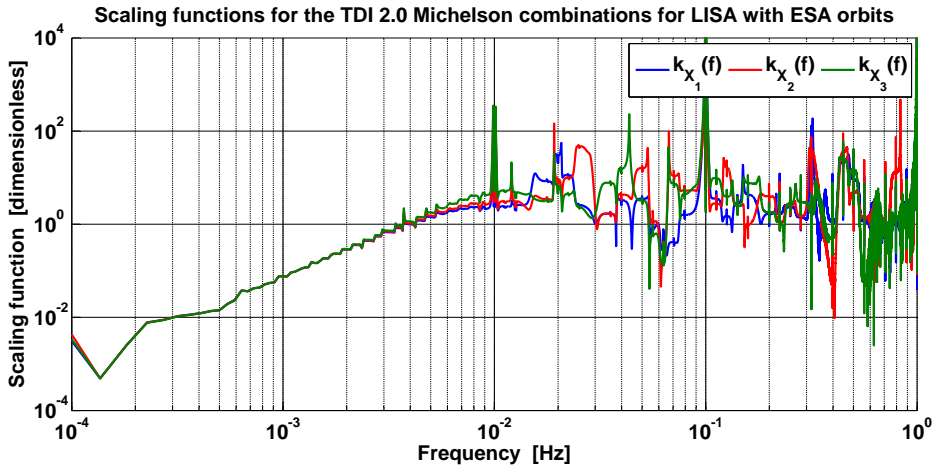
Figure 6.55: Scaling functions for the TDI 2.0 Michelson combinations X_1, X_2 and X_3 (ESA orbits). They show a remarkably similar low frequency behaviour. At $4\,\mathrm{mHz}$, all scaling functions have the value of $k_{X_i}(4\,\mathrm{mHz}) \approx 1$.
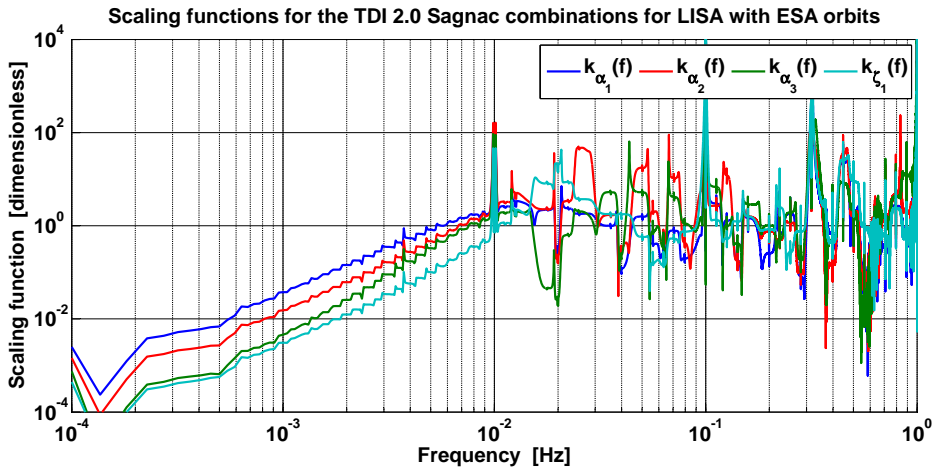
Figure 6.56: Scaling functions for the TDI 2.0 Sagnac and fully symmetric Sagnac combinations $\alpha_1, \alpha_2, \alpha_3$ and ζ_1 (ESA orbits). The latter shows the poorest scaling for $f < 0.01\,\mathrm{Hz}$. However, the roll-off of k_{α_3} is slightly steeper than $\propto f^{-2}$, which needs further investigation in the future. At $4\,\mathrm{mHz}$, the scaling functions yield the values $k_{\alpha_1}(4\,\mathrm{mHz}) \approx 0.5$, $k_{\alpha_2}(4\,\mathrm{mHz}) \approx 0.3$, $k_{\alpha_3}(4\,\mathrm{mHz}) \approx 0.2$ and $k_{\zeta_1}(4\,\mathrm{mHz}) \approx 0.06$.
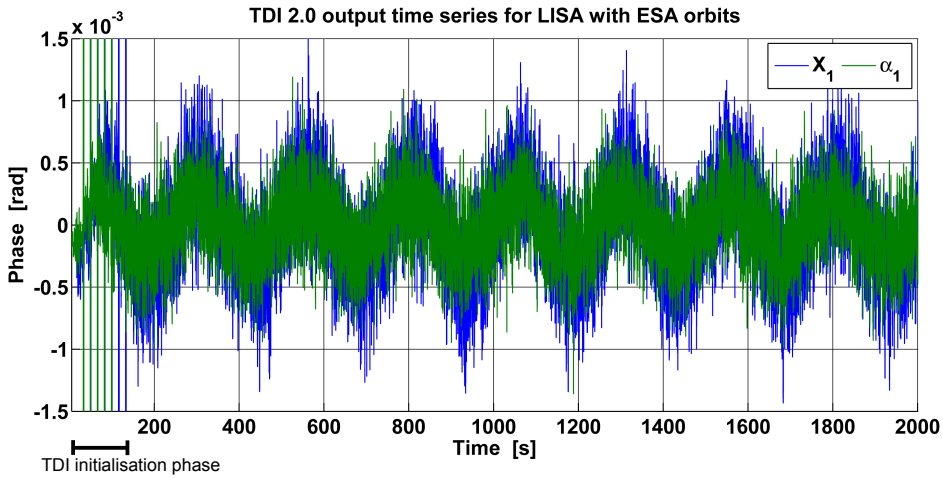
Figure 6.57: TDI output time series for Michelson and Sagnac combinations. Both are displayed for the first 2000 s. The TDI formation begins successfully after the initialisation phase of $\approx 8 \cdot 17\,\text{s} = 136\,\text{s}$. Compared to first generation TDI, the residual noise is larger by approximately a factor of two in amplitude.

The formation of α_1 and X_1 suppresses the laser frequency noise sufficiently such that the GW modulation is directly visible in the time series, while the fully symmetric Sagnac combination ζ_1 reduces the noise only by three orders of magnitude to some 1000 rad variation and is not plotted here (cf. Fig. 6.59).

The linear spectral densities for the TDI 2nd generation Michelson combinations are shown in Fig. 6.58. The most demonstrative difference to the static case in Fig. 6.49 is the low frequency behaviour. For TDI 2.0 Michelson, the noise rises with f^2 towards low frequencies, which is in accordance with the noise sensitivity function $\text{NSF}(f)$ included in the 40 pm-requirement. The lower power law of the frequency dependence agrees with our observation concerning the X_1-formation in the static LISA case (Fig. 6.44). For both static and flexing LISA, the time series X_1 does not diverge, which makes the difference in the steepness of the low frequency ramp in the linear spectral densities between TDI 1.0 and 2.0.

As for TDI 1.0, the residual noise level for $f > 0.01\,\text{Hz}$ is comparable to $40\,\frac{\text{pm}}{\sqrt{\text{Hz}}}$, which proofs a sufficient laser frequency noise suppression to establish GW extraction, even in the flexing LISA case. Note that first generation combinations are not sufficient here for laser frequency noise removal, exemplarily demonstrated for X.

Chapter 6
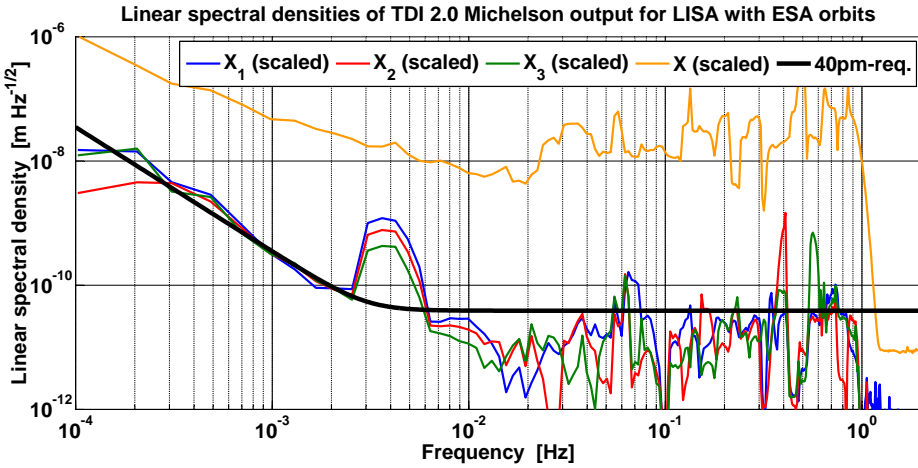
Figure 6.58: Linear spectral densities of TDI 2.0 Michelson outputs for LISA with ESA orbits. The GW peak at 4 mHz is visible, and for low frequencies, the output is slightly above the 40 pm-requirement. Moreover, in contrast to first generation TDI, the LSD rises with f^2 towards low frequencies. Application of first generation TDI variables, exemplarily shown here for X, are not sufficient in a flexing LISA constellation.
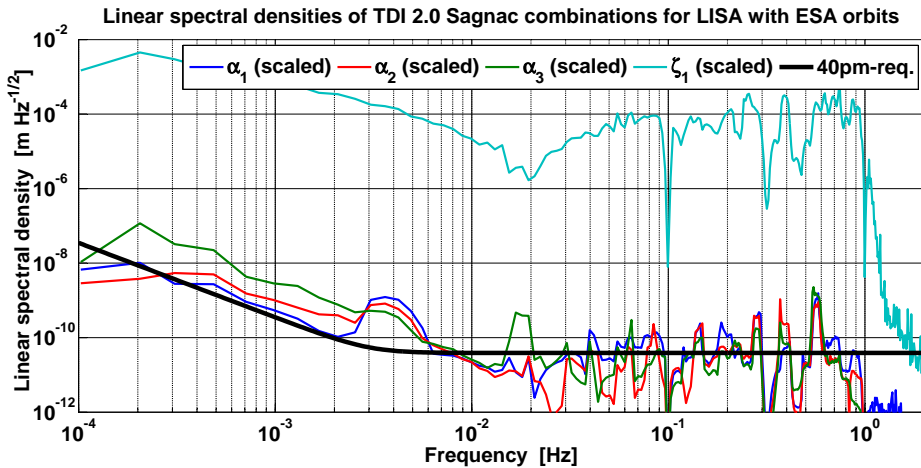
Figure 6.59: Linear spectral densities of TDI 2.0 Sagnac output noise suppression performance for LISA with ESA orbits. α_1 reduces the laser frequency noise down to a level where GW extraction becomes possible, while for α_2 and α_3 the low frequency residual noise is too high. Note that ζ_1 (and ζ_2, ζ_3 as well) is not sufficient for the suppression and lies more than four orders of magnitude in displacement above the requirement.

The linear spectral densities of the TDI 2.0 Sagnac combinations for LISA with ESA orbits are presented in Fig. 6.59. As for Michelson, the residual noise grows with f^2 towards low frequencies ($f < 3\,\mathrm{mHz}$) and comprises a flat noise level for high frequencies. At least the noise level for α_1 comes close to the 40 pm-requirement, while α_2 and α_3 have noise contributions that are up to one order of magnitude above the requirement for low frequencies.

Fully symmetric Sagnac variables are by far not sufficient for laser frequency noise suppression in the flexing LISA case since the residual noise lies, e.g., for ζ_1, more than four orders of magnitude in amplitude above that of $X_{\underline{i}}$ and $\alpha_{\underline{i}}$ (cf. Figs. 6.58 and 6.59, the same for ζ_2 and ζ_3). Hence, GW extraction is not possible anymore.

The GW peak is visible in the LSDs of at least $X_{\underline{i}}$ and $\alpha_{\underline{i}}$ and we can compute the carrier-to-receiver noise ratios presented in Tab. 6.3.

TDI variable	PS($f = 4\,\mathrm{mHz}$)	PSD($f \approx 4\,\mathrm{mHz}$)	C/N$_0$
X_1	$19.2 \cdot 10^{-22}\,\mathrm{m^2}$	$3 \ldots 5 \cdot 10^{-22}\,\frac{\mathrm{m^2}}{\mathrm{Hz}}$	$3.8 \ldots 6.4\,\mathrm{Hz}$
X_2	$7.9 \cdot 10^{-22}\,\mathrm{m^2}$	$1 \ldots 3 \cdot 10^{-22}\,\frac{\mathrm{m^2}}{\mathrm{Hz}}$	$2.6 \ldots 7.9\,\mathrm{Hz}$
X_3	$2.8 \cdot 10^{-22}\,\mathrm{m^2}$	$5 \ldots 15 \cdot 10^{-22}\,\frac{\mathrm{m^2}}{\mathrm{Hz}}$	$0.2 \ldots 0.6\,\mathrm{Hz}$
α_1	$10.5 \cdot 10^{-22}\,\mathrm{m^2}$	$3 \ldots 14 \cdot 10^{-22}\,\frac{\mathrm{m^2}}{\mathrm{Hz}}$	$0.75 \ldots 3.2\,\mathrm{Hz}$
α_2	$1.9 \cdot 10^{-22}\,\mathrm{m^2}$	$10 \ldots 50 \cdot 10^{-22}\,\frac{\mathrm{m^2}}{\mathrm{Hz}}$	$0.04 \ldots 0.19\,\mathrm{Hz}$
α_3	$0.2 \cdot 10^{-22}\,\mathrm{m^2}$	$10 \ldots 25 \cdot 10^{-22}\,\frac{\mathrm{m^2}}{\mathrm{Hz}}$	$0.008 \ldots 0.02\,\mathrm{Hz}$

Table 6.3: C/N$_0$-values for second generation TDI with ESA orbits. The values for $\zeta_{\underline{i}}$ are ignored here since no GW extraction is possible due to the high residual noise level (Fig. 6.59).

Concluding, we could show a sufficient laser frequency noise removal of input noise in $\eta_i^{\mathrm{sim}}(t)$ by the formation of the second generation Michelson combinations with C/N$_0$-values of the order $1 \ldots 10\,\mathrm{Hz}$. The Sagnac variables partially suppress the input noise to a level where GW extraction becomes possible and yield C/N$_0$-values of the order $0.01 \ldots 1\,\mathrm{Hz}$. Hereby, equivalent displacement noise of centimeters to meters in the input could be reduced down to some 10 picometer for $f > 3\,\mathrm{mHz}$, i.e., by 9 orders of magnitudes. Note that the fully symmetric Sagnac variables are not sufficient, and the same holds true for TDI 1.0 combinations.

Chapter 6
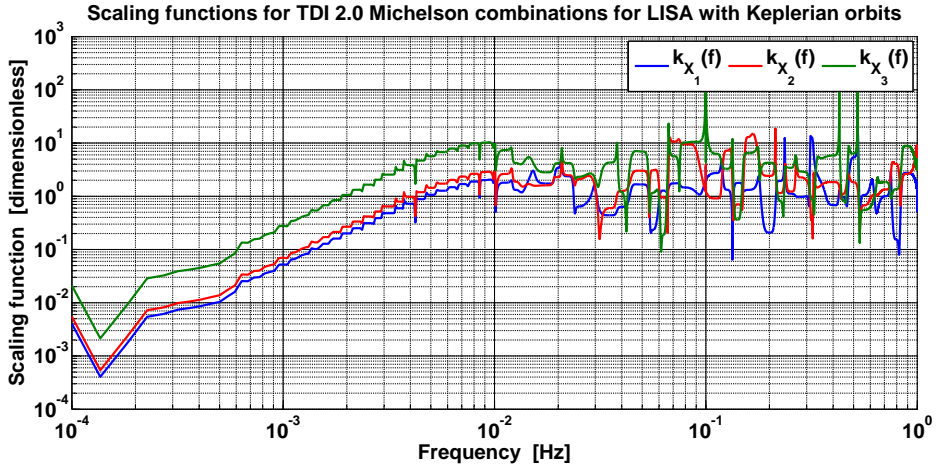
Figure 6.60: Scaling functions for TDI 2.0 Michelson combinations (Keplerian orbits). The signal amplification is here even worse than for the ESA orbits, since the GW signal at $4\,\text{mHz}$ is scaled by a factor 0.7 in X_1, by 1 in X_2 and 3.9 in X_3.

TDI 2.0 for LISA with Keplerian Orbits

For comparison, the 2nd generation TDI combinations are also synthesised for a LISA constellation with Keplerian orbits. At time origin, the spacecraft are placed as in the static LISA case, and then begin to flex. We can therefore directly compare between static and flexing mode.

First of all, the scaling functions for Michelson and Sagnac combinations presented in Figs. 6.60 and 6.61 show again the f^2-slope for low frequencies and a zero slope for some tens of milihertz. They lie different to the curves for ESA orbits which is due to the different constellation position and hence the changed relative direction of GW incidence with respect to the link orientation. It happens here that for X_3, the scaling value at the signal frequency is greater than one, while for X_1 and X_2, the scaling values are smaller one. The same effect could be discovered in the first generation combinations (Fig. 6.41). This again emphasises that the residual noise levels appear to be on different levels, if compared to a common noise requirement defined with respect to a reference Michelson interferometer. Finally, it is noticable that the scaling functions $k_{\zeta_i}(f)$ in Fig. 6.62 appear to have a roll-off $\propto f^{-2.5}$, which was not the case before. Further investigation is needed here as well.
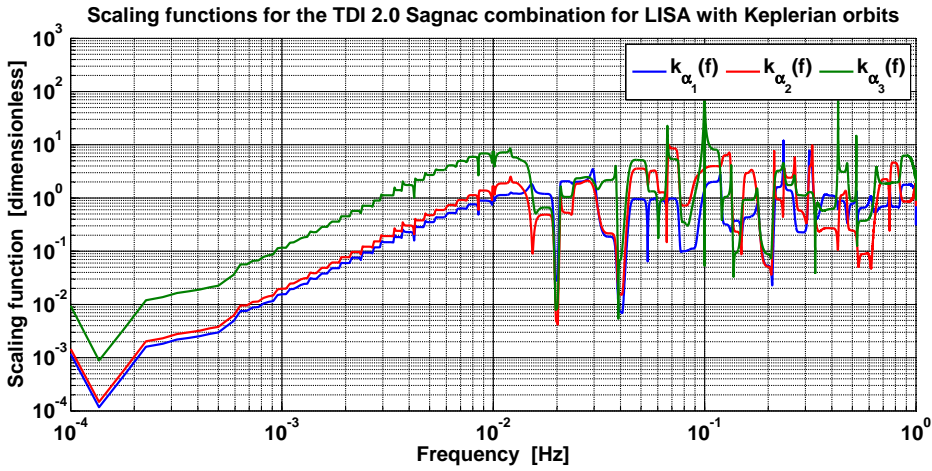
Figure 6.61: Scaling functions for TDI 2.0 Sagnac combinations (Keplerian orbits). The scaling values at the signal frequency are $k_{\alpha_1}(4\,\mathrm{mHz}) = 0.2$, $k_{\alpha_2}(4\,\mathrm{mHz}) = 0.3$ and $k_{\alpha_3}(4\,\mathrm{mHz}) = 1.8$.
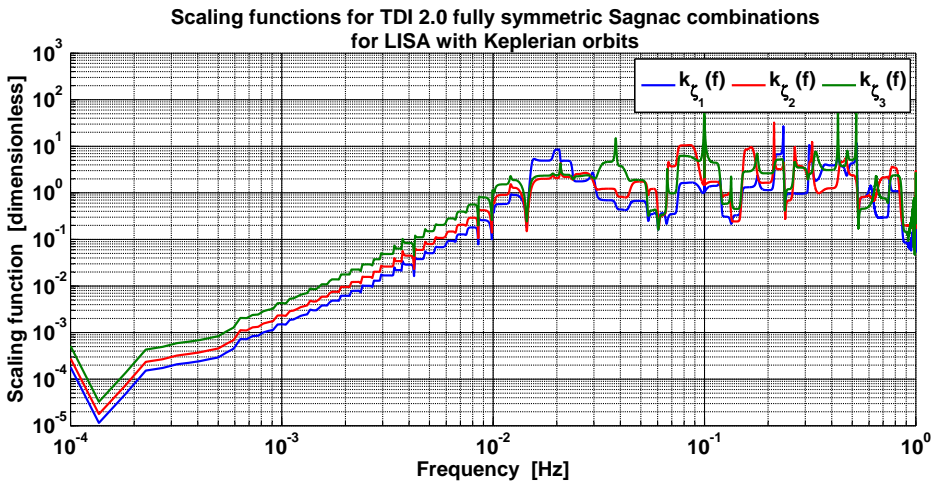
Figure 6.62: Scaling functions for TDI 2.0 fully symmetric Sagnac combinations (Keplerian orbits). The scaling values at the signal frequency are $k_{\zeta_1}(4\,\mathrm{mHz}) = 0.03$, $k_{\zeta_2}(4\,\mathrm{mHz}) = 0.04$ and $k_{\zeta_3}(4\,\mathrm{mHz}) = 0.08$.

Chapter 6

The resulting time series for X_1 and α_1 are displayed in Fig. 6.63. Again, the time series for ζ_1 is not plotted here, since it comprises too much noise to identify the GW modulation. Here, the imprinted noise is weaker than for the ESA orbit and has approximately a magnitude of ± 0.15 mrad for Sagnac and ± 0.3 mrad for Michelson (cf. Fig. 6.57).

The TDI noise suppression performance for Michelson, Sagnac, and fully symmetric Sagnac combinations in terms of linear spectral densities is given in Figs. 6.64 – 6.66. The spectral densities for X_i and α_i follow the envelope of the noise sensitivity function, but, as for ESA orbits, the requirement is violated for several frequencies. ζ_i comprises noise that is larger than the allowed level, but only by approximately one order of magnitude in contrast to four orders of magnitude for ESA orbits. This may come due to the smoother orbits. Future investigations are needed here.

In terms of signal-to-noise ratio, Tab. 6.4 provides information about C/N_0 for X_i, α_i and ζ_i. The latter can be included here since the noise level does not completely cover the GW peak in the spectrum, as was the case for ESA orbits.

TDI variable	PS($f = 4$ mHz)	PSD($f \approx 4$ mHz)	C/N_0
X_1	$14 \cdot 10^{-22}$ m^2	$6 \ldots 15 \cdot 10^{-22} \frac{\text{m}^2}{\text{Hz}}$	$1 \ldots 2.3$ Hz
X_2	$7 \cdot 10^{-22}$ m^2	$4 \ldots 6 \cdot 10^{-22} \frac{\text{m}^2}{\text{Hz}}$	$1.1 \ldots 1.75$ Hz
X_3	$9 \cdot 10^{-22}$ m^2	$1 \ldots 5 \cdot 10^{-22} \frac{\text{m}^2}{\text{Hz}}$	$1.8 \ldots 9$ Hz
α_1	$4 \cdot 10^{-22}$ m^2	$50 \ldots 80 \cdot 10^{-22} \frac{\text{m}^2}{\text{Hz}}$	$0.05 \ldots 0.08$ Hz
α_2	$2 \cdot 10^{-22}$ m^2	$30 \ldots 80 \cdot 10^{-22} \frac{\text{m}^2}{\text{Hz}}$	$0.025 \ldots 0.07$ Hz
α_3	$4 \cdot 10^{-22}$ m^2	$10 \ldots 20 \cdot 10^{-22} \frac{\text{m}^2}{\text{Hz}}$	$0.2 \ldots 0.4$ Hz
ζ_1	$0.4 \cdot 10^{-22}$ m^2	$50 \ldots 200 \cdot 10^{-22} \frac{\text{m}^2}{\text{Hz}}$	$8 \cdot 10^{-4} \ldots 0.005$ Hz
ζ_2	$0.3 \cdot 10^{-22}$ m^2	$40 \ldots 120 \cdot 10^{-22} \frac{\text{m}^2}{\text{Hz}}$	$0.0025 \ldots 0.0075$ Hz
ζ_3	$0.2 \cdot 10^{-22}$ m^2	$30 \ldots 70 \cdot 10^{-22} \frac{\text{m}^2}{\text{Hz}}$	$0.003 \ldots 0.007$ Hz

Table 6.4: C/N_0-values for second generation TDI with Keplerian orbits. As expected, ζ_i has no suitable carrier-to-receiver noise ratio, but even the Sagnac variables show a poor ratio compared with the Michelson variable.

As a conclusion, we could demonstrate TDI functionality in the case of Keplerian orbits, too, with C/N_0-values comparable to the ESA orbit case. Though the residual noise level in the fully symmetric Sagnac variables is three to four orders of magnitude lower than in the ESA case, it still makes GW extraction impossible.
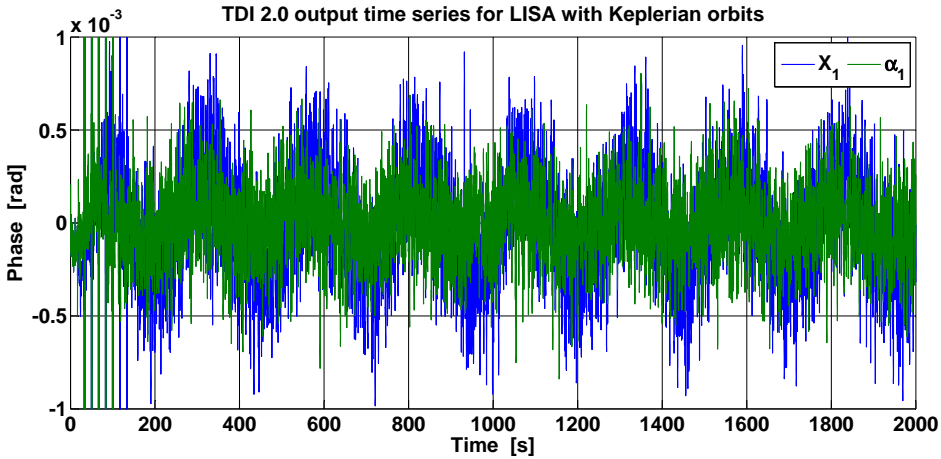
Figure 6.63: TDI output time series for LISA with Keplerian orbits, presented for the first 2000 s. The residual noise in X_1 and α_1 compared to the ESA orbits is smaller by approximately a factor of 2.
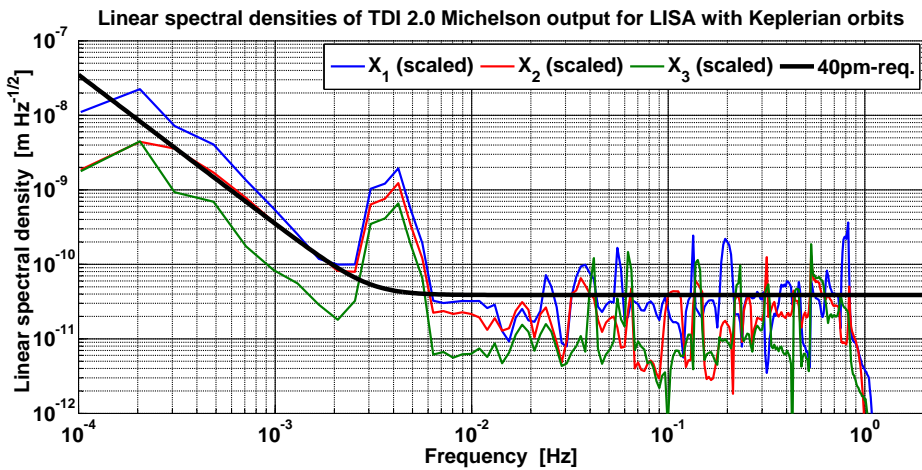
Figure 6.64: Linear spectral densities of TDI 2.0 Michelson output for LISA with Keplerian orbits. As expectable from the scaling functions, X_1 violates the 40 pm-requirement due to the low scaling values, while especially X_3 is for both low and high frequencies adequate below the requirement, except for the peaks at high frequencies.

Chapter 6
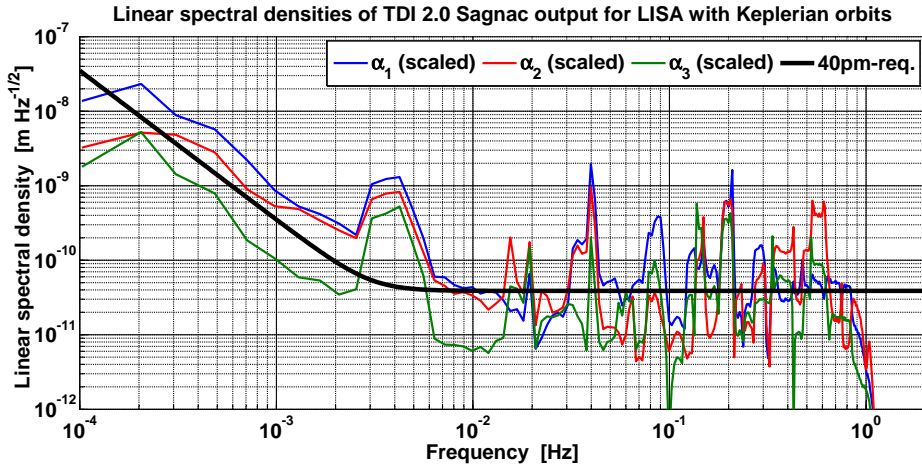
Figure 6.65: Linear spectral densities of TDI 2.0 Sagnac output for LISA with Keplerian orbits. α_3 is due to the advantageous scaling below the requirement except for the spikes.
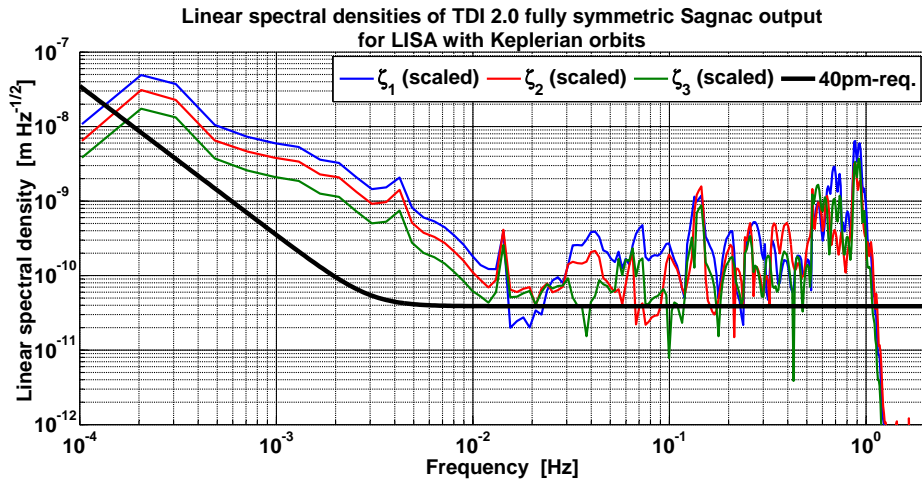
Figure 6.66: Linear spectral densities of TDI 2.0 fully symmetric Sagnac output for LISA with Keplerian orbits. All combinations comprise residual noise that is violating the requirement over the complete frequency band by one order of magnitude or more. GW extraction is thus impossible here.

6.5.6 TDI Performance Limits

The simulations have shown that all primary noise sources can be suppressed to a level that is comparable with the 40 pm-requirement. Even if the residual noise violates the requirement at some frequencies, it could be shown that the signal-to-noise ratio is large in the Michelson combinations such that GW extraction might be possible. However, it is worthwhile here to investigate the residual noise level and the TDI performance limits more deeply.

First of all, one should note that we have regarded a worst-case scenario of free-running lasers with huge phase noise contributions of Mrad. Using pre-stabilised laser phase noise with $\widetilde{\nu}_{\mathrm{stab}} = 280 \, \frac{\mathrm{Hz}}{\sqrt{\mathrm{Hz}}} \cdot \mathrm{NSF}(f)$ (Sec. 2.3), it can be checked if the residual noise in the TDI 2.0 combinations gets smaller and possibly fulfill completely the 40 pm-requirement. The linear spectral density of the TDI 2.0 output X_1 for stabilised lasers can be found in Fig. 6.67. The residual noise levels after TDI-X_1 formation for both free-running and stabilised lasers are almost equal except for $f > 1 \, \mathrm{Hz}$, and we can deduce from this result that the amount of input laser frequency noise does not limit the TDI performance.

Next, a simulation run with lasers and GW only yields the blue-coloured linear spectral density presented in Fig. 6.68. Evidently, laser frequency noise is not the limiting noise source, since it is possible to suppress it below the 40 pm-requirement over the complete frequency band by the formation of the TDI 2nd generation combinations. Moreover, input data with GW signal and displacement noise is processed through TDI and gives the red-coloured output linear spectral density. Compared with the complete X_1-output LSD presented in Fig. 6.67, it can be deduced that the residual noise for low frequencies is dominated by residual displacement noise.

For data with readout noise and GW signal only, the residual noise reaches the 40 pm-requirement in the high frequency band, as can be seen from Fig. 6.69 and is analytically established in appendix E.2. The input level is around $10 \, \frac{\mathrm{pm}}{\sqrt{\mathrm{Hz}}}$ in the band of interest, and this adds up by X_1-formation to $40 \, \frac{\mathrm{pm}}{\sqrt{\mathrm{Hz}}}$ or higher, i.e., by a factor of 4 or more in amplitude. Lowering the level of input readout noise does also lower the residual noise floor. Therefore, it is crucial to minimise the input readout noise in the measurement design since its appearance is inevitable.

Concluding, laser frequency noise does not limit the TDI performance in the case of *perfectly known* light travel times. Instead, readout noise limits the performance for frequencies $f > 3 \, \mathrm{mHz}$ and the displacement noise for $f < 3 \, \mathrm{mHz}$. With TDISim, it was thus possible to demonstrate successfully the laser frequency removal by 9 orders of magnitude in amplitude.

Chapter 6
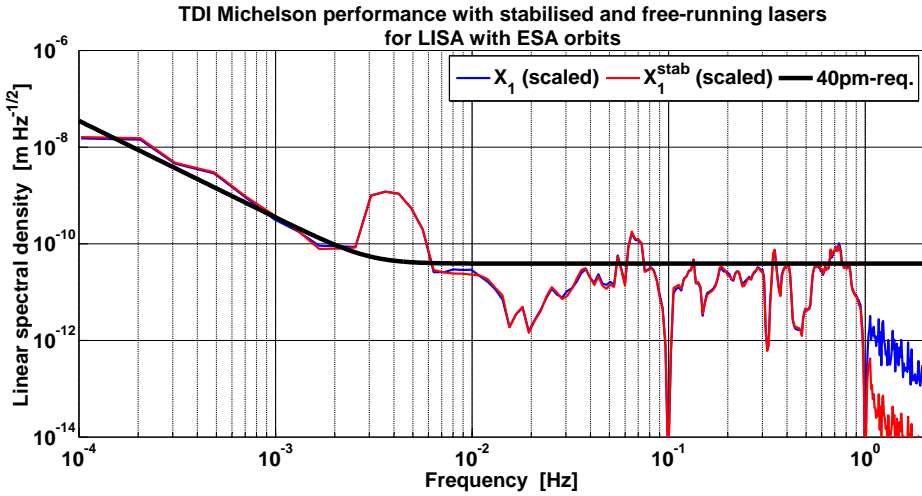
Figure 6.67: Linear spectral density comparison of TDI 2.0 output between stabilised and free-running lasers. The noise suppression performance for stabilised lasers is almost equal compared with that of free-running lasers in the band of interest $10^{-4}\,\mathrm{Hz} < f < 1\,\mathrm{Hz}$, and both LSDs are exceeding the 40 pm-requirement at some frequencies.
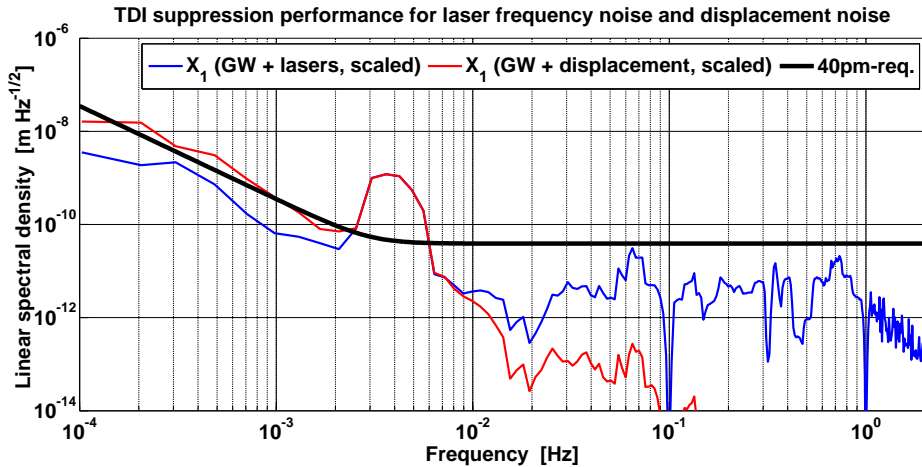
Figure 6.68: TDI 2.0 performance for X_1 with laser frequency noise and displacement noise only. For frequencies $f > 1\,\mathrm{mHz}$ both are well below the 40 pm-requirement. At low frequencies, the displacement noise slightly exceeds the requirement. This might be here the case due to the few sample points at low frequencies in the linear spectral density.
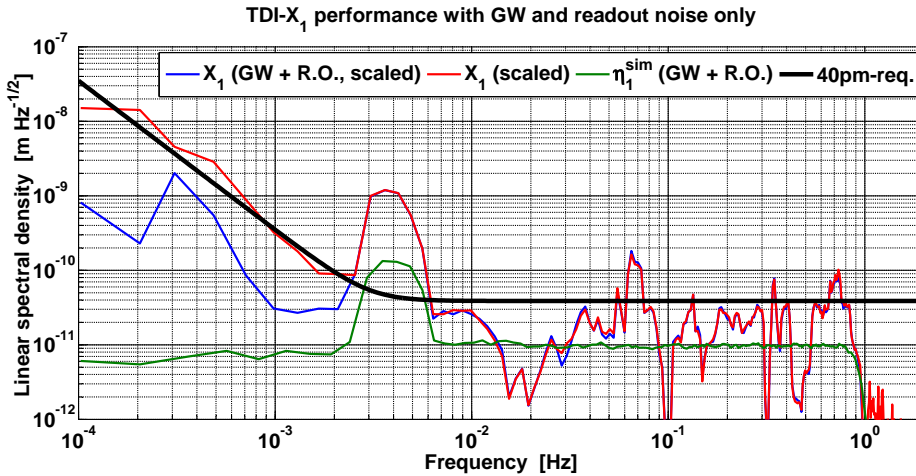
Figure 6.69: Linear spectral density for TDI with readout (R.O.) noise only, exemplarily presented for X_1. The input data to TDI, η_1^{sim}, comprises flat readout noise of $10\,\frac{\mathrm{pm}}{\sqrt{\mathrm{Hz}}}$. Combining the input data in the TDI combinations raise the noise limit to $40\,\frac{\mathrm{pm}}{\sqrt{\mathrm{Hz}}}$ and even higher at some frequencies. One can see in comparison with the full TDI-X_1 including all noise sources that readout noise is for $f > 3\,\mathrm{mHz}$ the limiting noise source.

Ranging Inaccuracy

An important question for TDI functionality is how accurate one needs to know the light travel times for each link. In order to simulate a ranging error (e.g., due to phasemeter inaccuracies), we can insert random timing errors δt in the synthesised time delays used for the data processing on ground. Thus, the delays in the construction of $\xi_i^{\mathrm{sim}}(t)$, $\eta_i^{\mathrm{sim}}(t)$ and in the 2nd generation TDI combinations are defective, and we expect the post-TDI residual noise level to be raised, depending on the ranging error. Note, however, that the physical delays in the onboard science signals use the ideally known light travel times as before.

For TDI with perfect knowledge of the armlengths, the pre-stabilisation of the lasers had only a small effect on the noise suppression performance, as demonstrated in Fig. 6.67, and furthermore the performance is limited for high frequencies by readout noise. However, the stabilisation should now establish the laser frequency noise removal for small ranging inaccuracies. We have tested this for TDI 2.0 with ESA orbits, and Figs. 6.70 and 6.71 present the results. For both second generation Michelson and Sagnac combinations, TDI with a ranging error of $10^{-7}\,\mathrm{s}$ (translates to $30\,\mathrm{m}$) violates the $40\,\mathrm{pm}$-requirement, while for ranging errors of $3\,\mathrm{m}$ or less, a noise residual level comparable to $40\,\frac{\mathrm{pm}}{\sqrt{\mathrm{Hz}}}$ remains.

Chapter 6
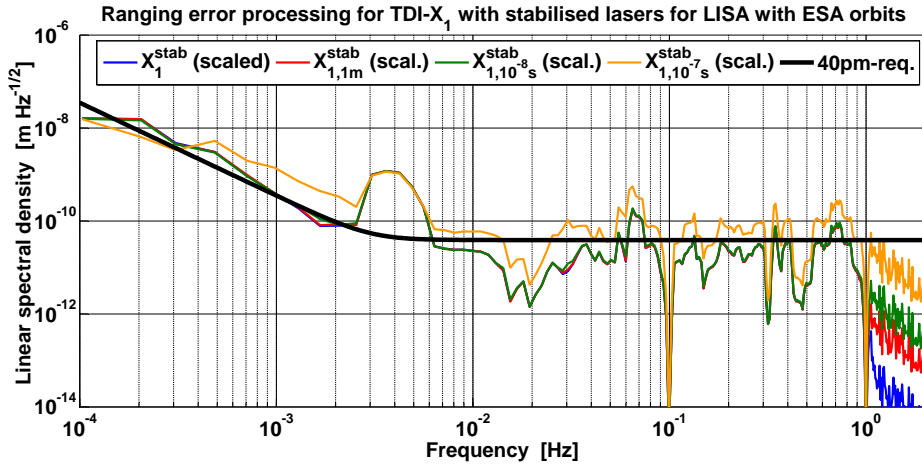
Figure 6.70: Ranging error impact for stabilised lasers in X_1 (ESA orbits). For a ranging error of more than $3\,\mathrm{m}$ (i.e., $10^{-8}\,\mathrm{s}$ in light travel time accuracy), the residual noise is above the requirement. Below $3\,\mathrm{m}$, the residual noise is limited by readout noise and comparable to the $40\,\mathrm{pm}$-requirement.
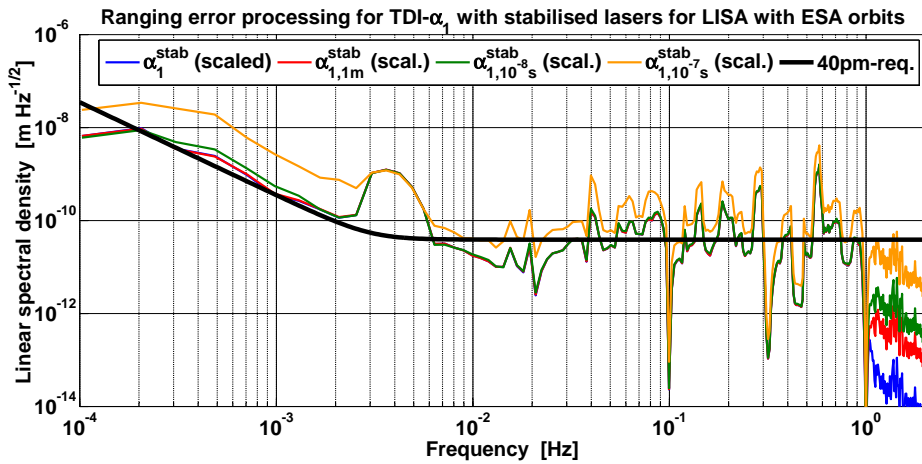
Figure 6.71: Ranging error impact for stabilised lasers in α_1 (ESA orbits). As before, for a ranging error of more than $3\,\mathrm{m}$, the residual noise is above the requirement. Below $3\,\mathrm{m}$, the residual noise is limited by readout noise and comparable to the $40\,\mathrm{pm}$-requirement.

In summary, the laser stabilisation is not crucial for TDI functionality in the case of perfectly known armlengths. However, if ranging errors are included, the laser frequency stabilisation ensures the sufficient suppression by TDI below the 40 pm-requirement. This becomes even more accurate if the readout noise is minimised, since TDI processing is limited by readout noise and in particular shot noise.

6.6 The Next Steps

TDISim offers a new starting point for the developement of a comprehensive LISA data processing chain simulation. However, it is clear that currently TDISim is an extremely simplified toy model and only covers basic aspects. Crucial parts are not implemented yet. In TDISim, well-defined test cases are missing to solidify the analysis and a comparison with existing simulators, especially the LISACode, are of high priority in the future. In the following, possible next steps in the simulation developement are listed, without the claim of completeness. Note, however, that parts of the issues are already dealt with in- and externally, and one of the main tasks will be to merge all of it in future work.

Concerning TDI, it is of utmost priority to compute the transfer functions analytically and to cross-check the numerical results of this thesis. With the analytical transfer functions at hand, it should be possible to derive smooth scaling functions and to perform a smooth TDI output spectral density scaling. Moreover, in the TDI algorithm the frequency dependence of displacement noise at low frequencies should be investigated carefully. If the test mass is removed, one would expect the OB to not limit the TDI performance. Together with a careful noise processing analysis including other noise sources like optical path length noise, this would finally lead to a revision of the 40 pm-requirement.

Next, the 'realistic' orbits used in TDISim rely on computations for the year 2011. Since a possible launch period for LISA might be in 2034, the ESA orbits should be computed for 2034, as well with higher sampling frequency than one data point per day. This would also give new Doppler data, which can in a later step be used for frequency locking schemes.

A further straightforward improvement in TDISim is to include auxiliary secondary noise sources like optical path length noise due to temperature fluctuations and misalignments of the optical components, noise due to the telescopes and the clipping of the laser beam from the distant spacecraft, etc. These can be directly implemented in the link computation. Additionally, by the inclusion of the primary fibre noise, its suppression within the post-processing full removal algorithm needs to be verified.

A far more complex issue is to implement three free-running clocks, one per S/C, which jitter and suffer relative drifts. This clock noise enters the phasemeter data according to Eqn. (4.5a) – (4.5h). Subsequently, supplementing the onboard sideband detection with the modulated clock signal from the different S/C is

Chapter 6

inevitable and the implemented removal algorithms need additionally the clock noise suppression, as discussed in Ch. 4. Furthermore, the inclusion of clock noise is directly connected with the data pre-processing. Since each S/C has its own clock ticking at a jittering frequency which also drifts with respect to the other clocks, it is necessary to synchronise the clocks. That is, the transmitted data has to be resampled on a common time stamp, the 'constellation time', that was introduced in Ch. 2. Therefore, the clock drifts have to be determined by Kalman filters, as was performed in [Wan14]. In order to estimate the armlengths and Doppler velocities again by Kalman, a ranging signal implementation would be helpful, together with the PRN signal transmission.

Subsequently, a frequency plan could be set up, and therefore Doppler shifts in the laser frequencies and an offset locking scheme must be accounted for. The Doppler shifts need to be computed from the orbit data (or can be directly taken from the ESA simulation) and a frequency order of the six onboard lasers needs to be introduced. From this, the heterodyne beat-notes according to Eqn. (4.3a) and (4.3b) can be computed and used for the factors θ_i^j in order to account for the beat-note frequency polarity. This would be a crucial test for TDI functionality, as discussed for the full removal algorithm in Ch. 4.

For TDISim, one-dimensional TM displacement noise is generated externally, while each TM noise is uncorrelated. However, this is of course not the case in reality, since the adjacent test masses are close by and therefore exhibit roughly the same gravitational field. Furthermore, the thruster model is applied to the S/C and hence both optical benches will also exhibit correlated displacements. Hence, a 3-D TM model also including rotations, is crucial to simulate 'realistic' TM interferometric output data. Moreover, the connection between the orbits, TM motion and thruster firing to correct for the relative S/C position is completely absent in TDISim. A sophisticated TM simulation is currently under developement [IAA+15]. More generally, the inclusion of non-linear satellite behaviour as attitude control loops are another great enhancement and could use several insights and tools from LISA Pathfinder modelling. In terms of subsystems, a rather minor issue, the satellite downlink to Earth, is also neglected up to now. However, we expect the data loss due to transmission to be minimal.

Finally, a completely different research point is the inclusion of (much) more than one GW signal in order to simulate the confusion noise due to impossible simultaneous resolution of all GW sources. Instead, a sophisticated data analysis part including noise projection methods and parameter estimation need to be added. This helps to check if the GW signal can be extracted properly from the interferometric measurements and gives a test for the proper LISA DPC functionality.

7 Summary and Outlook

Laser frequency noise is by far the dominating noise source in the onboard interferometric measurements of the Laser Interferometer Space Antenna. An algorithm to remove laser frequency noise is Time-Delay Interferometry. It cleverly adds and time-shifts the onboard measurements to form combinations that synthesise the output of virtual equal-arm Michelson interferometers. However, TDI was formulated for direct test mass to test mass displacement measurements. In the currently considered split interferometry configuration, this measurement is divided into separate parts which are combined in post-processing. Furthermore, it was neglected that any changes in the frequency order of the involved lasers and hence in the beat-note frequencies have to be compensated by the TDI algorithm.

For the first time, we formulated the LISA-like data streams conforming to the split interferometry configuration that provide the gravitational wave signal, test mass and optical bench displacement noise, dominant laser phase noise and further noise contributions. We then derived a compliant algorithm which removes optical bench motion and clock noise in a first step. In a second step, it provides the functionality of TDI which suppresses the laser frequency noise and back-link fibre noise. Moreover, the algorithm tracks the beat-note polarity of the lasers for the first time.

The onboard test mass and reference interferometer measurements are disturbed by straylight from the back-link fibres. By the use of a recently discussed auxiliary laser source and interferometer, it should be possible to reduce the straylight influence. We showed that the compliant algorithm can be extended to this new setup and that its noise suppression perfomance is unaffected by the additional interferometer.

The analytical results were verified by numerical computations with help of a simulation developed within the thesis. It includes as a worst-case scenario frequency noise of free-running lasers, test mass and optical bench displacement noise, readout noise and a monochromatic GW signal. In order to benchmark the performance, we developed a novel scheme where the numerical transfer function of the TDI output is put in relation to the transfer function of a 90°-Michelson interferometer.

237

Using this ratio, the residual noise after TDI can be scaled and then compared to the $40\,\frac{\mathrm{pm}}{\sqrt{\mathrm{Hz}}}$-requirement. This requirement includes test mass to test mass displacement noise contributions mainly due to shot noise, clock noise, laser phase noise and laser beam-pointing instability. However, it does not rely on the split interferometry configuration, and it had been further formulated for a simplified TDI algorithm. Therefore, to have a figure of merit at hand, we introduced the carrier-to-noise density which is directly related to a signal-to-noise ratio. We could show that our algorithm suppresses the laser frequency noise and optical bench displacement noise sufficiently below the $40\,\frac{\mathrm{pm}}{\sqrt{\mathrm{Hz}}}$-requirement for frequencies $f > 3\,\mathrm{mHz}$. For the TDI combinations that form a Michelson-like output, the simulation yielded a carrier-to-noise density of some Hz for certain standard source assumptions, while for Sagnac-like outputs, this value was one order of magnitude or more smaller.

Further investigations revealed that the gravitational wave extraction is limited by readout noise. Except for few frequencies, the TDI Michelson output fulfilled the requirement in the relevant frequency band. The exceptions are caused by the numerical procedure for the determination of the scaling functions. However, we expect the TDI Michelson output to be in agreement with the $40\,\frac{\mathrm{pm}}{\sqrt{\mathrm{Hz}}}$-requirement if the scaling functions are determined analytically.

The most important future steps are the inclusion of clock noise in the simulation as well as the implementation of a realistic test mass model which is connected to the orbits. Additionally, the TDI scaling functions need to be derived analytically and a careful noise contribution and propagation analysis is crucial in order to revise the common post-TDI noise requirement. The long time prospect is a comprehensive LISA simulation that combines all existing code parts and makes extensive use of the proven LISA Pathfinder data analysis tools.

A Spectral Densities

This thesis investigates inter alia the post-processing noise suppression for the phasemeter data taken onboard the LISA spacecraft. A deterministic target signal, the optical phase shift induced by passing gravitational waves, is buried in stochastic noise, first and foremost the laser frequency noise. The deterministic GW can be analytically represented by Eq. (1.59), while the noise contributions are described in terms of functions depending on the Fourier frequency f, the power and linear spectral density.

Let $s(t)$ be a noisy time series as, e.g., depicted in Fig. 6.16. In order to characterise the noise dependent on the frequency contributions, the power spectral density (PSD) $\mathcal{P}(f)$ is used. It is defined for stationary random time series as

$$\mathcal{P}(f) := \frac{1}{2\pi} \int\limits_{-\infty}^{+\infty} \mathrm{d}\tau \, (s \star s)(\tau) \mathrm{e}^{-\mathrm{i}\cdot 2\pi f \tau} \tag{A.1}$$

and could be read as the Fourier transform of the autocorrelation function

$$(s \star s)(\tau) := \int\limits_{-\infty}^{+\infty} \mathrm{d}t \, s(t) s(t + \tau). \tag{A.2}$$

Basically, the PSD measures the amount of time variation in the time series $s(t)$ that occurs with frequency f. Since the PSD (A.1) is defined for frequencies $f \in (-\infty, +\infty)$, where negative frequencies are technically irrelevant, a so-called one-sided power spectral density, denoted here by $\widetilde{s}^2(f)$, could be introduced instead:

$$\widetilde{s}^2(f) := \left\{ \begin{array}{ll} 2\,\mathcal{P}(f), & f \geq 0 \\ 0 \end{array} \right. . \tag{A.3}$$

The unit of the PSD depends on the quantity described by $\widetilde{s}^2(f)$. Consider, e.g., a time series of optical bench displacement jitter $s(t)$ with units of m. Subsequently,

the power spectral density has units of m²s according to Eq. (A.1), or, $[\widetilde{s}^{\,2}(f)] = 1\,\frac{\mathrm{m}^2}{\mathrm{Hz}}$. In order to compare the noise in terms of its amplitude directly, the linear spectral density (LSD) is derived from the PSD:

$$\widetilde{s}(f) := \sqrt{\widetilde{s}^{\,2}(f)}\,. \tag{A.4}$$

Using the previous example with the displacement, the LSD has units of $\mathrm{m}/\sqrt{\mathrm{Hz}}$. Furthermore, the linear definition reminds one to take the square when adding up the noise, and, equivalently, their LSDs, as exhibited in Ch. 2 for the readout noise (Eq. (2.6a)). For more details about spectral densities and spectra, we suggest to consult [HRS02].

In the course of Ch. 6, several plots of noise linear spectral densities are presented and discussed. Technically, they are computed from noisy time series with help of the LTPDA toolbox command `lpsd()` by use of the flat-top window `SFT3f` and a default overlap of 50 %. The number of averages is set to 100 and the average is subtracted for each converted data point.

B Derivation of the Monochromatic Gravitational Wave Signal

In Ch. 1, Eq. (1.59), the light travel time modulation $\Delta T(t)$ due to a *monochromatic* gravitational signal was given between two moving spacecraft. We will now derive this special case from the general integral formulation in Eq. (1.56):

$$\Delta T(t_{\text{recv}}) = \frac{1}{2} \cdot \frac{(n_{\text{recv}}(t_{\text{recv}}) \otimes \vec{n}_{\text{recv}}(t_{\text{recv}}))}{1 + \hat{k} \cdot \vec{n}_{\text{recv}}(t_{\text{recv}})} \; : \; \int_{\xi(0)}^{\xi(w_{\text{recv}})} \mathrm{d}\xi \, \boldsymbol{h}(\xi)$$

with the integral limits determined by Eqn. (1.57a) and (1.57b):

$$\xi(0) \quad = \quad t_{\text{recv}} - \frac{\hat{k} \cdot \vec{x}_{\text{recv}}(t_{\text{recv}})}{c} - \frac{L_0(t_{\text{recv}})}{c}(1 + \hat{k} \cdot \vec{n}_{\text{recv}}(t_{\text{recv}})),$$

$$\xi(w_{\text{recv}}) \quad = \quad t_{\text{recv}} - \frac{\hat{k} \cdot \vec{x}_{\text{recv}}(t_{\text{recv}})}{c}.$$

A monochromatic GW signal can be written tensorially as $\boldsymbol{h}(\xi) = \boldsymbol{h}_0 \mathrm{e}^{\mathrm{i}\omega_{\text{gw}}\xi}$ with

$$\xi(w) = t_{\text{recv}} - \frac{w_{\text{recv}} - w}{c} - \frac{\hat{k} \cdot (\vec{x}_{\text{recv}}(t_{\text{recv}}) + (w_{\text{recv}} - w)\vec{n}_{\text{recv}}(t_{\text{recv}}))}{c}$$

according to Eq. (1.53c). With this, we will now explicitly compute the integral and therefore simplify the notation by $a = \xi(0)$ and $b = \xi(w_{\text{recv}})$:

$$\int_a^b \mathrm{d}\xi \, \boldsymbol{h}(\xi) = \boldsymbol{h}_0 \int_a^b \mathrm{d}\xi \, \mathrm{e}^{\mathrm{i}\omega_{\text{gw}}\xi} = \frac{\boldsymbol{h}_0}{\mathrm{i}\omega_{\text{gw}}} \mathrm{e}^{\mathrm{i}\omega_{\text{gw}}\xi} \Big|_a^b = \frac{\boldsymbol{h}_0}{\mathrm{i}\omega_{\text{gw}}} \left(\mathrm{e}^{\mathrm{i}\omega_{\text{gw}}b} - \mathrm{e}^{\mathrm{i}\omega_{\text{gw}}a}\right).$$

The following algebraic manipulations of the bracket lead to the sinc-form of (1.59):

$$\left(\mathrm{e}^{\mathrm{i}\omega_{\text{gw}}b} - \mathrm{e}^{\mathrm{i}\omega_{\text{gw}}a}\right) \quad = \quad \left(\mathrm{e}^{\mathrm{i}\omega_{\text{gw}}(b-a)} - 1\right) \mathrm{e}^{\mathrm{i}\omega_{\text{gw}}a}$$

$$= \quad \left(\mathrm{e}^{\mathrm{i}\omega_{\text{gw}}\frac{b-a}{2}} - \mathrm{e}^{-\mathrm{i}\omega_{\text{gw}}\frac{b-a}{2}}\right) \mathrm{e}^{\mathrm{i}\omega_{\text{gw}}a} \mathrm{e}^{\mathrm{i}\omega_{\text{gw}}\frac{b-a}{2}},$$

and thus, with $\sin(x) = \frac{e^{ix} - e^{-ix}}{2i}$ and $\mathrm{sinc}(x) = \frac{\sin(x)}{x}$:

$$
\begin{aligned}
\int_a^b \mathrm{d}\xi\, \boldsymbol{h}(\xi) &= \frac{\boldsymbol{h}_0}{i\omega_{\mathrm{gw}}}\left(e^{i\omega_{\mathrm{gw}}\frac{b-a}{2}} - e^{-i\omega_{\mathrm{gw}}\frac{b-a}{2}}\right)e^{i\omega_{\mathrm{gw}}a}e^{i\omega_{\mathrm{gw}}\frac{b-a}{2}} \\[2mm]
&= \frac{2\boldsymbol{h}_0}{\omega_{\mathrm{gw}}}\frac{\left(e^{i\omega_{\mathrm{gw}}\frac{b-a}{2}} - e^{-i\omega_{\mathrm{gw}}\frac{b-a}{2}}\right)}{2i}e^{i\omega_{\mathrm{gw}}a}e^{i\omega_{\mathrm{gw}}\frac{b-a}{2}} \\[2mm]
&= \frac{2\boldsymbol{h}_0}{\omega_{\mathrm{gw}}}\sin\left(\omega_{\mathrm{gw}}\frac{b-a}{2}\right)e^{i\omega_{\mathrm{gw}}a}e^{i\omega_{\mathrm{gw}}\frac{b-a}{2}} \\[2mm]
&= \boldsymbol{h}_0(b-a)\frac{\sin\left(\omega_{\mathrm{gw}}\frac{b-a}{2}\right)}{\frac{\omega_{\mathrm{gw}}}{2}(b-a)}e^{i\omega_{\mathrm{gw}}a}e^{i\omega_{\mathrm{gw}}\frac{b-a}{2}} \\[2mm]
&= \boldsymbol{h}_0(b-a)\mathrm{sinc}\left(\omega_{\mathrm{gw}}\frac{b-a}{2}\right)e^{i\omega_{\mathrm{gw}}\frac{b-a}{2}}e^{i\omega_{\mathrm{gw}}a}\,.
\end{aligned}
$$

We resubstitute $a = \xi(0)$, $b = \xi(w_{\mathrm{recv}})$ and

$$
b - a = \xi(w_{\mathrm{recv}}) - \xi(0) = \frac{L_0(t_{\mathrm{recv}})}{c}\left(1 + \hat{k}\cdot\vec{n}_{\mathrm{recv}}(t_{\mathrm{recv}})\right),
$$

which yields

$$
\int_{\xi(0)}^{\xi(w_{\mathrm{recv}})} \mathrm{d}\xi\, \boldsymbol{h}(\xi) = \boldsymbol{h}_0\frac{L_0(t_{\mathrm{recv}})}{c}\left(1 + \hat{k}\cdot\vec{n}_{\mathrm{recv}}(t_{\mathrm{recv}})\right)\mathrm{sinc}\left(\frac{\omega_{\mathrm{gw}}L_0(t_{\mathrm{recv}})}{2c}\left(1 + \hat{k}\cdot\vec{n}_{\mathrm{recv}}(t_{\mathrm{recv}})\right)\right)\cdot
$$

$$
\cdot e^{i\frac{\omega_{\mathrm{gw}}L_0(t_{\mathrm{recv}})}{2c}\left(1 + \hat{k}\cdot\vec{n}_{\mathrm{recv}}(t_{\mathrm{recv}})\right)}e^{i\omega_{\mathrm{gw}}\xi(0)}\,.
$$

Inserted in $\Delta T(t_{\mathrm{recv}})$, the factor $\left(1 + \hat{k}\cdot\vec{n}_{\mathrm{recv}}(t_{\mathrm{recv}})\right)$ cancels and we end up with Eq. (1.59), where we finally used a generalised time coordinate t:

$$
\begin{aligned}
\Delta T(t) &= \frac{1}{2}\cdot\frac{(n_{\mathrm{recv}}(t) \otimes \vec{n}_{\mathrm{recv}}(t))}{1 + \hat{k}\cdot\vec{n}_{\mathrm{recv}}(t)} : \boldsymbol{h}_0\frac{L_0(t)}{c}\left(1 + \hat{k}\cdot\vec{n}_{\mathrm{recv}}(t)\right)\cdot \\[2mm]
&\quad \mathrm{sinc}\left(\frac{\omega_{\mathrm{gw}}L_0(t)}{2c}\left(1 + \hat{k}\cdot\vec{n}_{\mathrm{recv}}(t)\right)\right)\cdot e^{i\frac{\omega_{\mathrm{gw}}L_0(t)}{2c}\left(1 + \hat{k}\cdot\vec{n}_{\mathrm{recv}}(t)\right)}e^{i\omega_{\mathrm{gw}}\xi(0)} \\[2mm]
&= \frac{L_0(t)}{2c}\cdot\left(\vec{n}_{\mathrm{recv}}(t) \otimes \vec{n}_{\mathrm{recv}}(t)\right)\cdot\mathrm{sinc}\left(\frac{\omega_{\mathrm{gw}}L_0(t)}{2c}\left(1 + \hat{k}\cdot\vec{n}_{\mathrm{recv}}(t)\right)\right)\cdot \\[2mm]
&\quad \cdot e^{i\frac{\omega_{\mathrm{gw}}L_0(t)}{2c}\left(1 + \hat{k}\cdot\vec{n}_{\mathrm{recv}}(t)\right)} : \boldsymbol{h}_0 e^{i\omega_{\mathrm{gw}}\xi(0)}\,.
\end{aligned}
$$

C Time-Delay Operator Algebra

We will now show in C.1 – C.3 how the approximation formula (3.37) could be substantiated. This is achieved by expanding multiple time-dependent time delays to first order in $\frac{\dot{L}}{c} \approx 10^{-8}$ and $\frac{\ddot{L}L^2}{c^2} \simeq 0$ (cf. Sec. 3.3.1). Starting with twofold time delays, we will expand the considerations to multiple delays.

C.1 Twofold Time Delays

In order to get an idea of the expansion, we start with a twofold delay of the form (3.16b),

$$f(t)_{;jk} = f\left(t - \frac{L_k(t)}{c} - \frac{L_j\left(t - \frac{L_k(t)}{c}\right)}{c}\right).$$

Due to the implicitly nested functions of the armlengths, the above analytical treatment of time-dependent time delays in a closed form is extremely messy and complex. It it obvious that there is a need for 'direct' equations to compute the time shifts of a function $f(t)$. Therefore, we perform Taylor expansions of the nested terms. Using

$$g(t - a) = g(t) + \dot{g}(t)(-a) + \mathcal{O}\left((-a)^2 \ddot{g}\right) \tag{C.1}$$

with an arbitrary function $g(t)$, one can expand $f(t)_{;jk}$ to first order in $\frac{\dot{L}(t)}{c}$. We start with $\frac{L_j\left(t - \frac{L_k(t)}{c}\right)}{c}$ and find

$$
\begin{aligned}
L_j\left(t - \frac{L_k(t)}{c}\right) &= L_j(t) + \dot{L}_j(t)\left(-\frac{L_k(t)}{c}\right) + \frac{1}{2}\ddot{L}_j(t)\left(\frac{L_k(t)}{c}\right)^2 + \dots \\
&\simeq L_j(t) - \frac{1}{c}\dot{L}_j L_k.
\end{aligned}
$$

This approximation can be inserted in $f(t)_{;jk}$ to expand again:

$$
\begin{aligned}
f(t)_{;jk} &= f\left(t - \frac{L_k(t)}{c} - \frac{L_j\left(t - \frac{L_k(t)}{c}\right)}{c}\right) \simeq f\left(t - \frac{L_k}{c} - \frac{1}{c}\left[L_j - \frac{1}{c}\dot{L}_j L_k\right]\right) \\
&= f\left(t - \frac{1}{c}(L_k + L_j) + \frac{1}{c^2}\dot{L}_j L_k\right) = f\left(t + \frac{1}{c^2}\dot{L}_j L_k\right)_{,jk}.
\end{aligned}
$$

Note here that the comma operator applies to parts of the $f(t)$ argument with explicit t-dependence only, but not to $f(g(t))$. That is, the armlengths $L_j(t)$ and $L_k(t)$ within the argument of f are not shifted since they are taken to be constant in time (cf. Sec. 3.1.4), but the explicit t is. Finally, we perform a Taylor expansion for small $\frac{1}{c^2}\dot{L}_j L_k$,

$$
f\left(t + \tfrac{1}{c^2}\dot{L}_j L_k\right)_{,jk} \simeq \left(f(t) + \dot{f}(t)\tfrac{1}{c^2}\dot{L}_j L_k\right)_{,jk} = f(t)_{,jk} + \dot{f}(t)_{,jk} \cdot \tfrac{1}{c^2}\dot{L}_j L_k,
$$

and get the result for an approximated twofold time delay:

$$
f(t)_{;jk} \simeq f(t)_{,jk} + \dot{f}(t)_{,jk} \cdot \tfrac{1}{c^2}\dot{L}_j L_k.
$$

C.2 Threefold Time Delays

With similar algebra, one can derive formulars for threefold time delays. That is,

$$
\begin{aligned}
f(t)_{;jk\ell} &= f\left(t - \frac{L_j(t)}{c}\right)_{;k\ell} = f\left(t - \frac{L_k(t)}{c} - \frac{L_j(t - \frac{L_k(t)}{c})}{c}\right)_{;\ell} \\
&= f\left(t - \frac{L_\ell(t)}{c} - \frac{L_k\left(t - \frac{L_\ell(t)}{c}\right)}{c} - \frac{L_j\left(t - \frac{L_\ell(t)}{c} - \frac{L_k\left(t - \frac{L_\ell(t)}{c}\right)}{c}\right)}{c}\right).
\end{aligned}
$$

Expanding this by using $L_k\left(t - \frac{L_\ell(t)}{c}\right) \simeq L_k(t) - \frac{1}{c}\dot{L}_k L_\ell$ yields in a first step

$$
\begin{aligned}
f(t)_{;jk\ell} &\simeq f\left(t - \frac{L_\ell(t)}{c} - \frac{1}{c}\left(L_k(t) - \frac{\dot{L}_k L_\ell}{c}\right) - \frac{1}{c}L_j\left(t - \frac{L_\ell(t)}{c} - \frac{1}{c}(L_k(t) - \frac{\dot{L}_k L_\ell}{c})\right)\right) \\
&= f\left(t - \frac{1}{c}(L_\ell + L_k) + \frac{\dot{L}_k L_\ell}{c^2} - \frac{1}{c}L_j\left(t - \frac{1}{c}(L_\ell + L_k) + \frac{1}{c^2}\dot{L}_k L_\ell\right)\right).
\end{aligned}
$$

Next, the inner nesting $L_j(\dots)$ needs to be disentangled with the same tools as before:

$$
\begin{aligned}
L_j(t - \tfrac{1}{c}(L_\ell + L_k) + \tfrac{1}{c^2}\dot{L}_k L_\ell) &\simeq L_j(t) + \dot{L}_j(t) \cdot \left(-\tfrac{1}{c}(L_\ell + L_k) + \tfrac{1}{c^2}\dot{L}_k L_\ell\right) \\
&\simeq L_j(t) - \tfrac{1}{c}\dot{L}_j(t)(L_\ell + L_k),
\end{aligned}
$$

due to small $\frac{L\ddot{L}}{c^2}$ and $\frac{1}{c^2}\dot{L}_j\dot{L}_k L_\ell$. Hence,

$$
\begin{aligned}
f(t)_{;jk\ell} &\simeq f\left(t - \tfrac{1}{c}(L_\ell + L_k) + \tfrac{\dot{L}_k L_\ell}{c^2} - \tfrac{L_j}{c} + \tfrac{1}{c^2}\dot{L}_j(t)(L_\ell + L_k)\right) \\
&= f\left(t - \tfrac{1}{c}(L_\ell + L_k + L_j) + \tfrac{1}{c^2}(\dot{L}_k L_\ell + \dot{L}_j L_\ell + \dot{L}_j L_k)\right) \\
&= f\left(t + \tfrac{1}{c^2}(\dot{L}_k L_\ell + \dot{L}_j L_\ell + \dot{L}_j L_k)\right)_{,jk\ell}.
\end{aligned}
$$

Since $\frac{1}{c^2}\dot{L}_k L_\ell$, $\frac{1}{c^2}\dot{L}_j L_\ell$ and $\frac{1}{c^2}\dot{L}_j L_k$ are all of the order $10^{-6}\,\mathrm{s}$, the sum is also small and we can again Taylor expand the function:

$$
\begin{aligned}
f(t)_{;jk\ell} &\simeq \left[f(t) + \tfrac{1}{c^2}\dot{f}(t)(\dot{L}_k L_\ell + \dot{L}_j L_\ell + \dot{L}_j L_k)\right]_{,jk\ell} \\
&= f(t)_{,jk\ell} + \tfrac{1}{c^2}\dot{f}(t)_{,jk\ell}(\dot{L}_k L_\ell + \dot{L}_j L_\ell + \dot{L}_j L_k) \\
&= f(t)_{,jk\ell} + \tfrac{1}{c^2}\dot{f}(t)_{,jk\ell}(\dot{L}_j(L_k + L_\ell) + \dot{L}_k L_\ell)
\end{aligned}
$$

C.3 General Time-Delay Formula

Similar calculations give in a more generalised notation for the threefold time delay:

$$
\begin{aligned}
f(t)_{;j_1 j_2 j_3} &\simeq f(t)_{,j_1 j_2 j_3} + \tfrac{1}{c^2}\dot{f}(t)_{,j_1 j_2 j_3}(\dot{L}_{j_1}(L_{j_2} + L_{j_3}) + \dot{L}_{j_2} L_{j_3}) \\
&= f(t)_{,j_1 j_2 j_3} + \tfrac{1}{c^2}\dot{f}(t)_{,j_1 j_2 j_3}\left[\dot{L}_{j_1}\sum_{k=2}^{3} L_{j_k} + \dot{L}_{j_2}\sum_{k=3}^{3} L_{j_k}\right] \\
&= f(t)_{,j_1 j_2 j_3} + \tfrac{1}{c^2}\dot{f}(t)_{,j_1 j_2 j_3}\cdot\sum_{k=1}^{2}\left(\dot{L}_{j_k}\sum_{\ell=k+1}^{3} L_{j_\ell}\right)
\end{aligned}
$$

and furthermore for fourfold delays:

$$
\begin{aligned}
f(t)_{;j_1 j_2 j_3 j_4} &\simeq f(t)_{,j_1 j_2 j_3 j_4} + \tfrac{1}{c^2}\dot{f}(t)_{,j_1 j_2 j_3 j_4}\left[\dot{L}_{j_1}(L_{j_2} + L_{j_3} + L_{j_4})\right. \\
&\quad\left. + \dot{L}_{j_2}(L_{j_3} + L_{j_4}) + \dot{L}_{j_3} L_{j_4}\right] \\
&= f(t)_{,j_1 j_2 j_3 j_4} \\
&\quad + \tfrac{1}{c^2}\dot{f}(t)_{,j_1 j_2 j_3 j_4}\left[\dot{L}_{j_1}\sum_{k=2}^{4} L_{j_k} + \dot{L}_{j_2}\sum_{k=3}^{4} L_{j_k} + \dot{L}_{j_3}\sum_{k=4}^{4} L_{j_k}\right]
\end{aligned}
$$

or, condensed to a double sum,

$$
f(t)_{;j_1 j_2 j_3 j_4} \simeq f(t)_{,j_1 j_2 j_3 j_4} + \tfrac{1}{c^2}\dot{f}(t)_{,j_1 j_2 j_3 j_4}\cdot\sum_{k=1}^{3}\left(\dot{L}_{j_k}\sum_{\ell=k+1}^{4} L_{j_\ell}\right).
$$

This can exhibited for more delays. Finally, the underlying system can then be determined to

$$f(t)_{;j_1 \ldots j_n} \simeq f(t)_{,j_1 \ldots j_n} + \frac{1}{c^2} \dot{f}(t)_{,j_1 \ldots j_n} \cdot \sum_{k=1}^{n-1} \left(\dot{L}_{j_k} \sum_{\ell=k+1}^{n} L_{j_\ell} \right).$$

And now for something completely different.

C.4 Inverse Operator

In order to compute the second generation TDI monitor combinations (3.51) and cyclic, we introduced the inverse delay operator $\mathcal{D}_i^{-1}$, defined as

$$\mathcal{D}_i^{-1} f(t) = f(t)_{;\bar{i}} := f\left(t + \frac{L_i\left(t + \frac{L_i(t)}{c}\right)}{c} \right)$$

with $\mathcal{D}_i \mathcal{D}_i^{-1} = \mathbb{1}$. We will now prove this statement to first order in $\frac{\dot{L}}{c}$. Consider

$$\begin{aligned}
\mathcal{D}_i \mathcal{D}_i^{-1} f(t) &= \mathcal{D}_i f\left(t + \frac{L_i\left(t + \frac{L_i(t)}{c}\right)}{c} \right) \\
&= f\left(t - \frac{L_i(t)}{c} + \frac{L_i\left(t - \frac{L_i(t)}{c} + \frac{L_i\left(t - \frac{L_i(t)}{c}\right)}{c}\right)}{c} \right),
\end{aligned}$$

where we used the definition of the inverse delay operator. Again, the nesting could be expanded in a Taylor series with $\frac{\dot{L}}{c} \ll 1$ as follows:

$$L_i\left(t - \frac{L_i(t)}{c} \right) \simeq L_i(t) - \frac{\dot{L}_i(t) L_i(t)}{c},$$

and further

$$\begin{aligned}
L_i\left(t - \frac{L_i(t)}{c} + \frac{L_i\left(t - \frac{L_i(t)}{c}\right)}{c} \right) &\simeq L_i\left(t - \frac{L_i(t)}{c} + \frac{1}{c}\left(L_i(t) - \frac{\dot{L}_i(t) L_i(t)}{c} \right) \right) \\
&= L_i\left(t - \frac{\dot{L}_i(t) L_i(t)}{c^2} \right) \\
&\simeq L_i(t) + \dot{L}_i(t)\left(-\frac{\dot{L}_i(t) L_i(t)}{c^2} \right) \\
&= L_i(t) + \mathcal{O}\left(\frac{\dot{L}^2}{c^2} \right).
\end{aligned}$$

We thus end up with

$$
\mathcal{D}_i \mathcal{D}_i^{-1} f(t) \;=\; f\left(t - \frac{L_i(t)}{c} + \frac{L_i\left(t - \frac{L_i(t)}{c} + \frac{L_i\left(t - \frac{L_i(t)}{c} \right)}{c} \right)}{c} \right)
$$

$$
\simeq \; f\left(t - \frac{L_i(t)}{c} + \frac{L_i(t)}{c} \right) = f(t)
$$

and have proven the proposition:

$$
\mathcal{D}_i \mathcal{D}_i^{-1} f(t) = f(t) = \mathbb{1} f(t) \implies \mathcal{D}_i \mathcal{D}_i^{-1} = \mathbb{1} \,.
$$

D Translation Tables for the Index Notation

In this section, we will show two tables for notation comparison between the various TDI literature. Unfortunately, no unique notation exists up to now and one has to convert the equations between different authors by hand.

Both tables D.1 and D.2 are helpful for translating the TDI combinations to our convention. Exemplarily, we will do this for the unequal-arm Michelson combination, X, for first generation TDI given in [TEA04] (written by Armstrong, Estabrook and Tinto), Eq. (42), by

$$X_1 = [(\eta_{31} + \eta_{13,2'}) + (\eta_{21} + \eta_{12,3}),_{2'2}] - [(\eta_{21} + \eta_{12,3}) + (\eta_{31} + \eta_{13,2'}),_{33'}].$$

First of all, they use for the time-independent time delay a comma. According to Tab. D.1 (cf. the row 'Delay'), this corresponds to our colon notation. Next, as explained in their paper, the signals are formulated in terms of phase, and they use the Shaddock convention for the indices. Hence, the used notation is s_{sr} (Tab. D.1, row 'Inter-S/C meas.') and the same index notation does apply for η. With use of Tab. D.2 it is not hard to convert:

$$\eta_{31} \; \widehat{=} \; \eta_{1'}, \quad \eta_{13} \; \widehat{=} \; \eta_3, \quad \eta_{21} \; \widehat{=} \; \eta_1, \quad \eta_{12} \; \widehat{=} \; \eta_{2'}.$$

Thus, we find in the notation of this thesis:

$$
\begin{aligned}
X &= [(\eta_{31} + \eta_{13,2'}) + (\eta_{21} + \eta_{12,3}),_{2'2}] - [(\eta_{21} + \eta_{12,3}) + (\eta_{31} + \eta_{13,2'}),_{33'}] \\
&\widehat{=} [(\eta_{1'} + \eta_{3:\mathbf{2'}}) + (\eta_1 + \eta_{2':\mathbf{3}}):\mathbf{2'2}] - [(\eta_1 + \eta_{2':\mathbf{3}}) + (\eta_{1'} + \eta_{3:\mathbf{2'}}):\mathbf{33'}] \\
&= [\eta_{1'} + \eta_{3:\mathbf{2'}} + \eta_{1:\mathbf{2'2}} + \eta_{2':\mathbf{32'2}}] - [\eta_1 + \eta_{2':\mathbf{3}} + \eta_{1':\mathbf{33'}} + \eta_{3:\mathbf{2'33'}}].
\end{aligned}
$$

Rearranging the terms and indices order (which is allowed in the time-independent case, Eq. (3.19b)) gives exactly the TDI-X combination (3.26a):

$$X = (\eta_{2':\mathbf{322'}} + \eta_{1:\mathbf{22'}} + \eta_{3:\mathbf{2'}} + \eta_{1'}) - (\eta_{3:\mathbf{2'3'3}} + \eta_{1':\mathbf{3'3}} + \eta_{2':\mathbf{3}} + \eta_1).$$

Issue	**Us**	**AET**	**DhuVi**	**Shad**	**Vallis**
Inter-S/C meas.	s_{R} (ph.)	y_{ar} (fr.) s_{sr} (ph.)	$U^{\mathrm{r}}, V^{\mathrm{r}}$ (fr.)	s_{sr} (ph.)	y_{slr} (fr.)
Intra-S/C meas.	τ_{R} (ph.) ε_{R} (ph.)	z_{ar} (fr.) τ_{sr} (ph.)	$z_{\mathrm{r}}, z_{\mathrm{r}}^{*}$	τ_{sr} (ph.)	$z_{\mathrm{slr}}, \tau_{\mathrm{ar}}$ (fr.)
Direction (ccw.) Direction (cw.)	$\vec{n}_1$	$\hat{n}_1$ $-\hat{n}_1$	$\hat{n}_1$ $-\hat{n}_1$		
Armlength	L_1	L_{a}	L_{sr} L_1	$L_{\mathrm{a}}, L_{\mathrm{a}}'$ L_{sr}	L_1
Delay	$\boldsymbol{:}\, /\, \boldsymbol{;}$ $\widehat{\mathbf{D}}_1\, /\, \boldsymbol{\mathcal{D}}_1$	$,\, /\, ;$ $D_1, D_{1'}$	E_1, E_{sr} D_1, E_1	$,\, /\, ;$ D_{sr}	$;$ $\mathcal{D}_1$
GW signal	H_{R} (ph.)	$y_{\mathrm{ar}}^{\mathrm{gw}}$ (fr.) Ψ_1 (ph.)	$h_{U\mathrm{r}}, h_{V\mathrm{r}}$	h_{sr}	
Laser noise	p_{R} (ph.)	$C_{\mathrm{r}}, C_{\mathrm{r}}^{*}$ (fr.) p_{sr} (ph.)	$C_{\mathrm{r}}, C_{\mathrm{r}}^{*}$ (fr.) C_{sr}	p_{sr} (ph.)	$C_{\mathrm{r}}, C_{\mathrm{r}}^{*}$ (fr.)
Shot noise	$N_{\mathrm{R}}^{s,\epsilon,\tau}$	$y_{\mathrm{ar}}^{\mathrm{shot}}$ (fr.) n_{ar}^{s} (ph.)	$Y_{U\mathrm{r}}^{\mathrm{shot}}, Y_{V\mathrm{r}}^{\mathrm{shot}}$	n_{sr}	
TM disp. noise	$\vec{\delta}_{\mathrm{r}}$	$\vec{v}_{\mathrm{r}}, \vec{v}_{\mathrm{r}}^{*}$	$\vec{v}_{\mathrm{r}}, \vec{v}_{\mathrm{r}}^{*}$ $\vec{\delta}_{\mathrm{sr}}$	δ_{sr}	$pm_{\mathrm{r}}, pm_{\mathrm{r}}^{*}$
OB disp. noise	$\vec{\Delta}_{\mathrm{R}}$	$\vec{V}_{\mathrm{r}}, \vec{V}_{\mathrm{r}}^{*}$ $\vec{\Delta}_{\mathrm{sr}}$	$\vec{V}_{\mathrm{r}}, \vec{V}_{\mathrm{r}}^{*}$ $\vec{\Delta}_{\mathrm{sr}}$	Δ_{sr}	
Fibre noise	μ_{R}	η_{r} μ_{r}	η_{r}		
Optical noise	$N_{\mathrm{R}}^{\mathrm{opt}}$		$Y_{U\mathrm{r}}^{\mathrm{opt}}$		$y_{\mathrm{sr}}^{\mathrm{op}}$

Table D.1: Translation table for signals and noise contributions in the common literate. The first column shows the issue, the second column the notation of this thesis ('Us'), the third gives the Armstrong, Estabrook and Tinto ('AET') notation, followed by Dhurandhar and Vinet ('DhuVi'), Shaddock ('Sha') and Vallisneri ('Vallis'). The Indices 's', 'r', 'l' and 'a' stand for sender, receiver, link and arm. Capital R emphasises that the index of the receiving OB is used (instead of the receiving S/C, small r). The abbreviations 'fr.' and 'ph.' mean frequency and phase, respectively. Since all of the above authors worked in collaborations with each other, the notations got even more mixed.

As another example, we will translate the inter-spacecraft measurement given by Eqn. (2.1) of [ETA00] into our notation. It is given by

$$y_{21} = C_{3,2} - \hat{n}_2 \cdot \vec{V}_{3,2} + 2\hat{n}_2 \cdot \vec{v}_1^{*} - \hat{n}_2 \cdot \vec{V}_1^{*} - C_1^{*} + y_{21}^{\mathrm{gw}} + y_{21}^{\mathrm{shot}} ,$$

First of all, Tab. D.1 provides the insight that the signal here is formulated in terms of frequency by the authors Armstrong, Estabrook and Tinto (AET) (first row). In terms of phase (what we prefer and stringently use in this thesis), the analogies are, without indices, $y \leftrightarrow s$, $C \leftrightarrow p$, $\vec{V} \leftrightarrow \vec{\Delta}$, $\vec{v} \leftrightarrow \vec{\delta}$, $\hat{n} \leftrightarrow \vec{n}$, $y^{\mathrm{shot}} \leftrightarrow N^s$, and $y^{\mathrm{gw}} \leftrightarrow H$. With Tab. D.2, we can directly identify that $y_{21} \mathrel{\widehat{=}} s_{1'}$ since here the receiving S/C is r = 1 and the regarded arm a = 2 (compare with y_{ar}).

Us	AET	DhuVi	Shad	Vallis
s_1	y_{31}	$-V^1$	s_{21}	y_{231}
s_2	y_{12}	$-V^2$	s_{32}	y_{312}
s_3	y_{23}	$-V^3$	s_{13}	y_{123}
$s_{1'}$	y_{21}	U^1	s_{31}	$y_{32'1}$
$s_{2'}$	y_{32}	U^2	s_{12}	$y_{13'2}$
$s_{3'}$	y_{13}	U^3	s_{23}	$y_{21'3}$
τ_1	z_{31}, τ_{21}	z_1	τ_{21}	z_{231}, τ_{31}
τ_2	z_{12}, τ_{32}	z_2	τ_{32}	z_{312}, τ_{12}
τ_3	z_{23}, τ_{13}	z_3	τ_{13}	z_{123}, τ_{23}
$\tau_{1'}$	z_{21}, τ_{31}	z_1^*	τ_{31}	$z_{32'1}, \tau_{21}$
$\tau_{2'}$	z_{32}, τ_{12}	z_2^*	τ_{12}	$z_{13'2}, \tau_{32}$
$\tau_{3'}$	z_{13}, τ_{23}	z_3^*	τ_{23}	$z_{21'3}, \tau_{13}$

Table D.2: Translation table for onboard data stream notations in the common TDI literature. It also applies to the TDI input data, in this thesis denoted by $\eta_i(t)$.

The notation of [ETA00] denotes the entities on the OBs pointing in a counter-clockwise direction by the asterisk '$*$', which corresponds to our primed indices. That is, e.g., $C_i^* \,\widehat{=}\, p_{\underline{i}'}$. Furthermore, one has to be cautious with the links to be delayed, since the notation only distinguishes the arms, but not the links or their directions. From the deduction $y_{21} \,\widehat{=}\, s_{1'}$ above, it follows directly that the regarded link in our notation must be $2'$. We can thus formulate in phase:

$$
\begin{aligned}
y_{21} \,\widehat{=}\, s_{1'} \quad \widehat{=}\quad & p_{3,2} - \vec{n}_2 \cdot \vec{\Delta}_{3,2} + 2\vec{n}_2 \cdot \vec{\delta}_{1'} - \vec{n}_2 \cdot \vec{\Delta}_{1'} - p_{1'} + H_{1'} + N_{1'}^s \\
\widehat{=}\quad & p_{3:\mathbf{2}'} - \vec{n}_2 \cdot \vec{\Delta}_{3:\mathbf{2}'} + 2\vec{n}_2 \cdot \vec{\delta}_{1'} - \vec{n}_2 \cdot \vec{\Delta}_{1'} - p_{1'} + H_{1'} + N_{1'}^s
\end{aligned}
$$

One could now ask why the TM displacement noise enters the science interferometer. This is here due to the old optical bench layout used in [ETA00], where the input laser light directly hits the test mass, as sketched in Sec. 2.5. Hence, we can leave the term out and result in

$$
s_{1'} = p_{3:\mathbf{2}'} - \vec{n}_2 \cdot \vec{\Delta}_{3:\mathbf{2}'} - \vec{n}_2 \cdot \vec{\Delta}_{1'} - p_{1'} + H_{1'} + N_{1'}^s \,.
$$

Finally, a more careful consideration of the signatures and pre-factors yields in a simplified manner with time-independent time delays the onboard signal of the science interferometer for OB $1'$ given in Eq. (2.28d).

E Explicit Time-Delay Interferometry Outputs

E.1 TDI-X_1 Output – Primary Noises and Gravitational Wave Signal

We will now show explicitly that TDI-X_1 cancels laser frequency noise in terms of optical phase to first order in the relative LoS velocities. This was claimed in Sec. 3.3, where the combination X_1 was given by

$$
\begin{aligned}
X_1 \quad = \quad & \eta_{1'} + \eta_{3;\mathbf{2'}} + \eta_{1;\mathbf{22'}} + \eta_{2';\mathbf{322'}} + \eta_{1;\mathbf{3'322'}} + \eta_{2';\mathbf{33'322'}} \\
& + \eta_{1';\mathbf{3'33'322'}} + \eta_{3;\mathbf{2'3'33'322'}} - \eta_1 - \eta_{2';\mathbf{3}} - \eta_{1';\mathbf{3'3}} - \eta_{3;\mathbf{2'3'3}} \\
& - \eta_{1';\mathbf{22'3'3}} - \eta_{3;\mathbf{2'22'3'3}} - \eta_{1;\mathbf{22'22'3'3}} - \eta_{2';\mathbf{322'22'3'3}} \, .
\end{aligned}
$$

Therefore, TDI input data of the form (4.16a) – (4.16f),

$$
\begin{aligned}
\eta_1(t) &\sim H_1 + p_{2;\mathbf{3}} - p_1 + \tfrac{\mu_{2;\mathbf{3}} - \mu_{2';\mathbf{3}}}{2} \, , &\quad \eta_{1'}(t) &\sim H_{1'} + p_{3;\mathbf{2'}} - p_1 - \tfrac{\mu_1 - \mu_{1'}}{2} \\
\eta_2(t) &\sim H_2 + p_{3;\mathbf{1}} - p_2 + \tfrac{\mu_{3;\mathbf{1}} - \mu_{3';\mathbf{1}}}{2} \, , &\quad \eta_{2'}(t) &\sim H_{2'} + p_{1;\mathbf{3'}} - p_2 - \tfrac{\mu_2 - \mu_{2'}}{2} \\
\eta_3(t) &\sim H_3 + p_{1;\mathbf{2}} - p_3 + \tfrac{\mu_{1;\mathbf{2}} - \mu_{1';\mathbf{2}}}{2} \, , &\quad \eta_{3'}(t) &\sim H_{3'} + p_{2;\mathbf{1'}} - p_3 - \tfrac{\mu_3 - \mu_{3'}}{2}
\end{aligned}
$$

is inserted in X_1 and (3.37) applied,

$$
f(t)_{;\boldsymbol{j_1}\dots\boldsymbol{j_n}} \simeq f(t)_{,\boldsymbol{j_1}\dots\boldsymbol{j_n}} + \frac{1}{c^2} \dot{f}(t)_{,\boldsymbol{j_1}\dots\boldsymbol{j_n}} \cdot \sum_{k=1}^{n-1} \left(\dot{L}_{j_k} \sum_{\ell=k+1}^{n} L_{j_\ell} \right),
$$

to expand the result to first order in the LoS velocities. We find then

$$
\begin{aligned}
X_1 \sim\ & +(H_{1'}+p_{3;\mathbf{2'}}-p_1-\tfrac{\mu_1-\mu_{1'}}{2})+(H_3+p_{1;\mathbf{2}}-p_3+\tfrac{\mu_{1;\mathbf{2}}-\mu_{1';\mathbf{2}}}{2})_{;\mathbf{2'}} \\
& +(H_1+p_{2;\mathbf{3}}-p_1+\tfrac{\mu_{2;\mathbf{3}}-\mu_{2';\mathbf{3}}}{2})_{;\mathbf{22'}}+(H_{2'}+p_{1;\mathbf{3'}}-p_2-\tfrac{\mu_2-\mu_{2'}}{2})_{;\mathbf{322'}} \\
& +(H_1+p_{2;\mathbf{3}}-p_1+\tfrac{\mu_{2;\mathbf{3}}-\mu_{2';\mathbf{3}}}{2})_{;\mathbf{3'322'}}+(H_{2'}+p_{1;\mathbf{3'}}-p_2-\tfrac{\mu_2-\mu_{2'}}{2})_{;\mathbf{33'322'}} \\
& +(H_{1'}+p_{3;\mathbf{2'}}-p_1-\tfrac{\mu_1-\mu_{1'}}{2})_{;\mathbf{3'33'322'}} \\
& +(H_3+p_{1;\mathbf{2}}-p_3+\tfrac{\mu_{1;\mathbf{2}}-\mu_{1';\mathbf{2}}}{2})_{;\mathbf{2'3'33'322'}} \\
& -(H_1+p_{2;\mathbf{3}}-p_1+\tfrac{\mu_{2;\mathbf{3}}-\mu_{2';\mathbf{3}}}{2})-(H_{2'}+p_{1;\mathbf{3'}}-p_2-\tfrac{\mu_2-\mu_{2'}}{2})_{;\mathbf{3}} \\
& -(H_{1'}+p_{3;\mathbf{2'}}-p_1-\tfrac{\mu_1-\mu_{1'}}{2})_{;\mathbf{3'3}}-(H_3+p_{1;\mathbf{2}}-p_3+\tfrac{\mu_{1;\mathbf{2}}-\mu_{1';\mathbf{2}}}{2})_{;\mathbf{2'3'3}} \\
& -(H_{1'}+p_{3;\mathbf{2'}}-p_1-\tfrac{\mu_1-\mu_{1'}}{2})_{;\mathbf{22'3'3}}-(H_3+p_{1;\mathbf{2}}-p_3+\tfrac{\mu_{1;\mathbf{2}}-\mu_{1';\mathbf{2}}}{2})_{;\mathbf{2'22'3'3}} \\
& -(H_1+p_{2;\mathbf{3}}-p_1+\tfrac{\mu_{2;\mathbf{3}}-\mu_{2';\mathbf{3}}}{2})_{;\mathbf{22'22'3'3}} \\
& -(H_{2'}+p_{1;\mathbf{3'}}-p_2-\tfrac{\mu_2-\mu_{2'}}{2})_{;\mathbf{322'22'3'3}}\ . \\[4pt]
=\ & H_{1'}+p_{3;\mathbf{2'}}-p_1-\tfrac{\mu_1}{2}+\tfrac{\mu_{1'}}{2}+H_{3;\mathbf{2'}}+p_{1;\mathbf{22'}}-p_{3;\mathbf{2'}}+\tfrac{\mu_{1;\mathbf{22'}}}{2}-\tfrac{\mu_{1';\mathbf{22'}}}{2} \\
& +H_{1;\mathbf{22'}}+p_{2;\mathbf{322'}}-p_{1;\mathbf{22'}}+\tfrac{\mu_{2;\mathbf{322'}}}{2}-\tfrac{\mu_{2';\mathbf{322'}}}{2}+H_{2';\mathbf{322'}}+p_{1;\mathbf{3'322'}} \\
& -p_{2;\mathbf{322'}}-\tfrac{\mu_{2;\mathbf{322'}}}{2}+\tfrac{\mu_{2';\mathbf{322'}}}{2}+H_{1;\mathbf{3'322'}}+p_{2;\mathbf{33'322'}}-p_{1;\mathbf{3'322'}}+\tfrac{\mu_{2;\mathbf{33'322'}}}{2} \\
& -\tfrac{\mu_{2';\mathbf{33'322'}}}{2}+H_{2';\mathbf{33'322'}}+p_{1;\mathbf{3'33'322'}}-p_{2;\mathbf{33'322'}}-\tfrac{\mu_{2;\mathbf{33'322'}}}{2}+\tfrac{\mu_{2';\mathbf{33'322'}}}{2} \\
& +H_{1';\mathbf{3'33'322'}}+p_{3;\mathbf{2'3'33'322'}}-p_{1;\mathbf{3'33'322'}}-\tfrac{\mu_{1;\mathbf{3'33'322'}}}{2}+\tfrac{\mu_{1';\mathbf{3'33'322'}}}{2} \\
& +H_{3;\mathbf{2'3'33'322'}}+p_{1;\mathbf{22'3'33'322'}}-p_{3;\mathbf{2'3'33'322'}}+\tfrac{\mu_{1;\mathbf{22'3'33'322'}}}{2} \\
& -\tfrac{\mu_{1';\mathbf{22'3'33'322'}}}{2}-H_1-p_{2;\mathbf{3}}+p_1-\tfrac{\mu_{2;\mathbf{3}}}{2}+\tfrac{\mu_{2';\mathbf{3}}}{2}-H_{2';\mathbf{3}}-p_{1;\mathbf{3'3}}+p_{2;\mathbf{3}} \\
& +\tfrac{\mu_{2;\mathbf{3}}}{2}-\tfrac{\mu_{2';\mathbf{3}}}{2}-H_{1';\mathbf{3'3}}-p_{3;\mathbf{2'3'3}}+p_{1;\mathbf{3'3}}+\tfrac{\mu_{1;\mathbf{3'3}}}{2}-\tfrac{\mu_{1';\mathbf{3'3}}}{2}-H_{3;\mathbf{2'3'3}} \\
& -p_{1;\mathbf{22'3'3}}+p_{3;\mathbf{2'3'3}}-\tfrac{\mu_{1;\mathbf{22'3'3}}}{2}+\tfrac{\mu_{1';\mathbf{22'3'3}}}{2}-H_{1';\mathbf{22'3'3}}-p_{3;\mathbf{2'22'3'3}} \\
& +p_{1;\mathbf{22'3'3}}+\tfrac{\mu_{1;\mathbf{22'3'3}}}{2}-\tfrac{\mu_{1';\mathbf{22'3'3}}}{2}-H_{3;\mathbf{2'22'3'3}}-p_{1;\mathbf{22'22'3'3}}+p_{3;\mathbf{2'22'3'3}} \\
& -\tfrac{\mu_{1;\mathbf{22'22'3'3}}}{2}+\tfrac{\mu_{1';\mathbf{22'22'3'3}}}{2}-H_{1;\mathbf{22'22'3'3}}-p_{2;\mathbf{322'22'3'3}}+p_{1;\mathbf{22'22'3'3}} \\
& -\tfrac{\mu_{2;\mathbf{322'22'3'3}}}{2}+\tfrac{\mu_{2';\mathbf{322'22'3'3}}}{2}-H_{2';\mathbf{322'22'3'3}}-p_{1;\mathbf{3'322'22'3'3}} \\
& +p_{2;\mathbf{322'22'3'3}}+\tfrac{\mu_{2;\mathbf{322'22'3'3}}}{2}-\tfrac{\mu_{2';\mathbf{322'22'3'3}}}{2} \\[4pt]
=\ & +H_{1'}+H_{3;\mathbf{2'}}+H_{1;\mathbf{22'}}+H_{2';\mathbf{322'}}+H_{1;\mathbf{3'322'}}+H_{2';\mathbf{33'322'}}+H_{1';\mathbf{3'33'322'}} \\
& +H_{3;\mathbf{2'3'33'322'}}-H_1-H_{2';\mathbf{3}}-H_{1';\mathbf{3'3}}-H_{3;\mathbf{2'3'3}}-H_{1';\mathbf{22'3'3}}-H_{3;\mathbf{2'22'3'3}} \\
& -H_{1;\mathbf{22'22'3'3}}-H_{2';\mathbf{322'22'3'3}}+p_{1;\mathbf{22'3'33'322'}}-p_{1;\mathbf{3'322'22'3'3}}+\tfrac{\mu_{1'}-\mu_1}{2} \\
& +\tfrac{\mu_{1;\mathbf{22'}}-\mu_{1';\mathbf{22'}}}{2}+\tfrac{\mu_{1;\mathbf{3'3}}-\mu_{1';\mathbf{3'3}}}{2}+\tfrac{\mu_{1';\mathbf{3'33'322'}}-\mu_{1;\mathbf{3'33'322'}}}{2}+ \\
& +\tfrac{\mu_{1';\mathbf{22'22'3'3}}-\mu_{1;\mathbf{22'22'3'3}}}{2}+\tfrac{\mu_{1;\mathbf{22'3'33'322'}}-\mu_{1';\mathbf{22'3'33'322'}}}{2}\ .
\end{aligned}
$$

In the last step, several laser phase noise terms cancel out and we are left with only two of them. The remainders of the fibre noise all appear in a difference with their counterparts, even if time-delayed, and hence will cancel in the case of

fibre reciprocity. However, note, that the fibre noise does not cancel naturally and requires therefore the reciprocity.

In order to simplify the laser phase noise terms, we can make use of the Taylor expansion:

$$
\begin{aligned}
p_{1;\mathbf{22'3'33'322'}} &= p_{1,\mathbf{22'3'33'322'}} + \frac{1}{c^2}\dot{p}_{1,\mathbf{22'3'33'322'}}\big[\dot{L}_2(L_{2'} + L_{3'} + L_3 + L_{3'} \\
&\quad + L_3 + L_2 + L_{2'}) + \dot{L}_{2'}(L_{3'} + L_3 + L_{3'} + L_3 + L_2 + L_{2'}) \\
&\quad + \dot{L}_{3'}(L_3 + L_{3'} + L_3 + L_2 + L_{2'}) + \dot{L}_3(L_{3'} + L_3 + L_2 + L_{2'}) \\
&\quad + \dot{L}_{3'}(L_3 + L_2 + L_{2'}) + \dot{L}_3(L_2 + L_{2'}) + \dot{L}_2 L_{2'}\big] \\
&= p_{1,\mathbf{22'3'33'322'}} + \frac{1}{c^2}\dot{p}_{1,\mathbf{22'3'33'322'}}\big[3\dot{L}_2 L_{2'} + 2\dot{L}_2 L_{3'} + 2\dot{L}_2 L_3 \\
&\quad + \dot{L}_2 L_2 + 2\dot{L}_{2'} L_{3'} + 2\dot{L}_{2'} L_3 + \dot{L}_{2'} L_2 + \dot{L}_{2'} L_{2'} + 3\dot{L}_{3'} L_3 \\
&\quad + \dot{L}_{3'} L_{3'} + 2\dot{L}_{3'} L_2 + 2\dot{L}_{3'} L_{2'} + \dot{L}_3 L_{3'} + \dot{L}_3 L_3 + 2\dot{L}_3 L_2 \\
&\quad + 2\dot{L}_3 L_{2'}\big]
\end{aligned}
$$

and furthermore

$$
\begin{aligned}
p_{1;\mathbf{3'322'22'3'3}} &= p_{1,\mathbf{3'322'22'3'3}} + \frac{1}{c^2}\dot{p}_{1,\mathbf{3'322'22'3'3}}\big[\dot{L}_{3'}(L_3 + L_2 + L_{2'} + L_2 \\
&\quad + L_{2'} + L_{3'} + L_3) + \dot{L}_3(L_2 + L_{2'} + L_2 + L_{2'} + L_{3'} + L_3) \\
&\quad + \dot{L}_2(L_{2'} + L_2 + L_{2'} + L_{3'} + L_3) + \dot{L}_{2'}(L_2 + L_{2'} + L_{3'} + L_3) \\
&\quad + \dot{L}_2(L_{2'} + L_{3'} + L_3) + \dot{L}_{2'}(L_{3'} + L_3) + \dot{L}_{3'} L_3\big] \\
&= p_{1,\mathbf{3'322'22'3'3}} + \frac{1}{c^2}\dot{p}_{1,\mathbf{3'322'22'3'3}}\big[3\dot{L}_{3'} L_3 + 2\dot{L}_{3'} L_2 + 2\dot{L}_{3'} L_{2'} \\
&\quad + \dot{L}_{3'} L_{3'} + 2\dot{L}_3 L_2 + 2\dot{L}_3 L_{2'} + \dot{L}_3 L_{3'} + \dot{L}_3 L_3 + 3\dot{L}_2 L_{2'} + \dot{L}_2 L_2 \\
&\quad + 2\dot{L}_2 L_{3'} + 2\dot{L}_2 L_3 + \dot{L}_{2'} L_2 + \dot{L}_{2'} L_{2'} + 2\dot{L}_{2'} L_{3'} + 2\dot{L}_{2'} L_3\big]\,.
\end{aligned}
$$

The difference then gives

$$
\begin{aligned}
&p_{1;\mathbf{22'3'33'322'}} - p_{1;\mathbf{3'322'22'3'3}} \\
&= (p_{1,\mathbf{22'3'33'322'}} - p_{1,\mathbf{3'322'22'3'3}}) + \frac{1}{c^2}\dot{p}_{1,\mathbf{22'3'33'322'}}\big[3\dot{L}_2 L_{2'} + 2\dot{L}_2 L_{3'} \\
&\quad + 2\dot{L}_2 L_3 + \dot{L}_2 L_2 + 2\dot{L}_{2'} L_{3'} + 2\dot{L}_{2'} L_3 + \dot{L}_{2'} L_2 + \dot{L}_{2'} L_{2'} + 3\dot{L}_{3'} L_3 + \dot{L}_{3'} L_{3'} \\
&\quad + 2\dot{L}_{3'} L_2 + 2\dot{L}_{3'} L_{2'} + \dot{L}_3 L_{3'} + \dot{L}_3 L_3 + 2\dot{L}_3 L_2 + 2\dot{L}_3 L_{2'}\big] \\
&\quad - \frac{1}{c^2}\dot{p}_{1,\mathbf{3'322'22'3'3}}\big[3\dot{L}_{3'} L_3 + 2\dot{L}_{3'} L_2 + 2\dot{L}_{3'} L_{2'} + \dot{L}_{3'} L_{3'} + 2\dot{L}_3 L_2 + 2\dot{L}_3 L_{2'} \\
&\quad + \dot{L}_3 L_{3'} + \dot{L}_3 L_3 + 3\dot{L}_2 L_{2'} + \dot{L}_2 L_2 + 2\dot{L}_2 L_{3'} + 2\dot{L}_2 L_3 + \dot{L}_{2'} L_2 + \dot{L}_{2'} L_{2'} \\
&\quad + 2\dot{L}_{2'} L_{3'} + 2\dot{L}_{2'} L_3\big]\,.
\end{aligned}
$$

Since the time shifts denoted by comma do commute (Eq. (3.19c)), we can resort

the indices of the delays such that

$$
p_{1;\mathbf{22'3'33'322'}} - p_{1;\mathbf{3'322'22'3'3}}
$$

$$
\begin{aligned}
= \ & (p_{1,\mathbf{22'3'33'322'}} - p_{1,\mathbf{22'3'33'322'}}) + \frac{1}{c^2}\dot{p}_{1,\mathbf{22'3'33'322'}}\left[3\dot{L}_2 L_{2'} + 2\dot{L}_2 L_{3'}\right. \\
& + 2\dot{L}_2 L_3 + \dot{L}_2 L_2 + 2\dot{L}_{2'}L_{3'} + 2\dot{L}_{2'}L_3 + \dot{L}_{2'}L_2 + \dot{L}_{2'}L_{2'} + 3\dot{L}_{3'}L_3 + \dot{L}_{3'}L_{3'} \\
& \left. + 2\dot{L}_{3'}L_2 + 2\dot{L}_{3'}L_{2'} + \dot{L}_3 L_{3'} + \dot{L}_3 L_3 + 2\dot{L}_3 L_2 + 2\dot{L}_3 L_{2'}\right] \\
& - \frac{1}{c^2}\dot{p}_{1,\mathbf{22'3'33'322'}}\left[3\dot{L}_{3'}L_3 + 2\dot{L}_{3'}L_2 + 2\dot{L}_{3'}L_{2'} + \dot{L}_{3'}L_{3'} + 2\dot{L}_3 L_2 + 2\dot{L}_3 L_{2'}\right. \\
& + \dot{L}_3 L_{3'} + \dot{L}_3 L_3 + 3\dot{L}_2 L_{2'} + \dot{L}_2 L_2 + 2\dot{L}_2 L_{3'} + 2\dot{L}_2 L_3 + \dot{L}_{2'}L_2 + \dot{L}_{2'}L_{2'} \\
& \left. + 2\dot{L}_{2'}L_{3'} + 2\dot{L}_{2'}L_3\right].
\end{aligned}
$$

Hence, the round bracket vanishes and we can factor out $\frac{1}{c^2}\dot{p}_{1,\mathbf{2'233'33'2'2}}$:

$$
p_{1;\mathbf{22'3'33'322'}} - p_{1;\mathbf{3'322'22'3'3}}
$$

$$
\begin{aligned}
= \ & \frac{1}{c^2}\dot{p}_{1,\mathbf{22'3'33'322'}}\left[3(\dot{L}_2 L_{2'} - \dot{L}_2 L_{2'}) + 2(\dot{L}_2 L_{3'} - \dot{L}_2 L_{3'}) + 2(\dot{L}_2 L_3 - \dot{L}_2 L_3)\right. \\
& + (\dot{L}_2 L_2 - \dot{L}_2 L_2) + 2(\dot{L}_{2'}L_{3'} - \dot{L}_{2'}L_{3'}) + 2(\dot{L}_{2'}L_3 - \dot{L}_{2'}L_3) \\
& + (\dot{L}_{2'}L_2 - \dot{L}_{2'}L_2) + (\dot{L}_{2'}L_{2'} - \dot{L}_{2'}L_{2'}) + 3(\dot{L}_{3'}L_3 - \dot{L}_{3'}L_3) \\
& + (\dot{L}_{3'}L_{3'} - \dot{L}_{3'}L_{3'}) + 2(\dot{L}_{3'}L_2 - \dot{L}_{3'}L_2) + 2(\dot{L}_{3'}L_{2'} - \dot{L}_{3'}L_{2'}) \\
& + (\dot{L}_3 L_{3'} - \dot{L}_3 L_{3'}) + (\dot{L}_3 L_3 - \dot{L}_3 L_3) \\
& \left. + 2(\dot{L}_3 L_2 - \dot{L}_3 L_2) + 2(\dot{L}_3 L_{2'} - \dot{L}_3 L_{2'})\right] = 0.
\end{aligned}
$$

Finally, all terms in the bracket vanishes and we end up with

$$
\begin{aligned}
X_1 \ \simeq \ & +H_{1'} + H_{3;\mathbf{2'}} + H_{1;\mathbf{22'}} + H_{2';\mathbf{322'}} + H_{1;\mathbf{3'322'}} + H_{2';\mathbf{33'322'}} + H_{1';\mathbf{3'33'322'}} \\
& + H_{3;\mathbf{2'3'33'322'}} - H_1 - H_{2';\mathbf{3}} - H_{1';\mathbf{3'3}} - H_{3;\mathbf{2'3'3}} - H_{1';\mathbf{22'3'3}} - H_{3;\mathbf{2'22'3'3}} \\
& - H_{1;\mathbf{22'22'3'3}} - H_{2';\mathbf{322'22'3'3}} + \frac{\mu_{1'}-\mu_1}{2} + \frac{\mu_{1;\mathbf{22'}}-\mu_{1';\mathbf{22'}}}{2} + \frac{\mu_{1;\mathbf{3'3}}-\mu_{1';\mathbf{3'3}}}{2} \\
& + \frac{\mu_{1';\mathbf{3'33'322'}}-\mu_{1;\mathbf{3'33'322'}}}{2} + \frac{\mu_{1';\mathbf{22'22'3'3}}-\mu_{1;\mathbf{22'22'3'3}}}{2} \\
& + \frac{\mu_{1;\mathbf{22'3'33'322'}}-\mu_{1';\mathbf{22'3'33'322'}}}{2}.
\end{aligned}
$$

This comprises a data stream with GW signal only in the case of fibre reciprocity (plus secondary noise).

E.2 TDI-X_1 Output – Readout Noise Only

Readout noise is the dominant contribution to the residual noise budget after TDI processing as the simulations in Ch. 6 showed. We will now list here all readout noise instances in the TDI processing explained in Ch. 4. In the following, the readout noise contributions in the data stream $f(t)$ are denoted by the operator $\mathcal{R}[f(t)]$. $\mathcal{R}$ emphasises that only the respective readout noise is regarded (in some sense related with the symbol '$\sim$'). For example,

$$\mathcal{R}[s_1^c(t)] = N_1^s(t), \quad \mathcal{R}[\varepsilon_3(t)] = N_3^\varepsilon(t).$$

As before, we do not write the time dependence explicitly for the sake of brevity.

The telemetered data $s_i^c(t), s_i^{sb}(t), \varepsilon_i(t)$ and $\tau_i(t)$ each contain a single instance of readout noise. In the first step of the full removal algorithm discussed in Sec. 4.3, the OB displacement noise is suppressed by the construction of the combination $\xi_i(t)$. It is defined by

$$\xi_1(t) \equiv s_1^c(t) - \theta_1^{2'}\theta_1^{1'}\frac{\lambda_{1'}}{\lambda_{2'}}\frac{\varepsilon_1(t) - \tau_1(t)}{2} - \theta_1^{2'}\theta_{2'}^2\frac{\lambda_2}{\lambda_{2'}}\frac{\varepsilon_{2';\mathbf{3}}(t) - \tau_{2';\mathbf{3}}(t)}{2},$$

$$\xi_{1'}(t) \equiv s_{1'}^c(t) - \theta_{1'}^3\theta_{1'}^1\frac{\lambda_1}{\lambda_3}\frac{\varepsilon_{1'}(t) - \tau_{1'}(t)}{2} - \theta_{1'}^3\theta_3^{3'}\frac{\lambda_{3'}}{\lambda_3}\frac{\varepsilon_{3;\mathbf{2'}}(t) - \tau_{3;\mathbf{2'}}(t)}{2},$$

others cyclic. Hence, the readout noise contributions are

$$\mathcal{R}[\xi_1(t)] = N_1^s - \frac{\theta_1^{2'}\theta_1^{1'}\lambda_{1'}}{2\lambda_{2'}}N_1^\varepsilon + \frac{\theta_1^{2'}\theta_1^{1'}\lambda_{1'}}{2\lambda_{2'}}N_1^\tau - \frac{\theta_1^{2'}\theta_{2'}^2\lambda_2}{2\lambda_{2'}}N_{2';\mathbf{3}}^\varepsilon + \frac{\theta_1^{2'}\theta_{2'}^2\lambda_2}{2\lambda_{2'}}N_{2';\mathbf{3}}^\tau,$$

$$\mathcal{R}[\xi_{1'}(t)] = N_{1'}^s - \frac{\theta_{1'}^3\theta_{1'}^1\lambda_1}{2\lambda_3}N_{1'}^\varepsilon + \frac{\theta_{1'}^3\theta_{1'}^1\lambda_1}{2\lambda_3}N_{1'}^\tau - \frac{\theta_{1'}^3\theta_3^{3'}\lambda_{3'}}{2\lambda_3}N_{3;\mathbf{2'}}^\varepsilon + \frac{\theta_{1'}^3\theta_3^{3'}\lambda_{3'}}{2\lambda_3}N_{3;\mathbf{2'}}^\tau.$$

$\xi_i(t)$ already provide five readout noise contributions each.

In a next step, the data streams are reduced to three free-running lasers by the formation of

$$Q_1(t) \equiv \theta_1^{2'}\xi_1(t) + \kappa_{2;\mathbf{3}}(t) = \theta_1^{2'}\xi_1(t) + \frac{\theta_{2'}^2\tau_{2';\mathbf{3}}(t) - \theta_2^{2'}\tau_{2;\mathbf{3}}(t)}{2},$$

$$Q_{1'}(t) \equiv \theta_{1'}^3\xi_{1'}(t) - \kappa_1(t) = \theta_{1'}^3\xi_{1'}(t) - \frac{\theta_{1'}^1\tau_{1'}(t) - \theta_1^{1'}\tau_1(t)}{2},$$

and cyclic with the readout noise ($(\theta_j^i)^2 = 1!$):

$$
\begin{aligned}
\mathcal{R}[Q_1(t)] &= \theta_1^{2'} N_1^s - \frac{\theta_1^{1'}\lambda_{1'}}{2\lambda_{2'}} N_1^\varepsilon + \frac{\theta_1^{1'}\lambda_{1'}}{2\lambda_{2'}} N_1^\tau - \frac{\theta_{2'}^2\lambda_2}{2\lambda_{2'}} N_{2';\mathbf{3}}^\varepsilon + \frac{\theta_{2'}^2\lambda_2}{2\lambda_{2'}} N_{2';\mathbf{3}}^\tau \\
&\quad + \frac{\theta_{2'}^2}{2} N_{2';\mathbf{3}}^\tau - \frac{\theta_{2'}^2}{2} N_{2;\mathbf{3}}^\tau \,, \\
\mathcal{R}[Q_{1'}(t)] &= \theta_{1'}^3 N_{1'}^s - \frac{\theta_{1'}^1\lambda_1}{2\lambda_3} N_{1'}^\varepsilon + \frac{\theta_{1'}^1\lambda_1}{2\lambda_3} N_{1'}^\tau - \frac{\theta_3^{3'}\lambda_{3'}}{2\lambda_3} N_{3;\mathbf{2'}}^\varepsilon + \frac{\theta_3^{3'}\lambda_{3'}}{2\lambda_3} N_{3;\mathbf{2'}}^\tau \\
&\quad - \frac{\theta_{1'}^1}{2} N_{1'}^\tau + \frac{\theta_1^{1'}}{2} N_1^\tau \,.
\end{aligned}
$$

The $Q_i(t)$ are then used to remove clock jitter by the choice of a master clock. In the algorithm discussed in Sec. 4.3, the master clock is provided by S/C 1 (hence the notation $Q_i^{q_1}(t)$). However, the choice of a master clock breaks the cyclical symmetry in the data combinations. The clock noise free data is constructed via

$$
\begin{aligned}
\eta_1(t) &\equiv Q_1^{q_1}(t) - \frac{\theta_{2'}^2(b_{2'}+b_2)}{2} \frac{s_{2';\mathbf{3}}^c(t) - s_{2';\mathbf{3}}^{sb}(t)}{a_{2'} + \theta_{2'}^1 m_{2'} - c_{2'}} \,, \\
\eta_{1'}(t) &\equiv Q_{1'}^{q_1}(t) \,, \\
\eta_2(t) &\equiv Q_2^{q_1}(t) - \theta_2^{3'} a_2 \frac{s_{2'}^c(t) - s_{2'}^{sb}(t)}{a_{2'} + \theta_{2'}^1 m_{2'} - c_{2'}} - \frac{\theta_{3'}^3(b_{3'}+b_3)}{2} \frac{s_{3;\mathbf{1}}^c(t) - s_{3;\mathbf{1}}^{sb}(t)}{a_3 + \theta_3^{1'} m_3 - c_3} \,, \\
\eta_{2'}(t) &\equiv Q_{2'}^{q_1}(t) - \theta_{2'}^1 a_{2'} \frac{s_{2'}^c(t) - s_{2'}^{sb}(t)}{a_{2'} + \theta_{2'}^1 m_{2'} - c_{2'}} + \frac{\theta_{2'}^2(b_{2'}+b_2)}{2} \frac{s_{2'}^c(t) - s_{2'}^{sb}(t)}{a_{2'} + \theta_{2'}^1 m_{2'} - c_{2'}} \,, \\
\eta_3(t) &\equiv Q_3^{q_1}(t) - \theta_3^{1'} a_3 \frac{s_3^c(t) - s_3^{sb}(t)}{a_3 + \theta_3^{1'} m_3 - c_3} \,, \\
\eta_{3'}(t) &\equiv Q_{3'}^{q_1}(t) - \theta_{3'}^2 a_{3'} \frac{s_3^c(t) - s_3^{sb}(t)}{a_3 + \theta_3^{1'} m_3 - c_3} + \frac{\theta_{3'}^3(b_{3'}+b_3)}{2} \frac{s_3^c(t) - s_3^{sb}(t)}{a_3 + \theta_3^{1'} m_3 - c_3} \,.
\end{aligned}
$$

Since $\mathcal{R}[Q_i^{q_1}(t)] = \mathcal{R}[Q_i(t)]$, we can directly compute the readout noise contributions of $\eta_i(t)$:

$$
\begin{aligned}
\mathcal{R}[\eta_1(t)] &= \theta_1^{2'} N_1^s - \frac{\theta_1^{1'}\lambda_{1'}}{2\lambda_{2'}} N_1^\varepsilon + \frac{\theta_1^{1'}\lambda_{1'}}{2\lambda_{2'}} N_1^\tau - \frac{\theta_{2'}^2\lambda_2}{2\lambda_{2'}} N_{2';\mathbf{3}}^\varepsilon + \frac{\theta_{2'}^2\lambda_2}{2\lambda_{2'}} N_{2';\mathbf{3}}^\tau \\
&\quad + \frac{\theta_{2'}^2}{2} N_{2';\mathbf{3}}^\tau - \frac{\theta_{2'}^2}{2} N_{2;\mathbf{3}}^\tau - \frac{b_{2'}\theta_{2'}^2}{2(a_{2'}+\theta_{2'}^1 m_{2'}-c_{2'})} N_{2';\mathbf{3}}^s + \frac{b_{2'}\theta_{2'}^2}{2(a_{2'}+\theta_{2'}^1 m_{2'}-c_{2'})} N_{2';\mathbf{3}}^{sb} \\
&\quad - \frac{b_2\theta_{2'}^2}{2(a_{2'}+\theta_{2'}^1 m_{2'}-c_{2'})} N_{2';\mathbf{3}}^s + \frac{b_2\theta_{2'}^2}{2(a_{2'}+\theta_{2'}^1 m_{2'}-c_{2'})} N_{2';\mathbf{3}}^{sb} \,, \\
\mathcal{R}[\eta_{1'}(t)] &= \theta_{1'}^3 N_{1'}^s - \frac{\theta_{1'}^1\lambda_1}{2\lambda_3} N_{1'}^\varepsilon + \frac{\theta_{1'}^1\lambda_1}{2\lambda_3} N_{1'}^\tau - \frac{\theta_3^{3'}\lambda_{3'}}{2\lambda_3} N_{3;\mathbf{2'}}^\varepsilon + \frac{\theta_3^{3'}\lambda_{3'}}{2\lambda_3} N_{3;\mathbf{2'}}^\tau \\
&\quad - \frac{\theta_{1'}^1}{2} N_{1'}^\tau + \frac{\theta_1^{1'}}{2} N_1^\tau \,,
\end{aligned}
$$

$$\mathcal{R}[\eta_2(t)] = \theta_2^{3'} N_2^s - \frac{\theta_2^{2'}\lambda_{2'}}{2\lambda_{3'}} N_2^\varepsilon + \frac{\theta_2^{2'}\lambda_{2'}}{2\lambda_{3'}} N_2^\tau - \frac{\theta_{3'}^3\lambda_3}{2\lambda_{3'}} N_{3';\mathbf{1}}^\varepsilon + \frac{\theta_{3'}^3\lambda_3}{2\lambda_{3'}} N_{3';\mathbf{1}}^\tau$$

$$+ \frac{\theta_{3'}^3}{2} N_{3';\mathbf{1}}^\tau - \frac{\theta_3^{3'}}{2} N_{3;\mathbf{1}}^\tau - \frac{\theta_2^{3'} a_2}{a_{2'}+\theta_{2'}^1 m_{2'}-c_{2'}} N_{2'}^s + \frac{\theta_2^{3'} a_2}{a_{2'}+\theta_{2'}^1 m_{2'}-c_{2'}} N_{2'}^{\text{sb}}$$

$$- \frac{b_{3'}\theta_{3'}^3}{2(a_3+\theta_3^{1'} m_3-c_3)} N_{3;\mathbf{1}}^s + \frac{b_{3'}\theta_{3'}^3}{2(a_3+\theta_3^{1'} m_3-c_3)} N_{3;\mathbf{1}}^{\text{sb}} - \frac{b_3\theta_{3'}^3}{2(a_3+\theta_3^{1'} m_3-c_3)} N_{3;\mathbf{1}}^s$$

$$+ \frac{b_3\theta_{3'}^3}{2(a_3+\theta_3^{1'} m_3-c_3)} N_{3;\mathbf{1}}^{\text{sb}} \,,$$

$$\mathcal{R}[\eta_{2'}(t)] = \theta_{2'}^1 N_{2'}^s - \frac{\theta_{2'}^2\lambda_2}{2\lambda_1} N_{2'}^\varepsilon + \frac{\theta_{2'}^2\lambda_2}{2\lambda_1} N_{2'}^\tau - \frac{\theta_1^{1'}\lambda_{1'}}{2\lambda_1} N_{1;\mathbf{3'}}^\varepsilon + \frac{\theta_1^{1'}\lambda_{1'}}{2\lambda_1} N_{1;\mathbf{3'}}^\tau$$

$$- \frac{\theta_{2'}^2}{2} N_{2'}^\tau + \frac{\theta_2^{2'}}{2} N_2^\tau - \frac{\theta_{2'}^1 a_{2'}}{a_{2'}+\theta_{2'}^1 m_{2'}-c_{2'}} N_{2'}^s + \frac{\theta_{2'}^1 a_{2'}}{a_{2'}+\theta_{2'}^1 m_{2'}-c_{2'}} N_{2'}^{\text{sb}}$$

$$+ \frac{b_{2'}\theta_{2'}^2}{2(a_{2'}+\theta_{2'}^1 m_{2'}-c_{2'})} N_{2'}^s - \frac{b_{2'}\theta_{2'}^2}{2(a_{2'}+\theta_{2'}^1 m_{2'}-c_{2'})} N_{2'}^{\text{sb}} + \frac{b_2\theta_{2'}^2}{2(a_{2'}+\theta_{2'}^1 m_{2'}-c_{2'})} N_{2'}^s$$

$$- \frac{b_2\theta_{2'}^2}{2(a_{2'}+\theta_{2'}^1 m_{2'}-c_{2'})} N_{2'}^{\text{sb}} \,,$$

$$\mathcal{R}[\eta_3(t)] = \theta_3^{1'} N_3^s - \frac{\theta_3^{3'}\lambda_{3'}}{2\lambda_{1'}} N_3^\varepsilon + \frac{\theta_3^{3'}\lambda_{3'}}{2\lambda_{1'}} N_3^\tau - \frac{\theta_{1'}^1\lambda_1}{2\lambda_{1'}} N_{1';\mathbf{2}}^\varepsilon + \frac{\theta_{1'}^1\lambda_1}{2\lambda_{1'}} N_{1';\mathbf{2}}^\tau$$

$$+ \frac{\theta_{1'}^1}{2} N_{1';\mathbf{2}}^\tau - \frac{\theta_1^{1'}}{2} N_{1;\mathbf{2}}^\tau - \frac{\theta_3^{1'} a_3}{a_3+\theta_3^{1'} m_3-c_3} N_{3'}^s + \frac{\theta_3^{1'} a_3}{a_3+\theta_3^{1'} m_3-c_3} N_{3'}^{\text{sb}} \,,$$

$$\mathcal{R}[\eta_{3'}(t)] = \theta_{3'}^2 N_{3'}^s - \frac{\theta_{3'}^3\lambda_3}{2\lambda_2} N_{3'}^\varepsilon + \frac{\theta_{3'}^3\lambda_3}{2\lambda_2} N_{3'}^\tau - \frac{\theta_{2'}^2\lambda_{2'}}{2\lambda_2} N_{2;\mathbf{1'}}^\varepsilon + \frac{\theta_2^{2'}\lambda_{2'}}{2\lambda_2} N_{2;\mathbf{1'}}^\tau$$

$$- \frac{\theta_{3'}^3}{2} N_{3'}^\tau + \frac{\theta_3^{3'}}{2} N_3^\tau - \frac{\theta_{3'}^2 a_{3'}}{a_3+\theta_3^{1'} m_3-c_3} N_{3'}^s + \frac{\theta_{3'}^2 a_{3'}}{a_3+\theta_3^{1'} m_3-c_3} N_{3'}^{\text{sb}}$$

$$+ \frac{b_{3'}\theta_{3'}^3}{2(a_3+\theta_3^{1'} m_3-c_3)} N_{3'}^s - \frac{b_{3'}\theta_{3'}^3}{2(a_3+\theta_3^{1'} m_3-c_3)} N_{3'}^{\text{sb}} + \frac{b_3\theta_{3'}^3}{2(a_3+\theta_3^{1'} m_3-c_3)} N_{3'}^s$$

$$- \frac{b_3\theta_{3'}^3}{2(a_3+\theta_3^{1'} m_3-c_3)} N_{3'}^{\text{sb}} \,.$$

This is finally inserted in the laser phase noise free data combinations discussed in Ch. 3 to synthesise Michelson-like interferometer outputs. Therefore, the data $\eta_i(t)$ is added and time-delayed properly 16 times. Obviously, an analytic expression of the output is extremely lengthy and not constructive here.

In order to compare with the simulation, we will derive a simplified readout noise dominated TDI output, since clock noise is neglected in TDISim and thus the formation of $\eta_i(t)$ is not necessary. Instead, as explained in Sec. 5.2.6, the combination $\eta_i^{\text{sim}}(t)$ that neglects the beat-note frequency polarity and ignores different laser wavelengths is used as TDI input in TDISim. The analytic expression for this was determined to

$$\eta_1^{\text{sim}}(t) \equiv s_1^{\text{sim}}(t) - \frac{\varepsilon_1^{\text{sim}}(t) - \tau_1^{\text{sim}}(t)}{2} - \frac{\varepsilon_{2';\mathbf{3}}^{\text{sim}}(t) - \tau_{2';\mathbf{3}}^{\text{sim}}(t)}{2} + \frac{\tau_{2';\mathbf{3}}^{\text{sim}}(t) - \tau_{2;\mathbf{3}}^{\text{sim}}(t)}{2} \,,$$

$$\eta_{1'}^{\text{sim}}(t) \equiv s_{1'}^{\text{sim}}(t) - \frac{\varepsilon_{1'}^{\text{sim}}(t) - \tau_{1'}^{\text{sim}}(t)}{2} - \frac{\varepsilon_{3;\mathbf{2'}}^{\text{sim}}(t) - \tau_{3;\mathbf{2'}}^{\text{sim}}(t)}{2} - \frac{\tau_{1'}^{\text{sim}}(t) - \tau_1^{\text{sim}}(t)}{2} \,,$$

and cyclic, with the corresponding readout noise

$$
\begin{aligned}
\mathcal{R}[\eta_1^{\text{sim}}(t)] &= N_1^s - \tfrac{1}{2}N_1^\varepsilon + \tfrac{1}{2}N_1^\tau - \tfrac{1}{2}N_{2';\mathbf{3}}^\varepsilon + \tfrac{1}{2}N_{2';\mathbf{3}}^\tau + \tfrac{1}{2}N_{2';\mathbf{3}}^\tau - \tfrac{1}{2}N_{2;\mathbf{3}}^\tau \\
&= N_1^s - \tfrac{1}{2}N_1^\varepsilon + \tfrac{1}{2}N_1^\tau - \tfrac{1}{2}N_{2';\mathbf{3}}^\varepsilon + N_{2';\mathbf{3}}^\tau - \tfrac{1}{2}N_{2;\mathbf{3}}^\tau \,, \\
\mathcal{R}[\eta_{1'}^{\text{sim}}(t)] &= N_{1'}^s - \tfrac{1}{2}N_{1'}^\varepsilon + \tfrac{1}{2}N_{1'}^\tau - \tfrac{1}{2}N_{3;\mathbf{2'}}^\varepsilon + \tfrac{1}{2}N_{3;\mathbf{2'}}^\tau - \tfrac{1}{2}N_{1'}^\tau + \tfrac{1}{2}N_1^\tau \\
&= N_{1'}^s - \tfrac{1}{2}N_{1'}^\varepsilon - \tfrac{1}{2}N_{3;\mathbf{2'}}^\varepsilon + \tfrac{1}{2}N_{3;\mathbf{2'}}^\tau + \tfrac{1}{2}N_1^\tau \,.
\end{aligned}
$$

We will now insert this into the laser phase noise free data combinations, exemplarily demonstrated for

$$
\begin{aligned}
X_1 &= \eta_{1'}^{\text{sim}} + \eta_{3;\mathbf{2'}}^{\text{sim}} + \eta_{1;\mathbf{22'}}^{\text{sim}} + \eta_{2';\mathbf{322'}}^{\text{sim}} + \eta_{1;\mathbf{3'322'}}^{\text{sim}} + \eta_{2';\mathbf{33'322'}}^{\text{sim}} \\
&\quad + \eta_{1';\mathbf{3'33'322'}}^{\text{sim}} + \eta_{3;\mathbf{2'3'33'322'}}^{\text{sim}} - \eta_1^{\text{sim}} - \eta_{2';\mathbf{3}}^{\text{sim}} - \eta_{1';\mathbf{3'3}}^{\text{sim}} - \eta_{3;\mathbf{2'3'3}}^{\text{sim}} \\
&\quad - \eta_{1';\mathbf{22'3'3}}^{\text{sim}} - \eta_{3;\mathbf{2'22'3'3}}^{\text{sim}} - \eta_{1;\mathbf{22'22'3'3}}^{\text{sim}} - \eta_{2';\mathbf{322'22'3'3}}^{\text{sim}} \,.
\end{aligned}
$$

The overall readout noise contribution in the second generation TDI variable $X_1(t)$ can then be calculated in a tedious computation and reads as

$$
\begin{aligned}
\mathcal{R}[X_1(t)] &= N_{1'}^s - N_1^s + \tfrac{1}{2}N_1^\varepsilon - \tfrac{1}{2}N_{1'}^\varepsilon - N_{2';\mathbf{3}}^s + N_{2';\mathbf{3}}^\varepsilon - N_{2';\mathbf{3}}^\tau + N_{3;\mathbf{2'}}^s - N_{3;\mathbf{2'}}^\varepsilon \\
&\quad + N_{3;\mathbf{2'}}^\tau - N_{1';\mathbf{3'3}}^s + \tfrac{1}{2}N_{1;\mathbf{3'3}}^\varepsilon + \tfrac{1}{2}N_{1';\mathbf{3'3}}^\varepsilon - N_{1;\mathbf{3'3}}^\tau + N_{1;\mathbf{22'}}^s - \tfrac{1}{2}N_{1;\mathbf{22'}}^\varepsilon \\
&\quad - \tfrac{1}{2}N_{1';\mathbf{22'}}^\varepsilon + N_{1';\mathbf{22'}}^\tau - N_{3;\mathbf{2'3'3}}^s + N_{3;\mathbf{2'3'3}}^\varepsilon - N_{3;\mathbf{2'3'3}}^\tau + N_{2';\mathbf{322'}}^s \\
&\quad - N_{2';\mathbf{322'}}^\varepsilon + N_{2';\mathbf{322'}}^\tau - N_{1';\mathbf{22'3'3}}^s + N_{1';\mathbf{22'3'3}}^\varepsilon - N_{1';\mathbf{22'3'3}}^\tau + N_{1;\mathbf{3'322'}}^s \\
&\quad - N_{1;\mathbf{3'322'}}^\varepsilon + N_{1;\mathbf{3'322'}}^\tau - N_{3;\mathbf{2'22'3'3}}^s + N_{3;\mathbf{2'22'3'3}}^\varepsilon - N_{3;\mathbf{2'22'3'3}}^\tau \\
&\quad + N_{2';\mathbf{33'322'}}^s - N_{2';\mathbf{33'322'}}^\varepsilon + N_{2';\mathbf{33'322'}}^\tau - N_{1;\mathbf{22'22'3'3}}^s + \tfrac{1}{2}N_{1;\mathbf{22'22'3'3}}^\varepsilon \\
&\quad + \tfrac{1}{2}N_{1';\mathbf{22'22'3'3}}^\varepsilon - N_{1';\mathbf{22'22'3'3}}^\tau + N_{1';\mathbf{3'33'322'}}^s - \tfrac{1}{2}N_{1;\mathbf{3'33'322'}}^\varepsilon \\
&\quad - \tfrac{1}{2}N_{1';\mathbf{3'33'322'}}^\varepsilon + N_{1;\mathbf{3'33'322'}}^\tau - N_{2';\mathbf{322'22'3'3}}^s + N_{2';\mathbf{322'22'3'3}}^\varepsilon \\
&\quad - N_{2';\mathbf{322'22'3'3}}^\tau + N_{3;\mathbf{2'3'33'322'}}^s - N_{3;\mathbf{2'3'33'322'}}^\varepsilon + N_{3;\mathbf{2'3'33'322'}}^\tau \\
&\quad + \tfrac{1}{2}N_{1;\mathbf{3'322'22'3'3}}^\varepsilon - \tfrac{1}{2}N_{1;\mathbf{3'322'22'3'3}}^\tau - \tfrac{1}{2}N_{1';\mathbf{22'3'33'322'}}^\varepsilon \\
&\quad - \tfrac{1}{2}N_{1;\mathbf{22'3'33'322'}}^\tau + N_{1';\mathbf{22'3'33'322'}}^\tau \,.
\end{aligned}
$$

16 instances of readout noise from the science interferometers occur in X_1. If we assume each to be uncorrelated with a noise level of $10\,\frac{\text{pm}}{\sqrt{\text{Hz}}}$, they already add up to an equivalent displacement noise of $\sqrt{16 \cdot (10\,\frac{\text{pm}}{\sqrt{\text{Hz}}})^2} = 40\,\frac{\text{pm}}{\sqrt{\text{Hz}}}$. Since further noise sources will contribute to the overall level (e.g., residual laser frequency noise), it becomes clear that the 40 pm-requirement is not applicable for TDI 2.0. Further research effort is needed here in the future.

E.3 TDI-α_1 Output

In this section we will compute the output of the Sagnac combination α_1:

$$\alpha_1 \;=\; \eta_{1'} + \eta_{3';\mathbf{2'}} + \eta_{2';\mathbf{1'2'}} + \eta_{1;\mathbf{3'1'2'}} + \eta_{2;\mathbf{33'1'2'}} + \eta_{3;\mathbf{133'1'2'}}$$
$$-\eta_1 - \eta_{2;\mathbf{3}} - \eta_{3;\mathbf{13}} - \eta_{1';\mathbf{213}} - \eta_{3';\mathbf{2'213}} - \eta_{2';\mathbf{1'2'213}} \,,$$

again to first order in the LoS velocities.

The principle of the derivation is the same as previously for X_1. We insert $\eta_i(t)$,

$$\alpha_1 \sim \left(H_{1'} + p_{3;\mathbf{2'}} - p_1 - \tfrac{\mu_1 - \mu_{1'}}{2}\right) + \left(H_{3'} + p_{2;\mathbf{1'}} - p_3 - \tfrac{\mu_3 - \mu_{3'}}{2}\right)_{;\mathbf{2'}}$$
$$+\left(H_{2'} + p_{1;\mathbf{3'}} - p_2 - \tfrac{\mu_2 - \mu_{2'}}{2}\right)_{;\mathbf{1'2'}} + \left(H_1 + p_{2;\mathbf{3}} - p_1 + \tfrac{\mu_{2;3} - \mu_{2';3}}{2}\right)_{;\mathbf{3'1'2'}}$$
$$+\left(H_2 + p_{3;\mathbf{1}} - p_2 + \tfrac{\mu_{3;1} - \mu_{3';1}}{2}\right)_{;\mathbf{33'1'2'}} + \left(H_3 + p_{1;\mathbf{2}} - p_3 + \tfrac{\mu_{1;2} - \mu_{1';2}}{2}\right)_{;\mathbf{133'1'2'}}$$
$$-\left(H_1 + p_{2;\mathbf{3}} - p_1 + \tfrac{\mu_{2;3} - \mu_{2';3}}{2}\right) - \left(H_2 + p_{3;\mathbf{1}} - p_2 + \tfrac{\mu_{3;1} - \mu_{3';1}}{2}\right)_{;\mathbf{3}}$$
$$-\left(H_3 + p_{1;\mathbf{2}} - p_3 + \tfrac{\mu_{1;2} - \mu_{1';2}}{2}\right)_{;\mathbf{13}} - \left(H_{1'} + p_{3;\mathbf{2'}} - p_1 - \tfrac{\mu_1 - \mu_{1'}}{2}\right)_{;\mathbf{213}}$$
$$-\left(H_{3'} + p_{2;\mathbf{1'}} - p_3 - \tfrac{\mu_3 - \mu_{3'}}{2}\right)_{;\mathbf{2'213}} - \left(H_{2'} + p_{1;\mathbf{3'}} - p_2 - \tfrac{\mu_2 - \mu_{2'}}{2}\right)_{;\mathbf{1'2'213}} \,,$$

and time-shift it properly:

$$\alpha_1 \;\sim\; H_{1'} + p_{3;\mathbf{2'}} - p_1 - \tfrac{\mu_1 - \mu_{1'}}{2} + H_{3';\mathbf{2'}} + p_{2;\mathbf{1'2'}} - p_{3;\mathbf{2'}} - \tfrac{\mu_{3;\mathbf{2'}} - \mu_{3';\mathbf{2'}}}{2}$$
$$+H_{2';\mathbf{1'2'}} + p_{1;\mathbf{3'1'2'}} - p_{2;\mathbf{1'2'}} - \tfrac{\mu_{2;\mathbf{1'2'}} - \mu_{2';\mathbf{1'2'}}}{2} + H_{1;\mathbf{3'1'2'}} + p_{2;\mathbf{33'1'2'}}$$
$$-p_{1;\mathbf{3'1'2'}} + \tfrac{\mu_{2;\mathbf{33'1'2'}} - \mu_{2';\mathbf{33'1'2'}}}{2} + H_{2;\mathbf{33'1'2'}} + p_{3;\mathbf{133'1'2'}} - p_{2;\mathbf{33'1'2'}}$$
$$+\tfrac{\mu_{3;\mathbf{133'1'2'}} - \mu_{3';\mathbf{133'1'2'}}}{2} + H_{3;\mathbf{133'1'2'}} + p_{1;\mathbf{2133'1'2'}} - p_{3;\mathbf{133'1'2'}}$$
$$+\tfrac{\mu_{1;\mathbf{2133'1'2'}} - \mu_{1';\mathbf{2133'1'2'}}}{2} - H_1 - p_{2;\mathbf{3}} + p_1 - \tfrac{\mu_{2;3} - \mu_{2';3}}{2} - H_{2;\mathbf{3}} - p_{3;\mathbf{13}}$$
$$+p_{2;\mathbf{3}} - \tfrac{\mu_{3;\mathbf{13}} - \mu_{3';\mathbf{13}}}{2} - H_{3;\mathbf{13}} - p_{1;\mathbf{213}} + p_{3;\mathbf{13}} - \tfrac{\mu_{1;\mathbf{213}} - \mu_{1';\mathbf{213}}}{2}$$
$$-H_{1';\mathbf{213}} - p_{3;\mathbf{2'213}} + p_{1;\mathbf{213}} + \tfrac{\mu_{1;\mathbf{213}} - \mu_{1';\mathbf{213}}}{2} - H_{3';\mathbf{2'213}} - p_{2;\mathbf{1'2'213}}$$
$$+p_{3;\mathbf{2'213}} + \tfrac{\mu_{3;\mathbf{2'213}} - \mu_{3';\mathbf{2'213}}}{2} - H_{2';\mathbf{1'2'213}} - p_{1;\mathbf{3'1'2'213}} + p_{2;\mathbf{1'2'213}}$$
$$+\tfrac{\mu_{2;\mathbf{1'2'213}} - \mu_{2';\mathbf{1'2'213}}}{2} \,.$$

We sort the terms and the most laser phase noise terms vanish already except of two:

$$\alpha_1 \;\sim\; H_{1'} + H_{3';\mathbf{2'}} + H_{2';\mathbf{1'2'}} + H_{1;\mathbf{3'1'2'}} + H_{2;\mathbf{33'1'2'}} + H_{3;\mathbf{133'1'2'}} - H_1 - H_{2;\mathbf{3}}$$
$$-H_{3;\mathbf{13}} - H_{1';\mathbf{213}} - H_{3';\mathbf{2'213}} - H_{2';\mathbf{1'2'213}} + p_{1;\mathbf{2133'1'2'}} - p_{1;\mathbf{3'1'2'213}}$$
$$-\tfrac{\mu_1 - \mu_{1'}}{2} - \tfrac{\mu_{3;\mathbf{2'}} - \mu_{3';\mathbf{2'}}}{2} - \tfrac{\mu_{2;\mathbf{1'2'}} - \mu_{2';\mathbf{1'2'}}}{2} + \tfrac{\mu_{2;\mathbf{33'1'2'}} - \mu_{2';\mathbf{33'1'2'}}}{2}$$
$$+\tfrac{\mu_{3;\mathbf{133'1'2'}} - \mu_{3';\mathbf{133'1'2'}}}{2} + \tfrac{\mu_{1;\mathbf{2133'1'2'}} - \mu_{1';\mathbf{2133'1'2'}}}{2} - \tfrac{\mu_{2;3} - \mu_{2';3}}{2}$$
$$-\tfrac{\mu_{3;\mathbf{13}} - \mu_{3';\mathbf{13}}}{2} + \tfrac{\mu_{3;\mathbf{2'213}} - \mu_{3';\mathbf{2'213}}}{2} + \tfrac{\mu_{2;\mathbf{1'2'213}} - \mu_{2';\mathbf{1'2'213}}}{2}$$

Appendix E

The difference of the two laser phase noise instances is Taylor-expanded again:

$$
\begin{aligned}
&p_{1;\mathbf{2133'1'2'}} - p_{1;\mathbf{3'1'2'213}} \\
\simeq\ & p_{1,\mathbf{2133'1'2'}} + \frac{1}{c^2}\dot{p}_{1,\mathbf{2133'1'2'}}\left[\dot{L}_2(L_1 + L_3 + L_{3'} + L_{1'} + L_{2'})\right. \\
&+ \dot{L}_1(L_3 + L_{3'} + L_{1'} + L_{2'}) + \dot{L}_3(L_{3'} + L_{1'} + L_{2'}) + \dot{L}_{3'}(L_{1'} + L_{2'}) \\
&+ \left.\dot{L}_{1'}L_{2'}\right] - p_{1,\mathbf{3'1'2'213}} - \frac{1}{c^2}\dot{p}_{1,\mathbf{3'1'2'213}}\left[\dot{L}_{3'}(L_{1'} + L_{2'} + L_2 + L_1 + L_3)\right. \\
&+ \left.\dot{L}_{1'}(L_{2'} + L_2 + L_1 + L_3) + \dot{L}_{2'}(L_2 + L_1 + L_3) + \dot{L}_2(L_1 + L_3) + \dot{L}_1 L_3\right]
\end{aligned}
$$

and we could sort the indices and factorise:

$$
\begin{aligned}
&p_{1;\mathbf{2133'1'2'}} - p_{1;\mathbf{3'1'2'213}} \\
=\ & p_{1,\mathbf{1231'2'3'}} - p_{1,\mathbf{1231'2'3'}} + \frac{1}{c^2}\dot{p}_{1,\mathbf{1231'2'3'}}\left[(\dot{L}_2 L_1 - \dot{L}_2 L_1) + (\dot{L}_2 L_3 - \dot{L}_2 L_3)\right. \\
&+ \dot{L}_2(L_{3'} + L_{1'} + L_{2'}) + (\dot{L}_1 L_3 - \dot{L}_1 L_3) + \dot{L}_1(L_{3'} + L_{1'} + L_{2'}) \\
&+ \dot{L}_3(L_{3'} + L_{1'} + L_{2'}) + (\dot{L}_{3'} L_{1'} - \dot{L}_{3'} L_{1'}) + (\dot{L}_{3'} L_{2'} - \dot{L}_{3'} L_{2'}) \\
&+ (\dot{L}_{1'} L_{2'} - \dot{L}_{1'} L_{2'}) - \dot{L}_{3'}(L_2 + L_1 + L_3) - \dot{L}_{1'}(L_2 + L_1 + L_3) \\
&\left. - \dot{L}_{2'}(L_2 + L_1 + L_3)\right].
\end{aligned}
$$

Several parts vanish and we could factor $(L_1 + L_2 + L_3)$ and $(L_{1'} + L_{2'} + L_{3'})$ out, respectively. Thus, we end up with

$$
\begin{aligned}
p_{1;\mathbf{2133'1'2'}} - p_{1;\mathbf{3'1'2'213}}\ \simeq\ & \frac{1}{c^2}\dot{p}_1(t)_{,\mathbf{1231'2'3'}}\left((\dot{L}_{1'} + \dot{L}_{2'} + \dot{L}_{3'})(L_1 + L_2 + L_3)\right. \\
& \left. - (\dot{L}_1 + \dot{L}_2 + \dot{L}_3)(L_{1'} + L_{2'} + L_{3'})\right) \neq 0.
\end{aligned}
$$

which was stated before in Sec. 3.3. The α_1-output is then finally given by

$$
\begin{aligned}
\alpha_1\ \sim\ & H_{1'} + H_{3';\mathbf{2'}} + H_{2';\mathbf{1'2'}} + H_{1;\mathbf{3'1'2'}} + H_{2;\mathbf{33'1'2'}} + H_{3;\mathbf{133'1'2'}} - H_1 - H_{2;\mathbf{3}} \\
& - H_{3;\mathbf{13}} - H_{1';\mathbf{213}} - H_{3';\mathbf{2'213}} - H_{2';\mathbf{1'2'213}} + p_{1;\mathbf{2133'1'2'}} - p_{1;\mathbf{3'1'2'213}} \\
& - \frac{\mu_1 - \mu_{1'}}{2} - \frac{\mu_{3;\mathbf{2'}} - \mu_{3';\mathbf{2'}}}{2} - \frac{\mu_{2;\mathbf{1'2'}} - \mu_{2';\mathbf{1'2'}}}{2} + \frac{\mu_{2;\mathbf{33'1'2'}} - \mu_{2';\mathbf{33'1'2'}}}{2} \\
& + \frac{\mu_{3;\mathbf{133'1'2'}} - \mu_{3';\mathbf{133'1'2'}}}{2} + \frac{\mu_{1;\mathbf{2133'1'2'}} - \mu_{1';\mathbf{2133'1'2'}}}{2} - \frac{\mu_{2;\mathbf{3}} - \mu_{2';\mathbf{3}}}{2} \\
& - \frac{\mu_{3;\mathbf{13}} - \mu_{3';\mathbf{13}}}{2} + \frac{\mu_{3;\mathbf{2'213}} - \mu_{3';\mathbf{2'213}}}{2} + \frac{\mu_{2;\mathbf{1'2'213}} - \mu_{2';\mathbf{1'2'213}}}{2} \\
\simeq\ & H_{1'} + H_{3';\mathbf{2'}} + H_{2';\mathbf{1'2'}} + H_{1;\mathbf{3'1'2'}} + H_{2;\mathbf{33'1'2'}} + H_{3;\mathbf{133'1'2'}} - H_1 - H_{2;\mathbf{3}} \\
& - H_{3;\mathbf{13}} - H_{1';\mathbf{213}} - H_{3';\mathbf{2'213}} - H_{2';\mathbf{1'2'213}} + \frac{1}{c^2}\dot{p}_1(t)_{,\mathbf{1231'2'3'}} \cdot \\
& \left((\dot{L}_{1'} + \dot{L}_{2'} + \dot{L}_{3'})(L_1 + L_2 + L_3) - (\dot{L}_1 + \dot{L}_2 + \dot{L}_3)(L_{1'} + L_{2'} + L_{3'})\right) \\
& - \frac{\mu_1 - \mu_{1'}}{2} - \frac{\mu_{3;\mathbf{2'}} - \mu_{3';\mathbf{2'}}}{2} - \frac{\mu_{2;\mathbf{1'2'}} - \mu_{2';\mathbf{1'2'}}}{2} + \frac{\mu_{2;\mathbf{33'1'2'}} - \mu_{2';\mathbf{33'1'2'}}}{2} \\
& + \frac{\mu_{3;\mathbf{133'1'2'}} - \mu_{3';\mathbf{133'1'2'}}}{2} + \frac{\mu_{1;\mathbf{2133'1'2'}} - \mu_{1';\mathbf{2133'1'2'}}}{2} - \frac{\mu_{2;\mathbf{3}} - \mu_{2';\mathbf{3}}}{2} \\
& - \frac{\mu_{3;\mathbf{13}} - \mu_{3';\mathbf{13}}}{2} + \frac{\mu_{3;\mathbf{2'213}} - \mu_{3';\mathbf{2'213}}}{2} + \frac{\mu_{2;\mathbf{1'2'213}} - \mu_{2';\mathbf{1'2'213}}}{2}.
\end{aligned}
$$

Bibliography

[AAA+11] T. Accadia, F. Acernese, F. Antonucci, P. Astone, G. Ballardin, F. Barone, M. Barsuglia, A. Basti, T. S. Bauer, and M. Bebronne et al. Status of the Virgo project. *Classical Quantum Gravity*, 28(11):114002, 2011.

[AAB+08] O. D. Aguiar, L. A. Andrade, J. J. Barroso, P. J. Castro, C. A. Costa, S. T. de Souza, A. de Waard, A. C. Fauth, C. Frajuca, G. Frossati, S. R. Furtado, X. Gratens, T. M. A. Maffei, and J. Weber. The Schenberg spherical gravitational wave detector: the first commissioning runs. *Classical Quantum Gravity*, 25:114042, 2008.

[ABB+09] M. Armano, M. Benedetti, J. Bogenstahl, D. Bortoluzzi, P. Bosetti, N. Brandt, A. Cavalleri, G. Ciani, I. Christofolini, A. M. Cruise, and K. Danzmann et al. LISA pathfinder: the experiment and the route to LISA. *Classical Quantum Gravity*, 26:094001, 2009.

[ABF+03] R. Ackermann, Y. Benzaim, G. Frossati, L. Gottardi, A. Karbalai-Sadegh, W. Reincke, A. Shumack, O. Usenko, A. de Waard, J. Flokstra, M. Podt, M. Bassan, E. Coccia, V. Fafone, Y. Minenkov, A. Moleti, G.V. Pallottino, A. Rocchi, and M. Visco, editors. *Present Status of MiniGRAIL*. Proceedings of the 10th Marcel Grossmann Meeting on General Relativity, 2003.

[AET99] J. W. Armstrong, F. B. Estabrook, and M. Tinto. Time-Delay Interferometry for space-based gravitational wave searches. *Astrophys. Journal*, 527:814 – 826, 1999.

[AET03] J. W. Armstrong, F. B. Estabrook, and M. Tinto. Time delay interferometry. *Classical Quantum Gravity*, 20:283 – 289, 2003.

[Ait32] A. C. Aitken. On interpolation by iteration of proportional parts, without the use of differences. *Proceedings of the Edinburgh Mathematical Society*, 3:56 – 76, 1932.

[Arm06] J. W. Armstrong. Low-frequency gravitational wave searches using spacecraft Doppler tracking. *Living Review Relativity*, 9, 2006.

[Bar15] S. Barke. *Inter-spacecraft frequency distributions for future gravitational wave observatories*. PhD thesis, QUEST-Leibniz-Forschungsschule der Leibniz Universität Hannover, 2015.

[BBB+10] S. Babak, J. G. Baker, M. J. Benacquista, N. J. Cornish, S. L. Larson, I. Mandel, S. T. McWilliams, A. Petiteau, E. K. Porter, E. L. Robinson, and M. Vallisneri et al. The mock LISA data challenges: from challenge 3 to challenge 4. *Classical Quantum Gravity*, 27:084009, 2010.

[BBB+14] S. Barke, N. Brause, I. Bykov, J. J. Esteban Delgado, A. Enggaard, O. Gerberding, G. Heinzel, J. Kullmann, S. M. Pedersen, and T. Rasmussen. LISA metrology system - final report. Technical report, DTU Space / AEI Hannover / Axcon ApS, 2014.

[BDF+11] M. Bonnar, N. Dunbar, E. Fitzsimons, P. Gath, G. Hummel, S. Kemble, K. Lau, S. Nikolov, M. Perreur-Lloyd, N. Saks, M. Stewart, C. Trenkel, P. Weimer, and D. Weise. Mission design description. Technical report, Astrium Deutschland, 2011.

[Bla00] E. D. Black. An introduction to Pound-Drever-Hall laser frequency stabilization. *American Journal of Physics*, 69(79), 2000.

[BMR+79] H. Billing, K. Maischberger, A. Rüdiger, R. Schilling, L. Schnupp, and W. Winkler. An argon laser interferometer for the detection of gravitational radiation. *J. Phys. E: Sci . Instrum.*, 12:1043, 1979.

[BTS+10] S. Barke, M. Tröbs, B. Sheard, G. Heinzel, and K. Danzmann. EOM sideband phase characteristics for the spaceborne gravitational wave detector LISA. *Applied Physics B: Lasers and Optics*, 98, 2010.

[Buc70] B. Buchberger. Ein algorithmisches Kriterium für die Lösbarkeit eines algebraischen Gleichungssystems. *Aequationes mathematicae*, 4:374 – 383, 1970.

[BWD+15] S. Barke, Y. Wang, J. J. Esteban Delgado, M. Tröbs, G. Heinzel, and K. Danzmann. Towards a gravitational wave observatory designer: sensitivity limits of spaceborne detectors. *Classical Quantum Gravity*, 32:095004, 2015.

[Cav97] C. M. Caves. Quantum nondemolition measurements. *Advanced Series in Applied Physics: Foundations of Quantum Mechanics in the Light of New Technology*, 4:94 – 104, 1997.

[CBSV+14] C. Cutler, S. Burke-Spolaor, M. Vallisneri, J. Lazio, and W. Majid. The gravitational-wave discovery space of Pulsar Timing Arrays. *Physical Review D: Particles and Fields*, 89(042003), 2014.

[CC05] J. Crowder and N. J. Cornish. Beyond LISA: Exploring future gravitational wave missions. *Physical Review D: Particles and Fields*, 72:083005, 2005.

[Cer09] F. G. Cervantes. *Gravitational Wave Observation from Space: Optical Measurement Techniques for LISA and LISA Pathfinder*. PhD thesis, Leibniz Universität Hannover, 2009.

[CH03] N. J. Cornish and R. W. Hellings. The effects of orbital motion on LISA time delay interferometry. *Classical Quantum Gravity*, 20:4581, 2003.

[CH06] C. Cutler and J. Harms. Big Bang Observer and the neutron-star-binary subtraction problem. *Physical Review D: Particles and Fields*, 73:042001, 2006.

[CK06] Y. Chen and S. Kawamura. Displacement- and timing-noise-free gravitational-wave detection. *Physical Review Letters*, 96:231102, 2006.

[Col14] The Planck Collaboration. The angular power spectrum of polarized dust emission at intermediate and high Galactic latitudes, arxiv:1409.5738 [astro-ph.co]. 2014.

[Cor09] N. J. Cornish. Alternative derivation of the response of interferometric gravitational wave detectors. *Physical Review D: Particles and Fields*, 80:087101, 2009.

[CPS06] Y. Chen, A. Pai, and K. Somiya. Interferometers for displacement-noise-free gravitational-wave detection. *Physical Review Letters*, 97:151103, 2006.

[CR03] N. J. Cornish and L. J. Rubbo. LISA response functions. *Physical Review D: Particles and Fields*, 67:022001, 2003.

[CRVP05] B. Chauvineau, T. Regimbau, J. Y. Vinet, and S. Pireaux. Relativistic analysis of the LISA long range optical links. *Physical Review D: Particles and Fields*, 72:122003, 2005.

[Deh12] M. Dehne. *Construction and noise behaviour of ultra-stable optical systems for space interferometers*. PhD thesis, Leibniz Universität Hannover, 2012.

[DHK+83] R. W. P. Drever, J. L. Hall, F. V. Kowalski, J. Hough, G. M. Ford, A. J. Munley, and H. Ward. Laser phase and frequency stabilization using an optical resonator. *Applied Physics B: Lasers and Optics*, 31:97–105, 1983.

[DNV02] S. V. Dhurandhar, K. R. Nayak, and J. Y. Vinet. Algebraic approach to time-delay data analysis for LISA. *Physical Review D: Particles and Fields*, 65:102002, 2002.

[DVN08] S. V. Dhurandhar, J. Y. Vinet, and K. R. Nayak. General relativistic treatment of LISA optical links. *Classical Quantum Gravity*, 25:245002, 2008.

[dVWM+10] G. de Vine, B. Ware, K. McKenzie, R. E. Spero, W. M. Klipstein, and D. A. Shaddock. Experimental demonstration of time-delay interferometry for the Laser Interferometer Space Antenna. *Physical Review Letters*, 104:211103, 2010.

[ea04] E. S. Phinney et al. The Big Bang Observer: Direct detection of gravitational waves from the North of the universe to the present. NASA Mission Concept Study, 2004.

[Edl14] D. Edler. Measurement and modelling of USO clock noise in space based applications. Master's thesis, Leibniz Universität Hannover, 2014.

[EGMB+09] J. J. Esteban, A. F. Garcia-Marin, I. Bykov, G. Heinzel, and K. Danzmann. Free-space laser ranging and data communication. *IEEE Conference Proceedings*, pages 275 – 281, 2009.

[EGMB+11] J. J. Esteban, A. F. Garcia-Marin, S. Barke, A. M. Peinado, F. G. Cervantes, I. Bykov, G. Heinzel, and K. Danzmann. Experimental demonstration of weak-light laser ranging and data communication for LISA. *Optics Express*, 19:15937 – 15946, 2011.

[Ein] http://www.einstein-online.info/vertiefung/gw_wellen.

[Ein16] A. Einstein. Die Grundlage der Allgemeinen Relativitätstheorie. *Annalen der Physik*, 354(7):769 – 822, 1916.

[Ein17] A. Einstein. Kosmologische Betrachtungen zur Allgemeinen Relativitätstheorie. *Sitzungsberichte der Königlich Preußischen Akademie der Wissenschaften (Berlin)*, pages 142 – 152, 1917.

[Ein18] A. Einstein. Über Gravitationswellen. *Sitzungsberichte der Königlich Preußischen Akademie der Wissenschaften (Berlin)*, pages 154 – 167, 1918.

[EN09] ESA and NASA. Laser Interferometer Space Antenna (LISA): Measurement requirements flowdown guide. 2009.

[ER37] A. Einstein and N. Rosen. On gravitational waves. *Journal of the Franklin Institute*, 223:43–54, 1937.

[ESA00] ESA. Laser Interferometer Space Antenna: A cornerstone mission for the observation of gravitational waves system and technology study report. Internal ESA Report ESA-SCI(2000)11, ESA, 2000.

[ESA11] ESA. LISA yellow book - assessment study report. 2011.

[Est12] J. J. Esteban. *Laser ranging and data communication for the Laser Interferometer Space Antenna*. PhD thesis, Leibniz Universität Hannover, 2012.

[ETA00] F. B. Estabrook, M. Tinto, and J. W. Armstrong. Time-delay analysis of LISA gravitational wave data: Elimination of spacecraft motion effects. *Physical Review D: Particles and Fields*, 62:042002, 2000.

[EW75] F. B. Estabrook and H. D. Wahlquist. Response of Doppler spacecraft tracking to gravitational radiation. *General Relativity and Gravitation*, 6(5):439–447, 1975.

[Fin09] L. S. Finn. The response of the interferometric gravitational wave detectors. *Physical Review D: Particles and Fields*, 79:022002, 2009.

[Fle12] R. Fleddermann. *Interferometry for a space-based gravitational wave observatory - Reciprocity of an optical fiber*. PhD thesis, Leibniz Universität Hannover, 2012.

[FS10] A. Freise and K. Strain. Interferometer techniques for gravitational-wave detection. *Living Review Relativity*, 13(1), 2010.

[FST+04] W. Folkner, D. A. Shaddock, M. Tinto, R. E. Spero, R. Schilling, and O. Jennrich. Candidate LISA frequency (modulation) plan. In *LISA Symposium 5*, 2004.

[FST+09] R. Fleddermann, F. Steier, M. Tröbs, J. Bogenstahl, C. Killow, G. Heinzel, and K. Danzmann. Measurement of the non-reciprocal phase noise of a polarization maintaining single-mode optical fiber. *Journal Physics: Conference Series*, 154:012022, 2009.

[ftec13] K. Danzmann for the eLISA consortium. The gravitational universe. 2013.

[ftLSC10a] G. M. Harry for the LIGO Scientific Collaboration. Advanced LIGO: the next generation of gravitational wave detectors. *Classical Quantum Gravity*, 27:084006, 2010.

[ftLSC10b] H. Grote for the LIGO Scientific Collaboration. The GEO 600 status. *Classical Quantum Gravity*, 27(8):084003, 2010.

[Ger14] O. Gerberding. *Phase readout for satellite interferometry*. PhD thesis, Leibniz Universität Hannover, 2014.

[GHTF96] G. Giampieri, R. W. Hellings, M. Tinto, and J. E. Faller. Algorithms for unequal-arm Michelson interferometers. *Optics Communications*, 123:669–678, 1996.

[GKSftLSC11] H. Grote, A. Khalaidovski, R. Schnabel, and H. Vahlbruch for the LIGO Scientific Collaboration. A gravitational wave observatory operating beyond the quantum shot-noise limit. *Nature Physics*, 7:962–965, 2011.

[GTV⁺13] C. Gräf, A. Thüring, H. Vahlbruch, K. Danzmann, and R. Schnabel. Length sensing and control of a Michelson interferometer with Power Recycling and Twin Signal Recycling cavities. *Optics Express*, 21(5):5287–5299, 2013.

[Gut81] A. H. Guth. Inflationary universe: A possible solution to the horizon and flatness problem. *Physical Review D: Particles and Fields*, 23(2):347–356, 1981.

[HEB⁺11] G. Heinzel, J. J. Esteban, S. Barke, M. Otto, Y. Wang, and K. Danzmann. Auxiliary functions of the LISA laser link: ranging, clock noise transfer and data communication. *Classical Quantum Gravity*, 28:094008, 2011.

[Hei95] G. Heinzel. Resonant sideband extraction - neuartige Interferometrie für Gravitationswellendetektoren. Universität Hannover und Max-Planck-Institut für Quantenoptik Garching, 1995.

[Hei08] G. Heinzel. Generation of random time series with prescribed spectra. Technical Report S2-AEI-TN-3034, Albert-Einstein-Institut Hannover, 2008.

[Hel01] R. W. Hellings. Elimination of clock jitter noise in spaceborne laser interferometers. *Physical Review D: Particles and Fields*, 64:022002, 2001.

[Hen13] J.-S. Hennig. Mitigation of straylight effects in the LISA back-link. Master's thesis, Leibniz Universität Hannover, 2013.

[HGGT⁺96] R. W. Hellings, L. Maleki G. Giampieri, M. Tinto, K. Danzmann, J. Hough, and D. Robertson. Heterodyne laser tracking at high Doppler rates. *Optics Communications*, 124:313–320, 1996.

[HMOP08] J. Harms, C. Mahrdt, M. Otto, and M. Prieß. Subtraction-noise projection in gravitational-wave detector networks. *Physical Review D: Particles and Fields*, 77:123010, 2008.

[HRS02] G. Heinzel, A. Rüdiger, and R. Schilling. Spectrum and spectral density estimation by discrete Fourier transform (DFT), including a comprehensive list of window functions and some new flat-top windows. *Max Planck Society eDoc Server*, 2002.

[HT98] S. A. Hughes and K. S. Thorne. Seismic gravity-gradient noise in interferometric gravitational-wave detectors. *Physical Review D: Particles and Fields*, 58:122002, 1998.

[IAA⁺15] H. Inchauspé, M. Armano, H. Audley, G. Auger, J. Baird, P. Binetruy, M. Born, D. Bortoluzzi, N. Brandt, A. Bursi, and M. Caleni et al. A noise simulator for eLISA: Migrating LISA Pathfinder knowledge to the eLISA mission. *Journal of Physics: Conference Series*, 610:012036, 2015.

[Inc15] H. Inchauspé. *From LISA Pathfinder to eLISA: building of a dynamics simulator for the eLISA space mission.* PhD thesis, Francois Arago Centre - APC, 2015.

[Jen09] O. Jennrich. LISA technology and instrumentation. *Classical Quantum Gravity*, 26:153001, 2009.

[KAN⁺08] S. Kawamura, M. Ando, T. Nakamura, K. Tsubono, T. Tanaka, I. Funaki, N. Seto, K. Numata, S. Sato, and K. Ioka et al. The Japanese space gravitational wave antenna - DECIGO. *Journal Physics: Conference Series*, 122:012006, 2008.

[KC04] S. Kawamura and Y. Chen. Displacement-noise-free gravitational-wave detection. *Physical Review Letters*, 93:211103, 2004.

[KJLS09] F. Kefelian, H. Jiang, P. Lemonde, and G. Santarelli. Ultralow-frequency-noise stabilization of a laser by locking to an optical fiber-delay line. *Optics Letters*, 34(7):914 – 916, 2009.

[Kur10] K. Kuroda. Status of LCGT. *Classical Quantum Gravity*, 27(8):084004, 2010.

[LHH00] S. L. Larson, W. A. Hiscock, and R. W. Hellings. Sensitivity curves for spaceborne gravitational wave interferometers. *Physical Review D: Particles and Fields*, 62:062001, 2000.

[Lin82] A. D. Linde. A new inflationary universe scenario: a possible solution of the horizon, flatness, homogeneity, isotropy and primordial monopole problems. *Physics Letters B*, 108B(6):389–393, 1982.

[MAA⁺13] P. McNamara, F. Antonucci, M. Armano, H. Audley, G. Auger, M. Benedetti, P. Binetruy, J. Bogenstahl, D. Bortoluzzi, and N. Brandt et al. The LISA pathfinder mission. In G. Auger, P. Binetruy, and E. Plagnol, editors, *9th LISA Symposium (Paris), ASP Conference Series*, volume 467, 2013.

[Mag08] M. Maggiore. *Gravitational waves - Vol. 1: Theory and Experiments.* Oxford University Press, 2008.

[MG11] O. Montenbruck and E. Gill. *Satellite Orbits: Models, Methods and Applications.* Springer-Verlag Berlin/Heidelberg, 2011.

[MMS12] S. J. Mitryk, G. Müller, and J. Sanjuan. Hardware-based demonstration of time-delay interferometry and TDI-ranging with spacecraft motion effects. *Physical Review D: Particles and Fields*, 86:122006, 2012.

[MTW73] C. Misner, K. Thorne, and J. A. Wheeler. *Gravitation.* 1973.

[MWM10] S. J. Mitryk, V. Wand, and G. Müller. Verification of time-delay interferometry techniques using the University of Florida LISA interferometry simulator. *Classical Quantum Gravity*, 27:084012, 2010.

[NAS] NASA. http://ssd.jpl.nasa.gov/?ephemerides.

[NAS04] NASA. Laser Interferometer Space Antenna (LISA) - technology development plan. Technical report, National Aeronautics and Space Administration, 2004.

[New87] Sir I. Newton. *Philosophiae Naturalis Principia Mathematica*. apud Sa. Smith, London, 1687.

[NKDV05] K. R. Nayak, S. Koshti, S. V. Dhurandhar, and J. Y. Vinet. Reducing the flexing of the arms of LISA. *General Relativity and Quantum Cosmology*, 2005.

[NV04] K. R. Nayak and J. Y. Vinet. Algebraic approach to time-delay data analysis for orbiting LISA. *Physical Review D: Particles and Fields*, 70:102003, 2004.

[NV05] K. R. Nayak and J. Y. Vinet. Algebraic approach to time-delay data analysis: orbiting case. *Classical Quantum Gravity*, 22:437–443, 2005.

[OHD12] M. Otto, G. Heinzel, and K. Danzmann. TDI and clock noise removal for the split interferometry configuration of LISA. *Classical Quantum Gravity*, 29:205003, 2012.

[Ott08] M. Otto. Simulation und Messung des stochastischen Hintergrundes in einem TDI-Netzwerk. Diplomarbeit, Leibniz Universität Hannover, 2008.

[Ott11] M. Otto. *Rechenmethoden für Studierende der Physik im ersten Jahr*. Spektrum Akademischer Verlag Heidelberg/Berlin, 2011.

[Pac14] S. Paczkowski. Modelling the S/C and TM motion for LISA. Master's thesis, Leibniz Universität Hannover, 2014.

[PAH+08] A. Petiteau, G. Auger, H. Halloin, O. Jeannin, E. Plagnol, S. Pireaux, T. Regimbau, and J. Y. Vinet. LISACode: A scientific simulator of LISA. *Physical Review D: Particles and Fields*, 77:023002, 2008.

[PR10] J. A. C. M. Pijnenburg and N. Rijnveld. Picometer stable scan mechanism for gravitational wave detection in space: LISA PAAM. In *Proceedings of the International Conference on Space Optics*, 2010.

[PTLA02] T. A. Prince, M. Tinto, S. L. Larson, and J. W. Armstrong. LISA optimal sensitivity. *Physical Review D: Particles and Fields*, 66:122002, 2002.

[RCP04] L. J. Rubbo, N. J. Cornish, and O. Poujade. Forward modeling of space-borne gravitational wave detectors. *Physical Review D: Particles and Fields*, 69:082003, 2004.

[RHT08] A. Rüdiger, G. Heinzel, and M. Tröbs. LISA, the Laser Interferometer Space Antenna, requires the ultimate in lasers, clocks and drag-free control. In Hansjörg Dittus, Claus Lämmerzahl, and Slava Turyshev, editors, *Lasers, Clocks and Drag-Free Control*, volume 349 of *Astrophysics and Space Science Library*. Springer-Verlag Berlin/Heidelberg, 2008.

[Sau94] P. R. Saulson. *Fundamentals of Interferometric Gravitational Wave Detectors*. World Scientific Publishing, River Edge, 1994.

[SC09] LIGO Scientific Collaboration. LIGO: The laser interferometer gravitational-wave observatory. *Reports on Progress in Physics*, 72(7):076901, 2009.

[Sch09] B. F. Schutz. *A First Course in General Relativity*. Cambridge University Press, New York, 2009.

[Sch13] A. Schreiber. Time-delay interferometry simulations for space-based gravitational wave detectors. Master's thesis, Leibniz Universität Hannover, 2013.

[SCVC16] LIGO Scientific Collaboration and Virgo Collaboration. Observation of gravitational waves from a binary black hole merger. *Physical Review Letters*, 116:061102, 2016.

[SGMS03] B. Sheard, M. B. Gray, D. E. McClelland, and D. A. Shaddock. Laser frequency stabilization by locking to a LISA arm. *Physical Letters A*, 320(1):9 – 21, 2003.

[Sha49] C. E. Shannon. Communication in the presence of noise. *Proc. IRE*, 37(1), 1949.

[Sha64] I. I. Shapiro. Fourth test of general relativity. *Physical Review Letters*, 13:789, 1964.

[Sha04] D. A. Shaddock. Operating LISA as a Sagnac interferometer. *Physical Review D: Particles and Fields*, 69:022001, 2004.

[SLL12] B. R. Scanlon, L. Longuevergne, and D. Long. Ground referencing GRACE satellite estimates of groundwater storage changes in the California Central Valley, USA. *Water Resources Research*, 48(W04520), 2012.

[spa] http://spacegravity.org.

[SS09] B. S. Sathyaprakash and B. F. Schutz. Physics, astrophysics and cosmology with gravitational waves. *Living Review Relativity*, 2009.

[SSM+12] D. Schütze, G. Stede, V. Müller, O. Gerberding, C. Mahrdt, B. S. Sheard, G. Heinzel, and K. Danzmann. LISA-like laser ranging for GRACE Follow-On. In G. Auger, P. Binetruy, and E. Plagnol, editors, *9th LISA Symposium, ASP Conference Series*, volume 467 of *ASP Conference Series*, pages 285–289, 2012.

[STEA03] D. A. Shaddock, M. Tinto, F. B. Estabrook, and J. W. Armstrong. Data combinations accounting for LISA spacecraft motion. *Physical Review D: Particles and Fields*, 68:061303(R), 2003.

[Sut14] A. Sutton. TDI ranging for the GRACE-FO laser ranging interferometer. In *LISA Symposium X*, 2014.

[SWSV04] D. A. Shaddock, B. Ware, R. E. Spero, and M. Vallisneri. Post-processed time-delay interferometry for LISA. *Physical Review D: Particles and Fields*, 70:081101, 2004.

[TA99] M. Tinto and J. W. Armstrong. Cancellation of laser noise in an unequal-arm interferometer detector of gravitational radiation. *Physical Review D: Particles and Fields*, 59:102003, 1999.

[TBWR04] B. D. Tapley, S. Bettadpur, M. Watkins, and C. Reigber. The Gravity Recovery and Climate Experiment: Mission overview and early results. *Geophysical Research Letters*, 31(9), 2004.

[TD14] M. Tinto and S. V. Dhurandhar. Time-delay interferometry. *Living Reviews in Relativity*, 17(6), 2014.

[TDB+12] M. Tröbs, L. D'Arcio, S. Barke, J. Bogenstahl, and I. Bykov et al. Testing the LISA optical bench. *9th LISA Symposium*, 2012.

[Tea98] The LISA Study Team. *Laser Interferometer Space Antenna for the Detection and Observation of Gravitational Waves: Pre-Phase A Report*. Max Planck Institute for Quantum Optics, 1998.

[TEA02] M. Tinto, F. B. Estabrook, and J. W. Armstrong. Time-delay interferometry for LISA. *Physical Review D: Particles and Fields*, 65:082003, 2002.

[TEA04] M. Tinto, F. B. Estabrook, and J. W. Armstrong. Time delay interferometry with moving spacecraft arrays. *Physical Review D: Particles and Fields*, 69:082001, 2004.

[Tea11a] The E.T. Science Team. Einstein gravitational wave Telescope conceptual design study. Technical report, 2011.

[Tea11b] The LISA Study Team. LISA - unveiling a hidden universe: Assessment study report. *Max Planck Institute for Gravitational Physics*, 2011.

[TFM79] J. H. Taylor, L. A. Fowler, and P. M. McCulloch. Measurement of general relativistic effects in the binary pulsar PSR1913+16. *Nature*, 277(437), 1979.

[Tho11] J. I. Thorpe. LISA long-arm interferometry. *Classical Quantum Gravity*, 27:084008, 2011.

[Tin08a] M. Tinto. Frequency and timing requirements for the LISA missions. In *Frequency Control Symposium, IEEE International*, 2008.

[Tin08b] M. Tinto. Unequal-arm interferometry and ranging in space. In Hansjörg Dittus, Claus Lämmerzahl, and Slava Turyshev, editors, *Lasers, Clocks, and Drag-Free Control*, volume 349 of *Astrophysics and Space Science Library*. Springer-Verlag Berlin/Heidelberg, 2008.

[TML11] J. I. Thorpe, P. Maghami, and J. Livas. Time domain simulations of arm locking in LISA. *Physical Review D: Particles and Fields*, 83:122002, 2011.

[TSSA03] M. Tinto, D. A. Shaddock, J. Sylvestre, and J. W. Armstrong. Implementation of time-delay interferometry for LISA. *Physical Review D: Particles and Fields*, 67, 2003.

[TVA05] M. Tinto, M. Vallisneri, and J. W. Armstrong. Time-delay interferometric ranging for space-borne gravitational wave detectors. *Physical Review D: Particles and Fields*, 71:041101(R), 2005.

[Val05] M. Vallisneri. Synthetic LISA: Simulating time delay interferometry in a model LISA. *Physical Review D: Particles and Fields*, 71:022001, 2005.

[VCT08] M. Vallisneri, J. Crowder, and M. Tinto. Sensitivity and parameter-estimation precision for alternate LISA configurations. *Classical Quantum Gravity*, 25:065005, 2008.

[VSvdB14] I. Velicogna, T. C. Sutterley, and M. R. van den Broeke. Regional acceleration in ice mass loss from Greenland and Antartica using GRACE time-variable gravity data. *Geophysical Research Letters*, 41(22):8130–8137, 2014.

[Wan10] G. Wanner. *Complex optical systems in space: numerical modelling of the heterodyne interferometry of LISA Pathfinder and LISA*. PhD thesis, Leibniz Universität Hannover, 2010.

[Wan14] Y. Wang. *On inter-satellite laser ranging, clock synchronization and gravitational wave data analysis*. PhD thesis, QUEST-Leibniz-Forschungsschule der Leibniz Universität Hannover, 2014.

[WBC+14] B. Wouters, J. A. Bonin, D. P. Chambers, R. E. M. Riva, I. Sasgen, and J. Wahr. GRACE, time-varying gravity, Earth system dynamics and climate change. *Reports on Progress in Physics*, 77:116801, 2014.

[Web67] J. Weber. Gravitational radiation. *Physical Review Letters*, 18:498–501, 1967.

[WHK+12] G. Wanner, G. Heinzel, E. Kochkina, C. Mahrdt, B. S. Sheard, S. Schuster, and K. Danzmann. Methods for simulating the readout of lengths and angles in laser interferometers with Gaussian beams. *Optics Communications*, 285(24):4831–4839, 2012.

[Wil85] C. M. Will. *Theory and Experiment in Gravitational Physics*. Cambridge University Press, 1985.

[WKB+13] Y. Wang, D. Keitel, S. Babak, A. Petiteau, M. Otto, S. Barke, F. Kawazoe, A. Khalaidovski, V. Müller, D. Schütze, H. Wittel, K. Danzmann, and B. F. Schutz. Octahedron configuration for a displacement noise-cancelling gravitational wave detector in space. *Physical Review D: Particles and Fields*, 88:104021, 2013.

[YMM14] Y. Yu, S. Mitryk, and G. Müller. Arm-locking for space-based laser interferometry gravitational wave observatories. *Physical Review D: Particles and Fields*, 90:062005, 2014.

[ZD76] L. A. Zadeh and C. A. Desoer, editors. *Linear System Theory - The State Space Approach*. McGraw-Hill Book Company, Inc., 1976.

Software Tools

- **MATLAB**, version 2013(a) (Mathworks)

- **LTPDA Toolbox**, version 2.7

- **Mathematica**, version 8 (Wolfram)

- **MikTex**, version 2.9 (open source)

- **TexStudio**, version 2.3 (open source)

- **Adobe Illustrator CS 5**, version 15.0.2 (Adobe)

- **Photoshop**, version 12.0.4 (Adobe)

- **Component Library**, version 3 (Alexander Franzen)

- **Inkscape**, version 0.48 (open source)

- **Pdf Creator**, version 1.7.3 (open source)

- **Gravitational Wave Observatory Designer** (http://spacegravity.org)

- And last but not least: **Winamp**, version 5.623 (Nullsoft)

Curriculum Vitae

Markus Otto
Odeonstraße 19
30159 Hannover
`markus.otto@gmx.de`

Born on May 19, 1982
in Hildesheim

Work Experience

10/2008 – today	Research Associate (PhD candidate) and Lecture Assistant, Max Planck Institute for Gravitational Physics (Albert Einstein Institute) and Institute for Gravitational Physics, Leibniz Universität Hannover
03/2013 – today	Assistant Lecturer, University for Applied Sciences Hannover, Faculty of Mechanical Engineering and Bioprocess Engineering
12/2004 – 04/2008	Student Research Assistant, Institute for Applied Mathematics and Institute for Theoretical Physics, Leibniz Universität Hannover
2003 – 2014	Instructor, annual beginner's mathematical courses (uni:fit), Leibniz Universität Hannover
08/2001 – 05/2002	Community Service, Kreiskrankenhaus Diekholzen

Academic Career

05/2007 – 04/2008	Diploma Thesis, Max Planck Institute for Gravitational Physics (Albert Einstein Institute) and Institute for Gravitational Physics, Leibniz Universität Hannover
04/2004 – 07/2008	Studies of Physics, Leibniz Universität Hannover, degree: Diploma
10/2002 – 07/2008	Studies of Master of Education for Mathematics and Physics, Leibniz Universität Hannover, no degree
06/2001	Abitur, secondary school education at Scharnhorstgymnasium Hildesheim

Further Qualifications

11/2013 – 10/2015	PhD representative (deputy) at the Max Planck Institute for Gravitational Physics in Hannover, PhDnet membership of the Max Planck Society
10/2011 – 08/2012	International Teaching Professionals, University of Potsdam, training program of the Potsdam Graduate School
10/2010 – 07/2011	Executive Development Program Promotion plus+ qualifiziert, Leibniz Universität Hannover, Graduiertenakademie
06/2010	Summer School on Gravitational Wave Physics, South Padre Island (TX), USA

List of Publications

Scientific Publications

2013   Y. Wang, S. Babak, A. Petiteau, D. Keitel, **M. Otto**, S. Barke, F. Kawazoe, A. Khalaidovski, V. Müller, D. Schütze, H. Wittel, K. Danzmann, B. F. Schutz: Octahedron configuration for a displacement noise-cancelling gravitational wave detector in space, Physical Review D 88, 104021

2013   The eLISA Consortium (140 authors): The Gravitational Universe; arXiv:1305.5720v1 [astro-ph.CO] (ESA White Paper)

2012   **M. Otto**, G. Heinzel, K. Danzmann: TDI and clock noise removal for the split interferometry configuration of LISA; Classical Quantum Gravity 29, 205003

2011   G. Heinzel, J. J. Esteban, S. Barke, **M. Otto**, Y. Wang, A. F. Garcia and K. Danzmann: Auxiliary functions of the LISA laser link: Ranging, clock noise transfer and data communication; Classical Quantum Gravity 28, 094008

2008   J. Harms, C. Mahrdt, **M. Otto**, M. Prieß: Subtraction-noise projection in gravitational-wave detector networks; Physical Review D 77, 123010

Teaching-related Publications

2011   **M. Otto**: Rechenmethoden für Studierende der Physik im ersten Jahr; Spektrum Akademischer Verlag Heidelberg/Berlin (380 Seiten)

2008   S. Steinlechner, S. Barke, J. Dück, L. Hoppe, R. A. Lorbeer, **M. Otto**, A. Samblowski, T. Westphal: Der Lifter - Ein Flugobjekt mit Ionenantrieb; Physik und Didaktik in Schule und Hochschule (PhyDid) 2/7, S. 20-26

Thesis Supervision

2013 – 2014   Sarah Paczkowski: Modelling the Spacecraft and Test Mass Motion for LISA (Master's Thesis)

2012 – 2013   Andreas Schreiber: Time-Delay Interferometry Simulations for Space-Based Gravitational Wave Detectors (Master's Thesis)

Danksagung

letzten beiden versorgten mich in den Tagen vor der Abgabe mit leckerer Schokolade, Cookies und Pizza.

Für viele Korrekturen und Zerstreuung zwischendurch bin ich meinem Keller-büromitbewohner Christoph Krüger zu Dank verpflichtet. Vielleicht schaffen wir es mal gemeinsam zum Nordkap? Achso, und vor meiner Zeit als Kellerkind habe ich eine schöne Bürozeit mit Dr. Johanna Bogenstahl und unserem Bürohund Banja verbracht. Auch euch danke für die tolle Zeit! Darüber hinaus grüßt das Kellerkind den gesamten Flur der Callinstraße 36 (Space Interferometry Group) für die vielen netten Stunden auf Fahrten, Geburtstagen oder Ähnlichem. Hierbei danke ich insbesondere für Korrekturen Vitali Müller, Katharina-Sophie Isleif, Nils Brause und Daniel Penkert.

Auf gar keinen Fall darf die freundliche und nie versiegende Hilfe der IT und der Sekretariate vergessen werden. Bei den Letztgenannten möchte ich Kirsten Labove, Sabine Rehmert und Sandra Bruns meinen Dank aussprechen. Auf der Fakultätsseite muss Birgit Ohlendorf herausgehoben werden, die sich immer fast schon mütterlich um ihre Promovierenden kümmert. Weiterhin danke ich natürlich meinen vielen Freunden und Bekannten und allen, die ich hier vergessen habe. Ihr alle habt immer mit mir mitgefiebert und mich in dem Vorhaben, diese Dissertation zu schreiben, unterstützt. Demnächst fliegt 'ne Kuh, versprochen!

Zu guter Letzt möchte ich meinen engsten Weggefährten und vor allem meiner Familie von ganzem Herzen danken, die immer für mich dagewesen sind und mich aufgebaut und motiviert haben, wenn ich es brauchte. Ohne Euch hätte ich den Marathonlauf 'Promotion' nicht geschafft!

Danke, thanks, et merci!

Eigenständigkeitserklärung

Hiermit versichere ich, die vorliegende Arbeit selbstständig verfasst und keine anderen als die angegebenen Quellen und Hilfsmittel benutzt sowie die Zitate deutlich kenntlich gemacht zu haben.

Hannover, im August 2016   Markus Otto